

2011-01-01

Evaluating Suspended Dust Particulate Matter From Anthropogenically - Altered Lands

Roberto Velarde

University of Texas at El Paso, rvelarde2@miners.utep.edu

Follow this and additional works at: https://digitalcommons.utep.edu/open_etd



Part of the [Geology Commons](#), and the [Geophysics and Seismology Commons](#)

Recommended Citation

Velarde, Roberto, "Evaluating Suspended Dust Particulate Matter From Anthropogenically - Altered Lands" (2011). *Open Access Theses & Dissertations*. 2406.

https://digitalcommons.utep.edu/open_etd/2406

This is brought to you for free and open access by DigitalCommons@UTEP. It has been accepted for inclusion in Open Access Theses & Dissertations by an authorized administrator of DigitalCommons@UTEP. For more information, please contact lweber@utep.edu.

EVALUATING SUSPENDED DUST PARTICULATE MATTER FROM
ANTHROPOGENICALLY – ALTERED LANDS

ROBERTO VELARDE

Department of Geological Sciences

APPROVED:

Thomas E. Gill, Ph.D., Chair

Philip C. Goodell, Ph.D., Co-Chair

David Borrok, Ph.D.

Laura F. Serpa, Ph.D.

Rosa Fitzgerald, Ph.D.

Benjamin C. Flores, Ph.D.
Acting Dean of the Graduate School

Copyright
by
Roberto Velarde
2011

Dedication

I dedicate this dissertation to my family.

EVALUATING SUSPENDED DUST PARTICULATE MATTER FROM
ANTHROPOGENICALLY – ALTERED LANDS

by

ROBERTO VELARDE

DISSERTATION

Presented to the Faculty of the Graduate School of

The University of Texas at El Paso

in Partial Fulfillment

of the Requirements

for the Degree of

DOCTOR OF PHILOSOPHY

Department of Geological Sciences

THE UNIVERSITY OF TEXAS AT EL PASO

August 2011

Acknowledgements

The culmination of this endeavor was sustained by the collective efforts of a few key individuals. With respect and gratitude, I recognize Dr. Thomas E. Gill and Dr. Philip C. Goodell as the vital colleagues that made this possible. Their steadfast encouragement is immeasurable. I also recognize the following colleagues for their friendship and help: Oscar Romero, Victor Avila, Antony Wamalwa, Fotios Christos Kafantaris, John Olgin, Sarah N. Cervera, Carlos Montana, Pam Hart, Tina L. Carrick, and Sandra S. Ladewig.

Special thanks are extended to Dr. Richard Arimoto, Dr. Barry Huebert, Dr. Joe Prospero, Dr. Chang-Hee Kang, Dr. Minghua Ren, Dr. Scott Van Pelt, and Dr. Ralf Sudowe for their collective efforts.

Funding sources were as follows:

Dr. Philip Goodell made personal donations for the Peña Blanca study.

DOE-LANL-OSTI Grant to UTEP for Peña Blanca, Natural Analog Study.

NSF Grant #ATM 0404944 for the plutonium study.

Department of Defense Contract No. W912DY-07-2-0047 for the White Sands Missile Range (WSMR) study.

Abstract

Substantial dust loads are transported from drylands including the Saharan, Asian, and Chihuahuan Desert deposits by localized to planetary-scale processes to nearby and distal sites. These dusts may carry harmful constituents. To evaluate dust movement patterns and characteristics relative to carried constituents, three studies are presented comprising (A) Localized displacement of uranium and progeny radionuclides from high-grade uranium ore storage piles at Peña Blanca, Chihuahua, Mexico; (B) Long-distance transport of plutonium via Saharan and Asian aeolian pathways; and (C) Dust movement patterns in military maneuvering and non-maneuvering areas at White Sands Missile Range (WSMR), New Mexico. Study (A) evaluated surface soil, resuspended and naturally accreted sediment over a 2.4 year period from three sites on, upwind, and downwind of the ore piles. Study (B) investigated plutonium levels in dust aerosols at Izaña, Canary Islands (IZT); Barbados (BAT); Gosan, South Korea (GOS); and Mauna Loa Observatory, Hawaii (MLO). In study (C), 24 sampling sites amassed sediment in military maneuvering and non-maneuvering areas over ten seasonal phases. Methodologies applied to collect and analyze data at the various sites included passive sediment/dust collectors and high volume aerosol samplers; laser diffraction particle-sizing; X-ray diffraction for mineralogy; gamma-ray spectroscopy for nuclide radioactivity levels; electron microprobe analysis for element mapping; inductively coupled plasma mass spectroscopy (ICP-MS) for element concentrations; and alpha spectrometry for plutonium levels. Key findings included for: (A) Geochemical analyses indicated uranophane and uranium progeny radionuclides displaced in aeolian pathways to a small degree downwind from the ore pile via saltation, but effectively not at all upwind. (B) Plutonium activity/dust mass concentrations (Bq/μg) at the four sites had the following rank order: GOS > MLO > BAT > IZT. GOS reflected Pu levels plausibly attributable to new wind erosion of Asian deserts, while IZT, BAT, and MLO aerosol plutonium levels derived from re-entrained global fallout. (C) Spring and summer yielded the highest and least sediment mass amounts, respectively. Sediment yield was greater

for dune areas than for shrublands irrespective of location in maneuvering or non-maneuvering areas;
local geomorphology appears to play the key role in aeolian sediment transport at WSMR.

Table of Contents

Acknowledgements.....	v
Abstract.....	vi
Table of Contents.....	viii
List of Tables	xii
List of Figures.....	xiii
Chapter 1 Introduction.....	1
1. References.....	4
Chapter 2 Transport of Radionuclide Bearing Dust by Aeolian Processes, Peña Blanca, Chihuahua, Mexico.....	5
1. Introduction.....	5
1.1 Problem Statement.....	6
2. Background.....	9
2.1 Meteorology.....	9
2.2 Field Equipment.....	10
2.2.1 BSNE (Big Spring Number Eight) Sediment Traps	10
2.3 Lab Equipment.....	11
2.3.1 Laser Particle Sizing Theory	11
2.4 Colloid and Adsorption Theory	12
2.4.1 Colloids.....	12
2.4.2 Adsorption	12
2.5 Radionuclide Transport Processes.....	13
2.5.1 Aeolian Processes	13
2.5.2 Hydrological Processes.....	17
3. Methodology.....	19
3.1 Sample Acquisition.....	19
3.1.1 Sediment Trap Deployment.....	19
3.1.2 Wind Gust Simulation	21
3.1.3 Natural Long-Term Accretion	22
3.2 Data Acquisition	22
3.2.1 X-Ray Diffraction (XRD) Analysis.....	22

3.2.2 Particle Size Analysis	22
3.2.3 Electron Microprobe Analyzer (EMPA)	23
3.2.4 Inductively Coupled Plasma-Mass Spectrometry.....	23
(ICP-MS) Analysis	23
3.2.5 Gamma-Ray Spectroscopy Analysis	23
3.3 Data Processing	24
3.3.1 Horizontal Flux of Total Airborne Particle Mass (q_{tot}).....	24
3.3.2 AP-42 Emission Factor Equation	24
3.3.3 Radioactive Decay Computation	25
3.3.4 Radioactivity and Distance Computation	26
3.3.5 Friction Velocity (u_*) Computation	27
4. Results.....	27
4.1 X-Ray Diffraction (XRD) Analysis.....	28
4.2 Particle Size Analysis of Simulated Wind Gust Sediment	28
4.3 Particle Size Analysis of Topsoil Sediment.....	29
4.4 Particle Size Analysis of Accreted Sediment	29
4.5 Electron Microprobe Analysis of Simulated	30
Wind Gust Sediment.....	30
4.6 Electron Microprobe Analysis of Accreted Sediment.....	31
4.7 Inductively Coupled Plasma-Mass Spectrometry.....	31
(ICP-MS) Analysis	31
4.8 Gamma-Ray Spectroscopy Analysis	32
4.9 Horizontal Flux of Total Airborne Particle Mass (q_{tot}).....	32
4.10 AP-42 Emission Factor Equation	33
4.11 Radioactive Decay Computation	34
4.12 Radioactivity and Distance Computation	34
4.13 Meteorology.....	34
5. Discussion.....	35
6. Conclusions.....	40
8. References.....	92

Chapter 3 Evaluating Global Atmospheric Transport of Plutonium with Dust

Aerosols	95
1. Introduction.....	95
1.1 Site Selection	97

2.	Methodology.....	98
3.	Results.....	101
	3.1 Izaña, Canary Islands (IZT).....	101
	3.2 Barbados (BAT).....	102
	3.3 Gosan, South Korea (GOS)	102
	3.4 Mauna Loa Observatory, Hawaii (MLO)	102
4.	Discussion.....	102
	4.1 Saharan Pathways	103
	4.2 Asian Pathways.....	104
5.	Conclusions.....	108
6.	References.....	110

Chapter 4 Wind Erosion Patterns in Coppice Dune Maneuver Areas, White Sands

	Missile Range, New Mexico	130
1.	Introduction.....	130
	1.1 Problem Statement.....	131
2.	Background.....	132
	2.1 Field Equipment.....	132
	2.1.1 MDCO (Marble Dust Collector) Sediment Traps	132
	2.1.2 MWAC (Modified Wilson and Cooke) Sediment Traps	133
	2.1.3 BSNE (Big Spring Number Eight) Sediment Traps	133
	2.2 Lab Equipment.....	134
	2.2.1 Laser Particle Sizing Theory	134
	2.3 Dust Suspension Theory	135
	2.4 Terrain Effects of Vehicular Activity from	139
	Military Maneuvers	139
	2.5 Meteorology.....	140
3.	Methodology.....	141
	3.1 Staging Areas.....	141
	3.2 Sediment Traps	152
	3.3 Sample Collection.....	154
	3.4 Meteorology.....	155
	3.5 Particle Size Analysis	158
	3.6 Deposition Mean, Standard Deviation, and.....	161
	Confidence Intervals.....	161

3.7	Horizontal Flux of Total Airborne Particle Mass (q_{tot}).....	161
3.8	MDCO, BSNE, and MWAC Scattergrams.....	162
3.9	U-test Statistics	162
3.10	AP-42 Emission Factor Equation	163
4.	Results.....	164
4.1	Particle Size Analysis	164
4.2	Sediment Deposition Mean, Standard Deviation,	172
	and Confidence Intervals	172
4.3	Horizontal Flux of Total Airborne Particle Mass (q_{tot})	172
4.4	MDCO, BSNE, and MWAC Scattergrams.....	173
4.5	Non-maneuver and Maneuver Area Scattergrams.....	173
4.6	U-test Statistics	173
4.7	AP-42 Emission Factor Equation	173
5.	Discussion.....	174
6.	Conclusions.....	201
7.	References.....	285
	Chapter 5 Conclusions.....	289
	Appendix A.....	293
	Appendix B.....	304
	Curriculum Vita	340

List of Tables

CHAPTER 2

Table 1: BSNE horizontal flux quantities.....	32
Table 2: AP-42 emission factor equation results.	33
Table 3: Nuclide activity decrease with distance.	34
Table 4: Friction velocities from measured wind speeds.	34
Table 5: Sample index for all samples collected with corresponding analysis techniques.	42
Table 6: X-Ray diffraction mineralogy results for stations S-1, S-2, and S-3.....	43
Table 7: Volume percentage values of collected sediment at stations S-1, S-2, and S-3.....	45
Table 8: ICP-MS results of major and trace element concentrations for topsoil.....	50
Table 9: Element enrichment factor between stations S-1 and S-2.....	53
Table 10: Radionuclide activity and sediment mass values	54
Table 11: Progeny/Parent ratios for BSNE pans at stations S-2 and S-3	55
Table 12: Uranium Decay Series	55

CHAPTER 3

Table 1: Dust concentration/ ^{239,240} Pu activities for MLO, BAT, IZT, and GOS.....	118
Table 2: ^{239,240} Pu activity values per filter for MLO, BAT, IZT, and GOS.....	119
Table 3: Collection composites for IZT, BAT, GOS, and BAT.....	120

CHAPTER 4

Table 1: Collecting site list and description of surrounding topography.....	146
Table 2: Station UTM coordinates, longitudes/latitudes, and elevations	147
Table 3: Sampling stations' terrain/land cover description.	148
Table 4: Collecting stations' fetch lengths and vegetation heights.	149
Table 5: Calculated fetch lengths for each station.....	150
Table 6: Timeline for Phases 1 through 10.....	151
Table 7: Meteorology data for Phases 1 through 10.....	156
Table 8: American Geological Institute (AGI) sediment grain-size scale.....	160
Table 9: AP-42 emission factor equation results	174
Table 10: MDCO statistical results for varied areas for Phase 5.....	199
Table 11: MDCO statistical results for varied areas for Phase 6.....	199
Table 12: MDCO Sediment Mass and deposition quantities for Phases 1-10.....	203
Table 13: Deposition mean and standard deviation values for various specific conditions.....	213
Table 14: MWAC and BSNE horizontal flux quantities for Phases 5-10	214
Table 15: U-test result values for Groups A, B, C, and D for Phase 5-10.....	232
Table 16: U-test result for single stations 3, 10, 13, and 14 for Phase 5-10.....	236

List of Figures

CHAPTER 2

Figure 1: Peña Blanca location.	7
Figure 2: Maps of study area showing collection stations S-1, S-2, and S-3.	8
Figure 3: Photos of the high-grade uranium ore piles.	9
Figure 4: Profile of terrain across S-1, S-2, and S-3.	9
Figure 5: Particle size ranges under different transport modes.	15
Figure 6: Typical BSNE mast construction specifications.	19
Figure 7: BSNE masts installation in progress at S-1.	20
Figure 8: Completed BSNE sediment trap.	20
Figure 9: Suspending dust material from the high-grade uranium stockpile.	21
Figure 10: X-Ray Diffraction mineralogy diffractogram for S-1.	56
Figure 11: X-Ray Diffraction mineralogy diffractogram for S-2.	57
Figure 12: X-Ray Diffraction mineralogy diffractogram for S-3.	58
Figure 13: Volume percentage/particle size distribution graphs for simulated wind gust.	59
Figure 14: Volume percentage/particle size distribution graphs for topsoil.	60
Figure 15: Volume percentage/particle size distribution graphs for accreted sediment at S-1	61
Figure 16: Volume percentage/particle size distribution graphs for accreted sediment at S-2	62
Figure 17: Volume percentage/particle size distribution graphs for accreted sediment at S-3	63
Figure 18: BSE image of a composite mineral from simulated wind gust at S-1	64
Figure 19: Wavelength Dispersive Spectroscopy (WDS) X-ray scan for Figure 18.	65
Figure 20: Wavelength Dispersive Spectroscopy (WDS) X-ray scan for Figure 18.	66
Figure 21: Wavelength Dispersive Spectroscopy (WDS) X-ray scan for Figure 18.	67
Figure 22: BSE image of uranophane from simulated wind gust at S-2	68
Figure 23: Wavelength Dispersive Spectroscopy (WDS) X-ray scan for Figure 22.	69
Figure 24: Wavelength Dispersive Spectroscopy (WDS) X-ray scan for Figure 22.	70
Figure 25: BSE image of carnotite from simulated wind gust at S-2	71
Figure 26: Wavelength Dispersive Spectroscopy (WDS) X-ray scan for Figure 25.	72
Figure 27: Wavelength Dispersive Spectroscopy (WDS) X-ray scan for Figure 25.	73
Figure 28: Wavelength Dispersive Spectroscopy (WDS) X-ray scan for Figure 25.	74
Figure 29: BSE image of smithsonite from simulated wind gust at S-3	75
Figure 30: Wavelength Dispersive Spectroscopy (WDS) X-ray scan for Figure 29.	76
Figure 31: Wavelength Dispersive Spectroscopy (WDS) X-ray scan for Figure 29.	77
Figure 32: Wavelength Dispersive Spectroscopy (WDS) X-ray scan for Figure 29.	78
Figure 33: BSE image of uranophane from accreted sediment at S-2.	79
Figure 34: Wavelength Dispersive Spectroscopy (WDS) X-ray scan for Figure 33.	80
Figure 35: BSE image of uranophane from accreted sediment at S-2.	81
Figure 36: Wavelength Dispersive Spectroscopy (WDS) X-ray scan for Figure 35.	82
Figure 37: ICP-MS results of major element concentrations in topsoil	83
Figure 38: ICP-MS results of trace element concentrations in topsoil.	84
Figure 39: ICP-MS results of trace element concentrations in topsoil.	85
Figure 40: ICP-MS results of trace element concentrations in topsoil.	86
Figure 41: Trend line model of major and trace element concentrations	87
Figure 42: Particle size analysis graphs of accreted sediment.	88
Figure 43: EMPA/XRD mineralogy results of simulated wind gust and accreted sediment	89
Figure 44: ICP-MS results of topsoil sediment	90
Figure 45: Gamma-ray spectroscopy results of accreted sediment	91

CHAPTER 3

Figure 1: Study sites MLO, BAT, IZT, and GOS.	123
Figure 2: Dust concentration/ ^{239,240} Pu activities for MLO, BAT, IZT, and GOS.	124
Figure 3: ^{239,240} Pu activity/dust mass for MLO, BAT, IZT, and GOS.....	125
Figure 4: Al concentrations with respect to time for IZT.....	126
Figure 5: Dust concentrations with respect to time for BAT.....	127
Figure 6: Al concentrations with respect to time for GOS.....	128
Figure 7: Ca concentrations with respect to time for MLO.....	129

CHAPTER 4

Figure 1: Particle size ranges under different transport modes.	137
Figure 2: Staging areas showing all 24 collecting sites.....	144
Figure 3: Map of staging areas and surrounding geological features.....	145
Figure 4: Completed MWAC sediment trap.....	153
Figure 5: Completed BSNE sediment trap	153
Figure 6: Completed MDCO sediment trap.....	153
Figure 7: Completed MWAC, BSNE, and MDCO station.....	154
Figure 8: Characteristic MWAC volume percentage/particle size curve at 0.2 m height	175
Figure 9: Characteristic MWAC volume percentage/particle size curve at 1 m height	176
Figure 10: Characteristic MDCO volume percentage/particle size curve at 1.7 m height	177
Figure 11: Du1.5K-m and Du1K-u satellite images of areas with long fetch distances	183
Figure 12: Du3K-u and Du400m-m satellite images of areas with long fetch distances	184
Figure 13: Horizontal mass quantities and fetch lengths for all sites for Phase 5	185
Figure 14: Horizontal mass quantities and fetch lengths for high yield sites for Phase 5	186
Figure 15: Horizontal mass quantities and fetch lengths for all sites for Phase 9.....	186
Figure 16: Horizontal mass quantities and fetch lengths for high yield sites for Phase 9.....	187
Figure 17: Contours showing the PM10 percentages at 1.7 m for all sites for Phase 5	192
Figure 18: Contours showing the PM10 percentages at 1.7 m for all sites for Phase 6	193
Figure 19: Contours showing the PM10 percentages at 1.7 m for all sites for Phase 9	194
Figure 20: Contours showing the PM10 percentages at 1.7 m for all sites for Phase 10	195
Figure 21: Contours showing topsoil silt percentages at 0 m for all sites	196
Figure 22: Mass deposition quantities for Phases 5-6 and 9-10 for all sites	197
Figure 23: MDCO statistical results for varied areas for Phases 5 and 6.....	200
Figure 24: Particle size distribution for Du1K-u and Du400m-m at 0.2 m for Phase 5.....	238
Figure 25: Particle size distribution for Du1K-u and Du400m-m at 1 m for Phase 5.....	239
Figure 26: Particle size distribution for Du1K-u and Du400m-m at 1.7 m for Phase 5.....	240
Figure 27: Particle size distribution for Sh1K-d and Sh3K-m-u at 0.2 m for Phase 5	241
Figure 28: Particle size distribution for Sh1K-d and Sh3K-m-u at 1 m for Phase 5	242
Figure 29: Particle size distribution for Sh1K-d and Sh3K-m-u at 1.7 m for Phase 5	243
Figure 30: Particle size distribution for Du1K-u and Du400m-m at 0.2 m for Phase 6.....	244
Figure 31: Particle size distribution for Du1K-u and Du400m-m at 1 m for Phase 6.....	245
Figure 32: Particle size distribution for Du1K-u and Du400m-m at 1.7 m for Phase 6.....	246
Figure 33: Particle size distribution for Sh1K-d and Sh3K-m-u at 0.2 m for Phase 6	247
Figure 34: Particle size distribution for Sh1K-d and Sh3K-m-u at 1 m for Phase 6	248
Figure 35: Particle size distribution for Sh1K-d and Sh3K-m-u at 1.7 m for Phase 6	249
Figure 36: Particle size distribution for Du400m-m and Sh1K-d at 1.7 m for Phase 5.....	250
Figure 37: Particle size distribution for Du400m-m and Sh1K-d at 1.7 m for Phase 6.....	251

Figure 38: Particle size distribution for Du1K-u and Sh3K-m-u at 1.7 m for Phase 5	252
Figure 39: Particle size distribution for Du1K-u and Sh3K-m-u at 1.7 m for Phase 6	253
Figure 40: MDCO deposition mass (g) values versus station number for Phase 1.	254
Figure 41: MDCO deposition mass (g) values versus station number for Phase 2.	254
Figure 42: MDCO deposition mass (g) values versus station number for Phase 3.	255
Figure 43: MDCO deposition mass (g) values versus station number for Phase 4.	255
Figure 44: MDCO deposition mass (g) values versus station number for Phase 5.	256
Figure 45: MDCO deposition mass (g) values versus station number for Phase 6.	256
Figure 46: MDCO deposition mass (g) values versus station number for Phase 7.	257
Figure 47: MDCO deposition mass (g) values versus station number for Phase 8.	257
Figure 48: MDCO deposition mass (g) values versus station number for Phase 9.	258
Figure 49: MDCO deposition mass (g) values versus station number for Phase 10.	258
Figure 50: BSNE horizontal mass (g) values versus station number at 0.2 m for Phase 7.	259
Figure 51: MWAC horizontal mass (g) values versus station number at 0.2 m for Phase 7.	259
Figure 52: BSNE versus MWAC horizontal mass (g) scattergram at 0.2 m for Phase 7.	260
Figure 53: BSNE horizontal mass (g) values versus station number at 1 m for Phase 7.	260
Figure 54: MWAC horizontal mass (g) values versus station number at 1 m for Phase 7.	261
Figure 55: BSNE versus MWAC horizontal mass (g) scattergram at 1 m for Phase 7.	261
Figure 56: BSNE horizontal mass (g) values versus station number at 0.2 m for Phase 8.	262
Figure 57: MWAC horizontal mass (g) values versus station number at 0.2 m for Phase 8.	262
Figure 58: BSNE versus MWAC horizontal mass (g) scattergram at 0.2 m for Phase 8.	263
Figure 59: BSNE horizontal mass (g) values versus station number at 1 m for Phase 8.	263
Figure 60: MWAC horizontal mass (g) values versus station number at 1 m for Phase 8.	264
Figure 61: BSNE versus MWAC horizontal mass (g) scattergram at 1 m for Phase 8.	264
Figure 62: BSNE horizontal mass (g) values versus station number at 0.2 m for Phase 9.	265
Figure 63: MWAC horizontal mass (g) values versus station number at 0.2 m for Phase 9.	265
Figure 64: BSNE versus MWAC horizontal mass (g) scattergram at 0.2 m for Phase 9.	266
Figure 65: BSNE horizontal mass (g) values versus station number at 1 m for Phase 9.	266
Figure 66: MWAC horizontal mass (g) values versus station number at 1 m for Phase 9.	267
Figure 67: BSNE versus MWAC horizontal mass (g) scattergram at 1 m for Phase 9.	267
Figure 68: Maneuver/non-maneuver MDCO mass (g) scattergram at 1.7 m for Phase 5.	268
Figure 69: Maneuver/non-maneuver MDCO mass (g) scattergram at 1.7 m for Phase 6.	268
Figure 70: Maneuver/non-maneuver MDCO mass (g) scattergram at 1.7 m for Phase 7.	269
Figure 71: Maneuver/non-maneuver MDCO mass (g) scattergram at 1.7 m for Phase 8.	269
Figure 72: Maneuver/non-maneuver MDCO mass (g) scattergram at 1.7 m for Phase 9.	270
Figure 73: Maneuver/non-maneuver MDCO mass (g) scattergram at 1.7 m for Phase 10.	270
Figure 74: Volume percentages/soil textural composition for Du1K-u at 1.7 m for Phase 5.	271
Figure 75: Volume percentages/soil textural composition for Du1K-u at 1.7 m for Phase 6.	271
Figure 76: Volume percentages/soil textural composition for Sh1K-d at 1.7 m for Phase 5.	272
Figure 77: Volume percentages/soil textural composition for Sh1K-d at 1.7 m for Phase 6.	272
Figure 78: Volume percentages/soil textural composition for Du400m-m.	273
at 1.7 m for Phase 5.	273
Figure 79: Volume percentages/soil textural composition for Du400m-m.	273
at 1.7 m for Phase 6.	273
Figure 80: Volume percentages/soil textural composition for Sh3K-m-u.	274
at 1.7 m for Phase 5.	274
Figure 81: Volume percentages/soil textural composition for Sh3K-m-u.	274
at 1.7 m for Phase 6.	274
Figure 82: Phase 1 averaged vector wind direction and maximum wind speed.	275
Figure 83: Phase 2 averaged vector wind direction and maximum wind speed.	276

Figure 84: Phase 3 averaged vector wind direction and maximum wind speed.....	277
Figure 85: Phase 4 averaged vector wind direction and maximum wind speed.....	278
Figure 86: Phase 5 averaged vector wind direction and maximum wind speed.....	279
Figure 87: Phase 6 averaged vector wind direction and maximum wind speed.....	280
Figure 88: Phase 7 averaged vector wind direction and maximum wind speed.....	281
Figure 89: Phase 8 averaged vector wind direction and maximum wind speed.....	282
Figure 90: Phase 9 averaged vector wind direction and maximum wind speed.....	283
Figure 91: Phase 10 averaged vector wind direction and maximum wind speed.....	284

Chapter 1. Introduction

Dust suspension has occurred for millennia via natural processes (e.g., dust storms, volcanic eruptions, etc.) prior to the advent of anthropogenic sources (Péwé, 1981; Shao et al, 2011). Copious dust loadings typically originate in arid areas where abundant aeolian deposits reside, notably, Africa, Asia, Australia, and North America (Thomas and Wiggs, 2008). Numerous prominent deserts (e.g., Taklamakan, Saharan, and Chihuahuan Deserts) are located in these continents approximately between the 20° and 40° latitudes where high pressure systems have spawned long-sustained aeolian processes (Péwé, 1981; Thomas and Wiggs, 2008; Shao et al, 2011). These perennial venting processes have deprived these areas of moisture over time which subsequently led to desertification (Shao et al, 2011).

Substantial amounts of dust material from these arid deposits are annually transported hundreds to thousands of kilometers in their respective aeolian pathways at global, regional, and local scales (Péwé, 1981; Pye, 1987). Approximately $2,000 \text{ Mtyr}^{-1}$ of dust material is suspended in the atmosphere (Shao et al, 2011). Augmenting these aeolian sediment systems are ongoing global dynamic changes in the atmosphere and 21st century anthropogenic impacts (e.g., social development, military enterprise, etc.) (Thomas and Wiggs, 2008). Consequential impacts vary in magnitude and can range from the disruption of radiation budgets, rainfall regimes, and climate stability to transporting dust plumes and their mineral carrier particles which nourish ocean plankton or terrestrial vegetation (Eby, 2004; Okin et al., 2004; Mahowald et al., 2006).

Responding to landscape sensitivity, geomorphologists, sedimentologists, and agricultural scientists continue modern aeolian research initially introduced by Ralph Bagnold 70 years ago (Thomas and Wiggs, 2008). Methodological advances in sample collection and analysis such as passive (not powered) and active collectors (powered), laser particle sizers, robust dispersion codes, and satellite/remote sensing techniques have vastly expanded the aeolian research scope. These advancements have enhanced sediment flux monitoring/measurement and provided a means for modeling dust entrainment and transport behavior.

With the advent of the nuclear age during World War II, radionuclide containment has become a formidable and delicate undertaking. Core contributing factors are: uranium mining and milling, nuclear weapons manufacturing/testing, nuclear waste storage, nuclear fuel reprocessing, nuclear power plant operation, and nuclear accidents (Hu et al., 2010). A total volume of radioactive waste in the US has been estimated to be 5.5 million m³ with a 1.2×10^9 TBq (tera becquerel; 1 TBq = 27.03 Ci) (Ahearne, 1997) radioactivity level. An estimated 2×10^8 TBq of radioactivity attributable to worldwide nuclear weapons testing has been introduced into the atmosphere since 1945 (Choppin, 2003).

Plutonium is a manmade element, although trace amounts of plutonium have been found in pitchblende and in natural reactors (e.g., Oklo, Gabon) (Brady et al, 2002). Of the 15 Pu known isotopes (²³²Pu to ²⁴⁶Pu), ²³⁹Pu (94%), ²⁴⁰Pu (6%), and ²⁴¹Pu (0.4%) are the most common (Zhang et al, 2002). Isotopes ²³⁸Pu to ²⁴²Pu are identified as reactor grade plutonium, whereas ^{239,240}Pu (²³⁹Pu + ²⁴⁰Pu) are identified as weapons grade plutonium (Zhang et al, 2002; Hu et al., 2010). Tetravalent Pu⁴⁺ is most stable in soils and sorbs to Fe hydroxides, and to a lesser degree, soluble hydroxides (Brady et al, 2002). The mobility of plutonium depends on pH, clay content, calcium carbonate presence, and organic matter (Brady et al, 2002).

Naturally occurring uranium, which is employed to make weapons grade plutonium, modifies naturally from uraninite (UO₂) to (UO₂)²⁺ as U⁴⁺ oxidizes to mobile U⁶⁺. Mobile U⁶⁺ can reside in hydrated oxides and hydroxides (e.g., hematite, limonite), clays (e.g., kaolinite, montmorillonite), silicates (e.g., uranophane), and calcium carbonates (e.g., calcite) (Durrance, 1986; Langmuir, 1997; Goodell, personal communication, 2011).

Therefore, the following three investigations were conducted utilizing modern methodologies in order to better understand geological containment of nuclear waste and subsequent radionuclide sorption and displacement via geochemical and aeolian processes:

The first study entailed localized wind displacement of uranium and its byproducts by carrier particulates on and around abandoned surplus high-grade uranium ore storage piles at Peña Blanca,

Chihuahua, Mexico. The objective was to establish and determine whether and to what extent radionuclide carrier particulates (clays, silicates, and iron oxyhydroxides) and minerals themselves were being displaced from the storage piles.

The second study encompassed intercontinental migration of dust particulate matter (PM) bearing plutonium via Saharan and Asian aeolian pathways. The objective was to determine how plutonium radionuclide concentrations and activity levels correspond to dust events with respect to seasonal wind pathways.

The third investigation involved quantifying suspended PM with respect to volume, size, and mass of sediment collected at 24 sites deployed in military maneuvering and non-maneuvering areas at White Sands Missile Range, New Mexico.

The objective was to determine variances in dust sediment characteristics with respect to volume, particle size, and mineral constituents (i.e., clay, silt, and sand ranges) collected at the 24 sites at varied heights above ground. This was done in correlation with meteorological variables (i.e., wind speed and direction, temperature, precipitation, etc.) corresponding to time phases (season to season over three years) and existing land use/land cover (i.e., dunes, shrubland, grassland, and unpaved road systems).

This research addresses ongoing effects of suspension and re-suspension of geological particulate matter from anthropogenically altered lands by localized wind gusts in the Chihuahuan Desert and protracted intercontinental aeolian pathways, namely, Saharan trade winds and Asian jet streams. These aeolian processes traverse source deposits at local to global scales and are the driving mechanisms by which geological particulate matter potentially laden with anthropogenic constituents (e.g., radionuclides) are ejected and displaced to flanking or distal recipients.

Moreover, this research can prove to be useful in terms of monitoring airborne particulates and managing nuclear waste storage sites and uranium mine operations worldwide. It also offers valuable insight into global cycling and dispersion of nuclear test fallout and has applications in varied settings such as agriculture, military settings, and respiratory health of the public.

1. References

- Ahearne, J.F., 1997. Radioactive waste: the size of the problem. *Physics Today* 50 (6), 24-29.
- Brady, P.V., Jove-Colon, C., Carr G., Huang, F., 2002. Soil Radionuclide Plumes. In *Geochemistry of Soil Radionuclides*, SSSA Special Publication Number 59 (eds. P. Zhang and P. Brady). Soil Science Society of America, Madison, Wisconsin, pp.165-190.
- Choppin, G.R., 2003. Actinide speciation in the environment. *Radiochimica Acta* 91 (11), 645-649.
- Durrance, E.M., 1986. *Radioactivity in Geology, Principles and Applications*. John Wiley and Sons, New York, New York, pp. 106-108.
- Eby, G.N., 2004. *Principles of Environmental Geochemistry*. Brooks/Cole - Thomson Learning, Inc., Pacific Grove, California, pp. 289-290.
- Goodell, P.C., 2011. Department of Geological Sciences, University of Texas at El Paso. Personal communication.
- Hu, Q.H., Weng, J.Q., Wang, J.S., 2010. Sources of anthropogenic radionuclides in the environment: a review. *Journal of Environmental Radioactivity* 101(6): 426-437.
- Langmuir, D., 1997. *Aqueous Environmental Geochemistry*. Prentice Hall, Englewood Cliffs, New Jersey, pp. 495-514.
- Mahowald, N. M., Muhs, D. R., Levis, S., Rasch, P. J., Yoshioka, M., Zender, C. S., Luo, C., 2006, Change in atmospheric mineral aerosols in response to climate: Last glacial period, preindustrial, modern, and doubled carbon dioxide climates, *Journal of Geophysical Research*, 111, D10202, doi:10.1029/2005JD006653.
- Okin, G., Mahowald, N., Chadwick, O., Artaxo, P., 2004. The impact of desert dust on the biogeochemistry of phosphorus in terrestrial ecosystems. *Global Biogeochemical Cycles* 18: GB2005. DOI: 10.1029/2003GB002145.
- Péwé, T.L., 1981. Desert dust: an overview. *Geological Society of America Special Paper*, 186, 1-4.
- Pye, K., 1987. *Aeolian Dust and Dust Deposits*. Academic Press, London, pp. 29-51.
- Shao, Y., Wywoll, K.H., Chappell, A., Huang, J., Lin, Z., McTainsh, G.H., Mikami, M., Tanaka, T.Y., Wang, Xulong, W., Yoon, S., 2011. Dust cycle: An emerging core theme in Earth system science. *Aeolian Research*, 2, 181-204.
- Thomas, D.S.G., Wiggs, G.F.S., 2008. Aeolian system responses to global change: challenges of scale, process and temporal integration. *Earth Surface Processes and Landforms* 33: 1396-1418.
- Zhang, P., Krumhansl, J.A., Brady, P.V., 2002. Introduction to Properties, Sources and Characteristics of Soil Radionuclides, *Geochemistry of Soil Radionuclides*. In *Geochemistry of Soil Radionuclides*, SSSA Special Publication Number 59 (eds. P. Zhang and P. Brady). Soil Science Society of America, Madison, Wisconsin, pp.10-11.

Chapter 2. Transport of Radionuclide Bearing Dust by Aeolian Processes, Peña Blanca, Chihuahua, Mexico

1. Introduction

There is currently an ongoing global nuclear renaissance. According to the World Nuclear Association, approximately 60 nuclear power reactors are under construction in 15 countries plus Taiwan, namely, China, South Korea and Russia. There are approximately 440 reactors operating in 30 countries plus Taiwan (www.world-nuclear.org/info/inf17.html). Subsequently, inactive uranium mines worldwide will become active again and the need for monitoring mining operations and storage facilities is steadily on the increase.

In order to minimize radiation health hazards to the public, Congress passed the Uranium Mill Tailings Radiation Control Act (UMTRA) in 1978 directing the Department of Energy to take control of uranium mill tailings from inactive sites (Murray, 2003). The act made DOE responsible for safely undertaking environmental remedial operations at 24 inactive tailings piles remaining from mining and milling processes done under contracts with the Atomic Energy Commission. Additionally, DOE was responsible for restoring over 5,000 contaminated vicinity properties (Wiltshire, 1993). Consequently, there are no more tailings piles in the U.S.

This investigation evaluates radionuclide transport by wind erosion of high-grade uranium ore piles in the Sierra Peña Blanca (50 km north of Chihuahua City), Chihuahua, Mexico (Figures 1 – 4). Active mining operations ceased at Peña Blanca in 1983 (French, 2006); however, the study site contains exposed stockpiles of high-grade uranium ore in an arid environment which are susceptible to re-suspension as dust by aeolian processes. Since similar sites do not presently exist in the United States, this site can serve as an analog to study similar uranium mines (Lottermoser and Ashley, 2006) worldwide. Natural wind gust simulations, such as the one conducted in this study, have not been done elsewhere.

1.1 Problem Statement

The purpose of this study is to determine if radionuclides and any of their byproducts are being transported or displaced from the uranium ore piles by aeolian mechanisms. How these radionuclides associate with discrete minerals and ongoing weathering processes needs to be better understood. This requires establishing size fractionation of sampled soil and suspended dust along with concentrations of radionuclides therein. Specifically, the purpose of this study is to determine particulate matter (PM) grain size and mineralogy as well as uranium daughter concentrations and radioactivity levels in radionuclide-bearing PM. Also to be determined is secular equilibrium, that is, whether the steady-state ratio of parent to daughter is continuous throughout the decay chain.

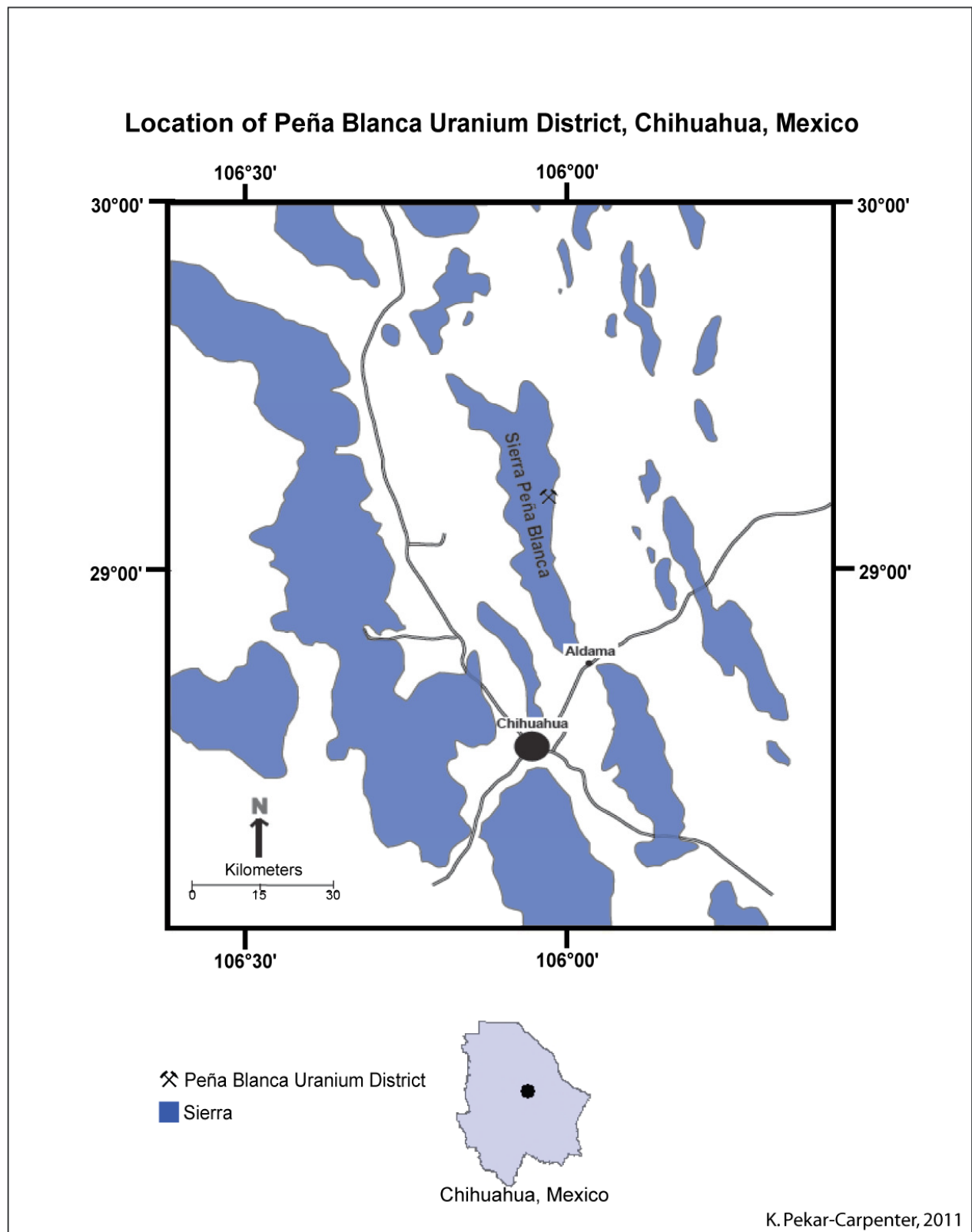


Figure 1: Peña Blanca location (Pekar-Carpenter, personal communication, 2011).

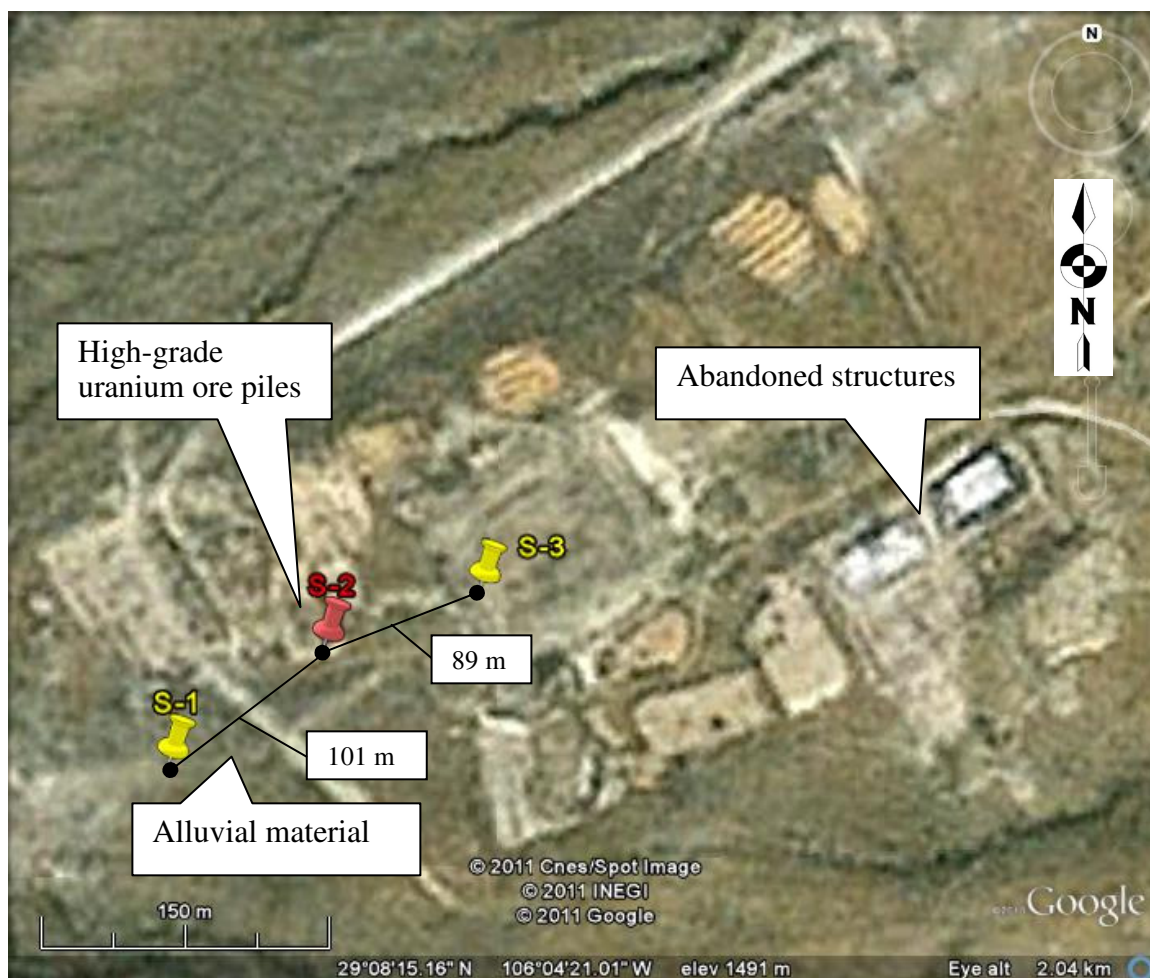
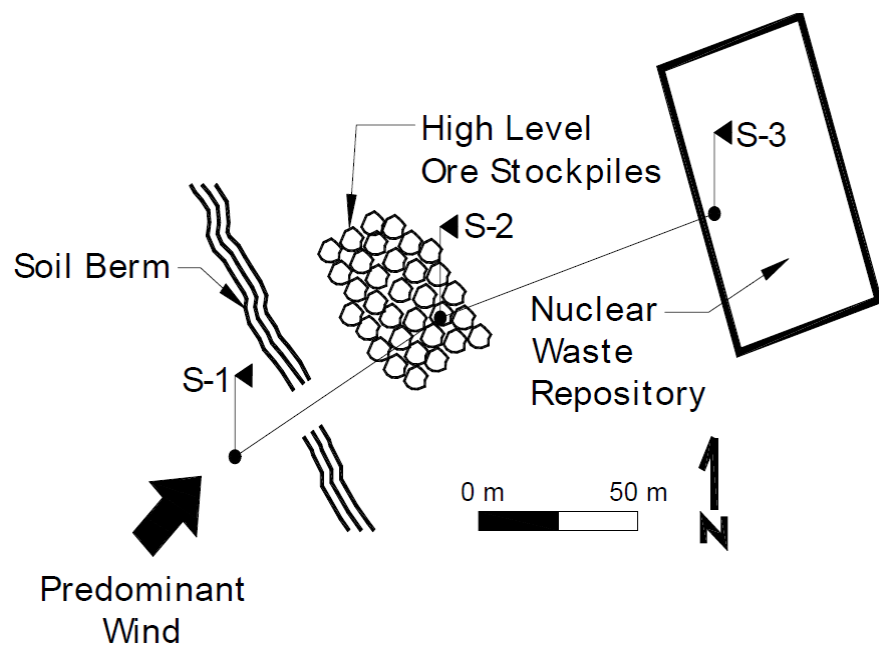


Figure 2: Schematic diagram (top) and satellite image (bottom) of study area showing sample collection stations S-1, S-2, and S-3.

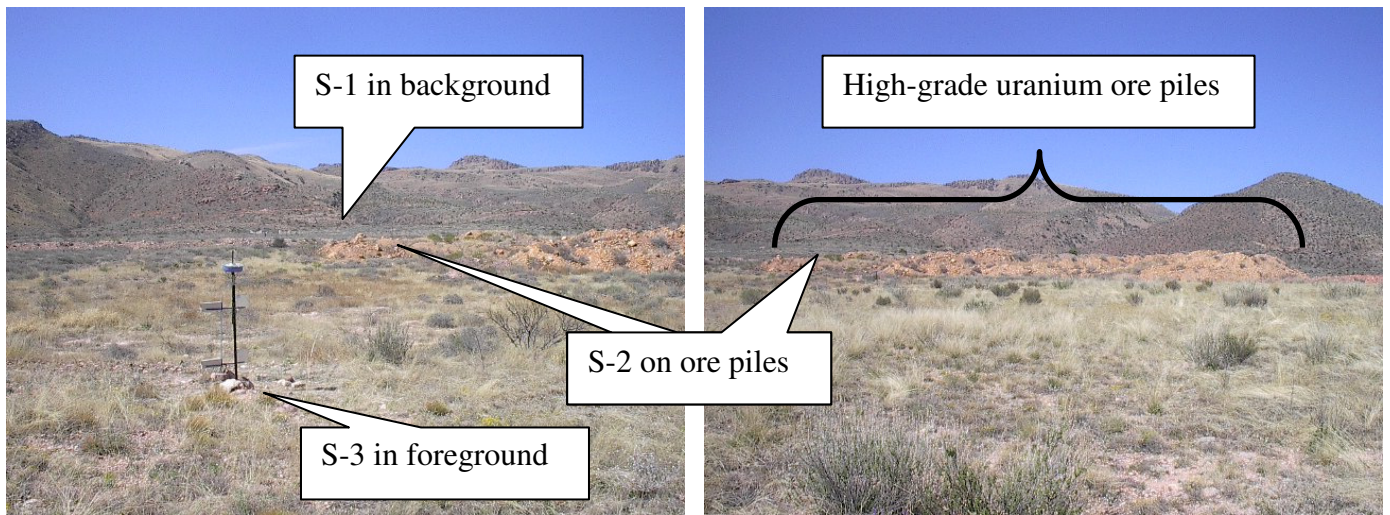


Figure 3: High-grade uranium ore piles looking west.

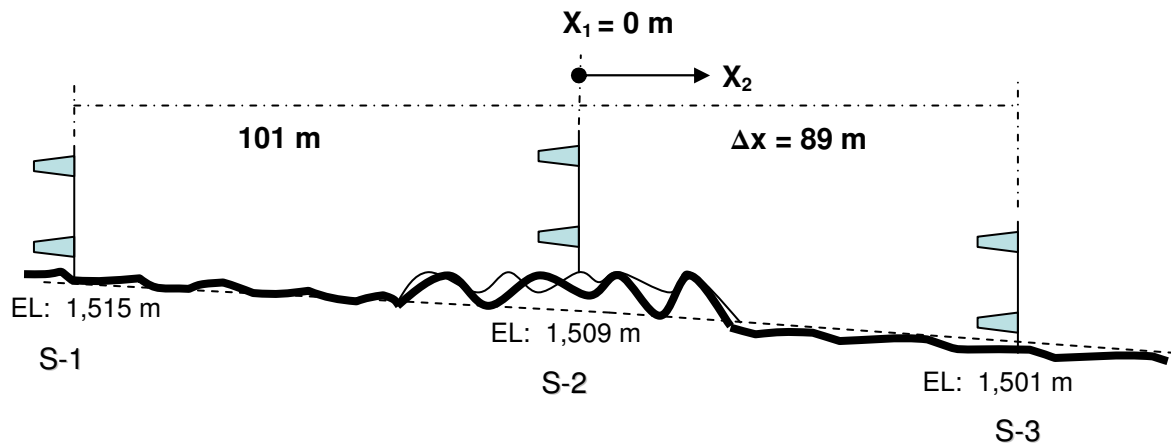


Figure 4: Profile of terrain across S-1, S-2, and S- 3.

2. Background

2.1 Meteorology

Sierra Peña Blanca is situated in the Chihuahuan Desert where the desert is affected by local and regional meteorological conditions such as high-velocity arid winds (predominantly during the spring) (Novlan et al., 2007; Perez and Gill, 2009) and precipitation (predominantly during the summer) (Reheis, 2006; Novlan et al., 2007). In the Chihuahuan Desert, spring is defined as March, April, and May; summer occurs during the months of June, July, and

August; autumn occurs during the months of September, October, and November; and winter occurs during the months of December, January, and February.

A weather station installed by the Department of Energy (DOE) 4.65 km southwest of the uranium ore stockpiles provided wind speed and direction and number days of with at least 0.254 mm of precipitation in 2006 (P. Dobson, personal communication, 2006). There were 94 days with at least 0.254 mm of precipitation in 2006. Maximum winds from the west to northwest (18.7 ms^{-1}) occurred in spring, whereas the minimum winds from the north to east (0.7 ms^{-1}) occurred in the summer. Spring wind velocity vectors measured approximately 20° from the S-2 – S-3 transect. These seasonal winds are plausibly augmented by the surrounding irregular terrain (e.g., gaps and canyons). Stations S-1, S-2, and S-3 rest on an alluvial fan which slopes towards the east (west is higher than east). S-1 is about 6 m higher than S-2 and 14 m higher than S-3 (Figures 1 – 4). The stockpiles at S-2 have been exposed to Chihuahuan aeolian processes since the 1980s. Roughness length (z_0) values (0.05 – 0.1 m) (Seinfeld and Pandis, 1998) were established by field observation of land cover features such as vegetation (creosote, grass, yucca, mesquite, and cacti) height and rock grain size.

2.2 Field Equipment

2.2.1 BSNE (Big Spring Number Eight) Sediment Traps

The BSNE sediment trap was developed by Fryrear (1986) (Figures 6 – 8). The BSNE pans are made of 28-gauge galvanized sheet metal with apertures covered with galvanized mesh screen and stainless steel 60-mesh screen. Air flow loaded with sediment enters an inlet of approximately 2 cm x 5 cm (Goosens and Offer, 2000). Air flow is diffused and decreased as the sampler width increases; consequently, dust particles settle in the collection pan. The air mass flow discharges through the 60-mesh screen. The 18-mesh screen helps prevent fine dust from mobilizing and escaping (Goosens and Offer, 2000). A rubber strap similar to a large rubber band retains the tray and plugs any holes in back and front of the sampler. The samplers are kept facing the wind with a wind vane at the rear of the

sampler. Typical sampling heights are 0.05 m, 0.1 m, 0.25 m, 0.5 m, and 1.0 m (Stout and Fryrear, 1989).

2.3 Lab Equipment

2.3.1 Laser Particle Sizing Theory

The Malvern Mastersizer laser diffraction granulometer is used to measure the size of particles of collected sediment. Chappell (1998) conducted dispersion studies with the Malvern 2600 and the Coulter LS-100 laser particle sizers to assess the most appropriate mediums for suspension and dispersion methods for sandy soil from a semi-arid environment. Even though there is no set of standard procedure for dispersion treatment of soil samples, recommendations were made by Chappell (1998). Even though some tap water may not be suitable due to impurities, tap water with sodium hexametaphosphate (Calgon) or sodium carbonate dispersant agent combined with mechanical agitation and ultrasonic action in the laser particle sizer were suggested to break up aggregates. Zobeck (2004) prepared samples with sodium hexametaphosphate shaking “overnight”. Ultrasonic action for not more than six minutes was recommended. Optimum duration is difficult to assess although three minutes was considered minimum by Chappell (1998). A combination pretreatment with Calgon mixed with tap water and ultrasonic action was most efficient.

Sperazza et al. (2004) systematically analyzed fine grained sediment ($<1\text{-}50\ \mu\text{m}$) from fluvial and volcanic soil systems with the Malvern Mastersizer 2000. Preparation protocols and observations were as follows: (1) Optimal fine-grained sediment dispersion was achieved by mixing sediment in 5.5 g/l of sodium hexametaphosphate solution and shaking the blend for 24 hours prior to analysis. Ultrasonication was set for 60 seconds during analysis. (2) Obscuration that produced the most reproducible results was approximately 20%, but actual obscuration values ranged from 2-40%. (3) Excessive modification of refractive-index settings may produce varied estimates in grain-size distributions. Zobeck (2004) tested refractive index values which ranged between 1.48 and 1.61 by citing Deer et al. (1962). (4) The amount of light absorbed by the sediment regulated by absorption

values may affect grain-size results. Procedures recommended by Sperazza et al. (2004) and Zobeck (2004) for granulometry in the laboratory were generally utilized in this study.

2.4 Colloid and Adsorption Theory

2.4.1 Colloids

Electrically charged small particles in liquids which remain dispersed but do not dissolve or suspend, are known as colloids. A species is considered in solution if it passes a $0.45\ \mu\text{m}$ filter (Eby, 2004). The size range of a colloid range (0.01 and $10\ \mu\text{m}$) (Eby, 2004) lies somewhere between particles that have dissolved (i.e., solutions) and suspensions (i.e., particles in suspension). Colloids typically found in natural waters are clay minerals, silica, oxyhydroxides, organic matter, and bacteria (Eby, 2004). The solubility of oxyhydroxides such as aluminum hydroxides ($\text{Al}(\text{OH})_3$) and iron hydroxides ($\text{Fe}(\text{OH})_3$) depends on the pH value of the water and subsequent charge (positive or negative) of the surface of the particle. Oxyhydroxides are very insoluble at intermediate pH levels and can exist in colloidal form (Eby, 2004).

2.4.2 Adsorption

The surface charge of clay minerals is attributable to three factors (Eby, 2004): (1) Tetrahedral and octahedral layer substitution, that is, Al^{3+} for Si^{4+} or Mg^{2+} for Al^{3+} . This substitution can decrease the positive charge resulting in a negative charge. (2) Imperfections in the crystal structure such as missing cations can result in a negative charge. (3) Broken or unsatisfied bonds at the edges or corners on the surface of the crystal can expose the O^{2-} or OH^- ions. Decreasing pH means H^+ ions will be in competition with cations at the crystal surface and adsorption will decrease. Smaller particles have larger relative surface areas that will yield more broken bonds and will increase cation exchange the capacity (CEC). The cation exchange capacity (CEC) is a measure of a soil's capacity to exchange and retain positively charged ions (cations) and can subsequently affect the negative charge of soils. Factors (1) and (2) apply to 2:1 clays (e.g., montmorillonite) where minerals have a relatively constant

permanent negative surface charge. Factor (3) applies to 1:1 clays in which most of the surface charge is attributable to broken bonds at crystallite edges (Kim, et al., 1996).

Kaolinite is a 1:1 (tetrahedral layer : octahedral layer) clay mineral with stacked layers which form plate-shaped particles (7.5 Angstroms thick) (McCarthy, 1988). The octahedral layer sites are occupied by Al^{3+} at the center of the unit cell; however, Fe^{2+} may on occasion substitute for Al^{3+} . Hydroxyls (OH^-) occupy the corners of the unit cell. The tetrahedral sites are occupied by Si^{4+} at the center of the unit cell and oxygen (O^{2-}) at the corners of the crystal structure. The cation exchange capacity of kaolinite is low (3-15) due to the limited substitution in the kaolinite structure (Eby, 2004). Mobile U^{6+} can be attracted to negatively charged edges (O^{2-} and OH^-) of the tetrahedral and octahedral layers.

2.5 Radionuclide Transport Processes

2.5.1 Aeolian Processes

Kirchner et al. (2002) conducted surface radionuclide studies in a grid area around the U.S. DOE Waste Isolation Pilot Plant (WIPP) and a background grid 20 km southeast of WIPP. Each grid had 16 sampling nodes which were methodically distributed over an area of 16,580 hectares. Since sampling was completed prior to the arrival of the first waste delivery to WIPP, ^{137}Cs and $^{239, 240}\text{Pu}$ found in the soil was attributed to global fallout. The background grid yielded higher concentrations of natural radionuclides and fallout than the WIPP grid. Regarding radionuclide concentrations between the two grids, most of the inconsistencies were attributed to spatial differences between grid nodes. Radionuclide concentrations were normalized to relative percentages of sand, silt, clay and the presence of Al and Pb as a means of adjusting differences in soil textures.

Emets et al. (1998) states that topsoil structure, topography, and rate of near surface wind can contribute to dust generation. Wind speeds above $4\text{-}5 \text{ ms}^{-1}$ can suspend sediment (dust particulates). Radioactive sediments can suspend or re-suspend from the topsoil from wind action. Moreover, dust can be generated without wind action via electrical and thermodynamic phenomenon (Emets et al., 1998).

Convection produced by solar radiation can dry and lead to dust suspension. Wind tube experiments which entailed suspension and re-suspension of radioactive sediments in natural environments were simulated. Various compounds representing dust suspension mediums were utilized. Wind speeds were between 0 to 25 ms⁻¹ and particle size suspension ranged from 0.3 to 10 mcm (micrometers).

Saltation occurs when vertical turbulent forces (velocity components) have nearly no effect on particle trajectory (Pye, 1987). Suspension occurs when the settling velocity of the particle is nearly insignificant relative to the friction velocity (Pye, 1987). The particle's trajectory between saltation and suspension is affected by the inertia and settling velocity of the particle (Pye, 1987). Sand-sized grains carried by wind rarely rise above 1 m, whereas the average carrying height is approximately 10 cm (Bagnold, 1954). Sand grains begin to mobilize on the ground at a wind velocity of approximately 5 ms⁻¹ (Bagnold, 1954), however this number is quite variable with soil and land cover conditions. The saltating-dominated zone of aeolian transport generally extends from the surface up to 0.2 to 0.3 m (Fryrear and Saleh, 1993). Typical diameter values for fine wind-blown sand range between 0.3 to 0.15 mm, whereas the finest wind-blown sand is not less than 0.08 mm in diameter (Bagnold, 1954). Other researchers found in their studies that saltating sand particles ranged between 25 to 125 μm (Visher, 1969) and 50 to 100 μm (Grini et al., 2002). Smaller particles are susceptible to transport and dispersal as dust by upward eddy currents (Bagnold, 1954). Past dust deposition studies indicate that 50 μm is a typical median grain diameter which characterizes most suspended dust mixtures near their source well (Goossens, 2005).

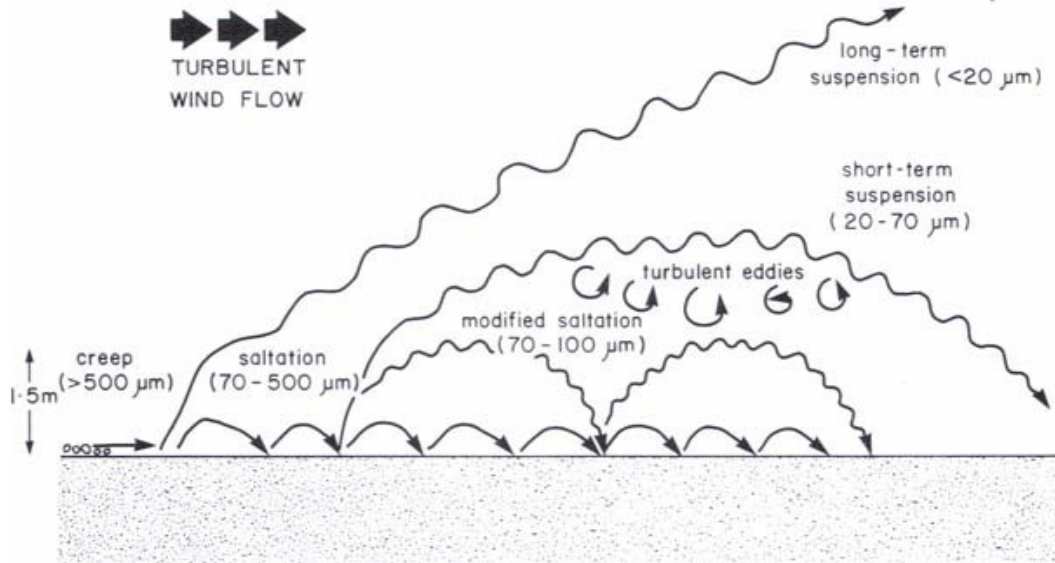


Figure 5: Particle size ranges in different transport modes under moderate wind storm conditions (Pye, 1987).

Under moderate wind storm conditions, the friction velocity (u_*) approximately ranges between $0.20 - 0.60 \text{ ms}^{-1}$. Within this friction velocity range, particles greater than $500 \mu\text{m}$ will creep (roll); particles 70 to $500 \mu\text{m}$ will saltate; particles 70 to $100 \mu\text{m}$ will undergo modified saltation; particles 20 to $70 \mu\text{m}$ will undergo short-term suspension; and particles less than $20 \mu\text{m}$ will undergo long-term suspension (Pye, 1987) (Figure 1). Equations pertinent to suspension and saltation of sediment by the wind are the settling velocity equation (1) (Van der Hoven, 1968; Pye, 1987; Seinfeld and Pandis, 1998; Eby, 2004) and the Prandtl-von Kármán equation (2) which defines the slope of the logarithmic wind profile (Pye, 1987).

The Prandtl-von Kármán equation determines the slope of the logarithmic wind profile:

$$U = \frac{u_*}{k} \ln \frac{z}{z_0} \quad (1)$$

U = Wind velocity (ms^{-1}) at height z above the ground

u_* = Friction velocity (ms^{-1})

z = Height above surface (m)

k = Dimensionless von Karman constant of 0.4

z_0 = Roughness length, the height at which the velocity is zero (roughness length is related to the height of the roughness elements on the surface)

The roughness length (z_0) depends on surface cover (e.g., urban, trees, grass, crops, desert, water, snow, ice, etc.) and can range from 10 m (urban terrain) to 10^{-5} m (smooth ice cover) (Seinfeld and Pandis, 1998). The roughness length z_0 is approximately 1/30 the diameter of the surface particles on bare surfaces (von Kármán, 1934; Prandtl, 1935; Bagnold, 1941 cited in Pye, 1987) or $\approx 1/30$ the height of the roughness elements covering the surface (Seinfeld and Pandis, 1998). The friction velocity (u_*) is directly proportional to the rate of increase of wind velocity with respect to logarithmic height (Bagnold, 1954).

The threshold friction velocity (3) is the critical point at which saltation occurs:

$$u_{*t} = A \sqrt{\frac{\rho_p - \rho_a}{\rho_a} g D} \quad (2)$$

The coefficient A is equal to 0.1 for particle friction Reynolds numbers (Re_p) greater than 3.5 (i.e., $Re_p > 3.5$). Reynolds number = friction velocity (u_*) x mean particle diameter (D) / kinematic viscosity of air (μ). Re_p is a numerical value which indicates how turbulent the flow is around the particle (Bagnold, 1954; Pye, 1987).

$$\begin{aligned} u_{*t} &= \text{the threshold friction velocity (cms}^{-1}\text{)} \\ \rho_p &= \text{the particle density (gcm}^{-3}\text{)} \\ \rho_a &= \text{the air density (0.001225 gcm}^{-3}\text{)} \\ g &= \text{the acceleration due to gravity (980.665 cms}^{-2}\text{)} \\ D &= \text{the mean particle diameter (cm)} \end{aligned}$$

In regards to the settling of a dust particle once suspended, Stokes' law determines the settling velocity of a spherical particle:

$$u_s = \frac{g(\rho_p - \rho_a) D_p^2}{18\mu} \quad (3)$$

(It should be noted that the slip correction factor C_c is factored in when small particles are considered. If D_p is greater than $10 \mu\text{m}$, C_c is usually neglected (Seinfeld and Pandis, 1998). C_c is a function of the mean free path (λ) and particle diameter (D_p). The mean free path is the average distance traveled by a molecule before colliding with another molecule.)

$$\begin{aligned} u_s &= \text{settling velocity (cms}^{-1}\text{)} \\ D_p &= \text{the particle diameter (cm)} \\ \rho_p &= \text{the particle density (gcm}^{-3}\text{)} \end{aligned}$$

ρ_a = air density (0.001225 gcm⁻³)
 g = the acceleration due to gravity (980.665 cms⁻²)
 μ = the dynamic viscosity of the air (1.789 x 10⁻⁴ g cm⁻¹s⁻¹ for standard atmosphere at sea level)

2.5.2 Hydrological Processes

This section concisely discusses the research findings of several investigators involving mobilization, leaching, and precipitation of radionuclides on surface environments and soil horizons at Peña Blanca and South Australia.

French (2006) studied leaching from high-grade ore stockpile boulders from the Nopal I mine at Sierra Peña Blanca, Chihuahua, Mexico. Gamma-ray spectroscopy via Canberra Ge (Li) detector and GENIE 2000 software analyzed collected soil samples and determined isotope peak areas. Uranium decay chain isotopes ²¹⁰Pb, ²³⁴U, ²³⁰Th, ²²⁶Ra, ²¹⁴Pb, and ²¹⁴Bi were detected. Disequilibrium between parent-daughter pairs (i.e., mobilization was multistage) and ²²⁶Ra were found in soil and organic material. A scarcity of ²³⁴U was attributed to the solubility and rapid interchange of uranium in soils. The scarcity of ²¹⁰Pb was attributed to the assimilation of ²²²Rn into the atmosphere. Water was the main means of transport since the highest concentrations of radionuclides occurred near the boulder drip zone.

Lottermoser and Ashley (2006) conducted studies of Radium Hill uranium deposit which is hosted on high-grade metamorphic rocks located in South Australia in a semiarid environment similar to Peña Blanca. This waste material lies exposed to weathering processes of rain and wind. The aim of these studies was to determine radiometric, mineralogical, and geochemical characteristics and properties of materials potentially affected by mining operations. A radiometric survey of waste rock piles, tailings material, and surrounding soil was completed in a succession of transects and loops with an Exploranium GR-320 spectrometer. Tailings, uncrushed and crushed waste rock, stream sediment, topsoil, and vegetation samples were collected for offsite analysis. Mineralized particles from waste sources have dispersed over the past 20 years in surrounding soils and vegetation. It was determined that supplementary capping and terrain design was required to minimize environmental impacts.

Radionuclide mobility utilizing Peña Blanca, Chihuahua, Mexico as a natural analog has been extensively studied (Wong, 1994; Wong et al., 1996; Wong, 1998a; Wong et al., 1998b). Analog I was selected to geochemically evaluate long term behavior of uranium radionuclides in host rocks. Analog II was selected to evaluate short term radionuclide activity at an abandoned dump site. Gamma-ray spectrometry with the Canberra lithium-compensated germanium detector was utilized to analyze and measure U-series nuclide radioactivity on bulk rock samples. For Analog I, X-ray diffraction analysis revealed alteration mineralogy consisting of pure kaolinite and a mixture of Fe-oxyhydroxide (goethite, hematite). Activity ratios ($^{230}\text{Th}/^{238}\text{U}$ compared to $^{226}\text{Ra}/^{230}\text{Th}$) results indicated a minor disequilibrium (Ra enrichment and U depletion) in the majority of the Fe-oxyhydroxides from the breccia zone. This reveals a multiple-event of U mobility. Two Fe phase samples from outside of the breccia zone, one kaolinite sample from inside the breccia zone, and one Fe-oxyhydroxide sample from an east-west fracture indicate Ra and U enrichment. This reveals a single-stage Ra and U precipitation event. For Analog II, isotopic analysis indicated U and Ra leached from the stockpile into the alluvium and bedrock. Thorium did not mobilize but lead had fluctuated mobility. According to isotope data and mineralogical results, Fe-oxyhydroxides and clay minerals attract uranium.

Wong (1994) states no radionuclide migration has taken place in the past million years if secular equilibrium occurs for all parent-daughter pairs. It takes approximately 1 million years to reach secular equilibrium. Conversely, radionuclide migration must have occurred in the span of five half-life durations of the daughter radionuclide, if disequilibrium is evident. Disequilibrium of specific radionuclides means either the parent or daughter isotope have migrated (Wong, 1994). When parent-daughter ratios are less than one is when parent isotope leaching is favored. When parent-daughter ratios are greater than one is when daughter isotopes leach or parent isotopes precipitate (Wong, 1994). This is the case for radionuclide ratios $^{234}\text{U}/^{238}\text{U}$ (Prikryl et al., 1997).

Gamma-ray spectroscopy results of ore samples from Nopal I indicate that kaolinite samples and most of the oxide samples such as hematite, limonite, and manganese oxide were deficient in ^{226}Ra

relative to ^{230}Th and ^{234}Th indicating leaching of ^{226}Ra . However, two hematite samples from outside the ore zone were high in ^{226}Ra relative to ^{230}Th indicating migration of ^{226}Ra (Wong, 1994).

3. Methodology

3.1 Sample Acquisition

3.1.1 Sediment Trap Deployment

On December 10, 2006, six BSNE (Big Spring Number Eight) (Fryrear, 1986) were installed (Figure 7) on and around the high-grade uranium ore piles at stations S-1, S-2, and S-3. S-1 is 101 meters upwind of the uranium ore piles, S-2 is on the uranium ore piles, and S-3 is 89 downwind of the uranium ore piles. A dual configuration was employed, that is, top and bottom BSNE sediment catchers were installed approximately 1 m and 30 cm from the ground surface, respectively (Fryrear and Saleh, 1993).

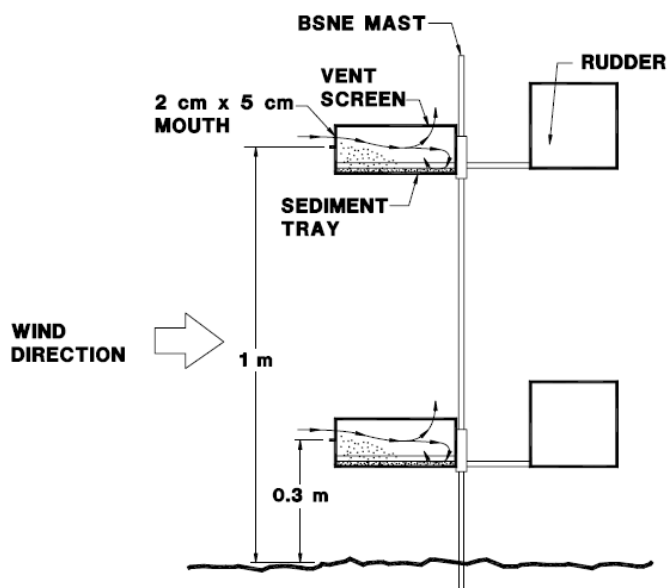


Figure 6: Typical BSNE mast construction specifications (Fryrear, 1986).

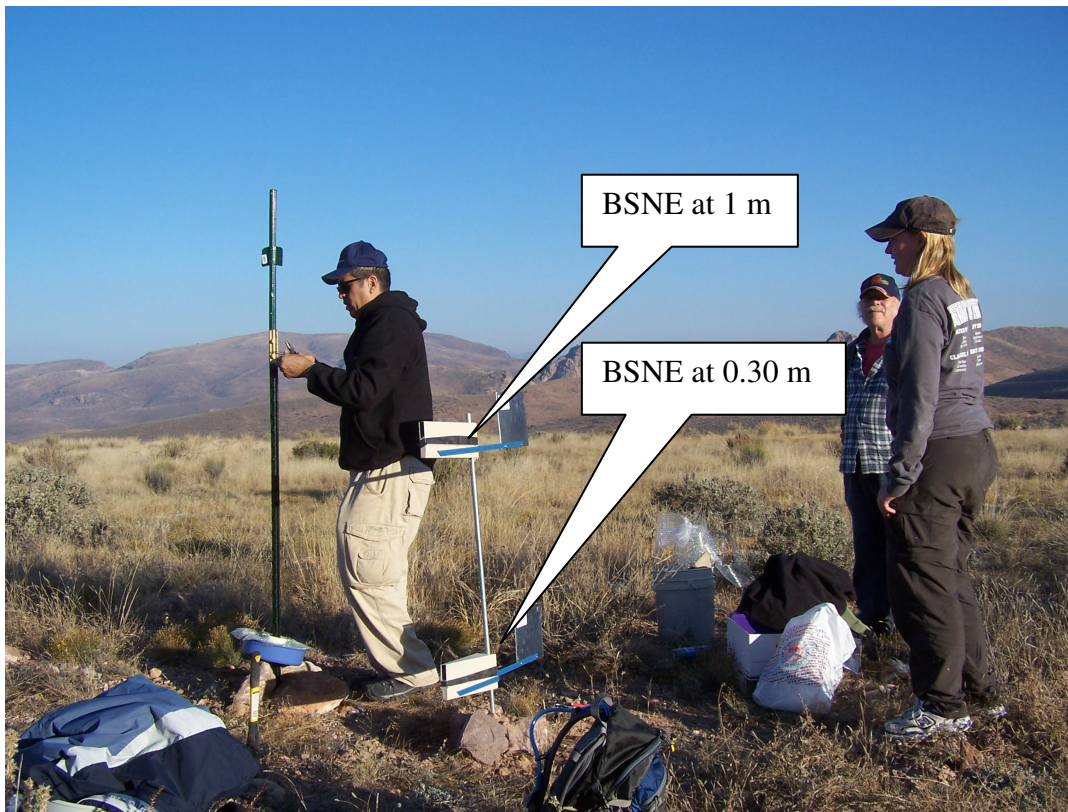


Figure 7: BSNE mast installation in progress at S-1 (looking east).



Figure 8: Completed BSNE sediment trap (top view).

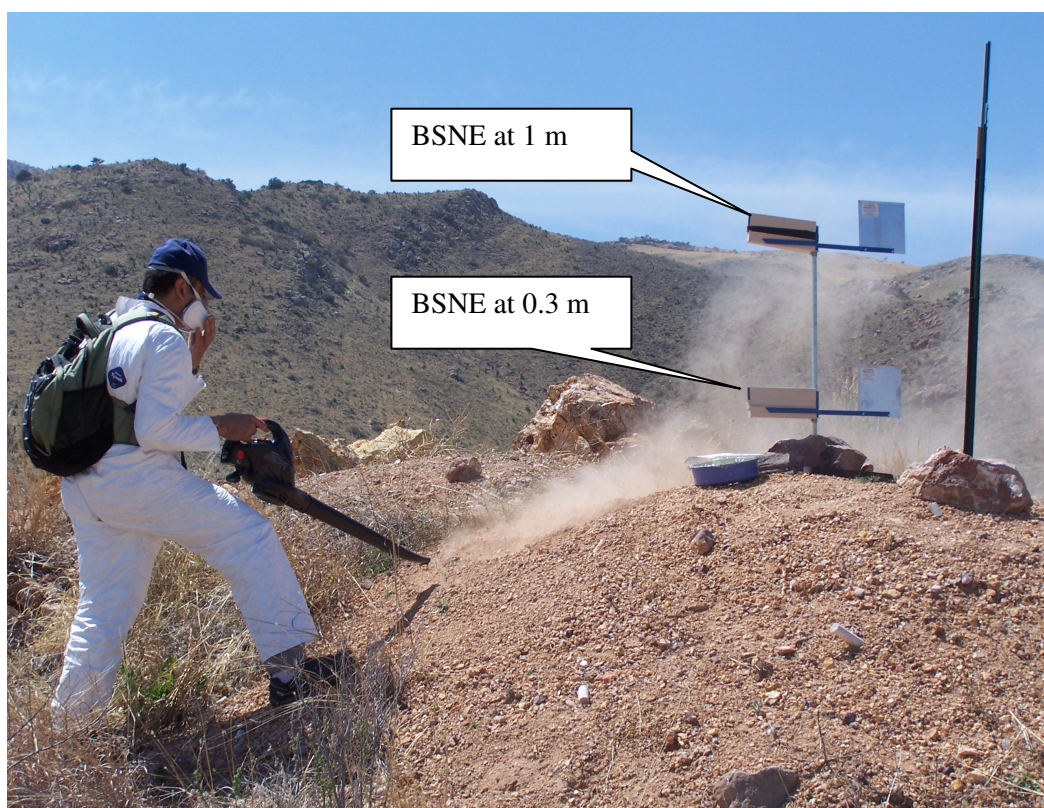


Figure 9: Suspending dust material from the high-grade uranium stockpile with a leaf blower at station S-2 (looking west).

3.1.2 Wind Gust Simulation

On March 17, 2007, it was observed that no sediment had deposited in the sediment traps (i.e., BSNE and MDCO pans); therefore, a wind gust was simulated to suspend sediment by employing a Task Force 18 volt battery operated leaf blower (Figure 9). Approximately 1 cm of topsoil was loosened with a rake prior to applying the leaf blower. The blower had a nozzle air exit velocity of 85 to 120 mph (Task Force mfr. specifications). Protective coveralls (Grainger mfr.) and respirator (Grainger mfr.) were utilized during the collection process. Dust samples were collected dry in the BSNE pans and wet in the MDCO pans. Dust collected in the marbles pans was washed out with distilled water into bottles. All bottles and utensils were washed out with distilled water.

3.1.3 Natural Long-Term Accretion

On July 30, 2009, naturally accumulated sediment samples were collected from the BSNE sediment traps at stations S-1, S-2, and S-3 which were reinstalled on March 17, 2007 after the wind gust simulation. The accretion duration period for S-1, S-2, and S-3 was from March 17, 2007 to July 30, 2009 which is approximately 2.4 years of accretion time. On July 30, 2009, all stations were disassembled.

3.2 Data Acquisition

3.2.1 X-Ray Diffraction (XRD) Analysis

XRD is a technique utilized to identify and quantify mineral content, determine crystallographic structure, and identify unknown substances. Sediment collected from simulated wind gust simulation wind gusts at stations S-1, S-2, and S-3 were analyzed utilizing the Bruker D2 PHASER X-ray Diffractometer which included a 30 kV/10 mA power tube. This XRD analysis was done by Bruker-AXS Incorporated in Madison, Wisconsin.

3.2.2 Particle Size Analysis

Particle size analysis fractionates particle grains into discrete textural constituents (i.e., clay, silt, and clay) with respect to particle sizes and volume percentages. Approximately 0.2 to 0.5 grams of collected topsoil, simulated wind gust sediment, and naturally accreted sediment from stations S-1, S-2, and S-3, were analyzed with the Malvern Hydro 2000G particle sizer. All samples were pretreated overnight with sodium hexametaphosphate for dispersion of particulate crusts (e.g., iron oxides).

Optimal fine-grained sediment dispersion was achieved by mixing sediment in 5.5 g/l of sodium hexametaphosphate solution and shaking the blend “overnight” prior to analysis (Sperazza et al., 2004); and ultrasonic action was applied and set for 60 seconds during analysis (Chappell, 1998; Sperazza et al., 2004).

3.2.3 Electron Microprobe Analyzer (EMPA)

An EMPA determines element mapping and chemical composition of the dust samples without destroying them. Based on the element mapping, mineralogy was inferred. Simulated wind gust sediment collected at S-1, S-2, and S-3 and naturally accreted sediment from S-2 and S-3 at 0.3 m was analyzed utilizing the CAMECA SX 50 EMPA.

3.2.4 Inductively Coupled Plasma - Mass Spectrometry (ICP-MS) Analysis

ICP-MS analysis determines multi-elemental concentration levels as low as parts per trillion (ppt). Collected topsoil was sieved for particles $< 75 \mu\text{m}$ and between $75 - 1,000 \mu\text{m}$ from stations S-1 and S-2 and analyzed by Actlabs. Three replicate samples of sieved $< 75 \mu\text{m}$ and $75 - 1,000 \mu\text{m}$ topsoil from S-1 and S-2 were analyzed, that is, six replicate samples for each station yields a total of twelve replicate samples. The following analytical code protocol was followed by Actlabs (<http://www.actlabs.com/>):

Code 4E-Res (11+) INAA (INAAGEO)/Major Elements Fusion
ICP (WRA)/Total Digestion ICP (TOTAL)
Code 4E-Res (FeO) (11+) INAA(INAAGEO)/Major Elements
Fusion ICP (WRA)/Total Digestion ICP (TOTAL)
Code 4F-F Fusion Specific Ion Electrode-ISE
Code 4F-FeO Titration
Code 5D-C-Organic Infrared

3.2.5 Gamma-Ray Spectroscopy Analysis

A gamma spectrometer determines the gamma energy emitted by nuclides in radioactive material. A spectrum of gamma energy specific to atoms in the sample is generated by the energy and intensity of the radioactive material. Radionuclides are identified and quantified by the resulting spectrum. Naturally accumulated sediment from stations S-1, S-2, and S-3 were analyzed with high-purity germanium gamma detectors (i.e., Canberra Model HPGe Detectors).

3.3 Data Processing

3.3.1 Horizontal Flux of Total Airborne Particle Mass (q_{tot})

Horizontal fluxes of total airborne particle mass (q_{tot}) (9) values were derived from the empirical equation (Gillette et al., 1997; Shao, 2000).

$$q_{tot} = \frac{\int_0^{1m} Q(z)dz}{\Delta t} \quad (4)$$

q_{tot} = Horizontal Flux of Total Airborne Particle Mass ($\text{gm}^{-1}\text{yr}^{-1}$)
 $Q(z)$ = Mass of sediment sample divided by the inlet area (gm^{-2})
 dz = Change in height of the sampler (m) = 0.3 m and 1 m
 Δt = Sampling time interval (yr) = 2.4 years

3.3.2 AP-42 Emission Factor Equation

The AP-42 Compilation of Air Pollutant Emission Factors, was originally published by the U.S. Public Health Service in 1968; and was revised and issued as the second edition by the U.S. Environmental Protection Agency (EPA) in 1972. Since then, the EPA has formulated equations for particulate matter (PM) emission factors from vehicles traveling on unpaved roads and published them in their AP-42 guidance document for emissions (EPA, 1998). The AP-42 PM emissions factor (E) equation (5) is as follows:

$$E = k(1.7) \left[\frac{s}{12} \right] \left[\frac{S}{48} \right] \left[\frac{W}{2.7} \right]^{0.7} \left[\frac{w}{4} \right]^{0.5} \left[\frac{365-p}{365} \right] \quad (5)$$

E = Emission factor, (kilograms [kg]/VKT)
 k = Particle size multiplier dependant on the aerodynamic size (dimensionless) = 0.36 for PM10
 s = Silt content of road surface material (%)
 S = Mean vehicle speed (km/hr)
 W = Mean vehicle weight in megagrams (Mg)
 w = Mean number of wheels
 p = Number of days with at least 0.254 mm of precipitation per year
 VKT = Vehicle Kilometers Traveled

The silt percentage values of 26.65 % and 38.42 % were obtained from particle size analysis results of artificially suspended sediment from stations S-1 and S-2, respectively. This percentage value

falls within the silt percentage range (1.6 – 68 %) for dirt roads prescribed by the AP-42 guidance document for unpaved roads (EPA, 1998). PM10 emissions were calculated since particulate matter less than 10 μm (PM10) aerodynamic diameter can be inhaled and have ill respiratory effects (Choi et al., 2008).

Emissions of uranium (U) from S-1 and S-2 were estimated by utilizing the U concentration ICP-MS results for sieved particles less than 75 μm and PM10 emission factor (E) results. Since fine ($\leq 75 \mu\text{m}$) and coarse (75 μm – 1,000 μm) particles yielded similar U concentration values, PM10 ($\leq 10 \mu\text{m}$) emission factor results were utilized to compute uranium emissions by multiplying PM10 emission factor (E) values with U ppm concentration values, that is, U emissions = $E \times U$ (ppm).

3.3.3 Radioactive Decay Computation

Gamma spectrometry does not provide ^{238}U activity levels; therefore, equations (6) – (9) expressing decay (disintegration) laws were employed to derive ^{238}U activity levels at S-2 from ^{235}U activity levels provided by the gamma spectrometry analysis.

$$N = N_0 e^{-\lambda t} \quad (6)$$

N = Number of unchanged (remaining) atoms

N_0 = Number of atoms at time zero

λ = Instantaneous fraction of atoms decaying per unit time

t = Time

$$\lambda = \frac{\ln 2}{t_{1/2}} \quad (7)$$

λ = Instantaneous fraction of atoms decaying per unit time

$t_{1/2}$ = Time it takes for half of the atoms to decay in a sample

$$a = \lambda N \quad (8)$$

a = Rate of decay or rate of disintegration

λ = Instantaneous fraction of atoms decaying per unit time

N = Number of unchanged (remaining) atoms

$$R = \frac{a_{U-238}}{a_{U-235}} = \frac{\lambda_{U-238}}{\lambda_{U-235}} \times \frac{U_{238} \%}{U_{235} \%} \quad (9)$$

R = Ratio of ^{238}U and ^{235}U activity

a = Rate of decay of ^{238}U and ^{235}U

λ = Instantaneous fraction of atoms decaying per unit time for ^{238}U and ^{235}U

^{238}U = Percentage of ^{238}U in nature (99.2745%)

^{235}U = Percentage of ^{235}U in nature (0.7200%)

3.3.4 Radioactivity and Distance Computation

Activities levels for radionuclides ^{226}Ra , ^{214}Pb , ^{214}Bi , and ^{210}Pb common to S-2 and S-3 in the saltating zone (0.3 m) were provided by the gamma spectrometry analysis. It was hypothesized minerals potentially bearing these four radionuclides displaced 89 m from S-2 to S-3 over a period of 2.4 years. Equations (10) – (11) were employed to compute the distance at which point radioactivity is zero, that is, no radionuclides are present (Figure 4).

$$A = \frac{a_{S-2} - a_{S-3}}{\Delta x} \quad (10)$$

A = Activity change/distance change between S-2 and S-3

$a_{S-2} - a_{S-3}$ = Change in activity of radionuclide between S-2 and S-3

Δx = Change in distance between S-2 and S-3

$$A_x = A_{S-2} - \int_{x_1}^{x_2} A dx \quad (11)$$

A_x = Activity of radionuclide at a given distance from S-2 towards S-3

A_{S-2} = Activity of radionuclide at S-2

A = Activity change/distance change between S-2 and S-3

x_1 = Initial distance (0 m) at S-2

x_2 = Distance of interest from S-2 towards S-3

dx = Change in distance ($x_2 - x_1$)

3.3.5 Friction Velocity (u_*) Computation

Measured maximum (18.7 ms^{-1}) and minimum (0.7 ms^{-1}) wind speeds were provided by a weather station installed 4.65 km southwest of station S-2. Maximum winds from the west to northwest occurred in spring, whereas the minimum winds from the north to east occurred in the summer. Roughness length (z_0) values ($0.05 - 0.1 \text{ m}$) (Seinfeld and Pandis, 1998) were estimated by observing land cover features such as vegetation (creosote, grass, yucca, mesquite, and cacti) height and rock grain size. Utilizing the logarithmic wind profile equation (1) (Pye, 1987), friction velocity (u_*) values were computed by applying measured Peña Blanca wind speeds at 0.3 m and 1 m heights and subsequently compared to friction velocity ranges ($0.2 - 0.6 \text{ ms}^{-1}$) (Pye, 1987) to mathematically verify if short-term suspension and modified saltation of medium and coarse silt grains ($20 - 100 \mu\text{m}$) (Pye, 1987) had occurred.

The Prandtl-von Kármán equation determines the slope of the logarithmic wind profile:

$$U = \frac{u_*}{k} \ln \frac{z}{z_0} \quad (1)$$

U = Wind velocity (ms^{-1}) at height z above the ground

u_* = Friction velocity (ms^{-1})

z = Height above surface (m)

k = Dimensionless von Karman constant of 0.4

z_0 = Roughness length, the height at which the velocity is zero (roughness length is related to the height of the roughness elements on the surface)

4. Results

This section presents the results of all analytical techniques applied for data acquisition from S-1, S-2, and S-3 selected sediment (Table 5). Sieved topsoil was analyzed via ICP-MS and particle sizer techniques. Sediment from the wind gust simulation was analyzed via XRD and particle sizer techniques. Naturally accreted sediment was analyzed via EMPA, gamma spectrometry techniques, and particle sizer techniques. For each analytical technique, results for S-1, S-2, and S-3 are displayed separately for clarity.

4.1 X-Ray Diffraction (XRD) Analysis

For the diffractograms generated by XRD, X-Ray counts (intensity) correspond to the y-axis, whereas the angle 2θ corresponds to the x-axis.

S-1) XRD mineralogy results indicate that the minerals with the highest concentrations were quartz and orthoclase, whereas the minerals of lesser abundance were hematite and dolomite (Figure 10; Table 6).

S-2) XRD mineralogy results indicate that the minerals with the highest concentrations were quartz and kaolinite, whereas the minerals of lesser abundance were uranophane, carnotite, and uraninite (Figure 11; Table 6).

S-3) XRD mineralogy results indicate that the minerals with the highest concentrations were calcite and quartz, whereas the minerals of lesser abundance were microcline, hematite, and smithsonite (Figure 12; Table 6).

4.2 Particle Size Analysis of Simulated Wind Gust Sediment

S-1) The volume percentage/particle size distribution graph displays a non-steady increase with a large tail and 7% volume peak ranging between $100\ \mu\text{m}$ to $1000\ \mu\text{m}$. The cumulative volume percent values for clay, silt, and sand sediment textural classes (AGI, 1982) are 7%, 17%, and 73%, respectively (Figure 13 top graph; Table 7).

S-2) The volume percentage/particle size distribution graph displays a bimodal distribution with a small 2% volume peak ranging between $1\ \mu\text{m}$ to $10\ \mu\text{m}$ and a large 4.5 % peak ranging between $100\ \mu\text{m}$ to greater than $1000\ \mu\text{m}$. The cumulative volume percent values for clay, silt, and sand sediment textural classes (AGI, 1982) are 17%, 20%, and 57%, respectively (Figure 13 middle graph; Table 7).

S-3) The volume percentage/particle size distribution graph displays a non-steady increase with a large tail, modest shoulder, and large 4.5% volume peak ranging between $100\ \mu\text{m}$ to greater than $1000\ \mu\text{m}$. The cumulative volume percent values for clay, silt, and sand sediment textural classes (AGI, 1982) are 13%, 23%, and 57%, respectively (Figure 13 middle graph; Table 7).

4.3 Particle Size Analysis of Topsoil Sediment

S-1) The volume percentage/particle size distribution graph displays a non-steady increase with a tail and a large 8% volume peak ranging between 15 μm to greater than 100 μm . The cumulative volume percent values for clay, silt, and sand sediment textural classes (AGI, 1982) are 7%, 71%, and 23%, respectively (Figure 14 top graph; Table 7).

S-2) The volume percentage/particle size distribution graph displays a non-steady increase with a small tail, large 3.3 % volume shoulder, and a large 5% volume peak ranging between 20 μm to greater than 100 μm . The cumulative volume percent values for clay, silt, and sand sediment textural classes (AGI, 1982) are 20%, 69%, and 11%, respectively (Figure 14 middle graph; Table 7).

S-3) The volume percentage/particle size distribution graph displays a non-steady increase with a large tail and 6.3 % volume peak ranging between 15 μm to greater than 100 μm . The cumulative volume percent values for clay, silt, and sand sediment textural classes (AGI, 1982) are 17%, 67%, and 16%, respectively (Figure 14 bottom graph; Table 7).

4.4 Particle Size Analysis of Accreted Sediment

S-1 top BSNE) The volume percentage/particle size distribution graph displays a steady increase with a large tail and 5% volume peak ranging between 10 μm to greater than 150 μm . The cumulative volume percent values for clay, silt, and sand sediment textural classes (AGI, 1982) are 13%, 62%, and 24%, respectively (Figure 15 top graph; Table 7).

S-1 bottom BSNE) The volume percentage/particle size distribution graph displays a steady increase with a large tail, 4% volume peak ranging between 10 μm to greater than 200 μm , and small shoulder ranging between 200 μm to greater than 1,000 μm . The cumulative volume percent values for clay, silt, and sand sediment textural classes (AGI, 1982) are 11%, 53%, and 36%, respectively (Figure 15 top graph; Table 7).

S-2 top BSNE) The volume percentage/particle size distribution graph displays a steady increase with a large tail, 5% volume peak ranging between 10 μm to greater than 150 μm , and a small heel

ranging between 150 μm to 1,000 μm . The cumulative volume percent values for clay, silt, and sand sediment textural classes (AGI, 1982) are 16%, 60%, and 24%, respectively (Figure 16 top graph; Table 7).

S-2 bottom BSNE) The volume percentage/particle size distribution graph displays a non-steady increase with a large tail, 4% volume peak ranging between 10 μm to 200 μm , and small shoulder ranging between 200 μm to greater than 1,000 μm . The cumulative volume percent values for clay, silt, and sand sediment textural classes (AGI, 1982) are 15%, 51%, and 33%, respectively (Figure 16 bottom graph; Table 7).

S-3 top BSNE) The volume percentage/particle size distribution graph displays a steady increase with a large tail and 4.8% volume peak ranging between 7 μm to greater than 200 μm , and a small heel ranging between 200 μm to greater than 1,000 μm . The cumulative volume percent values for clay, silt, and sand sediment textural classes (AGI, 1982) are 14%, 61%, and 24%, respectively (Figure 17 top graph; Table 7).

S-3 bottom BSNE) The volume percentage/particle size distribution graph displays a steady increase with a large tail and a large 3.5% volume peak ranging between 10 μm to greater than 1,000 μm . The cumulative volume percent values for clay, silt, and sand sediment textural classes (AGI, 1982) are 14%, 46%, and 39%, respectively (Figure 17 top graph; Table 7).

4.5 Electron Microprobe Analysis of Simulated Wind Gust Sediment

For the spectra generated by the electron microprobe, the X-Ray counts correspond to the y-axis, whereas $\sin\theta$ corresponds to the x-axis.

S-1) Elements detected by the electron microprobe with the highest counts per second were Si and Al, whereas the element with the lowest counts per second was Fe (Figures 18 – 21; Appendices 1 and 2).

S-2) Elements detected by the electron microprobe with the highest counts per second were Si, Ca, Al, and U, whereas the elements with the lowest counts per second were Fe and V (Figures 22 – 24; Appendices 1 and 2).

S-3) Elements detected by the electron microprobe with the highest counts per second were Pb and Zn, whereas the elements with the lowest counts per second were Ca and Si (Figures 29 – 32; Appendices 1 and 2).

4.6 Electron Microprobe Analysis of Accreted Sediment

For the spectra generated by the electron microprobe, the X-Ray counts correspond to the y-axis, whereas $\sin\theta$ corresponds to the x-axis.

S-2) Elements detected by the electron microprobe with the highest counts per second were Si, Ca, and U (Figures 33 – 34).

S-3) Elements detected by the electron microprobe with the highest counts per second were Si, Ca, and U (Figures 35 – 36).

4.7 Inductively Coupled Plasma - Mass Spectrometry (ICP-MS) Analysis

S-1) Oxide compound and elemental concentrations for sediment $< 75 \mu\text{m}$ (fine) and between $75 \mu\text{m} - 1,000 \mu\text{m}$ (coarse) are listed by samples numbers 101-103 and 104 -106, respectively (Table 8).

S-2) Oxide compound and elemental concentrations for sediment $< 75 \mu\text{m}$ (fine) and between $75 \mu\text{m} - 1,000 \mu\text{m}$ (coarse) are listed by samples numbers 107-109 and 110 -112, respectively (Table 8).

Concentrations of oxide compounds and elements for S-1 and S-2 are demonstrated on Figures 37-40. Enrichment factors (i.e., Enrichment Factor = S-2 concentration/S-1 concentration) are listed in Table 9.

The trend line scattergram model for major and trace elements detected by the ICP-MS analysis in S-1 and S-2 topsoil indicates an $r^2 = 0.98$ value with line slope of 1.86 for S-1 and an $r^2 = 0.84$ value with line slope of 0.63 for S-2.

4.8 Gamma-Ray Spectroscopy Analysis

S-1) No radionuclide activity above the detection limit was measured in the bottom BSNE pan. ^{210}Pb was the only radionuclide with a measurable activity level in the top BSNE pan (Table 10).

S-2) ^{234}Pa had the highest activity level, whereas ^{211}Bi had the lowest activity level in the bottom BSNE pan. ^{234}Pa had the highest activity level, whereas ^{211}Bi had the lowest activity level in the top BSNE pan (Table 10).

S-3) ^{226}Ra had the highest activity level, whereas ^{214}Bi had the lowest activity level in the bottom BSNE pan. ^{210}Pb was the only radionuclide with a measurable activity level in the top BSNE pan (Table 10).

4.9 Horizontal Flux of Total Airborne Particle Mass (q_{tot})

The results of horizontal fluxes of total airborne particle mass (q_{tot}) calculations are listed in Table 1.

Table 1: Naturally accreted sediment mass and horizontal flux quantities in top (1 m) and bottom (0.3 m) BSNE pans over 2.4 years at stations S-1, S-2, and S-3.

Station and BSNE pan height	Accreted Sediment Mass (g)	Total Horizontal Flux (g/m/yr)
S-1 top (1 m)	0.54	225
S-1 bottom (0.3 m)	1.39	173.8
S-2 top (1 m)	0.51	212.5
S-2 bottom (0.3 m)	1.10	137.5
S-3 top (1 m)	0.52	216.7
S-3 bottom (0.3 m)	1.18	147.5

4.10 AP-42 Emission Factor Equation

The results of the AP-42 emissions factor (E) equation (5) calculations are listed in Table 2.

Table 2: AP-42 emissions factor (E) equation results of PM10 and uranium emissions per vehicle kilometer traveled.

$$E = k(1.7) \left[\frac{s}{12} \right] \left[\frac{S}{48} \right] \left[\frac{W}{2.7} \right]^{0.7} \left[\frac{w}{4} \right]^{0.5} \left[\frac{365 - p}{365} \right]$$

Vehicle type	Number of wheels (w)	Weight (tons) (W)	Speed (km/hr) (S)	Number of days per year with precipitation > 0.254mm > 0.01 inches (p)	Sample source station	Topsoil (dry) Silt % (s)	(kg/VKT) (E)	U (ppm)	grams of U/VKT
Pick-up truck	4	1.93	32.2	95	S-1	26.65	0.54	7	0.004
Dump truck	6	252	32.2	95	S-1	26.65	19.84	7	0.14
Dump truck	10	231	32.2	95	S-1	26.65	24.10	7	0.17
Wheel Loader	4	208	22.6	95	S-1	26.65	4.58	7	0.03
Grader	6	15	32.2	95	S-1	26.65	3.60	7	0.03
Pick-up truck	4	1.93	32.2	95	S-2	38.42	0.77	2,300	1.77
Dump truck	6	252	32.2	95	S-2	38.42	28.61	2,300	65.79
Dump truck	10	231	32.2	95	S-2	38.42	34.75	2,300	79.92
Wheel Loader	4	208	22.6	95	S-2	38.42	6.60	2,300	15.18
Grader	6	15	32.2	95	S-2	38.42	5.19	2,300	11.94

4.11 Radioactive Decay Computation

S-2) The detected ^{235}U activity (14.5 pCi) value yielded a computed ^{238}U activity (323.8 pCi) value at 0.3 m. The detected ^{235}U activity (20 pCi) value yielded a computed ^{238}U activity (446.7 pCi) value at 1 m.

4.12 Radioactivity and Distance Computation

The results of the radioactivity and distance computations are listed in Table 3.

Table 3: These are the nuclide activities at S-2 and S-3, distance at which activity is no longer detected, and the rate at which displacement occurred from S-2 to S-3.

Nuclide	pCi at S-2	pCi at S-3	pCi = 0 at Δx (m)	$\Delta x/\Delta t$ (m/day)
Ra-226	131	14.2	99.8	0.114
Pb-214	175	5.28	91.8	0.105
Bi-214	193	4.8	91.3	0.104
Pb-210	143	10	95.7	0.109

4.13 Meteorology

The results of the friction velocity (u_*) equation (1) computations are listed in Table 4.

Table 4: Friction velocities computed with the friction velocity (u_*) equation (1) from measured wind speeds.

Measured Wind Speed	BSNE Height	Roughness Length Height	Computed Friction Velocity
U_{\max} (ms^{-1})	z (m)	z_0 (m)	u_* (ms^{-1})
18.7	0.3	0.1	6.81
18.7	0.3	0.05	4.17
18.7	1	0.1	3.25
18.7	1	0.05	2.49
U_{\min} (ms^{-1})	z (m)	z_0 (m)	u_* (ms^{-1})
0.71	0.3	0.1	0.26
0.71	0.3	0.05	0.16
0.71	1	0.1	0.12
0.71	1	0.05	0.10

5. Discussion

This section discusses the results of all analytical techniques applied: X-Ray Diffraction (XRD) Analysis, Particle Size Analysis, Electron Microprobe Analyzer (EMPA), Inductively Coupled Plasma-Mass Spectrometry (ICP-MS) Analysis, and Gamma-ray Spectroscopy Analysis. Also discussed are the data processing applications: Horizontal Flux (q_t), Radioactive Decay Computation, and Radioactivity and Distance Computation. Stations S-1, S-2, and S-3 are discussed in sequential order with corresponding acquired data for clarity.

S-1) Station S-1 is upwind of station S-2. S-1 serves as a background station since the predominant wind comes from the west as previously mentioned in the meteorology section. Elements detected by the EMPA infer that minerals kaolinite, feldspar, and iron oxide were present (Appendix A and B). The EMPA findings coincide with the XRD findings in which quartz, orthoclase, kaolinite, and hematite (ferric oxide Fe^{3+}) were quantified (Table 6).

The particle size analysis of the naturally accreted sediment at 0.3 m and 1 m heights revealed nearly identical volume percentage/particle size distribution curves for sediment collected at 1 m and much less similarity for sediment collected in the saltating zone (0.3 m) (Figure 15 top graph; Figure 16 top graph; Figure 17 top graph). Similar mass quantities for S-1, and S-2, and S-3 were also observed (Table 1). For all modes of collection (wind gust simulation, topsoil, and accreted sediment), the rank order of fine particle ($< 4 \mu\text{m}$) availability is $\text{S-2} > \text{S-3} > \text{S-1}$. For naturally accreted sediment collected within the saltating zone (0.3 m), the volume percentages between $62 - 1,000 \mu\text{m}$ (AGI, 1982) were very similar, but have a rank order of $\text{S-3} > \text{S-2} > \text{S-1}$. Furthermore, the volume percentages less than $62 \mu\text{m}$ (AGI, 1982) are also very similar and have a rank order of $\text{S-1} > \text{S-2} > \text{S-3}$ (Figure 15 bottom graph; Figure 16 bottom graph; Figure 17 bottom graph; Table 7).

The ICP-MS results indicated that the concentration of crustal oxide compounds SiO_2 and Al_2O_3 in fine ($< 70 \mu\text{m}$) and coarse ($70 - 1,000 \mu\text{m}$) sediment had a small degree of variation between S-1 and S-2, whereas FeO_3 yielded a higher concentration level at S-2 than at S-1. However, CaO and K_2O

yielded higher concentration levels at S-1 than at S-2 (Figure 37). With the exception of Rb, elements Ag, As, Br, Cd, Co, Cr, Cu, Mo, Ni, Pb, Sb, Sr, Th, U, V, W, Y, Zn, Zr, La, Ce, and Nd in fine and coarse sediment yielded higher concentration levels at S-2 than at S-1 (Figures 38 – 40).

The gamma-ray spectroscopy analysis detected the ^{210}Pb radionuclide with an activity level of 8.5 pCi in sediment collected at 1 m height, whereas no radiogenic activity was detected in the sediment collected at 0.3 m (Table 10). Sediment material on which S-1 was installed consisted of alluvial felsic igneous material (silicate minerals in igneous rocks) with an abundance of coarse (4 – 256 mm) particle grains. Similar mass amounts of sediment accreted at S-1, S-2, and S-3 at heights 0.3 m and 1 m. The ^{210}Pb activity levels at S-1 and S-3 at 1 m were 8.5 pCi and 10.6 pCi. This similarity suggests the ^{210}Pb radionuclide detected at 1 m at S-1 and S-3 originated from transported material from S-2. It is probable no radionuclide activity was detected in the saltating zone (0.3 m) at S-1 since it is unlikely sediment particles saltated uphill under weak easterly (towards the west) wind conditions, which is counter to predominant strong westerly winds (towards the east).

S-2) Station S-2 sits on high-grade uranium ore piles. Elements detected by the EMPA in the wind gust simulation sediment infer that minerals kaolinite, K-feldspar, carnotite, and uranophane were present (Appendix A and B); BSE images of carnotite ($\sim 10\ \mu\text{m}$) and uranophane ($\sim 100\ \mu\text{m} \times 300\ \mu\text{m}$) particles are displayed in Figures 22 and 25. These findings coincide with the XRD findings in which quartz, orthoclase, kaolinite, uranophane, and carnotite were determined (Table 6). The EMPA also detected Si, Ca, and U pertaining to a uranophane particle (Figures 33 and 34) found in the accreted sediment at S-2 in the saltating zone (0.3 m). The uranophane particle hosts ^{238}U and ^{235}U which generated the progeny radionuclides ^{234}Pa , ^{226}Ra , ^{214}Pb , ^{214}Bi , ^{210}Pb , and ^{211}Bi (Table 10). Alteration of uraninite (UO_2) produces U^{6+} oxyhydroxides as U^{4+} oxidizes to U^{6+} which yields $(\text{UO}_2)^{2+}$. Uranophane forms when $(\text{UO}_2)^{2+}$ in solution encounters calcium and silica H_4SiO_4 at saturation uranophane precipitates (Langmuir, 1997). Carnotite forms when uranyl ion in solution reacts with calcium and the complex ion vanadate $(\text{VO}_4)^{4-}$ (Durrance, 1986) and at saturation carnotite precipitates. The $10\ \mu\text{m}$

carnotite particle (Figure 25) can conceivably be transported long-term (Pye, 1987) and inhaled (Choi et al., 2008). The uranophane particle (Figure 33) has an elongated asymmetrical form ($\sim 80 \mu\text{m} \times 20 \mu\text{m}$) which falls within the modified saltation range ($70 - 100 \mu\text{m}$) (Pye, 1987).

The ICP-MS results indicated that averaged concentrations of U in fine ($< 70 \mu\text{m}$) and coarse ($70 - 1,000 \mu\text{m}$) sediment were 7 ppm and 9.1 ppm, respectively (Table 8). These values are higher than U concentrations found in sedimentary rocks, which range between 1.2 – 1.3 ppm in sedimentary rocks and 4.4 ppm in granites (Langmuir, 1997). Moreover, ICP-MS results indicated that the sieved background sediment had Pb concentration levels which ranged between 19 – 45 ppm. Concentration levels of Pb average about 24 ppm for granites (Maynard, 1983; Faure, 1986). The concentration levels of U and Pb in fine ($< 70 \mu\text{m}$) and coarse ($70 - 1,000 \mu\text{m}$) sediment had a small degree of variation between S-1 and S-2. The enrichment factor (EF) is the element concentration ratio between stations S-1 and S-2 ($\text{EF} = \text{S-2 concentration} / \text{S-1 concentration}$). The EF values for U and Pb in fine and coarse sediment ranged between 309 – 400 and 28 – 19, respectively (Table 9).

The trend line scattergram model results for the S-1 and S-2 ICP-MS results are fairly close; however, the r^2 value for S-2 is slightly smaller due to the outlier Zr, Zn, and U trace elements. Removing the Zr, Zn, and U outliers would raise the r^2 value and highlight the major elements (e.g., SiO_2 and Al_2O_3), but the U value cannot be omitted since it is essential to this study.

The gamma-ray spectroscopy results detected daughter radionuclides within the ^{238}U decay chain in sediment collected at 0.3 m and 1 m heights (Tables 10, 13). Activity (pCi) levels between 0.3 m and 1 m had a small degree of variation. In the saltating zone (0.3 m), activity levels of ^{226}Ra (131 pCi), ^{214}Pb (175 pCi), ^{214}Bi (193 pCi), and ^{210}Pb (143 pCi) (Tables 10 and 11) are comparable ($\lambda_{\text{daughter}}N_{\text{daughter}} \sim \lambda_{\text{parent}}N_{\text{parent}}$) (Murray, 2009) and are considered to be in secular equilibrium. Radionuclides with activity levels which are equal or approximately equal are considered to be in secular equilibrium which is obtained within five half-lives of the daughter radionuclide (Bourdon, 2003). The activity level of

^{234}Pa (392 pCi) is about twice greater than the activity of ^{226}Ra , ^{214}Pb , ^{214}Bi , and ^{210}Pb and is considered not to be in secular equilibrium (Table 10).

The computed ^{238}U activity value (323.8 pCi) at 0.3 m is in secular equilibrium with the detected ^{234}Pa activity value (392 pCi), whereas the computed ^{238}U activity value (446.7 pCi) at 1 m is in secular equilibrium with the detected ^{234}Pa activity value (486 pCi) (Table 10).

S-3) Station S-3 is situated downwind of station S-2. Elements detected by the EMPA in the wind gust simulation sediment infer that minerals smithsonite and calcite were present (Appendices A). These findings coincide with the XRD findings in which calcite, quartz, orthoclase, albite, kaolinite, hematite (ferric oxide Fe^{3+}), and smithsonite were quantified (Table 6). Oxyhydroxides (Fe^{3+}) are potential sorbents for uranium and they commonly occur in sediments having strong sorptive behavior toward U^{6+} (Langmuir, 1997). The EMPA also detected Si, Ca, and U pertaining to the uranophane particle (Figures 35 and 36) found in the accreted sediment at S-3 in the saltating zone (0.3 m). The uranophane particle was the source of progeny radionuclides ^{226}Ra , ^{214}Pb , ^{214}Bi , and ^{210}Pb . The EMPA did not reveal any evidence of U^{6+} sorption by kaolinite, hematite, or limonite. Kaolinite a negatively charged clay mineral with O^{2-} and (OH^-) ; hematite is an oxyhydroxide (Fe^{3+}) with a sorptive bias, and limonite is an iron oxide-hydroxide with (OH^-) .

The particle size analysis reflecting all the modes of collection (wind gust simulation, topsoil, and accreted sediment) indicate there is an ample volume percentage of fine particles $< 4 \mu\text{m}$ at S-3 (Figure 13 bottom graph; Figure 14 bottom graph; Figure 17 bottom graph; Table 7). The uranophane particle (Figure 35) has an “L” shape ($\sim 20 \mu\text{m} \times 5 \mu\text{m}$) which falls within the short-term suspension range (20 – 70 μm) (Pye, 1987).

The gamma-ray spectroscopy results detected the ^{210}Pb radionuclide with an activity level of 10.6 pCi in sediment collected at 1 m height. Similar to S-2, some daughter radionuclides (^{226}Ra , ^{214}Pb , ^{214}Bi , and ^{210}Pb) within the ^{238}U decay chain (Table 13) were detected in sediment collected at 0.3 m (Table 10). Activity levels of ^{214}Pb (5.28 pCi) and ^{214}Bi (4.8 pCi) are almost equal due to their short

half-lives; moreover, activity levels of ^{226}Ra (14.2 pCi) and ^{210}Pb (10.0 pCi) are also almost equal but with longer half-lives. However, the uncertainty values are greater for ^{210}Pb and ^{226}Ra than for ^{214}Bi and ^{214}Pb . This suggests secular equilibrium is plausible for ^{226}Ra , ^{214}Pb , ^{214}Bi , and ^{210}Pb at S-3, particularly when compared to the same four radionuclides at S-2 which are much closer to secular equilibrium (Tables 10, 11). These findings suggest these radionuclides were transported by wind in the saltating zone (0.3 m) from the upwind station S-2.

The AP-42 PM emissions factor (E) equation results entailed assumptions such as vehicle type, speed, and weight (Table 2). The silt percentage values 26.65% and 38.42% utilized in this study correspond to sediment from S-1 and S-2, respectively. Particulate emissions from unpaved roads bearing uranium bearing soil will vary depending on the above factors and site meteorology. Computation results indicate that speed, number of wheels, and weight of the vehicle were the factors which most influenced PM10 emissions.

Radioactivity/distance computations were determined by applying the detected activity level differentials of ^{226}Ra , ^{214}Pb , ^{214}Bi , and ^{210}Pb over the 89 m distance between S-2 and S-3 to equations (10) and (11). The resulting projected distances ranged between 91.3 – 99.8 m. This suggests the activity levels of these uranium progeny radionuclides are near zero approximately at the 100 m mark. Specifically, westerly aeolian processes did not transport significant amounts of radionuclide carrier particles or minerals (e.g., uranophane) beyond 100 m from S-2 over the 2.4 year period. Therefore, this radionuclide migration range is considered to be significantly localized.

The measured maximum spring wind speed from the west (18.7 ms^{-1}) yielded friction velocity (u_*) ranges ($2.49 - 6.81 \text{ ms}^{-1}$) which exceeded friction velocity ranges ($0.2 - 0.6 \text{ ms}^{-1}$) (Pye, 1987). Hypothetically, this indicates that medium and coarse silt grains ($20 - 100 \mu\text{m}$) would encounter short-term suspension and modified saltation (Pye, 1987). Conversely, the measured minimum summer wind speed from the east (0.71 ms^{-1}) would not eject medium or coarse silt grains ($20 - 100 \mu\text{m}$).

6. Conclusions

These studies revealed localized migration patterns of radioactive particle matter from S-2 to S-3 via natural aeolian processes. Radioactivity levels detected at the three stations by the gamma spectrometry analysis fell in the rank order of S-2 > S-3 > S-1. Since S-1 is upwind of S-2, less radioactivity was detected at S-1 than at the downwind station S-3. The radionuclides detected at S-2 by the gamma analysis are also within the ^{238}U and ^{235}U decay chains (Table 13). As expected, S-2 had the highest activity levels. Since S-3 is downwind of S-2, more radioactivity was detected at S-3 in the saltating zone than upwind at station S-1. EMPA detected uranophane ranging between 20 – 300 μm at S-2 (Figures 22 and 33) and S-3 (Figure 35) and a 10 μm carnotite particle.

Based on the activity levels of ^{226}Ra , ^{214}Pb , ^{214}Bi , and ^{210}Pb detected at S-2 and S-3 in the saltating zone at 0.3 m, empirically computed radionuclide migration limits (91.3 – 99.8 m) marginally exceeded the 89 m distance between S-1 and S-3 over a 2.4 year period. The activity levels at S-1 and S-3 at 1 m had a comparable nuclide activity baseline which ranged between 8.5 and 10.6 pCi, respectively. This is indicative that minimal radionuclide carrier particles suspended above 1 m and the bulk of radionuclide displacement occurred in the saltation zone (0.3 m).

Radionuclide displacements presumably occurred during spring seasons when conditions are typically arid and dynamic aeolian processes lead to copious dust loadings (Gillette, 1999; Gillette and Chen, 2001; Novlan et al., 2007; Perez and Gill, 2009). Weather station data revealed measured maximum spring wind speeds (18.7 ms^{-1}) greatly exceeded the 5 ms^{-1} necessary for sand grains to mobilize (Bagnold, 1954) and computed friction velocity (u_*) ranges ($2.49 - 6.81 \text{ ms}^{-1}$) had a large margin over friction velocity thresholds ($0.2 - 0.6 \text{ ms}^{-1}$) necessary for short-term suspension or modified saltation to occur (Pye, 1987). Such wind strengths would eject medium and coarse silt grains (20 – 100 μm) (Pye, 1987), whereas measured minimum summer wind speeds (0.71 ms^{-1}) lack the strength necessary to eject particles this size.

In summary, this study has yielded valuable data regarding the emission and depositional behavior of radionuclides from exposed uranium ore stockpiles in remote arid locations. Enrichment Factor (EF) values for U were approximately 309 – 400 greater at S-2 than at background levels. Based on the radionuclide activity levels provided by the gamma-ray spectroscopy analysis, the 2.4 year migration of radionuclides from S-2 was minimal and localized, and displayed an eastward asymmetrical pattern nearly paralleling predominant westerly wind direction vectors. Peña Blanca's rough terrain tends to enhance wind potency and subsequently promote radionuclide displacement. These findings can aid scientists better understand radionuclide migration behavior in comparative terms, that is, radionuclide migration under localized aeolian processes in contrast to intercontinental trade wind and jet stream pathways needs to be better understood. Moreover, the AP-42 PM emissions factor (E) equation can be applied to active and inactive uranium mining operations worldwide; and with a renewed global interest in nuclear reactor construction, these results have important implications in terms of public health and safety.

Tables

Table 5: Sample index for all samples collected with corresponding analysis techniques.

Experiment	Field Situation	Laboratory Studies					Data Processing				
Collection Method	Stations and Heights	XRD	PSA	EMPA	ICP	γ -ray	HF	AP-42	Distance/Radiation Decrease	U-238 Activity	Friction Velocity
Long Term Accretion	S-1 (0.3 m)		Figures 15, 42			Tables 10-11; Figure 45	Table 1			Table 10	Table 4
	S-1 (1m)		Figures 15, 42			Tables 10-11; Figure 45	Table 1			Table 10	
	S-2 (0.3 m)		Figures 16, 42	Figures 33-34, 43		Tables 10-11; Figure 45	Table 1		Table 3	Table 10	
	S-2 (1m)		Figures 16, 42			Tables 10-11; Figure 45	Table 1			Table 10	
	S-3 (0.3 m)		Figures 17, 42	Figures 35-36, 43		Tables 10-11; Figure 45	Table 1		Table 3	Table 10	
	S-3 (1m)		Figures 17, 42			Tables 10-11; Figure 45	Table 1			Table 10	
Simulated Wind Gust	S-1	Table 6; Figure 10	Figure 13; Table 7	Figures 18-21, 43; Appendix A and B							
	S-2	Table 6; Figure 11	Table 7; Figure 13	Figures 22-28, 43; Appendix A and B							
	S-3	Table 6; Figure 12	Table 7; Figure 13	Figures 29-32, 43; Appendix A and B							
Topsoil Scoop	S-1	Figure 43	Table 7; Figure 14		Tables 8-9; Figures 37-41, 44			Table 2			
	S-2	Figure 43	Table 7; Figure 14		Tables 8-9; Figures 37-41, 44			Table 2			
	S-3	Figure 43	Table 7; Figure 14								

Table 6: X-Ray diffraction mineralogy results for stations S-1, S-2, and S-3.

S-1 Mineralogy		
Mineral	Mineral Equation	Concentrations in weight percent
Quartz	SiO_2	51.57
Calcite	CaCO_3	3.91
Orthoclase	$\text{K(AlSi}_3\text{)O}_8$	23.45
Albite	$(\text{Na}_{0.98}\text{Ca}_{0.02})(\text{Al}_{1.02}\text{Si}_{2.98}\text{O}_8)$	9.43
Dolomite	$\text{CaMg(CO}_3\text{)}_2$	0.7
Hematite	Fe_2O_3	1.64
Microcline	KAlSi_3O_8	4.82
Kaolinite	$\text{Al}_2(\text{Si}_2\text{O}_5)(\text{OH})_4$	4.48
S-2 Mineralogy		
Mineral	Mineral Equation	Concentrations in weight percent
Quartz	SiO_2	47.21
Calcite	CaCO_3	3.76
Orthoclase	$\text{K(AlSi}_3\text{)O}_8$	10.67
Albite	$(\text{Na}_{0.98}\text{Ca}_{0.02})(\text{Al}_{1.02}\text{Si}_{2.98}\text{O}_8)$	2.94
Kaolinite	$\text{Al}_2(\text{Si}_2\text{O}_5)(\text{OH})_4$	35
Uranophane	$\text{Ca(UO}_2\text{)}_2(\text{SiO}_3\text{OH})_2 \cdot 5\text{H}_2\text{O}$	0.33
Carnotite	KUO_2VO_4	0.08
Uraninite	UO_2	0.01

Table 6 cont'd

S-3 Mineralogy		
Mineral	Mineral Equation	Concentrations in weight percent
Quartz	SiO_2	23.8
Calcite	CaCO_3	45.13
Orthoclase	$\text{K(AlSi}_3\text{)O}_8$	17.93
Albite	$\text{Na(AlSi}_3\text{)O}_8$	6.15
Hematite	Fe_2O_3	0.57
Microcline	KAlSi_3O_8	1.27
Kaolinite	$\text{Al}_2(\text{Si}_2\text{O}_5)(\text{OH})_4$	5.12
Smithsonite	ZnCO_3	0.03

Table 7: Corresponding volume percentage values for PM1 to PM1000, sand, silt, and clay textures of simulated wind gust, topsoil, and accreted sediment at stations S-1, S-2, and S-3.

S-1 (Simulated Wind Gust)				
Sediment Type	PM Size	Percent	Sediment Textural Classes	Percent
Clay	2.5	5		
	4	7	Clay	7
Silt	10	13		
	20	17		
	30	19		
	62	25	Silt	17
Sand	70	26		
	75	27		
	100	30		
	300	60		
	500	82		
	1000	97	Sand	73
S-2 (Simulated Wind Gust)				
Sediment Type	PM Size	Percent	Sediment Textural Classes	Percent
Clay	2.5	10		
	4	17	Clay	17
Silt	10	26		
	20	30		
	30	32		
	62	37	Silt	20
Sand	70	38		
	75	38		
	100	41		
	300	63		
	500	78		
	1000	93	Sand	57
S-3 (Simulated Wind Gust)				
Sediment Type	PM Size	Percent	Sediment Textural Classes	Percent
Clay	2.5	9		
	4	13	Clay	13
Silt	10	21		
	20	26		
	30	29		
	62	35	Silt	23
Sand	70	37		
	75	38		
	100	42		
	300	61		
	500	73		
	1000	92	Sand	57

Table 7 cont'd

S-1 (Topsoil)				
Sediment Type	PM Size	Percent	Sediment Textural Classes	Percent
Clay	2.5	5		
	4	7	Clay	7
Silt	10	14		
	20	26		
	30	41		
	62	77	Silt	71
Sand	70	83		
	75	86		
	100	95		
	300	100		
	500	-		
	1000	-	Sand	23
S-2 (Topsoil)				
Sediment Type	PM Size	Percent	Sediment Textural Classes	Percent
Clay	2.5	12		
	4	20	Clay	20
Silt	10	40		
	20	55		
	30	67		
	62	89	Silt	69
Sand	70	92		
	75	94		
	100	98		
	300	100		
	500	-		
	1000	-	Sand	11
S-3 (Topsoil)				
Sediment Type	PM Size	Percent	Sediment Textural Classes	Percent
Clay	2.5	12		
	4	17	Clay	17
Silt	10	30		
	20	43		
	30	55		
	62	84	Silt	67
Sand	70	88		
	75	91		
	100	97		
	300	100		
	500	-		
	1000	-	Sand	16

Table 7 cont'd

S-1 (Accreted in top BSNE)				
Sediment Type	PM Size	Percent	Sediment Textural Classes	Percent
Clay	2.5	9		
	4	13	Clay	13
Silt	10	25		
	20	41		
	30	53		
	62	76	Silt	62
Sand	70	79		
	75	80		
	100	86		
	300	96		
	500	99		
	1000	100	Sand	24
S-1 (Accreted in bottom BSNE)				
Sediment Type	PM Size	Percent	Sediment Textural Classes	Percent
Clay	2.5	7		
	4	11	Clay	11
Silt	10	21		
	20	34		
	30	45		
	62	64	Silt	53
Sand	70	67		
	75	69		
	100	75		
	300	93		
	500	98		
	1000	100	Sand	36

Table 7 cont'd

S-2 (Accreted in top BSNE)				
Sediment Type	PM Size	Percent	Sediment Textural Classes	Percent
Clay	2.5	11		
	4	16	Clay	16
Silt	10	27		
	20	42		
	30	53		
	62	76	Silt	60
Sand	70	79		
	75	81		
	100	87		
	300	97		
	500	99		
	1000	100	Sand	24
S-2 (Accreted in bottom BSNE)				
Sediment Type	PM Size	Percent	Sediment Textural Classes	Percent
Clay	2.5	10		
	4	15	Clay	15
Silt	10	26		
	20	38		
	30	47		
	62	65	Silt	51
Sand	70	68		
	75	70		
	100	75		
	300	89		
	500	92		
	1000	98	Sand	33

Table 7 cont'd

S-3 (Accreted in top BSNE)				
Sediment Type	PM Size	Percent	Sediment Textural Classes	Percent
Clay	2.5	10		
	4	14	Clay	14
Silt	10	26		
	20	42		
	30	54		
	62	75	Silt	61
Sand	70	78		
	75	80		
	100	86		
	300	96		
	500	98		
	1000	99	Sand	24
S-3 (Accreted in bottom BSNE)				
Sediment Type	PM Size	Percent	Sediment Textural Classes	Percent
Clay	2.5	10		
	4	14	Clay	14
Silt	10	25		
	20	36		
	30	44		
	62	60	Silt	46
Sand	70	62		
	75	64		
	100	70		
	300	89		
	500	95		
	1000	99	Sand	39

Table 8: ICP-MS results of major and trace element concentrations for topsoil fine (< 75 μm) and coarse (75 μm – 1,000 μm) sediment for stations S-1 and S-2. There are six replicate sediment samples (three fine and three coarse) representing S-1 and S-2.

Analyte Symbol	SiO ₂	Al ₂ O ₃	Fe ₂ O ₃ (T)	MnO	MgO	CaO	Na ₂ O	K ₂ O	TiO ₂	P ₂ O ₅	LOI	Total
Unit Symbol	%	%	%	%	%	%	%	%	%	%	%	%
Detection Limit	0.01	0.01	0.01	0.001	0.01	0.01	0.01	0.01	0.001	0.01		0.01
Analysis Method	FUS-ICP	FUS-ICP	FUS-ICP	FUS-ICP	FUS-ICP	FUS-ICP	FUS-ICP	FUS-ICP	FUS-ICP	FUS-ICP	FUS-ICP	FUS-ICP
101 sample from S-1 (75 μm size)	60.33	10.98	3.59	0.067	0.83	6.21	1.23	3.41	0.738	0.1	13.43	100.9
102 sample from S-1 (75 μm size)	60.86	10.93	3.63	0.068	0.81	6.02	1.26	3.44	0.799	0.09	12.92	100.8
103 sample from S-1 (75 μm size)	60.48	11.05	3.64	0.067	0.81	6.02	1.26	3.44	0.781	0.11	13.18	100.8
104 sample from S-1 (75-1,000 μm size)	68.62	10.02	2.96	0.085	0.44	4.2	1.29	4.4	0.452	0.07	7.83	100.3
105 sample from S-1 (75-1,000 μm size)	67.67	9.96	2.89	0.071	0.44	4.61	1.33	4.45	0.441	0.05	8.26	100.2
106 sample from S-1 (75-1,000 μm size)	69.29	9.78	3.01	0.068	0.42	4.3	1.34	4.46	0.492	0.04	6.96	100.2
107 sample from S-2 (75 μm size)	58.98	17.58	4.45	0.045	0.34	3.18	0.21	1.34	0.409	0.11	11.09	97.72
108 sample from S-2 (75 μm size)	58.85	17.21	4.34	0.046	0.33	3.15	0.21	1.33	0.405	0.11	11.02	97
109 sample from S-2 (75 μm size)	60.52	17.73	4.43	0.047	0.33	3.21	0.21	1.38	0.413	0.11	11.07	99.46
110 sample from S-2 (75-1,000 μm size)	67.54	14.85	4.54	0.029	0.2	1.64	0.33	1.51	0.33	0.1	9.01	100.1
111 sample from S-2 (75-1,000 μm size)	66.27	15.1	4.46	0.03	0.21	1.86	0.33	1.48	0.329	0.09	9.32	99.48
112 sample from S-2 (75-1,000 μm size)	65.84	15.17	4.45	0.034	0.21	1.8	0.31	1.33	0.327	0.08	9.25	98.79

Table 8 cont'd

Analyte Symbol	Au	Ag	As	Ba	Be	Bi	Br	Cd	Co	Cr	Cs	Cu	Hf	Hg	Ir	Mo	Ni	Pb	Rb	Sb
Unit Symbol	ppb	ppm	ppm	ppm	ppm	ppm	ppm	ppm	ppm	ppm	ppm	ppm	ppm	ppm	ppb	ppm	ppm	ppm	ppm	ppm
Detection Limit	1	0.5	1	1	1	2	0.5	0.5	0.1	0.5	0.2	1	0.2	1	1	2	1	5	10	0.1
Analysis Method	INAA	MULT INAA / TD-ICP	INAA	FUS- ICP	FUS- ICP	TD- ICP	INAA	TD- ICP	INAA	INAA	INAA	TD- ICP	INAA	INAA	INAA	TD- ICP	TD- ICP	TD- ICP	INAA	INAA
101 sample from S-1 (75 μ m size)	< 1	< 0.5	19	416	3	< 2	11.1	0.7	5.9	37.8	11.3	24	13.7	< 1	< 1	< 2	15	25	140	1.6
102 sample from S-1 (75 μ m size)	< 1	< 0.5	20	420	3	< 2	11.3	0.6	6.2	44.6	11.3	17	16.1	< 1	< 1	< 2	14	25	140	1.6
103 sample from S-1 (75 μ m size)	2	< 0.5	27	416	3	< 2	15.2	0.7	8	55.5	16	12	21.2	< 1	< 1	< 2	15	25	200	2.4
104 sample from S-1 (75-1,000 μ m size)	< 1	< 0.5	32	320	4	< 2	6.6	< 0.5	4.1	26.1	11.3	6	11.4	< 1	< 1	< 2	8	45	220	1.8
105 sample from S-1 (75-1,000 μ m size)	< 1	< 0.5	24	309	3	< 2	5.5	< 0.5	3.8	20.9	9	6	8	< 1	< 1	< 2	7	19	160	1.2
106 sample from S-1 (75-1,000 μ m size)	< 1	< 0.5	25	312	3	< 2	4.9	< 0.5	4.6	19.1	12.2	5	10.4	< 1	< 1	4	8	26	170	1.4
107 sample from S-2 (75 μ m size)	50	21.9	540	443	3	< 2	3.5	7.5	17	96.3	8	61	25.3	< 1	< 1	398	64	687	50	31
108 sample from S-2 (75 μ m size)	132	18.2	651	436	2	< 2	5.3	7.4	19.1	111	9.1	70	30.5	< 1	< 1	401	67	682	60	36.8
109 sample from S-2 (75 μ m size)	85	17.1	638	487	3	< 2	5.2	7.6	19.8	112	8.8	60	29.3	< 1	< 1	410	67	710	50	36.8
110 sample from S-2 (75-1,000 μ m size)	< 1	14.5	717	309	3	< 2	< 0.5	6.1	20.5	162	9.6	37	17.2	< 1	< 1	261	32	513	< 10	22.5
111 sample from S-2 (75-1,000 μ m size)	43	11.1	532	304	2	< 2	4.2	6.4	15.2	111	7	41	20.8	< 1	< 1	330	29	616	50	21.1
112 sample from S-2 (75-1,000 μ m size)	< 1	8.2	751	325	3	< 2	< 0.5	6.7	19.4	143	9.3	44	16.9	< 1	< 1	287	33	608	< 10	22.3

Table 8 cont'd

Analyte Symbol	Sr	Ta	Th	U	V	W	Y	Zn	Zr	La	Ce	Nd	Sm	Eu	Tb	Yb	Lu	Mass
Unit Symbol	ppm	ppm	ppm	ppm	ppm	ppm	ppm	ppm	ppm	ppm	ppm	ppm	ppm	ppm	ppm	ppm	ppm	g
Detection Limit	2	0.3	0.1	0.1	5	1	1	1	2	0.05	1	1	0.01	0.05	0.1	0.05	0.01	
Analysis Method	FUS-ICP	INAA	INAA	INAA	FUS-ICP	INAA	FUS-ICP	MULT INAA / TD-ICP	FUS-ICP	INAA	INAA	INAA	INAA	INAA	INAA	INAA	INAA	INAA
101 sample from S-1 (75 μ m size)	149	1.3	16	5.9	54	< 1	30	78	596	31.7	64	35	3.46	1.23	< 0.1	3.69	0.73	1.621
102 sample from S-1 (75 μ m size)	148	1.8	16.9	6.6	56	< 1	29	80	611	34.9	69	32	3.69	1.31	< 0.1	4.06	0.78	1.538
103 sample from S-1 (75 μ m size)	149	1.6	23.6	8.5	57	< 1	30	77	657	46.5	91	48	4.65	1.71	1	5.57	1.05	1.144
104 sample from S-1 (75-1,000 μ m size)	97	1.7	21.9	8.3	34	< 1	50	57	382	43.7	65	36	4.07	1.09	0.8	4.45	0.82	1.037
105 sample from S-1 (75-1,000 μ m size)	95	1.5	17.4	6.5	30	< 1	31	51	274	33.2	67	35	2.96	0.84	0.6	3.5	0.64	1.209
106 sample from S-1 (75-1,000 μ m size)	92	1.4	17.2	12.6	31	4	30	55	339	38.2	78	33	5.71	0.91	1	3.84	0.47	1.265
107 sample from S-2 (75 μ m size)	326	< 0.3	27.8	1910	432	31	128	1610	1128	136	312	383	39.5	< 0.05	2.9	9.13	< 0.01	1.388
108 sample from S-2 (75 μ m size)	310	2.9	33.7	2300	422	37	121	1620	1067	164	334	465	48.2	< 0.05	3.5	10	< 0.01	1.248
109 sample from S-2 (75 μ m size)	317	2.3	33.8	2280	433	35	123	1660	1110	162	352	461	48	< 0.05	3.3	11	< 0.01	1.123
110 sample from S-2 (75-1,000 μ m size)	225	< 0.3	27.1	4620	279	36	77	1220	728	230	< 1	< 1	< 0.01	< 0.05	1.4	6.52	< 0.01	1.083
111 sample from S-2 (75-1,000 μ m size)	217	2.9	25.3	2550	281	31	82	1280	772	146	301	543	49.9	< 0.05	2.1	6.96	< 0.01	1.11
112 sample from S-2 (75-1,000 μ m size)	222	< 0.3	26.7	3760	318	36	80	1280	714	198	< 1	< 1	< 0.01	< 0.05	< 0.1	7.59	< 0.01	1.117

Table 9: The enrichment factor is the element concentration ratio between stations S-1 and S-2 (Enrichment Factor = S-2 concentration/S-1 concentration). Averaged concentration values were taken from Table 8. Enrichment factor values are approximate.

Strongly Enriched Elements														
Element	Au	Ag	As	Cr	Cu	Mo	Ni	Pb	Sb	Sr	U	V	W	Y
Enrichment Factor (75μm size)	135	19	28	2.5	4	403	4.5	28	18	2	309	8	34	4
Enrichment Factor (75-1,000 μm size)	14	11	25	6	7	225	4	19	15	2	400	9	26	2
Element	Zn	Zr	La	Ce	Nd									
Enrichment Factor (75μm size)	21	2	4	4.5	11									
Enrichment Factor (75-1,000 μm size)	23	2	5	1.5	5									
Element	Br	Cd	Co	Rb	Th	Tb	Yb	Lu						
Enrichment Factor (75μm size)	0.5	11	3	0.5	2	10	2	0						
Enrichment Factor (75-1,000 μm size)	0.25	6.5	4.5	0.1	1.5	1.5	2	0						

Table 10: Radionuclide, corresponding activity, and sediment mass list for bottom (0.3 m) and top (1 m) BSNE pans for stations S-1, S-2, and S-3.

Nuclide	Activity (pCi)	Uncertainty (pCi)	Uncertainty (%)	Sediment mass (g)	Activity/Sediment Mass (pCi/g)
S-1 top (1 m) BSNE pan					
Pb-210	8.5	3.5	41	0.54	15.7
S-1 bottom (0.3 m) BSNE pan					
none	0	-	-	1.39	0.0
S-2 top (1 m) BSNE pan					
U-238	446.7	-	-	0.51	875.9
Pa-234	486	83	17	0.51	952.9
Ra-226	87	30	35	0.51	170.6
Pb-214	156	2.0	1	0.51	305.9
Bi-214	168	2.4	1	0.51	329.4
Pb-210	128	16	13	0.51	251.0
U-235	20	1.7	9	0.51	39.2
Bi-211	15.1	8.2	54	0.51	29.6
S-2 bottom (0.3 m) BSNE pan					
U-238	323.8	-	-	1.1	294.4
Pa-234	392	115	29	1.1	356.4
Ra-226	131	22	17	1.1	119.1
Pb-214	175	1.9	1	1.1	159.1
Bi-214	193	3.1	2	1.1	175.5
Pb-210	143	17	12	1.1	130.0
U-235	14.5	0.83	6	1.1	13.2
Bi-211	0.71	0.26	37	1.1	0.6
S-3 top (1 m) BSNE pan					
Pb-210	10.6	3.6	34	0.52	20.4
S-3 bottom (0.3 m) BSNE pan					
Ra-226	14.2	3.3	23	1.18	12.0
Pb-214	5.28	0.42	8	1.18	4.5
Bi-214	4.8	0.56	12	1.18	4.1
Pb-210	10.0	2.2	22	1.18	8.5

Table 11: Progeny/Parent ratios for top (1 m) and bottom (0.3 m) BSNE pans at stations S-2 and S-3.

Station	Progeny/Parent	Ratio = Activity _{progeny} /Activity _{parent}
S-2 (at 1 m)	$^{210}\text{Pb}/^{214}\text{Bi}$	0.76
S-2 (at 1 m)	$^{214}\text{Bi}/^{214}\text{Pb}$	1.08
S-2 (at 1 m)	$^{226}\text{Ra}/^{234}\text{Pa(m)}$	0.18
S-2 (at 1 m)	$^{211}\text{Bi}/^{235}\text{U}$	0.76
S-2 (at 0.3 m)	$^{210}\text{Pb}/^{214}\text{Bi}$	0.74
S-2 (at 0.3 m)	$^{214}\text{Bi}/^{214}\text{Pb}$	1.10
S-2 (at 0.3 m)	$^{226}\text{Ra}/^{234}\text{Pa(m)}$	0.33
S-2 (at 0.3 m)	$^{211}\text{Bi}/^{235}\text{U}$	0.05
S-3 (at 0.3 m)	$^{210}\text{Pb}/^{214}\text{Bi}$	2.08
S-3 (at 0.3 m)	$^{214}\text{Bi}/^{214}\text{Pb}$	0.91

Table 12: Uranium Decay Series.

U-238			U-235		
Isotope	Emitted Particle	Half-life	Isotope	Emitted Particle	Half-life
$^{238}_{92}\text{U}$	α	4.47 (10) ⁹ y	$^{235}_{92}\text{U}$	α	7.038 (10) ⁸ y
$^{234}_{90}\text{Th}$	β^-	24.1 d	$^{231}_{90}\text{Th}$	β^-	1.063 d
$^{234}_{91}\text{Pa}$	β^-	1.17 min	$^{231}_{91}\text{Pa}$	α	3.248 (10) ⁴ y
$^{234}_{92}\text{U}$	α	2.48 (10) ⁵ y	$^{227}_{89}\text{Ac}$	β^-	21.77 y
$^{230}_{90}\text{Th}$	α	7.52 (10) ⁴ y	$^{227}_{90}\text{Th}$	α	18.72 d
$^{226}_{88}\text{Ra}$	α	1.60 (10) ³ y	$^{223}_{88}\text{Ra}$	α	11.435 d
$^{222}_{86}\text{Rn}$	α	3.8235 d	$^{219}_{86}\text{Rn}$	α	3.96 s
$^{218}_{84}\text{Po}$	α	3.10 min	$^{215}_{84}\text{Po}$	α	1.78 (10) ⁻³ s
$^{214}_{82}\text{Pb}$	β^-	27 min	$^{211}_{82}\text{Pb}$	β^-	36.1 min
$^{214}_{83}\text{Bi}$	β^-	19.9 min	$^{211}_{83}\text{Bi}$	α	2.14 min
$^{214}_{84}\text{Po}$	α	1.64 (10) ⁻⁴ s	$^{207}_{81}\text{Tl}$	β^-	4.77 min
$^{210}_{82}\text{Pb}$	β^-	22.3 y	$^{207}_{82}\text{Pb}$		Stable
$^{210}_{83}\text{Bi}$	β^-	5.01 d			
$^{210}_{84}\text{Po}$	α	138.38 d			
$^{206}_{82}\text{Pb}$		Stable			

Figures

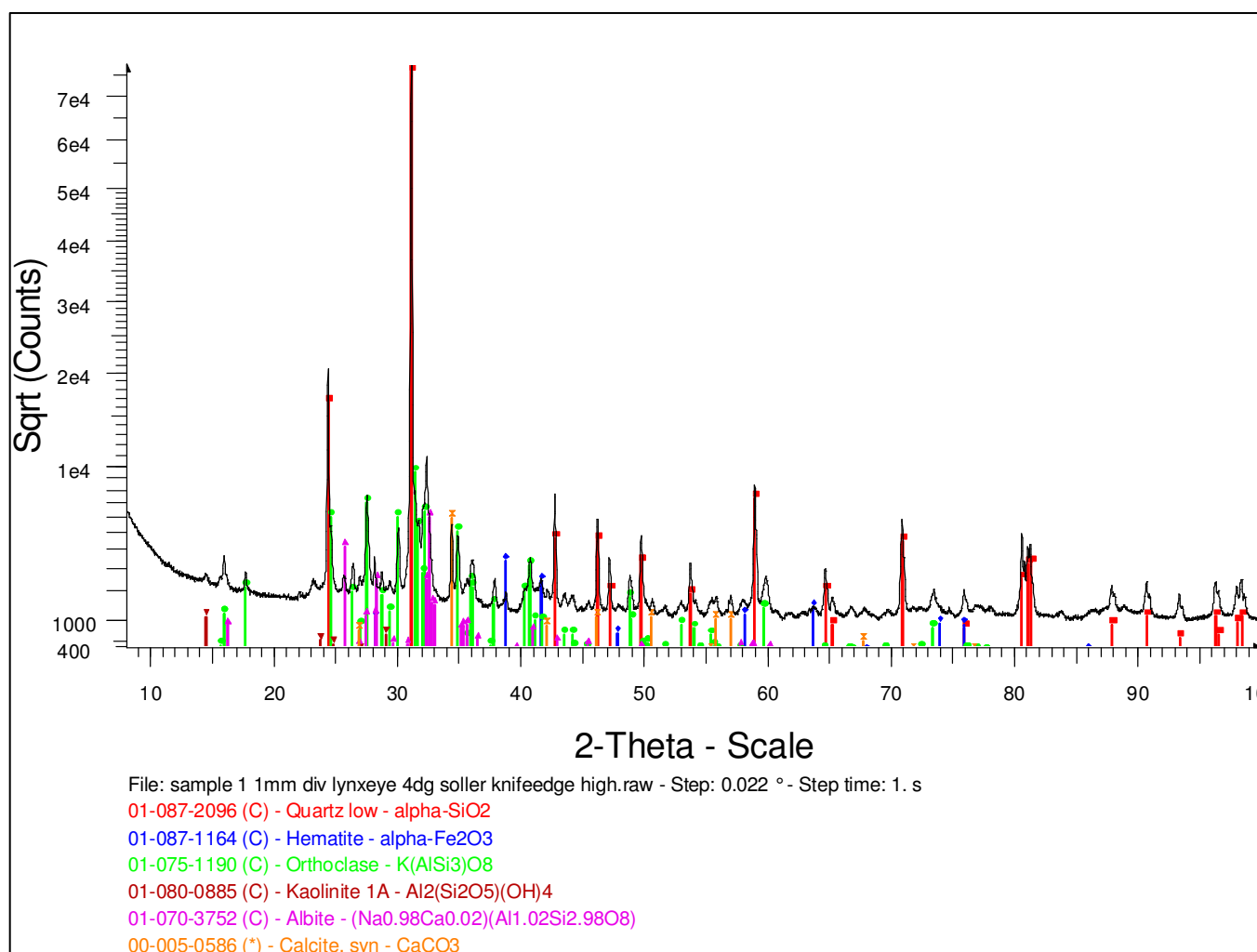


Figure 10: X-Ray Diffraction mineralogy diffractogram for station S-1.

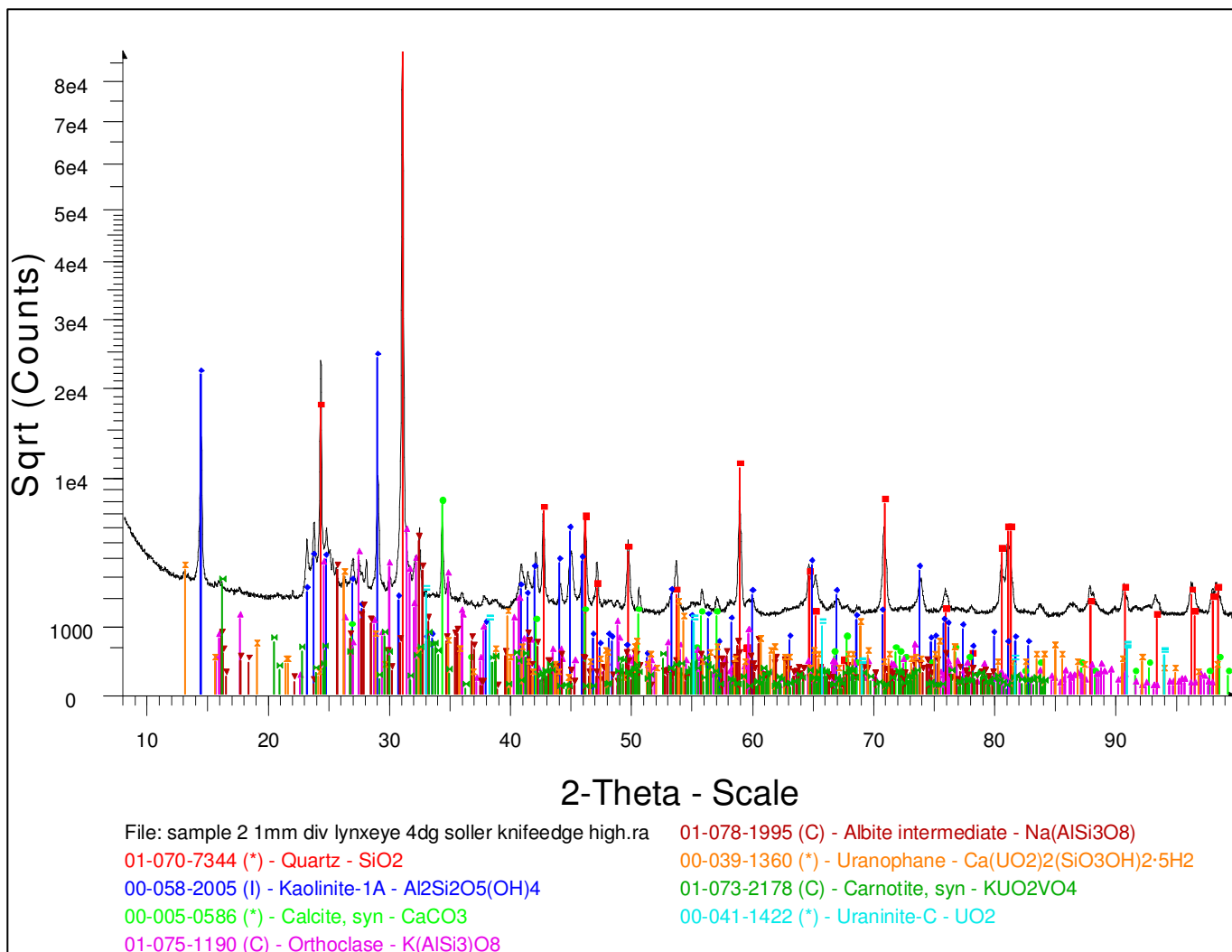


Figure 11: X-Ray Diffraction mineralogy diffractogram for station S-2.

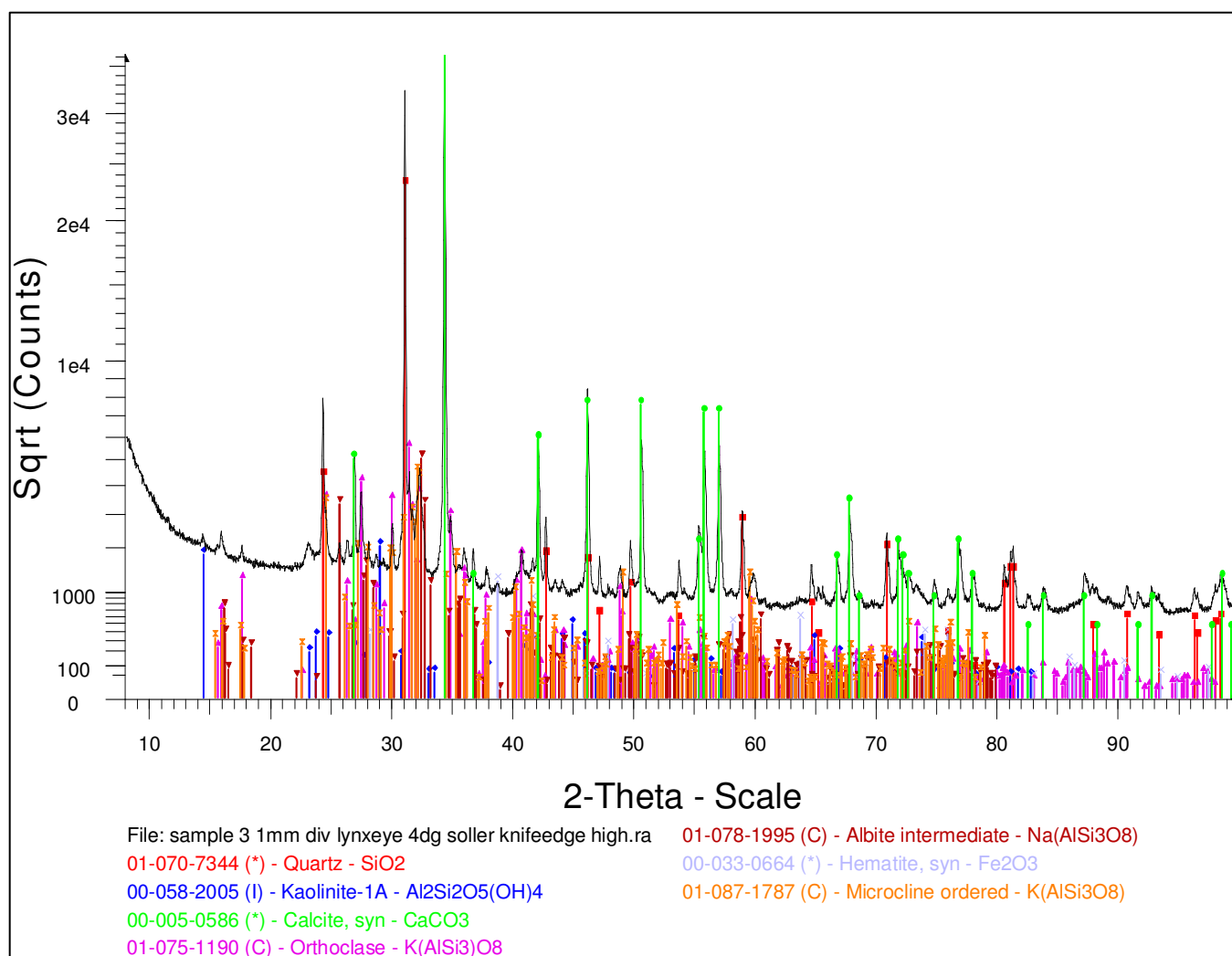


Figure 12: X-Ray Diffraction mineralogy diffractogram for station S-3.

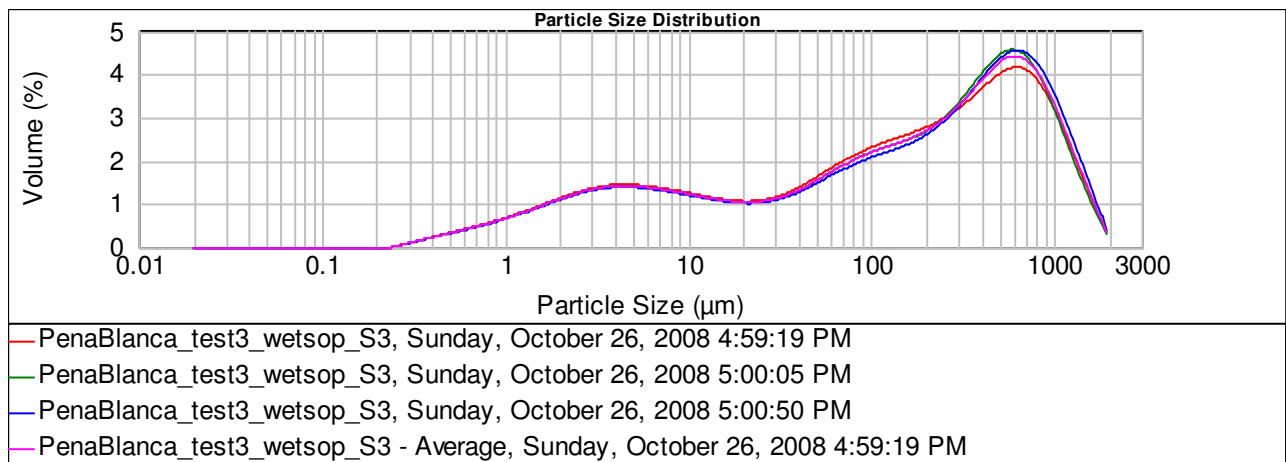
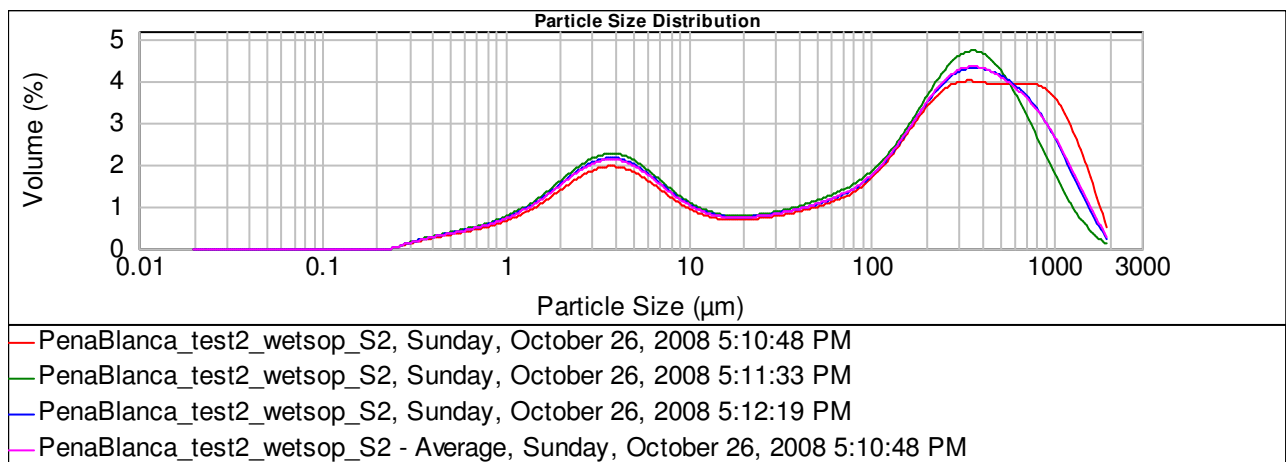
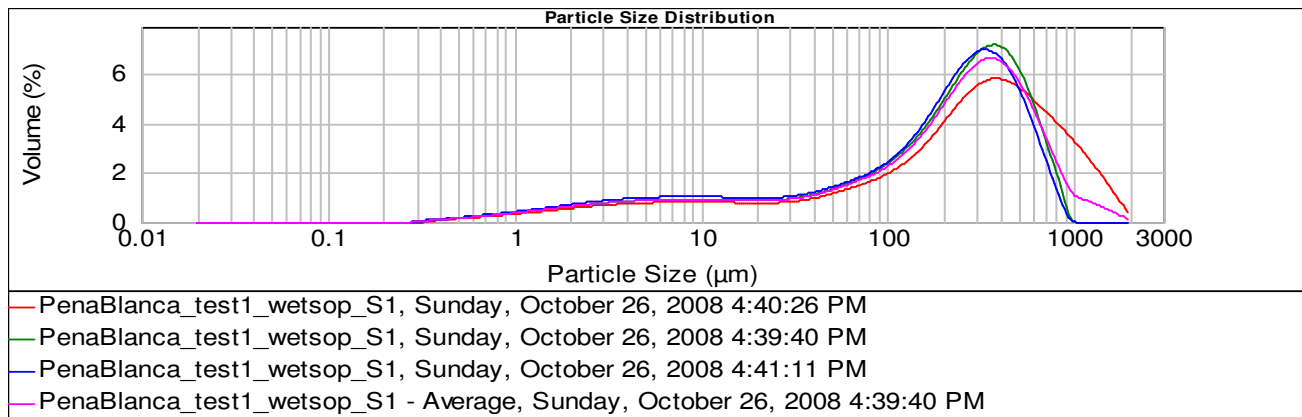


Figure 13: Volume percentage versus particle size distribution of a 0.5 g sample from the simulated wind gust at stations S-1 (top graph), S-2 (middle graph), and S-3 (bottom graph).

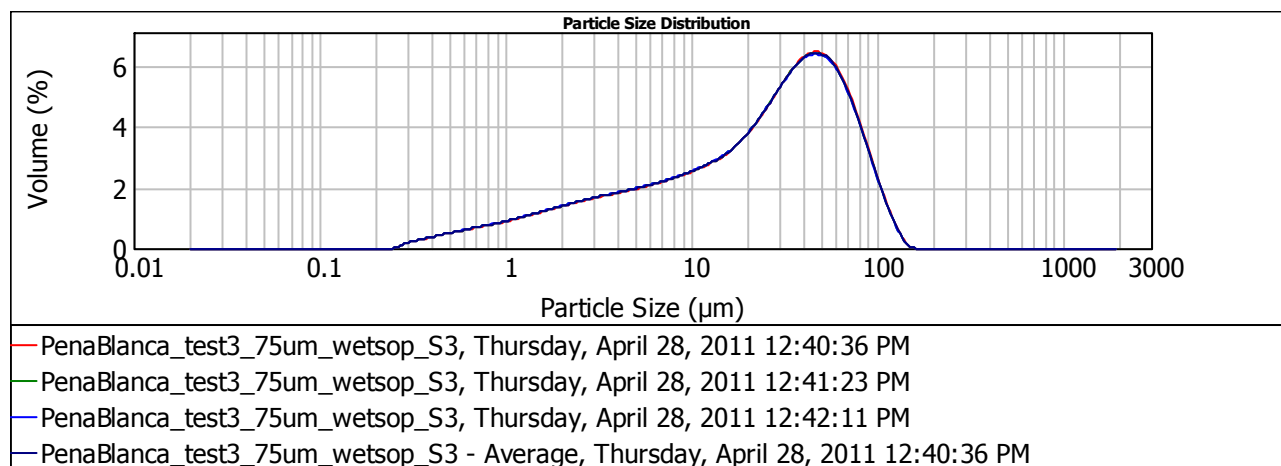
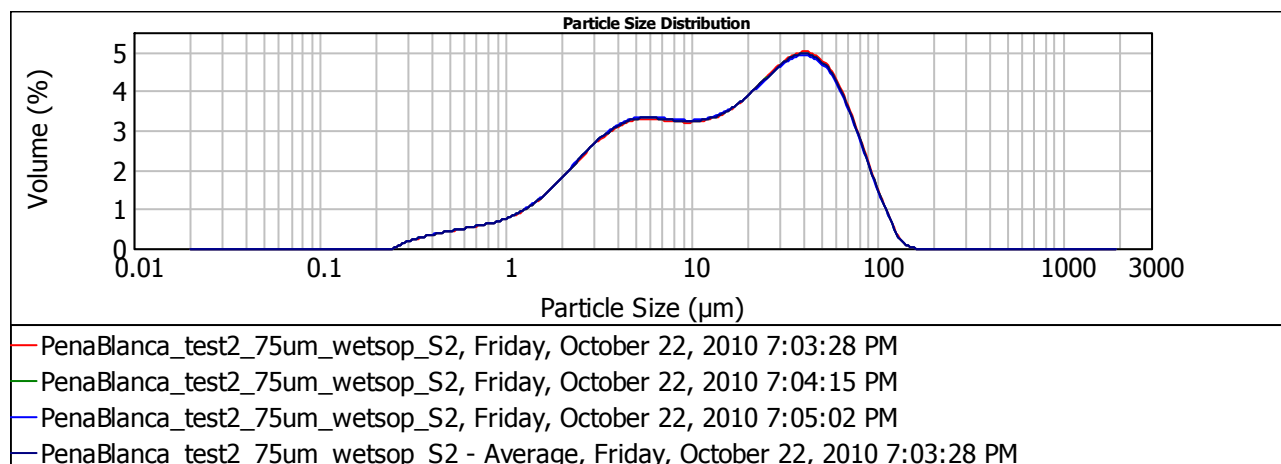
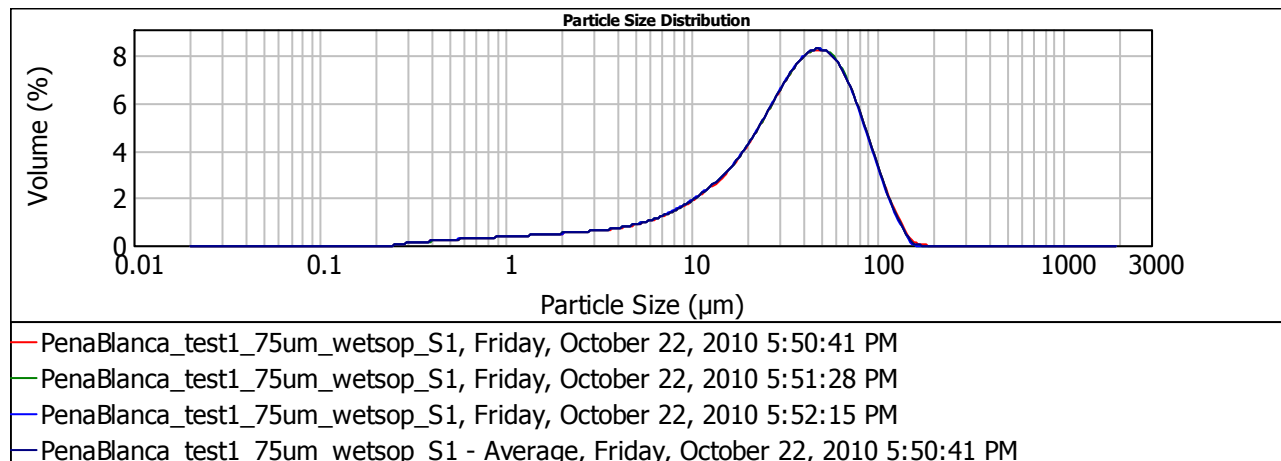


Figure 14: Volume percentage versus particle size distribution of a 0.5 g sample from topsoil at stations S-1 (top graph), S-2 (middle graph), and S-3 (bottom graph).

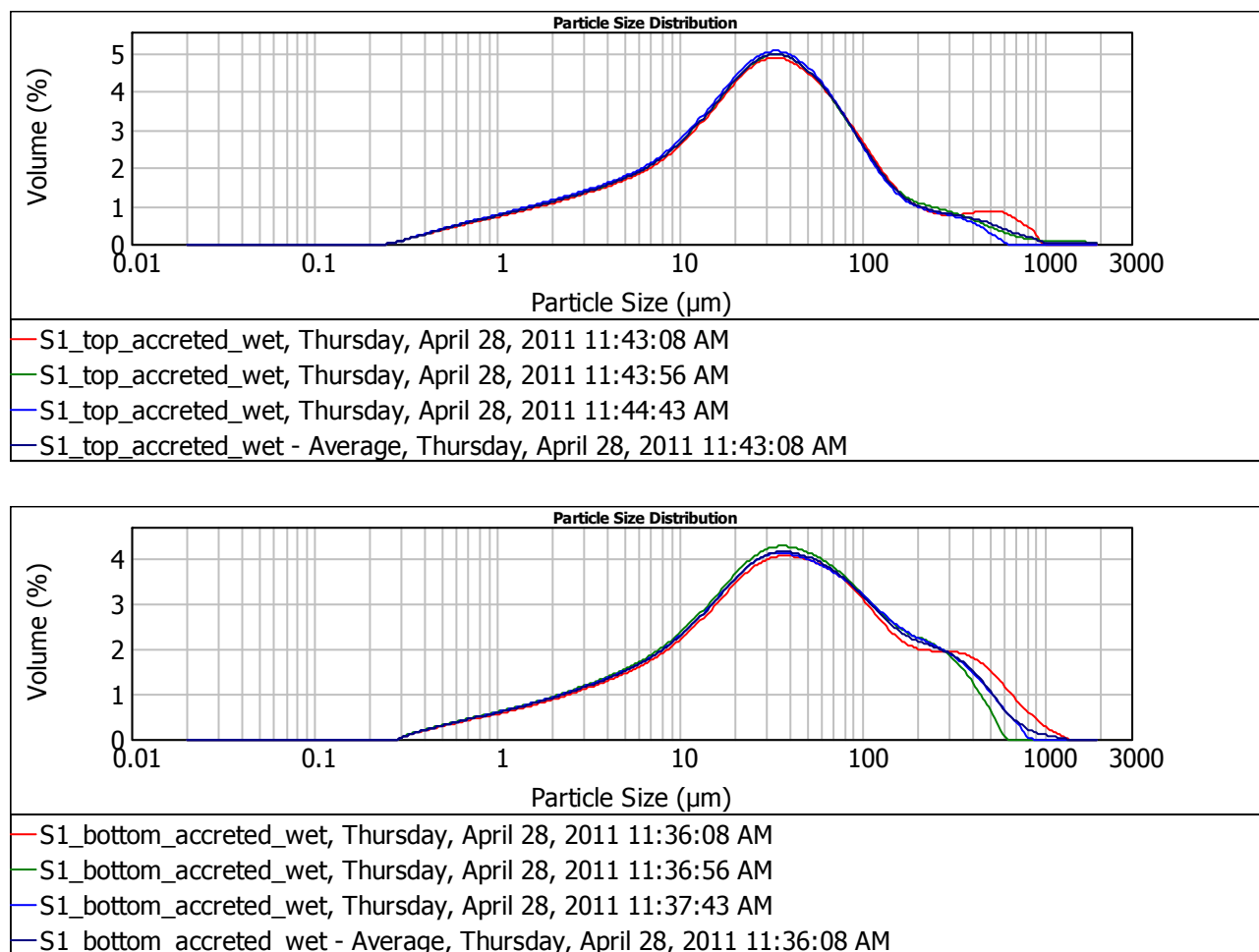


Figure 15: Volume percentage versus particle size distribution of a ~ 0.12 g sample from accreted sediment at station S-1 for the top (1 m) BSNE pan (top graph) and bottom (0.3 m) BSNE pan (bottom graph).

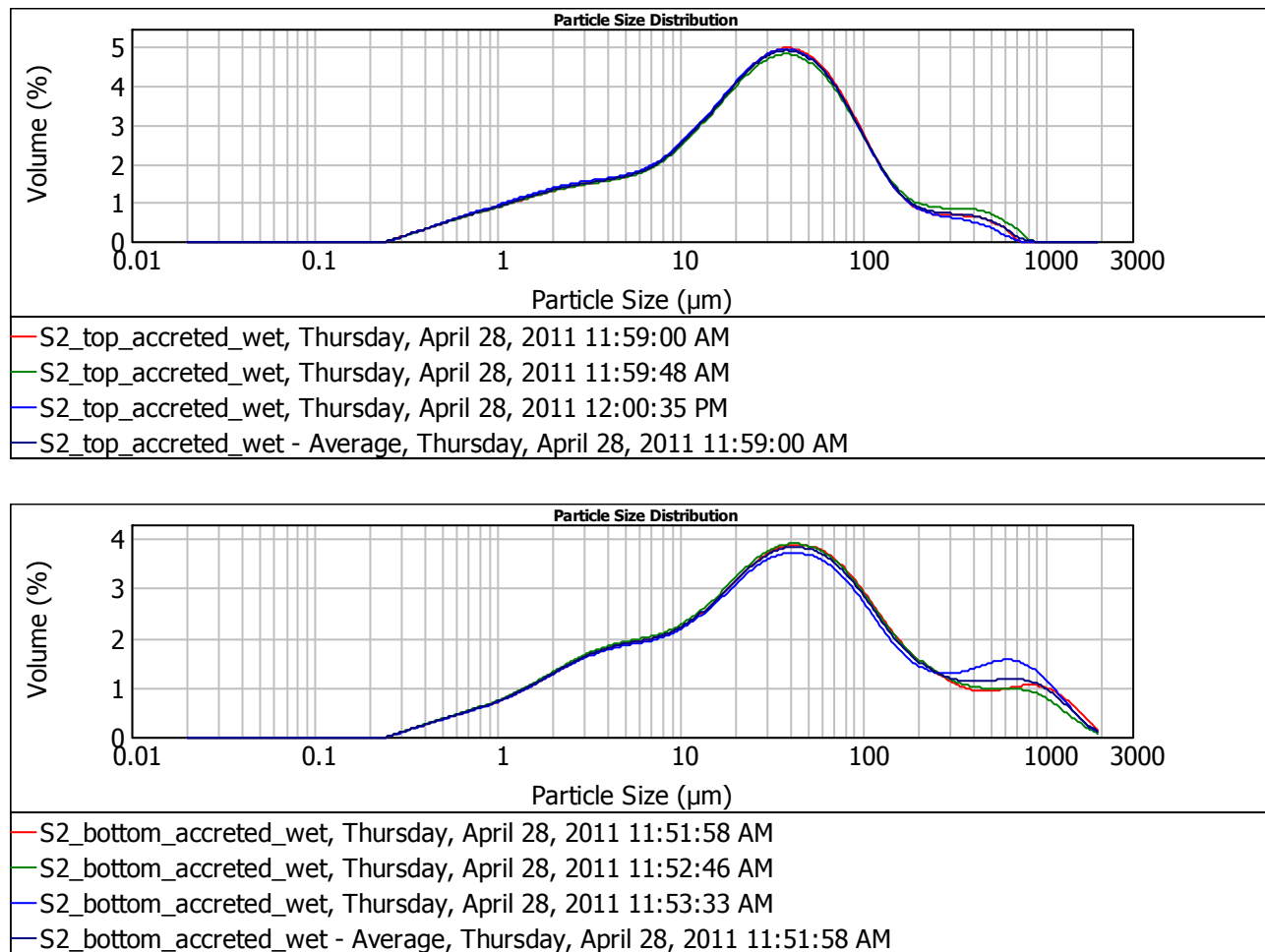


Figure 16: Volume percentage versus particle size distribution of a ~ 0.12 g sample from accreted sediment at station S-2 for the top (1 m) BSNE pan (top graph) and bottom (0.3 m) BSNE pan (bottom graph).

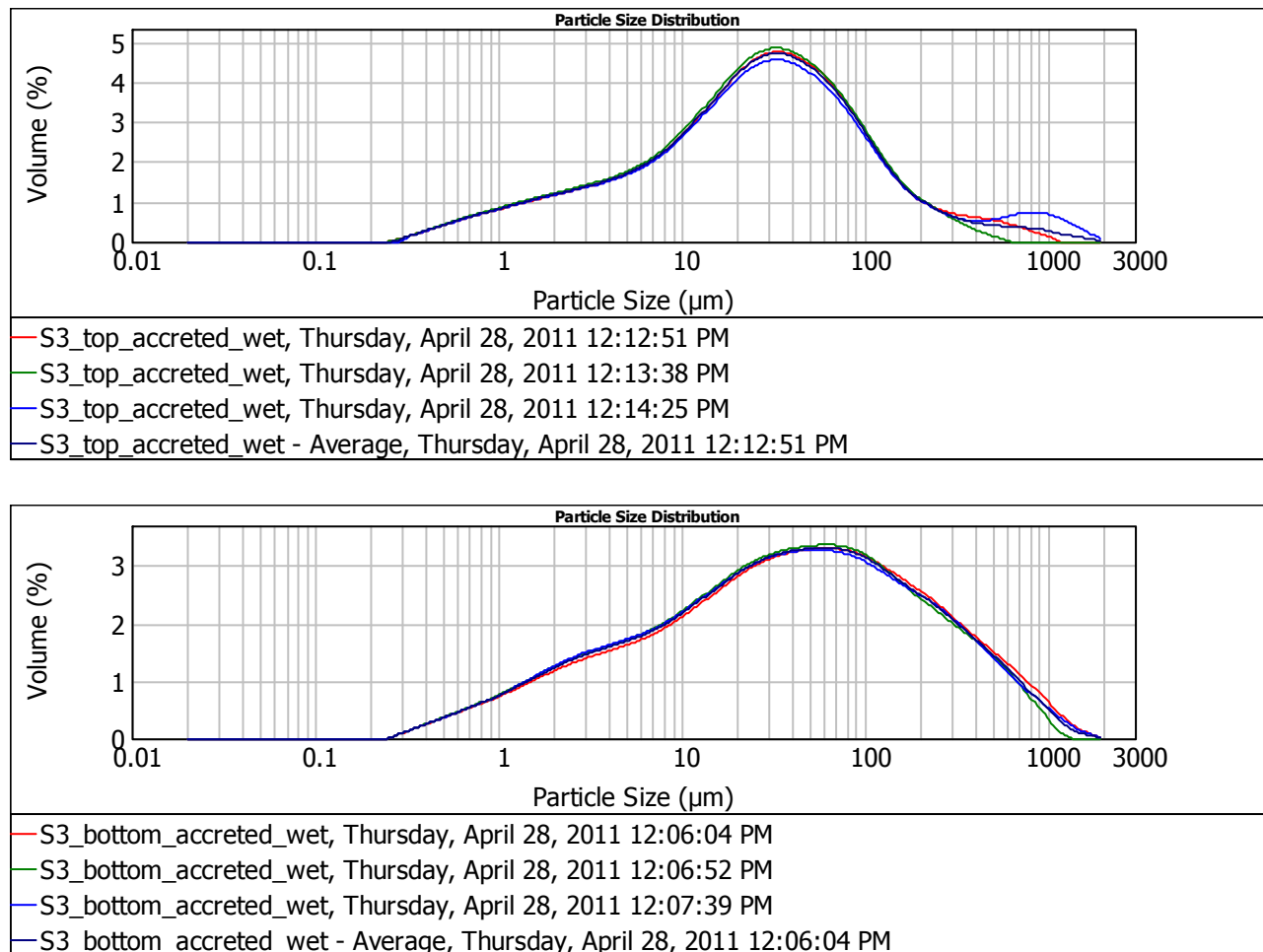
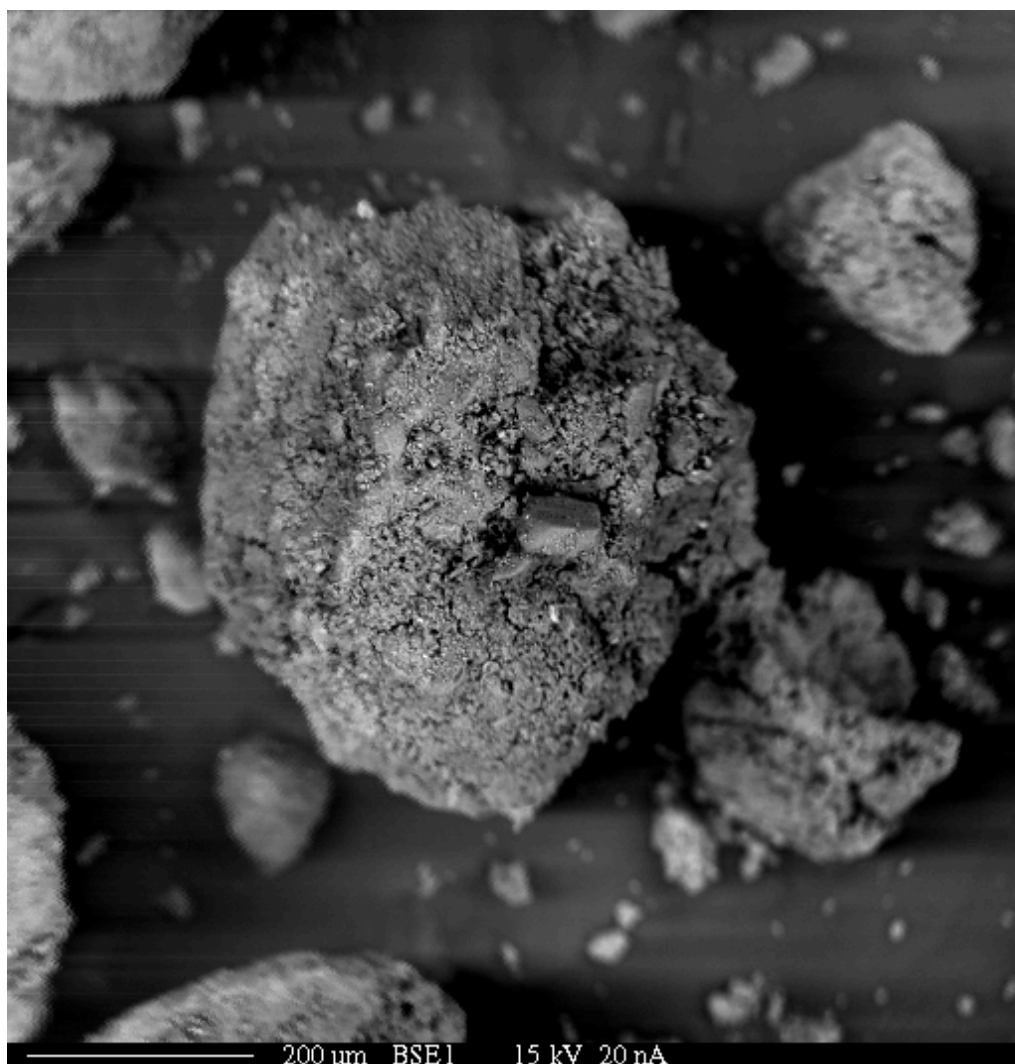


Figure 17: Volume percentage versus particle size distribution of a ~ 0.12 g sample from accreted sediment at station S-3 for the top (1 m) BSNE pan (top graph) and bottom (0.3 m) BSNE pan (bottom graph).



rb-s1-4BSE1

Figure 18: The back-scattered electron (BSE) sample is from station S-1. According to the generated WDS spectra (Figures 19-21), the inferred minerals are kaolinite, feldspar, and iron oxide. The sample is from the simulated wind gust.

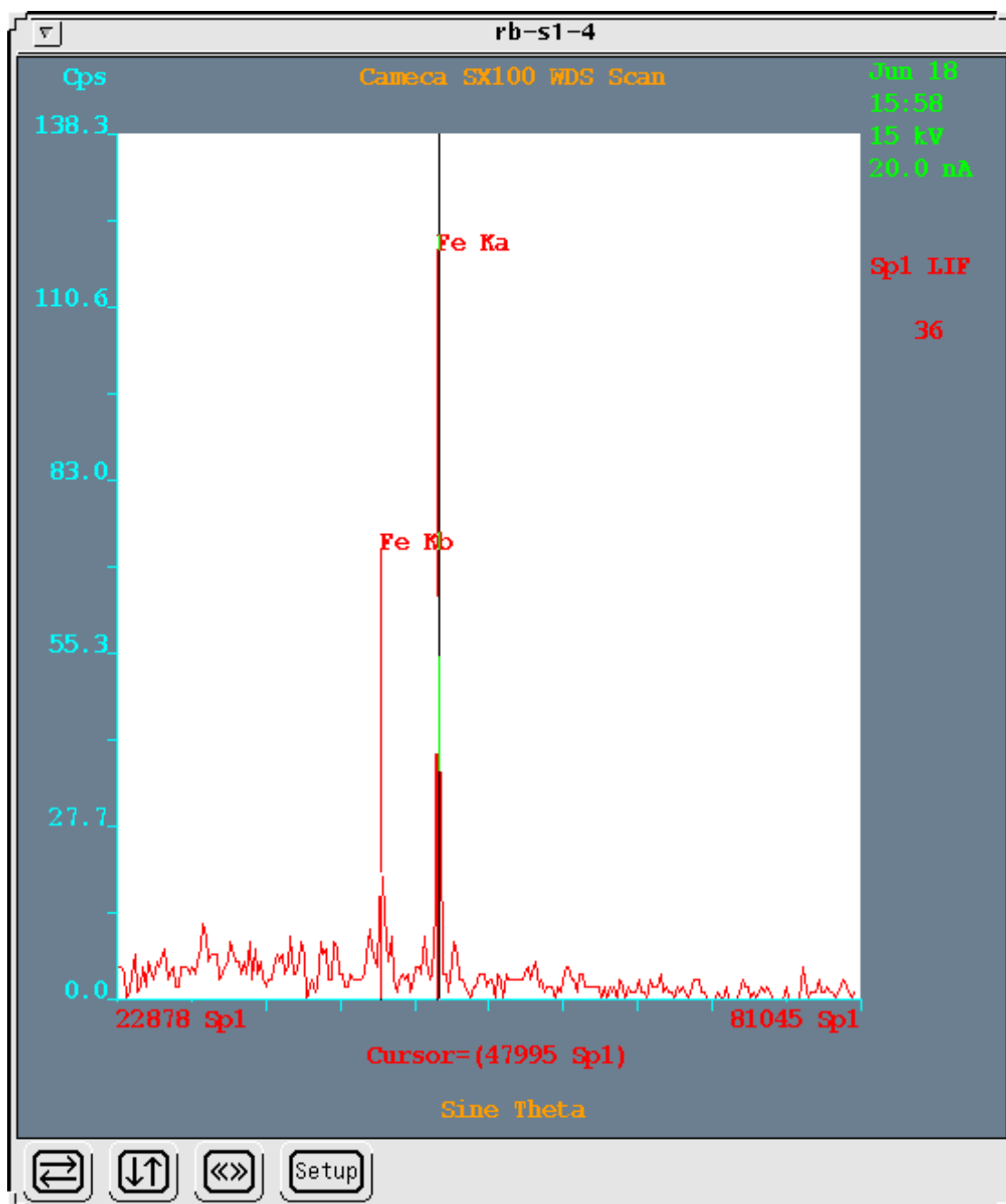


Figure 19: Wavelength Dispersive Spectroscopy (WDS) X-ray scan for image (Figure 18) from station S-1.

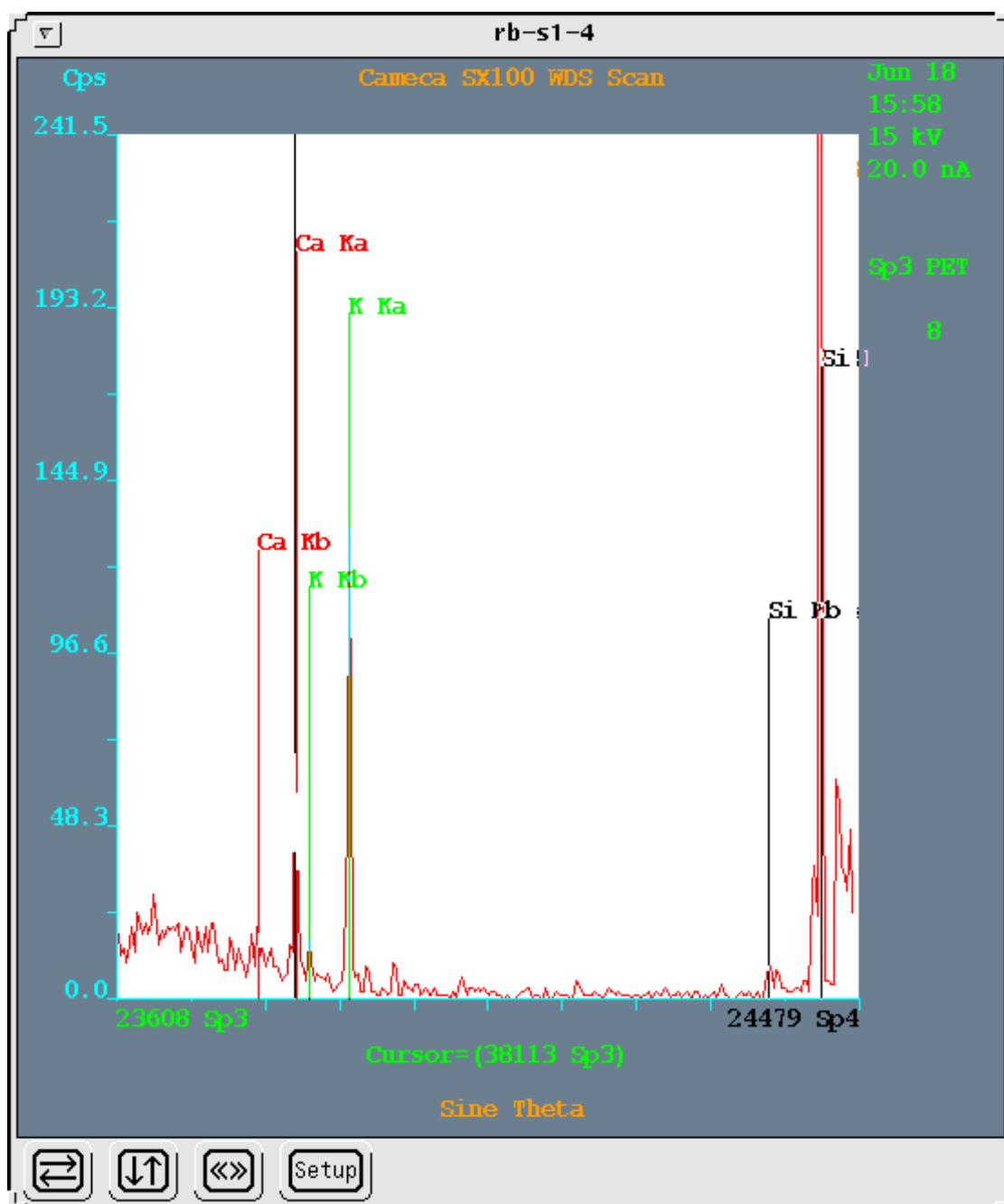


Figure 20: Wavelength Dispersive Spectroscopy (WDS) X-ray scan for image (Figure 18) from station S-1.

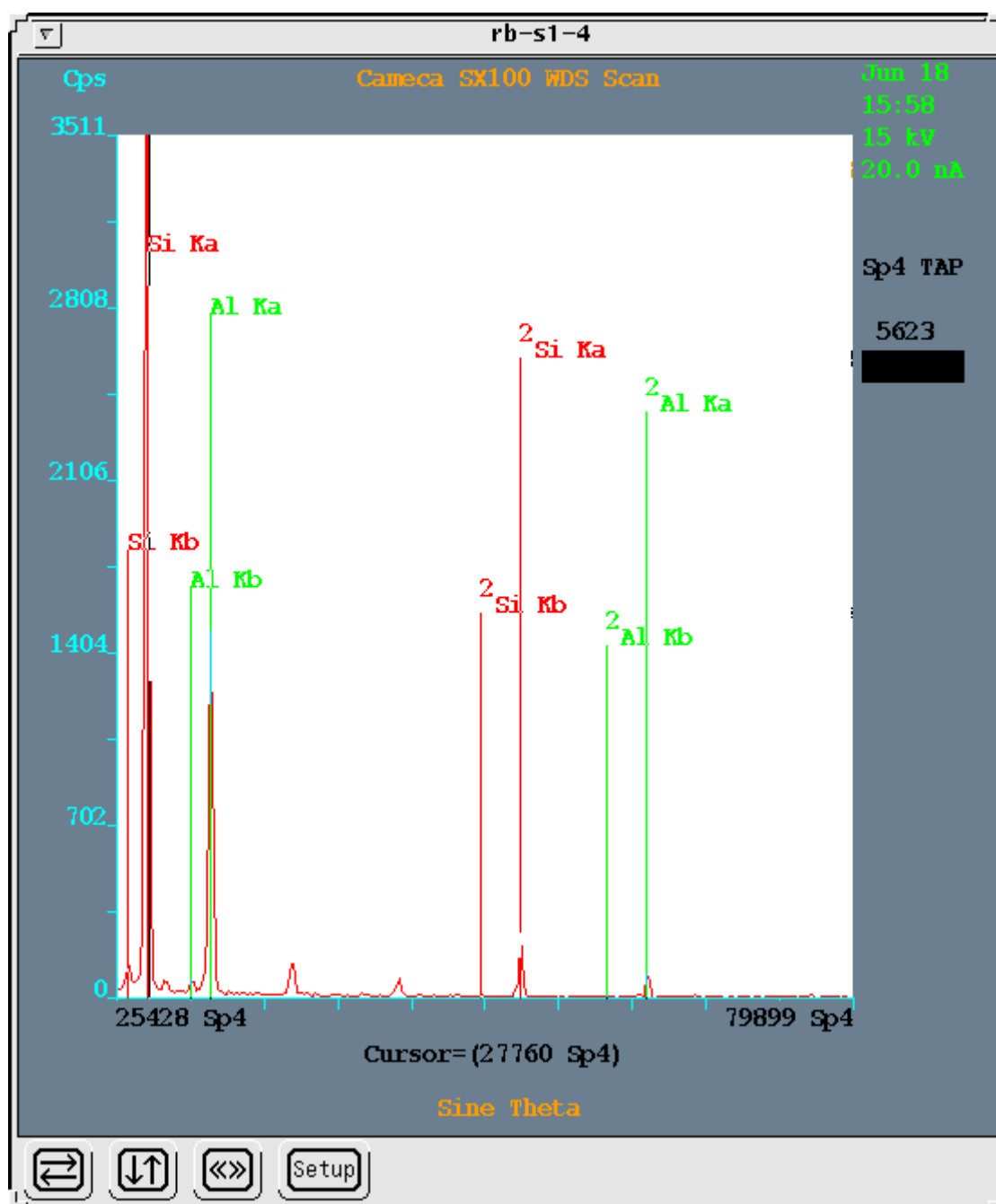
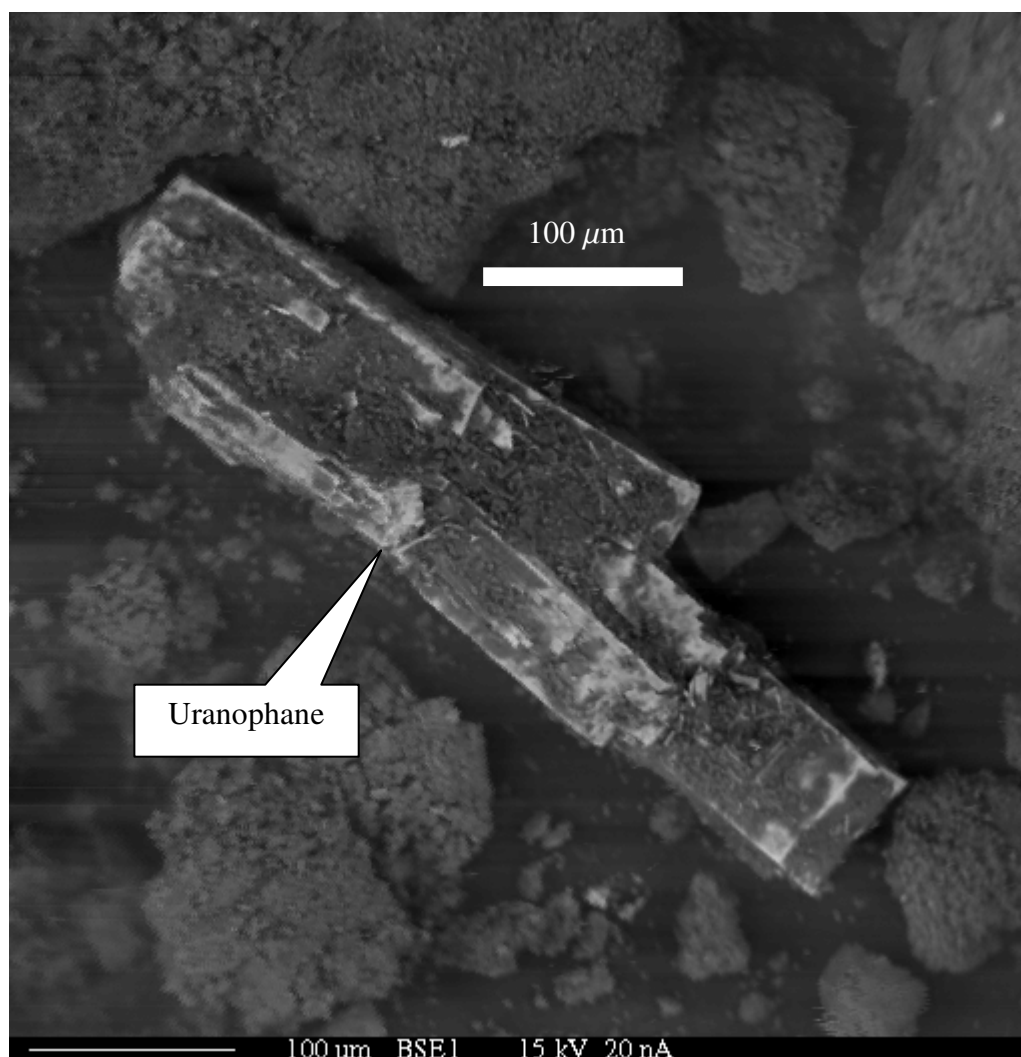


Figure 21: Wavelength Dispersive Spectroscopy (WDS) X-ray scan for image (Figure 18) from station S-1.



rb-s2-6bse1BSE1

Figure 22: The back-scattered electron (BSE) sample image is from station S-2. According to the generated WDS spectra (Figures 23-24), the inferred mineral is uranophane. The sample is from the simulated wind gust.

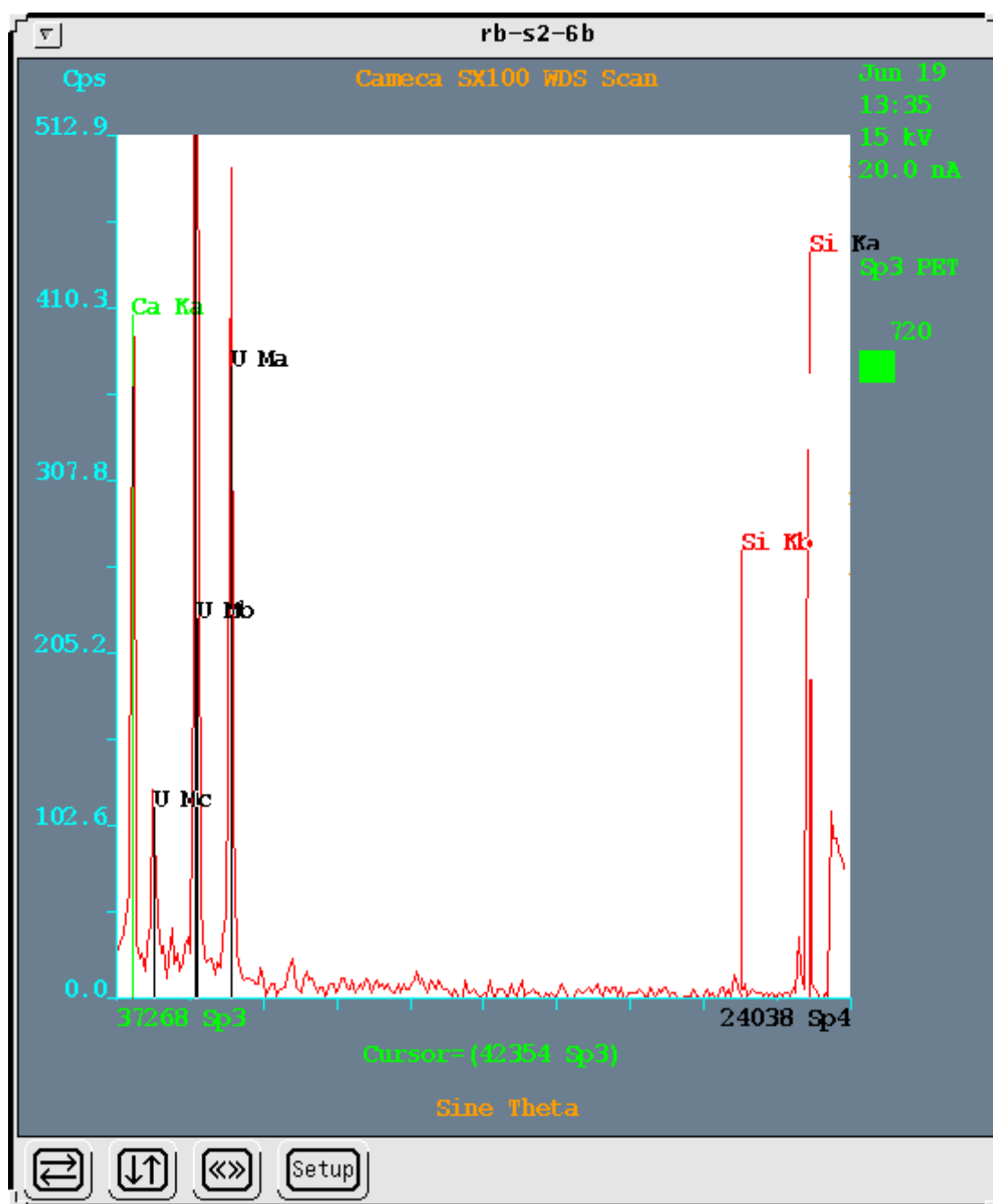


Figure 23: Wavelength Dispersive Spectroscopy (WDS) X-ray scan for image (Figure 22) from station S-2.

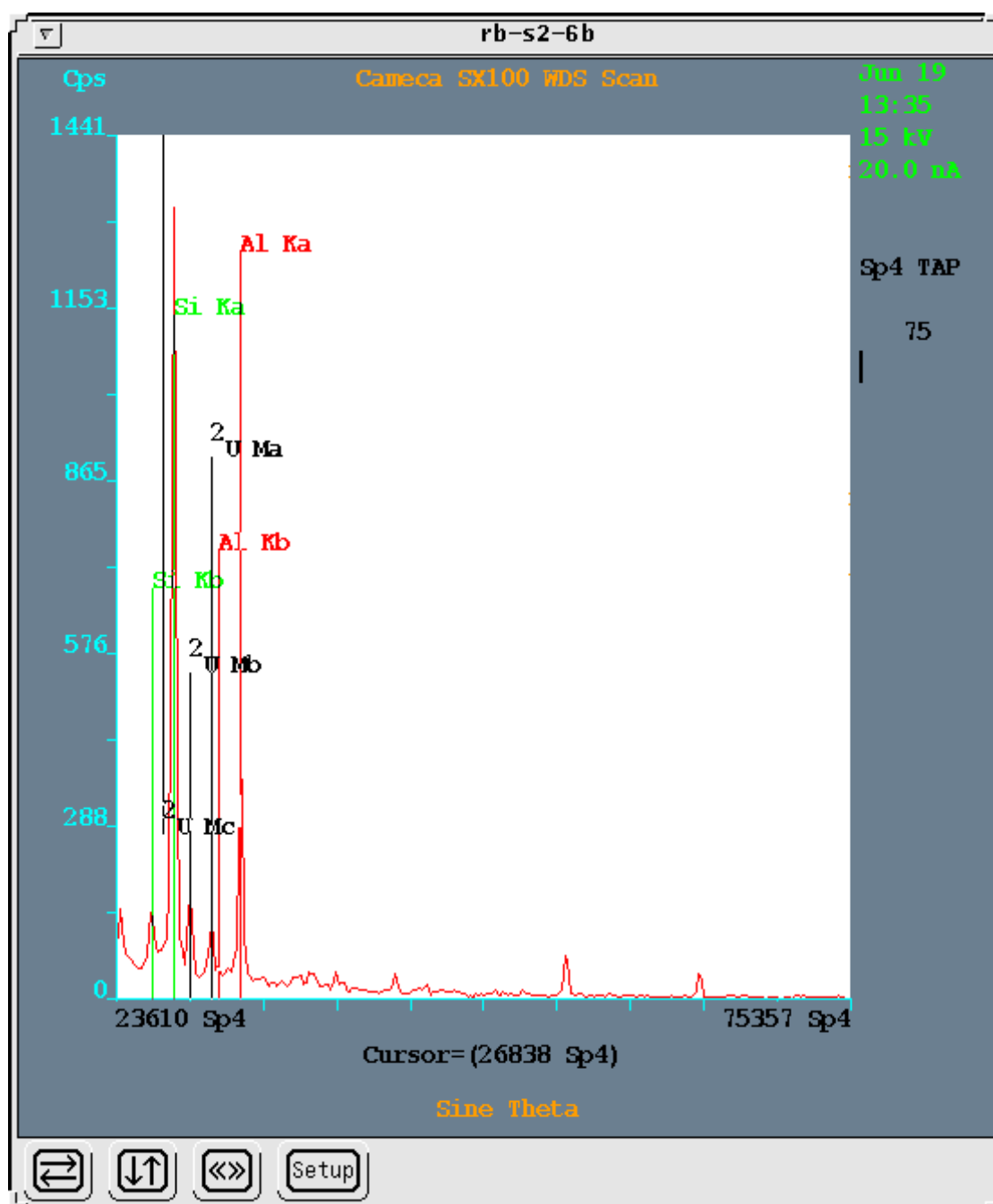


Figure 24: Wavelength Dispersive Spectroscopy (WDS) X-ray scan for image (Figure 22) from station S-2.

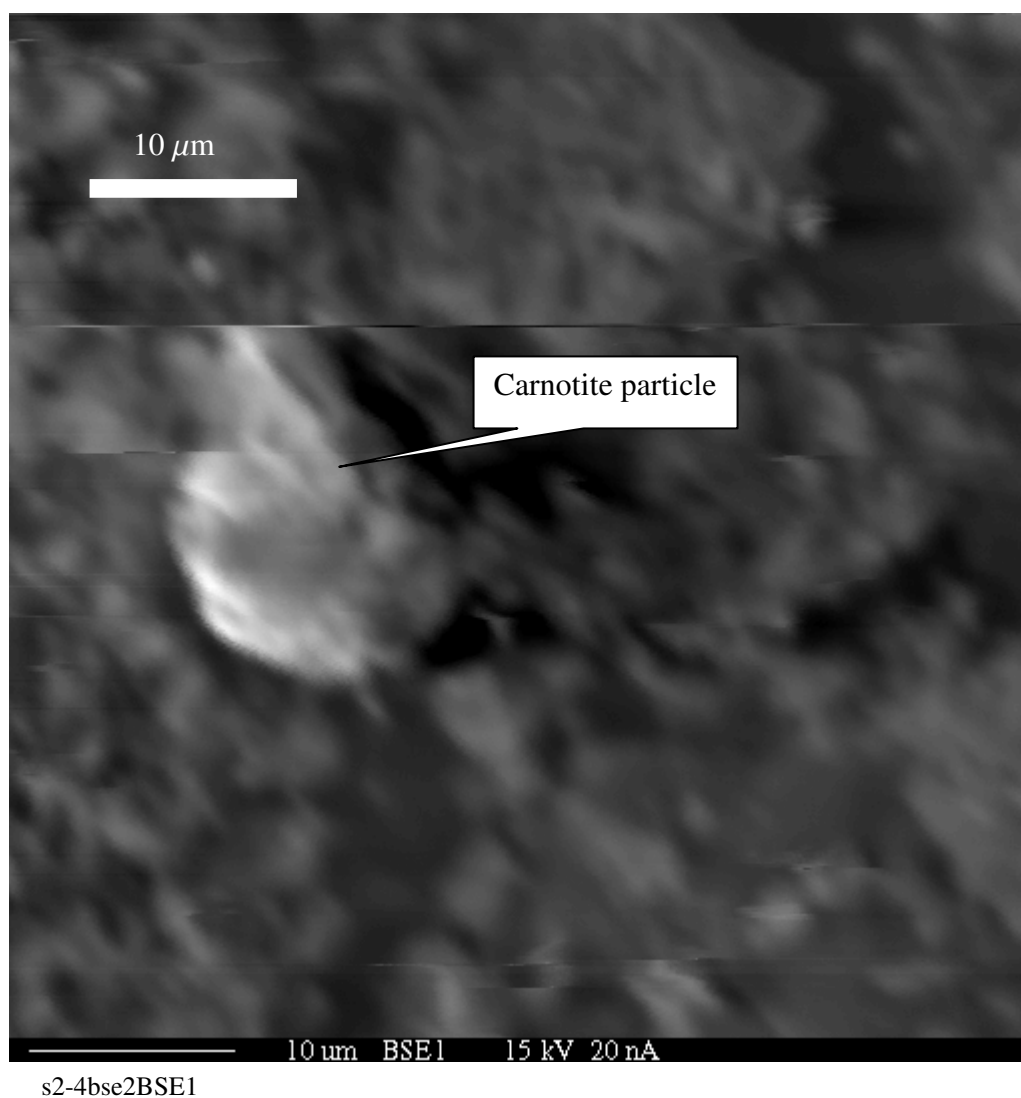


Figure 25: The back-scattered electron (BSE) sample image is from station S-2. According to the generated WDS spectra (Figures 26-28), the inferred mineral is carnotite. The sample (10 μm particle) is from the simulated wind gust.

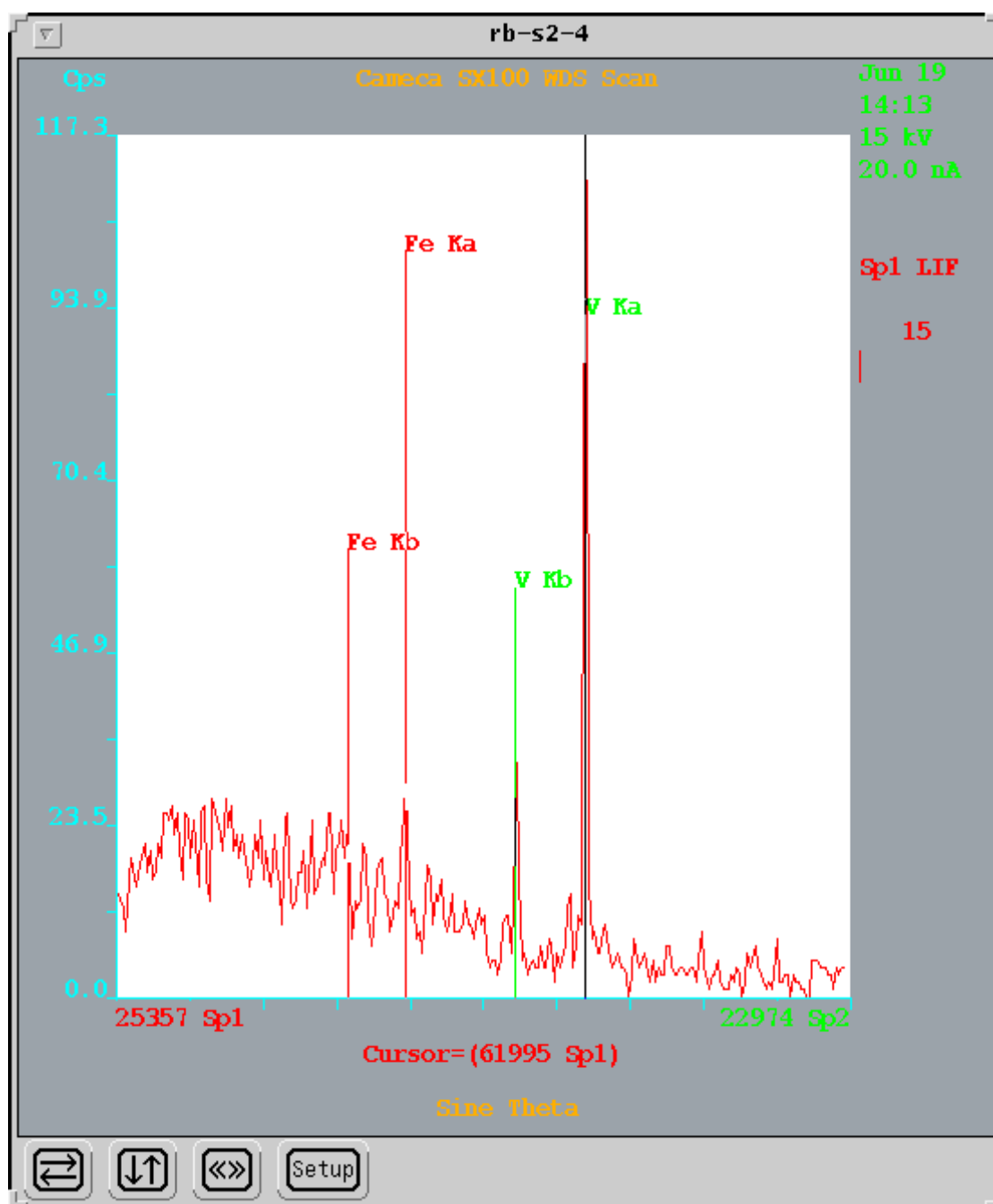


Figure 26: Wavelength Dispersive Spectroscopy (WDS) X-ray scan for image (Figure 25) from station S-2.

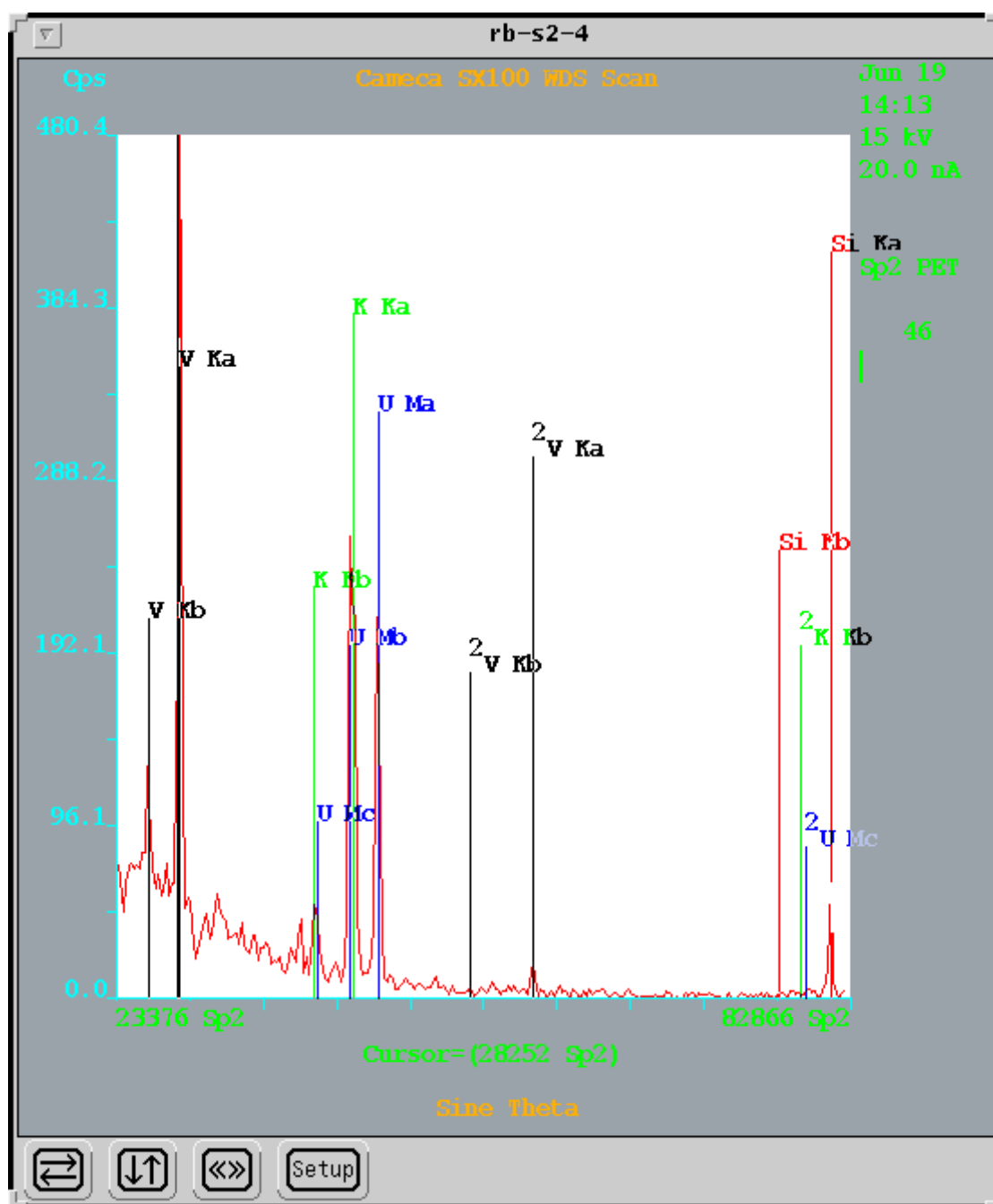


Figure 27: Wavelength Dispersive Spectroscopy (WDS) X-ray scan for image (Figure 25) from station S-2.

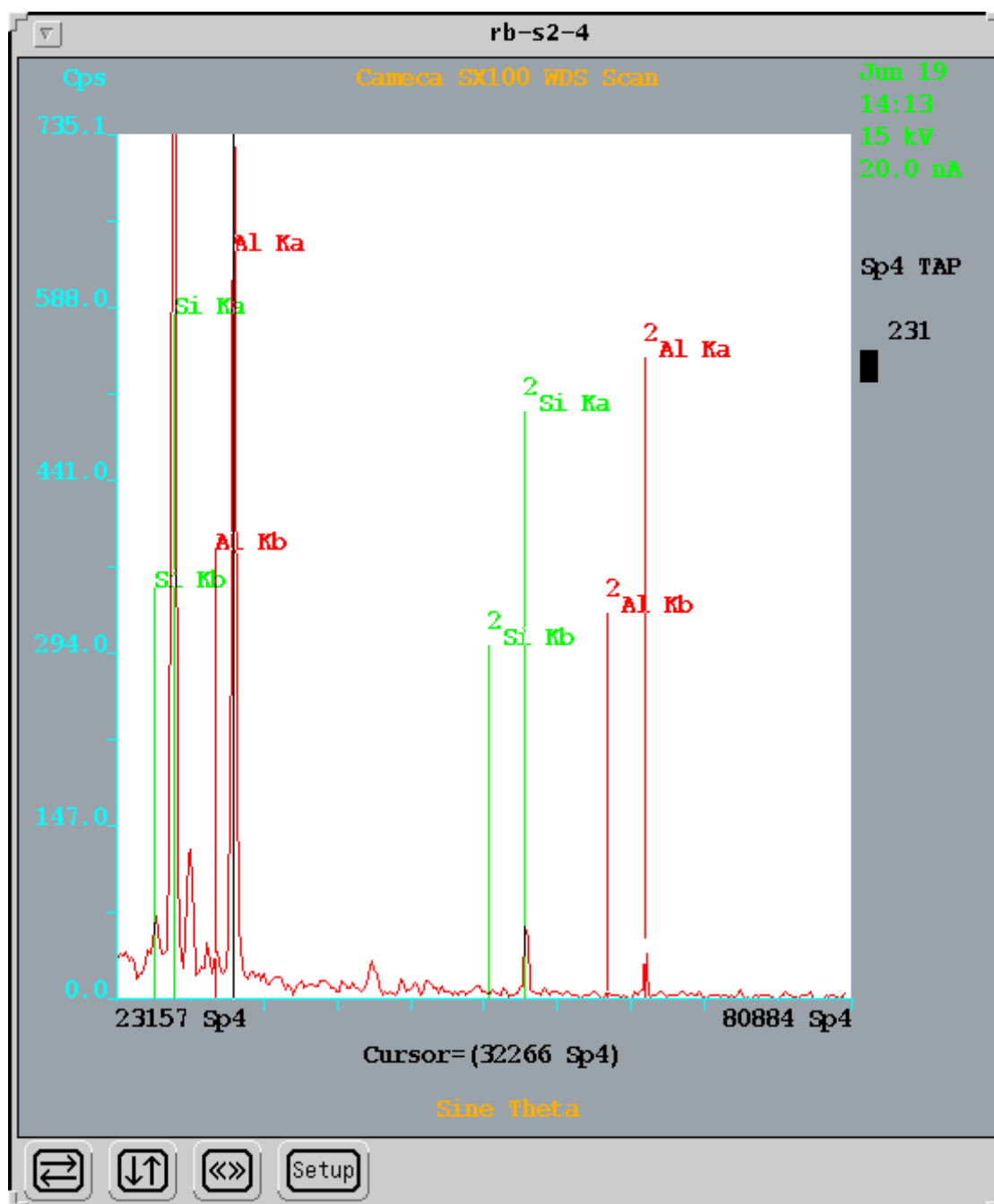


Figure 28: Wavelength Dispersive Spectroscopy (WDS) X-ray scan for image (Figure 25) from station S-2.

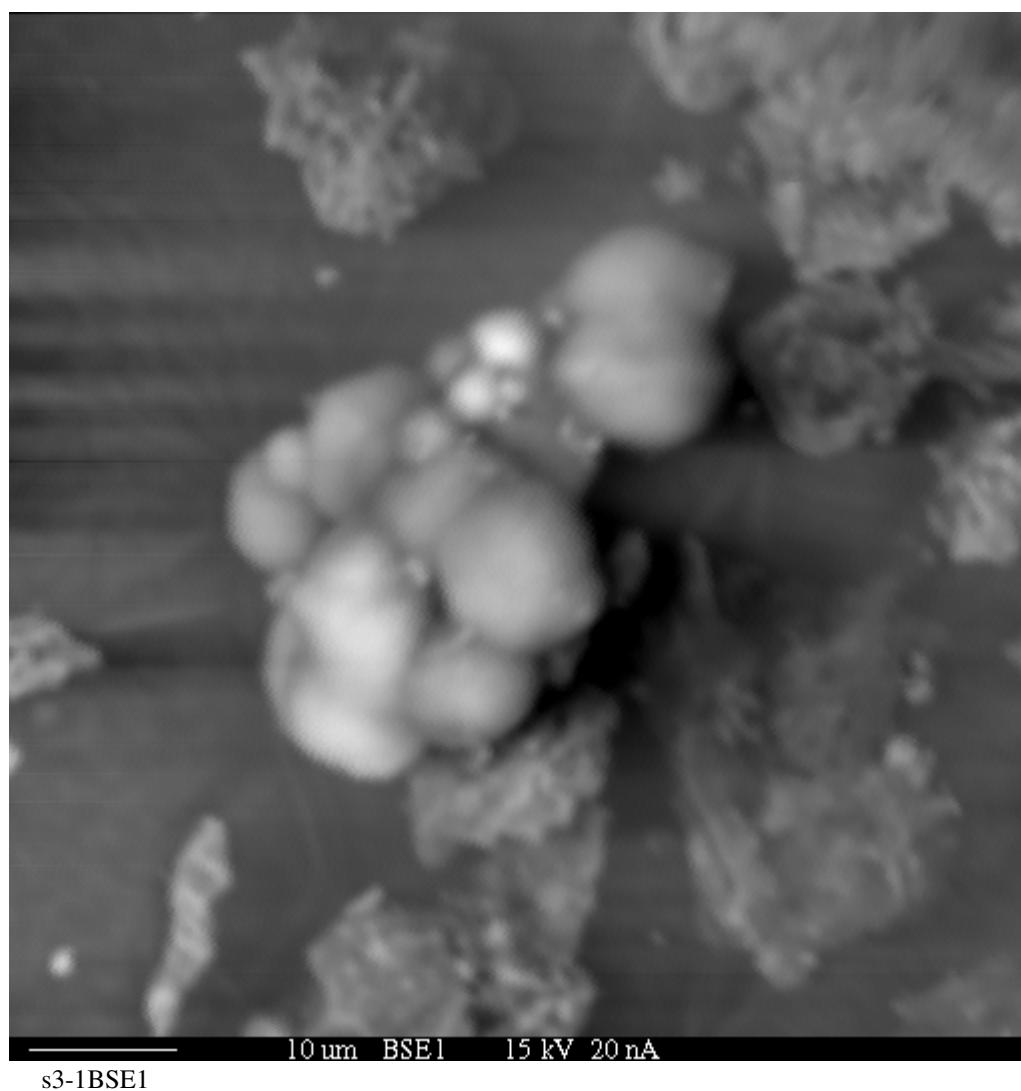


Figure 29: The back-scattered electron (BSE) sample image is from station S-3. According to the generated WDS spectra (Figures 30-32), the inferred mineral is smithsonite. The sample is from the simulated wind gust.

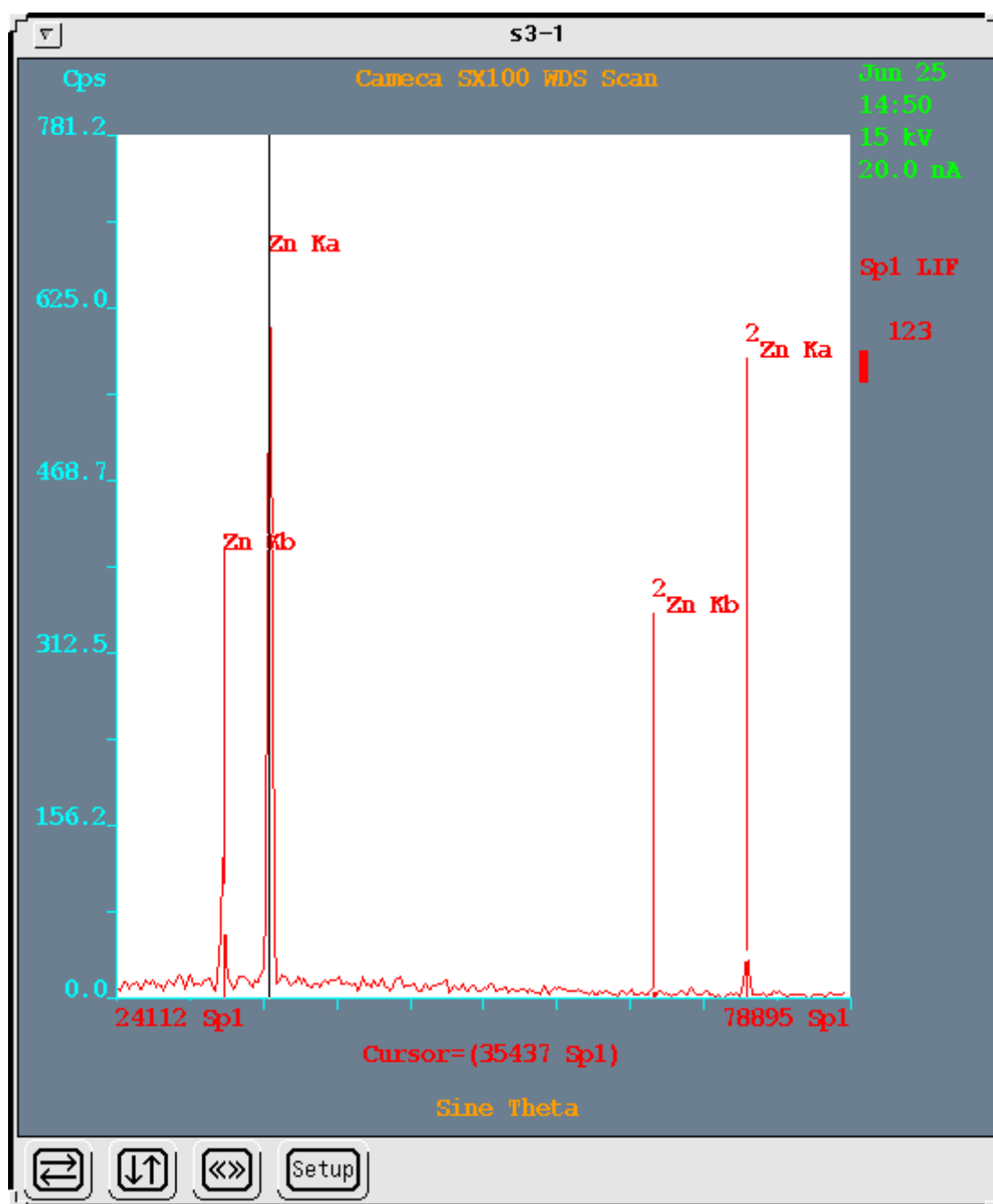


Figure 30: Wavelength Dispersive Spectroscopy (WDS) X-ray scan for image (Figure 29) from station S-3.

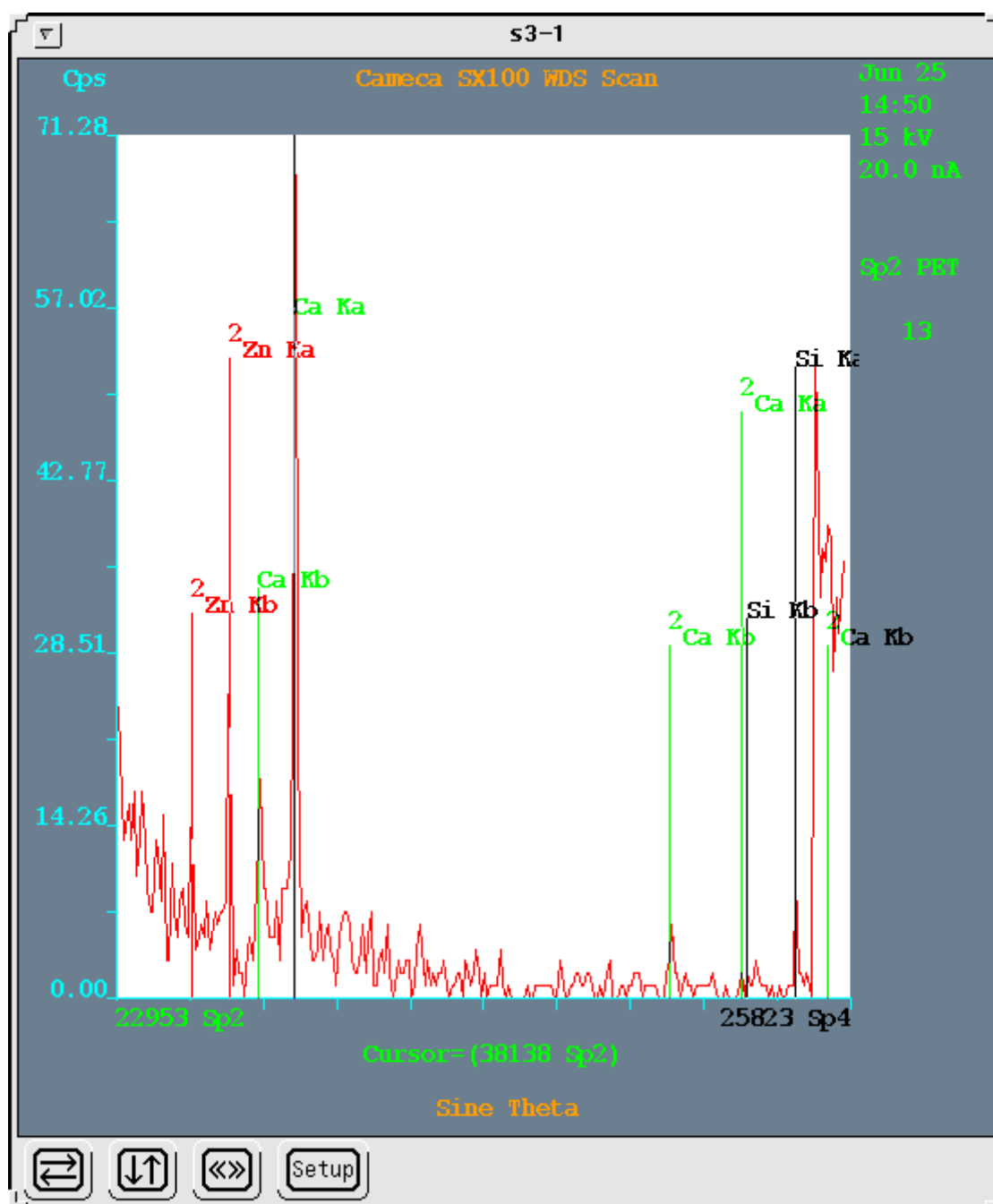


Figure 31: Wavelength Dispersive Spectroscopy (WDS) X-ray scan for image (Figure 29) from station S-3.

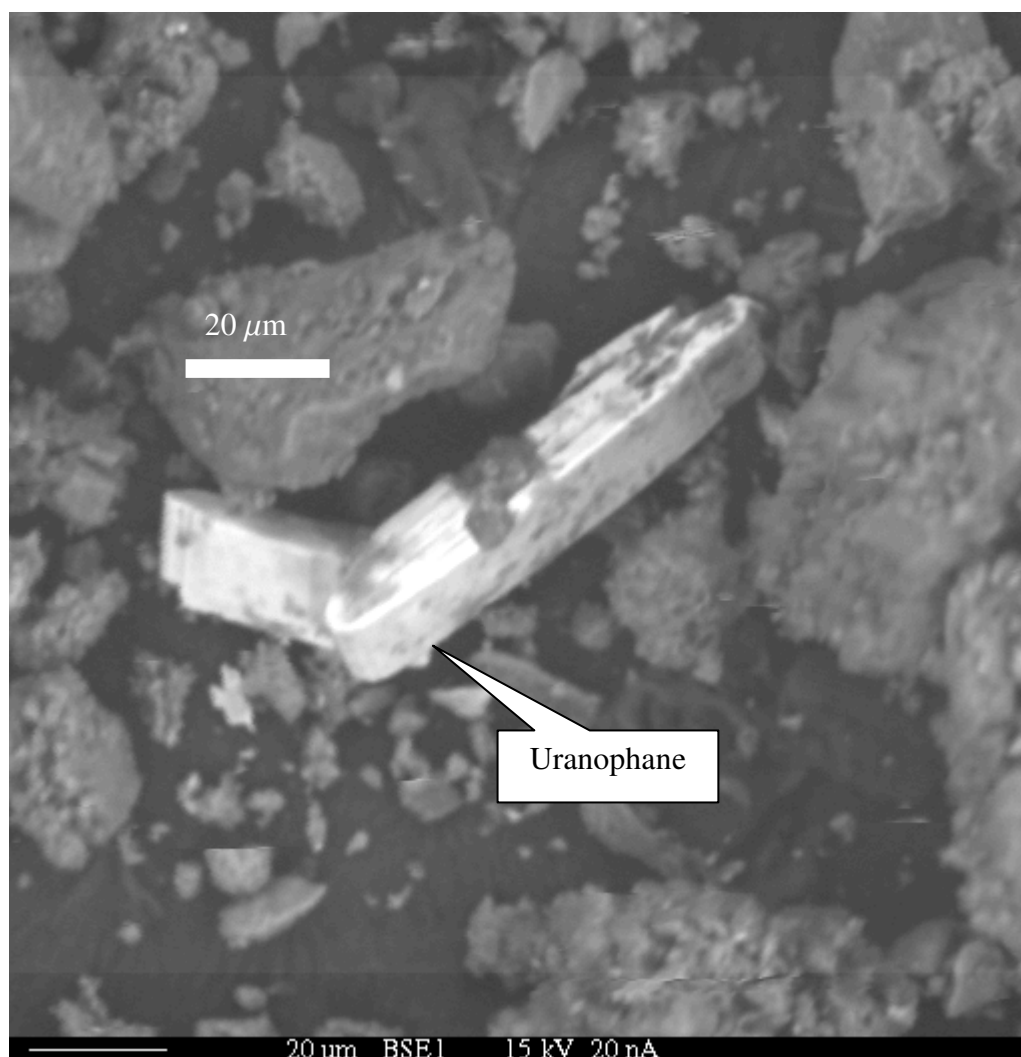


Figure 33: The back-scattered electron (BSE) sample image is from station S-3. According to the generated WDS spectra (Figure 34), the inferred mineral is uranophane. The sample is from naturally accreted sediment in the saltating zone (0.3 m) at S-2.

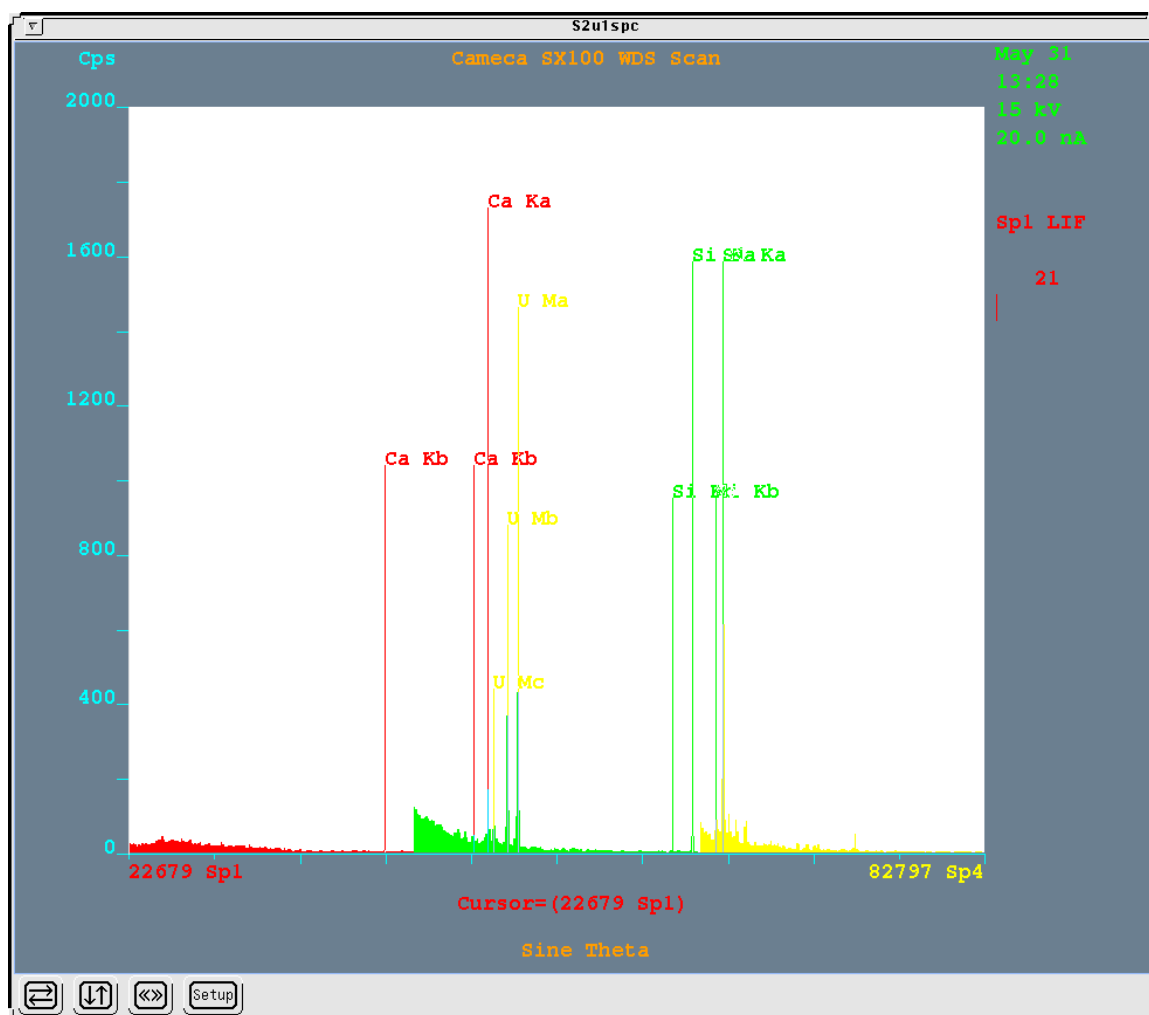


Figure 34: Wavelength Dispersive Spectroscopy (WDS) X-ray scan for image (Figure 33) from station S-2.

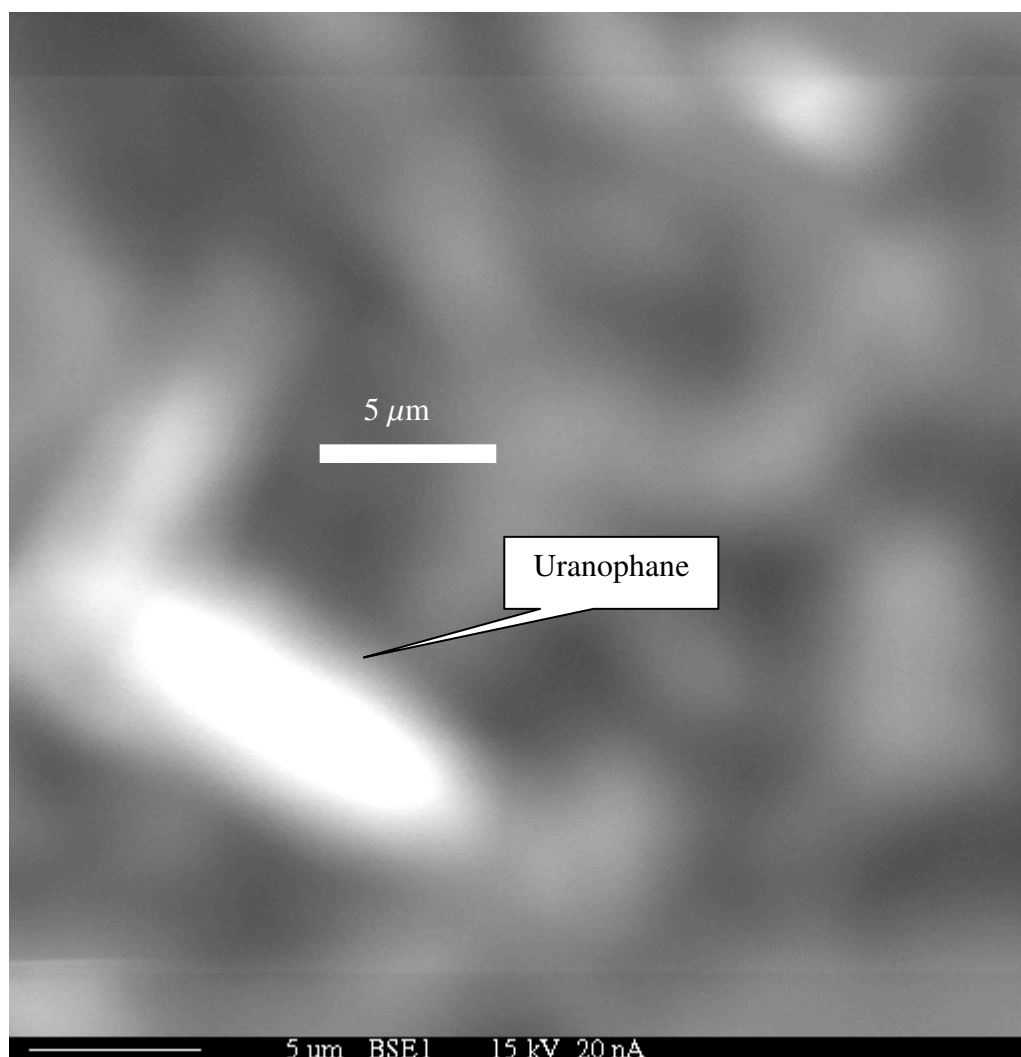


Figure 35: The back-scattered electron (BSE) sample image is from station S-3. According to the generated WDS spectra (Figure 36), the inferred mineral is uranophane. The sample is from naturally accreted sediment in the saltating zone (0.3 m) at S-3.

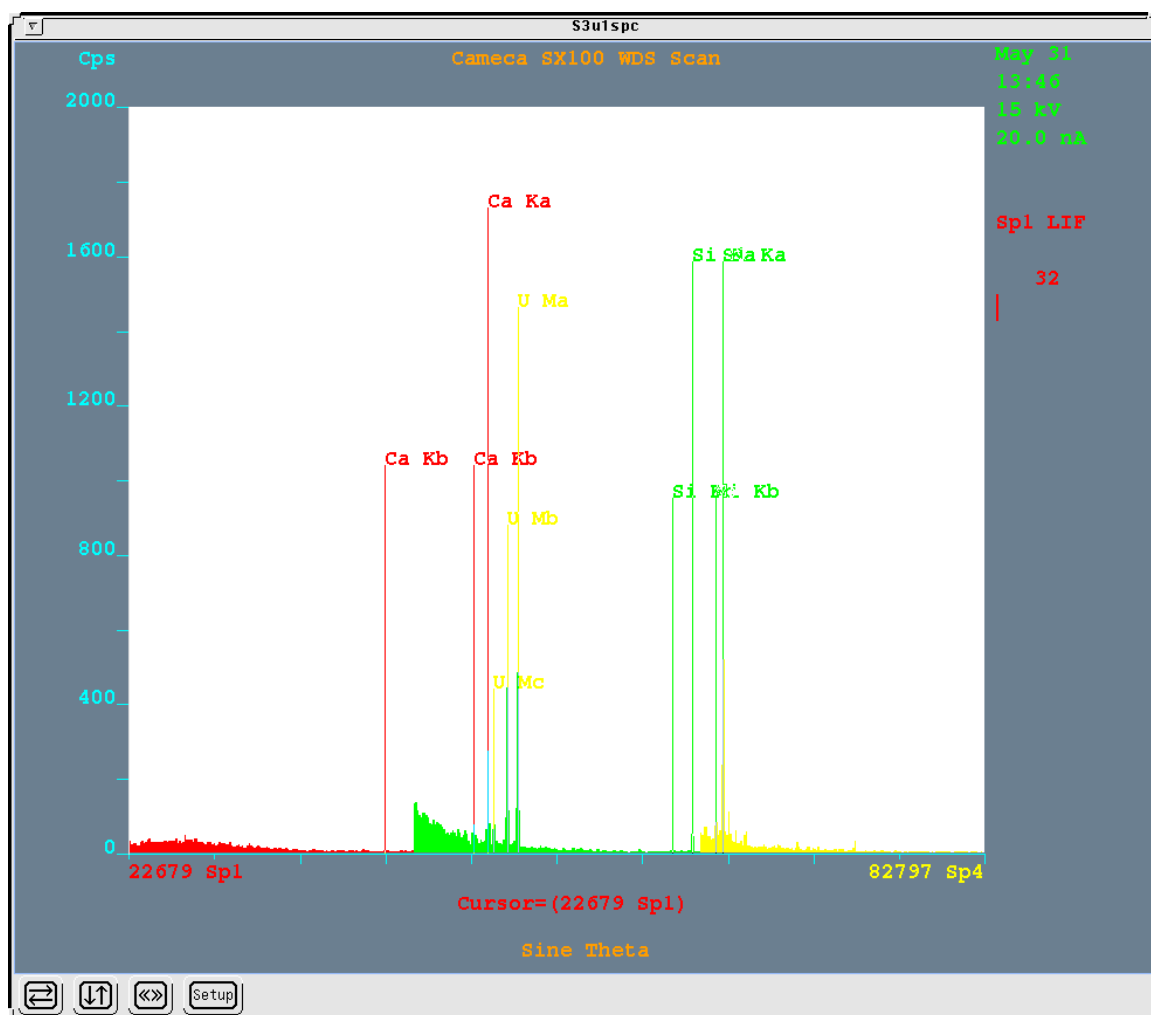


Figure 36: Wavelength Dispersive Spectroscopy (WDS) X-ray scan for image (Figure 35) from station S-3.

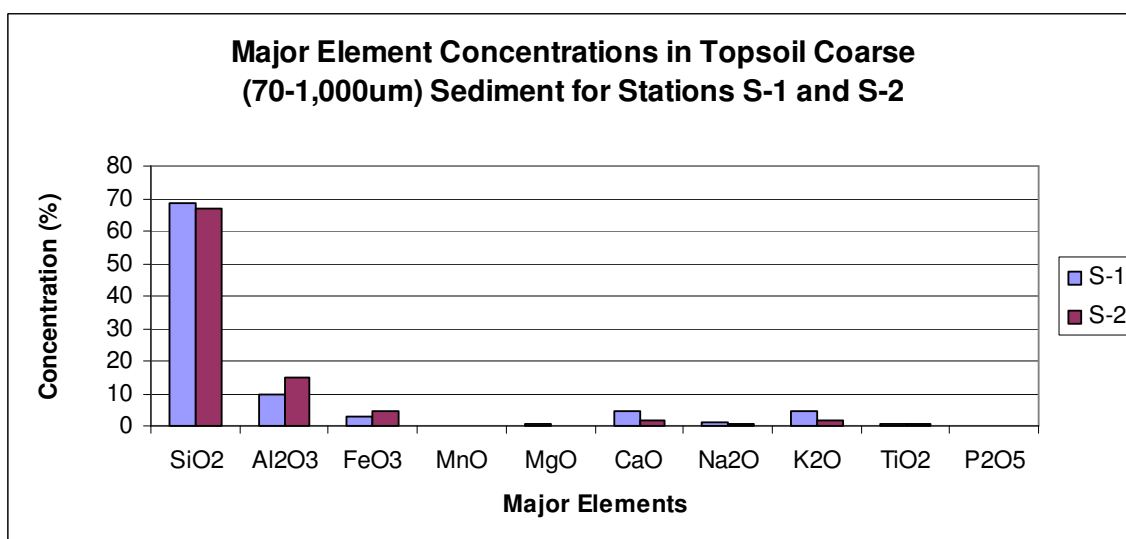
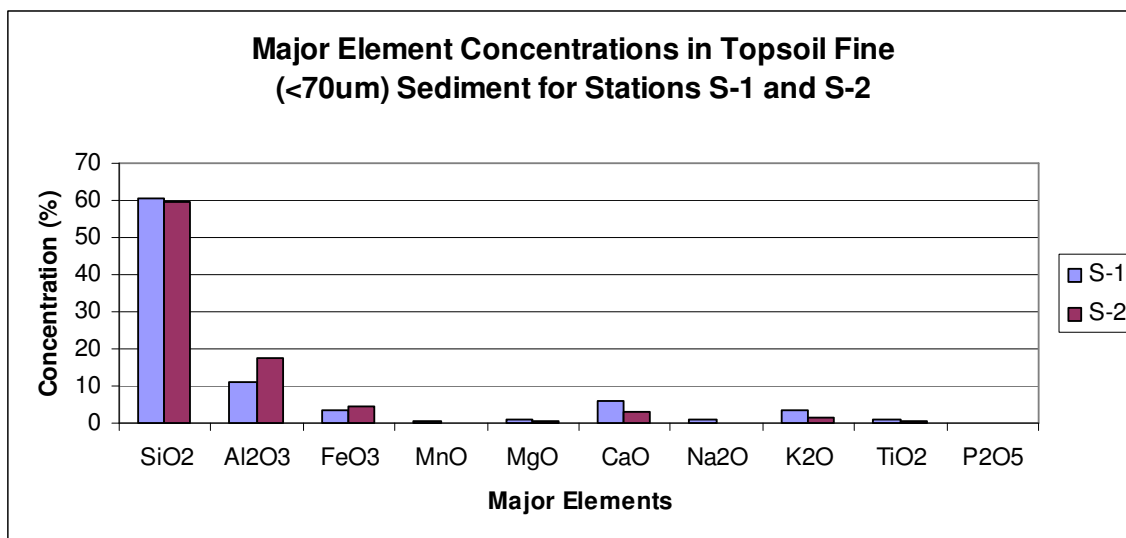


Figure 37: ICP-MS results of major element concentrations in topsoil fine ($< 70 \mu\text{m}$) (top graph) and coarse ($70 - 1,000 \mu\text{m}$) (bottom graph) sediment for stations S-1 and S-2.

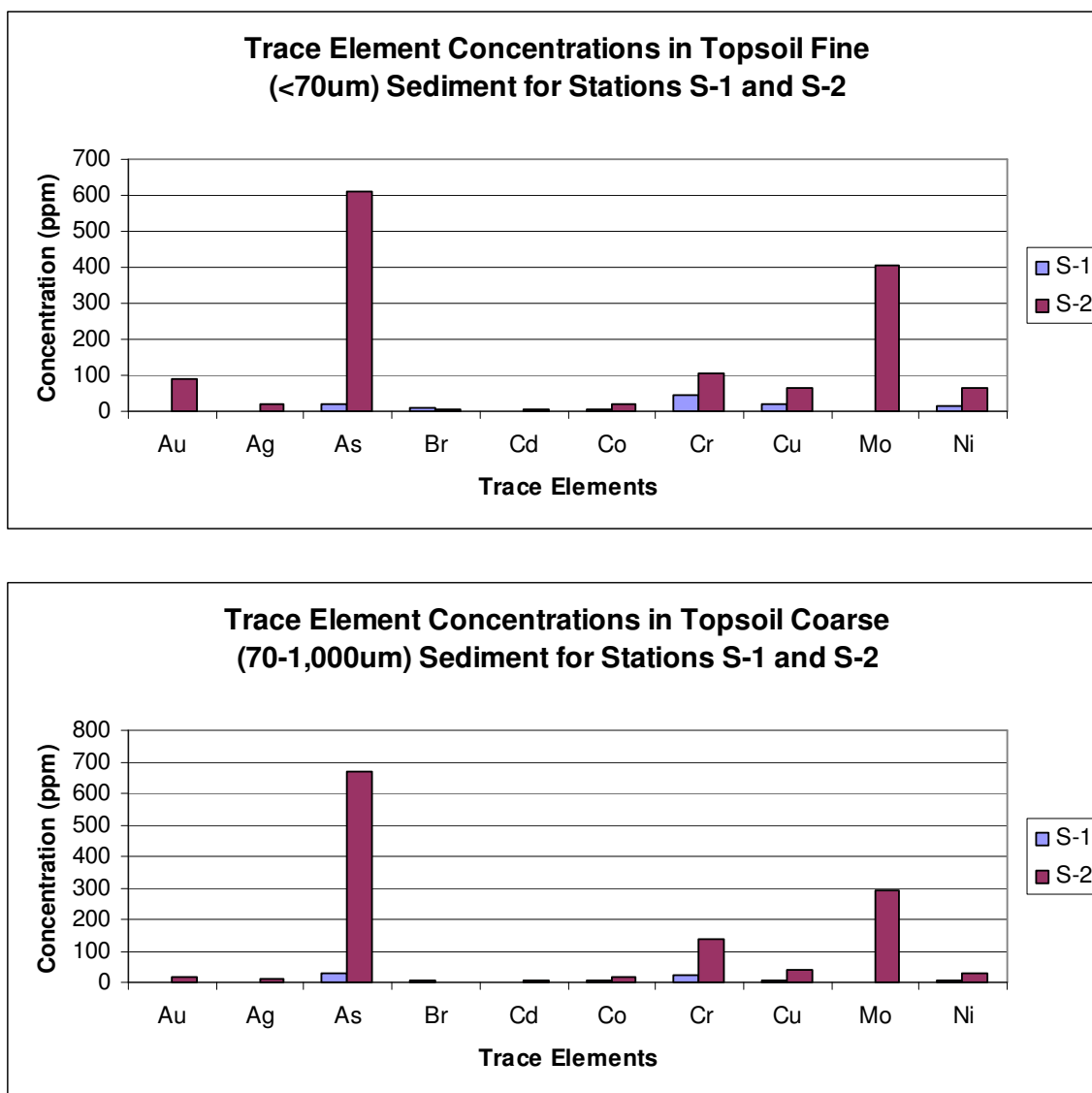


Figure 38: ICP-MS results of trace element concentrations in topsoil fine (< 70 µm) (top graph) and coarse (70 – 1,000 µm) (bottom graph) sediment for stations S-1 and S-2. Only for Au, the concentration units are ppb.

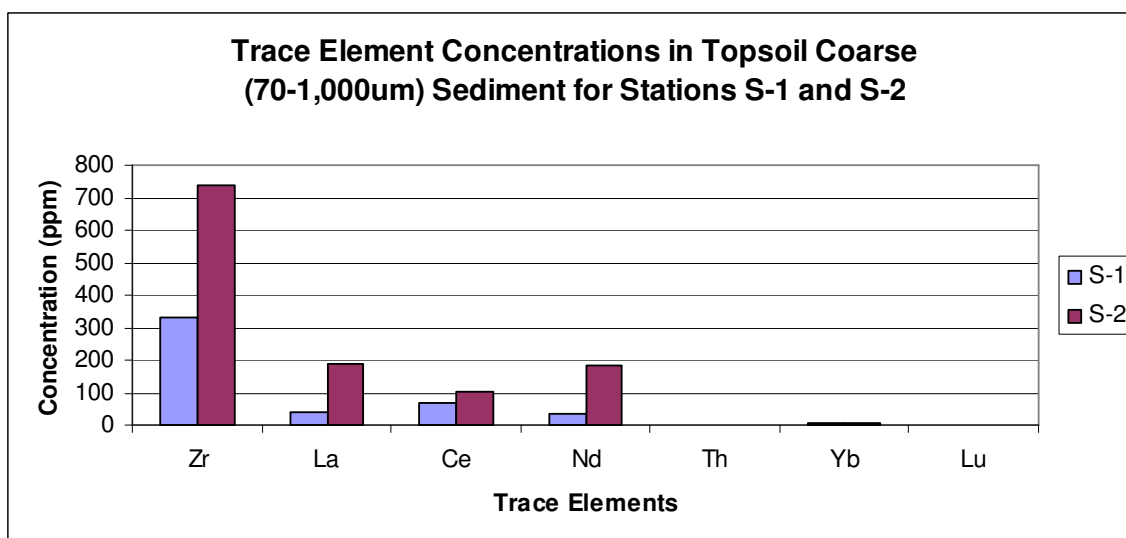
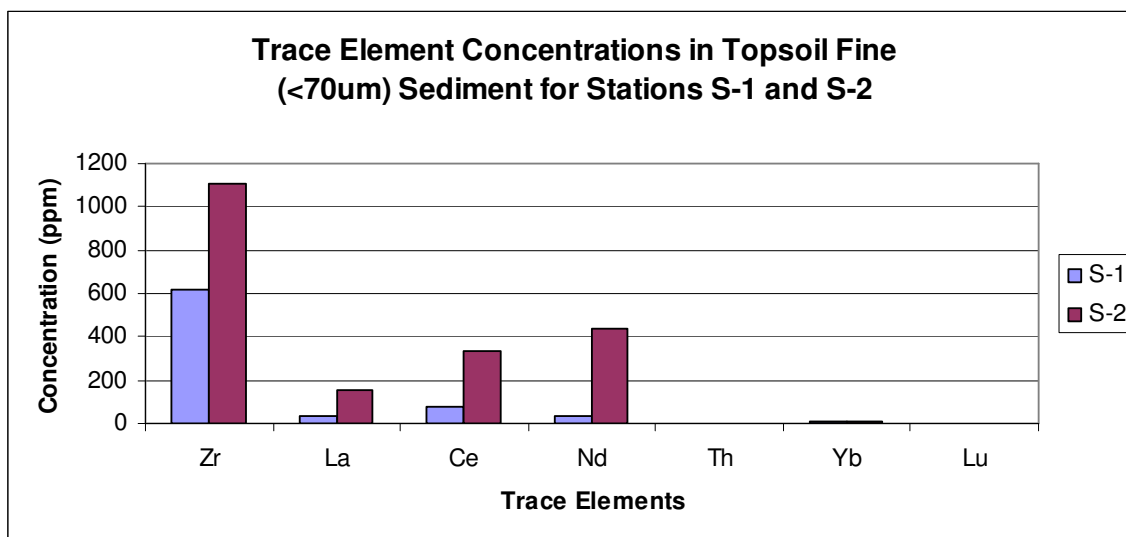


Figure 39: ICP-MS results of trace element concentrations in topsoil fine (< 70 μ m) (top graph) and coarse (70 – 1,000 μ m) (bottom graph) sediment for stations S-1 and S-2.

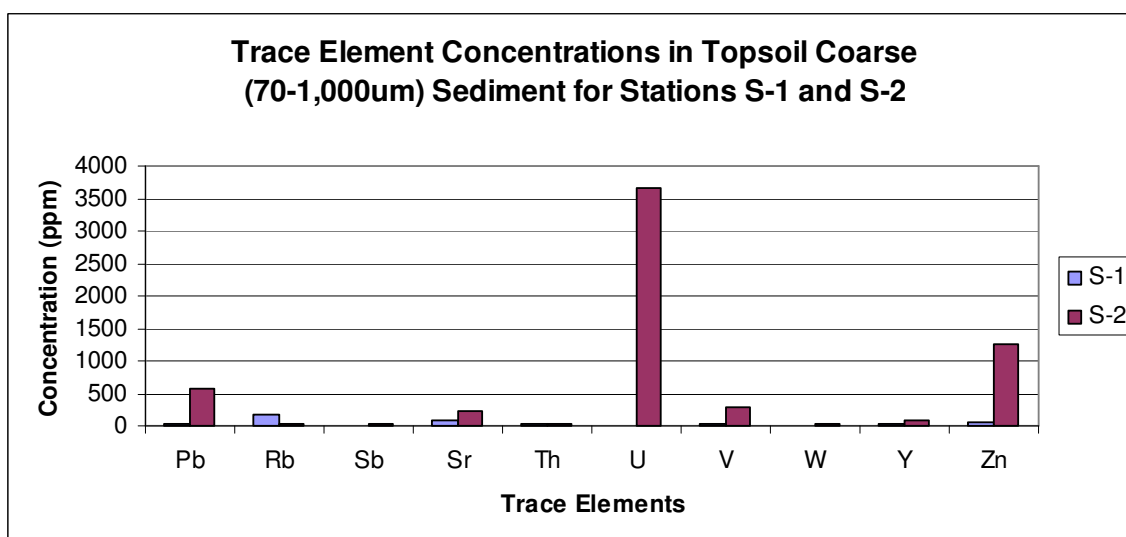
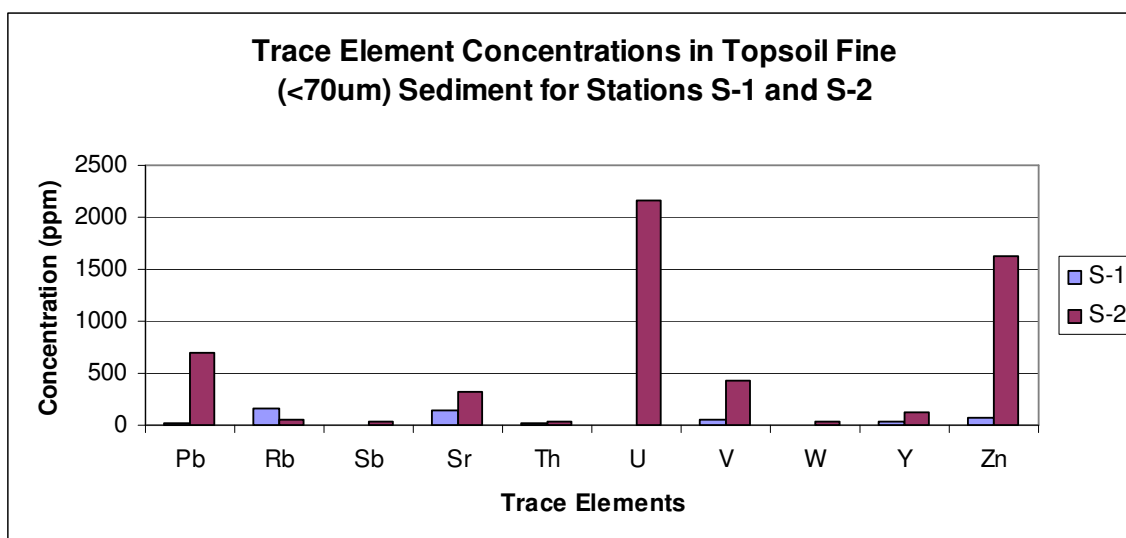


Figure 40: ICP-MS results of trace element concentrations in topsoil fine (< 70 μ m) (top graph) and coarse (70 – 1,000 μ m) (bottom graph) sediment for stations S-1 and S-2.

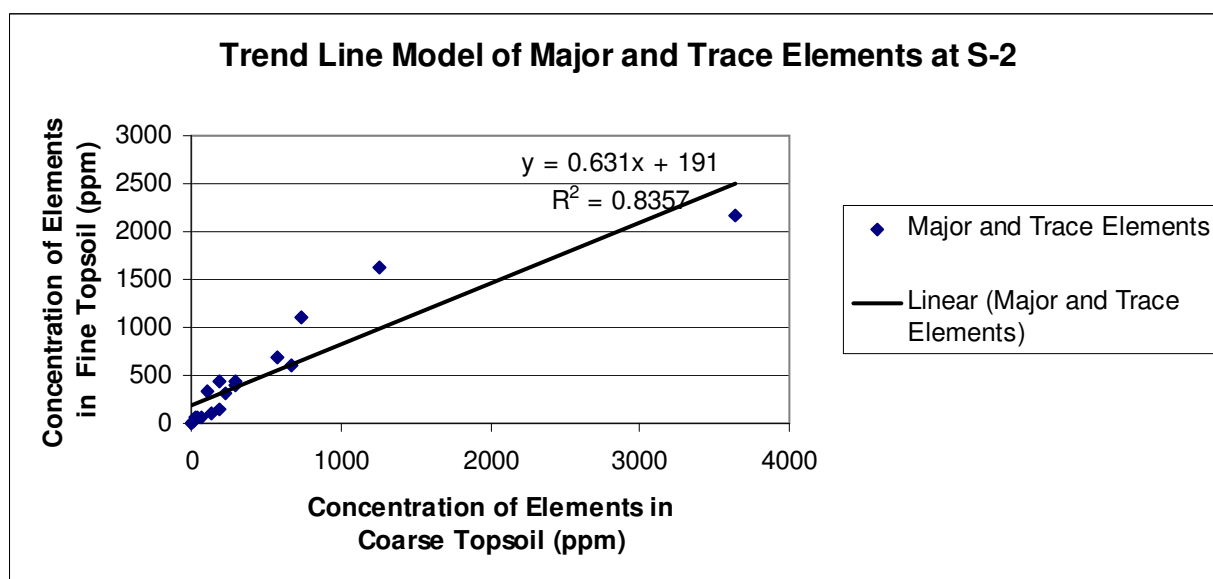
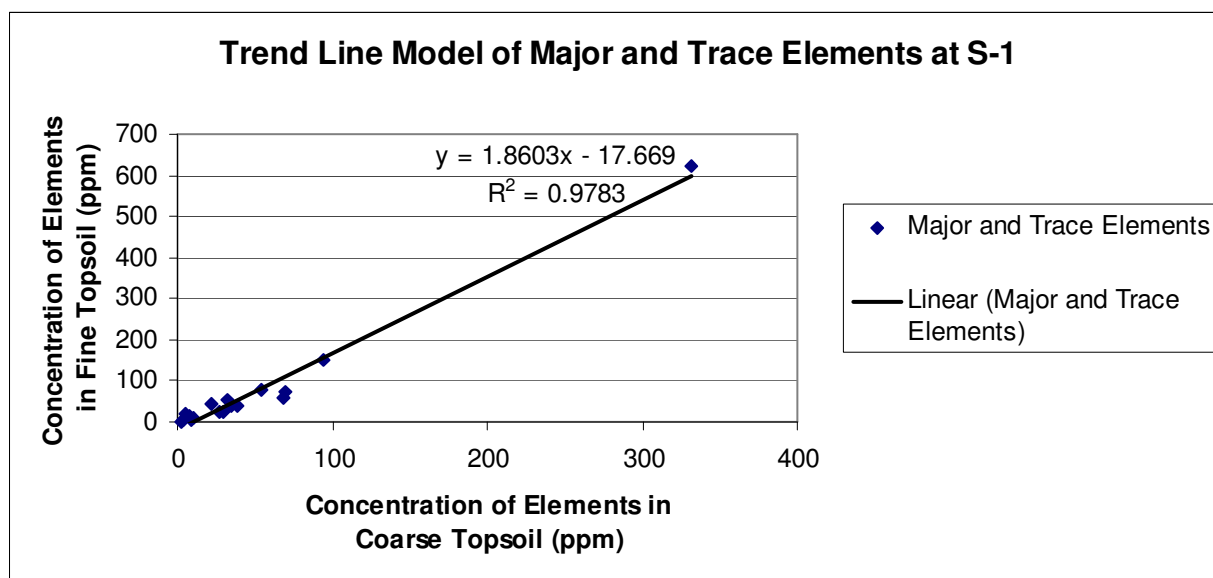


Figure 41: Trend line model of major and trace element concentrations detected by ICP-MS in topsoil fine ($< 70 \mu\text{m}$) (top graph) and coarse ($70 - 1,000 \mu\text{m}$) (bottom graph) sediment for stations S-1 and S-2.

The major and trace elements used to construct the trend linear model are as follows: SiO_2 , Al_2O_3 , CaO , As, Cr, Cu, Mo, Ni, Zr, La, Ce, Nd, Pb, Sr, U, V, and Zn (Table 8).

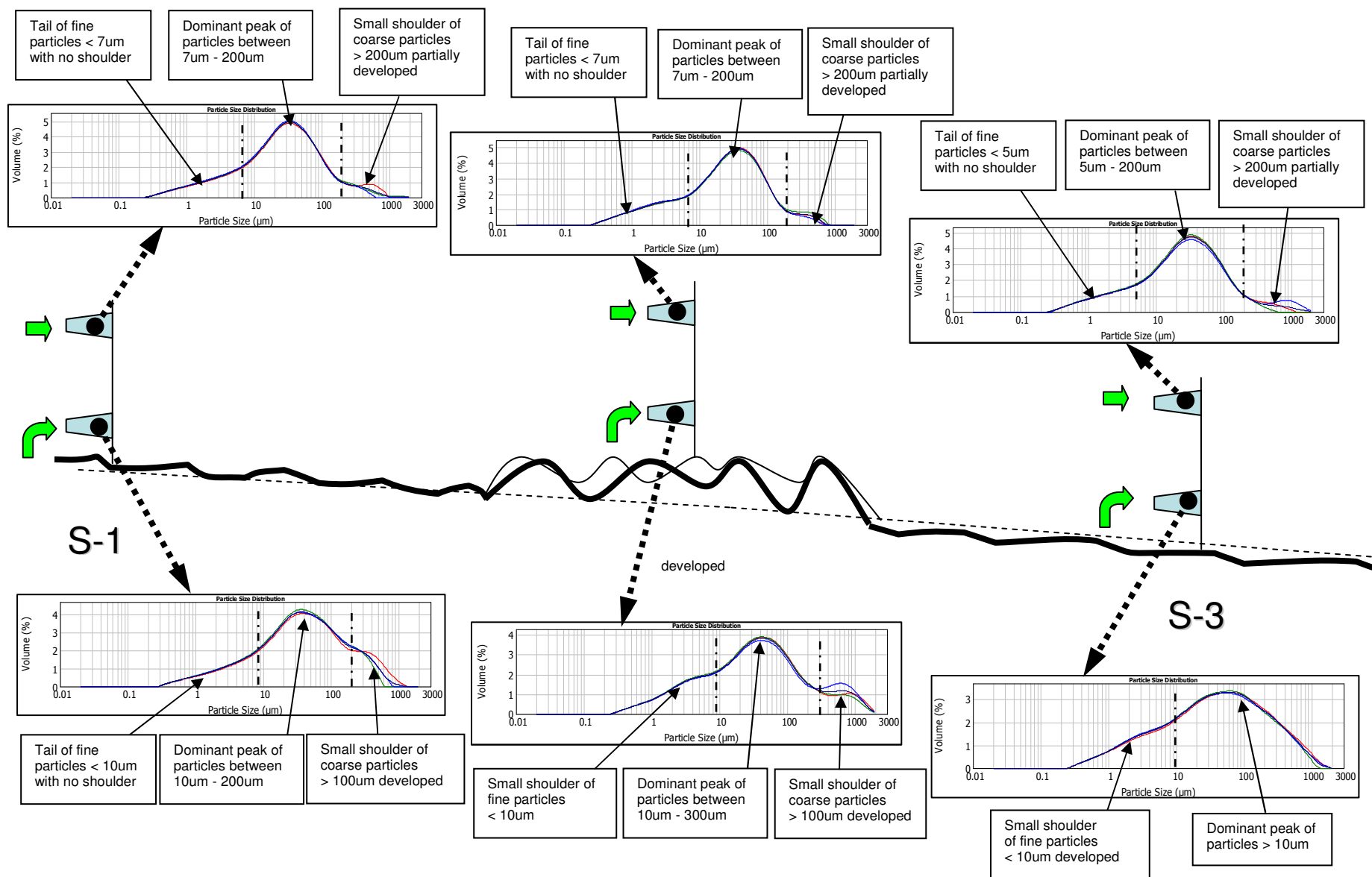


Figure 42: This diagram displays particle size analysis graphs of accreted sediment from S-1, S-2, and S-3.

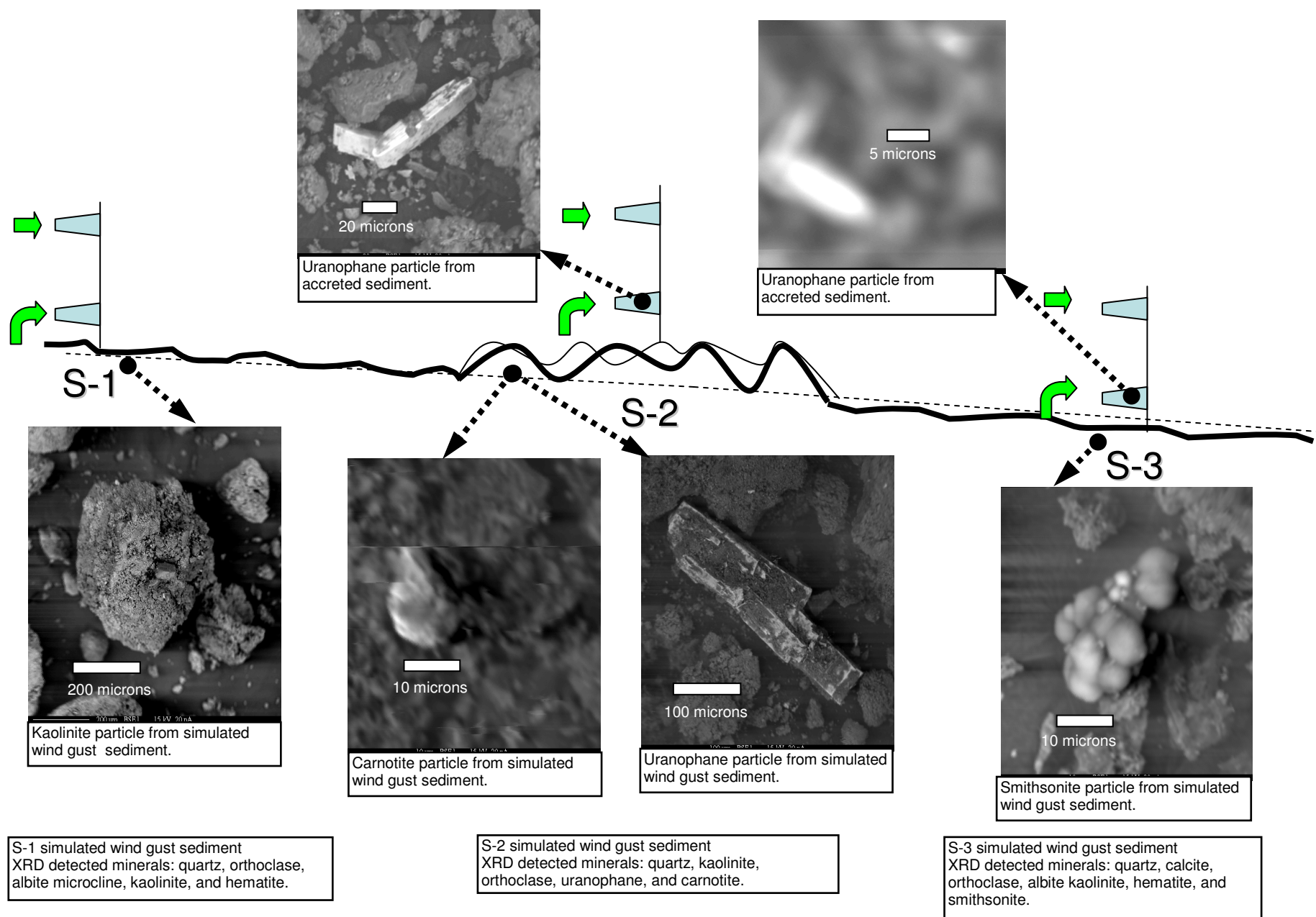


Figure 43: This diagram displays EMPA images and XRD mineralogy results of simulated wind gust and accreted sediment from S-1, S-2, and S-3.

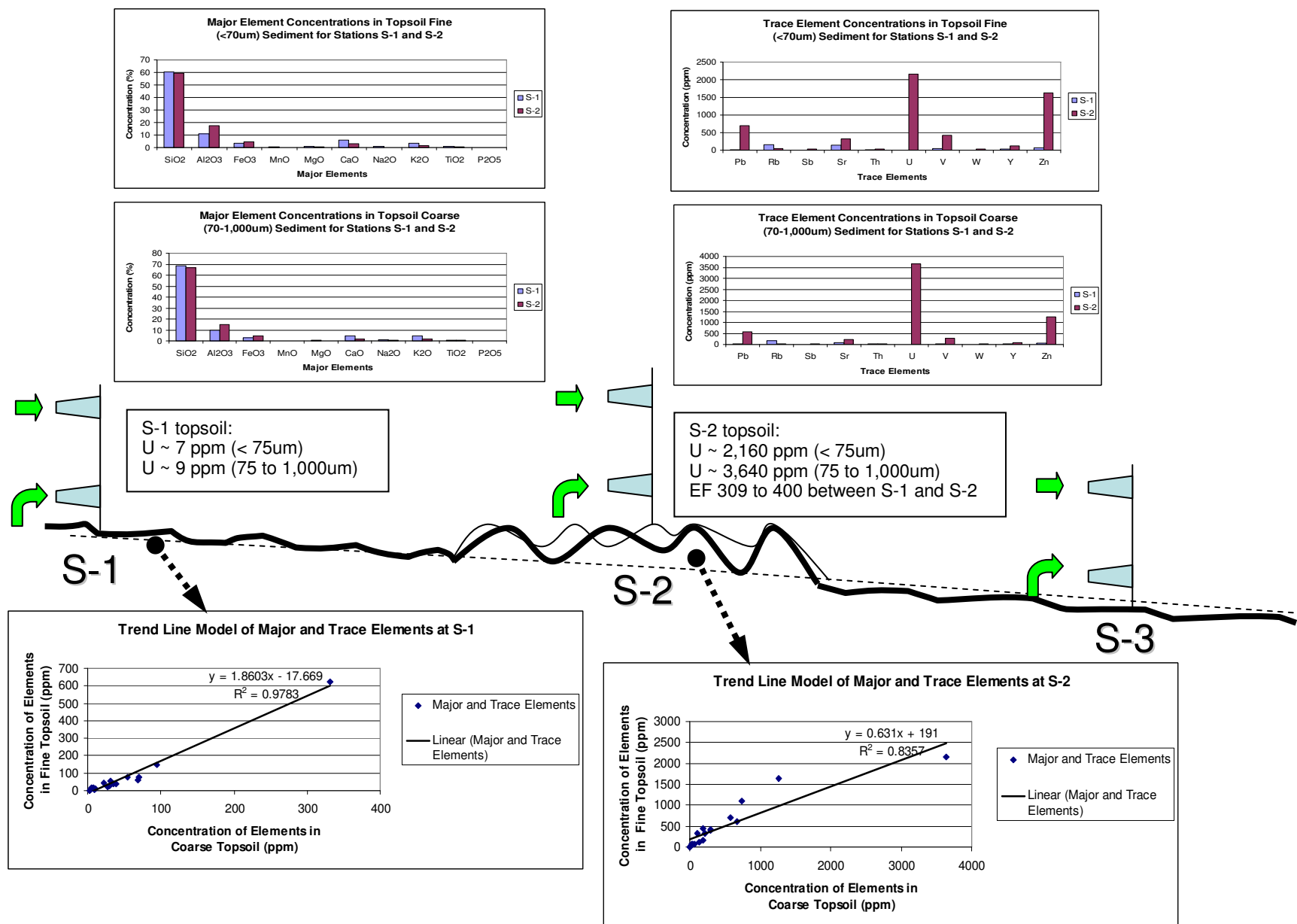


Figure 44: This diagram displays ICP-MS results of topsoil sediment from S-1, S-2, and S-3.

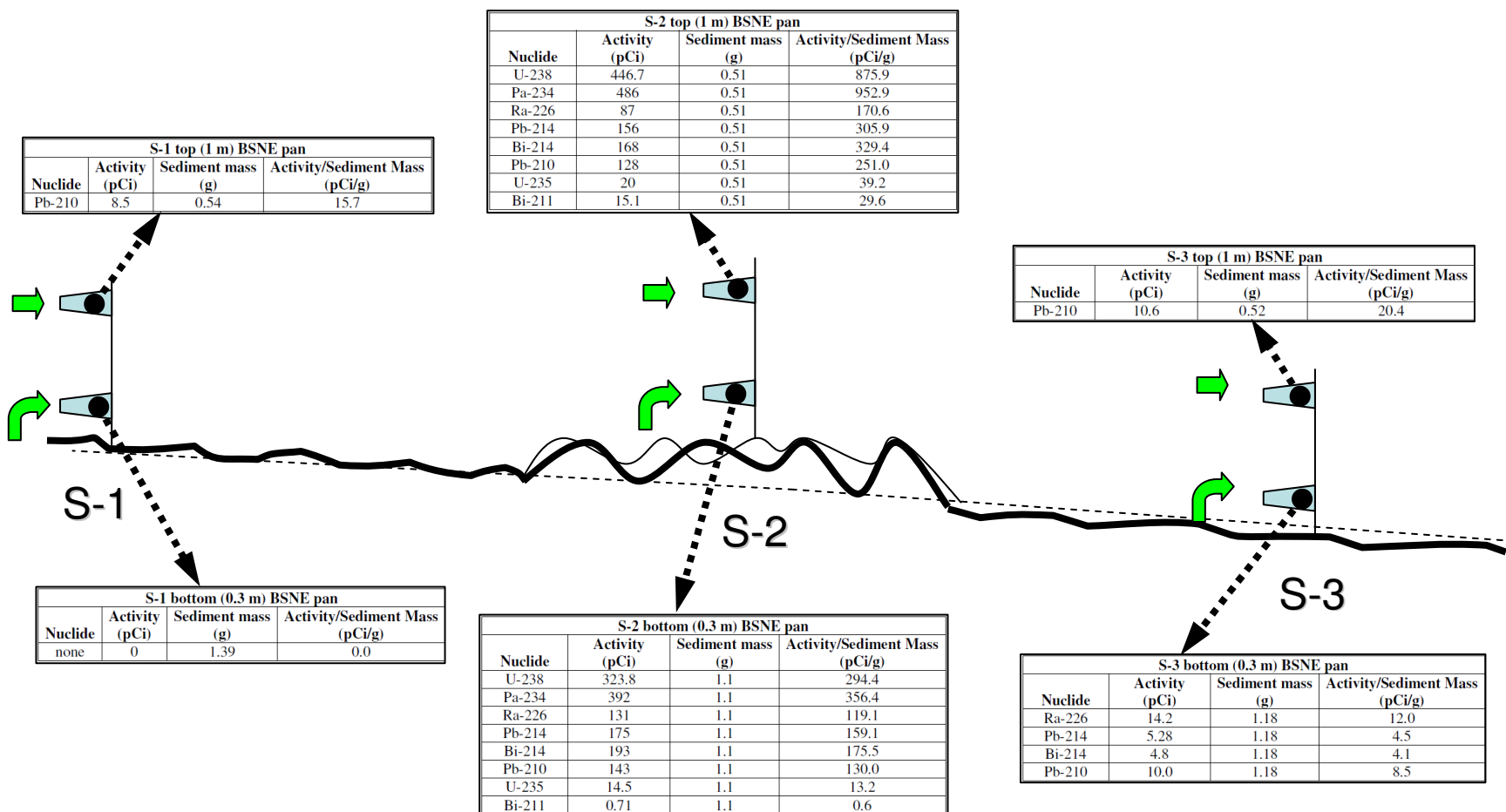


Figure 45: This diagram displays gamma-ray spectroscopy results of accreted sediment from S-1, S-2, and S-3.

8. References

- American Geological Institute (AGI), 1982, Data Sheet 17.1, Grain-size scale used by American Geologists, 2nd edition, Modified Wentworth Scale, AGI Data Sheets.
- Bourdon, B., Henderson, G.M., Lundstrom, C.C., Turner, S.P., 2003. Uranium-Series Geochemistry. *Reviews in Mineralogy and Geochemistry*, 52: 2-6.
- Chappell, A., 1998. Dispersing sandy soil for the measurement of particle size distribution using optical laser diffraction. *Catena* 31, 271-281.
- Choi, Y.-J., Hyde, P., Fernando, H.J.S., 2008. Implementation of a windblown dust parameterization into MODELS-3/CMAQ: Application to episodic PM events in the US/Mexico border. *Atmospheric Environment* 42, 6039–6046.
- Deer, W. A., Howie, R.A., Zussman, H., 1962. *Rock-Forming Minerals: Volume 3: Sheet Silicates*. Longman, London.
- Durrance, E.M., 1986. *Radioactivity in Geology, Principles and Applications*. John Wiley and Sons, New York, New York, pp. 106-108.
- Eby, G.N., 2004. *Principles of Environmental Geochemistry*. Brooks/Cole - Thomson Learning, Inc., Pacific Grove, California, pp. 214-362.
- Emets E., Kolomeytsev G., Mikheikin S., Poluektov P., Smirnov A., Timonin V., 1998. Investigation of dust generation processes over radioactive contaminated soil under wind action. *Journal of Aerosol Science* 29, Supplement 1, S211-S112.
- Environmental Protection Agency (EPA), 1998. *Emission Factor Documentation for AP-42, Section 13.2.2, Unpaved Roads*, Final Report: Midwest Research Institute, Kansas City, Missouri.
- Faure, G., 1986. *Principles of Isotope Geology, Second Edition*. John Wiley and Sons, New York, New York, pp. 283-286.
- French, D.C., 2006. *Geologic Studies in the Sierra de Peña Blanca Chihuahua, Mexico*. M.S. Thesis, University of Texas at El Paso, pp. 1-7.
- Fryrear, D.W. 1986. A field dust sampler. *Journal of Soil and Water Conservation* 41, 17-120.
- Fryrear, D.W., Saleh, A., 1993. Field wind erosion: vertical distribution. *Soil Science* 155, 294-300.
- Ganor, E., 1975. *Atmospheric dust in Israel. Sedimentological and meteorological analysis of dust deposition*. Ph.D. Thesis, Hebrew University of Jerusalem.
- Gillette, D.A., 1999. A Qualitative Geophysical Explanation for "Hot Spot" Dust Emitting Source Regions. *Contributions to Atmospheric Physics* 72, 67-77.
- Gillette, D.A., Fryrear, D.W., Gill, T.E., Ley, T., Cahill, T.A., Gearhart, E.A., 1997. Relation of vertical flux of particles smaller than 10 μm to total aeolian horizontal mass flux at Owens Lake. *Journal of Geophysical Research* 102, 26,009-26,015.

- Gillette, D. A., Chen, W., 2001. Particle production and aeolian transport from a “supply-limited” source area in the Chihuahuan desert. *Journal of Geophysical Research* 106, 5267-5278.
- Kim, Y., Kirkpatrick, R. J., Cygan, T., 1996. ^{133}Cs NMR study of cesium on the surfaces of kaolinite and illite. *Geochimica et Cosmochimica Acta* 60, 4059- 4074.
- Kirchner, T.B., Webb, J.L., Webb, S.B., Arimoto, R., Schoep, D.A., Stewart, B.D., 2002. Variability in background levels of surface soil radionuclides in the vicinity of the US DOE waste isolation pilot plant. *Journal of Environmental Radioactivity* 60, 275-291.
- Langmuir, D., 1997. *Aqueous Environmental Geochemistry*. Prentice Hall, Englewood Cliffs, New Jersey, pp. 495-514.
- Lottermoser, B.G., Ashley, P.M., 2006. Physical Dispersion of Radioactive Mine Waste at the Rehabilitated Radium Hill Mine Site, South Australia. *Australian Journal of Earth Sciences* 53, 485-499.
- Maynard, J.B., 1983. *Geochemistry of Sedimentary Ore Deposits*. Springer-Verlag, New York, New York, pp. 181-182.
- McCarthy, D.F., 1988. *Essentials of Soil Mechanics and Foundations: Basic Geotechnics*. Prentice Hall, Englewood Cliffs, New Jersey, pp. 46-58.
- Murray, R.L., 2009. *Nuclear Energy, Sixth Edition: An Introduction to the Concepts, Systems, and Applications of Nuclear Processes*. Butterworth-Heinemann, Boston, Massachusetts, pp. 29-34.
- Novlan, D.J., Hardiman, M., Gill, T.E., 2007. A synoptic climatology of blowing dust events in El Paso, Texas from 1932-2005: 16th Conference on Applied Climatology, American Meteorological Society, paper J3.12.
- Perez, A.E., Gill, T.E., 2009. Salt Flat Basin’s Contribution to Regional Dust Production and Potential Influence on Dry Deposition in the Guadalupe Mountains (Texas, USA). *Natural Resources and Environmental Issues* 15, 118- 119.
- Prikryl, J.D., Pickett, D.A., Murphy, W.M., Percy, E.C., 1997. Migration behavior of naturally occurring radionuclides at the Nopal I uranium deposit, Chihuahua, Mexico. *Journal of Contaminant Hydrology* 26, 61-69.
- Pye, K., 1987. *Aeolian Dust and Dust Deposits*. Academic Press, London, pp. 29-51.
- Reheis, M.C., 2006. A 16-year record of eolian dust in Southern Nevada and California, USA: Controls on dust generation and accumulation. *Journal of Arid Environments* 67, 487-520.
- Shao, Y., 2000. *Physics and Modelling of Wind Erosion*. Kluwer Academic Publishers, pp. 145-158.
- Sperazza, M., Moore, J.N., Hendrix, M.S., 2004. High-Resolution Particle Size Analysis of Naturally Occurring Very Fine-Grained Sediment Through Laser Diffraction. *Journal of Sedimentary Research* 74, 736-743.
- Stout, J. E., Fryrear, D.W., 1989. Performance of a windblown-particle sampler. *Transactions of the American Society of Agricultural Engineers* 32, 2041-2045.

Wiltshire, S.D., 1993. The Nuclear Waste Primer. The League of Women Voters Education Fund, New York, New York, pp. 125-126.

Wong, V., 1994. Nopal I Uranium Deposit, Peña Blanca District, Chihuahua, Mexico: A Study of Radionuclide Migration in a Natural Analogue to Yucca Mountain, Nevada. Master of Science Thesis, University of Texas at El Paso, pp. 30-40.

Wong, Virginia, E.Y. Anthony, and P.C. Goodell, 1996, Nopal I uranium deposit: A study of radionuclide migration: Proceed., 7th Ann. Internat. Conf., High Level Radioactive Waste Management; p. 43-45.

Wong, V., 1998a. Gamma-Ray Characterization of the Uranium-Series Nuclides and its Application to the Study of the Peña Blanca Natural Analog Site, Chihuahua, Mexico. Ph.D. Thesis, University of Texas at El Paso, pp. 66-96.

Wong, V., P.C. Goodell, and E.Y. Anthony, 1998b, Characterization of U-Series disequilibrium at the Pena Blanca Natural Analogue Site, Chihuahua, México: In Scientific Basis for Nuclear Waste Management XXII (eds. Wronkiewicz, D. J. and Lee, J. H.) Materials Research Soc. Symp. Proc. Vol. 556, p. 801-808.

Zobeck, T.E., 2004. Rapid Soil Particle Size Analyses Using Laser Diffraction. Applied Engineering in Agriculture 20, 633-639.

Chapter 3. Evaluating Global Atmospheric Transport of Plutonium with Dust Aerosols

1. Introduction

Approximately 2,000 Mt of dust is suspended in the atmosphere each year, predominantly from the great deserts of Africa and Asia (Prospero et al., 2002; Shao et al., 2011). Above-ground tests of nuclear weapons also were conducted in arid, dust-producing regions (Hirose et al., 1987, 2001), and the soils at nuclear test sites are known to be enriched in radionuclides (Turner et al., 2003). Pu injected into the stratosphere by high-yield nuclear weapons tests gradually deposits to the earth's surface via fallout (Hirose et al., 2010) from where it can be resuspended. Additional Pu has been mobilized by the wind from sites of low-yield nuclear events (Garcia-Olivares and Iranzo, 1997), especially during dust storms (Johnston et al., 1993). Other fallout radionuclides are also known to be released to the atmosphere via biomass burning (Pazukhin et al., 2004; Wotawa et al., 2006), and thus some Pu may be dispersed into the atmosphere by this mechanism as well.

When a nuclear device is detonated above ground, released radionuclides integrate with materials in the nuclear air burst (cloud), which may include soil particles (Schery, 2001), to form fused glass particles, crystals, or refractory oxides when mineral elements (e.g., Al, Si, Fe, Mg, Na, K, Ca, and their oxides) are exposed to temperatures high above their melting points (Zhang et al., 2002). Radionuclides from the detonations also attach to pre-existing particles suspended in the atmosphere, especially clay minerals. Pu from high-yield nuclear tests is initially concentrated in the stratosphere but then slowly falls out to the ground after exchange with the troposphere (Lee et al., 1998). The mean stratospheric residence time from atmospheric nuclear tests for Pu before re-entering the troposphere is ~1 year, so stratospheric Pu has long since been deposited to the land surface and oceans (Chamizo et al., 2010; Simon et al., 2004). The fallout of stratospheric “background” Pu was higher in the subtropics and mid-latitudes than at high latitudes owing to stronger stratosphere-troposphere exchange (Cizdziel et al., 2008). In the cases of low-yield nuclear tests and nuclear accidents, local soils and sediments receive radionuclides directly, and the Pu is dispersed mainly in the troposphere near and downwind of

the test site. Thus, Pu in soils represent a mixture of Pu from global stratospheric fallout and any Pu sourced from locally deposited material (Cizdziel et al., 2008).

Pu is relatively insoluble in water and exists in soils and sediments as the oxide PuO_2 (McDowell and Whicker, 1978; Wilkins et al., 1996). Tetravalent Pu has an affinity for sorption onto sediment surfaces (Powell et al., 2002), especially iron oxide coatings (Arimoto et al., 2006). Studies at the site of the Palomares contamination accident in Spain (Garcia-Olivares and Iranzo, 1997; Wilkins et al., 1996) suggested that Pu there is largely associated with large (sand-sized) soil particles. On the other hand, McDowell and Whicker (1978) suggested that Pu oxide particles in the soil at the Rocky Flats nuclear facility in Colorado (USA) were predominantly submicron in size. With regards to plutonium in aerosols, Wilkins et al. (1996) noted that areas secondarily contaminated by resuspended plutonium from the Palomares site had most of their Pu activity associated with particles smaller than $5\text{ }\mu\text{m}$. Similarly, samples from the vicinity of the Waste Isolation Pilot Plant in New Mexico (USA) (Arimoto et al., 2002) showed Pu was predominantly in PM_{10} (particulate matter $\geq 10\text{ }\mu\text{m}$ in diameter).

Global Pu contamination of soils is therefore ultimately a result of radionuclides from atmospheric nuclear weapons testing and to a lesser extent nuclear accidents such as the burn-up of a satellite (SNAP 9A), the nuclear weapons accident in Palomares, Spain, and the nuclear reactor accident in Chernobyl, Ukraine; and to a very minor degree leakage of radionuclides from underground nuclear weapons testing (Choi, et al., 2006; Chamizo et al., 2010; Garcia-Olivares and Iranzo, 1997; Hardy et al., 1973; Hirose et al., 2003; Kinoshita et al., 2011; Perkins and Thomas, 1980). Pu isotopes (^{238}Pu , half-life $T_{1/2} = 87.8$ years; ^{239}Pu , $T_{1/2}=24,110$ years); and ^{240}Pu , $T_{1/2}=6,400$ years) in contaminated soils can be resuspended by the wind and transported through the atmosphere in dust episodes (Arimoto et al., 2005; Johnston et al., 1993; Masson et al., 2010). Given the widespread contamination and long half-lives of the Pu isotopes, the redistribution of pre-existing Pu in the environment would have continued even if no further atmospheric nuclear releases were to occur. However, the recent radionuclide releases

from the damaged nuclear reactors in Fukushima, Japan (Buck and Upton, 2011) have brought increased attention to the movements of radionuclides in the environment.

In this investigation, we seek to better understand the global atmospheric transport of Pu by analyzing aerosols from four sites downwind of two major global dust sources. To determine whether Pu was associated with mineral aerosol particles, crustal elements including aluminum (Al) and calcium (Ca) were employed as dust tracers.

1.1 Site Selection

Aerosol samples were collected from Izaña, Canary Islands (IZT); Barbados (BAT); Gosan, South Korea (GOS); and Mauna Loa Observatory, Hawaii (MLO) (Figure 1). The IZT and BAT sites receive dust from Africa, especially the Sahara (Alpert et al., 2004; Arimoto et al., 1992, 1995; Gobbi et al., 2000; Pérez-Marrero et al., 2002; Pewe, 1981; Prospero and Carlson, 1981; Prospero et al., 1970, 2002) while GOS and MLO receive dust from Asia (Arimoto et al., 1996, 2004; Kang et al., 2009; Parrington et al., 1983; Perry et al., 1999).

Saharan dust transport over the Atlantic via easterly trade winds and its relationship with biogeochemical, and ecological processes led to the establishment of the Izaña and Barbados aerosol sampling sites (Arimoto et al., 1996, 1997; Kandler, 2007; Prospero, 1999b; Zhu et al., 1997). The Barbados site, which is more distal than Izaña from the African coast, was strategically positioned in the Saharan dust pathway and has been actively collecting dust samples since 1965 (Delany, 1967). Saharan dust events have been shown to represent a major pathway of regional injection of radionuclides into the atmosphere (Masson et al., 2010), and transport of radionuclides to the Canary Islands is known to be highest during African dust events (Hernandez et al., 2005a, 2005b).

Asian dust is lofted/mixed predominantly by strong westerly winds (Chen et al., 1997; Holmes and Zollar, 1996; Zhang et al., 1997) and transported via mid- and upper-tropospheric flow to Korea, Japan, and over the North Pacific Ocean as far as North America (Arimoto et al., 1996; Liu Tung-sheng et al., 1981; Yu et al., 2006). The Gosan site receives dust laden winds from dryland regions of Asia

including the Gobi and Takla Makan deserts and Loess Plateau (Arimoto et al., 2004; Igarashi et al., 1996, 2009; Kang et al., 2009; Kurosaki and Mikami, 2003; Rahn et al., 1981) and is an ideal to monitor atmospheric aerosol flow from east Asia since Gosan has an insignificant local industrial presence (Arimoto et al., 1996, 1999, 2004; Yu et al., 2006; Zhuang et al., 2001). The Mauna Loa Observatory receives aerosols primarily from Asia, with smaller contributions from North America and elsewhere (Braaten and Cahill, 1986; Perry et al., 1999; Shaw, 1980). Since 1979, the Mauna Loa Observatory site has been monitoring globally distributed natural and anthropogenic aerosol material due to its remoteness and high elevation (3,397 m) above the trade wind inversion layer (Arimoto et al., 1996; Braaten and Cahill, 1986; Holmes and Zollar, 1996; Huebert et al., 2001; Parrington et al., 1983; Perry and Cahill, 1999; Ziemann et al., 1995).

2. Methodology

High-volume aerosol samples were collected on Whatman® 41 paper filters (Whatman Ltd, Maidstone UK); these filters have low blanks for many trace elements and allow high flow rates (Arimoto et al., 1995; Trapp et al., 2010). The dates utilized for this study were 1989 – 1996 at Izaña, and 2005- 2006 at Barbados, Gosan, and Mauna Loa Observatory. Due to the low concentrations of Pu expected, the filters from each site were composited before analysis as detailed in Tables 1 and 2. The IZT site had five filters collected between 07-13-1989 and 05-26-1996 (Table 3). The BAT site had five composites (BAT-1 through BAT-5) with a total of 29 filters collected between 01-18-2005 and 11-27-2006 (Table 3). The GOS site had three composites (GOS-1 through GOS-3) with a total of 23 filters collected between 04-24-2005 and 05-10-2006 (Table 3). The MLO site had four composites (MLO-1 through MLO-4) with a total of 23 filters collected between 02-10-2005 and 07-24-2006 (Table 3). The dust and $^{239,240}\text{Pu}$ activity concentrations shown in Tables 1-2 for these composite samples correspond to all collection periods (composites) shown in Table 3.

Non-contaminating materials, including as anodized aluminum, stainless steel, polyethylene, and polypropylene, were used to fabricate the sampling equipment, and strict sampling protocols were

followed at all stations. With the exception of IZT, all the sites had pumping rates of $\sim 1 \text{ m}^3 \text{ min}^{-1}$. The IZT site had targeted collection periods and higher pumping rates (5 to $10 \text{ m}^3 \text{ min}^{-1}$) in order to enhance the collection of large quantities of dust. At BAT, there were days in which no data were collected because the winds were not from the clean oceanic sector. The negative values were omitted and remaining values averaged. The aerosol samples were stored in clean plastic bags for transport prior to analysis (Arimoto et al., 1992).

The activity of $^{239,240}\text{Pu}$ ($^{239}\text{Pu} + ^{240}\text{Pu}$) in the aerosol samples was determined by alpha spectrometry after the element was chemically separated and purified in a set of pretreatments as described in Arimoto et al. (2002, 2005). To prepare the filters for plutonium (Pu) and americium (Am) separation, the filters were heated (500°C) to where organics decompose along with most of the filter medium; the remaining portion was digested with $\text{HNO}_3/\text{HCl}/\text{HF}$ and dried for actinide removal (Arimoto et al., 1992). Pu was purified by a series of precipitation, co-precipitation and anion exchange steps. Pu activities were determined by alpha spectrometry for which the samples were counted for 5 to 12 days. The energies of the ^{239}Pu and ^{240}Pu α -particles are similar, and therefore the results for the two isotopes together are traditionally presented as $^{239,240}\text{Pu}$.

Here it is essential to point out that aliquots of the digested filters were analyzed for trace elements, but the elemental data were not considered reliable, most likely due to contamination introduced during the digestion process. The contamination was evident both in terms of absolute concentrations and elemental ratios. Note also that there was no indication of any contamination for Pu. Because of the problem with the elemental data we used dust proxy data for samples collected independently but in parallel with ours.

The relationship between Pu activity and mineral dust concentrations was evaluated by using aluminum (Al) or calcium (Ca^{2+}) concentrations, or ash free dry weight, as normalizing proxies for dust (Arimoto et al., 1997, 2002; Chamizo et al., 2010; Choi et al., 2006). Crustal reference elements have been employed to calculate soil aerosol concentrations with the assumption that the soil aerosols have

elemental contents approximately equal to those in the earth's upper continental crust or a specific dust source (Arimoto et al., 1995, 1997, 2002; Chamizo et al., 2010; Choi et al., 2006). Dust concentration values for BAT were obtained directly from collected in-situ ash free dry weight samples. Dust concentration values for IZT and GOS were derived from Al concentration values as related to its crustal weight percentage ($\text{Al}_{\text{concentration}}/8.13\%$). Dust concentration values for MLO were derived from measured water-soluble Ca^{2+} concentration values related to its crustal weight percentage ($\text{nssCa}^{2+}_{\text{concentration}}/3.63\%$). In the equation $\text{Ca}_{\text{total}} = (\text{Ca}^{2+}_{\text{soluble}} + \text{Ca}^{2+}_{\text{insoluble}}) + \text{ssCa}^{2+}$, only $\text{Ca}^{2+}_{\text{soluble}}$ was measured and $\text{Ca}^{2+}_{\text{insoluble}}$ not considered; therefore, the equation becomes $\text{Ca}_{\text{total}} = \text{Ca}^{2+}_{\text{soluble}} + \text{ssCa}^{2+}$. This equation was utilized in concurrence with equation $\text{Ca}_{\text{total}} = \text{nssCa}^{2+} + \text{ssCa}^{2+}$ to calculate nssCa^{2+} . The ssCa^{2+} value is considered negligible, but was included in the calculations for improved precision in equations (1) and (2) (Rothlisberger, 2002; Guinot, 2007). Equations (1) and (2) are combined to obtain equation (3) to solve for crustal Ca^{2+} (nssCa^{2+}).

$$\text{ssNa}^+ = \text{Na}^+ - \left[\frac{\text{nssCa}^{2+}}{R_t} \right] \quad (1)$$

$$\text{ssNa}^+ = \text{sea-salt Na}^+$$

$$\text{Na}^+ = \text{Measured Na}^+$$

$$\text{nssCa}^{2+} = \text{nonsea-salt Ca}^{2+} (\text{crustal Ca}^{2+})$$

$$R_t = \frac{\text{Ca}^{2+}}{\text{Na}^+} = 1.78 \quad (\text{Crustal ratio of Ca}^{2+}/\text{Na}^+)$$

$$\text{nssCa}^{2+} = \text{Ca}^{2+} - R_m \cdot \text{ssNa}^+ \quad (2)$$

$$\text{nssCa}^{2+} = \text{nonsea-salt Ca}^{2+}$$

$$\text{Ca}^{2+}_{\text{soluble}} = \text{Ca}^{2+}$$

$$\text{ssCa}^{2+} = R_m \cdot \text{ssNa}^+ = \text{sea-salt Ca}^{2+}$$

$$R_m = \frac{\text{Ca}^{2+}}{\text{Na}^+} = 0.038 \quad (\text{Marine ratio of Ca}^{2+}/\text{Na}^+)$$

$$nssCa^{2+} = Ca^{2+} - 0.038 \left[\frac{Na^+ - \frac{Ca^{2+}}{1.78}}{1 - \frac{0.038}{1.78}} \right] \quad (3)$$

Elemental concentrations representing mineral dust proxies were determined by inductively coupled plasma atomic emission spectrometry (ICP-AES) and/or instrumental neutron activation analyses (INAA), whereas water-soluble ions were determined by ion chromatography (IC). The application of these various techniques was site dependent, that is, INAA was used to determine Al concentrations at IZT (Arimoto et al., 1995); ICP-AES was used to determine Al concentrations at GOS (Kang et al., 1995); and IC was used to determine water-soluble Ca^{2+} concentrations at MLO (Huebert et al., 2001). The BAT site required no normalization since dust concentration values were available as the samples' ash free dry weights (Prospero, 1999a).

3. Results

The dust mass concentrations ($\mu g/m^3$) for all sites had the following rank order: IZT > BAT > GOS > MLO (Figure 2; Table 1). The overall results of total Pu activity concentrations (Bq/m^3) for all sites had the following rank order: GOS > IZT > BAT > MLO (Figure 2). Results suggest that $^{239,240}Pu$ activity, as well as dust concentrations, decrease with distance from continental aerosol sources. Combined, the overall results of Pu activity levels per unit of dust mass ($Bq/\mu g$) for all sites had the following rank order: GOS > MLO > BAT > IZT (Figure 3).

3.1 Izaña, Canary Islands (IZT)

The samples from IZT had been previously analyzed by INAA for the Atmosphere/Ocean Chemistry Program (Arimoto et al., 1995), and were specifically chosen for Pu analyses because of their high dust loadings (Figure 4). Utilizing Al as a dust proxy, the averaged dust concentration value was $412.3 \mu g/m^3$. The $^{239,240}Pu$ activity/volume was $2.8 \times 10^{-7} Bq/m^3$, whereas the $^{239,240}Pu$ activity/dust mass was $6.7 \times 10^{-10} Bq/\mu g$ (Table 1).

3.2 Barbados (BAT)

The dust concentration values ranged between $25.5 \mu\text{g}/\text{m}^3$ and $7.2 \mu\text{g}/\text{m}^3$ (Figure 5; Tables 1 and 3). The $^{239,240}\text{Pu}$ activity/volume values ranged between $8.3 \times 10^{-8} \text{ Bq}/\text{m}^3$ and $5.0 \times 10^{-8} \text{ Bq}/\text{m}^3$, whereas the $^{239,240}\text{Pu}$ activity/dust mass values ranged from $3.0 \times 10^{-9} \text{ Bq}/\mu\text{g}$ to $4.7 \times 10^{-9} \text{ Bq}/\mu\text{g}$ (Table 1). There was no $^{239,240}\text{Pu}$ activity value detected for the BAT-2 composite above the minimum detectable activity level ($2.6 \times 10^{-9} \text{ Bq}/\text{m}^3$) (Table 1) (Arimoto et al., 2005).

3.3 Gosan, South Korea (GOS)

Utilizing Al as a dust proxy, the dust concentration values ranged between $3.2 \mu\text{g}/\text{m}^3$ and $14.1 \mu\text{g}/\text{m}^3$ (Figure 6; Tables 1 and 3). There was no $^{239,240}\text{Pu}$ activity value detected for the GOS-1 and GOS-2 composites above the minimum detectable activity level ($2.6 \times 10^{-9} \text{ Bq}/\text{m}^3$) (Table 1) (Arimoto et al., 2005). The only detected $^{239,240}\text{Pu}$ activity/volume value was $5.0 \times 10^{-7} \text{ Bq}/\text{m}^3$, whereas the only $^{239,240}\text{Pu}$ activity/dust mass value was $3.5 \times 10^{-8} \text{ Bq}/\mu\text{g}$ (Table 1).

3.4 Mauna Loa Observatory, Hawaii (MLO)

Utilizing Ca as a dust proxy, the dust concentration values ranged between $0.2 \mu\text{g}/\text{m}^3$ and $1.6 \mu\text{g}/\text{m}^3$ (Figure 7; Tables 1 and 3). There was no $^{239,240}\text{Pu}$ activity value detected for MLO-1, MLO-2, and MLO-4 composites above the minimum detectable activity level ($2.6 \times 10^{-9} \text{ Bq}/\text{m}^3$) (Table 1) (Arimoto et al., 2005). The only $^{239,240}\text{Pu}$ activity/volume value was $1.2 \times 10^{-8} \text{ Bq}/\text{m}^3$ (Table 1), whereas the only $^{239,240}\text{Pu}$ activity/dust mass value was $8.6 \times 10^{-9} \text{ Bq}/\mu\text{g}$ (Table 1).

4. Discussion

Pu was detectable in at least some samples from all four locations. The $^{239,240}\text{Pu}$ activity values in the air for these samples are generally on the order of a magnitude higher than those reported for non-dusty aerosols with plutonium derived only from global background fallout (Arimoto et al., 2002, 2005; Chamizo et al., 2010; Gascó et al., 2007; Pan and Stevenson, 1996; Wershofen et al., 2001). But on the other hand, they are one to four magnitudes lower than those reported for sites known to be contaminated by Pu from nuclear accidents or low-yield nuclear tests (Chamizo et al., 2010, and

references therein). These findings suggest that Pu concentrations in the atmosphere vary as a function of their source area. Considering Pu activity per dust mass (Bq/ μ g) values determined here, it appears that Asian values were far greater than Saharan values (Figures 2 and 3; Table 1).

4.1 Saharan Pathways

Soil material from the Sahara is regularly spread over the Atlantic and Canary Islands as dust (Alastuey et al., 2005; Alpert et al., 2004; Gobbi et al., 2000; Pérez-Marrero et al., 2002). After trans-Atlantic transport, some Saharan dust eventually reaches the Caribbean, southeastern North America, and the Amazon Basin (Husar et al., 1997; Prospero, 1999b; Prospero et al., 1970; Trapp et al., 2010). African dust transport predominantly occurs in the spring and summer (Trapp et al., 2010), with annual dust levels peaking in June and July (Pewe, 1981; Prospero and Lamb, 2003; Prospero et al., 1970). The highest Saharan aerosol concentrations at Barbados occur in July and August (Prospero, 1999b; Prospero and Carlson, 1981; Prospero et al., 1987). Thus, Barbados (Trapp et al., 2010) and Izaña (Alastuey et al., 2005) receive dust (and would receive dust-associated Pu) originating from Africa.

Aerosol Pu activities in continental Spain have been demonstrated to be highest and most enriched over baseline hemispheric fallout values during Saharan dust intrusions (Chamizo et al., 2010), and gross alpha and beta radionuclide (^7Be , ^{210}Pb , ^{228}Ac , ^{226}Ra , ^{212}Pb , ^{214}Pb , ^{208}Tl , ^{214}Bi , ^{235}U , ^{40}K , ^{131}I and ^{137}Cs) activities in the Canary Islands also are highest during Saharan dust events (Hernandez et al., 2005a). On the other hand, the highest concentrations of actinides at free tropospheric sites in the Azores islands, north of the Canaries, are associated with transport from northern Europe rather than the Sahara (do Carmo Freitas and Pacheco, 2010). Several of France's atmospheric nuclear test sites were located the Sahara (Figure 1). However, the contamination of sediments from these tests was relatively minor and limited in spatial extent, with the nuclides predominantly residing in hard fused materials near the test sites and not in resuspendable sediments (Baggoura et al., 1998; Danesi, 2008; IAEA, 2005). Plutonium fallout from the Chernobyl accident primarily affected the northern regions of North Africa closest to the Mediterranean coast (Baggoura et al., 1998; do Carmo Freitas and Pacheco, 2010), thus

suggesting that the IZT and BAT sites are not likely recipients of Chernobyl plutonium fallout. Therefore, the origin of Pu in West African dust would be derived from the reuspension of surface soil particles bearing global fallout radionuclides.

The activity of Pu in the IZT aerosol samples (0.67 mBq/g) is just above the activity range of soils in the Sahara impacted by the general stratospheric fallout (Baggoura et al., 1998), and it ~ 36% lower than that measured during a Saharan dust event in France not associated with local resuspension from nuclear test sites (Masson et al., 2010). The IZT site is located at approximately 2,200 m altitude, where the local land surface might have received slightly more Pu than low elevations (Hirose et al., 2010). The samples from IZT had the highest mean dust concentration with respect to volume ($\mu\text{g}/\text{m}^3$), but the lowest Pu activity/dust mass ($\text{Bq}/\mu\text{g}$) value (Figures 2 and 3; Table 1). As previously noted the samples from IZT were specifically selected based on prior analyses to have high dust loadings, the intent being to maximize the chances for detecting Pu. In contrast, collections at BAT yielded the second highest mean dust concentration values with respect to volume ($\mu\text{g}/\text{m}^3$), and a slightly higher Pu activity/dust mass ($\text{Bq}/\mu\text{g}$) value (Figures 2 and 3; Table 1). The BAT-4 composite, which had the highest $^{239,240}\text{Pu}$ activity, was the only sample that was collected entirely within the annual dust peak period (Figure 5). The fact that the IZT samples, collected during intense dust events and closer to the dust source than BAT, had lower $^{239,240}\text{Pu}$ activity/dust mass ratios (Figure 3), could be explained by the preferential removal of dust relative to $^{239,240}\text{Pu}$ during transport. This would occur if the Pu was borne in the finer dust particles because their dry deposition velocities would be smaller.

4.2 Asian Pathways

Primarily between November and May, and most especially during the late winter and early spring, wind-suspended dust from the interior of Asia, especially the Gobi and Takla Makan deserts and the Chinese Loess Plateau is transported by prevailing westerlies in the middle and upper troposphere towards Korea and Japan. These events can last for up to several days (Duce, 1980; Liu Tung-sheng et al., 1981; Merrill et al, 1989; Mori et al., 2002; Shaw, 1980). Asian dust can reach Pacific island sites

including Hawaii (Braaten and Cahill, 1986; Parrington et al., 1983; Perry et al., 1999; Shaw, 1980) and western North America (VanCuren and Cahill, 2002; Zhao et al., 2008). The Lop Nor atmospheric nuclear test site in the Takla Makan desert of China and the Soviet nuclear testing grounds in Kazakhstan (Figure 1), would be upwind of Chinese deserts during dust-favoring synoptic weather patterns (Cao et al., 2005; Chung and Yoon, 1996; Chung et al., 2003; Hirose et al., 2001; Rahn et al., 1981; Sun, 2002), thus the GOS and MLO sites could receive material resuspended from these sites in addition to plutonium derived from the global fallout.

GOS, the highest-latitude of the study sites (~36 degrees North), would be expected to receive a slightly lower amount of Pu from global background fallout than the other sites (Hirose and Aoyama, 2003; Hirose et al., 2003). However, the GOS site yielded a greater gross $^{239,240}\text{Pu}$ activity per unit air volume ($5.0 \times 10^{-7} \text{ Bq/m}^3$ vs. $1.2 \times 10^{-8} \text{ Bq/m}^3$) and $^{239,240}\text{Pu}$ activity per dust concentration values ($3.5 \times 10^{-8} \text{ Bq/}\mu\text{g}$ vs. $8.6 \times 10^{-9} \text{ Bq/}\mu\text{g}$) than the MLO site (Table 1).

The Chinese atmospheric nuclear weapons testing program at Lop Nor, in addition to releasing Pu into the stratosphere, also contaminated soils in Gansu and Qinghai provinces of northwestern China, as far as ~600 km or more downwind from the tests, with additional local tropospheric fallout (Wu et al., 2010). It is possible that the prevailing westerly winds might have resuspended some Pu-bearing material from these contaminated lands, and/or the Semipalatinsk site in the former Soviet Union, adding additional plutonium to the Asian dust transport pathway. The path of the radionuclide cloud from a typical Chinese atmospheric nuclear test (and by analogy, resuspended dust from the area around and downwind of Lop Nor) would take it near Korea one to two days later (Rahn et al., 1981; <http://www.atomicarchive.com/Maps/LopNorMap.shtml>). These materials might initially seem to explain the higher $^{239,240}\text{Pu}$ values per air volume detected at Gosan (Table 1). The activity per unit mass of Pu in dust at GOS (35 mBq/g) (Figure 3; Table 1) is enriched by an order of magnitude over that in Mongolian surface soil (Hirose et al., 2010), also suggesting the possibility that some resuspended soils enriched with supplementary Pu (i.e., Pu derived from a source other than global

background fallout) were sampled at GOS. The Pu levels in aerosol at Gosan were, though, one to two orders of magnitude lower than measured directly over Pu-contaminated soils at Palomares, Spain (Iranzo et al., 1987) and Chernobyl (Holgye, 2008). What is more, the activity of $^{239,240}\text{Pu}$ per unit air volume at GOS ($\sim 0.5 \times 10^{-6} \text{ Bq/m}^3$, Figure 2) was only about half the maximum recorded in aerosol samples obtained on the Korean west coast (Korea Global Atmosphere Watch Observatory) during Asian dust events (Choi et al., 2006), in which the Pu isotopic ratios were indicative of Northern Hemisphere background fallout rather than contamination from Chinese test sites. Therefore, resuspended global background fallout alone is sufficient to explain the observed plutonium activity in dust aerosol at Gosan.

The greatest single influence on aerosol compositions and concentrations at the Gosan site is Asian dust events (Kang et al., 2009). The GOS-3 collection phase in which Pu concentrations could be detected (Figures 6 and 7; Tables 5 and 6) fell within the Asian dust season. Deposition of both ^{137}Cs and $^{239,240}\text{Pu}$ in Korea and Japan has been shown to reach a maximum in springtime, especially in association with strong Asian dust outbreaks (Akata et al., 2007; Hirose et al., 2004, 2010), and was highest at Gosan in this study between January and May 2006, matching the observed seasonal pattern and Pu activity levels documented for sites in Japan (Hirose et al., 2010), suggesting that Pu is preferentially transported to Gosan during Asian dust events. Hirose et al. (2010) pointed out that Asian dust has become somewhat enhanced in $^{239,240}\text{Pu}$ in recent years as newly desertified (i.e., not having eroded since the period of global atmospheric nuclear testing) lands became dust emission sources; the relatively high gross activity of Pu per unit air volume and unit dust mass measured at GOS (Figure 3; Table 1) therefore most likely reflects the initial historically recent wind erosion (which would resuspend the surface layer richest in anthropogenic Pu) from these contaminated soils.

Although Hawaii is not a particularly dusty environment (Pett-Ridge et al., 2007), the Mauna Loa Observatory receives aerosols predominantly comprised of continental crustal material (Parrington et al., 1983), primarily from Asia and primarily fine (~ 1.0 micron in mass median diameter) (Braaten

and Cahill, 1986), with smaller contributions from North America and other sources (Perry et al., 1999). Anthropogenic air pollutants such as nitrate (NO_3), sulfate (SO_4), and ammonium (NH_4) are adsorbed by Asian silicate mineral aerosols proportionally more than on dusts from other regions (Ministry of the Environment Government of Japan, 2008), and some of these anthropogenic Asian aerosols are also transported to MLO (Perry et al., 1999). Pett-Ridge et al. (2007) showed that mineral dust was the primary long-term geochemical pathway for deposition of naturally occurring radionuclides (uranium) in the Hawaiian Islands. The MLO-3 collection period, when Pu concentrations could be detected at Mauna Loa, occurred during the Asian dust season.

The proportionally high Pu activity/dust mass values at MLO during this period may be attributable to several factors. MLO receives predominantly fine aerosols, with mass median diameters during dust events on the order of ~ 1 micron; if Pu is carried on the surface of a soil aerosol, it would have a higher relative enrichment when transported with fine particles. The mountaintop location of Mauna Loa (altitude ~ 3400 m) above the mean trade wind inversion layer height (~ 1800 m) favors reception of far-traveled aerosols entrained in the free troposphere (Mendonca and Iwaoka, 1969). There are upslope winds occurring at MLO during daytime and downslope winds occurring at night (Perry et al., 1999). The downslope winds at MLO introduce free-tropospheric air from 1 km above the observatory to ground level (Ryan, 1997). This combination of high altitude, wind patterns, and a relatively low latitude (~ 19.5 degrees N) might have positioned Mauna Loa to receive a proportionally higher amount of Pu from stratospheric fallout (which would become available for resuspension), since the stratospheric “background” Pu fallout is stronger in the subtropics and midlatitudes due to stronger stratosphere- troposphere exchange (Cizdziel et al., 2008). Finally, MLO is located approximately downwind of the USA nuclear test sites in the Central Pacific, and at a latitude that may have received some additional dosage from those explosions (Kinoshita et al., 2011). However, it must be pointed out that the gross Pu activity per overall volume of air at MLO, 1.2×10^{-8} Bq/m³, is comparable to that

reported in Chicago, a site receiving global fallout Pu only (Pan and Stevenson, 1996), thus resuspended global fallout is sufficient to explain Pu levels in the air at Mauna Loa Observatory.

5. Conclusions

Plutonium activity was detected in some samples of mineral (resuspended soil) aerosols at global receptor sites relatively near and far from known African and Asian dust sources; moreover, evidence of an enhancement in concentration/detectability of atmospheric Pu transport associated with dust episodes was shown. The dust concentrations were consistent with previous observations at these sites. The dust mass/pumped air volume ($\mu\text{g}/\text{m}^3$) for all sites had the following rank order: IZT > BAT > GOS > MLO. The Pu activity levels/pumped air volume (Bq/m^3) for all sites had the following rank order: GOS > IZT > BAT > MLO. When combined, the Pu activity levels/dust mass ($\text{Bq}/\mu\text{g}$) for all sites had the following rank order: GOS > MLO > BAT > IZT.

The sites closer to dust sources (i.e., GOS and IZT) are recipients of relatively lower concentrations of fine aerosols (proportionally more coarse particles) which would result in a lesser surface-to-volume ratio (and thus lower Pu activity-to-mass ratio) of radionuclides if plutonium is carried on mineral surfaces. The more distal, lower-dust-mass sites along each pathway (i.e., MLO and BAT) are recipients of slightly higher relative concentrations of Pu in dust, suggesting that plutonium appears to be enriched in the finer fraction of aerosols. Publicly-available data on size-resolved Pu concentrations in sediments are difficult to obtain. However, since metal concentrations in dust and sediments generally increase as particle size decreases (al-Rajhi et al., 1996; Horowitz, 1984) as revealed in the PM10 fraction (Eleftheriadis and Colbeck, 2001; Gatz et al., 1986), the same behavior is suggested here for Pu and merits further investigation.

The Izaña samples were obtained during a limited number of high-dust-concentration episodes in which it was anticipated that greater amounts of Pu would be collected, but even so, the gross amount of Pu measured in IZT samples was only about half that detected under about 1/30th the dust loading at GOS. The Pu activity at GOS was clearly enriched over levels which would be expected solely from the

current global background dust bearing Pu from the global stratospheric fallout of Pu, and most likely represents additional Pu contributions from the surface soil of newly eroding lands. $^{239,240}\text{Pu}$ activity at the other three sites was reasonably consistent with location-adjusted global background fallout carried in dust.

Since ^{239}Pu has a half-life of 24,110 years and with numerous daughter products in its decay series, resuspension of Pu and other radionuclides via mineral aerosols will continue well into the future. These results regarding fate and global transport of Pu-bearing dust comprise another step towards establishing a residence time of Pu in the earth-atmosphere system, have implications to the biogeochemical and environmental impacts of other substances associated with atmospheric dust cycling, and may have further implications for land use dynamics, homeland security, and public health. It is predicted that better knowledge of the geochemical and nuclear chain behaviors of this system may lead to future research tools.

Finally, we suggest that fallout Pu may eventually have utility as a geochemical tracer of environmental change, just as fallout tritium and ^{137}Cs have been used as a geochemical tracer for groundwater (Eriksson, 1958; Schlosser et al., 1988) and sediment transport (Akata et al., 2007; Robbins et al., 1985; Van Pelt et al., 2007; Wan et al., 1987). The fallout process for Pu and ^{137}Cs is the same, and the $^{239,240}\text{Pu}$ peak would be preserved similarly to ^{137}Cs in sediments (Wu et al., 2010). Since $^{239,240}\text{Pu}$ should be less mobile than ^{137}Cs in sediments and thus less likely to migrate (Wu et al., 2010), and since ^{137}Cs activity relating to the global atmospheric fallout peak has been used as a geochronological and source apportionment tool for marine and lacustrine sediments (Robbins et al., 1975; Wan et al., 1987) and aeolian material (Akata et al., 2007; Van Pelt et al., 2007), therefore $^{239,240}\text{Pu}$ may also be applicable for measuring the short-term deposition chronology and understanding the dynamics of sources of wind-transported sediments, just as Wu et al. (2010) suggested it could be used for lacustrine sediments.

6. References

- Akata, N., Hasegawa, H., Kawabata, H., Chikuchi, Y., Sato, T., Ohtsuka, Y., Kondo, K., Hisamatsu, S., 2007. Deposition of ^{137}Cs in Rokkasho, Japan and its relation to Asian dust. *Journal of Environmental Radioactivity*, 95, 1-9.
- Al-Rajhi, M.A., Al-Shayeb, S.M., Seaward, M.R.D., Edwards, H.G.M., 1996. Particle size effect for metal pollution analysis of atmospherically deposited dust. *Atmospheric Environment*, 30, 145-153.
- Alastuey, A., Querol, X., Castillo, S., Escudero, M., Avila, A., Cuevas, E., Torres, C., Romero, P.M., Exposito, F., Garcia, O., Diaz, J.P., Van Dingenen, R., Putaud, J.P., 2005. Characterisation of TSP and PM_{2.5} at Izana and Sta. Cruz de Tenerife (Canary Islands, Spain) during a Saharan Dust Episode (July 2002). *Atmospheric Environment*, 39, 4715-4728.
- Alpert, P., Kishcha, P., Shtivelman, A., Krichack, S.O., Joseph, J.H., 2004. Vertical distribution of Saharan dust based on 2.5-year model predictions. *Atmospheric Research*, 70, 109-130.
- Aoyama, M., Hirose, K., Suzuki, Y., Inoue, H., Sugimura, Y., 1986. High level radioactive nuclides in Japan in May. *Nature*, 321, 819-820.
- Aoyama, M., Hirose, K., Sugimura, Y., 1991. The temporal variation of stratospheric fallout derived from the Chernobyl accident. *Journal of Environmental Radioactivity*, 13, 103-115.
- Arimoto, R., Duce, R.A., Savoie, D.L., Prospero, J.M., 1992, Trace Elements in Aerosol Particles from Bermuda and Barbados: Concentrations, Sources and Relationships to Aerosol Sulfate. *Journal of Atmospheric Chemistry*, 14, 439-457.
- Arimoto, R., Duce, R.A., Ray, B.J., Ellis Jr., Cullen, J.D., Merrill, J.T., 1995, Trace Elements in the Atmosphere over the North Atlantic. *Journal of Geophysical Research*, 100, 1199-1213.
- Arimoto, R., Duce, R. A., Savoie, D. L., Prospero, J. M., Talbot, R., Cullen, J. D., Tomza, U., Lewis, N. F., Ray, B. J., 1996. Relationships among aerosol constituents from Asia and the North Pacific during PEM West-A. *Journal of Geophysical Research*, 101, 2011-2023.
- Arimoto, R., Ray, B.J., Lewis, N.F., Tomza, U., Duce, R.A., 1997. Mass-particle size distributions of atmospheric dust and the dry deposition of dust to the remote ocean. *Journal of Geophysical Research*, 102, 15867-15874.
- Arimoto, R., Snow, J.A., Graustein, W.C., Moody, J.L., Ray, B.J., Duce, R.A., Turekian, K.K., and Maring, H.B., 1999. Influences of atmospheric transport pathways on radionuclide activities in aerosol particles from over the North Atlantic. *Journal of Geophysical Research*, 104, 21301-21316.
- Arimoto, R., Kirchner, T., Webb, J., Conley, M., Stewart, B., Schoep, D., Walthall, M., 2002. $^{239,240}\text{Pu}$ and inorganic substances in aerosols from the vicinity of the waste isolation pilot plant: the importance of resuspension. *Health Physics*, 83, 456-470.
- Arimoto, R., Zhang, X. Y., Huebert, B. J., Kang, C. H., Savoie, D. L., Prospero, J. M., Sage, S. K., Schloesslin, C. A., Khaing, H. M., Oh, S. N., 2004. Chemical composition of atmospheric aerosols from Zhenbeitai, People's Republic of China, and Gosan, South Korea, during the ACE-Asia. *Journal of Geophysical Research*, 109, D19S04, doi: 10.1029/2003JD004323.

- Arimoto, R., Webb, J.L., Conley, M., 2005. Radioactive contamination of atmospheric dust over southeastern New Mexico. *Atmospheric Environment*, 39, 4745–4754.
- Arimoto, R., Stewart, B., Khaing, H., Tatro, D. P., 2006. Biogeochemical Recycling on Aerosol Particles. American Geophysical Union, Fall Meeting 2006, abstract #A53A-0175.
- Baggoura, B., Noureddine, A., Benkrid, M., 1998. Level of natural and artificial radioactivity in Algeria. *Applied Radiation and Isotopes*, 49, 867- 873.
- Braaten, D.A., Cahill, T.A., 1986. Size and composition of Asian dust transported to Hawaii. *Atmospheric Environment*, 20, 1105- 1109.
- Buck, E.H., Upton, H.F., 2011. Effects of Radiation from Fukushima Daiichi on the U.S. Marine Environment. Congressional Research Service (CRS) Report R41751.
- Cao, J.J., Lee, S.C., Zhang, X.Y., Chow, J.C. An, Z.S., Ho, K.F., Watson, J.G., Fung, K., Wang, Y.Q., Shen, Z.X., 2005. Characterization of Airborne Carbonate over a Site on Asian Dust Source Regions during 2002 Spring and Its Climatic and Environmental Significance. *Journal of Geophysical Research*, 110: D03203.
- Chamizo, E., Garcia- Leon, M., Enamorado, S.M., Jimenez-Ramos, M.C., Wacker, L., 2010. Measurement of Pu isotopes, ^{239}Pu and ^{240}Pu , in air-filter samples from Seville (2001- 2002). *Atmospheric Environment*, 44, 1851- 1858.
- Chen, L.-L., Carmichael, G. R., Hong, M.-S., Ueda, H., Shim, S., Song, C. H., Kim, Y. P., Arimoto, R., Prospero, J., Savoie, D., Murano, K., Park, J. K., Lee, H.-G., and Kang, C., 1997. Influence of continental outflow events on the aerosol composition at Cheju Island, South Korea, *Journal of Geophysical Research*, 102, 28551–28574.
- Choi, M.S., Lee, D.S., Choi, J.C., Webb, J., Cha, H.J., Yi, H.I., 2006. 239 , ^{240}Pu Concentration and Isotope Ratio (239 , ^{240}Pu) in Aerosols During High Dust (Yellow Dust) Period, Korea. *Science of the Total Environment*, 370, 262-270.
- Chung, Y.-S., Yoon, M.-B., 1996. On the occurrence of yellow sand and atmospheric loadings. *Atmospheric Environment*, 30, 2387-2397.
- Chung, Y. S., Kim, H. S., Dulama, J., Harris, J., 2003. On heavy dustfall observed with explosive sandstorms in Chongwon-Chongju, Korea in 2002, *Atmospheric Environment*, 37, 425-443.
- Cizdziel, J.V., Ketterer, M.E., Farmer, D., Faller, S.H., Hodge, V.F., 2008. 239 , 240 , ^{241}Pu fingerprinting of western US soils using ICPMS: solution and laser ablation measurements. *Analytical and Bioanalytical Chemistry*, 390, 521- 530.
- Danesi, P., Moreno, J., Makarewicz, M., Louvat, D., 2008. Residual radionuclide concentrations and estimated radiation doses at the former French nuclear weapons test sites in Algeria. *Applied Radiation and Isotopes*, 66, 1671- 1674.
- Delany, A.C., Parkin, D.W., Griffin, J.J., Goldberg, E. D., Reimann, B.E.F., 1967. Airborne dust collected at Barbados. *Geochimica et Cosmochimica Acta*, 31, 885-909.

- Do Carmo Freitas, M., Pacheco, A.M.G., 2010. Remote sources of airborne lanthanoids and actinoids collected in the Azores' lower free troposphere, studied with k_0 -INAA. *Nuclear Instruments and Methods In Physics Research A*, 622, 456- 459.
- Duce, R.A., Unni, C.K., Ray, B.J., Prospero, J.M., Merrill, J.T., 1980. Long-range atmospheric transport of soil dust from Asia to the tropical North Pacific: Temporal variability. *Science*, 209, 1522- 1524.
- Eleftheriadis, K., Colbeck, I., 2001. Coarse atmospheric aerosol: size distributions of trace elements. *Atmospheric Environment*, 35, 5321- 5330.
- Eriksson, E., 1958, The Possible Use of Tritium for Estimating Groundwater Storage. *Tellus*, 10, 472-478.
- Garcia-Olivares, A., Iranzo, C.E., 1997. Resuspension and Transport of Pu in the Palomares Area. *Journal of Environmental Radioactivity*, 37, 101- 114.
- Gascó, C., Heras, M., Sánchez, M., Pozuelo, M., Fernández, E., Meral, J., Clavero, M.A., Gracia, J.A., González, P., 2007. Natural and anthropogenic radionuclides in an urban environment (Madrid). International Atomic Energy Agency Publication IAEA-CN-145-147P.
- Gatz, D.F., Miller, M.V., Stensland, G.J., Chu, L.C., 1986. Evidence of element fractionation in fine particle size classes of highly erodible soils. In: *Particulate Matter/Fugitive Dusts: Measurement and Control in Western Arid Regions*, Proceedings of the APCA International Specialty Conference, Tucson, AZ, Air and Waste Management Association, Pittsburgh, 1986, pp. 39-51.
- Gobbi, G.P., Barnaba, F., Giorgi, R., Santacasa, A., 2000. Altitude-resolved properties of a Saharan dust event over the Mediterranean. *Atmospheric Environment*, 34, 5119–5127.
- Guinot, B., Cachier, H., Oikonomou, K., 2007. Geochemical perspectives from a new aerosol chemical mass closure. *Atmospheric Chemistry and Physics*, 7, 1657-1670.
- Hardy, E.P., Krey, P.W., Volchok, H.L., 1973. Global inventory and distribution of fallout Pu. *Nature*, 241, 444- 445.
- Hernandez, F., Hernandez-Armas, J., Catalan, A., Fernandez-Aldecoa, J.C., Karlsson, L., 2005a. Gross-alpha, gross-beta activities and gamma emitting radionuclides composition of airborne particulate samples in an oceanic island. *Atmospheric Environment*, 39, 4057- 4066.
- Hernandez, F., Perez, S.A., Hernandez, J.A., Cuevas, E., Karlsson, L., Romero-Campos, P.M., 2005b. Influence of major African dust intrusions on the ^{137}Cs and ^{40}K activities in the lower atmosphere at the Island of Tenerife. *Atmospheric Environment*, 39, 4111- 4118.
- Hirose, K., Aoyama, M., Katsuragi, Y., Sugimura, Y., 1987. Annual Deposition of Sr-90, Cs-137 and Pu-239, 240 from the 1960-1980 Nuclear Explosions: A Simple Model. *Journal of the Meteorological Society of Japan*, 65, 259-277.
- Hirose, K., Igarashi, I., Aoyama, M., Miyao, T., 2001. Long-term trends of plutonium fallout observed in Japan. In: Kudo, A. (Ed.), *Plutonium in the Environment*. Elsevier Science, Amsterdam, pp. 251-266.

- Hirose, K., Aoyama, M., 2003. Present background levels of surface ^{137}Cs and $^{239,240}\text{Pu}$ concentrations in the Pacific. *Journal of Environmental Radioactivity*, 69, 53-60.
- Hirose, K., Igarashi, Y., Aoyama, M., Kim, C.K., Kim, C.S., Chang, B.W., 2003. Recent trends of Pu fallout observed in Japan: Pu as a proxy for desertification. *Journal of Environmental Monitoring*, 5, 302-307.
- Hirose, K., Kim, C.K., Kim, C.S., Chang, B.W., Igarashi, Y., Aoyama, M., 2004. Wet and dry deposition patterns of Pu in Daejeon, Korea. *Science of the Total Environment*, 332, 243-252.
- Hirose, K., Igarashi, Y., Aoyama, M., Inomata, Y., 2010. Depositional behaviors of Pu and thorium isotopes at Tsukuba and Mt. Haruna in Japan indicates the sources of atmospheric dust. *Journal of Environmental Radioactivity*, 101, 106-112.
- Holgye, Z., 2008. Pu isotopes in surface air of Prague in 1986- 2006. *Journal of Environmental Radioactivity*, 99, 1653- 1655.
- Holmes, J., and Zoller, W., 1996. The elemental curve of transported Asian dust at Mauna Loa observatory, *Tellus, Ser. B*, 48, 83-92.
- Horowitz, A.J., 1984. A primer on trace metal sediment chemistry. U.S. Geological Survey Water-Supply Paper, 84-2227, 67 pp.
- Huebert, B.J., Phillips, C.A., Zhuang, L., Kjellstrom, E., Rodhe, H., Feichter, J., Land, C., 2001. Long-term measurements of free-tropospheric sulfate at Mauna Loa: comparison with model simulations. *Journal of Geophysical Research*, 106, 5479-5492.
- Husar, R.B., Prospero, J.M., Stowe, L.L., 1997. Characterization of tropospheric aerosols over the oceans with the NOAA advanced very high resolution radiometer aerosol optical thickness operational product. *Journal of Geophysical Research*, 102, 16889-16909.
- Igarashi, Y., Otsuji-Hatori, J., Hirose, K., 1996. Recent deposition of ^{90}Sr and ^{137}Cs observed in Tsukuba. *Journal of Environmental Radioactivity*, 31, 157-169.
- Igarashi, Y., Inomata, Y., Aoyama, M., Hirose, K., Takahashi, H., Shinoda, Y., Sugimoto, N., Shimizu, A., Chiba, M., 2009. Possible change in Asian dust source suggested by atmospheric anthropogenic radionuclides during the 2000s, *Atmospheric Environment*, 43, 2971-2980.
- International Atomic Energy Agency, 2005. Radiological Conditions at the Former French Nuclear Test Sites in Algeria: Preliminary Assessment and Recommendations. IAEA, Vienna, STI/PUB/1215, 71 pp.
- Iranzo, E., Salvador, S., Iranzo, C.E., 1987. Air concentrations of ^{239}Pu and ^{240}Pu and potential radiation doses to persons living near Pu-contaminated areas in Palomares, Spain. *Health Physics*, 52, 453- 461.
- Johnston, P.N., Williams, G.A., Burns, P.A., and Coor, M.B., 1993. Pu Resuspension and Airborne Dust Loadings in the Desert Environment of Maralinga, South Australia. *Journal of Environmental Radioactivity*, 20, 117- 131.

- Kandler, K., Benker, N., Bundke, U., Cuevas, E., Ebert, M., Knippertz, P., Rodriguez, S., Schutz, L., Weinbruch, S., 2007. Chemical composition and complex refractive index of Saharan Mineral Dust at Izaña, Tenerife (Spain) derived by electron microscopy. *Atmospheric Environment*, 41, 8058-8074.
- Kang, C.H., Kim, W.H., Ko, H.J., Hong, S.B., 2009. Asian dust effects on total suspended particulate (TSP) compositions at Gosan in Jeju Island, Korea. *Atmospheric Research*, 94, 345- 355.
- Kinoshita, N., Sumi, T., Takimoto, K., Nagaoka, M., Yokoyama, A., Nakanishi, T., 2011. Anthropogenic Pu distribution in Tropical East Pacific. *Science of the Total Environment*, 409, 1889-1899.
- Kurosaki, Y., Mikami, M., 2003. Recent frequent dust events and their relation to surface wind in East Asia. *Geophysical Research Letters*, 30, 1736, doi:10.1029/2003GL017261.
- Lee, S.C., Orlandini, K.A., Webb, J., Schoep, D., Kirchner, T., Fingleton, D.J., 1998. Measurement of baseline atmospheric Pu-239, 240 and americium-241 in the vicinity of the waste isolation pilot plant. *Journal of Radioanalytical and Nuclear Chemistry*, 234, 267- 272.
- Li-Jones, X., Prospero, J.M., 1998. Variations in the size distribution of non-sea-salt sulfate aerosol in the marine boundary layer at Barbados: impact of Saharan Dust. *Journal of Geophysical Research*, 103, 16073- 16084.
- Liu Tung-sheng, Gu Xiong-fei, An Zhi-sheng, Fan Yong-xiang, 1981. The dustfall in Beijing, China, on April 18, 1980. *Geological Society of America Special Paper*, 186, 149-158.
- Masson, O., Piga, D., Gurriaran, R., D'Amico, D., 2010. Impact of an exceptional Saharan dust outbreak in France: PM10 and artificial radionuclides concentrations in air and in dust deposit. *Atmospheric Environment*, 44, 2478- 2486.
- McDowell, L.M., Whicker, F.W., 1978. Size characteristics of Pu particles in Rocky Flats soil. *Health Physics*, 35, 293-299.
- Mendonca, B.G., Iwaoka, W.T., 1969. The trade wind inversion at the slopes of Mauna Loa, Hawaii. *Journal of Applied Meteorology*, 8, 213-219.
- Merrill, J. T., Uematsu, M., Bleck, R., 1989. Meteorological analysis of long-range transport of mineral aerosol over the North Pacific. *Journal of Geophysical Research*, 94, 8584-8598.
- Ministry of the Environment Government of Japan, 2008. Dust and Sandstorms. <http://www.env.go.jp/en/earth/dss/pamph/pdf/full.pdf>.
- Mori, I., Nishikawa, M., Quanb, H., Morita, M., 2002. Estimation of the concentration and chemical composition of Kosa aerosols at their origin. *Atmospheric Environment*, 36, 4569- 4575.
- Pan, V., Stevenson, K.A., 1996. Temporal variation analysis of Pu baseline concentration in surface air from selected sites in the continental US. *Journal of Environmental Radioactivity*, 32, 239- 257.
- Parrington, J.R., Zoller, W.H., Aras, N.K., 1983. Asian dust: seasonal transport to the Hawaiian Islands. *Science*, 220, 195-197.

- Pazukhin, E.M., Borovoi, A.A., Ogorodnikov, B.I., 2004. Forest fire as a factor of environmental redistribution of radionuclides originating from Chernobyl accident. *Radiochemistry*, 46, 102- 106.
- Pérez-Marrero, J., Llinás, O., Maroto, L., Rueda, M.J., Cianca, A., 2002. Saharan dust storms over the Canary Islands during winter 1998 as depicted from the advanced very high-resolution radiometer. *Deep-Sea Research II*, 49, 3465–3479.
- Perkins, R. W., Thomas, C. W., 1980. Worldwide fallout. In: *Transuranic Elements in the Environment*, W. C. Hanson, ed., USDOE/TIC-22800, 55-82.
- Perry, K. D., Cahill, T. A., Schnell, R. C., Harris, J. M., 1999. Long-range transport of anthropogenic aerosols to the NOAA baseline station at Mauna Loa Observatory, Hawaii. *Journal of Geophysical Research*, 104, 18521-18533.
- Pett-Ridge, J.C., Monastra, V.M., Derry, L.A., Chadwick, O.A., 2007. Importance of atmospheric inputs and Fe-oxides in controlling soil uranium budgets and behavior along a Hawaiian chronosequence. *Chemical Geology*, 244, 691- 707.
- Péwé, T.L., 1981. Desert dust: an overview. *Geological Society of America Special Paper*, 186, 1-4.
- Powell, B.A., Field, R.A., Coates, J.T., Kaplan, D.I., Serkiz, S.M., 2002. Pu Oxidation State Geochemistry in the SRS Subsurface Environment (U). U.S. Department of Energy / Westinghouse Savannah River Company Report, WSRC-TR-2003-00035.
- Prospero, J.M., 1999a. Long-term measurements of the transport of African mineral dust to the south-eastern United States: implications for regional air quality. *Journal of Geophysical Research*, D104, 15917- 15927.
- Prospero, J.M., 1999b. Long-range transport of mineral dust in the global atmosphere: Impact of African dust on the environment of the southeastern United States. *Proceedings of the National Academy of Sciences (USA)*, 96, 3396–3403.
- Prospero, J.M., Carlson, T.N., 1981. Saharan air outbreaks over the tropical North Atlantic. *PAGEOP*, 119, 677-691.
- Prospero, J.M., Lamb, P.J., 2003. African droughts and dust transport to the Caribbean: Climate change implications. *Science*, 302, 1024-1027.
- Prospero, J.M., Bonatti, E., Schubert, C., Carlson, T.N., 1970. Dust in the Caribbean Atmosphere Traced to an African Dust Storm. *Earth and Planetary Science Letters*, 9, 287-293.
- Prospero, J.M., Nees, R.T., Uematsu, M., 1987. Deposition rate of particulate and dissolved aluminum derived from Saharan dust in precipitation at Miami, Florida. *Journal of Geophysical Research*, 92, 14723-14731.
- Prospero, J.M., Ginoux, P., Torres, O., Nicholson, S.E., Gill, T.E., 2002. Environmental characterization of global sources of atmospheric soil dust identified with the Nimbus 7 Total Ozone Mapping Spectrometer (TOMS) absorbing aerosol product. *Reviews of Geophysics*, 40, 1002.

- Rahn, K.A., Borys, R.D., Shaw, G.E., 1981. Asian desert dust over Alaska: Anatomy of an Arctic haze episode. *Geological Society of America Special Paper*, 186, 37-43.
- Robbins, J.A., Edginton, D.N., 1975. Determination of recent sedimentation rates in Lake Michigan using Pb-210 and Cs-137. *Geochimica et Cosmochimica Acta*, 39, 285- 304.
- Rothlisberger, R., Mulvaney, R., Wolff, E.W., Hutterli, M.A., Bigler, M., Sommer, S., Jouzel, J., 2002. Dust and sea salt variability in central East Antarctica (Dome C) over the last 45 kyrs and its implications for southern high-latitude climate. *Geophysical Research Letters*, 29, 1963.
- Ryan, S., 1997. The wind field around Mauna Loa derived from surface and balloon observations. *Journal of Geophysical Research*, 102, 10711-10725.
- Schery, S.D., 2001. *Understanding Radioactive Aerosols and Their Measurement*. Environmental Science and Technology Library, Vol. 19, Springer, 339 pp.
- Schlosser, P., Stute, M., Dorr, H., Sonntag, C., Munnich, K.O., 1988. Tritium/³He dating of shallow groundwater. *Earth and Planetary Science Letters*, 89, 353-362.
- Shao, Y., Wywoll, K.H., Chappell, A., Huang, J., Lin, Z., McTainsh, G.H., Mikami, M., Tanaka, T.Y., Wang, Xulong, W., Yoon, S., 2011. Dust cycle: An emerging core theme in Earth system science. *Aeolian Research*, 2, 181-204.
- Shaw, G.E., 1980. Transport of Asian Desert Aerosol to the Hawaiian Islands. *Journal of Applied Meteorology*, 19, 1254- 1259
- Simon, S., Bouville, A., Beck, H.L., 2004. The geographic distribution of radionuclide deposition across the continental US from atmospheric nuclear testing. *Journal of Environmental Radioactivity*, 74, 91- 105.
- Sun, J.M., 2002. Provenance of loess material and formation of loess deposits on the Chinese Loess Plateau. *Earth and Planetary Science Letters*, 203, 845-859.
- Trapp, J.M., Millero, F.J., Prospero, J.M., 2010. Temporal variability of the elemental composition of African dust measured in trade wind aerosols at Barbados and Miami. *Marine Chemistry*, 120, 71- 82.
- Turner, M., Rudin, M., Cizdziel, J., Hodge, V., 2003. Excess Pu in soil near the Nevada Test Site, USA. *Environmental Pollution*, 125, 193- 203.
- VanCuren, R.A., Cahill, T.A., 2002. Asian aerosols in North America: Frequency and concentration of fine dust. *Journal of Geophysical Research*, 107, D24, 4804, doi:10.1029/2002JD002204.
- Van Pelt, R.S., Zobeck, T.M., Ritchie, J.C., Gill, T.E., 2007. Validating the use of ¹³⁷Cs measurements to estimate rates of soil redistribution by wind. *Catena*, 70, 455- 464.
- Wan, G.J., Santschi, P.H., Sturm, M., Farrenkothen, K., Lueck, A., Werth, W., Schuler, C., 1987. Natural (²¹⁰Pb, ⁷Be) and fallout (¹³⁷Cs, ^{239,240}Pu, ⁹⁰Sr) radionuclides as geochemical tracers of sedimentation in Greifensee, Switzerland. *Chemical Geology*, 63, 181- 196.

- Wershofen, H., Arnold, D., Steinkopff, T., 2001. Measurement of plutonium isotopes in 14 ground-level air in Northern-Germany history and recent results. *Nukleonika*, 46,155-159.
- Wilkins, B.T., Paul, M., Nisbet, A.F., 1996. Speciation and foodchain availability of Pu accidentally released by nuclear weapons. London, Her Majesty's Scientific Office, 23 pp.
- Wotawa, G., DeGeer, L.E., Becker, A., D'Amours, R., Jean, M., Servanckx, R., Ungar, K., 2006. Inter- and intra-continental transport of radioactive cesium released by boreal forest fires. *Geophysical Research Letters*, 33, L12806, doi:10.1029/2006GL026206.
- Wu, Fengchang, Zheng, Jian, Liao, Haiqing, Yamada, M., 2010. Vertical distributions of Pu and ¹³⁷Cs in lacustrine sediments in northwestern China: quantifying sediment accumulation rates and source identifications. *Environmental Science and Technology*, 44, 2911- 2917.
- Yu X., Cheng, T., Chen, J., Lui, Y., 2006. A comparison of dust properties between China continent and Korea, Japan in East Asia. *Atmospheric Environment*, 40, 5787-5797.
- Zhang, X. Y., Arimoto, R., An, Z. S., 1997. Dust emission from Chinese desert sources linked to variations in atmospheric circulation. *Journal of Geophysical Research*, 102, 28, 041–28, 047.
- Zhang, P., Krumhansl, J.A., Brady, P.V., 2002. Introduction to Properties, Sources and Characteristics of Soil Radionuclides, *Geochemistry of Soil Radionuclides*. In *Geochemistry of Soil Radionuclides*, SSSA Special Publication Number 59 (eds. P. Zhang and P. Brady). Soil Science Society of America, Madison, Wisconsin, pp.10-11.
- Zhao, T. L., Gong, S. L., Zhang, X. Y., Jaffe, D. A., 2008. Asian dust storm influence on North American ambient PM levels: observational evidence and controlling factors, *Atmospheric Chemistry and Physics*, 8, 2717-2728, doi:10.5194/acp-8-2717-2008.
- Zhu, X.R., Prospero, J.M., Millero, F.J., 1997. Diel variability of soluble Fe (II) and soluble total Fe in North African dust in the trade winds at Barbados. *Journal of Geophysical Research*, 102, 21297- 21305.
- Zhuang, G.S., Guo, J.H., Yuan, H., Zhao, C.Y., 2001. The Compositions, Sources, and Size Distribution of the Dust Storm from China in Spring of 2000 and its Impact on the Global Environment. *Chinese Science Bulletin*, 46, 895- 900.
- Zieman, J. J., Holmes, J.L., Connor, D., Jensen, C.R., Zoller, W.H., 1995. Atmospheric aerosol trace element chemistry at Mauna Loa Observatory 1. 1979-1985. *Journal of Geophysical Research*, 100, 25979- 25994.

Tables

Table 1: Dust concentration versus $^{239,240}\text{Pu}$ activity values for all four study sites (MLO, BAT, IZT, and GOS).

Station	$^{239,240}\text{Pu}$ Activity (Bq/m^3)	Dust Concentration ($\mu\text{g/m}^3$)			$^{239, 240}\text{Pu/Dust Mass (Bq/ } \mu\text{g)}$
		Mean	Standard Deviation	Number of samples	
IZT	2.8E-07	412.3	310.5	11	6.7E-10
BAT-1 ^a	7.7E-08	17.7	21.8	182	4.3E-09
BAT-2		7.2	12.0	97	
BAT-3	5.0E-08	16.4	34.4	77	3.0E-09
BAT-4	8.3E-08	25.5	17.2	43	3.3E-09
BAT-5	7.2E-08	15.3	17.5	119	4.7E-09
GOS-1		3.2	2.7	53	
GOS-2		3.3	3.7	46	
GOS-3	5.0E-07	14.1	13.4	45	3.5E-08
MLO-1		1.6	4.0	114	
MLO-2		0.2	0.6	179	
MLO-3	1.2E-08	1.5	3.4	203	8.6E-09
MLO-4		0.2	0.2	5	

^a Composite number

Table 2: $^{239,240}\text{Pu}$ activity values per filter for all four study sites (MLO, BAT, IZT, and GOS).

Station Phases	$^{239,240}\text{Pu}$ Activity (Bq)	Vol (m³)	$^{239,240}\text{Pu}$ Activity (Bq/m³)	Filters in Batch
IZT-1	1.000E-03	3631	2.754E-07	5
BAT-1	1.018E-03	13237.68	7.691E-08	5
BAT-2		12733.86		7
BAT-3	4.832E-04	9757.12	4.952E-08	5
BAT-4	3.982E-04	4780.26	8.331E-08	5
BAT-5	7.709E-04	10693.83	7.209E-08	7
GOS-1				8
GOS-2				9
GOS-3	2.758E-04	554.94	4.970E-07	6
MLO-1				4
MLO-2				6
MLO-3	2.158E-04	18587.10	1.161E-08	8
MLO-4				5

Table 3: Collection composites for IZT, BAT, GOS, and BAT sites.

Izaña (IZT) Collection Periods		
Composite ID	Start	End
IZT-1	7/13/1989 12:00	7/14/1989 8:00
IZT-1	4/5/1993 16:40	4/6/1993 12:40
IZT-1	8/13/1993 16:15	8/14/1993 16:55
IZT-1	8/7/1994 15:30	8/8/1994 15:30
IZT-1	3/24/1995 18:05	3/25/1995 16:15
IZT-1	4/4/1995 14:30	Unknown
IZT-1	8/17/1995 16:00	8/18/1995 16:30
IZT-1	5/25/1996 10:00	5/26/1996 12:30
Barbados (BAT) Collection Periods		
Composite ID	Start	End
BAT-1	1/18/2005 10:53	4/9/2005 10:15
BAT-1	4/9/2005 10:51	6/4/2005 17:21
BAT-1	6/4/2005 17:36	6/25/2005 9:34
BAT-1	6/25/2005 9:50	7/16/2005 9:28
BAT-1	7/16/2005 9:45	8/6/2005 10:04
BAT-1	8/6/2005 10:17	9/21/2005 9:30
BAT-2	9/21/2005 9:48	10/10/2005 13:59
BAT-2	10/10/2005 14:23	10/24/2005 9:34
BAT-2	10/24/2005 9:50	11/14/2005 13:11
BAT-2	11/14/2005 13:27	12/5/2005 18:30
BAT-2	12/5/2005 19:06	12/26/2005 10:24
BAT-2	12/26/2005 10:48	1/16/2006 10:21
BAT-2	1/16/2006 10:22	2/5/2006 11:54
BAT-3	2/5/2006 11:54	2/26/2006 16:27
BAT-3	2/26/2006 17:09	3/12/2006 12:02
BAT-3	3/12/2006 11:15	3/26/2006 12:36
BAT-3	3/26/2006 13:55	4/9/2006 13:33
BAT-3	4/9/2006 15:35	5/21/2006 15:35
BAT-4	5/21/2006 15:58	6/6/2006 10:58
BAT-4	6/6/2006 12:10	6/9/2006 10:11
BAT-4	6/9/2006 10:26	6/18/2006 14:45
BAT-4	6/18/2006 15:00	6/25/2006 12:25
BAT-4	6/25/2006 12:45	7/12/2006 10:13
BAT-5	7/12/2006 10:26	7/26/2006 10:09
BAT-5	7/26/2006 10:22	8/14/2006 10:52
BAT-5	8/14/2006 11:18	8/25/2006 6:00
BAT-5	8/25/2006 10:52	9/17/2006 12:50
BAT-5	9/17/2006 13:37	10/16/2006 9:55
BAT-5	10/16/2006 10:07	11/5/2006 14:34
BAT-5	11/5/2006 14:55	11/27/2006 10:00

Table 3 cont'd

Gosan, South Korea (GOS) Collection Periods		
Composite ID	Start	End
GOS-1	4/23/2005 10:30	5/13/2005 14:50
GOS-1	5/13/2005 14:52	6/1/2005 15:03
GOS-1	6/1/2005 15:05	6/19/2005 15:15
GOS-1	6/19/2005 15:18	7/7/2005 14:00
GOS-1	7/7/2005 14:02	7/24/2005 14:27
GOS-1	7/24/2005 14:29	8/12/2005 12:00
GOS-1	8/12/2005 12:02	8/26/2005 12:20
GOS-1	8/26/2005 12:22	9/13/2005 14:30
GOS-1	9/13/2005 14:32	10/2/2005 13:30
GOS-2	10/2/2005 13:32	10/25/2005 09:00
GOS-2	10/25/2005 9:02	11/14/2005 8:45
GOS-2	11/14/2005 8:47	12/1/2005 14:50
GOS-2	12/1/2005 14:52	12/17/2005 8:55
GOS-2	12/17/2005 9:00	1/5/2006 10:10
GOS-2	1/5/2006 10:15	1/26/2006 16:00
GOS-3	1/26/2006 16:20	2/14/2006 11:40
GOS-3	2/14/2006 11:45	3/4/2006 10:10
GOS-3	3/4/2006 10:15	3/21/2006 11:20
GOS-3	3/21/2006 11:25	4/24/2006 16:15
GOS-3	4/24/2006 16:20	5/10/2006 11:30

Table 3 cont'd

Mauna Loa, Hawaii (MLO) Collection Periods		
Composite ID	Start	End
MLO-1	2/10/2005 14:35	3/8/2005 17:20
MLO-1	3/8/2005 17:40	4/5/2005 13:20
MLO-1	4/5/2005 13:23	5/2/2005 13:38
MLO-1	5/2/2005 13:39	6/7/2005 14:11
MLO-2	6/7/2005 14:32	7/5/2005 10:44
MLO-2	7/5/2005 10:44	8/2/2005 10:50
MLO-2	8/2/2005 10:53	9/6/2005 12:22
MLO-2	9/6/2005 12:24	10/4/2005 10:50
MLO-2	10/4/2005 10:50	11/1/2005 12:59
MLO-2	11/1/2005 13:00	12/6/2005 12:18
MLO-3	12/6/2005 12:43	1/10/2006 10:32
MLO-3	1/10/2006 10:36	2/7/2006 10:57
MLO-3	2/7/2006 10:59	3/7/2006 1:49
MLO-3	3/7/2006 1:51	3/28/2006 10:59
MLO-3	3/28/2006 12:50	4/25/2006 10:58
MLO-3	4/25/2006 11:12	5/23/2006 10:32
MLO-3	5/26/2006 10:40	6/20/2006 11:47
MLO-3	6/20/2006 11:50	7/18/2006 10:20
MLO-4	7/18/2006 10:32	8/15/2006 12:55
MLO-4	8/15/2006 12:56	9/12/2006 10:35
MLO-4	9/12/2006 10:26	10/10/2006 11:07
MLO-4	10/10/2006 11:17	11/7/2006 10:30
MLO-4	11/7/2006 10:40	12/5/2006 12:05

Figures

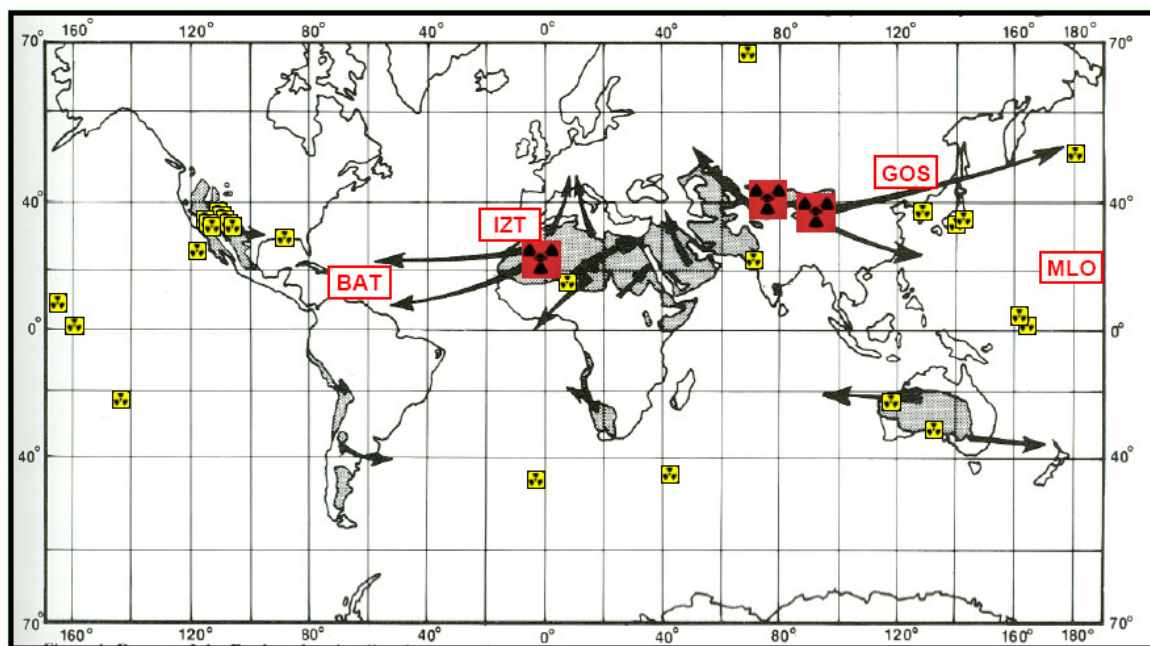


Figure 1: Study sites (MLO, BAT, IZT, and GOS), major dust sources and flow paths worldwide (after Pewe, 1981), and earth's nuclear test sites (www.atomicarchive.com) shown with radioactive symbol. The red radioactive symbols represent sites where atmospheric nuclear detonations took place pertinent to this study.

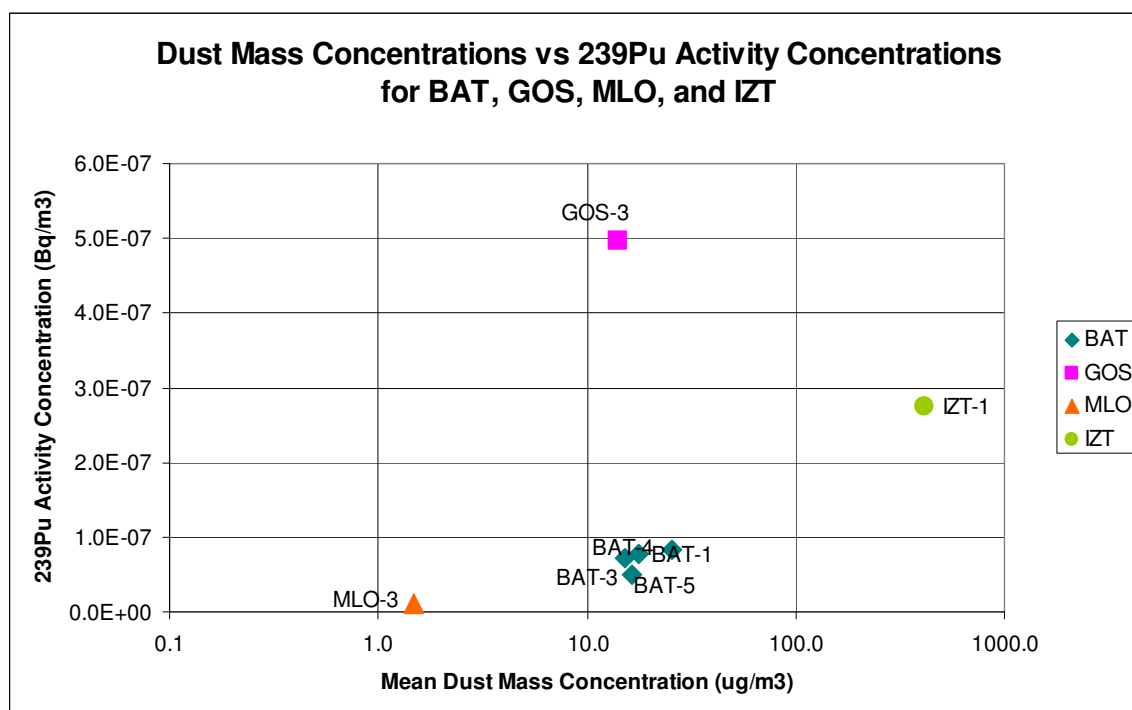


Figure 2: Dust concentration versus ^{239, 240}Pu activity values for all four study sites (MLO, BAT, IZT, and GOS).

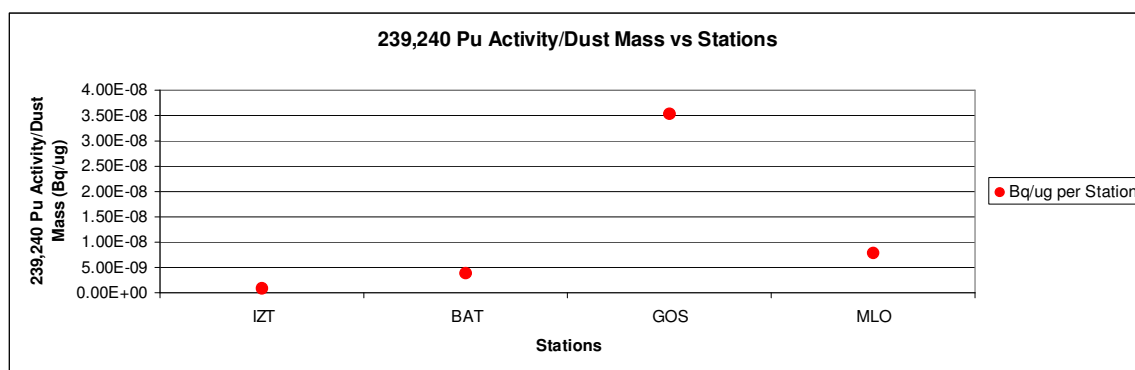


Figure 3: $^{239,240}\text{Pu}$ activity values versus dust mass values for all four study sites (MLO, BAT, IZT, and GOS).

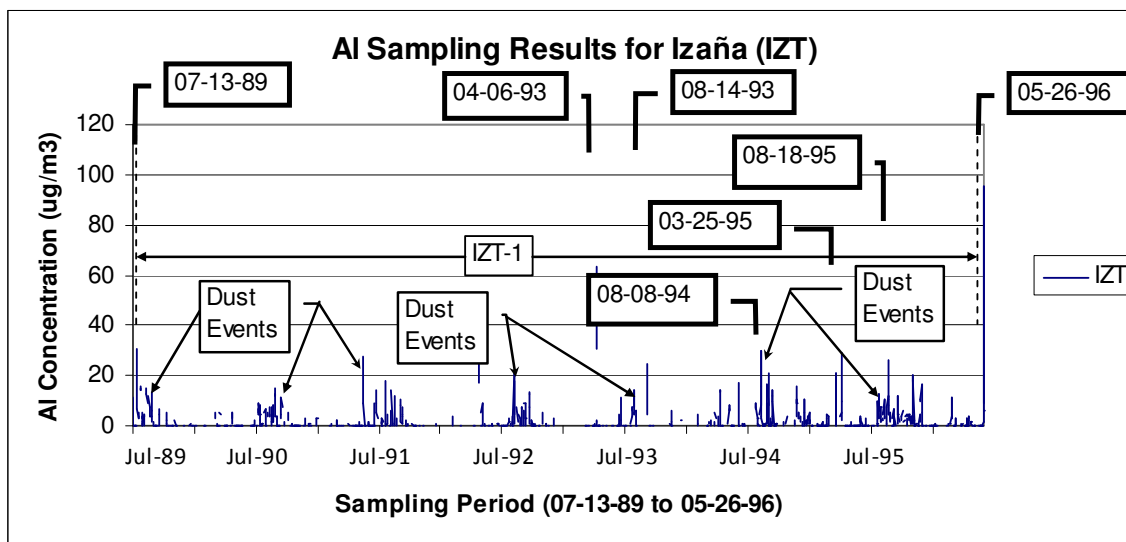


Figure 4: Al concentrations with respect to time for Izaña, Canary Islands (IZT).

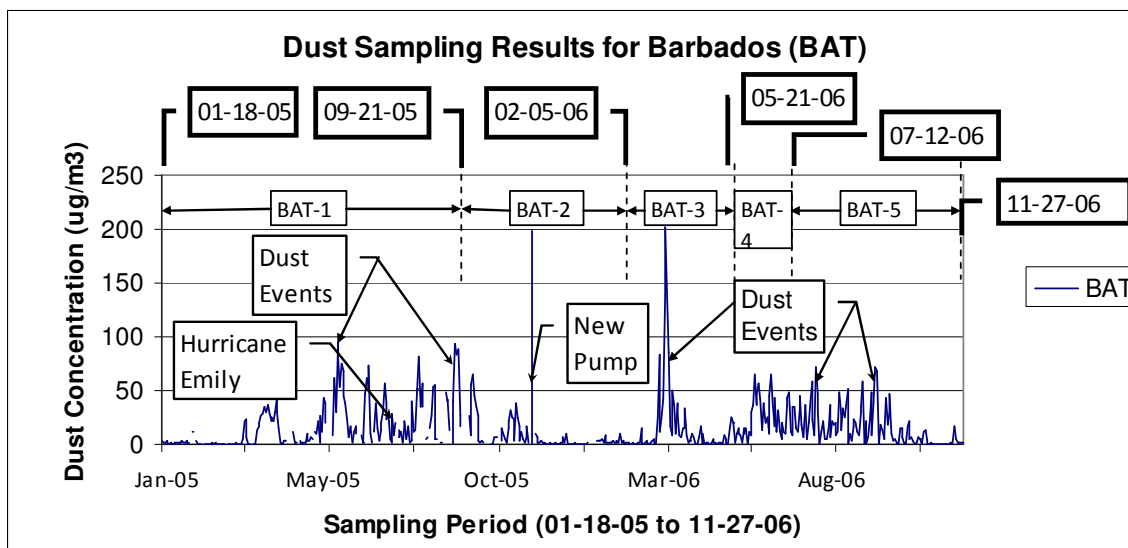


Figure 5: Dust concentrations with respect to time for Barbados (BAT).

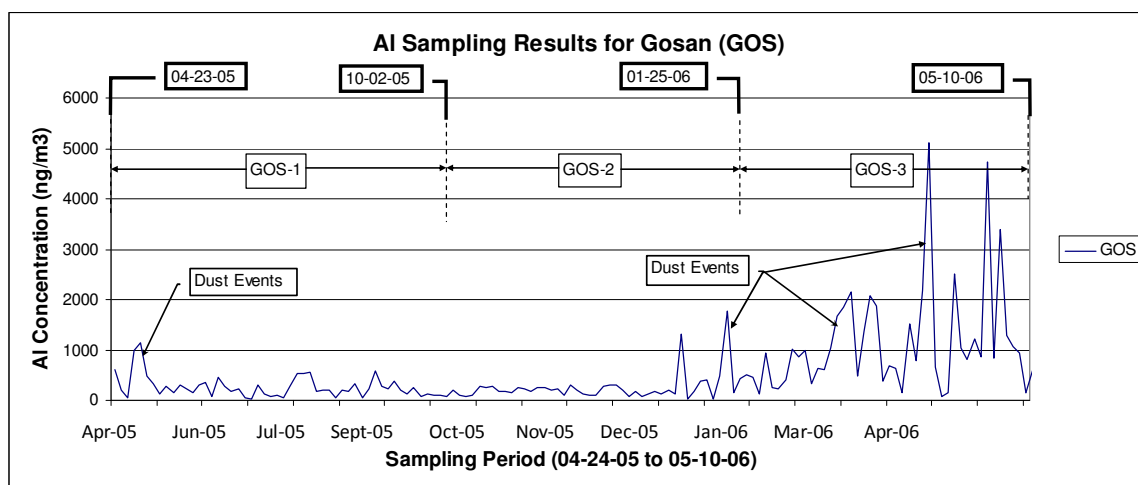


Figure 6: Al concentrations with respect to time for Gosan, South Korea (GOS).

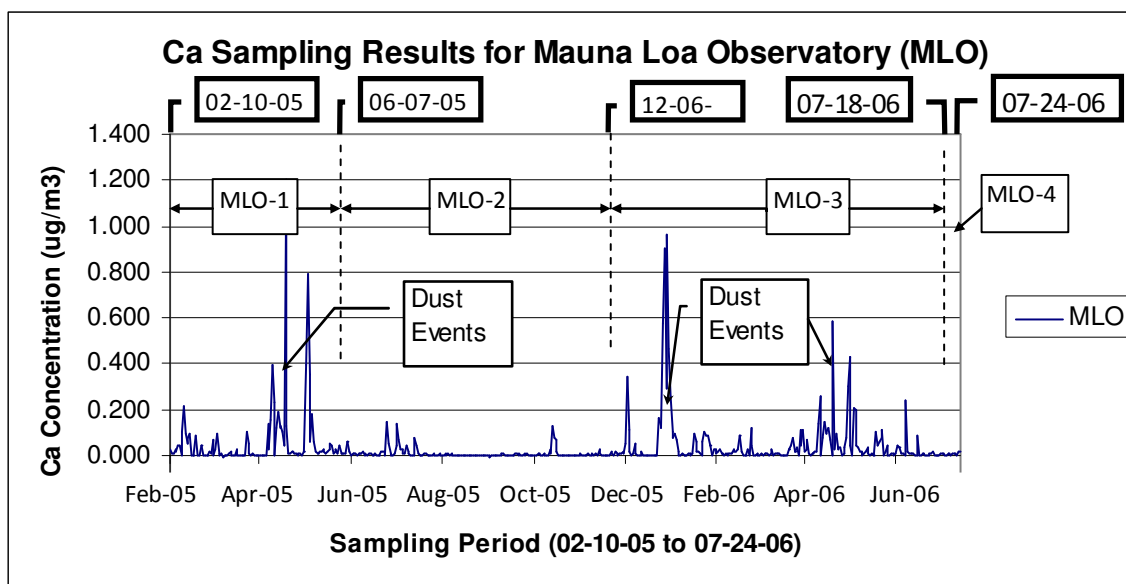


Figure 7: Ca concentrations with respect to time for Mauna Loa Observatory, Hawaii (MLO).

Chapter 4. Wind Erosion Patterns in Coppice Dune Maneuver Areas, White Sands Missile Range, New Mexico

1. Introduction

White Sands Proving Ground (now known as White Sands Missile Range), established in July 9, 1945, initiated the atomic age at the Trinity Test Site in July 16, 1945 (U.S. Government, 1986) and presently serves as missile testing grounds for the U.S. Department of Defense (Army, Navy, and Air Force), NASA, and other government agencies (U.S. Government, 1986; U.S. Army Corps of Engineers, 1993). White Sands Missile Range (WSMR) lies in south-central New Mexico in the Tularosa Basin and has an average elevation of 1,220 meters with approximately 1,900,000 acres (7,689 km²) of controlled land. WSMR lies in the Chihuahuan Desert near the U.S. Department of Agriculture (USDA) Jornada Experimental Range (JER), which is about 25 km northeast of Las Cruces, New Mexico.

Construction of defense structures (e.g., fortifications, scarping, and flooding) can significantly alter the surface of the earth while military operations (e.g., explosive ordnance, vehicular activity, and fuel leakage) can disfigure the surface of the earth (Rose, 2005). Land increasingly becomes susceptible to wind erosion as result of vegetation reduction, crust disintegration, and soil aggregate degradation caused by military activity (van Donk et al., 2003). Tank tracks break-down desert pavement clast sizes and compact soil while reducing vegetation (Prose and Wilshire, 2000). Heavy tanks divide dunes held in place by mesquite (*Prosopis glandulosa*), break-down surface crust, and increases interdune deflation (Martson, 1986). Dust episodes can wreak havoc on military operations and civilian transportation (Goudie, 2009). With the advent of modern warfare and sophisticated weaponry (e.g., fast ground vehicles, ground launched missiles, helicopters, turbine engines, etc. introduced during the Vietnam Era), Army equipment is increasingly subject to dust failure (Engelhardt and Knebel, 1968).

This type of study bears importance in terms of gaining understanding of aeolian processes impacting landscape characteristics such as geomorphology, vegetation type, and land cover (Floyd and Gill, 2011). Moreover, severe dust events which typically occur in March, April, and May often impede

visibility on highways and often carry dust particulate matter (PM) which can adversely affect respiratory tracts (Novlan et al., 2007; Rivera et al., 2009). Suspended PM with an aerodynamic diameter less than $2.5\ \mu\text{m}$ ($\text{PM}_{2.5}$) and $10\ \mu\text{m}$ (PM_{10}) can have ill effects on respiratory systems if inhaled (Choi et al., 2008).

This investigation estimates sediment transport and deposition due to desert dust suspension resulting from military vehicle maneuvers and aeolian processes at WSMR. This type of dust transport research has applications in varied research settings such as agriculture, military preparedness, planetary dust, and respiratory health of the public.

1.1 Problem Statement

The purpose of this study is to measure the amount and particle size of aeolian dust with respect to vertical deposition and horizontal suspension fluxes and corresponding textural constituents (i.e., clay, silt, and sand ranges) at varied heights (i.e., 0.2 m, 1 m, and 1.7 m) in maneuver and non-maneuver areas of WSMR. The sediment traps employed for these studies are passive type (MWAC and MDCO). The relationship of these variables to land use, land cover, military maneuvers, and meteorology needs to be better understood and has been requested of UTEP by the U.S. Army.

The maneuver and non-maneuver study zones area at WSMR has a total land area of approximately $100\ \text{km}^2$ (Figure 3). The non-maneuver area will generally serve as a control for the maneuver area. Both areas have shrubland, dunes, grassland, and sporadic manmade structures. Details regarding military activities in the maneuver area such as frequency, vehicle type, and hours of operation are not provided by the U.S. Army. WSMR personnel estimate 20 (minimum) to 1,000 (maximum) troops participated in military maneuvers during April 1, 2009 to July 31, 2009.

The objective is to gain a better understanding of dust emission behavior in anthropogenically disturbed and undisturbed open range settings in the northern Chihuahuan Desert by estimating desert dust suspension and deposition patterns over varied land cover types (i.e., dune and shrubland areas) at WSMR potentially attributable to wind erosion and military maneuvers at WSMR. Specifically, the

amount and particle size of surface soil and suspended and transported dust will be determined at a multitude of sampling sites. Transport (horizontal flux) and deposition (vertical flux) rates will be estimated using sediment collected in dust traps and correlated with seasonal averages of daily meteorological data provided by WSMR meteorologists.

2. Background

2.1 Field Equipment

2.1.1 MDCO (Marble Dust Collector) Sediment Traps

The marble dust collector (MDCO) was first described by Ganor (1975). The MDCO design and its variants have been widely used for estimating vertical dust deposition flux (settling) (Ganor, 1975; Hall et al., 1994; Goossens and Offer, 2000; Wiggs et al., 2002; Reheis, 2006). The MDCO design consists of a circular tray (outer diameter of 24.4 cm and height of 10 cm) with two layers of marbles (diameter of 1.5 cm). The marble pan can rest on the ground or be suspended (typically 1 to 2 m above the ground) from a mast (Goossens and Offer, 2000; Reheis, 2006). A wire mesh suspends the marbles 3 to 4 cm below the rim of the pan. The traps collect wet and dry deposition of airborne sediments. Reheis (2006) successfully used a modification of the MDCO concept by using 35 angel food cake pans filled with marbles to capture sediment for USGS studies in Southern Nevada and California. Results from the Reheis (2006) study indicated accretion rates (downward fluxes) of dust in the Mojave desert partly composed of silt-clay (which includes carbonates) ranged from 2 to 20 g/m²/yr depending on meteorology, location, and source types (e.g., alluvium and dry or wet playas).

Several dust deposition investigations have been previously done in the Chihuahuan Desert and surrounding areas. Perez and Gill (2009) conducted mineral aerosol studies at the Salt Flat Basin in west Texas near the Guadalupe Mountains, about 175 km southeast of the WSMR. Dry lakes (playas) are major sources of dust in the Salt Flat Basin. Dust traps of varied designs (including MDCO) were placed 0.5 m, 1.0 m, and 1.5 m above the ground at three sites in the basin. Analysis of the 32 collected MDCO samples indicated seasonal dust flux values ranged from 10 g/m²/yr to 150 g/m²/yr for summer of 2005

and spring 2007, respectively. The overall average for the 32 samples was $50 \text{ g/m}^2/\text{yr}$ for a 1.5 m height. Studies done at Las Cruces, New Mexico (near WSMR) and the Texas Panhandle yielded dust flux values ranging between 7.6 to $28.1 \text{ g/m}^2/\text{yr}$ for Las Cruces (Gile et al., 1981), up to $102 \text{ g/m}^2/\text{yr}$ for Lubbock, Texas (Crabtree, 2005), and 13 to $27 \text{ g/m}^2/\text{yr}$ for the northern Texas Panhandle (Machenberg, 1987), respectively.

2.1.2 MWAC (Modified Wilson and Cooke) Sediment Traps

The MWAC (Modified Wilson and Cooke) design consists of vertically installed plastic bottles (which serve as a sediment storage chamber) with lids fitted with inlet and outlet ventilation tubing. The tubing can be made of plastic, glass, or metal. The MWAC design is used for monitoring horizontal dust flux (horizontal transport of saltating and suspended particles). The MWAC design was initially successfully used by Kuntze et al. (1990). Eventually, MWAC sediment traps were mounted on wind vanes at different heights by Sterk (1993). Goossens and Offer (2000) performed wind tunnel efficiency experiments for six aeolian dust samplers which included the MWAC bottle type design; they stated that design factors such as size and shape, wind speed, grain inertia, time, and type of collector were most important. The MWAC design was rated as having the highest efficiency (Goossens and Offer, 2000).

2.1.3 BSNE (Big Spring Number Eight) Sediment Traps

The BSNE sediment trap was developed by Fryrear (1986). The sampler trays are made of 28-gauge galvanized sheet metal with apertures covered with galvanized mesh screen and stainless steel 60-mesh screen. Air flow loaded with sediment enters an inlet of approximately 2 cm x 5 cm (Goossens and Offer, 2000). Air flow is diffused and decreased as the sampler width increases; consequently, dust particles settle in the collection pan. The air mass flow discharges through the 60-mesh screen. The 18-mesh screen helps prevent fine dust from mobilizing and escaping (Goossens and Offer, 2000). A rubber strap (similar to a large rubber band) retains the tray and plugs any holes in back and front of the sampler. The samplers are kept facing the wind with a vane fixture (similar to a rudder) fixed at the rear

of the sampler. Typical sampling heights are 0.05 m, 0.1 m, 0.25 m, 0.5 m, and 1.0 m (Stout and Fryrear, 1989).

2.2 Lab Equipment

2.2.1 Laser Particle Sizing Theory

The Malvern Mastersizer laser diffraction granulometer is used to measure the size of particles collected by the above collection devices. Chappell (1998) conducted dispersion studies with the Malvern 2600 and the Coulter LS-100 laser particle sizers to assess the most appropriate mediums for suspension and dispersion methods for sandy soil from a semi-arid environment. Only 0.5 g of material was used for most measurements. Even though there is no set of standard procedure for dispersion treatment of soil samples, recommendations were made by Chappell (1998). Tap water (even though some tap water may not be suitable due to impurities) with dispersant agent (e.g., sodium hexametaphosphate (Calgon) or sodium carbonate) combined with mechanical agitation and ultrasonic action settings in the laser particle sizer were suggested to break up aggregates. (Zobeck (2004) prepared samples with sodium hexametaphosphate shaking “overnight”). Ultrasonic action for not more than six minutes was recommended (optimum duration is difficult to assess although three minutes was considered minimum) by Chappell (1998). A combination pretreatment with Calgon mixed with tap water and ultrasonic action was most efficient.

Sperazza et al. (2004) systematically analyzed fine grained sediment ($<1\text{-}50\text{ }\mu\text{m}$) from fluvial and volcanic soil systems with the Malvern Mastersizer 2000. Preparation protocols and observations were as follows: (1) Optimal fine-grained sediment dispersion was achieved by mixing sediment in 5.5 g/l of sodium hexametaphosphate solution and shaking the blend for 24 hours prior to analysis. Ultrasonication was set for 60 seconds during analysis. (2) Obscuration that produced the most reproducible results was approximately 20% (actual obscuration values ranged from 2-40%). (3) Excessive modification of refractive-index settings may produce varied estimates in grain-size distributions. Deer et al. (1962) proposed the following refractive index values relative to materials:

illites 1.54 – 1.57; smectites 1.48 – 1.61; kaolinites 1.55 – 1.56; and quartz 1.54. (4) Unspecified absorption (light absorption by the sediment) values may affect grain-size results. Procedures recommended by Sperazza et al. (2004) and Zobeck (2004) for granulometry in the laboratory will be generally utilized in this study.

2.3 Dust Suspension Theory

Gillette (1999) explained dust emitting areas (“hot spots”) in terms of eight geophysical dust production factors specific to a given area, that is, how air and particle interaction with terrain features contribute to dust suspension. WSMR Du1K-u and Du400m-m dune areas have high particle supply in the form of dune sand and upwind fetch areas with an abundance of mesquite and varied vegetation growth, while Sh1K-d and Sh3K-m-u shrubland areas have a higher land cover through abundance of creosote and other vegetation growth. These “hot spot” producing factors and how they relate to a northern Chihuahuan Desert sampling site, the Jornada Experimental Range (JER) adjacent to WSMR, are as follows:

- 1) High winds (meso-scale winds) above the threshold velocity (wind velocity that begins grain particle movement) must be present. High winds in the JER can sandblast the desert surface and produce sediment for transport (Gillette and Chen, 2001).

- 2) Surface obstruction such as vegetation, boulders, cobbles, and gravel must be low. These obstructions can breakup wind flow (Gillette refers to this as momentum partitioning). If grain sizes are between 80 to 120 μm , low threshold friction velocity will cause erosion. Long fetch areas (sediment deposits parallel to strong winds) will yield more suspension. Sand dunes can be stabilized by mesquite growth (mesquite coppice dunes) in the Chihuahuan Desert (Gillette et al., 2006). Creosote bush, black gramma grass, and mesquite are present in the JER (Gillette and Chen, 2001) and at the WSMR field site: however, aeolian activity occurs in vegetation-free “streets” parallel to the fetch of the wind (Gillette et al., 2006).

3) Aggregation (particle grouping and enlargement) and crusting (e.g., silts and clays tend to cement after moistening) must be low. Relative hardness crust tests in the JER ranged consistently between 4 and 7 kg cm⁻² with a low of 2 kg cm⁻² (Gillette and Chen, 2001).

4) An abundance of grains (a thick deposit has more available particles) must be present. More availability of particles leads to more suspension for longer periods of time. Particle depletion and particle supply at the JER varied after high wind episodes (Gillette and Chen, 2001). Supply and availability of loose particles on the surface is more significant than wind energy alone with regard to erosion rate (Gillette and Chen, 2001).

5) Airborne sediment (saltating particles) increases aerodynamic roughness height (i.e., drag coefficient increases with wind speed). This is known as the Owen effect. When this occurs, the ratio of friction velocity versus mean wind velocity increases; subsequently, sediment flux increases with length nonlinearly. It was observed that three sites at the JER equipped with Sensit and BSNE collectors 30 m apart yielded particle terminal velocity versus the friction velocity ratios higher downwind than upwind (Gillette and Ono, 2008).

6) Particle “trapping” by vegetation, large rock particles, or furrows must be low. Sand dunes can be stabilized by mesquite growth (mesquite coppice dunes) in the Chihuahuan Desert, but again, vegetation-free sediment “lanes” occur parallel to the prevailing wind direction (Gillette et al., 2006).

7) Soil moisture and cohesion in soil must be low (i.e., dry soil transports easier). It has already been observed from results to date for this project that Phase 2 (from Phase 1, 2, and 3 data) had the lowest mass deposition values, likely because Phase 2 (July and August, 2008) had the most precipitation.

8) Soil matrix must not be too tightly structured (i.e., low binding energies between particles). It was observed that surface conditions at the JER ranged from smooth hard crust (mostly non-erodible) to loose-sand cover (highly erodible) (Gillette and Ono, 2008), and similar conditions prevail at WSMR.

Saltation occurs when vertical turbulent forces (velocity components) have nearly no effect on particle trajectory (Pye, 1987). Suspension occurs when the settling velocity of the particle is nearly insignificant relative to the friction velocity (Pye, 1987). The particle's trajectory between saltation and suspension is affected by the inertia and settling velocity of the particle (Pye, 1987). Sand-sized grains carried by wind rarely rise above 1 m, whereas the average carrying height is approximately 10 cm (Bagnold, 1954). Sand grains begin to mobilize on the ground at a wind velocity of approximately 5 ms^{-1} (Bagnold, 1954), however this number is quite variable with soil and land cover conditions. The saltating-dominated zone of aeolian transport generally extends from the surface up to 0.2 to 0.3 m (Fryrear and Saleh, 1993). Typical diameter values for fine wind-blown sand range between 0.3 to 0.15 mm, whereas the finest wind-blown sand is not less than 0.08 mm in diameter (Bagnold, 1954). Other researchers found in their studies that saltating sand particles ranged between 25 to 125 μm (Visher, 1969) and 50 to 100 μm (Grini et al., 2002). Smaller particles are susceptible to transport and dispersal as dust by upward eddy currents (Bagnold, 1954). Past dust deposition studies indicate that < 63 or $< 50 \mu\text{m}$ is a typical median grain diameter which characterizes most suspended dust mixtures well near their source (Goossens and Gross, 2002).

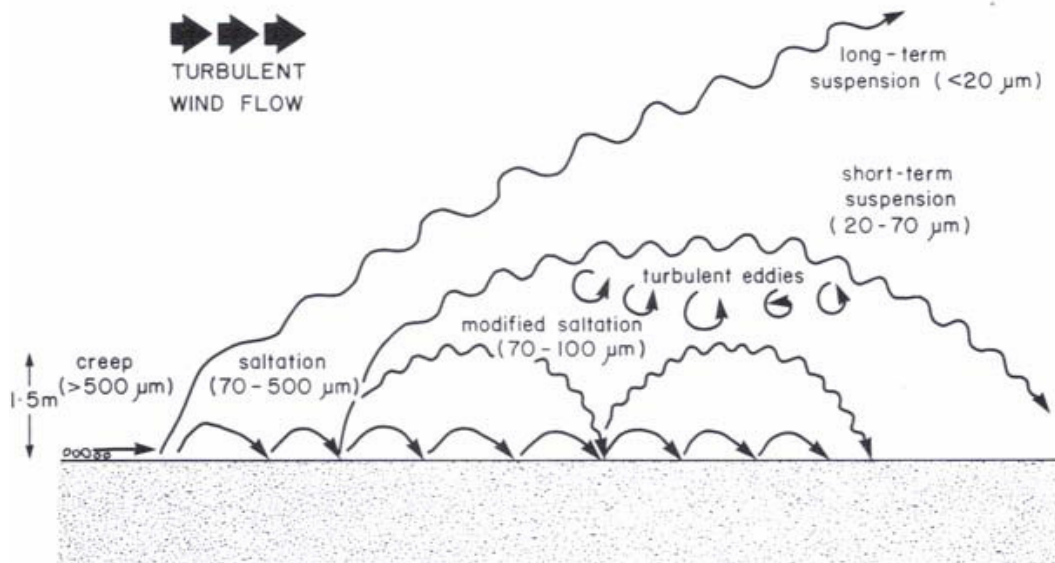


Figure 1: Particle size ranges in different transport modes under moderate wind storm conditions (Pye, 1987).

Under moderate wind storm conditions, the friction velocity (u_*) approximately ranges between $0.20 - 0.60 \text{ ms}^{-1}$. Within this friction velocity range, particles greater than $500 \mu\text{m}$ will creep (roll); particles 70 to $500 \mu\text{m}$ will saltate; particles 70 to $100 \mu\text{m}$ will undergo modified saltation; particles 20 to $70 \mu\text{m}$ will undergo short-term suspension; and particles less than $20 \mu\text{m}$ will undergo long-term suspension (Pye, 1987) (Figure 1). Equations pertinent to suspension and saltation of sediment by the wind are the settling velocity equation (Van der Hoven, 1968; Pye, 1987; Seinfeld and Pandis, 1998; Eby, 2004) and the Prandtl-von Kármán equation which defines the slope of the logarithmic wind profile (Pye, 1987).

The Prandtl-von Kármán equation (1) determines the slope of the logarithmic wind profile:

$$U = \frac{u_*}{k} \ln \frac{z}{z_0} \quad (1)$$

U = Wind velocity (ms^{-1}) at height z above the ground

u_* = Friction velocity (ms^{-1})

z = Height above surface (m)

k = Dimensionless von Karman constant of 0.4

z_0 = Roughness length, the height at which the velocity is zero (roughness length is related to the height of the roughness elements on the surface)

The roughness length (z_0) depends on surface cover (e.g., urban, trees, grass, crops, desert, water, snow, ice, etc.) and can range from 10 m (urban terrain) to 10^{-5} m (smooth ice cover) (Seinfeld and Pandis, 1998). The roughness length z_0 is approximately $1/30$ the diameter of the surface particles on bare surfaces (von Kármán, 1934; Prandtl, 1935; Bagnold, 1941 cited in Pye, 1987) or $\approx 1/30$ the height of the roughness elements covering the surface (Seinfeld and Pandis, 1998). The friction velocity (u_*) is directly proportional to the rate of increase of wind velocity with respect to logarithmic height (Bagnold, 1954).

The threshold friction velocity (2) is the critical point at which saltation occurs:

$$u_{*t} = A \sqrt{\frac{\rho_p - \rho_a}{\rho_a} g D} \quad (2)$$

The coefficient A is equal to 0.1 for particle friction Reynolds numbers (Re_p) greater than 3.5 (i.e., $Re_p > 3.5$). Reynolds number = friction velocity (u_*) x mean particle diameter (D) / kinematic viscosity of air (μ). Re_p is a numerical value which indicates how turbulent the flow is around the particle (Bagnold, 1954; Pye, 1987).

$$\begin{aligned} u_{*t} &= \text{the threshold friction velocity (cms}^{-1}\text{)} \\ \rho_p &= \text{the particle density (gcm}^{-3}\text{)} \\ \rho_a &= \text{the air density (0.001225 gcm}^{-3}\text{)} \\ g &= \text{the acceleration due to gravity (980.665 cms}^{-2}\text{)} \\ D &= \text{the mean particle diameter (cm)} \end{aligned}$$

In regards to the settling of a dust particle once suspended, Stokes' law determines the settling velocity (3) of a spherical particle:

$$u_s = \frac{g(\rho_p - \rho_a)D_p^2}{18\mu} \quad (3)$$

(It should be noted that the slip correction factor C_c is factored in when small particles are considered. If D_p is greater than 10 μm , C_c is usually neglected (Seinfeld and Pandis, 1998). C_c is a function of the mean free path (λ) and particle diameter (D_p). The mean free path is the average distance traveled by a molecule before colliding with another molecule.)

$$\begin{aligned} u_s &= \text{settling velocity (cms}^{-1}\text{)} \\ D_p &= \text{the particle diameter (cm)} \\ \rho_p &= \text{the particle density (gcm}^{-3}\text{)} \\ \rho_a &= \text{air density (0.001225 gcm}^{-3}\text{)} \\ g &= \text{the acceleration due to gravity (980.665 cms}^{-2}\text{)} \\ \mu &= \text{the dynamic viscosity of the air (1.789 x 10}^{-4} \text{ g cm}^{-1}\text{s}^{-1} \text{ for standard atmosphere at sea level)} \end{aligned}$$

2.4 Terrain Effects of Vehicular Activity from Military Maneuvers

Althoff and Thein (2005) conducted studies of the effect of heavy military tank activity on soil surface parameters. A 63-ton M1A1 tank with a speed of 12 ms^{-1} will invariably cause soil compaction; additionally, damage will increase substantially under wet conditions and with repeated turns and passes.

Monger et al. (1993) delineated landforms on military property (north and south Fort Bliss) approximately 10 km south of White Sands Missile Range maneuvering area. Monger reports on the

geomorphic surface described as La Mesa Basin floor east of the Organ Mountains which has large watershed areas and sediment sources from alluvial fans. These areas contain large dunes (> 1m in height) and small dunes (< 1m in height). Large dunes are characterized by wind ripples (indicating active sand movement) and interdune sheet deposits with sparse vegetation (mesquite and grasses). Creosote bush, which is abundant at WSMR, had a mean percent survivability of 38.9 % after vehicular impact (rubber tire wheels and metal tracks) (Hansen and Ostler, 2005). Small dunes are characterized by interdune sheet deposits and grasses. Established by Monger et al. (1993), sand, silt, and clay percentages found at 0 to 0.2 m depths in dune and interdune areas are approximately 80 %, 4 %, and 16 %, respectively.

Williams et al. (2008) measured dust suspension from a motor vehicle running on an unpaved road at Las Cruces, New Mexico. The height and width of the dust plume and the amount of clay-sized particles captured increased with vehicle speed, although the amount of particles larger than 2.5 microns did not correlate with vehicle speed.

Pinnick et al. (1985) conducted a dust suspension study which entailed constructing a 1 km unpaved road perpendicular to the prevailing wind about 10 km northwest of Orogrande, New Mexico. Heavy military type vehicles (tracked and rubber tire) such as a five-ton truck, M-47 tank, an M-113 armored personnel carrier were tested. The speeds of these vehicles ranged from 5 to 12 ms⁻¹. The dust particles suspended consisted of quartz, clay minerals (montmorillonite, kaolinite, and illite), calcite, and aragonite. Sand displayed a higher mass loading than silt. The size and composition of vehicle dust suspension at Orogrande was very similar to that of local wind blown dust. The maximum dust loading, which occurred a few meters from the dust source, was 0.05 to 10 gm⁻³.

2.5 Meteorology

This work will require use of collected meteorological data (i.e., average and high/low temperatures, wind speed and direction, peak gusts, precipitation, and presence of seasonal inversions) provided by meteorologists at WSMR. This data will be correlated with dust deposition data provided by

the sediment traps. How much dust is suspended and deposited is affected by meteorological conditions in the Chihuahuan Desert such as high-velocity arid winds (spring) (Novlan et al., 2007; Perez and Gill, 2009), precipitation (summer) (Reheis, 2006; Novlan et al., 2007), and temperature inversions (fall) (Strahler and Strahler, 1974).

Strahler and Strahler (1974) mention that the frequency of low level inversions (152 m to 305 m in the southwestern U.S.) during autumn season is relatively high; subsequently, less atmospheric air mass interaction is expected. Dust suspended by vehicular activity, such as overnight military maneuvers, during inversions may be trapped in the inversion and settle closer to its source. Particles greater than 1 μm in aerodynamic diameter will settle with constant velocity in air. Stokes' law can provide the terminal velocity of a settling particle (Seinfeld and Pandis, 1998). Suspended dust will eventually settle into the marble traps installed in the maneuvering and non-maneuvering areas, so maneuvers during inversions may lead to greater deposition in the maneuvering area during periods of inversions.

3. Methodology

3.1 Staging Areas

A total of twenty-four passive dust collecting sites (i.e., stations) were installed in two areas at WSMR between April 25, 2008 and May 6, 2008. The sites were strategically installed respective to military activity, vegetation type, and land cover in the area after consultation and negotiation with WSMR management staff. Each site is identified with a prefix and suffix (i.e., "Sh" = shrublands; "Du" = dunes; K = kilometer; m = meter; M = maneuver area; u = upwind; d = downwind) (Tables 1-3; Figures 2-3). Ten collecting sites were installed in the northernmost area and fourteen in the southernmost area. One area serves as a maneuver area collection platform (i.e., the southernmost sector) while the other serves as a control (non-maneuver) collection platform (i.e., the northernmost sector). The locations of the sites were chosen in consultation with Nicole Sikula, the WSMR RTLA (Range and Training Land Assessment) and Land Rehabilitation and Maintenance coordinator and

strategically installed respective to military activity, vegetation type, and land cover. Approximately 1 m x 1 m x 1 cm of surface sediment was collected at each site for characterizing soil properties at each site and comparing surface soil to airborne soil characteristics at each site.

Samples were collected from each site over a period of 10 phases in this project. Phase 1 started on April 25, 2008, while Phase 10 ended on August 31, 2010. Table 6 displays the project timeline.

It has been established that military maneuvers took place from April 1, 2009 through July 31, 2009 (Phases 5 and 6). Additional military activity took place from March, 2010 through August 31, 2010 (Phases 9 and 10) when the project terminated.

Sampling sites Du1K-u, Sh1K-d, Du400m-m, and Sh3K-m-u were selected for detailed analysis based on similarity as they relate to military activity presence, location relative to wind direction (upwind/downwind), terrain features, vegetation species, and soil structure (Figure 3). This was done in order to conduct a concentrated comparative analysis of these sites which are in the maneuver and non-maneuver areas.

Sites Du400m-m and Sh3K-m-u are in the maneuver areas, while sites Du1K-u and Sh1K-d are in the non-maneuver area. Sites Du1K-u and Du400m-m are in high dune density areas with an abundance of mesquite and varied vegetation species, whereas sites Sh3K-m-u and Sh1K-d are in areas comprising of alluvial deposits from the Jarilla Mountains to the east which are populated with creosote and varied vegetation species (Table 3).

Moreover, four groups (Groups A, B, C, and D) of sites were selected to represent upwind/downwind dust emission activity (Figure 2). Group A consists of sites Du1K-u, Du400m, and Du1k-d. Site Du400m is the pivot site with Du1K-d being upwind of pivot site and Du1K-u being downwind of the pivot site. Group B consists of sites Sh1K-u, Sh400m, and Sh1K-d. Site Sh400m is the pivot site with Sh1K-d being upwind of pivot site and Sh1K-u being downwind of the pivot site. Group C consists of sites Du1K-m-u, Du400m-m, and Du1K-m-d. Site Du400m-m is the pivot site with Du1K-m-d being upwind of pivot site and Du1K-m-u being downwind of the pivot site. Group D consists of

sites Sh1K-m-u, Sh400m-m, and Sh1K-m-d. Site Sh400m-m is the pivot site with Sh1K-m-d being upwind of pivot site and Sh1K-m-u being downwind of the pivot site. All pivot sites are adjacent to unpaved roads. This study was undertaken to compare sites with respect to natural setting similarities and anthropogenic dissimilarities, that is, military activity presence, location relative to wind direction (upwind/downwind), terrain features, vegetation species, and soil structure.

Table 4 displays measurements taken in the field of potential sediment yielding areas for each site. Rectangular areas were computed from these dimensions and converted to equivalent circular areas centered at the site; subsequently, radius lengths were obtained from the derived circular areas. The radius length represents the fetch length of the sediment source area which is aligned parallel to wind direction at the site (Table 5). Increasing the fetch length will tend to increase sediment flux nonlinearly which leads to the Owen Effect (i.e., drag coefficient increases with wind speed) (Gillette, 1997b).

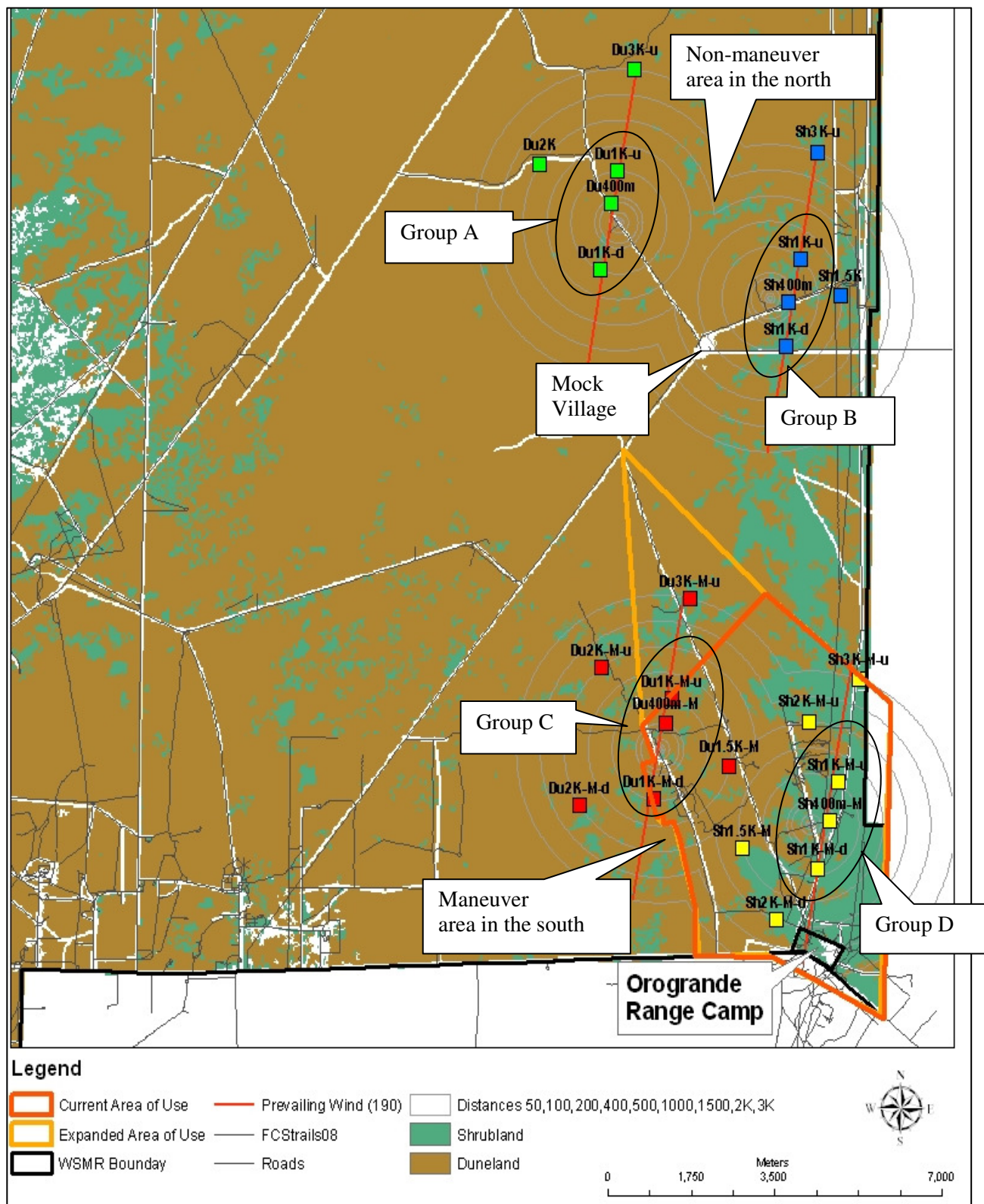


Figure 2: Staging areas showing all 24 collecting sites in maneuver and non-maneuver areas.

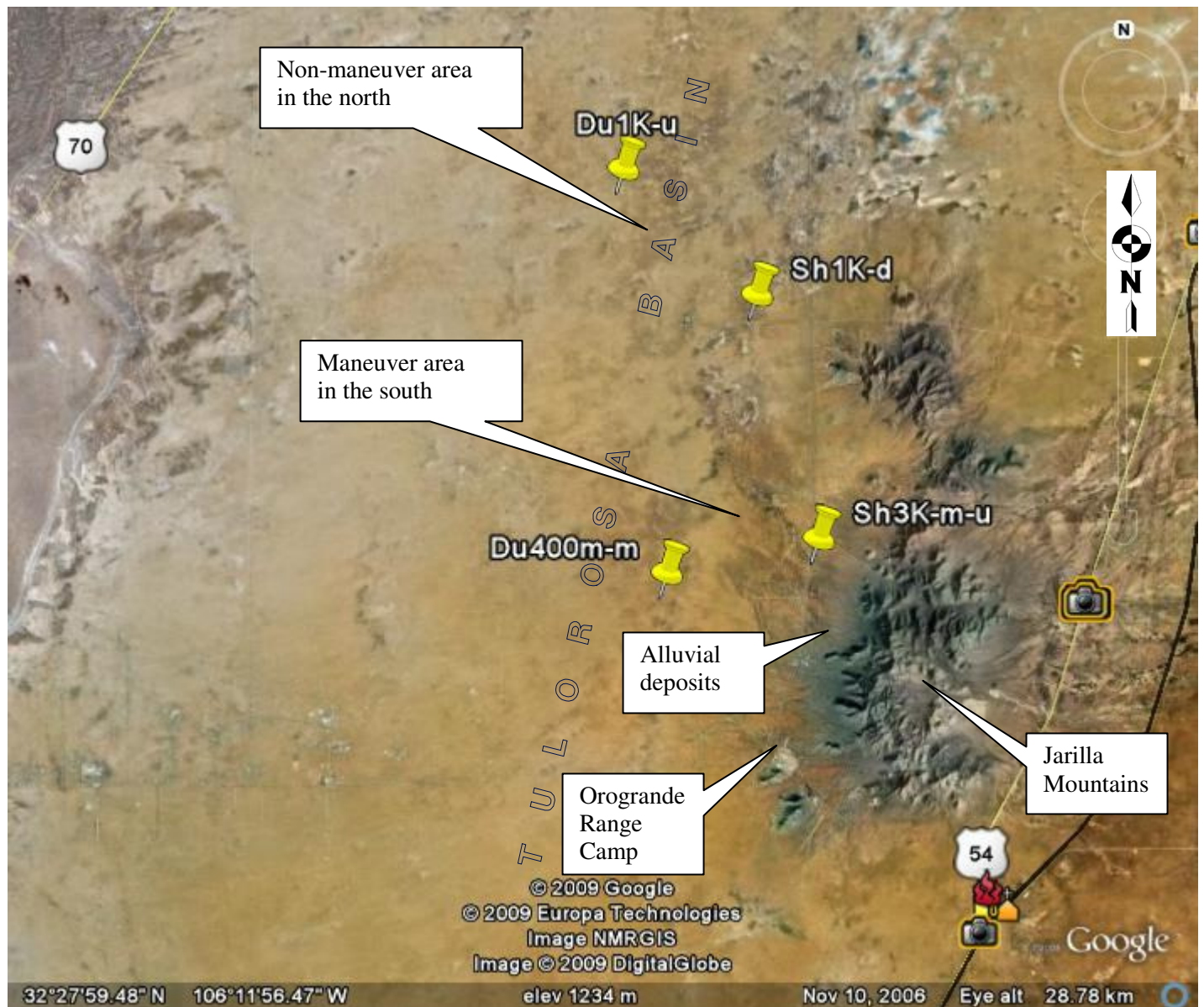


Figure 3: Map of staging areas and surrounding geological features.

Table 1: Collecting site list and description of surrounding topography. (Note: “Sh” = shrublands; “Du” = dunes; K = kilometer; m = meter; M= maneuver area; u = upwind; d = downwind)

(non-maneuver area in the northern sector)		
Station No.	Station ID	Description
1	Du3K-u	Dunes
2	Du2K	Dunes
3	Du1K-u	Dunes
4	Sh3K-u	Mixed Shrubland land
5	Du400m	Dunes
6	Du1K-d	Dunes
7	Sh1K-u	Mixed Shrubland land
8	Sh400m	Mixed Shrubland land
9	Sh1.5K	Mixed Shrubland land
10	Sh1K-d	Mixed Shrubland land
(maneuver area in the southern sector)		
11	Du3K-M-u	Dunes
12	Du2K-M-u	Dunes
13	Sh3K-M-u	Mixed Shrubland land
14	Du400m-M	Dunes
15	Sh2K-M-u	Mixed Shrubland land
16	Du1.5K-M	Dunes
17	Sh1K-M-u	Mixed Shrubland land
18	Du2K-M-d	Dunes
19	Du1K-M-d	Dunes
20	Sh400m-M	Mixed Shrubland land
21	Sh1.5K-M	Mixed Shrubland land
22	Sh1K-M-d	Mixed Shrubland land
23	Du1K-M-u	Dunes
24	Sh2K-M-d	Mixed Shrubland land

Table 2: Station UTM coordinates, longitudes/latitudes, and elevations.

Station Coordinates					
Station ID	(UTM) X	(UTM) Y	Longitude	Latitude	Elevation (m)
Du1.5K-M	390130.0168	3589532.402	-106° 10' 7.4784"	32° 26' 15.0102"	1249
Du1K-d	387438.2911	3599219.364	-106° 11' 54.7038"	32° 31' 28.5672"	1221
Du1K-M-d	388542.8419	3588883.927	-106° 11' 7.9722"	32° 25' 53.3892"	1243
Du1K-M-u	388935.5068	3590839.898	-106° 10' 53.7666"	32° 26' 57.0366"	1239
Du1K-u	387796.9968	3601147.152	-106° 11' 41.7876"	32° 32' 31.293"	1222
Du2K	386160.8201	3601277.04	-106° 12' 44.5608"	32° 32' 34.908"	1220
Du2K-M-d	386997.2569	3588779.288	-106° 12' 7.0986"	32° 25' 49.4286"	1237
Du2K-M-u	387458.962	3591467.596	-106° 11' 50.5788"	32° 27' 16.8834"	1234
Du3K-M-u	389303.1943	3592808.213	-106° 10' 40.5186"	32° 28' 1.077"	1235
Du3K-u	388154.0085	3603127.596	-106° 11' 28.9494"	32° 33' 35.7222"	1218
Du400m	387670.5977	3600521.746	-106° 11' 46.3632"	32° 32' 10.9392"	1222
Du400m-M	388793.6231	3590360.268	-106° 10' 58.9974"	32° 26' 41.4126"	1239
Sh1.5K	392468.5279	3598706.884	-106° 8' 41.7084"	32° 31' 13.7244"	1232
Sh1.5K-M	390405.3991	3587924.125	-106° 9' 56.2602"	32° 25' 22.89"	1257
Sh1K-d	391315.377	3597734.168	-106° 9' 25.4988"	32° 30' 41.7342"	1233
Sh1K-M-d	391985.5382	3587529.411	-106° 8' 55.608"	32° 25' 10.6278"	1278
Sh1K-M-u	392399.2829	3589221.314	-106° 8' 40.4622"	32° 26' 5.7084"	1277
Sh1K-u	391629.6028	3599422.909	-106° 9' 14.1582"	32° 31' 36.6774"	1228
Sh2K-M-d	391104.0593	3586536.293	-106° 9' 28.9404"	32° 24' 38.073"	1268
Sh2K-M-u	391807.6303	3590400.712	-106° 9' 3.603"	32° 26' 43.7958"	1261
Sh3K-M-u	392838.3097	3591225.444	-106° 8' 24.471"	32° 27' 10.9332"	1266
Sh3K-u	391974.6479	3601512.209	-106° 9' 1.7958"	32° 32' 44.6382"	1227
Sh400m	391358.8992	3598583.228	-106° 9' 24.1812"	32° 31' 9.321"	1228
Sh400m-M	392224.02	3588454.505	-106° 8' 46.8594"	32° 25' 40.749"	1281

Table 3: Sampling stations list corresponding to the maneuver and non-maneuver areas and terrain/land cover description.

(non-maneuver area in the northern sector)		
Station No.	Station ID	Description
1	Du3K-u	Mesquite, Saltbush, Snakeweed, Soaptree (few), Sand Dropseed (very few), and medium size dunes (many).
2	Du2K	Mesquite, Saltbush, Snakeweed, and small size dunes (many).
3	Du1K-u	Mesquite, Saltbush, Snakeweed, Soaptree, and dunes (many).
4	Sh3K-u	Saltbush flat, grass, and annuals (many).
5	Du400m	Mesquite, Saltbush, Snakeweed, Soaptree, and dunes (many).
6	Du1K-d	Mesquite, Saltbush, Sand Dropseed, many pedestals, annuals 6 weeks gramma (sparse), and dunes (many).
7	Sh1K-u	Mesquite, Saltbush, Creosote (small amount), Sand Dropseed, annuals 6 weeks gramma, and small mounds.
8	Sh400m	Mesquite, Saltbush, Sand Dropseed, grass, annuals 6 weeks gramma (many), and small mounds (few dunes).
9	Sh1.5K	Mesquite, Saltbush, Creosote, Sand Dropseed, and small mounds (few and mostly flat).
10	Sh1K-d	Soaptree, Creosote, Saltbush, Sand Dropseed, grass, annuals 6 weeks gramma, and dunes (few).
(maneuver area in the southern sector)		
11	Du3K-M-u	Mesquite, grass (patches), Snakeweed, Saltbush, Sage, red sand, and large dunes.
12	Du2K-M-u	Mesquite, Snakeweed, Saltbush, Yucca, Soaptree, Sand Dropseed grass, and dunes (less dense).
13	Sh3K-M-u	Soaptree, Creosote, Saltbush, Sand Dropseed, annuals 6 weeks gramma, and dunes (few).
14	Du400m-M	Mesquite, Snakeweed, Saltbush, Soaptree, Sand Dropseed grass, red sand, and dunes (many).
15	Sh2K-M-u	Mesquite, grass, and small dunes.
16	Du1.5K-M	Mesquite, Yucca (sparse), and dune streets with much available sediment.
17	Sh1K-M-u	Creosote, grass, and alluvial material.
18	Du2K-M-d	Mesquite, Saltbush, Yucca, annuals 6 weeks gramma, Snakeweed (sparse) and dunes (few but more to north).
19	Du1K-M-d	Mesquite, Saltbush, Yucca, annuals 6 weeks gramma, Snakeweed (sparse) and dunes (few but more to north).
20	Sh400m-M	Creosote, grass, and alluvial material.
21	Sh1.5K-M	Mesquite, Creosote (sparse), and grass (abundant) with exposed surface patches.
22	Sh1K-M-d	Creosote, grass, and alluvial material.
23	Du1K-M-u	Mesquite, Snakeweed, Saltbush, Soaptree, Sand Dropseed grass, red sand, and dunes (many).
24	Sh2K-M-d	Creosote, grass, red sand, dunes (sparse), and arroyo nearby.

Table 4: Collecting stations list corresponding to the maneuver (M) and non-maneuver (NM) areas fetch length and vegetation height. Fetch lengths are radius lengths obtained from derived circular areas. These circular areas are equal to areas computed from actual measurements done in the field. These measurements were made on March 1, 2, and 3 of 2010.

Fetch Length and Vegetation Height						
Area	Station Number	Station ID	L=Fetch Length (meters) and H=Height (meters minimum-maximum)			
NM			North	East	South	West
	1	Du3K-u	L=5; H=0.5-2.5	L=34; H=0.5-2.5	L=11; H=0.5-3.5	L=6; H=0.5-2.5
	2	Du2K	L=10; H=1-2	L=5; H=1-2	L=29; H=0.5-2	L=8; H=2-2.5
	3	Du1K-u	L=9; H=0.5-4.5	L=23; H=1-3	L=5; H=0.5-1.5	L=13; H=2-3.5
	4	Sh3K-u	L~0; H=0.5-1	L~0; H=0.5-1	L~0; H=0.5-1	L~0; H=0.5-1
	5	Du400m	L=13; H=1-3.5	L=3.5; H=1-2	L=8.5; H=1-2	L=5; H=1.5-2.5
	6	Du1K-d	L=6.5; H=2-4.5	L=9; H=0.5-2.5	L=10.5; H=1-2.5	L=6; H=1-2.5
	7	Sh1K-u	L=10; H=1-3	L=3; H=1-2	L=3; H=1-2	L=5; H=1-2
	8	Sh400m	L=3; H=1-3	L=0; H=1-2	L=4; H=1-1.5	L=6; H=1-2
	9	Sh1.5K	L=4; H=0-2	L=1; H=0-1.5	L=6; H=0-2	L=5; H=2-2.5
	10	Sh1K-d	L=5; H=0.5-2	L=5; H=0.5-2	L=5; H=0.5-2	L=5; H=0.5-2
M	11	Du3K-m-u	L=2; H=0.5-2	L=10; H=0.5-2.5	L=14; H=0.5-2	L=5; H=0.5-3
	12	Du2K-m-u	L=2; H=0.5-2.5	L=16; H=0.5-2.5	L=19; H=0.5-2.5	L=2; H=0.5-3
	13	Sh3K-m-u	L=12; H=1-2.5	L=6; H=1-4	L=6; H=1-2	L=5; H=1-5
	14	Du400m-m	L=9; H=0.5-2.5	L=17; H=0.5-2	L=6; H=0.5-2	L=38; H=0.5-2
	15	Sh2K-m-u	L=32; H=0.5-2	L=3; H=1-2.5	L=2; H=0.5-2	L=2; H=1-2.5
	16	Du1.5K-m	L=6; H=0.5-2	L=13; H=0.5-2	L=15; H=0.5-3	L=9; H=0.5-2
	17	Sh1K-m-u	L=5; H=1-2	L=5; H=1-2	L=5; H=1-2	L=5; H=1-2
	18	Du2K-m-d	L=6; H=0.5-3	L=12; H=0.5-2	L=14; H=0.5-2.5	L=5; H=0.5-3.5
	19	Du1K-m-d	L=8; H=0.5-1.5	L=3; H=0.5-3	L=11; H=0.5-2.5	L=20; H=0.5-3
	20	Sh400m-m	L=3; H=1-2	L=3; H=1-2	L=3; H=1-2	L=3; H=1-2
	21	Sh1.5K-m	L=8; H=0.5-1.5	L=10; H=0.5-2	L=3; H=0.5-2	L=7; H=0.5-2
	22	Sh1K-m-d	L=12; H=2-2.5	L=4; H=0.5-2	L=10; H=0.5-4	L=2; H=1-3
	23	Du1K-m-u	L=18; H=0.5-2	L=14; H=0.5-2	L=7; H=0.5-2.5	L=4; H=0.5-2
	24	Sh2K-m-d	L=5; H=1-4	L=5; H=1-2	L=5; H=1-2	L=5; H=1-2

Table 5: Calculated fetch lengths for each station.

Calculated Fetch Length			
Area	Station Number	Station ID	Calculated Fetch Length (m)
NM	1	Du3K-u	L=14
	2	Du2K	L=13
	3	Du1K-u	L=13
	4	Sh3K-u	L=0
	5	Du400m	L=5
	6	Du1K-d	L=9
	7	Sh1K-u	L=6
	8	Sh400m	L=4
	9	Sh1.5K	L=4
	10	Sh1K-d	L=6
M	11	Du3K-m-u	L=9
	12	Du2K-m-u	L=11
	13	Sh3K-m-u	L=8
	14	Du400m-m	L=16
	15	Sh2K-m-u	L=7
	16	Du1.5K-m	L=12
	17	Sh1K-m-u	L=6
	18	Du2K-m-d	L=10
	19	Du1K-m-d	L=12
	20	Sh400m-m	L=3
	21	Sh1.5K-m	L=8
	22	Sh1K-m-d	L=7
	23	Du1K-m-u	L=12
	24	Sh2K-m-d	L=6

Table 6: Timeline for Phases 1 through 10.

Timeline of Phases	
Spring 2008	<ul style="list-style-type: none"> • April 25 to May 6, 2008 (Phase 1 starts)
Summer 2008	<ul style="list-style-type: none"> • June 25 to 26, 2008 (Phase 1 ends/Phase 2 starts)
Fall 2008	<ul style="list-style-type: none"> • August 26 to 27, 2008 (Phase 2 ends/Phase 3 starts)
Winter 2008	<ul style="list-style-type: none"> • December, 17 to 18, 2008 (Phase 3 ends/Phase 4 starts)
Spring 2009	<ul style="list-style-type: none"> • February 25 to 27, 2009 (Phase 4 ends/Phase 5 starts) • March 23 to 24, 2009 (Kerr MWACs installed)
Summer 2009	<ul style="list-style-type: none"> • May 27 to 28, 2009 (Phase 5 ends/Phase 6 starts)
Fall 2009	<ul style="list-style-type: none"> • August 19, 20, 2009 (Phase 6 ends/Phase 7 starts) • August 19, 20, 2009 (BSNEs installed)
Winter 2010	<ul style="list-style-type: none"> • January 5, 6, 7 2010 (Phase 7 ends/Phase 8 starts) •
Spring 2010	<ul style="list-style-type: none"> • March 1, 2, 3, 2010 (Phase 8 ends/Phase 9 starts)
Summer 2010	<ul style="list-style-type: none"> • May 25, 26, 27, 28, 2010 (Phase 9 ends/Phase 10 starts) • May 25, 26, 27, 28, 2010 (BSNEs removed)
Fall 2010	<ul style="list-style-type: none"> • August 25, 31, 2010 (Phase 10 and project ends)

3.2 Sediment traps

The plastic bottle type sediment traps were constructed utilizing 250 ml and 500 ml plastic bottles resulting in a device similar to the MWAC design (Goossens and Offer, 2000) (Figure 4 left). The lids for these bottles were fitted with two plastic hose openings (6 mm inner diameter Polyethylene Tubing) which serve as inlets for dust particles. The 250 ml bottle was strapped horizontally onto a BSNE wind vane tray rack (Fryrear, 1986) 0.2 m from the desert surface to collect peak amounts of saltating particles (Fryrear and Saleh, 1993). In similar fashion, the 500 ml bottle was suspended 1 m from the desert surface to best collect particles in short term suspension. In addition to the plastic MWACs, glass MWAC type traps with 9 mm copper tube inlets (Figure 4 right) were installed on March 23 and 24, 2009 at matching heights. The glass type MWAC traps have a more efficient design patterned closely to designs by Goossens and Offer (2000).

BSNEs replaced the plastic MWAC type sediment traps on August 20, 2009. BSNE sediment traps have been widely used worldwide as aeolian sediment traps (Yaalon and Ganor, 1979; Fryrear, 1986; Goossens and Offer, 1988; Spann et al, 1990; Shao et al, 1993; Sterk, 1993), thus making the results of this project more easily correlated to many previous aeolian studies. Comparable to the MWAC, the BSNE dust traps were mounted onto custom made BSNE wind vane tray racks at 0.2 and 1 m from the desert surface (Figure 5).

Marble filled angel food cake tube pans (MDCOs) were used to trap vertically settling dust particles (Reheis, 2006). The brim of the MDCO pan was secured 1.7 m above the desert surface (Figure 6). The outer diameter of the marble pan (interior walls) is approximately 24.4 cm while the inner diameter is approximately 5 cm. These dimensions yield a collecting area of approximately 0.0458 m². The depth of the pan is approximately 10 cm. The marbles are 1.5 cm in diameter.

Each collecting site consists of three masts. Two masts are mounted with two MWACs or BSNEs for horizontal mass transport collection, while the remaining mast is mounted with one MDCO pan for vertical deposition collection (Goossens and Offer, 2000) (Figure 7).



Figure 4: Completed MWAC plastic (left) and glass (right) trap.



Figure 5: Completed BSNE sediment trap.



Figure 6: Completed MDCO sediment trap.

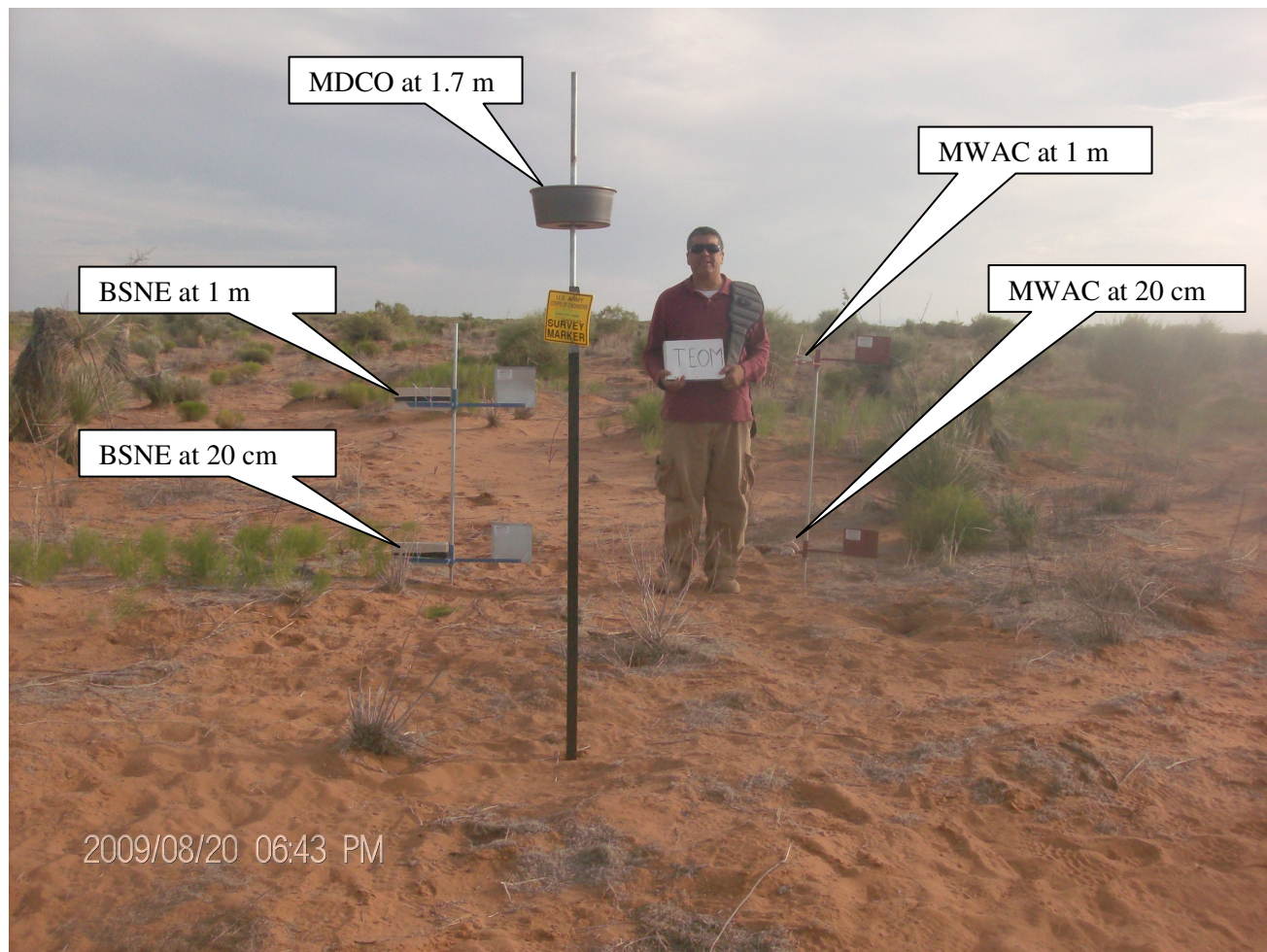


Figure 7: Completed MWAC, BSNE, and MDCO station.

3.3 Sample Collection

To collect samples for each phase, the MWAC bottle sediment traps were simply sealed and replaced with new bottles while the dust trapped by the marbles was washed out with distilled water from the marbles and marble pan. The wash water with dust particulate matter was secured in plastic containers (kitchen type) and subsequently dehydrated for dust extraction. This procedure is similar to methods practiced by the USGS for these samplers (Reheis, 2006). The collection timeline is outlined in Table 6.

3.4 Meteorology

Interpretation of the dust data requires use of collected meteorological data (i.e., average and high/low temperatures, wind speed and direction, peak gusts, precipitation, and presence of seasonal inversions) provided by meteorologists at WSMR. The amount of dust is suspended and deposited in the Chihuahuan Desert is affected by local and regional meteorological conditions such as high-velocity arid winds (predominantly during the spring) (Novlan et al., 2007; Perez and Gill, 2009) and precipitation (predominantly during the summer) (Reheis, 2006; Novlan et al., 2007). Annual and seasonal meteorological conditions in the region vary; individual collecting phases were established from best estimates of expected local climatology based on information provided by WSMR and NOAA meteorologists. That is, locally, spring is defined as March, April, and May; summer occurs during the months of June, July, and August; autumn occurs during the months of September, October, and November; and winter occurs during the months of December, January, and February. Phases 1, 5 and 9 took place during spring which is the windiest and driest season. Phases 2, 6, and 10 took place during summer which is the season with the most precipitation. Phases 3 and 7 took place during fall which is not as windy as spring or as wet as summer. Phases 4 and 8 took place during winter which is the second windiest season. A summary of all 10 phases (Table 6) is as follows: Phase 1 (spring, 2008); Phase 2 (summer, 2008); Phase 3 (fall, 2008); Phase 4 (winter, 2008/2009); Phase 5 (spring, 2009); Phase 6 (summer, 2009); Phase 7 (fall, 2009); Phase 8 (winter, 2009/2010); Phase 9 (spring, 2010); and Phase 10 (summer, 2010). Refer to Table 7 and Figures 82-91 for meteorological data.

Table 7: Meteorology data table for Phases 1 through 10 taken at Oro Grande Gate. Data were obtained from WSMR officials. NA¹ (not available) – Equipment malfunction.

Dates	Avg. of Min. Temp. (F)	Avg. of Avg. Temp. (F)	Avg. of Max. Temp. (F)	Avg. of Avg. RH %	Avg. of Avg. Wind Speed (mph)	Avg. of Max. Wind Speed (mph)	Dir. of Avg. Vector Wind Dir. (Deg.)	Avg. of Total Precip. (inches)
Apr 2008	50	65	78	12	10	33	241	0.00
May 2008	58	73	87	20	10	34	225	0.00
Jun 2008	70	85	98	18	9	36	193	0.00
Jul 2008	68	79	91	53	7	30	134	0.19
Aug 2008	66	77	89	55	7	26	126	0.14
Sep 2008	60	71	84	52	7	23	130	0.08
Oct 2008	50	65	79	40	7	25	135	0.06
Nov 2008	39	53	68	32	7	23	101	0.00
Dec 2008	35	48	61	41	9	28	203	0.06
Jan 2009	33	48	63	33	7	23	239	0.00
Feb 2009	38	54	68	20	9	28	200	0.00
Mar 2009	43	59	73	26	9	28	221	0.00
Apr 2009	50	65	78	17	10	33	226	0.00
May 2009	61	76	89	27	8	33	176	0.04
Jun 2009	67	80	93	31	8	33	203	0.04
Jul 2009	72	85	98	37	7	30	137	0.04
Aug 2009	69	82	96	39	7	27	135	0.04

Table 7 cont'd

Dates	Avg. of Min. Temp. (F)	Avg. of Avg. Temp. (F)	Avg. of Max. Temp. (F)	Avg. of Avg. RH %	Avg. of Avg. Wind Speed (mph)	Avg. of Max. Wind Speed (mph)	Dir. of Avg. Vector Wind Dir. (Deg.)	Avg. of Total Precip. (inches)
Sep 2009	61	74	87	45	7	25	NA ¹	0.02
Oct 2009	50	64	76	42	8	26	NA ¹	0.02
Nov 2009	40	54	68	35	6	19	117	0.04
Dec 2009	31	42	53	55	7	23	216	0.04
Jan 2010	30	42	55	49	6	20	138	0.03
Feb 2010	35	46	59	48	8	26	191	0.04
Mar 2010	39	53	67	31	9	28	237	0.00
Apr 2010	49	63	77	31	10	33	204	0.00
May 2010	57	73	87	21	9	32	204	0.00
Jun 2010	68	83	98	23	8	31	168	0.00
Jul 2010	69	80	93	51	8	29	131	0.00
Aug 2010	69	82	95	43	7	27	133	0.00

3.5 Particle Size Analysis

Particle sizing of the dust was performed with a Malvern Mastersizer 2000 laser diffraction particle sizer at the Geological Sciences Department at UTEP. Particle sizing is performed on dust samples when dry as collected in the sediment traps (dry aggregate size distribution) (Scirocco mode) and/or dispersed in liquid (Hydro mode), depending on the amount of material collected. Prior to analysis with the Malvern Hydro 2000G, the sample was treated with a sodium hexametaphosphate solution and agitated overnight (more than 12 hours) in order to break down soil aggregates (e.g., clay minerals and grain coatings) into individual grains and provide the best dispersion of the individual particulates during analysis (Sperazza et al., 2004). Bird waste was occasionally found in the marble pans (Drees and Manu, 1996) which is removed by pretreatment with hydrogen peroxide (M. Reheis, personal communication, 2008).

Approximately 0.5 grams of material from each sample was analyzed in the Hydro mode and 0.5-1.0 grams of material from each sample was analyzed in the Scirocco mode. Certain samples from certain phases and sites did not contain enough material to analyze by one and/or the other modes.

The Malvern particle sizer provides data as volume percentage values within specific particle size ranges shown in Table 8 (AGÍ, 1982) with mean and standard deviation values. Specifically, the Malvern particle sizer makes three separate measurements per aliquot (an aliquot is one sample put into the Malvern instrument for analysis) to produce three corresponding graphs for each of the three measurements and one averaged graph of the three measurements.

For the analysis of samples from all sites, results were selected depending on the comparison of sites desired mentioned in the staging areas discussion above. Resulting data sets were used to derive statistical values. The following statistical descriptive equations are employed by the Malvern particle size analyzer to produce mean (4) and standard deviation (5) values:

$$\bar{x} = \frac{\sum x}{n} \quad (4)$$

\bar{x} = Arithmetic mean of observed values

$\sum x$ = Summation of observed values

n = Number of observations

$$s = \sqrt{\frac{\sum (x - \bar{x})^2}{n-1}} \quad (5)$$

s = Standard deviation (measure of variation)

x = Observed value (x_1, x_2, \dots, x_n)

\bar{x} = Arithmetic mean of observed values

Table 8: American Geological Institute (AGI) sediment grain-size scale used by American geologists (AGI, 1982).

AGI DATA SHEET 17.1										
Grain-size Scales										
By Roy L. Ingram, University of North Carolina										
GRAIN-SIZE SCALE USED BY AMERICAN GEOLOGISTS										
Modified Wentworth Scale — after Lane, et al., 1947, Trans. American Geophysical Union, v. 28, p. 936-938										
phi	mm	GRADE LIMITS		inches	U.S. Standard Sieve Series		GRADE NAME			
-12	4096	-	-	-	161.3	-	-	-	-	-
-11	2048	-	-	-	80.6	-	-	-	-	-
-10	1024	-	-	-	40.3	-	-	-	-	Boulders
-9	512	-	-	-	20.2	-	-	-	-	-
-8	256	-	-	-	10.1	-	-	-	-	-
-7	128	-	-	-	5.0	-	-	-	-	Cobbles
-6	64	-	-	-	2.52	63 mm	-	-	-	GRAVEL
-5	32	-	-	-	1.26	31.5 mm	-	-	-	-
-4	16	-	-	-	0.63	16 mm	-	-	-	-
-3	8	-	-	-	0.32	8 mm	-	-	-	Pebbles
-2	4	-	-	-	0.16	No. 5	-	-	-	-
-1	2	-	-	-	0.08	No. 10	-	-	-	-
0	1	-	-	-	0.04	No. 18	-	-	-	-
+1	1/2	0.500	-	-	-	No. 35	-	-	-	-
+2	1/4	0.250	-	-	-	No. 60	-	-	-	Sand
+3	1/8	0.125	-	-	-	No. 120	-	-	-	SAND
+4	1/16	0.062	-	-	-	No. 230	-	-	-	-
+5	1/32	0.031	-	-	-	-	-	-	-	-
+6	1/64	0.016	-	-	-	-	-	-	-	Silt
+7	1/128	0.008	-	-	-	-	-	-	-	-
+8	1/256	0.004	-	-	-	-	-	-	-	MUD
+9	1/512	0.002	-	-	-	-	-	-	-	-
+10	1/1024	0.001	-	-	-	-	-	-	-	Clay size
+11	1/2048	0.0005	-	-	-	-	-	-	-	-
+12	1/4096	0.00025	-	-	-	-	-	-	-	-

AGI-DS-rvd-82

3.6 Deposition Mean, Standard Deviation, and Confidence Intervals

MDCO deposition values for all 24 sites for Phases 1 through 10 were applied to statistical descriptive equations shown below to produce mean (6), standard deviation (7), and confidence interval (8) values (Miller, et al., 1990). Calculation were conducted with a 0.05 level of significance ($\alpha=0.05$) to derive the 95 % confidence interval (μ).

$$\bar{x} = \frac{\sum x}{n} \quad (6)$$

\bar{x} = Arithmetic mean of observed values

$\sum x$ = Summation of observed values

n = Number of observations

$$s = \sqrt{\frac{\sum (x - \bar{x})^2}{n-1}} \quad (7)$$

s = Standard deviation (measure of variation)

x = Observed value (x_1, x_2, \dots, x_n)

\bar{x} = Arithmetic mean of observed values

$$\bar{x} - t_{\alpha/2} \cdot \frac{s}{\sqrt{n}} < \mu < \bar{x} + t_{\alpha/2} \cdot \frac{s}{\sqrt{n}} \quad (8)$$

\bar{x} = Arithmetic mean of observed values

$t_{\alpha/2}$ = Value of random variable having the t distribution

α = Significance level

s = Standard deviation (measure of variation)

n = Number of observations

μ = Small-sample confidence interval

3.7 Horizontal Flux of Total Airborne Particle Mass (q_{tot})

Horizontal fluxes of total airborne particle mass (q_{tot}) (9) values were derived from the empirical equation (Gillette et al., 1997a; Shao, 2000).

$$q_{tot} = \frac{\int_0^{1m} Q(z) dz}{\Delta t} \quad (9)$$

q_{tot} = Horizontal Flux of Total Airborne Particle Mass ($\text{gm}^{-1}\text{yr}^{-1}$)

$Q(z)$ = Mass of sediment sample divided by the inlet area (gm^{-2})

dz = Change in height of the sampler (m)

Δt = Sampling time interval (yr)

3.8 MDCO, BSNE, and MWAC Scattergrams

Phases 5 (spring, 2009) through 10 (fall, 2010) were selected to construct scattergrams and linear models to compare sediment mass deposition in MDOCs at 1.7 m in the non-maneuver and maneuver areas during varied seasons.

Moreover, scattergrams were constructed to compare sediment mass accumulation in BSNEs and MWACs sediment traps at 0.2 and 1 meter height for Phases 7 (fall, 2009), 8 (winter, 2009/2010), and 9 (spring, 2010). These three phases (7, 8, and 9) was the only time period in which both BSNE and MWAC traps were simultaneously collecting sediment.

3.9 U-test Statistics

Phases 5 (spring, 2009) through 10 (fall, 2010) were selected to conduct the U-test (i.e., Wilcoxon test or Mann Whitney test) (Miller, et al., 1990) since the time span of these phases is approximately one year. For each phase, four site groups (A, B, C, and D) were selected for analysis. As mentioned in the staging areas discussion, single sites Du1K-u, Sh1K-d, Du400m-m, and Sh3K-m-u and Groups A, B, C, and D were selected for this analysis based on similarity as they relate to military activity presence, location relative to wind direction (upwind/downwind), terrain features, vegetation species, and soil structure. Each group corresponds to dune or shrubland areas and upwind or downwind location with respect to a pivot reference point (Figure 2). Groups A and B are in the non-maneuver area, while Groups C and D are in the maneuver area. The U-test was employed to test whether there is a difference between populations with respect to volume percentages as they (percentages) correspond to 15 particle size range bins. The particle size bins fall between 1, 2, 2.5, 4, 8, 10, 16, 31, 62, 100, 125, 250, 300, 500, and 1000 μm . The volume percentage values are produced by the Malvern particle size analyzer utilizing sediment samples collected with MWACs and/or BSNEs. Once the above values are established, the U-test is conducted at the 0.01 level of significance ($\alpha=0.01$) to test the null hypothesis (two samples come from identical populations) against the alternative hypothesis in which the

populations are not identical. Therefore, the criterion is such that the null hypothesis is rejected if $Z < -2.575$ or $Z > 2.575$.

$$U_1 = W_1 - \frac{n_1(n_1 + 1)}{2} \quad (10)$$

$$U_2 = W_2 - \frac{n_2(n_2 + 1)}{2} \quad (11)$$

U_1 and $U_2 = U_I$ and U_2 statistics
 W_1 and $W_2 = W_I$ and W_2 sums of the ranks
 n_1 and $n_2 =$ Sizes of samples n_I and n_2

$$\mu_{v_1} = \frac{n_1 n_2}{2} \quad (12)$$

$\mu_{v_1} =$ Mean of U_I statistic
 n_1 and $n_2 =$ Sizes of samples n_I and n_2

$$\sigma_{v_1}^2 = \frac{n_1 n_2 (n_1 + n_2 + 1)}{12} \quad (13)$$

$\sigma_{v_1}^2 =$ Variance of U_I statistic
 n_1 and $n_2 =$ Sizes of samples n_I and n_2

$$Z = \frac{U_1 - \mu_{v_1}}{\sigma_{v_1}} \quad (14)$$

$Z =$ Statistic for large-sample U test
 $\mu_{v_1} =$ Mean of U_I statistic
 $\sigma_{v_1} =$ Variance of U_I statistic

3.10 AP-42 Emission Factor Equation

The AP-42 Compilation of Air Pollutant Emission Factors, was originally published by the U.S. Public Health Service in 1968; and was revised and issued as the second edition by the U.S. Environmental Protection Agency (EPA) in 1972. Since then, the EPA has formulated equations for particulate matter (PM) emission factors from vehicles traveling on unpaved roads and published them in their AP-42 guidance document for emissions (EPA, 1998). The AP-42 PM emissions factor (E) equation (15) is as follows:

$$E = k(1.7) \left[\frac{s}{12} \right] \left[\frac{S}{48} \right] \left[\frac{W}{2.7} \right]^{0.7} \left[\frac{w}{4} \right]^{0.5} \left[\frac{365-p}{365} \right] \quad (15)$$

E = Emission factor, (kilograms [kg]/VKT)

k = Particle size multiplier dependant on the aerodynamic size

(dimensionless) = 0.36 for PM10

s = Silt content of road surface material (%)

S = Mean vehicle speed (km/hr)

W = Mean vehicle weight in megagrams (Mg)

w = Mean number of wheels

p = Number of days with at least 0.254 mm of precipitation per year

VKT = Vehicle Kilometers Traveled

Emissions of particulate matter smaller than 10 μm in diameter (PM10) were estimated by applying silt volume percentages derived from Malvern analysis of dry topsoil from dune (Du400m and Du400m-m) and shrubland (Sh400m, Sh400m-m, and Sh3K-m-u) areas to the AP-42 dust emission factor equation. Details of military vehicular maneuvers are unknown; therefore, assumptions were made. These estimates are only for a 1 km stretch of dirt road of varied soil structure.

4. Results

4.1 Particle Size Analysis

4.1.1 Du1K-u (non-maneuver area) and Du400m-m (maneuver area) at 0.2 m for Phase 5

Figure 24 (top graph) shows Phase 5 (spring, 2009) volume versus particle size percentages for sites Du1K-u in the non-maneuver area and Du400m-m in the maneuver area collected by MWAC type sediment traps at 0.2 m height. Both Du1K-u and Du400m-m sites are in similar high dune density areas with an abundance of mesquite and varied vegetation species. The Du1K-u peak lies approximately at 13 % volume/180 μm , while the Du400m-m peak lies approximately at 11 % volume/280 μm .

Figure 24 (bottom graph) shows Phase 5 (spring, 2009) mean and standard deviation values of volume percentages versus particle size for sites Du1K-u in the non-maneuver area and Du400m-m in the maneuver area collected by MWAC type sediment traps at 0.2 m height. The largest standard deviation values, 16.26 % and 13.59 %, lie between the 125 to 250 μm and 300 to 500 μm ranges, respectively.

4.1.2 Du1K-u (non-maneuver area) and Du400m-m (maneuver area) at 1 m for Phase 5

Figure 25 (top graph) shows Phase 5 (spring, 2009) volume versus particle size percentages for sites Du1K-u in the non-maneuver area and Du400m-m in the maneuver area collected by MWAC type sediment traps at 1 m height. Both Du1K-u and Du400m-m sites are in similar high dune density areas with an abundance of mesquite and varied vegetation species. The Du1K-u peak lies approximately at 11.5 % volume/125 μm , while the Du400m-m peak lies approximately at 8.5 % volume/100 μm .

Figure 25 (bottom graph) shows Phase 5 (spring, 2009) mean and standard deviation values of volume percentages versus particle size for sites Du1K-u in the non-maneuver area and Du400m-m in the maneuver area collected by MWAC type sediment traps at 1 m height. The largest standard deviation value 14.88 %, lies between the 125 to 250 μm range.

4.1.3 Du1K-u (non-maneuver area) and Du400m-m (maneuver area) at 1.7 m for Phase 5

Figure 26 (top graph) shows Phase 5 (spring, 2009) volume versus particle size percentages for sites Du1K-u in the non-maneuver area and Du400m-m in the maneuver area collected by MDCO type sediment traps at 1.7 m height. Both Du1K-u and Du400m-m sites are in similar high dune density areas with an abundance of mesquite and varied vegetation species. Both Du1K-u and Du400m-m graphs have peaks and shoulders that approximately coincide with respect to particle size. The Du1K-u peak and shoulder lie approximately at 13 %/150 μm and 0.5 %/20 μm , respectively. The Du400m-m peak and shoulder lie approximately at 6 %/190 μm and 2 %/15 μm , respectively.

Figure 26 (bottom graph) shows Phase 5 (spring, 2009) mean and standard deviation values of volume percentages versus particle size for sites Du1K-u in the non-maneuver area and Du400m-m in the maneuver area collected by MDCO type sediment traps at 1.7 m height. The largest standard deviation value, 18.89 %, lies between the 125 to 250 μm range.

4.1.4 Sh1K-d (non-maneuver area) and Sh3K-m-u (maneuver area) at 0.2 m for Phase 5

Figure 27 (top graph) shows Phase 5 (spring, 2009) volume versus particle size percentages for sites Sh1K-d in the non-maneuver area and Sh3K-m-u in the maneuver area collected by MWAC type

sediment traps at 0.2 m height. Both Sh1K-d and Sh3K-m-u sites are in similar shrubland areas with an abundance of creosote and varied vegetation growth. The Sh1K-d peak lies approximately at 8.5 % volume/110 μm , while the Sh3K-m-u peak lies approximately at 6.5 % volume/80 μm .

Figure 27 (bottom graph) shows Phase 5 (spring, 2009) mean and standard deviation values of volume percentages versus particle size for sites Sh1K-d in the non-maneuver area and Sh3K-m-u in the maneuver area collected by MWAC type sediment traps at 0.2 m height. The largest standard deviation value, 5.69 %, lies between the 125 to 250 μm range.

4.1.5 Sh1K-d (non-maneuver area) and Sh3K-m-u (maneuver area) at 1 m for Phase 5

Figure 28 (top graph) shows Phase 5 (spring, 2009) volume versus particle size percentages for sites Sh1K-d in the non-maneuver area and Sh3K-m-u in the maneuver area collected by MWAC type sediment traps at 1 m height. Both Sh1K-d and Sh3K-m-u sites are in similar shrubland areas with an abundance of creosote and varied vegetation growth. The Sh3K-m-u peak lies approximately at 5.5 % volume/70 μm , while Sh1K-d lies approximately at 4.8 % volume/70 μm .

Figure 28 (bottom graph) shows Phase 5 (spring, 2009) mean and standard deviation values of volume percentages versus particle size for sites Sh1K-d in the non-maneuver area and Sh3K-m-u in the maneuver area collected by MWAC type sediment traps at 1 m height. The largest standard deviation value 1.80 %, lies between the 62 to 100 μm range.

4.1.6 Sh1K-d (non-maneuver area) and Sh3K-m-u (maneuver area) at 1.7 m for Phase 5

Figure 29 (top graph) shows Phase 5 (spring, 2009) volume versus particle size percentages for sites Sh1K-d in the non-maneuver area and Sh3K-m-u in the maneuver area collected by MDCO type sediment traps at 1.7 m height. Both Sh1K-d and Sh3K-m-u sites are in similar shrubland areas with an abundance of creosote and varied vegetation growth. Both Sh1K-d and Sh3K-m-u graphs have peaks and shoulders that approximately coincide with respect to particle size. The Sh3K-m-u peak and shoulder lie at about 5 %/180 μm and 3.5 %/20 μm , respectively. The Sh1K-d peak and shoulder lie at about 4 %/190 μm and 3.5 %/15 μm , respectively.

Figure 29 (bottom graph shows Phase 5 (spring, 2009) mean and standard deviation values of volume percentages versus particle size for sites Du1K-u in the non-maneuver area and Du400m-m in the maneuver area collected by MDCO type sediment traps at 1.7 m height. The largest standard deviation values, 2.71 % and 3.46 %, lie between the 4 to 8 μm and 125 to 250 μm ranges, respectively.

4.1.7 Du1K-u (non-maneuver area) and Du400m-m (maneuver area) at 0.2 m for Phase 6

Figure 30 (top graph) shows Phase 6 (summer, 2009) volume versus particle size percentages for sites Du1K-u in the non-maneuver area and Du400m-m in the maneuver area collected by MWAC type sediment traps at 0.2 m height. Both Du1K-u and Du400m-m sites are in high dune density areas with an abundance of mesquite and varied vegetation species. The Du1K-u peak lies approximately at 13.5 % volume/205 μm , while the Du400m-m peak lies approximately at 10.5 % volume/220 μm .

Figure 30 (bottom graph) shows Phase 6 (summer, 2009) mean and standard deviation values of volume percentages versus particle size for sites Du1K-u in the non-maneuver area and Du400m-m in the maneuver area collected by MWAC type sediment traps at 0.2 m height. The largest standard deviation values, 9.18 %, lies between the 125 to 250 μm range.

4.1.8 Du1K-u (non-maneuver area) and Du400m-m (maneuver area) at 1 m for Phase 6

Figure 31 (top graph) shows Phase 6 (summer, 2009) volume versus particle size percentages for sites Du1K-u in the non-maneuver area and Du400m-m in the maneuver area collected by MWAC type sediment traps at 1 m height. Both Du1K-u and Du400m-m sites are in high dune density areas with an abundance of mesquite and varied vegetation species. The Du1K-u peak lies approximately at 8.5 % volume/125 μm , while the Du400m-m peak lies approximately at 6.5 % volume/100 μm .

Figure 31 (bottom graph) shows Phase 6 (summer, 2009) mean and standard deviation values of volume percentages versus particle size for sites Du1K-u in the non-maneuver area and Du400m-m in the maneuver area collected by MWAC type sediment traps at 1 m height. The largest standard deviation value 4.90 %, lies between the 125 to 250 μm range.

4.1.9 Du1K-u (non-maneuver area) and Du400m-m (maneuver area) at 1.7 m for Phase 6

Figure 32 (top graph) shows Phase 6 (summer, 2009) volume versus particle size percentages for sites Du1K-u in the non-maneuver area and Du400m-m in the maneuver area collected by MDCO type sediment traps at 1.7 m height. Both Du1K-u and Du400m-m sites are in high dune density areas with an abundance of mesquite and varied vegetation species. Both Du1K-u and Du400m-m graphs have peaks and shoulders that approximately coincide with respect to particle size. The Du1K-u peak and shoulder lie at about 7 %/175 μm and 1.5 %/20 μm , respectively. The Du400m-m peak and shoulder lie at about 7 %/195 μm and 1.80 %/20 μm , respectively.

Figure 32 (bottom graph) shows Phase 6 (summer, 2009) mean and standard deviation values of volume percentages versus particle size for sites Du1K-u in the non-maneuver area and Du400m-m in the maneuver area collected by MDCO type sediment traps at 1.7 m height. The largest standard deviation values, 1.96 %, lies between the 62 to 100 μm range.

4.1.10 Sh1K-d (non-maneuver area) and Sh3K-m-u (maneuver area) at 0.2 m for Phase 6

Figure 33 (top graph) shows Phase 6 (summer, 2009) volume versus particle size percentages for sites Sh1K-d in the non-maneuver area and Sh3K-m-u in the maneuver area collected by MWAC type sediment traps at 0.2 m height. Both Sh1K-d and Sh3K-m-u sites are in similar shrubland areas with an abundance of creosote and varied vegetation growth. The Sh1K-d peak lies approximately at 7.8 % volume/200 μm , while the Sh3K-m-u peak lies approximately at 7.2 % volume/120 μm .

Figure 33 (bottom graph) shows Phase 6 (summer, 2009) mean and standard deviation values of volume percentages versus particle size for sites Sh1K-d in the non-maneuver area and Sh3K-m-u in the maneuver area collected by MWAC type sediment traps at 0.2 m height. The largest standard deviation values, 4.06 %, 3.80 %, and 5.48 %, lie between the 62 to 100 μm , 125 to 250 μm , and 300 to 500 μm ranges, respectively.

4.1.11 Sh1K-d (non-maneuver area) and Sh3K-m-u (maneuver area) at 1 m for Phase 6

Figure 34 (top graph) shows Phase 6 (summer, 2009) volume versus particle size percentages for sites Sh1K-d in the non-maneuver area and Sh3K-m-u in the maneuver area collected by MWAC type sediment traps at 1 m height. Both Sh1K-d and Sh3K-m-u sites are in similar shrubland areas with an abundance of creosote and varied vegetation growth. The Sh3K-m-u peak lies approximately at 6 % volume/80 μm , while Sh1K-d peak lies approximately a 5 % volume/70 μm .

Figure 34 (bottom graph) shows Phase 6 (summer, 2009) mean and standard deviation values of volume percentages versus particle size for sites Sh1K-d in the non-maneuver area and Sh3K-m-u in the maneuver area collected by MWAC type sediment traps at 1 m height. The largest standard deviation value 4.47 %, lies between the 125 to 250 μm range.

4.1.12 Sh1K-d (non-maneuver area) and Sh3K-m-u (maneuver area) at 1.7 m for Phase 6

Figure 35 (top graph) shows Phase 6 (summer, 2009) volume versus particle size percentages for sites Sh1K-d in the non-maneuver area and Sh3K-m-u in the maneuver area collected by MDCO type sediment traps at 1.7 m height. Both Sh1K-d and Sh3K-m-u sites are in similar shrubland areas with an abundance of creosote and varied vegetation growth. Both Sh1K-d and Sh3K-m-u graphs have peaks and shoulders that approximately coincide. The Sh3K-m-u peak and shoulder lie at about 5 %/180 μm and 2.3 %/25 μm , respectively. The Sh1K-d peak and shoulder lie at about 5.5 %/190 μm and 2.5 %/20 μm , respectively.

Figure 35 (bottom graph) shows Phase 6 (summer, 2009) mean and standard deviation values of volume percentages versus particle size for sites Du1K-u in the non-maneuver area and Du400m-m in the maneuver area collected by MDCO type sediment traps at 1.7 m height. The largest standard deviation values, 1.50 %, lies between the 62 to 100 μm range.

4.1.13 Sh1K-d (non-maneuver area) and Du400m-m (maneuver area) at 1.7 m for Phase 5

Figure 36 (top graph) shows Phase 5 (spring, 2009) volume versus particle size percentages for sites Sh1K-d in the non-maneuver area and Du400m-m in the maneuver area collected by MDCO type

sediment traps at 1.7 m height. Sh1K-d and Du400m-m sites are not in similar areas with respect to terrain features or vegetation; however, these sites lie parallel with predominant southwesterly winds. The Du400m-m peak and shoulder lie at about 6 %/190 μm and 3.5 %/12 μm , respectively. The Sh1K-d peak and shoulder lie at about 4 %/180 μm and 3.5 %/12 μm , respectively.

Figure 36 (bottom graph) shows Phase 5 (spring, 2009) mean and standard deviation values of volume percentages versus particle size for sites Sh1K-d in the non-maneuver area and Du400m-m in the maneuver area collected by MDCO type sediment traps at 1.7 m height. The largest standard deviation values, 3.85 % and 6.93 %, lie between the 16 to 31 μm and 125 to 250 μm ranges, respectively.

4.1.14 Sh1K-d (non-maneuver area) and Du400m-m (maneuver area) at 1.7 m for Phase 6

Figure 37 (top graph) shows Phase 6 (summer, 2009) volume versus particle size percentages for sites Sh1K-d in the non-maneuver area and Du400m-m in the maneuver area collected by MDCO type sediment traps at 1.7 m height. Sh1K-d and Du400m-m sites are not in similar areas with respect to terrain features or vegetation; however, these sites lie parallel with predominant southwesterly winds. Both Sh1K-d and Du400m-m graphs have peaks and shoulders that approximately coincide with respect to particle size. The Du400m-m peak and shoulder lie at about 7 %/200 μm and 2 %/20 μm , respectively. The Sh1K-d peak and shoulder lie at about 5.5 %/180 μm and 2.5 %/20 μm , respectively.

Figure 37 (bottom graph) shows Phase 6 (summer, 2009) mean and standard deviation values of volume percentages versus particle size for sites Sh1K-d in the non-maneuver area and Du400m-m in the maneuver area collected by MDCO type sediment traps at 1.7 m height. The largest standard deviation values, 2.35 % and 4.52 %, lie between the 16 to 31 μm and 125 to 250 μm ranges, respectively.

4.1.15 Sh3K-m-u (maneuver area) and Du1K-u (non-maneuver area) at 1.7 m for Phase 5

Figure 38 (top graph) shows Phase 5 (spring, 2009) volume versus particle size percentages for sites Sh3K-m-u in the maneuver area and Du1K-u in the non-maneuver area collected by MDCO type

sediment traps at 1.7 m height. Sh3K-m-u and Du1K-u sites are not in similar areas with respect to terrain features or vegetation; however, these sites lie parallel to southeasterly winds. Both Sh3K-m-u and Du1K-u graphs have peaks and shoulders that approximately coincide with respect to particle size. The Du1K-u peak and shoulder lie at about 13 %/150 μm and 1 %/20 μm , respectively. The Sh3K-m-u peak and shoulder lie at about 4.5 %/180 μm and 2.5 %/20 μm , respectively.

Figure 38 (bottom graph) shows Phase 5 (spring, 2009) mean and standard deviation values of volume percentages versus particle size for sites Sh3K-m-u in the maneuver area and Du1K-u in the non-maneuver area collected by MDCO type sediment traps at 1.7 m height. The largest standard deviation values, 6.57 % and 22.35 %, lie between the 16 to 31 μm and 125 to 250 μm ranges, respectively.

4.1.16 Sh3K-m-u (maneuver area) and Du1K-u (non-maneuver area) at 1.7 m for Phase 6

Figure 39 (top graph) shows Phase 6 (summer, 2009) volume versus particle size percentages for sites Sh3K-m-u in the maneuver area and Du1K-u in the non-maneuver area collected by MDCO type sediment traps at 1.7 m height. Sh3K-m-u and Du1K-u sites are not in similar areas with respect to terrain features or vegetation; however, these sites lie parallel to southeasterly winds. Both Sh3K-m-u and Du1K-u graphs have peaks and shoulders that approximately coincide with respect to particle size. The Du1K-u peak and shoulder lie at about 7 %/180 μm and 1.5 %/20 μm , respectively. The Sh3K-m-u peak and shoulder lie at about 5.8 %/150 μm and 2.3 %/25 μm , respectively.

Figure 39 (bottom graph) shows Phase 6 (summer, 2009) mean and standard deviation values of volume percentages versus particle size for sites Sh3K-m-u in the maneuver area and Du1K-u in the non-maneuver area collected by MDCO type sediment traps at 1.7 m height. The largest standard deviation values, 2.18 % and 3.84 %, lie between the 16 to 31 μm and 125 to 250 μm ranges, respectively.

4.2 Sediment Deposition Mean, Standard Deviation, and Confidence Intervals

Dune sites yielded the highest MDCO deposition values, whereas shrubland sites yielded the lowest. The seasons having the highest MDCO deposition values had the following rank order: spring > winter > fall > summer. Phase 9 (spring, 2010) values ranged between $33.7 \text{ gm}^{-2}\text{y}^{-1}$ – $1,172.6 \text{ gm}^{-2}\text{y}^{-1}$; Phase 8 (winter, 2009/2010) values ranged between $20.4 \text{ gm}^{-2}\text{y}^{-1}$ – $241.6 \text{ gm}^{-2}\text{y}^{-1}$; Phase 7 (fall, 2009) values ranged between $23.0 \text{ gm}^{-2}\text{y}^{-1}$ – $143.1 \text{ gm}^{-2}\text{y}^{-1}$; and Phase 10 (summer, 2010) values ranged between $41.1 \text{ gm}^{-2}\text{y}^{-1}$ – $126.0 \text{ gm}^{-2}\text{y}^{-1}$ (Table 12; Figures 40-49).

The minimum standard deviation value ($14.9 \text{ gm}^{-2}\text{y}^{-1}$) corresponded to Phase 6 (summer, 2009), whereas the maximum standard deviation value ($243.0 \text{ gm}^{-2}\text{y}^{-1}$) corresponded to Phase 9 (spring 2010). Deposition mean, standard deviation, and confidence interval values for Phases 1 through 10 and various conditions are listed in Table 13, respectively.

4.3 Horizontal Flux of Total Airborne Particle Mass (q_{tot})

The q_{tot} values for the MWAC design for Phases 1 (spring, 2008) through 4 (winter, 2008/2009) could not be determined due to the MWAC design bottle type; therefore, only results for MWAC and BSNE traps for Phases 5 (spring, 2009) through 10 (summer, 2010) were displayed in Table 14.

BSNE sediment traps collected more mass (g), but MWAC traps were more efficient, that is, MWAC traps collected more sediment per inlet area (gm^{-2}).

Dune sites yielded the highest q_{tot} values, whereas shrubland sites yielded the lowest q_{tot} values. The seasons having the highest MWAC q_{tot} values had the following rank order: spring > winter > fall > summer. Respective to 0.2 m and 1 m heights, Phase 9 (spring, 2009) values ranged between $917 \text{ gm}^{-1}\text{y}^{-1}$ – $274,166 \text{ gm}^{-1}\text{y}^{-1}$ and $6,550 \text{ gm}^{-1}\text{y}^{-1}$ – $176,839 \text{ gm}^{-1}\text{y}^{-1}$; Phase 8 (winter, 2009/2010) values ranged between $210 \text{ gm}^{-1}\text{y}^{-1}$ – $98,925 \text{ gm}^{-1}\text{y}^{-1}$ and $0 \text{ gm}^{-1}\text{y}^{-1}$ and $34,582 \text{ gm}^{-1}\text{y}^{-1}$; Phase 7 (fall, 2009) values ranged between $166 \text{ gm}^{-1}\text{y}^{-1}$ – $38,470 \text{ gm}^{-1}\text{y}^{-1}$ and $414 \text{ gm}^{-1}\text{y}^{-1}$ and $14,064 \text{ gm}^{-1}\text{y}^{-1}$; and Phase 10 (summer, 2010) values ranged between $1,209 \text{ gm}^{-1}\text{y}^{-1}$ and $7,134 \text{ gm}^{-1}\text{y}^{-1}$ and $157 \text{ gm}^{-1}\text{y}^{-1}$ and $1,572 \text{ gm}^{-1}\text{y}^{-1}$ (Table 14; Figures 50-67).

4.4 MDCO, BSNE, and MWAC Scattergrams

Scattergram results for sediment mass (g) accumulation in BSNEs and MWACs sediment traps at 0.2 and 1 m are displayed in Figures 52, 55, 58, 61, 64, and 67. Respective to 0.2 m and 1 m heights, Phase 7 (fall, 2009) r^2 values were 0.98 and 0.89; Phase 8 (winter, 2009/2010) values were 0.72 and 0.90; and Phase 9 (spring 2010) values were 0.91 and 0.92.

4.5 Non-maneuver and Maneuver Area Scattergrams

Scattergram results for deposition mass (g) in MDCOs at 1.7 m in the non-maneuver and maneuver areas are displayed in Figures 68-73. Respective to seasons, Phase 5 (spring, 2009) and Phase 9 (spring 2010) r^2 values were 0.92 and 0.55; Phase 6 (summer, 2009) and Phase 10 (summer, 2010) r^2 values were 0.18 and 0.02; Phase 7 (fall, 2009) r^2 value was 0.68; and Phase 8 (winter, 2009/2010) r^2 value was 0.63.

4.6 U-test Statistics

Seasonal weather fluctuations and topography features had the most pronounced effect on Z values listed in Tables 15 and 16. Phase 5 (spring, 2009), Phase 8 (winter, 2009/2010), and Phase 8 (winter, 2009/2010) and dune areas yielded the highest Z values ($Z=2.14$, 0.82 and $Z=2.05$, 1.06) at 0.2 m and 1 m heights, respectively. Phase 8 (winter, 2009/2010) and Phase 9 (spring 2010) and shrubland areas yielded the lowest Z values ($Z=0.02$, 0.23 and $Z=0.06$, 0.31) at 0.2 m and 1 m heights, respectively.

4.7 AP-42 Emission Factor Equation

Results for the AP-42 emissions factor equation are listed in Table 9.

Table 9: Annual emissions estimate of particulate matter less than PM10 (AGI, 1982) for two types of military vehicles in two types of terrain utilizing the AP-42 emissions equation.

Vehicle type	Number of wheels (w)	Weight (tons) (W)	Speed (km/hr) (S)	Number of days per year with precipitation > 0.254mm > 0.01 inches (p)	Sample source site	Topsoil (dry) Silt % (s)	E= (kg/VKT) (E)
Truck	6	5	72.4	35	Sh3K-m-u	8.23	1.08
HMMWV ¹	4	4	72.4	35	Sh3K-m-u	8.23	0.75
Truck	6	5	72.4	35	Du400m	6.26	0.82
Truck	6	5	72.4	35	Sh400m	8.08	1.06
Truck	6	5	72.4	35	Du400m-m	0.51	0.07
Truck	6	5	72.4	35	Sh400m-m	11.50	1.51
HMMWV ¹	4	4	72.4	35	Du400m	6.26	0.57
HMMWV ¹	4	4	72.4	35	Sh400m	8.08	0.74
HMMWV ¹	4	4	72.4	35	Du400m-m	0.51	0.05
HMMWV ¹	4	4	72.4	35	Sh400m-m	11.50	1.05

¹High Mobility Multipurpose Wheeled Vehicle (HMMWV)

5. Discussion

Volume percentage/particle size graphs show similar symmetrical and nonsymmetrical almost concurring peaks with tails and/or shoulders on the left side. The tails to the left are typical of fine aeolian sediment and indicative of clay and silt size sediment possibly deposited by long-term suspension and/or local entrainment (Pye, 1987). The large peaks are indicative of sand size sediment in extreme saltation trajectories or short-term suspension, potentially deposited by wind gusts (Pye, 1987). The two peaks are indicative of sand size sediment transported by saltation. This is typical for the saltating zone which typically extends above the land surface peaking at heights ranging between 0.2 m to 0.3 m (Fryrear and Saleh, 1993).

The graphs indicate that dune areas had a greater volume of sand size particles than the shrubland areas. The graphs also indicate that the shrubland areas had a greater volume of fine aeolian-transport size particles than the dune areas. The largest standard deviation values were approximately within the fine aeolian to sand particle size ranges and were on the whole larger for phases with higher

wind speeds and less precipitation (spring) than for phases with less wind but more precipitation (summer).

These graphs also indicate that on the whole quantities of fine aeolian particles are almost the same in the maneuver and non-maneuver areas, whereas more sand size particles are available in the non-maneuver area than in the maneuver area.

Both the maneuver (towards the north) and non-maneuver (towards the south) areas have dune (towards the east) and shrubland (towards the east) areas. Dune areas have similar terrain (coarse grain dunes and lanes) terrain and vegetation (e.g., mesquite, grass, yucca, and saltbush). Shrubland areas also have similar terrain (mostly alluvial material) and vegetation (e.g., creosote, saltbush, grass).

Based on the results of this study, there are three characteristic volumetric particle size curves. Contributing factors which form these volumetric particle size curves are location features (e.g., vegetation and surface features), meteorology, and collection height.

1) For MWAC type collectors at 0.2 m height, the typical volumetric particle size curve is a dominant symmetrical peak with small tail and no shoulder (Figure 8). This is the expected pattern for predominantly saltating aeolian sands (Fryrear and Saleh, 1993; Pye, 1987), but also note the tail representing emission of dust particles as small as submicron in size.

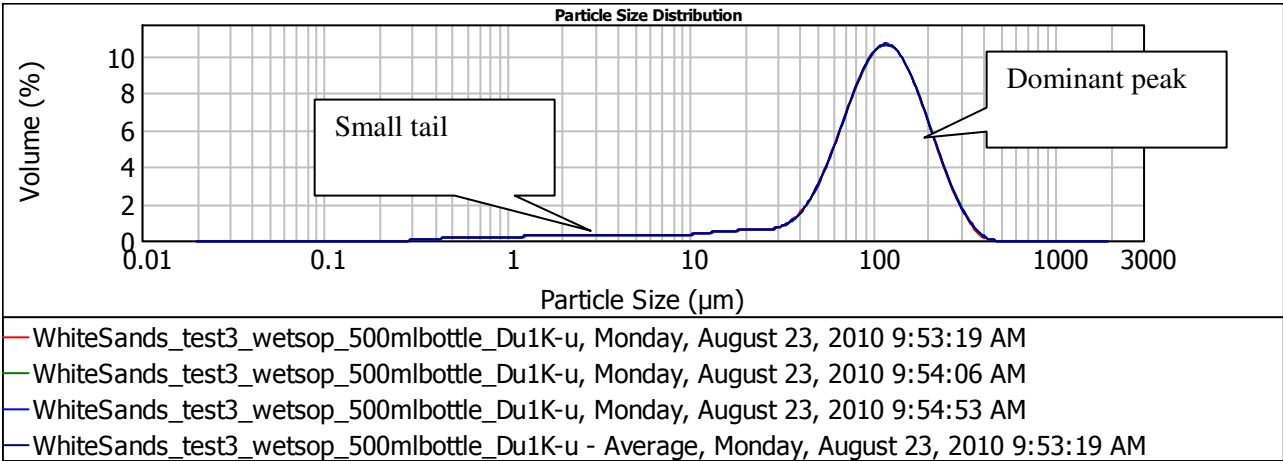


Figure 8: Characteristic MWAC volume percentage versus particle size curve at 0.2 m height.

2) For MWAC type collectors at 1 m height, the typical volumetric particle size curve is a less symmetrical peak with a larger tail of fines (Figure 9). The dominant peak is typical of fine sand particles. Particles between 70 to 100 μm can transport by modified saltation up to 1.5 m (Pye, 1987). Saltating particles can break down by impact and reach heights above the saltating zone. These saltating particles can be impeded or trapped by vegetation and/or land features (Gillette, 1999). The tail is typical of fine aeolian sediment (dust) comprised of clay and silt. Particles between 20 to 70 μm can be transported by short-term suspension, while particles less than 20 μm can be transported by long-term suspension (Pye, 1987).

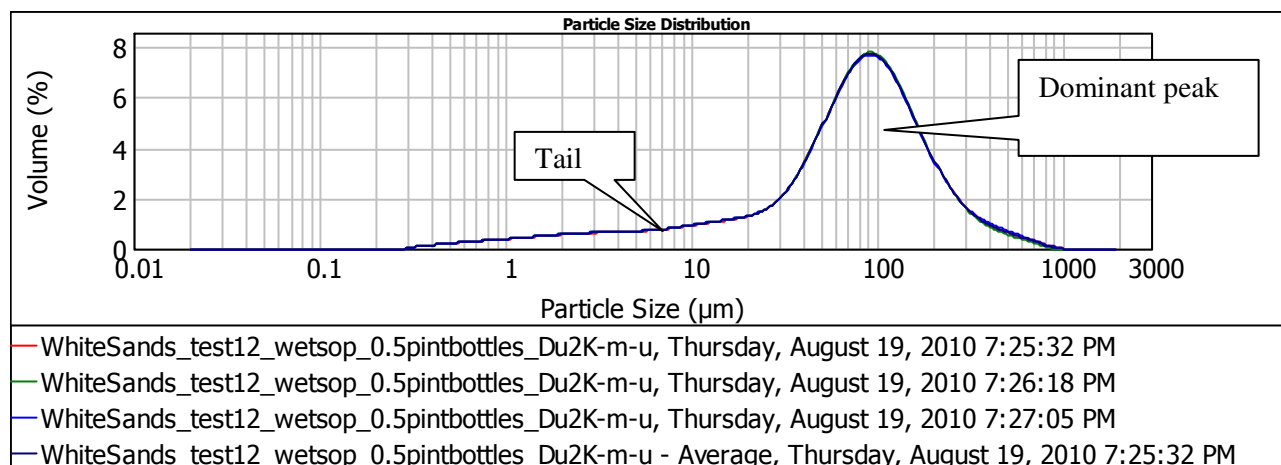


Figure 9: Characteristic MWAC volume percentage versus particle size curve at 1 m height.

3) For the MDCO type collector at 1.7 m height, the typical volume percentage versus particle size curve is a more composite curve comprised of a dominant peak with shoulders on either side (typically bimodal) and tail on the fine particle side (Figure 10). The dominant peak is typical of fine sand grains, while the shoulder and tail is typical of clay and silt (dust) particles with individual particles as small as a fraction of a micron in diameter. Particles between 20 to 70 μm can be transported by short-term suspension, while particles less than 20 μm can be transported by long-term suspension (Pye, 1987). Wind gusts can transport sand grains to this height, while typical wind entrainment can transport clay and silt size sediment into the MDCOs.

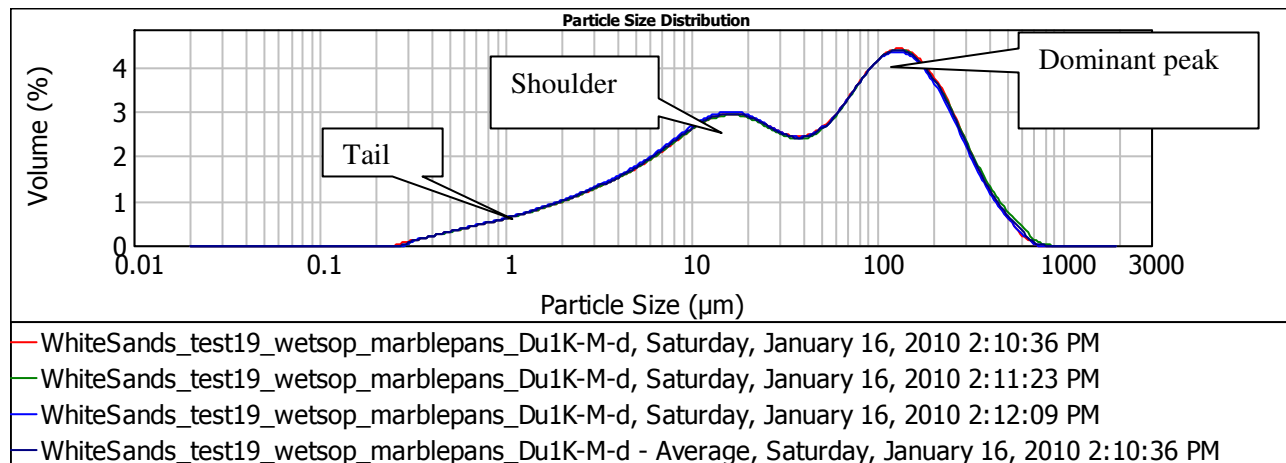


Figure 10: Characteristic MDCO volume percentage versus particle size curve at 1.7 m height.

These curves certainly do vary depending on factors (i.e., vegetation, surface features, meteorology, and collection height) which are particular to the collection site; however, these three rudimentary are typical for aeolian desert sand and dust (i.e., fine particles of clay and silt transported by wind). The particle size, density, and form will also dictate how the particle will transport.

Trends which are evident in Table 12 and Figures 40-49 show that deposition and standard deviation values were highest typically during spring, winter, and fall seasons (i.e., Phases 1, 3 4, 5, 7, and 8) as compared to summer. These seasons tended to be windier and dryer. In general, trends indicate that dune areas yielded the highest sediment deposition (dustfall) values, while shrubland areas yielded the lowest sediment deposition (dustfall) values. Sites Du1K-u, Du1.5K-m, and Du400m-m consistently yielded very high sample masses. Other dune area sites yielded moderately high sample masses, but these values were much less than those of Du1K-u, Du1.5K-m, and Du400m-m sites.

Anticipated problems such as damaged or lost MDCO sediment traps, contaminated MDCO sediment traps (with organic matter), field errors, and laboratory weighing uncertainties would invalidate a data set. However, due to the abundance of collecting sites, sufficient data was collected for each phase.

For Phases 1 (spring, 2008) through 4 (winter, 2008/2009), the MWAC design was experimental and horizontal flux (q_{tot}) calculations were not possible. However, a sediment Malvern particle size

analysis was completed for all phases. The latest MWAC design was introduced during Phase 5 (spring, 2009) in which made q_{tot} calculations possible. Phase 5 (spring, 2009) started on February 25, 2009 and ended on May 28, 2009. The latest MWAC design was introduced on March 23, 2009 (Table 6).

For Phases 7 (fall, 2009), 8 (winter, 2009/2010), and 9 (Spring 2010), Table 14 shows higher values of sediment weight for the BSNEs than for the MWACs at 0.2 and 1 meter heights. However, the MWACs predominantly show higher values for the total horizontal flux. That is, the MWACs typically had more accumulation per inlet area than the BSNEs. This is also generally true at 0.2 and 1 meter heights.

Sites Du3K-u, Du1K-u, Du400m-m, Du1.5K-m, and Du1K-m-d had the highest sample masses (i.e., horizontal flux) for Phases 7 (fall, 2009), 8 (winter, 2009/2010), and 9 (spring 2010). Of these five sites, Du1K-u, Du400m-m, and Du1.5K-m sites yielded the highest sample masses. All these sites are in dune areas. This trend is evident throughout all phases (Table 14; Figures 50-67).

For Phases 7 (fall, 2009), 8 (winter, 2009/2010), and 9 (spring 2010), the r^2 values for the BSNEs and MWACs at 0.2 and 1.0 m indicate the regression line approximates the real data points. That is, the fraction of variance (r^2) in the linear model approximates the value of 1. This means there is a good correlation between the sediment mass accumulated in the BSNEs and MWACs at their respective heights. For Phase 8 (winter, 2009/2010), the low r^2 value of 0.72 is likely attributable to atypical high sediment mass accumulation in the BSNE pans at 0.2 meters at Du400m-m and Du1.5K-m (Figure 58). Also for Phase 8 (winter, 2009/2010), the atypical sediment weight value (outlier) corresponding to site Du3K-u was removed which increased the r^2 value to 0.90 (Figure 61).

For Phase 5 (spring, 2009), Figure 68 indicates an $r^2 = 0.92$ value for the MDCOs which is higher than the r^2 value for other phases. This is probably attributable to this phase corresponding to the spring season which has high winds and little or no precipitation. Also, site Du1K-u yields higher deposition values than other dune area sites. This is probably attributable to the availability of sediment

surrounding the Du1K-u site area. This anomaly (outlier) at Du1K-u apparently decreased the r^2 value significantly.

For Phase 6 (summer, 2009), Figure 69 indicates an $r^2 = 0.18$ value for the MDCOs which is much lower than the other phase r^2 values. This is probably attributable to this phase corresponding to the summer season which has less wind and more precipitation. Soil moisture will result in less sediment suspension due to soil cohesion, soil crusting, and aggregation. Less sediment suspension means less particles are present to give sediment mass load information about the site which is highly dependent on individual site geomorphology (e.g., fetch length, vegetation type and density, soil structure, etc.); therefore, this leads to more ambiguity and lower r^2 values.

For Phase 7 (fall, 2009), Figure 70 indicates an $r^2 = 0.68$ value for the MDCOs which is similar to other phase r^2 values with the exception of Phases 5 (spring, 2009) and 6 (summer, 2009). This is probably attributable to this phase corresponding to the fall season in which precipitation drops and vegetation decreases; subsequently, this leads to more sediment suspension as soil matrix loosens with more wind flow and lack of moisture. More sediment suspension means more particles are present to give sediment mass load information about the site which is highly dependent on individual site geomorphology (e.g., fetch length, vegetation type and density, soil structure, etc.); therefore, compared to summer values, there is less ambiguity and greater r^2 values.

For Phase 8 (winter, 2009/2010), Figure 71 indicates an $r^2 = 0.63$ value for the MDCOs which is nearly the same as Phase 7 (fall, 2009) and similar to other phase r^2 values with the exception of Phases 5 (spring, 2009) and 6 (summer, 2009). This is probably attributable to this phase corresponding to the winter season. The winter season trends to have higher wind events with dry air. This will result in more dust as the barren surface yields more productive sources of sediment for suspension.

For Phase 9 (spring 2010), Figure 72 indicates an $r^2 = 0.55$ value for the MDCOs which is similar to other phase r^2 values with the exception of Phases 5 (spring, 2009) and 6 (summer, 2009).

Phase 9 (spring 2010) corresponds to the spring season which has high winds and minimal precipitation. Phase 9 (spring 2010) marks the end of the annual cycle which started with Phase 5 (spring, 2009).

For Phase 10 (summer, 2010), Figure 73 indicates an $r^2 = 0.02$ value for the MDCOs which is much smaller than the other r^2 values. Phase 10 (summer, 2010) corresponds to the summer season which has less wind and more precipitation. There was heavy rainfall during Phase 10 (summer, 2010) and many of the MDCO pans overfilled and some sample sediment was lost. Moreover, during this humid season, there was a substantial presence of insects and bird urine in the MDCOs which subsequently affected the results for Phase 10 (summer, 2010).

Even though the values shown in Tables 15-16 above are well below the criterion value ($Z < 2.575$) (mentioned in the methodology section), they are higher than the Z values for other groups. The Z values indicate that there is more variance with respect to volume percentages versus particle size in the dunes areas than in the shrubland sites. That is, the analysis indicates that upwind/downwind sites in the dune areas yielded the highest Z values indicating more variation in horizontal flux in the dune areas due to greater sediment displacement. Shrubland collecting sites were installed largely in areas made of alluvial material east of the dune areas and west of the Jarrilla Mountains. Amid the shrubland sites, Sh1K-m-d/Sh400m-m upwind site comparison yielded high Z values. However, site comparison of Du1K-u/Sh3K-m-u yielded the highest Z values ($Z = 2.14, 0.82$). This indicates that site Du1K-u yields atypical high sediment weight values. This is also the case for sites Du400m-m and Du1.5K-m. Sites Du3K-u and Du1K-m-d have relatively high sediment weight values when compared to other sites except Du1K-u, Du400m-m, and Du1.5K-m sites. Concisely, Du1K-u, Du1K-d, Du1K-m-u, and Du1K-m-d were the sites which had the highest effect on the Z outcome attributable to greater sediment displacement and horizontal flux variations. These sites were either downwind or upwind of the pivot station. The pivot station was deployed near a potential dust emitting source such a dirt road.

Comparatively, the Z value corresponding to Phase 9 (spring 2010) is greater than that for Phase 5 (spring, 2009) for sites Sh400m and Sh1K-d. Construction activity of the mock village during Phase 9

(spring 2010) may have caused this increase. There was also a significant increase in the Z value between Phase 7 (fall, 2009) and Phase 10 (summer, 2010) for sites Sh3K-m-u and Sh1K-d. There was heavy rainfall during Phase 10 (summer, 2010) which caused overflow in some of the MDCOs and organic matter such as insect remains, bird waste, and vegetation fragments. The sites with the highest MDCO deposition values were Du1k-u and Du1.5K-m.

These data suggest the dominant contributing suspension causing factors are station geomorphic features and seasonal variations meteorology. Specifically, mechanisms responsible for emission of particles from “hotspots” as defined by Gillette (1999), are the main reasons for dust suspension in the non-maneuver and maneuver areas (Gillette, 1999).

An increase in the Owen Effect (Gillette, 1997b) will increase the aerodynamic roughness height z_0 of the surface. That is, saltating motions of saltating particles amplify the drag coefficient. This is in essence a feedback mechanism caused by particles in motion which causes particle transport impedance. The Owen Effect can cause threshold friction velocities to be larger for eroding areas than for non-eroding areas. Also, the Owen Effect increases the nonlinear dust flux with a long fetch distance. Specifically, source areas having a long fetch (where the sediment lines up parallel with strong wind direction) and low-threshold friction velocity will yield greater dust fluxes with equal areas having a shorter fetch (Gillette, 1999). Sites Du1.5K-m, Du1K-u, Du3K-u, and Du400m-m had the greatest fetch distances (Table 5; Figures 11, 12, 14, and 16).

It was established that military activity took place within Phases 5-6 (spring-summer, 2009) and 9-10 (spring-summer, 2010). Since Phases 5 (spring, 2009) and 9 (spring 2010) took place during the spring when wind speeds are highest, these Phases (5 and 9) were selected to evaluate horizontally transported sediment mass at 0.2 and 1 m heights as they correspond to fetch length. Fetch lengths were measured as radii obtained from derived circular areas computed from actual measurements done in the field as listed on Table 4. Figures 13 (Phase 5) and 15 (Phase 9) indicate that sediment mass amounts at 0.2 and 1 m heights correlate with site fetch length, that is, sites with greater fetch lengths yielded higher

amounts of sediment. Dune sites had greater fetch lengths than shrubland sites; therefore, dune sites yielded higher sediment amounts. Figures 14 (Phase 5) and 16 (Phase 9) display the highest sediment yielding sites with respect to fetch length. These graphs indicate sediment amounts increase logarithmically beyond the 12 m mark and suggest that 12 m may be a critical fetch length beyond which saltating particle amounts began to maximize. This observation suggests substantiation of the Owen Effect in which the drag coefficient and nonlinear sediment flux increase with wind speed and fetch length.



Figure 11: Du1.5K-m (top) and Du1K-u (bottom) Google Earth images revealing areas with long fetch distances.

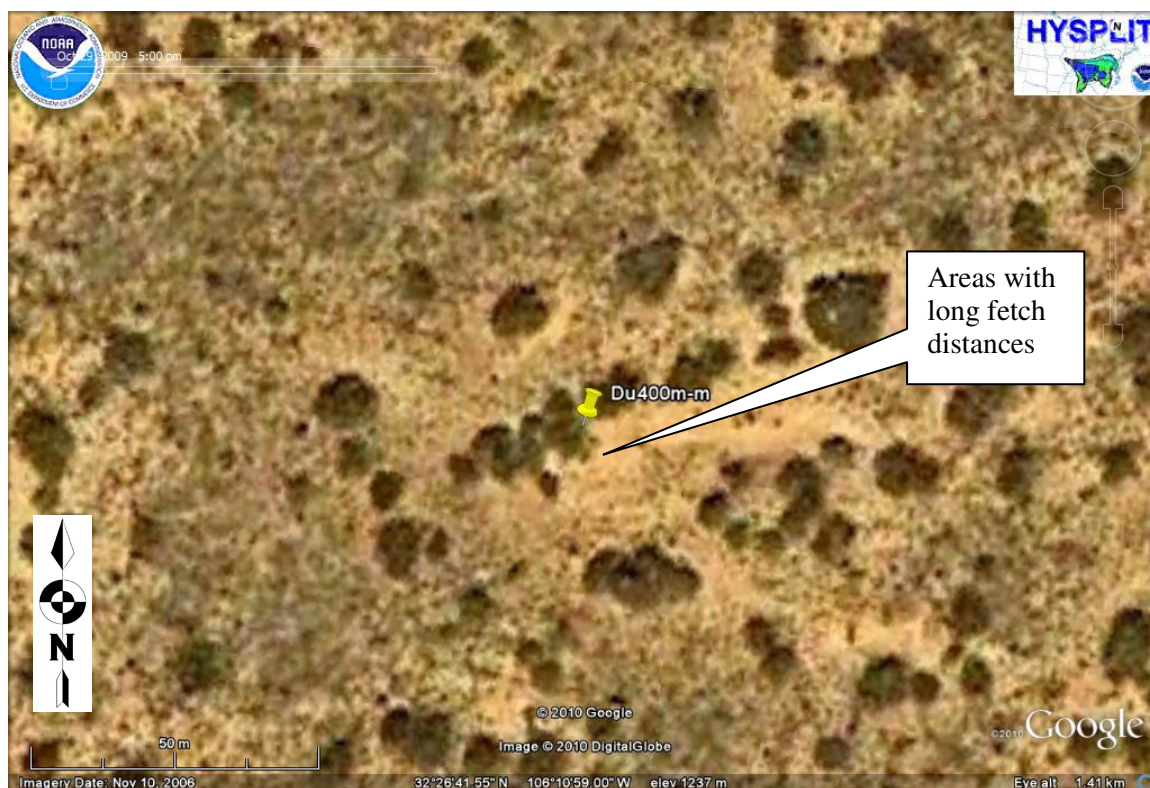


Figure 12: Du3K-u (top) and Du400m-m (bottom) Google Earth images revealing areas with long fetch distances.

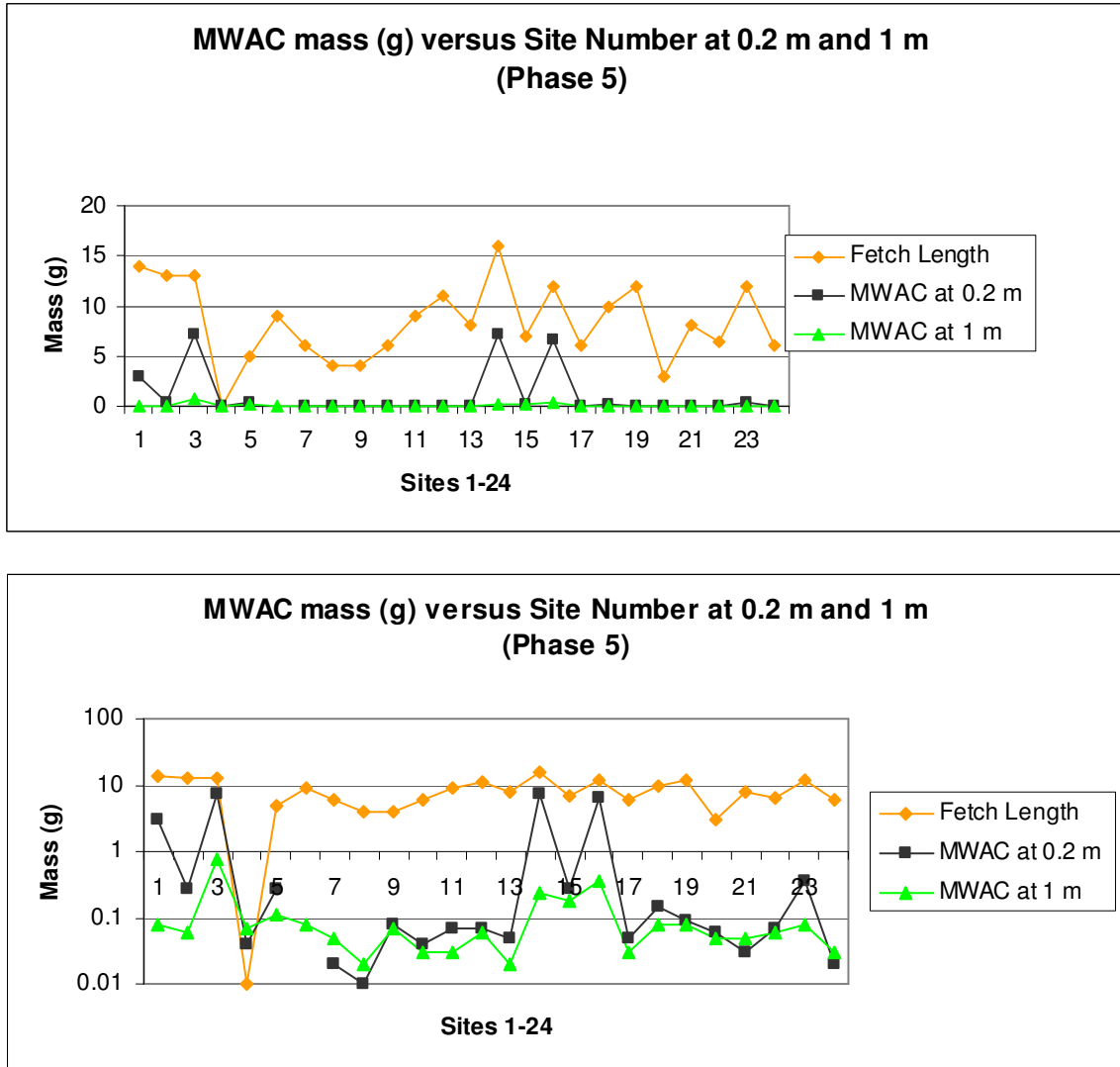


Figure 13: Horizontal mass quantities at 0.2 m and 1 m are shown with corresponding fetch lengths for all sites (i.e., stations) (top graph) for Phase 5. The y-axis is shown with logarithmic scale for clarity (bottom graph). Note: Fetch length magnitudes are shown accurately per site without units or scale.

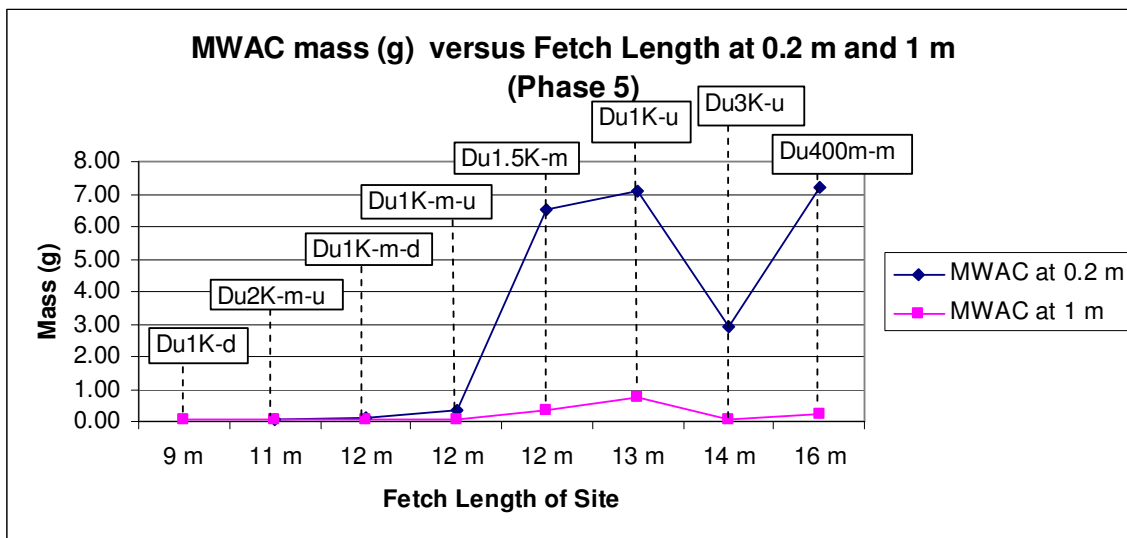


Figure 14: Horizontal mass quantities and corresponding fetch lengths for sites with significant sediment yield for Phase 5.

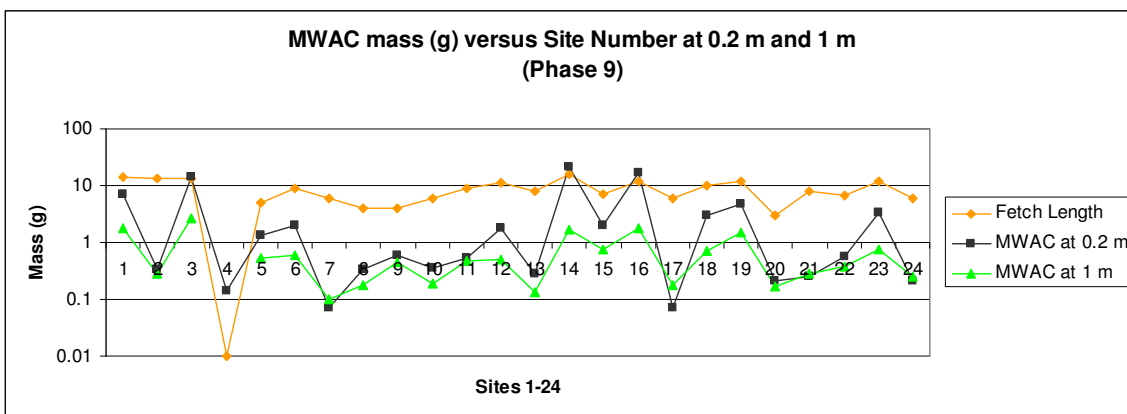
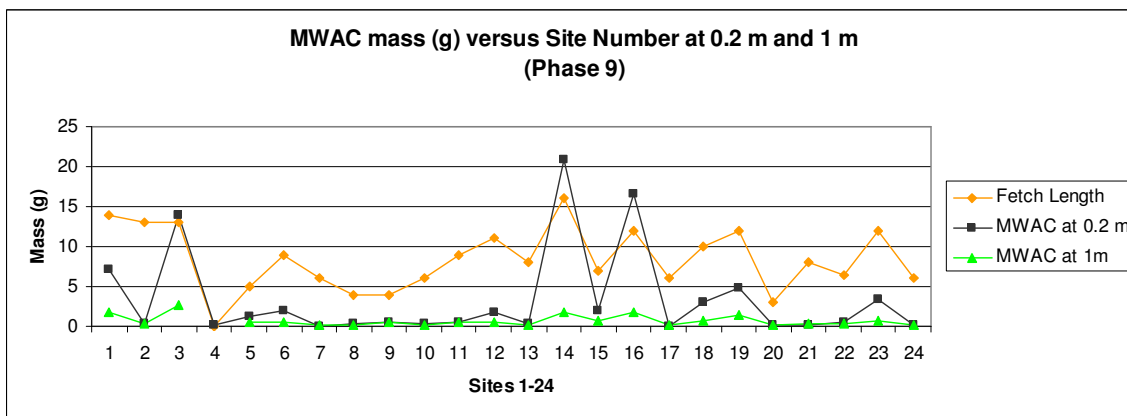


Figure 15: Horizontal mass quantities at 0.2 m and 1 m are shown with corresponding fetch lengths for all sites (i.e., stations) (top graph) for Phase 9. The y-axis is shown with logarithmic scale for clarity (bottom graph). Note: Fetch length magnitudes are shown accurately per site without units or scale.

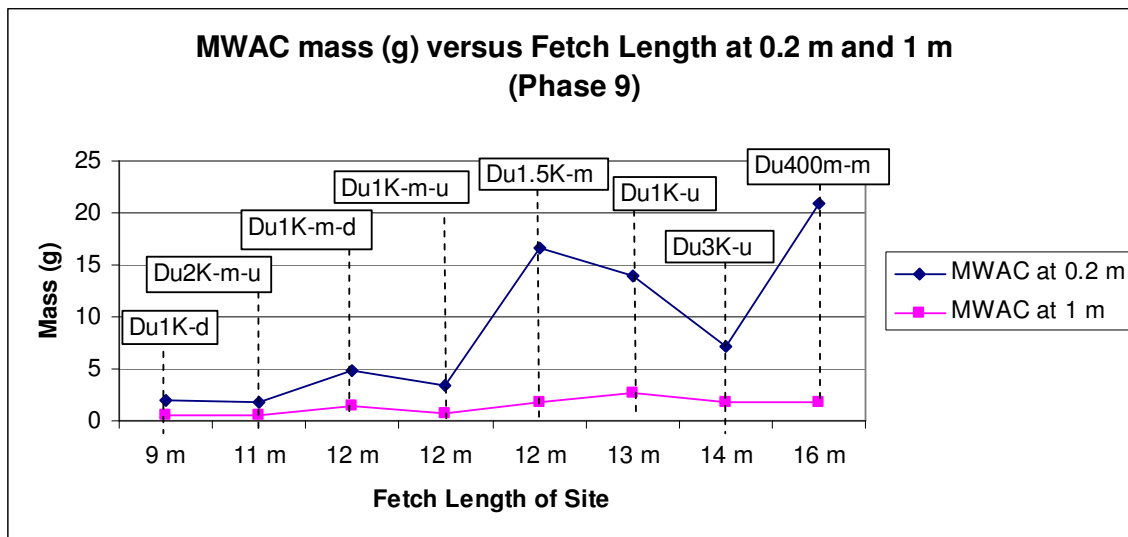


Figure 16: Horizontal mass quantities and corresponding fetch lengths for sites with significant sediment yield for Phase 9.

When wind velocities are greater than the threshold friction velocity, emission of particles will occur. The threshold friction velocity is the critical point at which saltation occurs. The threshold friction velocity will be at its minimum low for wind erosion if particles are $80 \mu\text{m} < d < 120 \mu\text{m}$ (Gillette, 1999).

Even if a site has exposed long fetch areas upwind, sediment particles must be available and unobstructed for transport to occur (Gillette, 1999; Gillette and Chen, 2001) as mentioned above. Crust that has developed over time, trapping by vegetation, or rough surface features can reduce the amount of sediment transport (Gillette and Chen, 2001; Gillette et al., 2006). This is especially true during dry periods coupled with high wind events that scour the desert surface (Gillette and Chen, 2001). However, hard crust can break down with anthropogenic presence (e.g., military activity) (Marston, 1986) and particle saltation impact during high wind events.

As previously mentioned, Du1K-u, Sh1K-d, Du400m-m, and Sh3K-m-u sites and Groups A, B, C, and D were selected for this report on the basis of location with respect to the presence or non-presence of military activity, terrain features, vegetation, and erosive wind mechanisms. Du1K-u and Sh1K-d sites and Groups A and B lie in the non-maneuver area, while Du400m-m and Sh3K-m-u and

Groups C and D lie in the maneuver area. Sites Du1K-u and Du400m-m along with Groups A and C are in high dune density areas with similar mesquite and varied vegetation species (Table 3; Figure 2). Station Sh1K-d and Sh3K-m-u along with Groups B and D are in flatter areas bearing more alluvial material from the Jarilla Mountains and creosote and varied vegetation species. Military maneuvers occurred during the months of April 1 to July 31, 2009 and March through August, 2010, overlapping Phases 5/6 and 9/10 as shown on Table 6. Table 7 displays meteorology data which indicates the strongest winds were from the southwest during spring, while the weaker winds were from the south to southeast during summer. Precipitation was lowest during spring and highest during summer.

MWAC type collectors trap horizontal mass transport of particles under short-term suspension, saltation (which is expected to peak at heights between 0.2 m to 0.3 m) (Fryrear and Saleh, 1993), and modified saltation (heights up to ~1.5 m) (Pye, 1987). Sand size particles can potentially be transported by short-term suspension and/or extreme wind gusts, while fine aeolian particles can potentially be transported by long-term suspension and/or local entrainment/resuspension. Since MWACs collect horizontally transported particles close to the surface, particles can be hindered or trapped from collection within them by surface features such as rocks, vegetation, and irregular terrain. Therefore, distance between the maneuver and non-maneuver areas is more pertinent for MDCO type traps than for MWAC type traps.

MDCO type collectors primarily trap vertically settling particles. However, it is possible for turbulent eddies caused by gust perturbations and severe wind conditions to entrain and transport sand particles into the MDCO at 1.7 m from the surface. Reheis (2006) mentions some drawbacks about the MDCO. Dry dust found in the top layer of marbles can be deflated by turbulence since the MDCO is not aerodynamic and that actual rates of dust accumulation may be 25-40% greater than measured in areas with 'low scrubby vegetation'. From field observations, rain laden with dust can contribute to MDCO deposition and the sample can often be contaminated with organics such as vegetation fragments, insects, and bird waste (Drees and Manu, 1996; Reheis, personal communication, 2008).

Relative to station Du400m-m and Group C in the maneuver area in the south, station Du1K-u and Group A lie approximately 10.7 km northwest ($\sim N355^\circ W$) in the non-maneuver area, while Sh1K-d and Group B lie approximately 7.6 km northeast ($\sim N18^\circ E$) in the non-maneuver area. Relative to station Sh3K-m-u and Group D in the maneuver area in the south, station Du1K-u and Group A lie approximately 11 km northwest ($\sim N333^\circ W$) in the non-maneuver area, while Sh1K-d and Group B lie approximately 6.7 km northwest ($\sim N346^\circ W$) in the non-maneuver area. As mentioned previously, Du400m-m, Du1K-u, Group C, and Group A have similar dune features and vegetation and they differ from Sh3K-m-u, Sh1K-d, Group B, and Group D which share similar shrubland terrain features and vegetation. Between these areas, large saltating particles will be impeded and trapped by surface features such as dunes, furrows, rocks, and vegetation growth. Therefore, for large distances such as those between the maneuver and non-maneuver areas, particles will not be expected to saltate between areas, and MDCOs provide data more relevant to transport. MWACs provide data which is significant with respect to local entrainment, transport, and saltation of particles. It is important to note that along with suspension caused by local natural and anthropogenic erosive mechanisms within WSMR remote upwind sources of dust may result in deposition into the MDCOs. For example, the Chihuahuan Desert southwest (and thus upwind) of WSMR can contribute significant quantities of dust during the windy and dry season (February, March, and April) (Novlan et al., 2007). During the rainy months (July and August), local dust suspension is generally more localized since sediment becomes more cohesive with precipitation and is less likely to transport large distances. The observations in the discussions were made considering dominant wind directions and magnitudes from the southeast to southwest as shown on Table 5.

PM10 (particles with an aerodynamic diameter less than or equal to $10\ \mu m$) percentage contours in the non-maneuver and maneuver areas for Phases 5 (spring, 2009) and 6 (summer, 2009) are displayed in Figures 17 and 18, respectively. PM10 quantity at 1.7 m is of particular interest since PM10 can be inhaled and the 1.7 m height is approximately within the respiratory zone of humans. These

contours indicate that Phase 5 (phase with higher wind speeds and less precipitation) have higher PM10 percentages than Phase 6 (phase with less wind but more precipitation). PM10 percentage contours in the non-maneuver and maneuver areas for Phases 9 (spring, 2010) and 10 (summer, 2010) are displayed in Figures 19 and 20, respectively. These contours indicate that Phase 9 (phase with higher wind speeds and less precipitation) have higher PM10 percentages than Phase 10 (phase with less wind but more precipitation). For Phases 5 and 9, the contours indicate that for the most part, there are higher PM10 concentrations values in the non-maneuvering area. Figure 21 displays topsoil (0 m height) silt percentage contours for the non-maneuver and maneuver areas. These contours indicate that the eastern part of the study area (maneuver and non-maneuver areas) towards the Jarilla Mountains have higher silt concentrations. This suggests vegetation type in the eastern area and alluvial material from the Jarilla Mountains may contribute to higher silt concentrations. Furthermore, this suggests the western part of the study area has coarser particles.

Figure 22 displays MDCO mass and deposition quantities for all sites during Phases 5-6 (top graph) and 9-10 (bottom graph). For Phases 5-6, the graph indicates sediment mass amounts are slightly greater for Phase 6 than for Phase 5. This is more apparent in the maneuver area. However, sites Du1K-u, Du1K-d, and Du1.5K-m show much greater amounts during Phase 5. Particularly, Du1K-u shows a significantly greater amount. With the exception of Du1.5K-m, these anomalies correspond to dune areas in the non-maneuver areas. For Phases 9-10, the graph reveals a similar trend; however, sediment masses for Phases 9 and 10 are roughly equivalent with the exception of sites Du1K-u, Du1K-d, and Du1.5K-m. This may be attributable to the predominant wind alleys (unvegetated lanes parallel to the wind direction with long fetch lengths in which sediment is available for suspension) which lie southwest of these sites. Strong spring winds and the availability of sediment in the fetch areas account for high sediment mass values in the dune areas. Some shrubland areas in the maneuvering area have a greater availability of particles than other shrubland areas and consequently yield higher sediment mass values.

Several previous studies of dust deposition in the Chihuahuan Desert and surrounding areas can provide useful data for comparative purposes to this study. Perez and Gill (2009) conducted mineral aerosol studies at the Salt Flat Basin in west Texas near the Guadalupe Mountains, about 175 km southeast of the WSMR. Dry lakes (playas) are major sources of dust in the Salt Flat Basin. Dust traps of varied designs (including MDCO) were placed 0.5 m, 1.0 m, and 1.5 m above the ground at three sites in the basin. Analysis of the 32 collected MDCO samples indicated seasonal dust flux values ranged from $10 \text{ gm}^{-2}\text{yr}^{-1}$ to $150 \text{ gm}^{-2}\text{yr}^{-1}$ for summer of 2005 and spring 2007, respectively. The overall average for the 32 samples was $50 \text{ gm}^{-2}\text{yr}^{-1}$ for a 1.5 m height. Studies done at Las Cruces, New Mexico (near WSMR) and the Texas Panhandle yielded dust flux values ranging between 7.6 to $28.1 \text{ gm}^{-2}\text{yr}^{-1}$ for Las Cruces (Gile et al., 1981), up to $102 \text{ gm}^{-2}\text{yr}^{-1}$ for Lubbock, Texas (Crabtree, 2005), and 13 to $27 \text{ gm}^{-2}\text{yr}^{-1}$ for the northern Texas Panhandle (Machenberg, 1987), respectively.

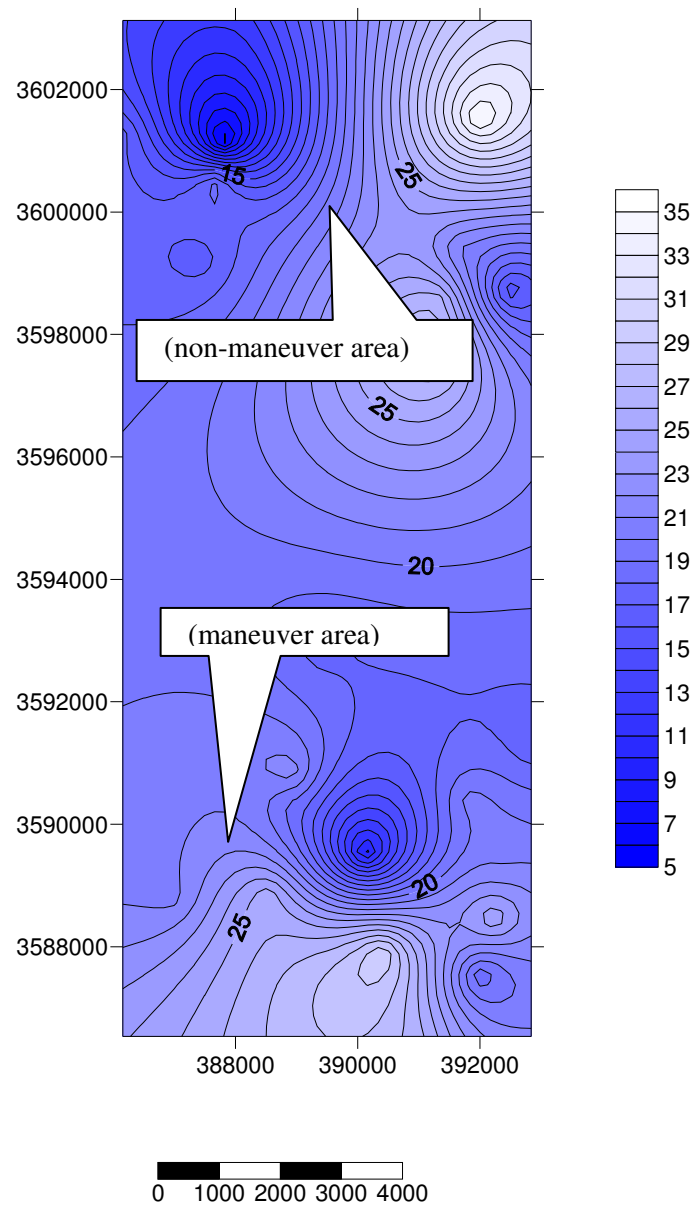


Figure 17: Contours showing the PM10 percentages in the maneuver and non-maneuver areas at 1.7 m for Phase 5. Scale is shown in meters.

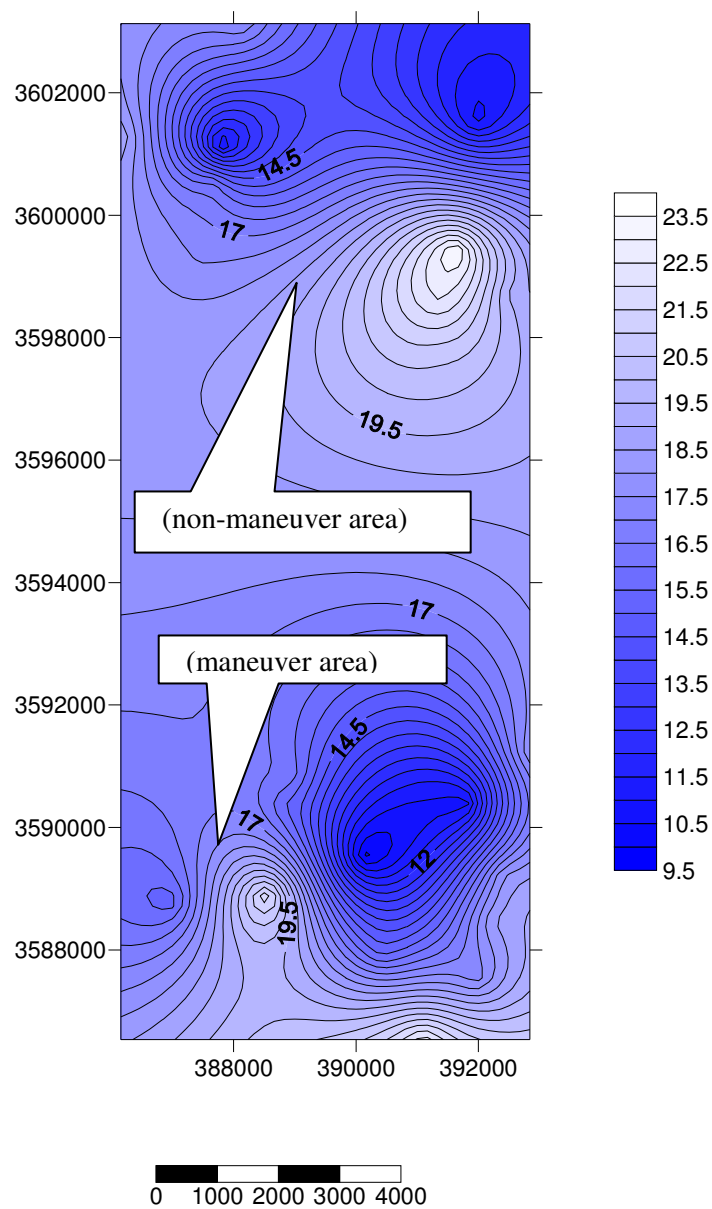


Figure 18: Contours showing the PM10 percentages in the maneuver and non-maneuver areas at 1.7 m for Phase 6. Scale is shown in meters.

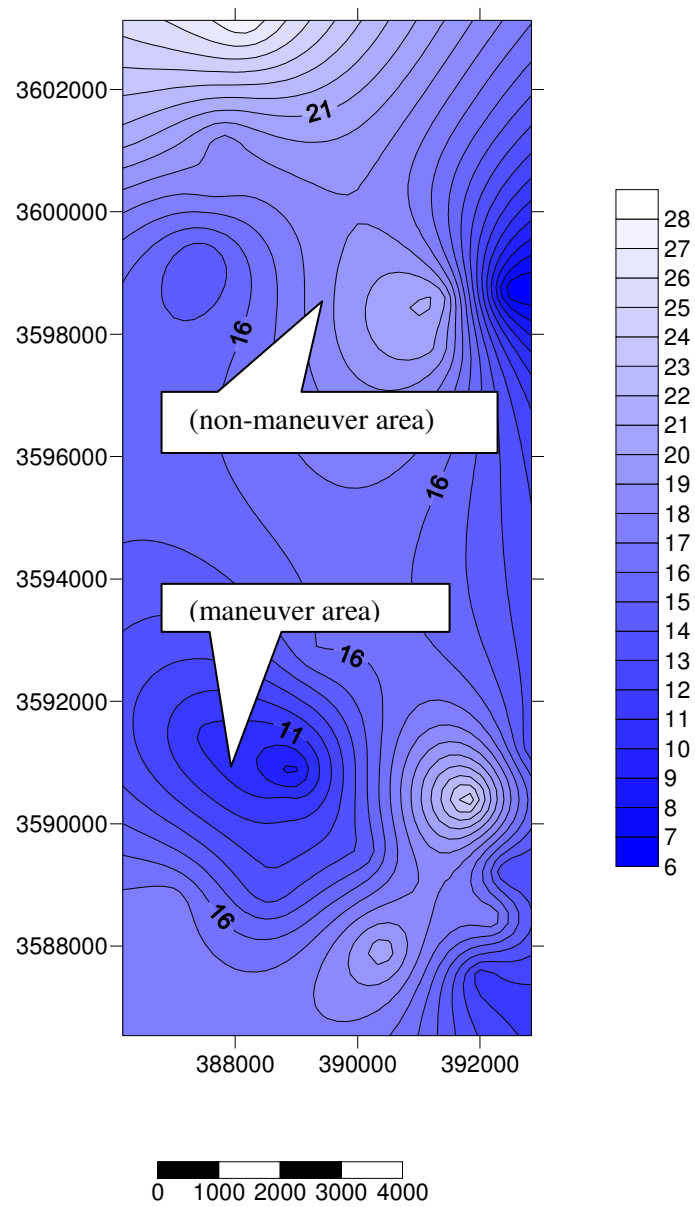


Figure 19: Contours showing the PM10 percentages in the maneuver and non-maneuver areas at 1.7 m for Phase 9. Scale is shown in meters.

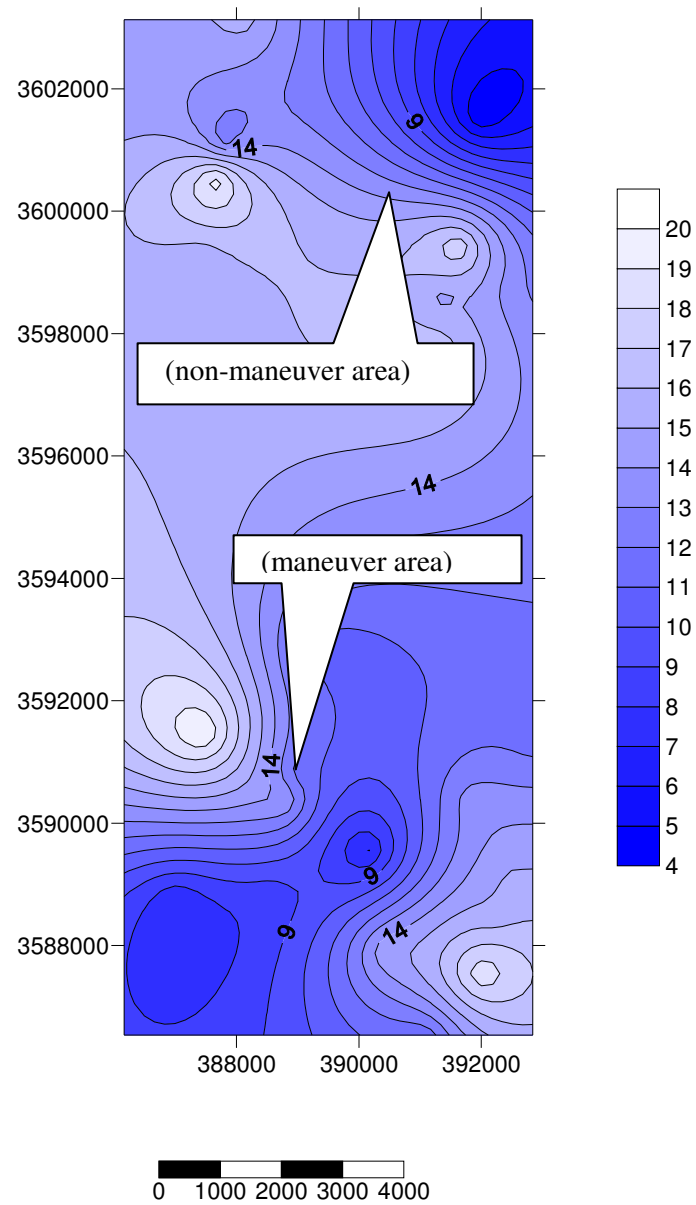


Figure 20: Contours showing the PM10 percentages in the maneuver and non-maneuver areas at 1.7 m for Phase 10. Scale is shown in meters.

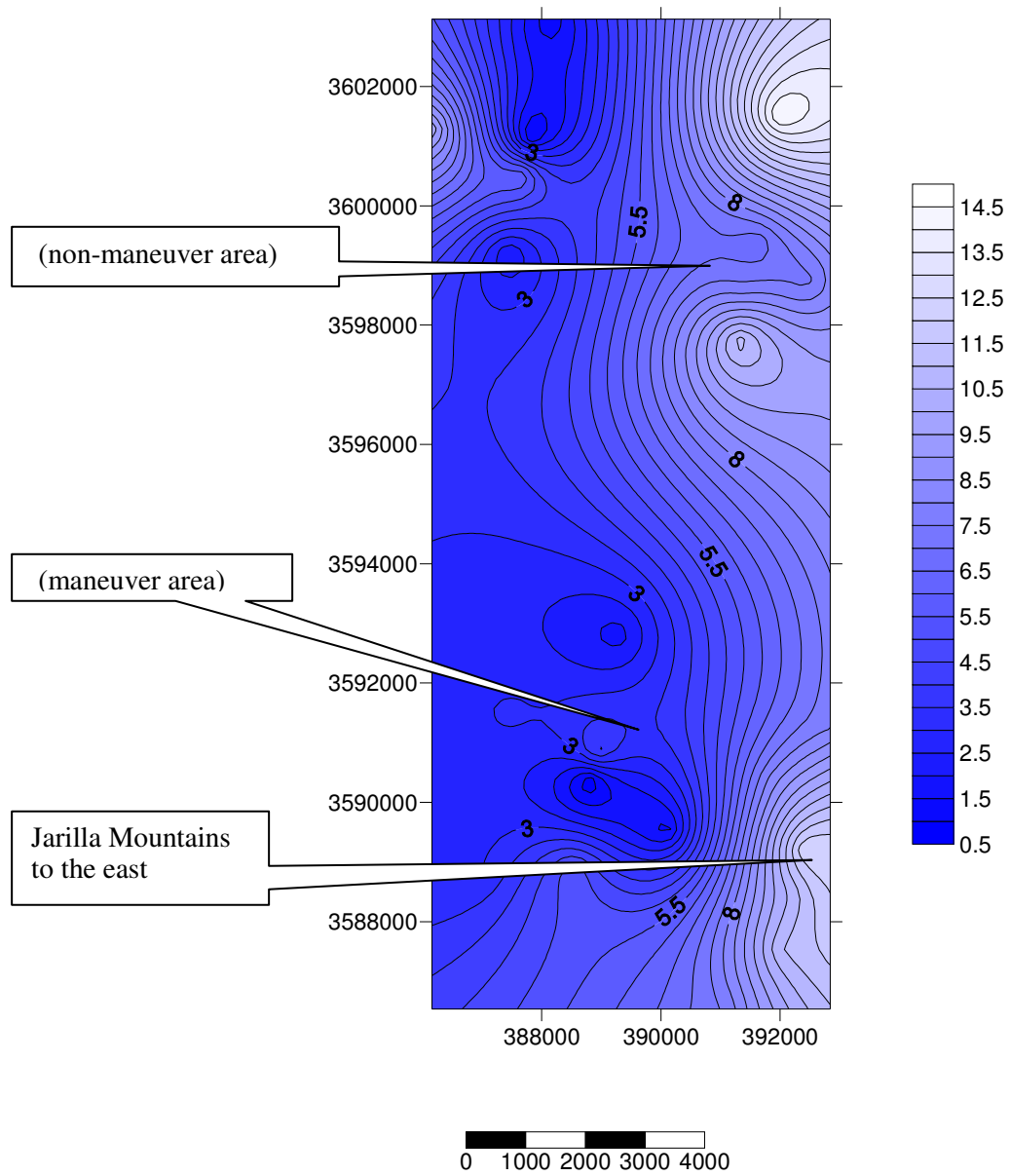


Figure 21: Contours showing topsoil silt percentages in the maneuver and non-maneuver areas at 0 m. Scale is shown in meters.

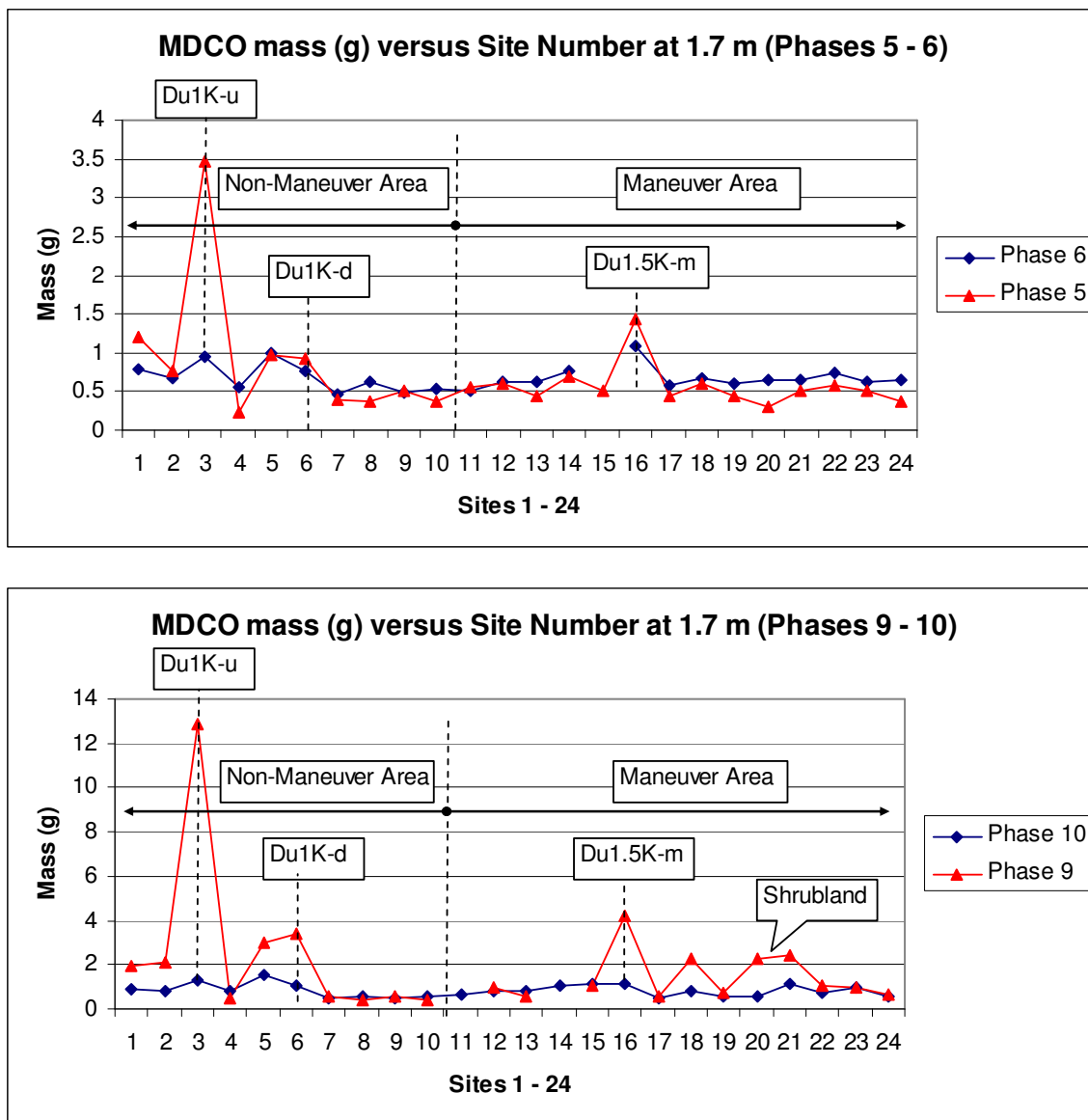


Figure 22: Mass deposition quantities for Phases 5-6 (top graph) and 9-10 (bottom graph) for all sites.

Figures 74-81 display clay, silt, sand, PM_{2.5}, PM₁₀, and PM₁₀₀ volume percentages for MDCOs pertaining to single sites Du1K-u, Sh1K-d, Du400m-m, and Sh3K-m-u in the non-maneuver and maneuver areas for Phases 5 and 6. These bar graphs indicate shrubland areas have more PM₁₀ than dune areas.)

Statistical results for MDCO PM₁₀ mass and volume percentages are displayed on Tables 10 and 11 for Phase 5 and 6, respectively. (An explanation of columns and rows precedes the tables.) There is greater variance between mean PM₁₀ volume percentage values than for mean PM₁₀ mass values (See

columns A – I). Furthermore, differences between confidence levels and standard deviations are greater for mean PM10 volume percentage values than for mean PM10 mass values. It should be noted that it is possible for smaller particles to weigh more than larger particles if their density is greater even though larger particles have a greater volume. Lastly, Phase 5 (phase with higher wind speeds and less precipitation) has greater mean PM10 volume percentages and generally greater mean PM10 mass values than Phase 6 (phase with less wind but more precipitation).

Phase 5 mass and volume percentages of PM10 estimates are displayed as a scattergram and trend line model on Figure 23 (top and middle graph), whereas the Phase 6 scattergram and trend line model are displayed on Figure 23 (bottom graph). The $r^2 = 0.52$ value on Figure 23 (top graph) is attributable to the high mass deposition anomaly (outlier) at station Du1K-u. The Du1K-u outlier is removed on Figure 23 (middle graph) and an $r^2 = 0.77$ value results. This indicates that there is more correlation (more linear relationship) between mass and volume percentages of PM10 in the non-maneuver area for Phase 5 (phase with higher wind speeds and less precipitation) than for Phase 6. Figure 23 (bottom graph) shows there is less correlation (less linear relationship) between mass and volume percentages of PM10 in the non-maneuver and maneuver areas for Phase 6 (phase with less wind but more precipitation). This is indicated by the smaller r^2 values.

Columns:

- A – All sites
- B – All sites in maneuver area
- C – All sites in non-maneuver area
- D – All dune sites
- E – All shrubland sites
- F – All dune sites in the non-maneuver area
- G – All dune sites in the maneuver area
- H – All shrubland sites in the non-maneuver area
- I – All shrubland sites in the maneuver area

Rows:

The PM10 mass = $\Sigma \text{ mass (g)} \times \text{PM10 volume \%} \div 100$ (for selected sites)

The PM10 volume % = $\Sigma \text{ PM10 volume \%}$ (for selected sites)

Mean = Average corresponding to selected sites

Standard Deviation = Variability of the mean corresponding to selected sites

Confidence Interval = $\text{Mean} \pm 1.96 [\text{Standard Deviation} / (\text{Number of Sites})^{1/2}]$

Table 10: MDCO statistical results for varied areas for Phase 5.

Phase 5 MDCO Statistics										
PM10 Mode	Statistical Description	A	B	C	D	E	F	G	H	I
PM10 Mass (g)	Mean	0.11	0.12	0.11	0.13	0.10	0.15	0.12	0.09	0.10
	Standard Deviation	0.03	0.04	0.02	0.02	0.02	0.02	0.01	0.01	0.03
	Significance Level for 95% Confidence Level	0.05	0.05	0.05	0.05	0.05	0.05	0.05	0.05	0.05
	Number of Sites	24	10	14	12	12	5	7	5	7
	Confidence Level \pm	0.01	0.02	0.01	0.01	0.01	0.01	0.01	0.01	0.02
	Confidence Interval	0.11 \pm 0.01	0.12 \pm 0.02	0.11 \pm 0.01	0.13 \pm 0.01	0.10 \pm 0.01	0.15 \pm 0.01	0.12 \pm 0.01	0.09 \pm 0.01	0.10 \pm 0.02
PM10 Volume %	Mean	20.4	19.7	20.9	17.0	23.7	13.9	19.2	25.4	22.6
	Standard Deviation	6.6	8.6	4.9	5.6	5.9	5.3	4.9	7.6	4.6
	Significance Level for 95% Confidence Level	0.05	0.05	0.05	0.05	0.05	0.05	0.05	0.05	0.05
	Number of Sites	24	10	14	12	12	5	7	5	7
	Confidence Level \pm	2.63	5.36	2.57	3.15	3.33	4.68	3.66	6.68	3.40
	Confidence Interval	20.4 \pm 2.63	19.7 \pm 5.36	20.9 \pm 2.57	17.0 \pm 3.15	23.7 \pm 3.33	13.9 \pm 4.68	19.2 \pm 3.66	25.4 \pm 6.68	22.6 \pm 3.40

Table 11: MDCO statistical results for varied areas for Phase 6.

Phase 6 MDCO Statistics										
PM10 Mode	Statistical Description	A	B	C	D	E	F	G	H	I
PM10 Mass	Mean	0.11	0.12	0.11	0.12	0.11	0.13	0.11	0.10	0.12
	Standard Deviation	0.02	0.03	0.02	0.02	0.02	0.02	0.02	0.03	0.02
	Significance Level for 95% Confidence Level	0.05	0.05	0.05	0.05	0.05	0.05	0.05	0.05	0.05
	Number of Sites	24	10	14	12	12	5	7	5	7
	Confidence Level \pm	0.01	0.02	0.01	0.01	0.01	0.02	0.01	0.03	0.01
	Confidence Interval	0.11 \pm 0.01	0.12 \pm 0.02	0.11 \pm 0.01	0.12 \pm 0.01	0.11 \pm 0.01	0.13 \pm 0.02	0.11 \pm 0.01	0.10 \pm 0.03	0.12 \pm 0.01
PM10 Volume %	Mean	17.1	17.8	16.6	16.1	18.1	16.2	16.1	19.4	17.2
	Standard Deviation	3.8	4.3	3.5	3.2	4.2	3.1	3.6	5.1	3.6
	Significance Level for 95% Confidence Level	0.05	0.05	0.05	0.05	0.05	0.05	0.05	0.05	0.05
	Number of Sites	24	10	14	12	12	5	7	5	7
	Confidence Level \pm	1.52	2.67	1.83	1.81	2.38	2.72	2.67	4.47	2.67
	Confidence Interval	17.1 \pm 1.52	17.8 \pm 2.67	16.6 \pm 1.83	16.1 \pm 1.81	18.1 \pm 2.38	16.2 \pm 2.72	16.1 \pm 2.67	19.4 \pm 4.47	17.2 \pm 2.67

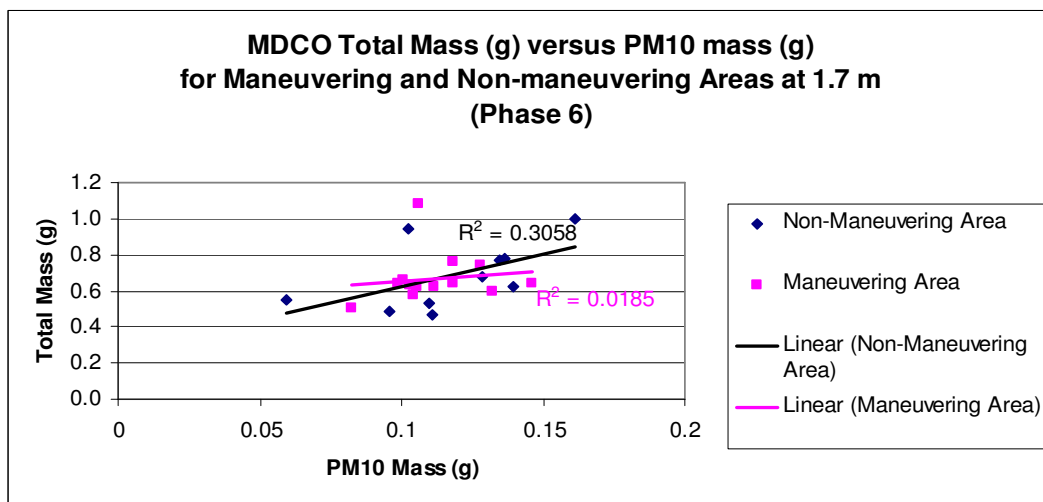
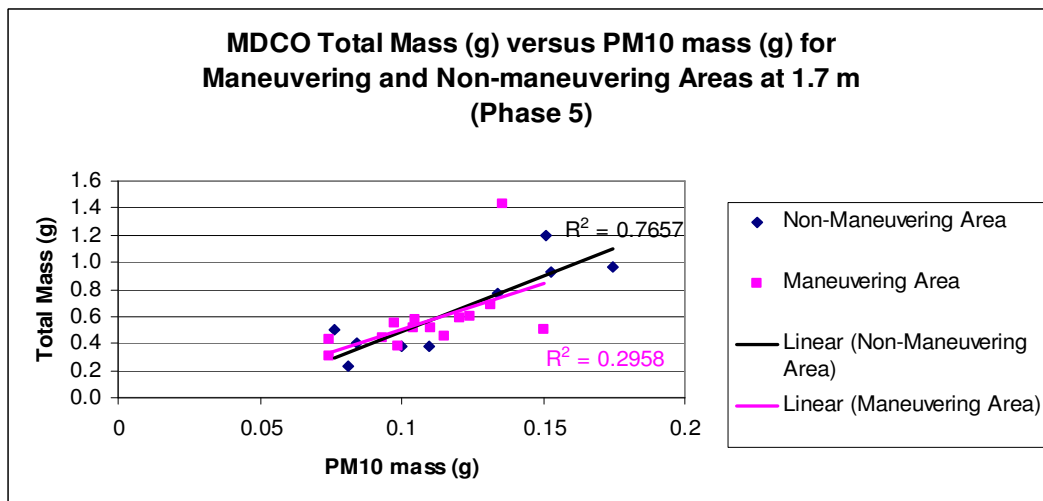
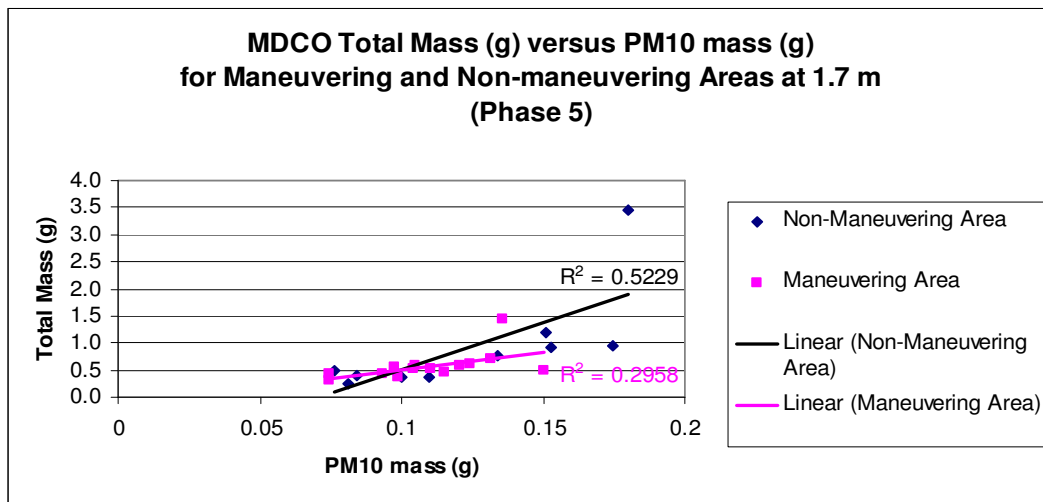


Figure 23: MDCO statistical results for varied areas for Phases 5 (top graph), Phase 5 without the outlier (middle graph), and Phase 6 (bottom graph).

Disturbed sediment on dirt roads can also be a source of dust emissions. According to the AP-42 emissions equation, heavier vehicles with more wheels at higher speeds yield more dust emissions. Attributable to higher silt percentage values, dirt roads in the shrubland areas yielded more dust emissions than dirt roads in dune areas; however, mechanical breakdown of soil can occur over time and subsequently increase dust emissions.

6. Conclusions

Geomorphology (terrain) and seasonal weather factors appeared to be the most significant factors affecting horizontal flux and vertical deposition values. Specifically, dune areas with long fetch areas (i.e., vegetation-free, wind-parallel lanes between coppice dunes) and abundant particle availability yielded the highest horizontal flux and deposition values. The lack of grass cover and sand abundance are significant geomorphic factors contributing to sediment transport. Shrubland sites were installed east of the dune areas and west of the Jarrilla Mountains mostly on alluvial material, which is vastly different from dune type material (mostly sand). Peak sediment transport occurred during spring which is the most dry and windy season. The least sediment transport occurred in summer which is the wettest season. Moisture causes cohesion and crusting soil which subsequently decreases particle suspension. Second to spring, fall and winter yielded the most deposition. Fall is not as windy as spring and not as moist as summer. Winds increase as the winter and spring seasons approach.

There were three types of volume percentage versus particle size graph curves: 1) A dominant symmetrical peak of sand-sized grains with no shoulder or tail. 2) A dominant less symmetrical peak of sand with a tail on the fine (dust) particle side. 3) A dominant peak with shoulders on either side (typically bimodal) with a tail on the fine particle side. The dominant peak and shoulders are typical of coarse (i.e., sand) and fine (i.e., dust = clay and silt) particles.

The horizontal flux U-test results indicate that upwind/downwind sites in the dune areas yielded the highest Z values and irregularities with respect to volume percentages versus particle size. Even though Sh1K-m-d/Sh400m-m upwind U-test results were relatively high when compared to other

shrubland sites, Du1K-u/Sh3K-m-u yielded the highest Z values ($Z=2.14, 0.82$). Station Du1K-u yielded the highest horizontal flux sediment weight values. Sites Du400m-m and Du1.5K-m also yielded high horizontal flux sediment weight values. Similarly, relative to other sites except Du1K-u, Du400m-m, and Du1.5K-m, Du3K-u and Du1K-m-d yielded high horizontal flux sediment weight values. Briefly, Du1K-u, Du1K-d, Du1K-m-u, and Du1K-m-d sites had the greatest effect on the U-test results. These sites were upwind or downwind of the pivot station which was installed near a possible dust emitting source (e.g., dirt road).

A mock village was constructed in spring (during Phase 9) near sites Sh400m and Sh1K-d. For these two sites, Z result values were higher for Phase 9 (spring season) than for Phase 5 (spring season). This may be attributable the construction of the mock village. The Z value increase between Phase 7 and 10 for sites Sh3K-m-u and Sh1K-d may be attributable to heavy rainfall MDCO overflow and organic matter contamination (e.g., insect remains, bird waste, and vegetation fragments). Sites Du1k-u and Du1.5K-m had the highest MDCO deposition values.

The AP-42 equation results indicate there is more dust emission from dirt roads in shrubland areas than from dirt roads in dune areas. The shrubland areas have a higher silt percentage the dune areas; therefore, dirt roads in shrubland areas yield more dust emissions.

These studies helped quantify dust suspension and map deposition patterns caused by natural aeolian processes, vehicle movement on unpaved roads, and military maneuvers. These studies will also add to the knowledge of how different land cover types absorb or impede aeolian sediment transport. Ultimately, these studies will help Department of Defense officials better manage military installations in desert environments. This type of study can also provide useful PM data to atmospheric scientists and health officials.

Tables

Table 12: MDCO Sediment Mass and deposition quantities in the non-maneuvering and maneuvering areas for Phases 1-10. NA¹ (not available) – MDCO Sediment Mass quantities for these stations had to be nullified due to laboratory weighing uncertainties or termite contamination.

MDCO Sediment Mass and Deposition Quantities for Phase 1					
Area	Station No.	Station ID	Sample Weight	Mass per Area	Deposition
	Number	ID	mass (g)	g/m ²	g/m ² /yr
Non-maneuvering	1	Du3K-u	1.3	28.4	167.0
	2	Du2K	0.9	19.6	115.6
	3	Du1K-u	3.2	69.9	411.0
	4	Sh3K-u	0.5	10.9	64.2
	5	Du400m	NA ¹	NA ¹	NA ¹
	6	Du1K-d	NA ¹	NA ¹	NA ¹
	7	Sh1K-u	0.3	6.5	38.5
	8	Sh400m	0.7	15.3	89.9
	9	Sh1.5K	0.4	8.7	51.4
	10	Sh1K-d	0.4	8.7	51.4
Maneuvering	11	Du3K-m-u	0.5	10.9	64.2
	12	Du2K-m-u	NA ¹	NA ¹	NA ¹
	13	Sh3K-m-u	NA ¹	NA ¹	NA ¹
	14	Du400m-m	0.3	6.5	38.5
	15	Sh2K-m-u	NA ¹	NA ¹	NA ¹
	16	Du1.5K-m	NA ¹	NA ¹	NA ¹
	17	Sh1K-m-u	NA ¹	NA ¹	NA ¹
	18	Du2K-m-d	0.4	8.7	51.4
	19	Du1K-m-d	NA ¹	NA ¹	NA ¹
	20	Sh400m-m	NA ¹	NA ¹	NA ¹
	21	Sh1.5K-m	NA ¹	NA ¹	NA ¹
	22	Sh1K-m-d	NA ¹	NA ¹	NA ¹
	23	Du1K-m-u	NA ¹	NA ¹	NA ¹
	24	Sh2K-m-d	NA ¹	NA ¹	NA ¹

Table 12 cont'd

MDCO Sediment Mass and Deposition Quantities for Phase 2					
Area	Station No.	Station ID	Sample Weight	Mass per Area	Deposition
	Number	ID	mass (g)	g/m ²	g/m ² /yr
Non-maneuvering	1	Du3K-u	0.6	13.1	77.1
	2	Du2K	0.4	8.7	51.4
	3	Du1K-u	0.4	8.7	51.4
	4	Sh3K-u	0.6	13.1	77.1
	5	Du400m	0.5	10.9	64.2
	6	Du1K-d	0.4	8.7	51.4
	7	Sh1K-u	0.3	6.5	38.5
	8	Sh400m	0.4	8.7	51.4
	9	Sh1.5K	0.1	2.2	12.8
	10	Sh1K-d	0.1	2.2	12.8
Maneuvering	11	Du3K-m-u	0.3	6.5	38.5
	12	Du2K-m-u	0.3	6.5	38.5
	13	Sh3K-m-u	0.2	4.4	25.7
	14	Du400m-m	0.6	13.1	77.1
	15	Sh2K-m-u	0.2	4.4	25.7
	16	Du1.5K-m	0.4	8.7	51.4
	17	Sh1K-m-u	0.1	2.2	12.8
	18	Du2K-m-d	0.3	6.5	38.5
	19	Du1K-m-d	0.4	8.7	51.4
	20	Sh400m-m	0.2	4.4	25.7
	21	Sh1.5K-m	0.9	19.6	115.6
	22	Sh1K-m-d	0.4	8.7	51.4
	23	Du1K-m-u	0.3	6.5	38.5
	24	Sh2K-m-d	0.3	6.5	38.5

Table 12 cont'd

MDCO Sediment Mass and Deposition Quantities for Phase 3					
Area	Station No.	Station ID	Sample Weight	Mass per Area	Deposition
	Number	ID	mass (g)	g/m ²	g/m ² /yr
Non-maneuvering	1	Du3K-u	0.9	19.6	61.4
	2	Du2K	1.2	26.2	81.9
	3	Du1K-u	1	21.8	68.2
	4	Sh3K-u	1.3	28.4	88.7
	5	Du400m	0.5	10.9	34.1
	6	Du1K-d	0.5	10.9	34.1
	7	Sh1K-u	0.3	6.5	20.5
	8	Sh400m	0.2	4.4	13.6
	9	Sh1.5K	0.3	6.5	20.5
	10	Sh1K-d	0.2	4.4	13.6
Maneuvering	11	Du3K-m-u	0.3	6.5	20.5
	12	Du2K-m-u	0.3	6.5	20.5
	13	Sh3K-m-u	0.2	4.4	13.6
	14	Du400m-m	0.7	15.3	47.8
	15	Sh2K-m-u	0.4	8.7	27.3
	16	Du1.5K-m	0.7	15.3	47.8
	17	Sh1K-m-u	0.2	4.4	13.6
	18	Du2K-m-d	0.3	6.5	20.5
	19	Du1K-m-d	0.2	4.4	13.6
	20	Sh400m-m	0.1	2.2	6.8
	21	Sh1.5K-m	0.3	6.5	20.5
	22	Sh1K-m-d	1	21.8	68.2
	23	Du1K-m-u	0.3	6.5	20.5
	24	Sh2K-m-d	0.4	8.7	27.3

Table 12 cont'd

MDCO Sediment Mass and Deposition Quantities for Phase 4					
Area	Station No.	Station ID	Sample Weight	Mass per Area	Deposition
	Number	ID	mass (g)	g/m ²	g/m ² /yr
Non-maneuvering	1	Du3K-u	0.7	15.3	80.4
	2	Du2K	0.7	15.3	80.4
	3	Du1K-u	1.7	37.1	195.4
	4	Sh3K-u	0.2	4.4	23.0
	5	Du400m	0.3	6.5	34.5
	6	Du1K-d	0.2	4.4	23.0
	7	Sh1K-u	0.2	4.4	23.0
	8	Sh400m	0.1	2.2	11.5
	9	Sh1.5K	0.2	4.4	23.0
	10	Sh1K-d	0.2	4.4	23.0
Maneuvering	11	Du3K-m-u	0.2	4.4	23.0
	12	Du2K-m-u	0.1	2.2	11.5
	13	Sh3K-m-u	0.2	4.4	23.0
	14	Du400m-m	0.2	4.4	23.0
	15	Sh2K-m-u	0.3	6.5	34.5
	16	Du1.5K-m	0.9	19.6	103.4
	17	Sh1K-m-u	0.5	10.9	57.5
	18	Du2K-m-d	0.1	2.2	11.5
	19	Du1K-m-d	0.2	4.4	23.0
	20	Sh400m-m	0.2	4.4	23.0
	21	Sh1.5K-m	0.1	2.2	11.5
	22	Sh1K-m-d	0.3	6.5	34.5
	23	Du1K-m-u	0.2	4.4	23.0
	24	Sh2K-m-d	0.2	4.4	23.0

Table 12 cont'd

MDCO Sediment Mass and Deposition Quantities for Phase 5					
Area	Station No.	Station ID	Sample Weight	Mass per Area	Deposition
	Number	ID	mass (g)	g/m ²	g/m ² /yr
Non-maneuvering	1	Du3K-u	1.2	26.2	104.8
	2	Du2K	0.77	16.8	67.2
	3	Du1K-u	3.46	75.5	302.2
	4	Sh3K-u	0.23	5.0	20.1
	5	Du400m	0.96	21.0	83.8
	6	Du1K-d	0.93	20.3	81.2
	7	Sh1K-u	0.4	8.7	34.9
	8	Sh400m	0.38	8.3	33.2
	9	Sh1.5K	0.5	10.9	43.7
	10	Sh1K-d	0.38	8.3	33.2
Maneuvering	11	Du3K-m-u	0.55	12.0	48.0
	12	Du2K-m-u	0.59	12.9	51.5
	13	Sh3K-m-u	0.43	9.4	37.6
	14	Du400m-m	0.69	15.1	60.3
	15	Sh2K-m-u	0.51	11.1	44.5
	16	Du1.5K-m	1.43	31.2	124.9
	17	Sh1K-m-u	0.44	9.6	38.4
	18	Du2K-m-d	0.6	13.1	52.4
	19	Du1K-m-d	0.45	9.8	39.3
	20	Sh400m-m	0.3	6.5	26.2
	21	Sh1.5K-m	0.5	10.9	43.7
	22	Sh1K-m-d	0.58	12.7	50.7
	23	Du1K-m-u	0.51	11.1	44.5
	24	Sh2K-m-d	0.38	8.3	33.2

Table 12 cont'd

MDCO Sediment Mass and Deposition Quantities for Phase 6					
Area	Station No.	Station ID	Sample Weight	Mass per Area	Deposition
	Number	ID	mass (g)	g/m ²	g/m ² /yr
Non-maneuvering	1	Du3K-u	0.78	17.0	74.0
	2	Du2K	0.68	14.8	64.6
	3	Du1K-u	0.94	20.5	89.2
	4	Sh3K-u	0.55	12.0	52.2
	5	Du400m	1	21.8	94.9
	6	Du1K-d	0.77	16.8	73.1
	7	Sh1K-u	0.47	10.3	44.6
	8	Sh400m	0.62	13.5	58.9
	9	Sh1.5K	0.49	10.7	46.5
	10	Sh1K-d	0.53	11.6	50.3
Maneuvering	11	Du3K-m-u	0.5	10.9	47.5
	12	Du2K-m-u	0.62	13.5	58.9
	13	Sh3K-m-u	0.62	13.5	58.9
	14	Du400m-m	0.76	16.6	72.1
	15	Sh2K-m-u	NA ¹	NA ¹	NA ¹
	16	Du1.5K-m	1.08	23.6	102.5
	17	Sh1K-m-u	0.58	12.7	55.1
	18	Du2K-m-d	0.66	14.4	62.7
	19	Du1K-m-d	0.6	13.1	57.0
	20	Sh400m-m	0.64	14.0	60.8
	21	Sh1.5K-m	0.64	14.0	60.8
	22	Sh1K-m-d	0.74	16.2	70.2
	23	Du1K-m-u	0.63	13.8	59.8
	24	Sh2K-m-d	0.64	14.0	60.8

Table 12 cont'd

MDCO Sediment Mass and Deposition Quantities for Phase 7					
Area	Station No.	Station ID	Sample Weight	Mass per Area	Deposition
	Number	ID	mass (g)	g/m ²	g/m ² /yr
Non-maneuvering	1	Du3K-u	0.64	14.0	36.8
	2	Du2K	0.52	11.4	29.9
	3	Du1K-u	2.49	54.4	143.1
	4	Sh3K-u	1.13	24.7	64.9
	5	Du400m	0.78	17.0	44.8
	6	Du1K-d	0.87	19.0	50.0
	7	Sh1K-u	0.40	8.7	23.0
	8	Sh400m	0.40	8.7	23.0
	9	Sh1.5K	0.41	9.0	23.6
	10	Sh1K-d	0.44	9.6	25.3
Maneuvering	11	Du3K-m-u	0.43	9.4	24.7
	12	Du2K-m-u	0.72	15.7	41.4
	13	Sh3K-m-u	0.76	16.6	43.7
	14	Du400m-m	0.85	18.6	48.8
	15	Sh2K-m-u	1.32	28.8	75.8
	16	Du1.5K-m	2.28	49.8	131.0
	17	Sh1K-m-u	0.59	12.9	33.9
	18	Du2K-m-d	1.02	22.3	58.6
	19	Du1K-m-d	1.12	24.5	64.4
	20	Sh400m-m	0.58	12.7	33.3
	21	Sh1.5K-m	0.72	15.7	41.4
	22	Sh1K-m-d	0.96	21.0	55.2
	23	Du1K-m-u	0.59	12.9	33.9
	24	Sh2K-m-d	0.75	16.4	43.1

Table 12 cont'd

MDCO Sediment Mass and Deposition Quantities for Phase 8					
Area	Station No.	Station ID	Sample Weight	Mass per Area	Deposition
	Number	ID	mass (g)	g/m ²	g/m ² /yr
Non-maneuvering	1	Du3K-u	0.37	8.1	53.9
	2	Du2K	0.30	6.5	43.7
	3	Du1K-u	1.66	36.2	241.6
	4	Sh3K-u	0.14	3.1	20.4
	5	Du400m	0.37	8.1	53.9
	6	Du1K-d	0.50	10.9	72.8
	7	Sh1K-u	0.16	3.5	23.3
	8	Sh400m	0.18	3.9	26.2
	9	Sh1.5K	0.22	4.8	32.0
	10	Sh1K-d	0.15	3.3	21.8
Maneuvering	11	Du3K-m-u	0.29	6.3	42.2
	12	Du2K-m-u	0.52	11.4	75.7
	13	Sh3K-m-u	0.29	6.3	42.2
	14	Du400m-m	0.52	11.4	75.7
	15	Sh2K-m-u	1.02	22.3	148.5
	16	Du1.5K-m	1.30	28.4	189.2
	17	Sh1K-m-u	0.25	5.5	36.4
	18	Du2K-m-d	0.43	9.4	62.6
	19	Du1K-m-d	0.37	8.1	53.9
	20	Sh400m-m	0.32	7.0	46.6
	21	Sh1.5K-m	0.30	6.5	43.7
	22	Sh1K-m-d	0.35	7.6	50.9
	23	Du1K-m-u	0.53	11.6	77.1
	24	Sh2K-m-d	0.37	8.1	53.9

Table 12 cont'd

MDCO Sediment Mass and Deposition Quantities for Phase 9					
Area	Station No.	Station ID	Sample Weight	Mass per Area	Deposition
	Number	ID	mass (g)	g/m ²	g/m ² /yr
Non-maneuvering	1	Du3K-u	1.98	43.2	180.1
	2	Du2K	2.11	46.1	192.0
	3	Du1K-u	12.89	281.4	1172.6
	4	Sh3K-u	0.50	10.9	45.5
	5	Du400m	2.99	65.3	272.0
	6	Du1K-d	3.43	74.9	312.0
	7	Sh1K-u	0.56	12.2	50.9
	8	Sh400m	0.40	8.7	36.4
	9	Sh1.5K	0.58	12.7	52.8
	10	Sh1K-d	0.37	8.1	33.7
Maneuvering	11	Du3K-m-u	NA ¹	NA ¹	NA ¹
	12	Du2K-m-u	0.95	20.7	86.4
	13	Sh3K-m-u	0.59	12.9	53.7
	14	Du400m-m	NA ¹	NA ¹	NA ¹
	15	Sh2K-m-u	1.05	22.9	95.5
	16	Du1.5K-m	4.20	91.7	382.1
	17	Sh1K-m-u	0.56	12.2	50.9
	18	Du2K-m-d	2.25	49.1	204.7
	19	Du1K-m-d	0.75	16.4	68.2
	20	Sh400m-m	2.29	50.0	208.3
	21	Sh1.5K-m	2.40	52.4	218.3
	22	Sh1K-m-d	1.03	22.5	93.7
	23	Du1K-m-u	0.95	20.7	86.4
	24	Sh2K-m-d	0.66	14.4	60.0

Table 12 cont'd

MDCO Sediment Mass and Deposition Quantities for Phase 10					
Area	Station No.	Station ID	Sample Weight	Mass per Area	Deposition
	Number	ID	mass (g)	g/m ²	g/m ² /yr
Non-maneuvering	1	Du3K-u	0.87	19.0	73.1
	2	Du2K	0.80	17.5	67.2
	3	Du1K-u	1.26	27.5	105.8
	4	Sh3K-u	0.83	18.1	69.7
	5	Du400m	1.50	32.7	126.0
	6	Du1K-d	1.09	23.8	91.5
	7	Sh1K-u	0.51	11.1	42.8
	8	Sh400m	0.59	12.9	49.5
	9	Sh1.5K	0.51	11.1	42.8
	10	Sh1K-d	0.57	12.4	47.9
Maneuvering	11	Du3K-m-u	0.68	14.8	57.1
	12	Du2K-m-u	0.82	17.9	68.9
	13	Sh3K-m-u	0.77	16.8	64.7
	14	Du400m-m	1.08	23.6	90.7
	15	Sh2K-m-u	1.10	24.0	92.4
	16	Du1.5K-m	1.10	24.0	92.4
	17	Sh1K-m-u	0.49	10.7	41.1
	18	Du2K-m-d	0.82	17.9	68.9
	19	Du1K-m-d	0.58	12.7	48.7
	20	Sh400m-m	0.54	11.8	45.3
	21	Sh1.5K-m	1.14	24.9	95.7
	22	Sh1K-m-d	0.74	16.2	62.1
	23	Du1K-m-u	0.97	21.2	81.5
	24	Sh2K-m-d	0.55	12.0	46.2

Table 13: Deposition mean and standard deviation values for various specific conditions.

Mean, Standard Deviation, and Confidence Intervals for Deposition Values (g/m²/yr)			
Condition	Mean	Standard Deviation	Confidence Interval (±)
Overall (all phases and stations)	68.7	93.7	-
Maneuver Area (all phases)	58.7	47.4	-
Non-Maneuver Area (all phases)	80.8	128.5	-
Dune (all phases)	90.8	124.9	-
Shrubland (all phases)	46.6	32.5	-
Spring 2008 (Phase 1)	103.9	108.9	64.4
Summer 2008 (Phase 2)	46.6	23.9	9.6
Fall 2008 (Phase 3)	33.6	23.7	9.5
Winter 2008/2009 (Phase 4)	39.3	40.9	16.4
Spring 2009 (Phase 5)	62.5	56.8	22.7
Summer 2009 (Phase 6)	64.1	14.9	6.1
Fall 2009 (Phase 7)	49.7	30.6	12.2
Winter 2009/2010 (Phase 8)	66.2	53.6	21.4
Spring 2010 (Phase 9)	179.8	243.0	101.5
Summer 2010 (Phase 10)	69.7	23.1	9.2

Table 14: MWAC and BSNE horizontal flux quantities at 0.2 m and 1 m heights for Phases 5-10. NA¹ (not available) - MWAC missing, displaced, or damaged by animals in the field.

MWAC Horizontal Flux Quantities at 0.2 m for Phase 5					
Area	Station No.	Station ID	Sample Weight	Horizontal Flux	Total Horizontal Flux
	Number	ID	mass (g)	g/m ²	g/m/yr
Non-maneuvering	1	Du3K-u	2.91	45742.3	50824.8
	2	Du2K	0.28	4401.3	4890.4
	3	Du1K-u	7.11	111762.1	124180.2
	4	Sh3K-u	0.04	628.8	698.6
	5	Du400m	0.28	4401.3	4890.4
	6	Du1K-d	NA ¹	NA ¹	NA ¹
	7	Sh1K-u	0.02	314.4	349.3
	8	Sh400m	0.01	157.2	174.7
	9	Sh1.5K	0.08	1257.5	1397.2
	10	Sh1K-d	0.04	628.8	698.6
Maneuvering	11	Du3K-m-u	0.07	1100.3	1222.6
	12	Du2K-m-u	0.07	1100.3	1222.6
	13	Sh3K-m-u	0.05	786.0	873.3
	14	Du400m-m	7.22	113491.2	126101.4
	15	Sh2K-m-u	0.27	4244.1	4715.7
	16	Du1.5K-m	6.52	102487.9	113875.5
	17	Sh1K-m-u	0.05	786.0	873.3
	18	Du2K-m-d	0.15	2357.9	2619.8
	19	Du1K-m-d	0.09	1414.7	1571.9
	20	Sh400m-m	0.06	943.1	1047.9
	21	Sh1.5K-m	0.03	471.6	524.0
	22	Sh1K-m-d	0.07	1100.3	1222.6
	23	Du1K-m-u	0.35	5501.7	6112.9
	24	Sh2K-m-d	0.02	314.4	349.3

Table 14 cont'd

MWAC Horizontal Flux Quantities at 1 m for Phase 5					
Area	Station No.	Station ID	Sample Weight	Horizontal Flux	Total Horizontal Flux
	Number	ID	mass (g)	g/m ²	g/m/yr
Non-maneuvering	1	Du3K-u	0.08	1257.5	6986.2
	2	Du2K	0.06	943.1	5239.7
	3	Du1K-u	0.76	11946.4	66369.1
	4	Sh3K-u	0.07	1100.3	6112.9
	5	Du400m	0.11	1729.1	9606.1
	6	Du1K-d	0.08	1257.5	6986.2
	7	Sh1K-u	0.05	786.0	4366.4
	8	Sh400m	0.02	314.4	1746.6
	9	Sh1.5K	0.07	1100.3	6112.9
	10	Sh1K-d	0.03	471.6	2619.8
Maneuvering	11	Du3K-m-u	0.03	471.6	2619.8
	12	Du2K-m-u	0.06	943.1	5239.7
	13	Sh3K-m-u	0.02	314.4	1746.6
	14	Du400m-m	0.24	3772.6	20958.7
	15	Sh2K-m-u	0.18	2829.4	15719.0
	16	Du1.5K-m	0.36	5658.8	31438.0
	17	Sh1K-m-u	0.03	471.6	2619.8
	18	Du2K-m-d	0.08	1257.5	6986.2
	19	Du1K-m-d	0.08	1257.5	6986.2
	20	Sh400m-m	0.05	786.0	4366.4
	21	Sh1.5K-m	0.05	786.0	4366.4
	22	Sh1K-m-d	0.06	943.1	5239.7
	23	Du1K-m-u	0.08	1257.5	6986.2
	24	Sh2K-m-d	0.03	471.6	2619.8

Table 14 cont'd

MWAC Horizontal Flux Quantities at 0.2 m for Phase 6					
Area	Station No.	Station ID	Sample Weight	Horizontal Flux	Total Horizontal Flux
	Number	ID	mass (g)	g/m^2	g/m/yr
Non-maneuvering	1	Du3K-u	0.79	12418.0	10798.3
	2	Du2K	0.11	1729.1	1503.6
	3	Du1K-u	0.73	11474.9	9978.2
	4	Sh3K-u	0.01	157.2	136.7
	5	Du400m	0.21	3301.0	2870.4
	6	Du1K-d	0.1	1571.9	1366.9
	7	Sh1K-u	0.03	471.6	410.1
	8	Sh400m	0.4	6287.6	5467.5
	9	Sh1.5K	0.06	943.1	820.1
	10	Sh1K-d	0.04	628.8	546.7
Maneuvering	11	Du3K-m-u	0.11	1729.1	1503.6
	12	Du2K-m-u	0.1	1571.9	1366.9
	13	Sh3K-m-u	NA ¹	NA ¹	NA ¹
	14	Du400m-m	1.02	16033.4	13942.1
	15	Sh2K-m-u	0.17	2672.2	2323.7
	16	Du1.5K-m	1.42	22321.0	19409.6
	17	Sh1K-m-u	0.04	628.8	546.7
	18	Du2K-m-d	0.24	3772.6	3280.5
	19	Du1K-m-d	0.14	2200.7	1913.6
	20	Sh400m-m	0.02	314.4	273.4
	21	Sh1.5K-m	0.16	2515.0	2187.0
	22	Sh1K-m-d	0.1	1571.9	1366.9
	23	Du1K-m-u	0.19	2986.6	2597.1
	24	Sh2K-m-d	0.11	1729.1	1503.6

Table 14 cont'd

MWAC Horizontal Flux Quantities at 1 m for Phase 6					
Area	Station No.	Station ID	Sample Weight	Horizontal Flux	Total Horizontal Flux
	Number	ID	mass (g)	g/m ²	g/m/yr
Non-maneuvering	1	Du3K-u	0.02	314.4	1366.9
	2	Du2K	0.02	314.4	1366.9
	3	Du1K-u	0.05	786.0	3417.2
	4	Sh3K-u	0.01	157.2	683.4
	5	Du400m	0.04	628.8	2733.7
	6	Du1K-d	0.03	471.6	2050.3
	7	Sh1K-u	0.03	471.6	2050.3
	8	Sh400m	0.03	471.6	2050.3
	9	Sh1.5K	0.02	314.4	1366.9
	10	Sh1K-d	0.02	314.4	1366.9
Maneuvering	11	Du3K-m-u	0.01	157.2	683.4
	12	Du2K-m-u	0.02	314.4	1366.9
	13	Sh3K-m-u	0.03	471.6	2050.3
	14	Du400m-m	0.05	786.0	3417.2
	15	Sh2K-m-u	0.03	471.6	2050.3
	16	Du1.5K-m	0.12	1886.3	8201.2
	17	Sh1K-m-u	0.02	314.4	1366.9
	18	Du2K-m-d	0.07	1100.3	4784.0
	19	Du1K-m-d	0.03	471.6	2050.3
	20	Sh400m-m	0.01	157.2	683.4
	21	Sh1.5K-m	0.04	628.8	2733.7
	22	Sh1K-m-d	0.02	314.4	1366.9
	23	Du1K-m-u	0.04	628.8	2733.7
	24	Sh2K-m-d	0.02	314.4	1366.9

Table 14 cont'd

BSNE Horizontal Flux Quantities at 0.2 m for Phase 7					
Area	Station No.	Station ID	Sample Weight	Horizontal Flux	Total Horizontal Flux
	Number	ID	mass (g)	g/m ²	g/m/yr
Non-maneuvering	1	Du3K-u	11.16	11160.0	5873.7
	2	Du2K	1.31	1310.0	689.5
	3	Du1K-u	32.32	32320.0	17010.5
	4	Sh3K-u	1.31	1310.0	689.5
	5	Du400m	2.16	2160.0	1136.8
	6	Du1K-d	3.11	3110.0	1636.8
	7	Sh1K-u	1.60	1600.0	842.1
	8	Sh400m	1.03	1030.0	542.1
	9	Sh1.5K	1.42	1420.0	747.4
	10	Sh1K-d	1.21	1210.0	636.8
Maneuvering	11	Du3K-m-u	4.42	4420.0	2326.3
	12	Du2K-m-u	1.34	1340.0	705.3
	13	Sh3K-m-u	2.79	2790.0	1468.4
	14	Du400m-m	40.70	40700.0	21421.1
	15	Sh2K-m-u	4.75	4750.0	2500.0
	16	Du1.5K-m	55.85	55850.0	29394.7
	17	Sh1K-m-u	1.89	1890.0	994.7
	18	Du2K-m-d	6.47	6470.0	3405.3
	19	Du1K-m-d	10.90	10900.0	5736.8
	20	Sh400m-m	2.21	2210.0	1163.2
	21	Sh1.5K-m	4.86	4860.0	2557.9
	22	Sh1K-m-d	2.49	2490.0	1310.5
	23	Du1K-m-u	6.57	6570.0	3457.9
	24	Sh2K-m-d	1.30	1300.0	684.2

Table 14 cont'd

BSNE Horizontal Flux Quantities at 1 m for Phase 7					
Area	Station No.	Station ID	Sample Weight	Horizontal Flux	Total Horizontal Flux
	Number	ID	mass (g)	g/m ²	g/m/yr
Non-maneuvering	1	Du3K-u	0.81	810.0	2131.6
	2	Du2K	0.2	200.0	526.3
	3	Du1K-u	2.08	2080.0	5473.7
	4	Sh3K-u	0.21	210.0	552.6
	5	Du400m	0.37	370.0	973.7
	6	Du1K-d	0.51	510.0	1342.1
	7	Sh1K-u	0.13	130.0	342.1
	8	Sh400m	0.15	150.0	394.7
	9	Sh1.5K	0.21	210.0	552.6
	10	Sh1K-d	0.16	160.0	421.1
Maneuvering	11	Du3K-m-u	0.43	430.0	1131.6
	12	Du2K-m-u	0.47	470.0	1236.8
	13	Sh3K-m-u	0.25	250.0	657.9
	14	Du400m-m	1.49	1490.0	3921.1
	15	Sh2K-m-u	0.54	540.0	1421.1
	16	Du1.5K-m	4.42	4420.0	11631.6
	17	Sh1K-m-u	0.24	240.0	631.6
	18	Du2K-m-d	1.22	1220.0	3210.5
	19	Du1K-m-d	1.7	1700.0	4473.7
	20	Sh400m-m	0.3	300.0	789.5
	21	Sh1.5K-m	0.61	610.0	1605.3
	22	Sh1K-m-d	0.77	770.0	2026.3
	23	Du1K-m-u	0.79	790.0	2078.9
	24	Sh2K-m-d	0.34	340.0	894.7

Table 14 cont'd

MWAC Horizontal Flux Quantities at 0.2 m for Phase 7					
Area	Station No.	Station ID	Sample Weight	Horizontal Flux	Total Horizontal Flux
	Number	ID	mass (g)	g/m ²	g/m/yr
Non-maneuvering	1	Du3K-u	0.85	13361.2	7032.2
	2	Du2K	0.06	943.1	496.4
	3	Du1K-u	2.77	43541.6	22916.7
	4	Sh3K-u	0.02	314.4	165.5
	5	Du400m	0.12	1886.3	992.8
	6	Du1K-d	0.14	2200.7	1158.2
	7	Sh1K-u	0.06	943.1	496.4
	8	Sh400m	0.05	786.0	413.7
	9	Sh1.5K	0.08	1257.5	661.9
	10	Sh1K-d	0.13	2043.5	1075.5
Maneuvering	11	Du3K-m-u	0.08	1257.5	661.9
	12	Du2K-m-u	0.11	1729.1	910.0
	13	Sh3K-m-u	0.02	314.4	165.5
	14	Du400m-m	3.05	47943.0	25233.1
	15	Sh2K-m-u	0.36	5658.8	2978.3
	16	Du1.5K-m	4.65	73093.4	38470.2
	17	Sh1K-m-u	0.08	1257.5	661.9
	18	Du2K-m-d	0.79	12418.0	6535.8
	19	Du1K-m-d	0.39	6130.4	3226.5
	20	Sh400m-m	0.03	471.6	248.2
	21	Sh1.5K-m	0.25	3929.8	2068.3
	22	Sh1K-m-d	0.13	2043.5	1075.5
	23	Du1K-m-u	0.63	9903.0	5212.1
	24	Sh2K-m-d	0.1	1571.9	827.3

Table 14 cont'd

MWAC Horizontal Flux Quantities at 1 m for Phase 7					
Area	Station No.	Station ID	Sample Weight	Horizontal Flux	Total Horizontal Flux
	Number	ID	mass (g)	g/m ²	g/m/yr
Non-maneuvering	1	Du3K-u	NA ¹	NA ¹	NA ¹
	2	Du2K	0.01	157.19	413.7
	3	Du1K-u	0.3	4715.70	12409.7
	4	Sh3K-u	0.01	157.19	413.7
	5	Du400m	0.04	628.76	1654.6
	6	Du1K-d	0.02	314.38	827.3
	7	Sh1K-u	0.02	314.38	827.3
	8	Sh400m	0.01	157.19	413.7
	9	Sh1.5K	0.01	157.19	413.7
	10	Sh1K-d	0.01	157.19	413.7
Maneuvering	11	Du3K-m-u	NA ¹	NA ¹	NA ¹
	12	Du2K-m-u	0.05	785.95	2068.3
	13	Sh3K-m-u	0.03	471.57	1241.0
	14	Du400m-m	0.12	1886.28	4963.9
	15	Sh2K-m-u	0.05	785.95	2068.3
	16	Du1.5K-m	0.34	5344.46	14064.4
	17	Sh1K-m-u	0.04	628.76	1654.6
	18	Du2K-m-d	0.12	1886.28	4963.9
	19	Du1K-m-d	0.17	2672.23	7032.2
	20	Sh400m-m	0.02	314.38	827.3
	21	Sh1.5K-m	0.07	1100.33	2895.6
	22	Sh1K-m-d	0.07	1100.33	2895.6
	23	Du1K-m-u	0.08	1257.52	3309.3
	24	Sh2K-m-d	0.02	314.38	827.3

Table 14 cont'd

BSNE Horizontal Flux Quantities at 0.2 m for Phase 8					
Area	Station No.	Station ID	Sample Weight	Horizontal Flux	Total Horizontal Flux
	Number	ID	mass (g)	g/m ²	g/m/yr
Non-maneuvering	1	Du3K-u	5.92	5920.0	7893.3
	2	Du2K	0.49	490.0	653.3
	3	Du1K-u	21.57	21570.0	28760.0
	4	Sh3K-u	0.45	450.0	600.0
	5	Du400m	0.75	750.0	1000.0
	6	Du1K-d	3.53	3530.0	4706.7
	7	Sh1K-u	0.83	830.0	1106.7
	8	Sh400m	0.52	520.0	693.3
	9	Sh1.5K	0.91	910.0	1213.3
	10	Sh1K-d	0.60	600.0	800.0
Maneuvering	11	Du3K-m-u	6.81	6810.0	9080.0
	12	Du2K-m-u	1.90	1900.0	2533.3
	13	Sh3K-m-u	1.08	1080.0	1440.0
	14	Du400m-m	72.60	72600.0	96800.0
	15	Sh2K-m-u	2.84	2840.0	3786.7
	16	Du1.5K-m	33.70	33700.0	44933.3
	17	Sh1K-m-u	0.52	520.0	693.3
	18	Du2K-m-d	4.33	4330.0	5773.3
	19	Du1K-m-d	11.44	11440.0	15253.3
	20	Sh400m-m	0.98	980.0	1306.7
	21	Sh1.5K-m	1.56	1560.0	2080.0
	22	Sh1K-m-d	0.79	790.0	1053.3
	23	Du1K-m-u	1.47	1470.0	1960.0
	24	Sh2K-m-d	0.81	810.0	1080.0

Table 14 cont'd

BSNE Horizontal Flux Quantities at 1 m for Phase 8					
Area	Station No.	Station ID	Sample Weight	Horizontal Flux	Total Horizontal Flux
	Number	ID	mass (g)	g/m ²	g/m/yr
Non-maneuvering	1	Du3K-u	0.7	700.0	4666.7
	2	Du2K	0.12	120.0	800.0
	3	Du1K-u	2.54	2540.0	16933.3
	4	Sh3K-u	0.14	140.0	933.3
	5	Du400m	0.24	240.0	1600.0
	6	Du1K-d	0.54	540.0	3600.0
	7	Sh1K-u	0.08	80.0	533.3
	8	Sh400m	0.17	170.0	1133.3
	9	Sh1.5K	0.3	300.0	2000.0
	10	Sh1K-d	0.15	150.0	1000.0
Maneuvering	11	Du3K-m-u	0.48	480.0	3200.0
	12	Du2K-m-u	0.7	700.0	4666.7
	13	Sh3K-m-u	0.2	200.0	1333.3
	14	Du400m-m	2.27	2270.0	15133.3
	15	Sh2K-m-u	0.51	510.0	3400.0
	16	Du1.5K-m	2.74	2740.0	18266.7
	17	Sh1K-m-u	0.14	140.0	933.3
	18	Du2K-m-d	1.01	1010.0	6733.3
	19	Du1K-m-d	1.41	1410.0	9400.0
	20	Sh400m-m	0.18	180.0	1200.0
	21	Sh1.5K-m	0.43	430.0	2866.7
	22	Sh1K-m-d	0.36	360.0	2400.0
	23	Du1K-m-u	0.32	320.0	2133.3
	24	Sh2K-m-d	0.28	280.0	1866.7

Table 14 cont'd

MWAC Horizontal Flux Quantities at 0.2 m for Phase 8					
Area	Station No.	Station ID	Sample Weight	Horizontal Flux	Total Horizontal Flux
	Number	ID	mass (g)	g/m ²	g/m/yr
Non-maneuvering	1	Du3K-u	0.47	7387.9	9850.6
	2	Du2K	0.02	314.4	419.2
	3	Du1K-u	2.44	38354.4	51139.2
	4	Sh3K-u	0.03	471.6	628.8
	5	Du400m	NA ¹	NA ¹	NA ¹
	6	Du1K-d	0.13	2043.5	2724.6
	7	Sh1K-u	0.01	157.2	209.6
	8	Sh400m	0.05	786.0	1047.9
	9	Sh1.5K	0.07	1100.3	1467.1
	10	Sh1K-d	0.08	1257.5	1676.7
Maneuvering	11	Du3K-m-u	0.06	943.1	1257.5
	12	Du2K-m-u	0.14	2200.7	2934.2
	13	Sh3K-m-u	0.09	1414.7	1886.3
	14	Du400m-m	3.74	58789.1	78385.4
	15	Sh2K-m-u	0.17	2672.2	3563.0
	16	Du1.5K-m	4.72	74193.7	98924.9
	17	Sh1K-m-u	0.02	314.4	419.2
	18	Du2K-m-d	0.53	8331.1	11108.1
	19	Du1K-m-d	0.26	4086.9	5449.3
	20	Sh400m-m	0.03	471.6	628.8
	21	Sh1.5K-m	0.09	1414.7	1886.3
	22	Sh1K-m-d	0.08	1257.5	1676.7
	23	Du1K-m-u	0.4	6287.6	8383.5
	24	Sh2K-m-d	0.04	628.8	838.3

Table 14 cont'd

MWAC Horizontal Flux Quantities at 1 m for Phase 8					
Area	Station No.	Station ID	Sample Weight	Horizontal Flux	Total Horizontal Flux
	Number	ID	mass (g)	g/m ²	g/m/yr
Non-maneuvering	1	Du3K-u	0.33	5187.3	34581.8
	2	Du2K	0.01	157.2	1047.9
	3	Du1K-u	0.21	3301.0	22006.6
	4	Sh3K-u	0	0.0	0.0
	5	Du400m	0.03	471.6	3143.8
	6	Du1K-d	0.02	314.4	2095.9
	7	Sh1K-u	0.01	157.2	1047.9
	8	Sh400m	0.02	314.4	2095.9
	9	Sh1.5K	0.02	314.4	2095.9
	10	Sh1K-d	0.01	157.2	1047.9
Maneuvering	11	Du3K-m-u	0.08	1257.5	8383.5
	12	Du2K-m-u	0.05	786.0	5239.7
	13	Sh3K-m-u	0.02	314.4	2095.9
	14	Du400m-m	0.12	1886.3	12575.2
	15	Sh2K-m-u	0.05	786.0	5239.7
	16	Du1.5K-m	0.19	2986.6	19910.7
	17	Sh1K-m-u	0.01	157.2	1047.9
	18	Du2K-m-d	0.08	1257.5	8383.5
	19	Du1K-m-d	0.12	1886.3	12575.2
	20	Sh400m-m	0.01	157.2	1047.9
	21	Sh1.5K-m	0.04	628.8	4191.7
	22	Sh1K-m-d	0.04	628.8	4191.7
	23	Du1K-m-u	0.06	943.1	6287.6
	24	Sh2K-m-d	0.03	471.6	3143.8

Table 14 cont'd

BSNE Horizontal Flux Quantities at 0.2 m for Phase 9					
Area	Station No.	Station ID	Sample Weight	Horizontal Flux	Total Horizontal Flux
	Number	ID	mass (g)	g/m ²	g/m/yr
Non-maneuvering	1	Du3K-u	93.08	93080.0	77566.7
	2	Du2K	14.90	14900.0	12416.7
	3	Du1K-u	117.53	117530.0	97941.7
	4	Sh3K-u	2.67	2670.0	2225.0
	5	Du400m	23.31	23310.0	19425.0
	6	Du1K-d	62.27	62270.0	51891.7
	7	Sh1K-u	3.11	3110.0	2591.7
	8	Sh400m	2.00	2000.0	1666.7
	9	Sh1.5K	3.99	3990.0	3325.0
	10	Sh1K-d	5.36	5360.0	4466.7
Maneuvering	11	Du3K-m-u	65.93	65930.0	54941.7
	12	Du2K-m-u	17.78	17780.0	14816.7
	13	Sh3K-m-u	3.76	3760.0	3133.3
	14	Du400m-m	275.10	275100.0	229250.0
	15	Sh2K-m-u	35.58	35580.0	29650.0
	16	Du1.5K-m	261.70	261700.0	218083.3
	17	Sh1K-m-u	1.20	1200.0	1000.0
	18	Du2K-m-d	25.15	25150.0	20958.3
	19	Du1K-m-d	93.29	93290.0	77741.7
	20	Sh400m-m	2.58	2580.0	2150.0
	21	Sh1.5K-m	3.59	3590.0	2991.7
	22	Sh1K-m-d	4.17	4170.0	3475.0
	23	Du1K-m-u	24.55	24550.0	20458.3
	24	Sh2K-m-d	3.52	3520.0	2933.3

Table 14 cont'd

BSNE Horizontal Flux Quantities at 1 m for Phase 9					
Area	Station No.	Station ID	Sample Weight	Horizontal Flux	Total Horizontal Flux
	Number	ID	mass (g)	g/m ²	g/m/yr
Non-maneuvering	1	Du3K-u	14.24	14240.0	59333.3
	2	Du2K	3.30	3300.0	13750.0
	3	Du1K-u	21.37	21370.0	89041.7
	4	Sh3K-u	1.79	1790.0	7458.3
	5	Du400m	5.87	5870.0	24458.3
	6	Du1K-d	8.37	8370.0	34875.0
	7	Sh1K-u	1.02	1020.0	4250.0
	8	Sh400m	1.48	1480.0	6166.7
	9	Sh1.5K	3.69	3690.0	15375.0
	10	Sh1K-d	1.49	1490.0	6208.3
Maneuvering	11	Du3K-m-u	5.39	5390.0	22458.3
	12	Du2K-m-u	6.35	6350.0	26458.3
	13	Sh3K-m-u	1.19	1190.0	4958.3
	14	Du400m-m	20.65	20650.0	86041.7
	15	Sh2K-m-u	6.64	6640.0	27666.7
	16	Du1.5K-m	20.56	20560.0	85666.7
	17	Sh1K-m-u	1.02	1020.0	4250.0
	18	Du2K-m-d	6.95	6950.0	28958.3
	19	Du1K-m-d	14.94	14940.0	62250.0
	20	Sh400m-m	1.32	1320.0	5500.0
	21	Sh1.5K-m	2.86	2860.0	11916.7
	22	Sh1K-m-d	3.71	3710.0	15458.3
	23	Du1K-m-u	5.01	5010.0	20875.0
	24	Sh2K-m-d	2.01	2010.0	8375.0

Table 14 cont'd

MWAC Horizontal Flux Quantities at 0.2 m for Phase 9					
Area	Station No.	Station ID	Sample Weight	Horizontal Flux	Total Horizontal Flux
	Number	ID	mass (g)	g/m ²	g/m/yr
Non-maneuvering	1	Du3K-u	7.15	112390.9	93659.1
	2	Du2K	0.34	5344.5	4453.7
	3	Du1K-u	13.95	219280.1	182733.5
	4	Sh3K-u	0.14	2200.7	1833.9
	5	Du400m	1.31	20591.9	17159.9
	6	Du1K-d	1.97	30966.4	25805.4
	7	Sh1K-u	0.07	1100.3	916.9
	8	Sh400m	0.33	5187.3	4322.7
	9	Sh1.5K	0.59	9274.2	7728.5
	10	Sh1K-d	0.36	5658.8	4715.7
Maneuvering	11	Du3K-m-u	0.52	8173.9	6811.6
	12	Du2K-m-u	1.79	28137.0	23447.5
	13	Sh3K-m-u	0.28	4401.3	3667.8
	14	Du400m-m	20.93	328998.8	274165.7
	15	Sh2K-m-u	2.03	31909.6	26591.3
	16	Du1.5K-m	16.67	262035.8	218363.2
	17	Sh1K-m-u	0.07	1100.3	916.9
	18	Du2K-m-d	3	47157.0	39297.5
	19	Du1K-m-d	4.8	75451.2	62876.0
	20	Sh400m-m	0.21	3301.0	2750.8
	21	Sh1.5K-m	0.25	3929.8	3274.8
	22	Sh1K-m-d	0.56	8802.6	7335.5
	23	Du1K-m-u	3.42	53759.0	44799.2
	24	Sh2K-m-d	0.21	3301.0	2750.8

Table 14 cont'd

MWAC Horizontal Flux Quantities at 1 m for Phase 9					
Area	Station No.	Station ID	Sample Weight	Horizontal Flux	Total Horizontal Flux
	Number	ID	mass (g)	g/m ²	g/m/yr
Non-maneuvering	1	Du3K-u	1.81	28451.4	118547.5
	2	Du2K	0.28	4401.3	18338.8
	3	Du1K-u	2.7	42441.3	176838.8
	4	Sh3K-u	NA ¹	NA ¹	NA ¹
	5	Du400m	0.54	8488.3	35367.8
	6	Du1K-d	0.59	9274.2	38642.6
	7	Sh1K-u	0.1	1571.9	6549.6
	8	Sh400m	0.18	2829.4	11789.3
	9	Sh1.5K	0.45	7073.6	29473.1
	10	Sh1K-d	0.19	2986.6	12444.2
Maneuvering	11	Du3K-m-u	0.46	7230.7	30128.1
	12	Du2K-m-u	0.51	8016.7	33402.9
	13	Sh3K-m-u	0.13	2043.5	8514.5
	14	Du400m-m	1.72	27036.7	112652.9
	15	Sh2K-m-u	0.74	11632.1	48466.9
	16	Du1.5K-m	1.82	28608.6	119202.5
	17	Sh1K-m-u	0.18	2829.4	11789.3
	18	Du2K-m-d	0.69	10846.1	45192.1
	19	Du1K-m-d	1.46	22949.7	95624.0
	20	Sh400m-m	0.17	2672.2	11134.3
	21	Sh1.5K-m	0.28	4401.3	18338.8
	22	Sh1K-m-d	0.38	5973.2	24888.4
	23	Du1K-m-u	0.74	11632.1	48466.9
	24	Sh2K-m-d	0.25	3929.8	16374.0

Table 14 cont'd

MWAC Horizontal Flux Quantities at 0.2 m for Phase 10					
Area	Station No.	Station ID	Sample Weight	Horizontal Flux	Total Horizontal Flux
	Number	ID	mass (g)	g/m ²	g/m/yr
Non-maneuvering	1	Du3K-u	0.23	3615.4	2781.1
	2	Du2K	0.16	2515.0	1934.6
	3	Du1K-u	0.48	7545.1	5803.9
	4	Sh3K-u	0.1	1571.9	1209.2
	5	Du400m	0.35	5501.7	4232.0
	6	Du1K-d	0.11	1729.1	1330.1
	7	Sh1K-u	0.13	2043.5	1571.9
	8	Sh400m	0.04	628.8	483.7
	9	Sh1.5K	0.12	1886.3	1451.0
	10	Sh1K-d	0.1	1571.9	1209.2
Maneuvering	11	Du3K-m-u	0.1	1571.9	1209.2
	12	Du2K-m-u	0.2	3143.8	2418.3
	13	Sh3K-m-u	0.42	6602.0	5078.4
	14	Du400m-m	0.59	9274.2	7134.0
	15	Sh2K-m-u	0.17	2672.2	2055.6
	16	Du1.5K-m	0.55	8645.5	6650.3
	17	Sh1K-m-u	0.1	1571.9	1209.2
	18	Du2K-m-d	0.17	2672.2	2055.6
	19	Du1K-m-d	0.22	3458.2	2660.1
	20	Sh400m-m	0.14	2200.7	1692.8
	21	Sh1.5K-m	0.16	2515.0	1934.6
	22	Sh1K-m-d	0.12	1886.3	1451.0
	23	Du1K-m-u	0.17	2672.2	2055.6
	24	Sh2K-m-d	0.16	2515.0	1934.6

Table 14 cont'd

MWAC Horizontal Flux Quantities at 1 m for Phase 10					
Area	Station No.	Station ID	Sample Weight	Horizontal Flux	Total Horizontal Flux
	Number	ID	mass (g)	g/m ²	g/m/yr
Non-maneuvering	1	Du3K-u	0.03	471.6	471.6
	2	Du2K	0.02	314.4	314.4
	3	Du1K-u	0.06	943.1	943.1
	4	Sh3K-u	0.07	1100.3	1100.3
	5	Du400m	0.04	628.8	628.8
	6	Du1K-d	0.01	157.2	157.2
	7	Sh1K-u	0.01	157.2	157.2
	8	Sh400m	0.01	157.2	157.2
	9	Sh1.5K	0.02	314.4	314.4
	10	Sh1K-d	0.01	157.2	157.2
Maneuvering	11	Du3K-m-u	0.01	157.2	157.2
	12	Du2K-m-u	0.02	314.4	314.4
	13	Sh3K-m-u	NA ¹	NA ¹	NA ¹
	14	Du400m-m	0.06	943.1	943.1
	15	Sh2K-m-u	0.06	943.1	943.1
	16	Du1.5K-m	0.1	1571.9	1571.9
	17	Sh1K-m-u	0.01	157.2	157.2
	18	Du2K-m-d	0.03	471.6	471.6
	19	Du1K-m-d	0.03	471.6	471.6
	20	Sh400m-m	0.01	157.2	157.2
	21	Sh1.5K-m	0.02	314.4	314.4
	22	Sh1K-m-d	0.03	471.6	471.6
	23	Du1K-m-u	0.03	471.6	471.6
	24	Sh2K-m-d	0.01	157.2	157.2

Table 15: U-test result values for Groups A, B, C, and D at 0.2 and 1 m heights in the non-maneuver (NM) and maneuver (M) areas for Phase 5-10.

Phase 5					
Area					
	Group	Station No.	Station ID	Z at 0.2 m	Z at 1 m
NM	A	3	Du1K-u (downwind)	1.56	1.60
		5	Du400m (center)	/	/
		6	Du1K-d (upwind)	0.85	0.39
	B	7	Sh1K-u (downwind)	0.39	0.19
		8	Sh400m (center)	/	/
		10	Sh1K-d (upwind)	0.06	0.06
M	C	23	Du1K-m-u (downwind)	0.48	0.10
		14	Du400m-m (center)	/	/
		19	Du1K-m-d (upwind)	1.31	0.27
	D	17	Sh1K-m-u (downwind)	0.31	0.52
		20	Sh400m-m (center)	/	/
		22	Sh1K-m-d (upwind)	0.89	0.52

Table 15 cont'd

Phase 6					
Area					
	Group	Station No.	Station ID	Z at 0.2 m	Z at 1 m
NM	A	3	Du1K-u (downwind)	1.22	1.06
		5	Du400m (center)	/	/
		6	Du1K-d (upwind)	0.15	0.98
	B	7	Sh1K-u (downwind)	0.15	0.15
		8	Sh400m (center)	/	/
		10	Sh1K-d (upwind)	0.89	0.06
M	C	23	Du1K-m-u (downwind)	0.89	0.06
		14	Du400m-m (center)	/	/
		19	Du1K-m-d (upwind)	1.18	0.23
	D	17	Sh1K-m-u (downwind)	0.27	0.48
		20	Sh400m-m (center)	/	/
		22	Sh1K-m-d (upwind)	0.31	0.10

Table 15 cont'd

Phase 9					
Area					
	Group	Station No.	Station ID	Z at 0.2 m	Z at 1 m
NM	A	3	Du1K-u (downwind)	0.73	0.31
		5	Du400m (center)	/	/
		6	Du1K-d (upwind)	0.85	0.81
	B	7	Sh1K-u (downwind)	0.23	0.39
		8	Sh400m (center)	/	/
		10	Sh1K-d (upwind)	0.62	0.21
M	C	23	Du1K-m-u (downwind)	0.145	0.933
		14	Du400m-m (center)	/	/
		19	Du1K-m-d (upwind)	0.52	1.71
	D	17	Sh1K-m-u (downwind)	0.270	0.021
		20	Sh400m-m (center)	/	/
		22	Sh1K-m-d (upwind)	0.518	0.62

Table 15 cont'd

Phase 10					
Area					
	Group	Station No.	Station ID	Z at 0.2 m	Z at 1 m
NM	A	3	Du1K-u (downwind)	0.726	0.643
		5	Du400m (center)	/	/
		6	Du1K-d (upwind)	0.56	0.31
	B	7	Sh1K-u (downwind)	0.73	0.02
		8	Sh400m (center)	/	/
		10	Sh1K-d (upwind)	0.27	0.21
M	C	23	Du1K-m-u (downwind)	0.93	0.48
		14	Du400m-m (center)	/	/
		19	Du1K-m-d (upwind)	0.27	0.52
	D	17	Sh1K-m-u (downwind)	0.52	0.39
		20	Sh400m-m (center)	/	/
		22	Sh1K-m-d (upwind)	0.39	0.44

Table 16: U-test result values for station numbers 3, 10, 13, and 14 at 0.2 and 1 m heights in the non-maneuver (NM) and maneuver (M) areas for Phase 5-10.

Phase 5					
Area					
	Single	Station No.	Station ID	Z at 0.2 m	Z at 1 m
NM	1	3	Du1K-u	1.39	1.64
M	3	14	Du400m-m		
NM	2	10	Sh1K-d	0.19	0.27
M	4	13	Sh3K-m-u		
Phase 5					
Area					
	Single	Station No.	Station ID	Z at 0.2 m	Z at 1 m
NM	1	3	Du1K-u	2.14	0.82
M	4	13	Sh3K-m-u		
NM	2	10	Sh1K-d	0.56	0.68
M	3	14	Du400m-m		
Phase 6					
Area					
	Single	Station No.	Station ID	Z at 0.2 m	Z at 1 m
NM	1	3	Du1K-u	0.68	0.89
M	3	14	Du400m-m		
NM	2	10	Sh1K-d	0.23	0.85
M	4	13	Sh3K-m-u		
Phase 7					
Area					
	Single	Station No.	Station ID	Z at 0.2 m	Z at 1 m
NM	1	3	Du1K-u	1.72	1.43
M	3	14	Du400m-m		
NM	2	10	Sh1K-d	0.10	0.44
M	4	13	Sh3K-m-u		

Table 16 cont'd

Phase 8					
Area					
	Single	Station No.	Station ID	Z at 0.2 m	Z at 1 m
NM	1	3	Du1K-u	2.05	1.06
M	3	14	Du400m-m		
NM	2	10	Sh1K-d	0.02	0.23
M	4	13	Sh3K-m-u		
Phase 9					
Area					
	Single	Station No.	Station ID	Z at 0.2 m	Z at 1 m
NM	1	3	Du1K-u	0.31	0.77
M	3	14	Du400m-m		
NM	2	10	Sh1K-d	0.06	0.31
M	4	13	Sh3K-m-u		
Phase 10					
Area					
	Single	Station No.	Station ID	Z at 0.2 m	Z at 1 m
NM	1	3	Du1K-u	0.56	0.44
M	3	14	Du400m-m		
NM	2	10	Sh1K-d	0.73	1.18
M	4	13	Sh3K-m-u		

Figures

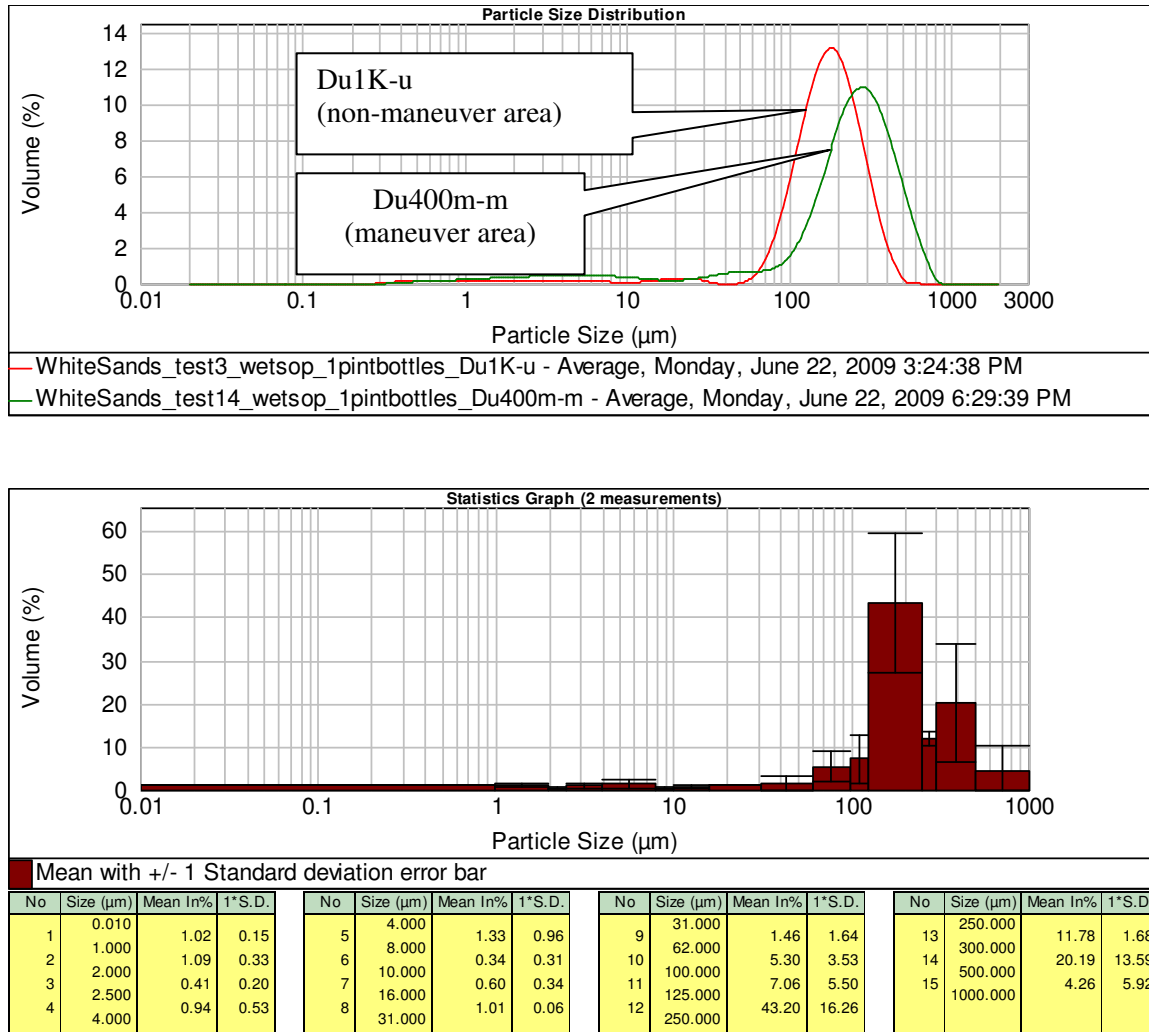


Figure 24: Volume percentage versus particle size distribution for MWAC stations Du1K-u in the non-maneuver area and Du400m-m in the maneuver area at 0.2 m height for Phase 5 (top graph).

Statistics graph showing mean and standard deviation values of volume percentages versus particle size distribution for MWAC sites Du1K-u in the non-maneuver area and Du400m-m in the maneuver area at 0.2 m height for Phase 5 (bottom graph).

(It should be noted that all mean and standard deviation values are derived from volume percentage values which correspond to specific particle size ranges produced by the Malvern particle sizer. This is mentioned in greater detail in the Particle Size Analysis discussion.)

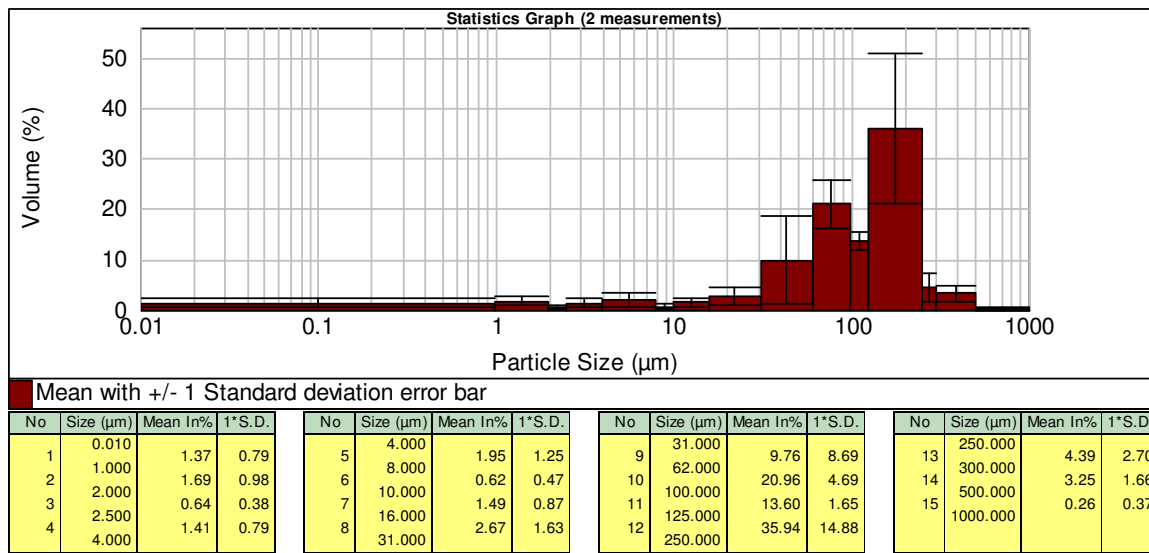
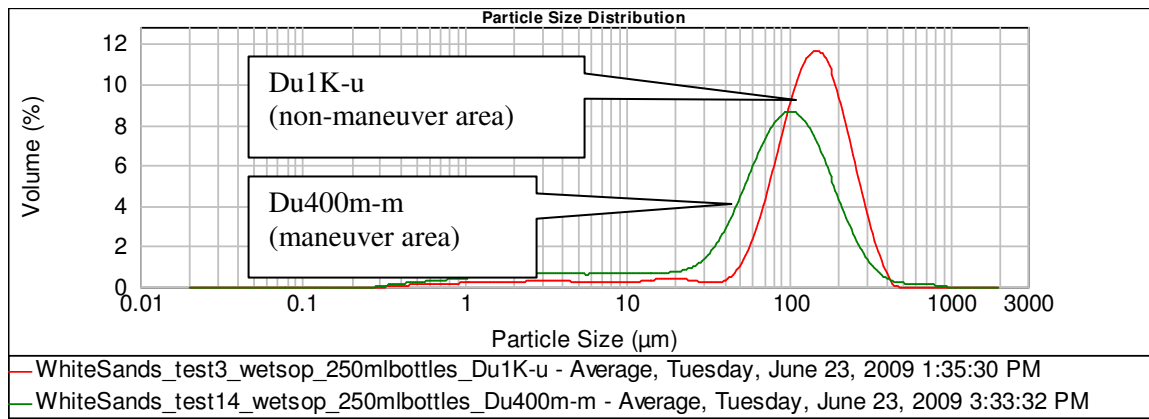


Figure 25: Volume percentage versus particle size distribution for MWAC sites Du1K-u in the non-maneuver area and Du400m-m in the maneuver area at 1 m height for Phase 5 (top graph).

Statistics graph showing mean and standard deviation values of volume percentages versus particle size distribution for MWAC sites Du1K-u in the non-maneuver area and Du400m-m in the maneuver area at 1 m height for Phase 5 (bottom graph).

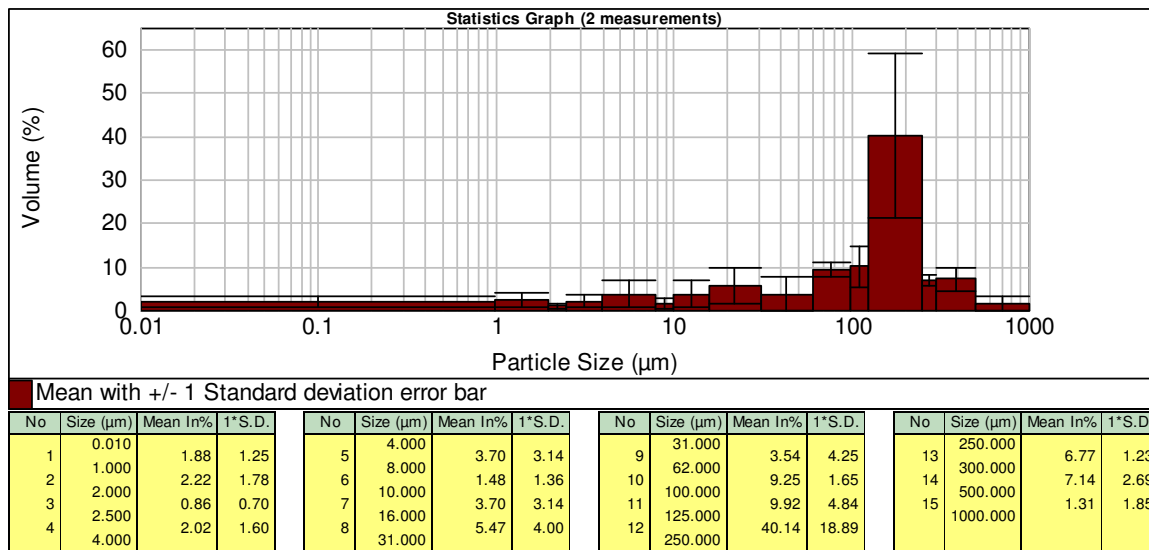
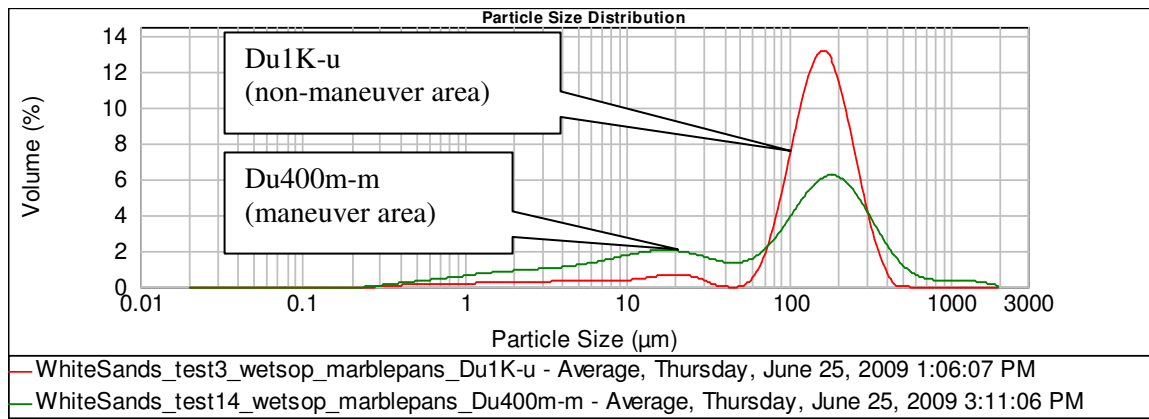


Figure 26: Volume percentage versus particle size distribution for MDCO sites Du1K-u in the non-maneuver area and Du400m-m in the maneuver area at 1.7 m height for Phase 5 (top graph).

Statistics graph and table showing mean and standard deviation values of volume percentages versus particle size distribution for MDCO sites Du1K-u in the non-maneuver area and Du400m-m in the maneuver area at 1.7 m height for Phase 5 (bottom graph).

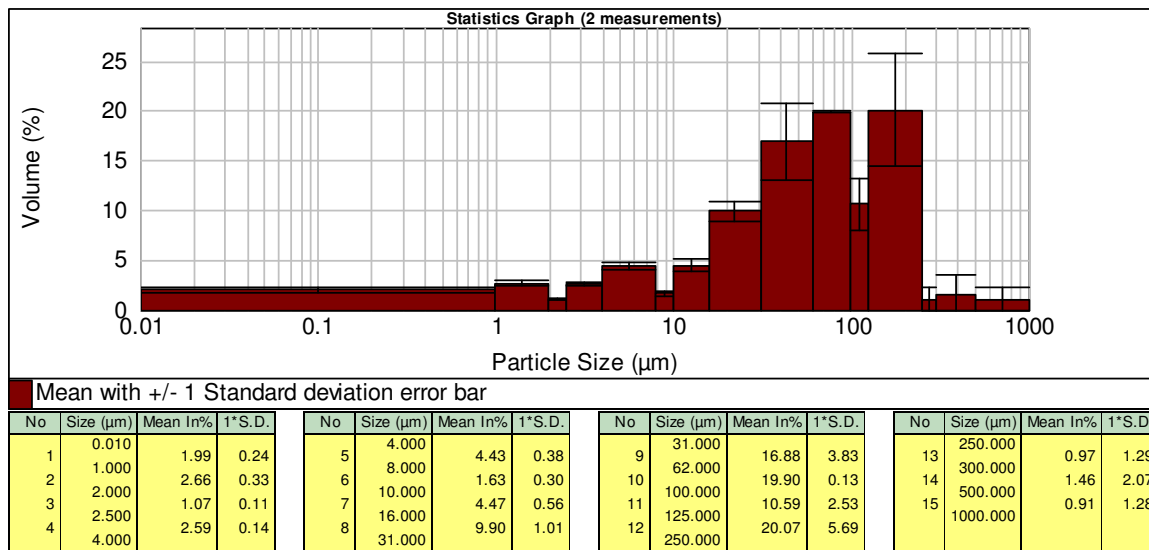
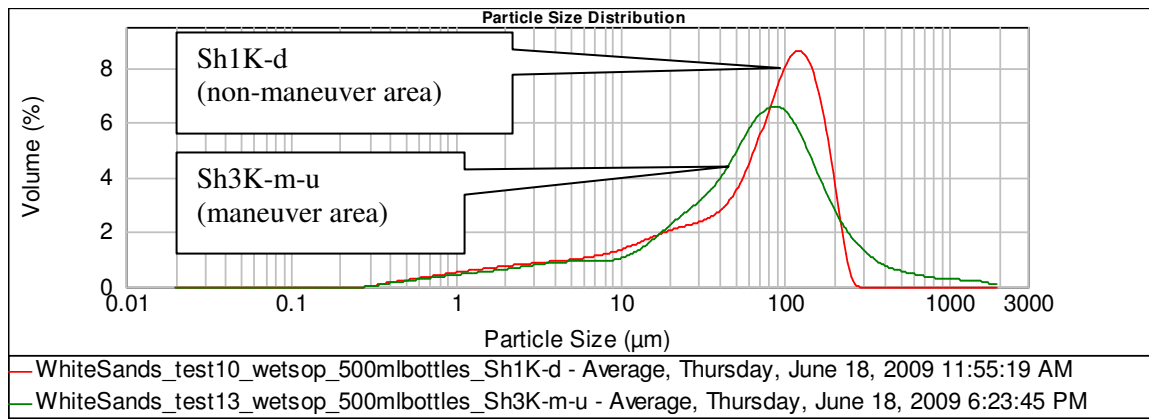


Figure 27: Volume percentage versus particle size distribution for MWAC sites Sh1K-d in the non-maneuver area and Sh3K-m-u in the maneuver area at 0.2 m for Phase 5 (top graph).

Statistics graph and table showing mean and standard deviation values of volume percentages versus particle size distribution for MWAC sites Sh1K-d in the non-maneuver area and Sh3K-m-u in the maneuver area at 0.2 m height for Phase 5 (bottom graph).

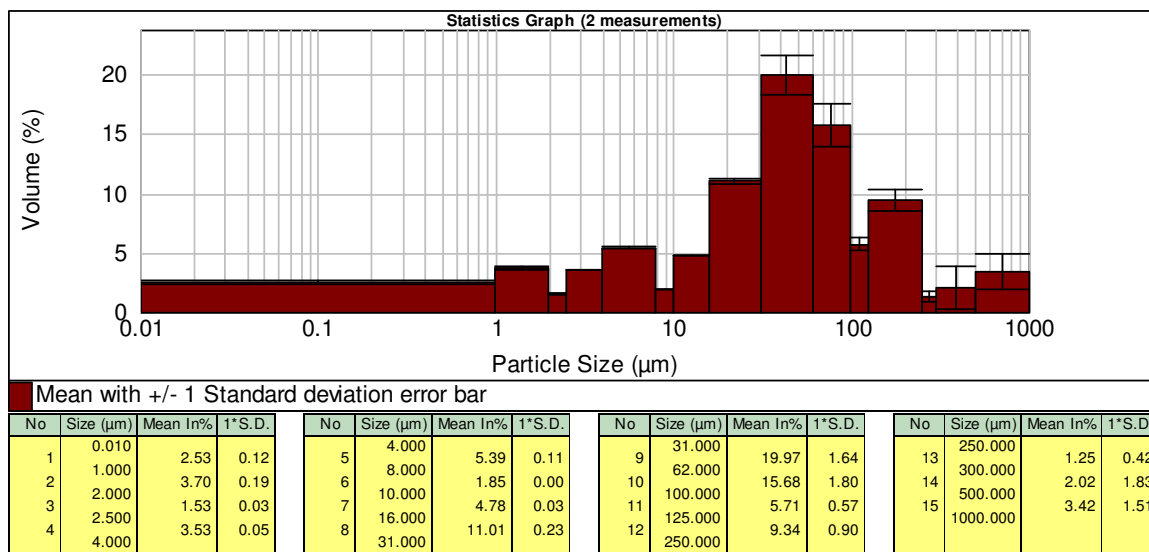
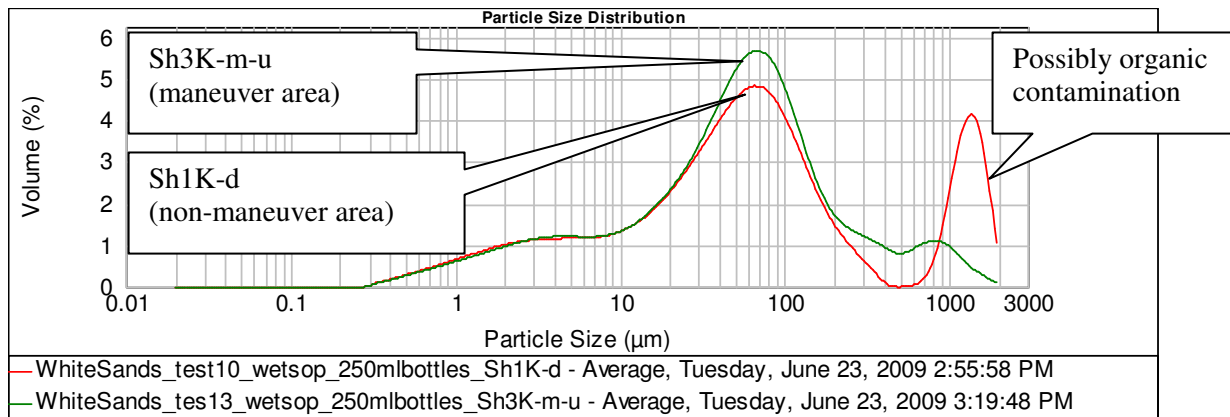


Figure 28: Volume percentage versus particle size distribution for MWAC sites Sh1K-d in the non-maneuver area and Sh3K-m-u in the maneuver area at 1 m for Phase 5 (top graph).

Statistics graph and table showing mean and standard deviation values of volume percentages versus particle size distribution for MWAC sites Sh1K-d in the non-maneuver area and Sh3K-m-u in the maneuver area at 1 m height for Phase 5 (bottom graph).

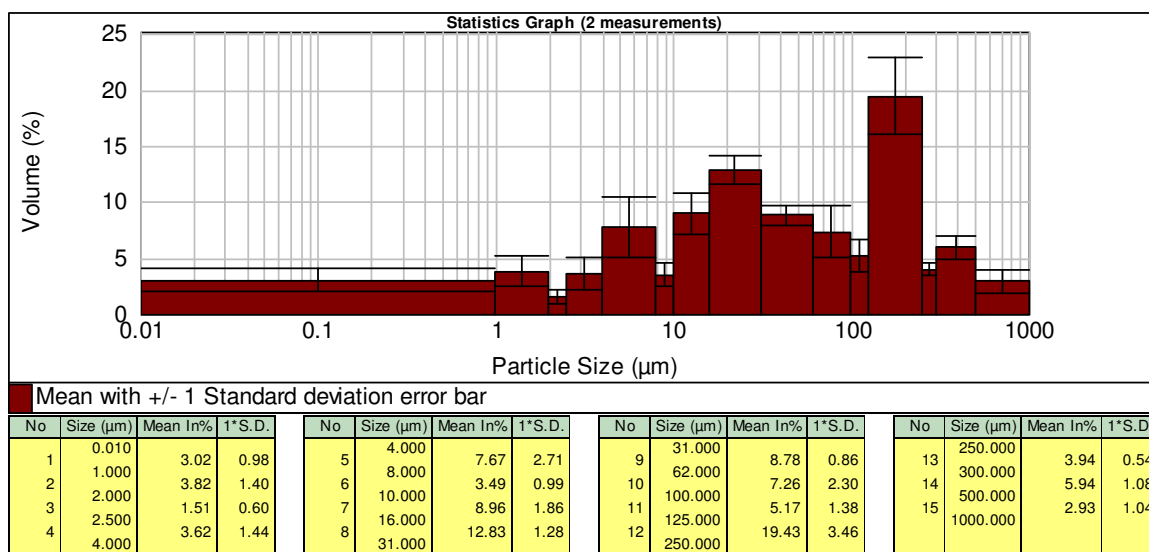
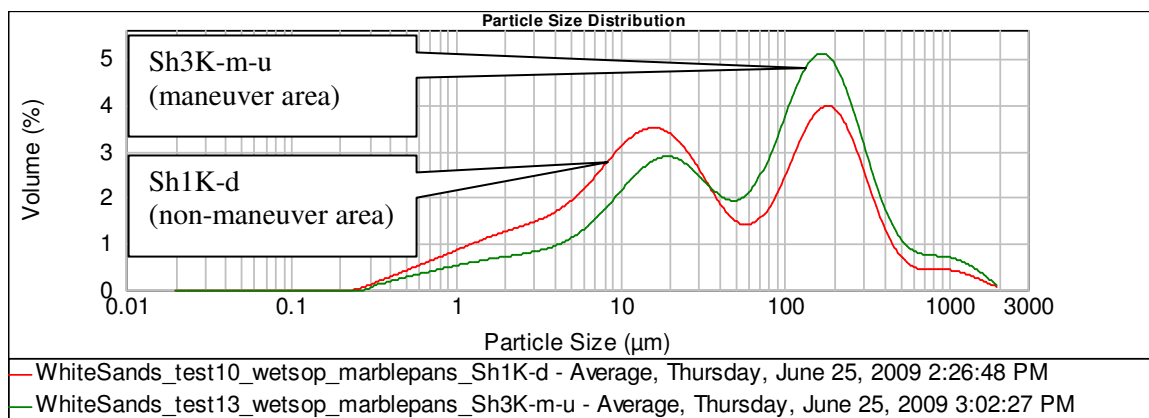


Figure 29: Volume percentage versus particle size distribution for MDCO sites Sh1K-d in the non-maneuver area and Sh3K-m-u in the maneuver area at 1.7 m for Phase 5 (top graph).

Statistics graph and table showing mean and standard deviation values of volume percentages versus particle size distribution for MDCO sites Sh1K-d in the non-maneuver area and Sh3K-m-u in the maneuver area at 1.7 m height for Phase 5 (bottom graph).

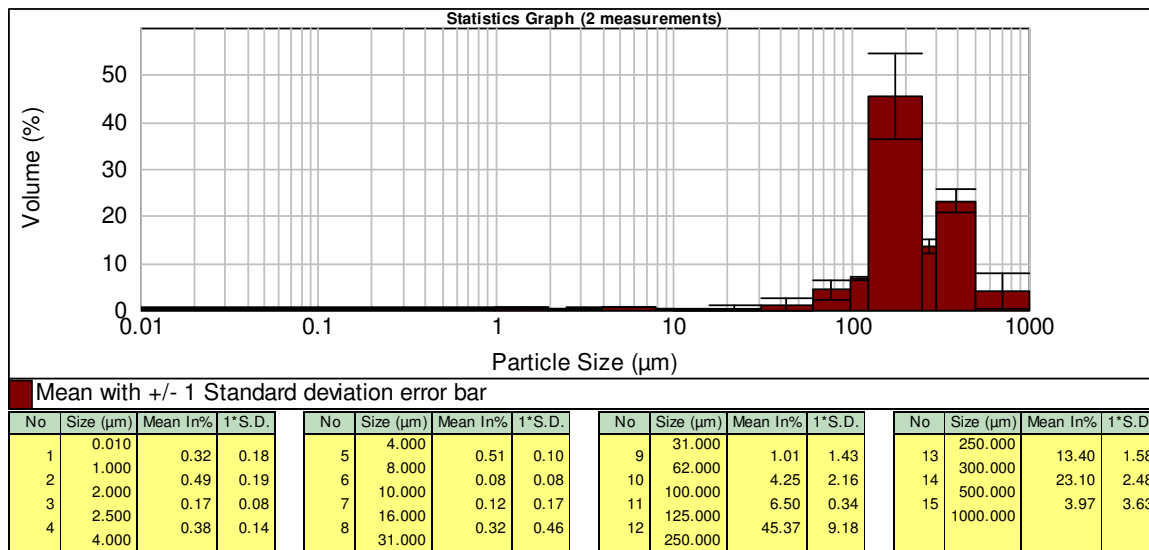
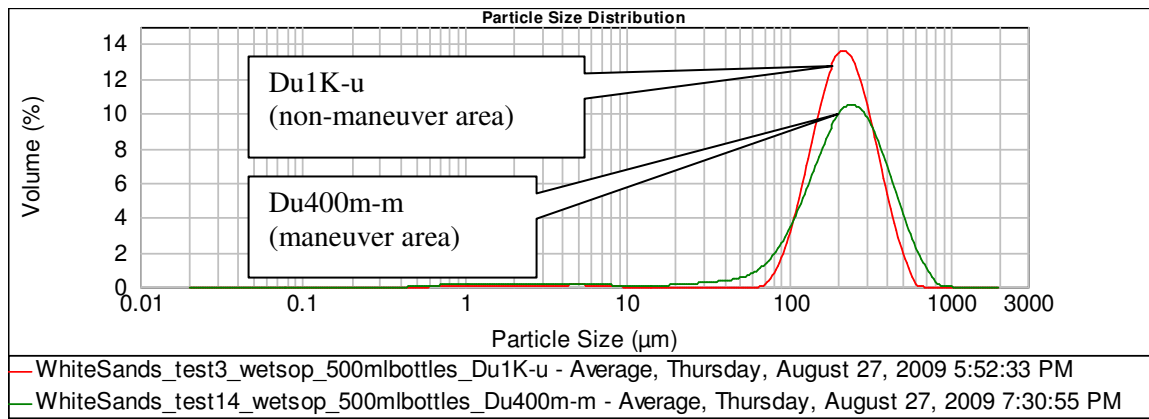


Figure 30: Volume percentage versus particle size distribution for MWAC sites Du1K-u in the non-maneuver area and Du400m-m in the maneuver area at 0.2 m height for Phase 6 (top graph).

Statistics graph showing mean and standard deviation values of volume percentages versus particle size distribution for MWAC sites Du1K-u in the non-maneuver area and Du400m-m in the maneuver area at 0.2 m height for Phase 6 (bottom graph).

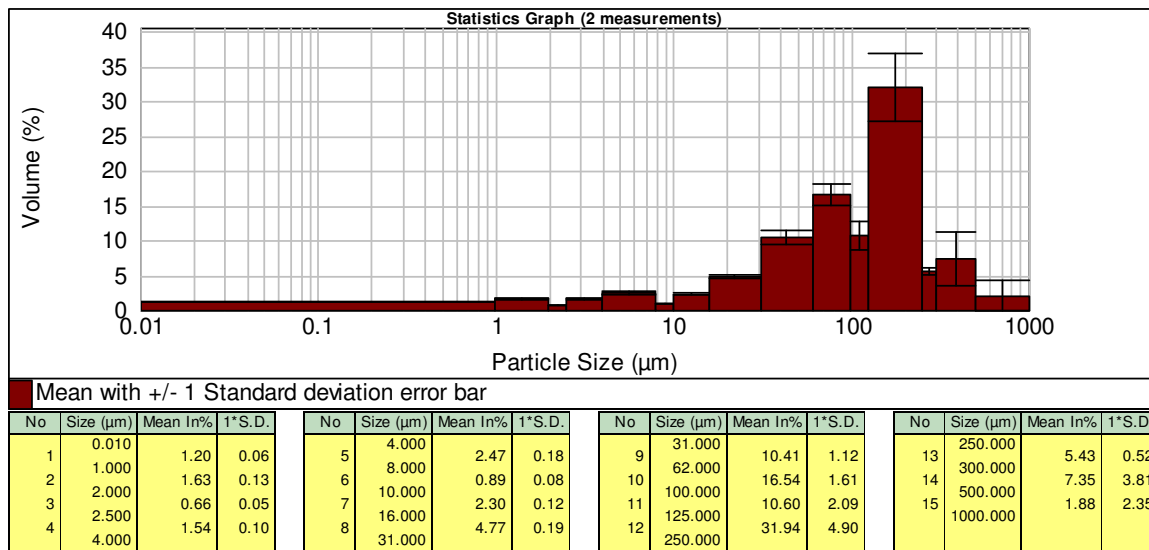
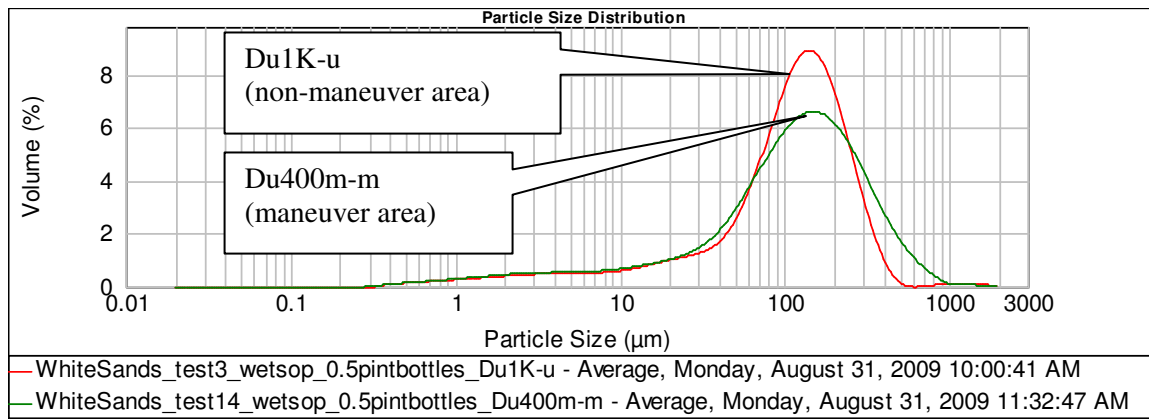


Figure 31: Volume percentage versus particle size distribution for MWAC sites Du1K-u in the non-maneuver area and Du400m-m in the maneuver area at 1 m height for Phase 6 (top graph).

Statistics graph showing mean and standard deviation values of volume percentages versus particle size distribution for MWAC sites Du1K-u in the non-maneuver area and Du400m-m in the maneuver area at 1 m height for Phase 6 (bottom graph).

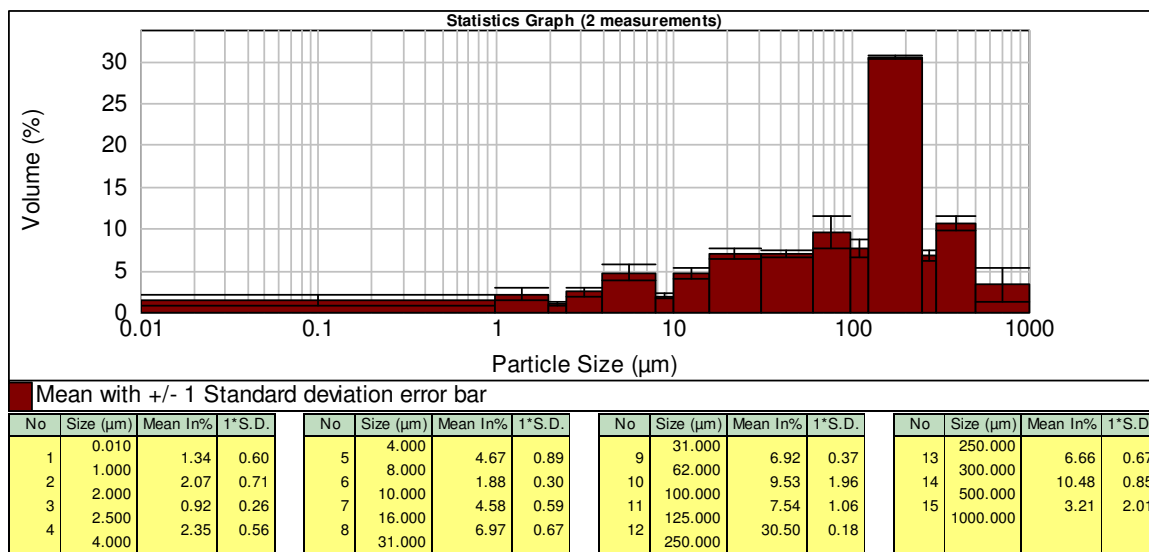
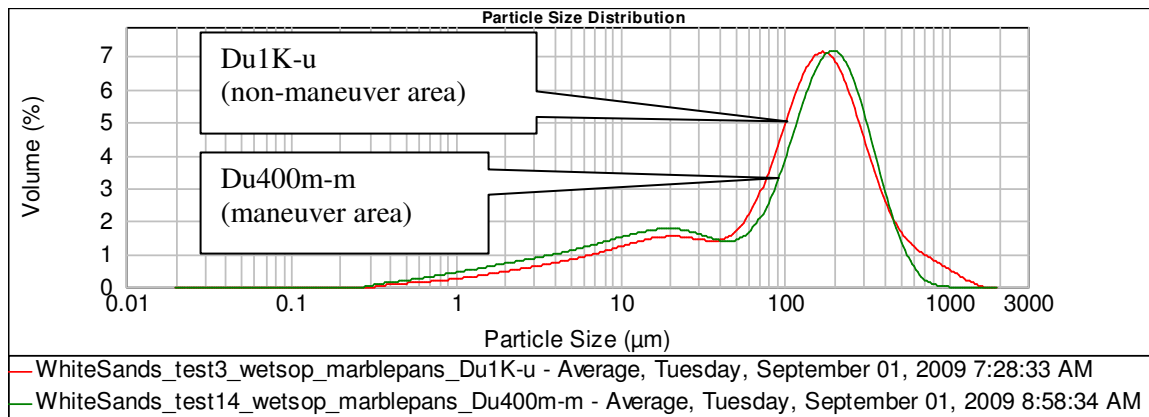


Figure 32: Volume percentage versus particle size distribution for MDCO sites Du1K-u in the non-maneuver area and Du400m-m in the maneuver area at 1.7 m height for Phase 6 (top graph).

Statistics graph and table showing mean and standard deviation values of volume percentages versus particle size distribution for MDCO sites Du1K-u in the non-maneuver area and Du400m-m in the maneuver area at 1.7 m height for Phase 6 (bottom graph).

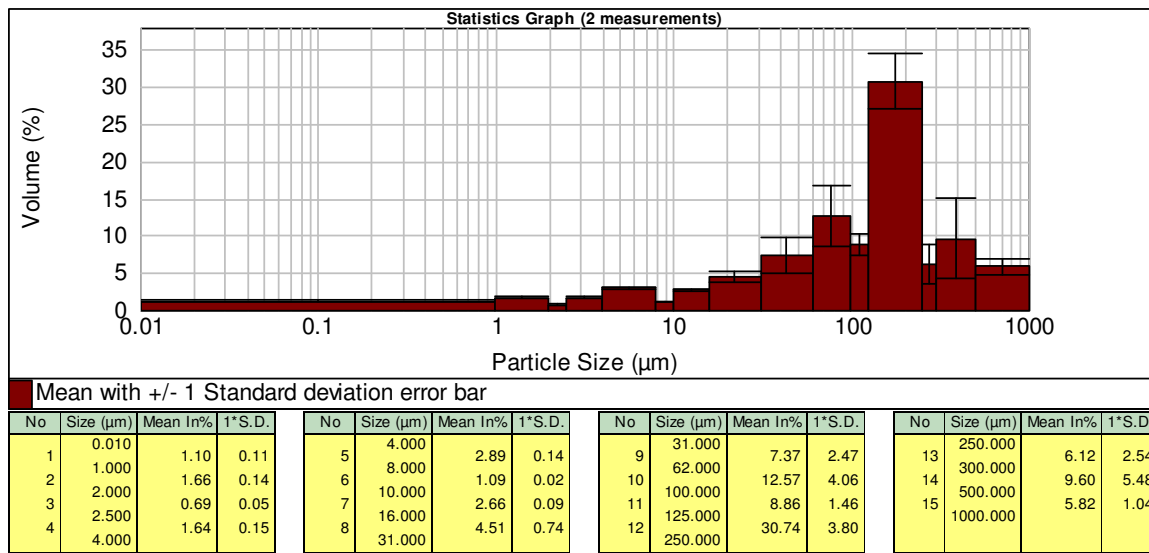
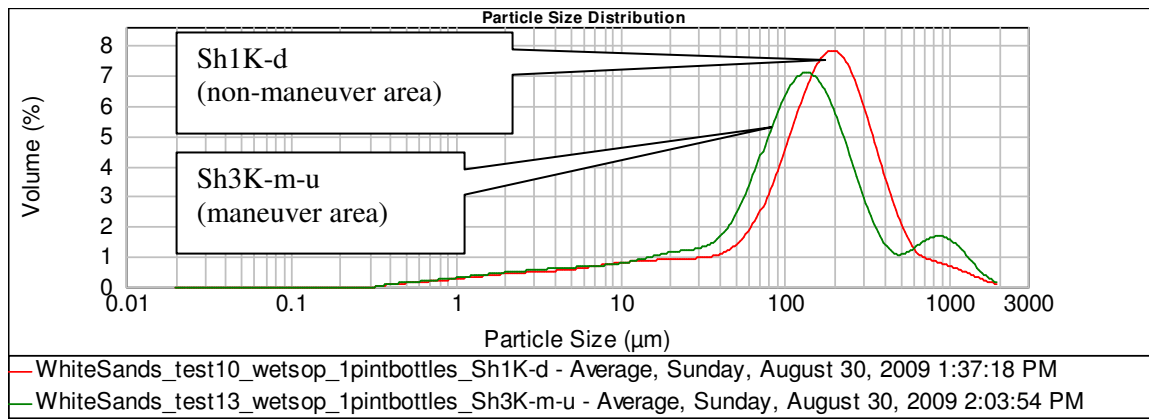


Figure 33: Volume percentage versus particle size distribution for MWAC sites Sh1K-d in the non-maneuver area and Sh3K-m-u in the maneuver area at 0.2 m for Phase 6.

Statistics graph and table showing mean and standard deviation values of volume percentages versus particle size distribution for MWAC sites Sh1K-d in the non-maneuver area and Sh3K-m-u in the maneuver area at 0.2 m height for Phase 6.

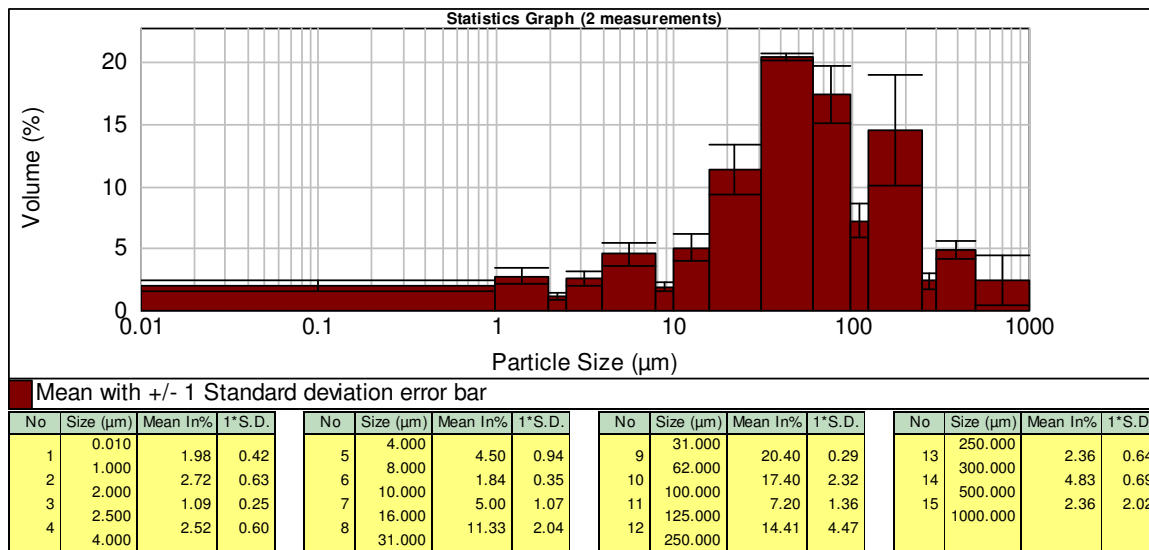
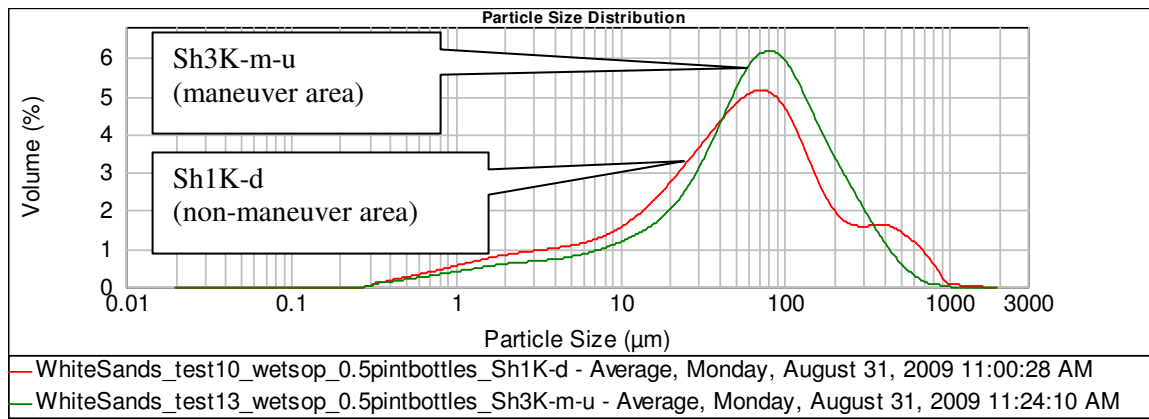


Figure 34: Volume percentage versus particle size distribution for MWAC sites Sh1K-d in the non-maneuver area and Sh3K-m-u in the maneuver area at 1 m for Phase 6 (top graph).

Statistics graph and table showing mean and standard deviation values of volume percentages versus particle size distribution for MWAC sites Sh1K-d in the non-maneuver area and Sh3K-m-u in the maneuver area at 1 m height for Phase 6 (bottom graph).

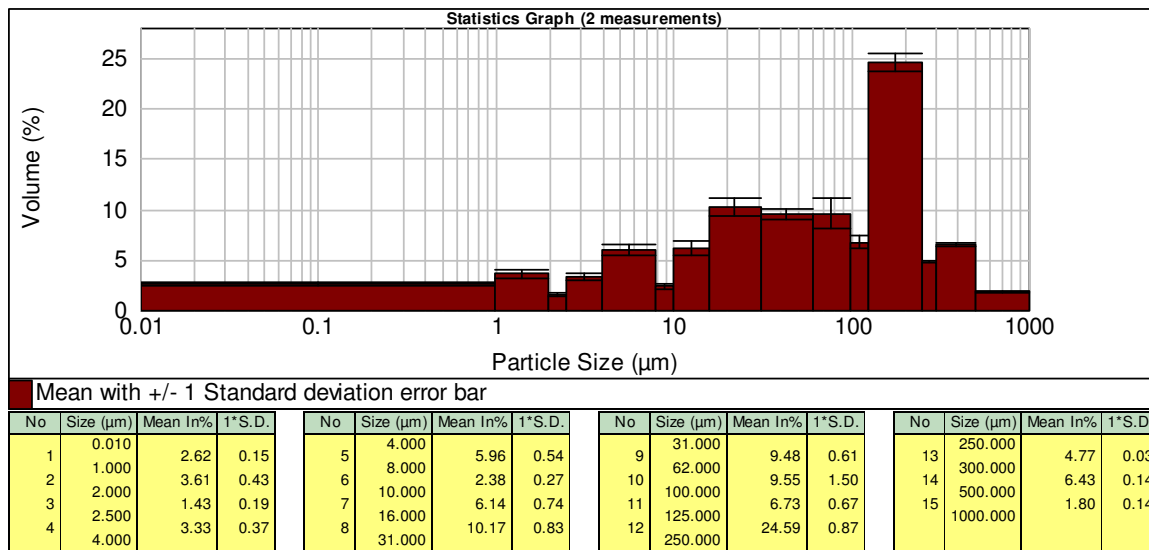
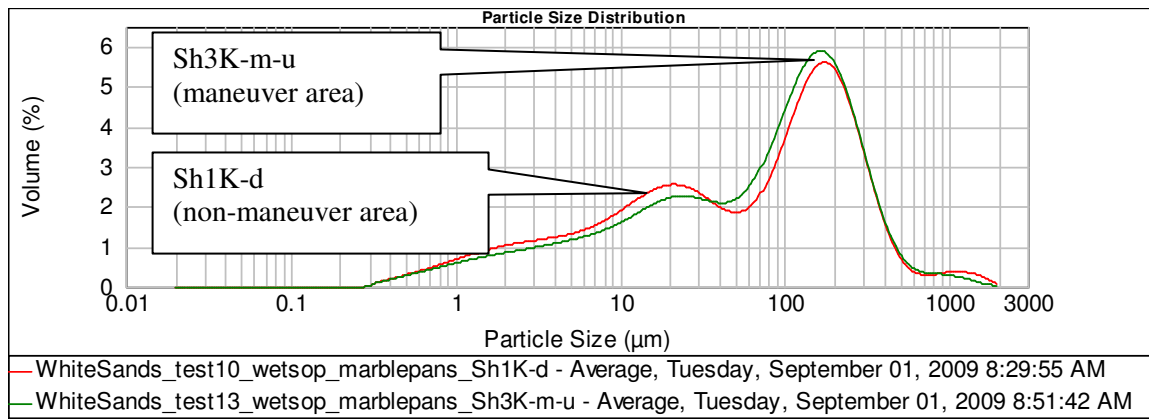


Figure 35: Volume percentage versus particle size distribution for MDCO sites Sh1K-d in the non-maneuver area and Sh3K-m-u in the maneuver area at 1.7 m height for Phase 6 (top graph).

Statistics graph and table showing mean and standard deviation values of volume percentages versus particle size distribution for MDCO sites Sh1K-d in the non-maneuver area and Sh3K-m-u in the maneuver area at 1.7 m height for Phase 6 (bottom graph).

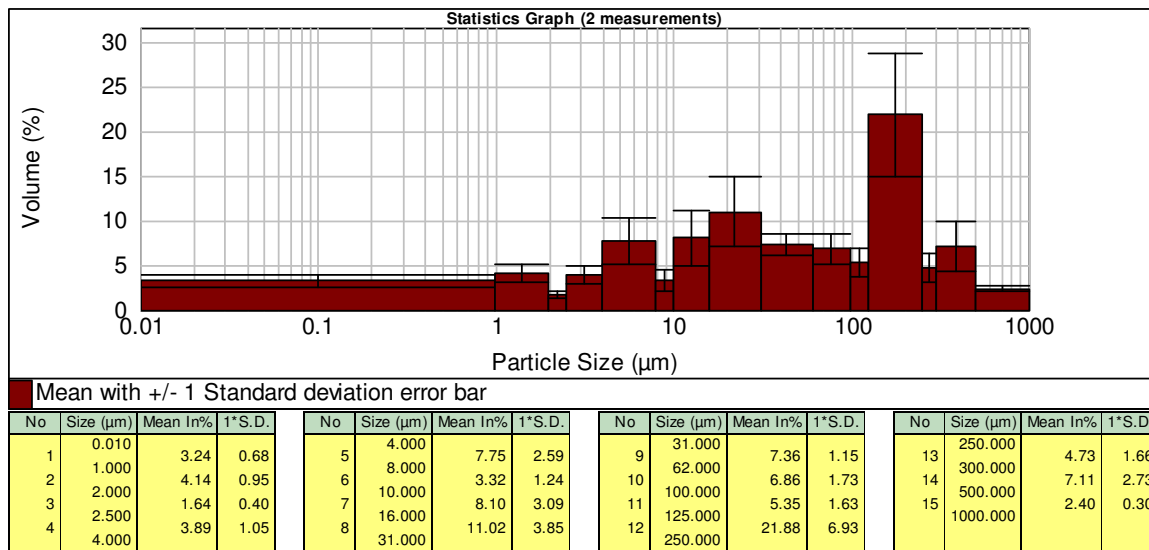
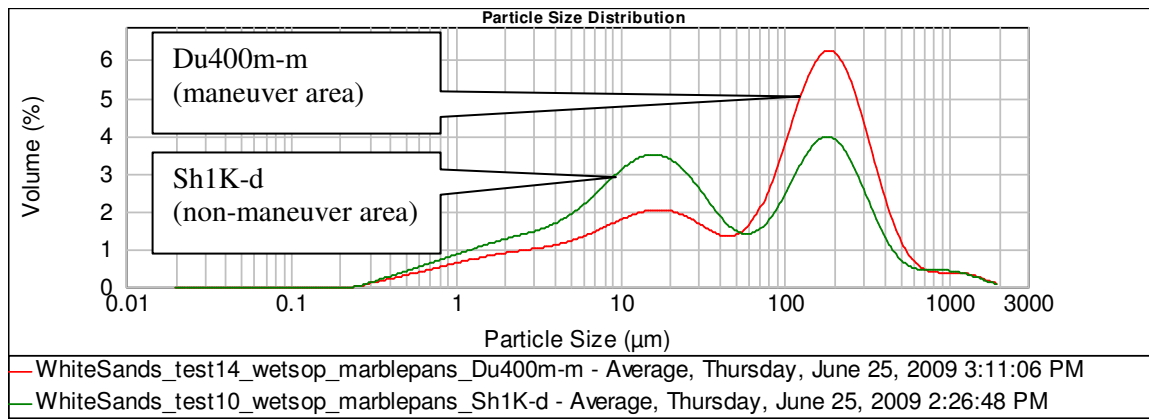


Figure 36: Volume percentage versus particle size distribution for MDCO sites Du400m-m in the maneuver area and Sh1K-d in the non-maneuver area at 1.7 m height for Phase 5 (top graph).

Statistics graph and table showing mean and standard deviation values of volume percentages versus particle size distribution for MDCO sites Du400m-m in the maneuver area and Sh1K-d in the non-maneuver area at 1.7 m height for Phase 5 (bottom graph).

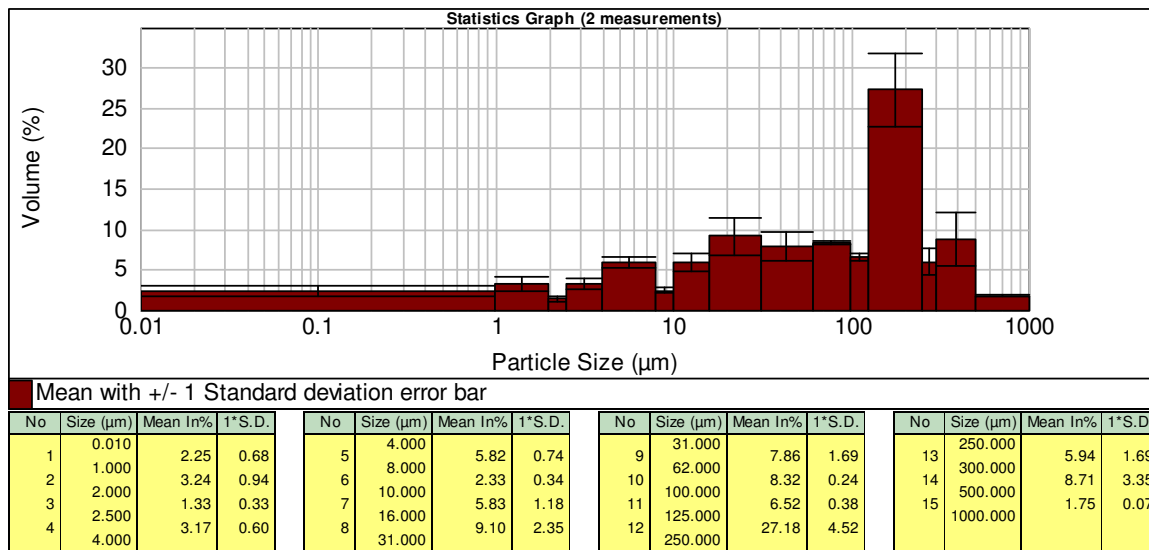
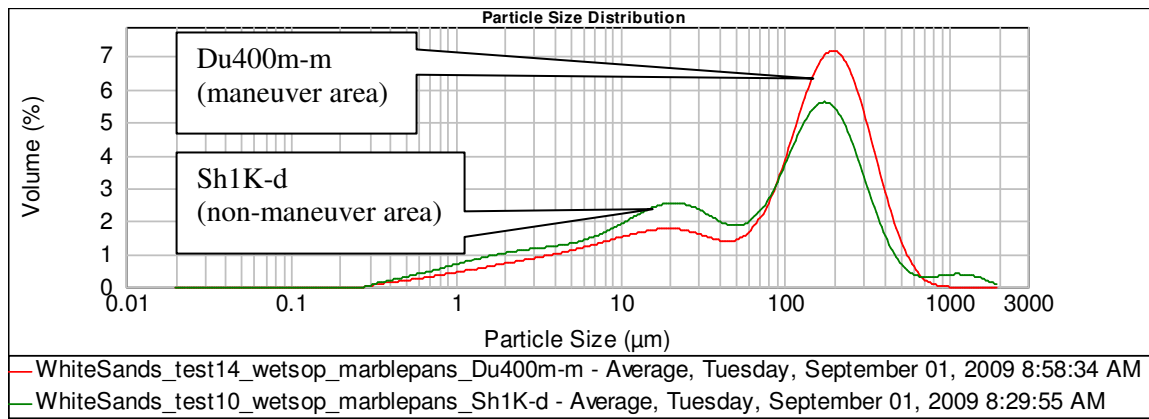


Figure 37: Volume percentage versus particle size distribution for MDCO sites Du400m-m in the maneuver area and Sh1K-d in the non-maneuver area at 1.7 m height for Phase 6 (top graph).

Statistics graph and table showing mean and standard deviation values of volume percentages versus particle size distribution for MDCO sites Du400m-m in the maneuver area and Sh1K-d in the non-maneuver area at 1.7 m height for Phase 6 (bottom graph).

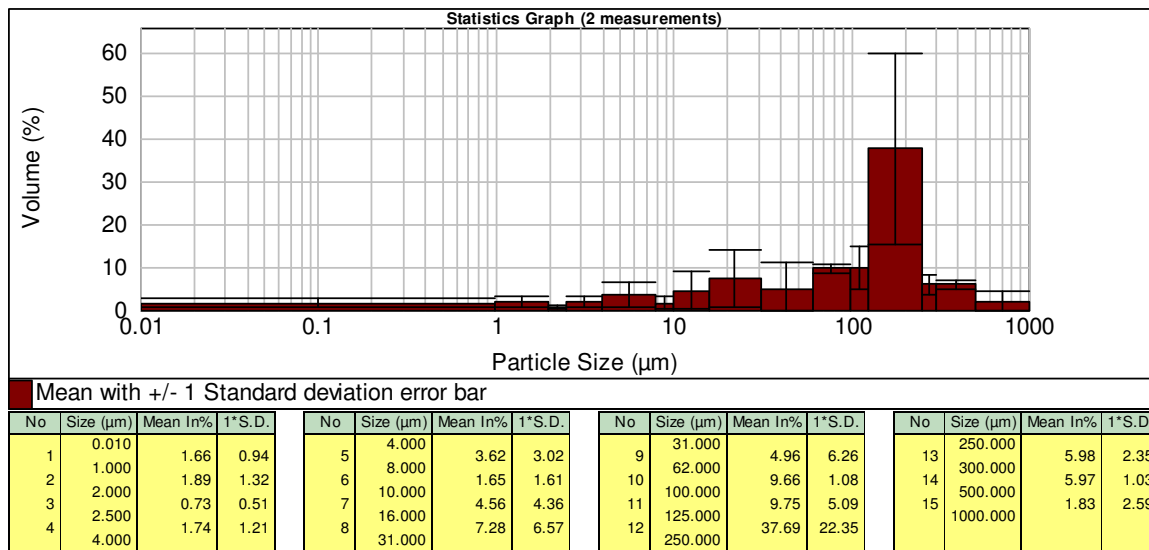
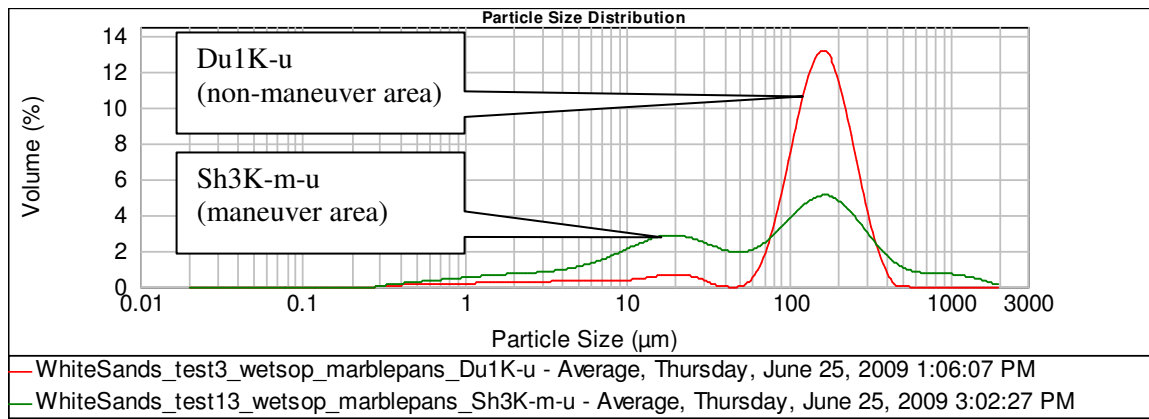


Figure 38: Volume percentage versus particle size distribution for MDCO sites Du1K-u in the maneuver area and Sh3K-m-u in the non-maneuver area at 1.7 m height for Phase 5 (top graph).

Statistics graph and table showing mean and standard deviation values of volume percentages versus particle size distribution for MDCO sites Du1K-u in the maneuver area and Sh3K-m-u in the non-maneuver area at 1.7 m height for Phase 5 (bottom graph).

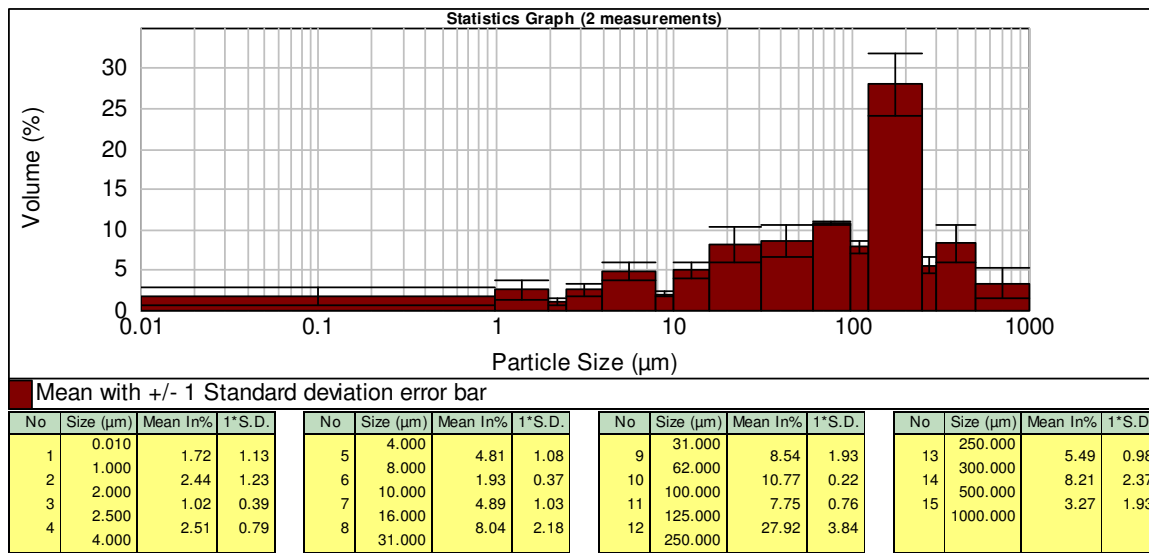
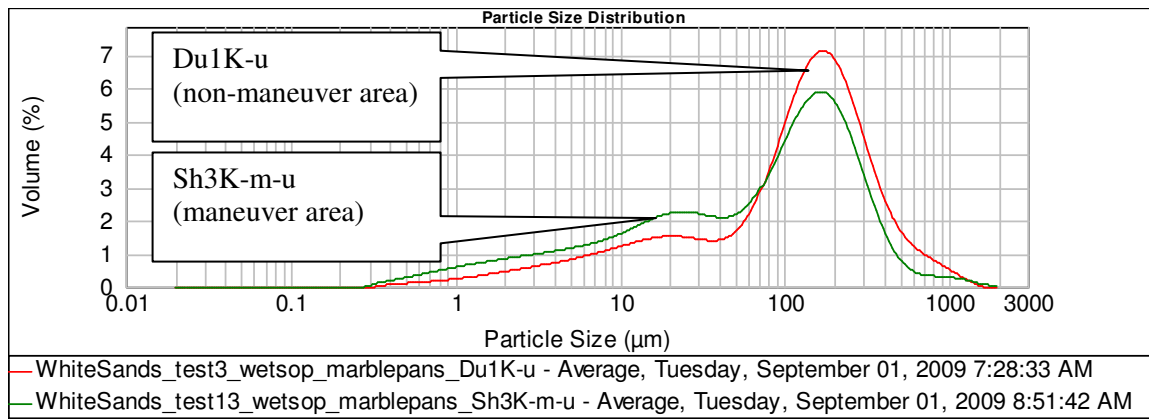


Figure 39: Volume percentage versus particle size distribution for MDCO sites Du1K-u in the maneuver area and Sh3K-m-u in the non-maneuver area at 1.7 m height for Phase 6 (top graph).

Statistics graph and table showing mean and standard deviation values of volume percentages versus particle size distribution for MDCO sites Du1K-u in the maneuver area and Sh3K-m-u in the non-maneuver area at 1.7 m height for Phase 6 (bottom graph).

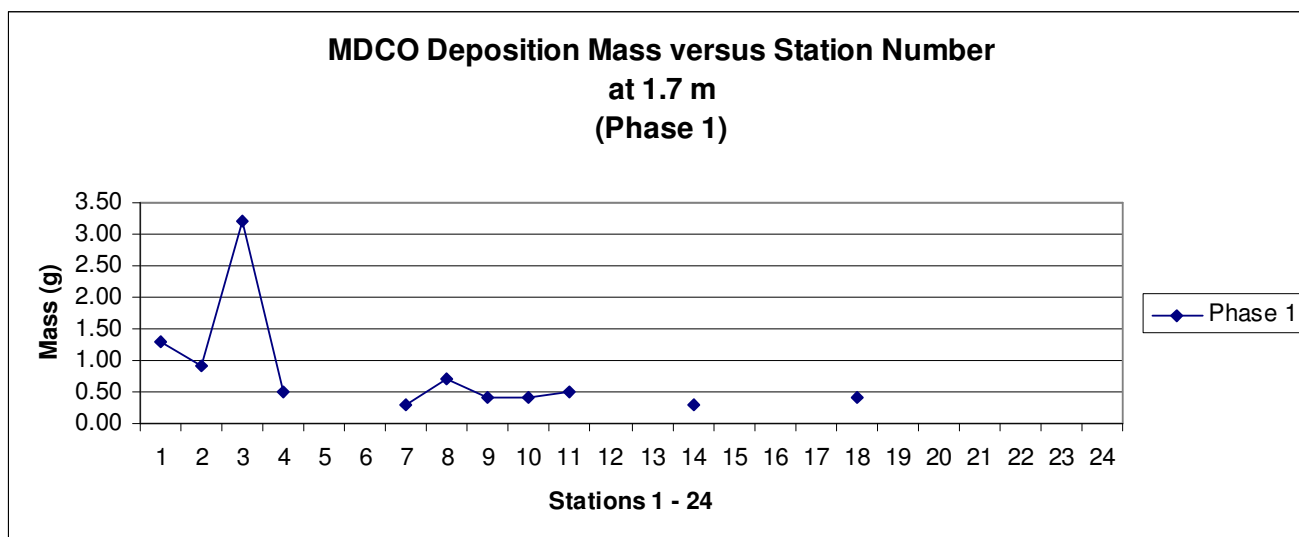


Figure 40: MDCO deposition mass (g) values versus station number for Phase 1.

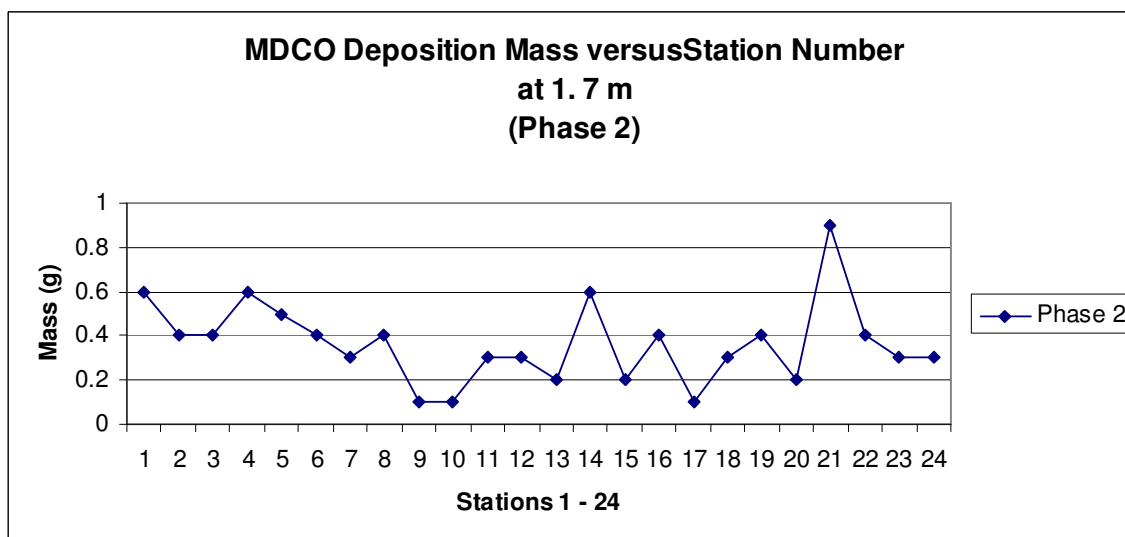


Figure 41: MDCO deposition mass (g) values versus station number for Phase 2.

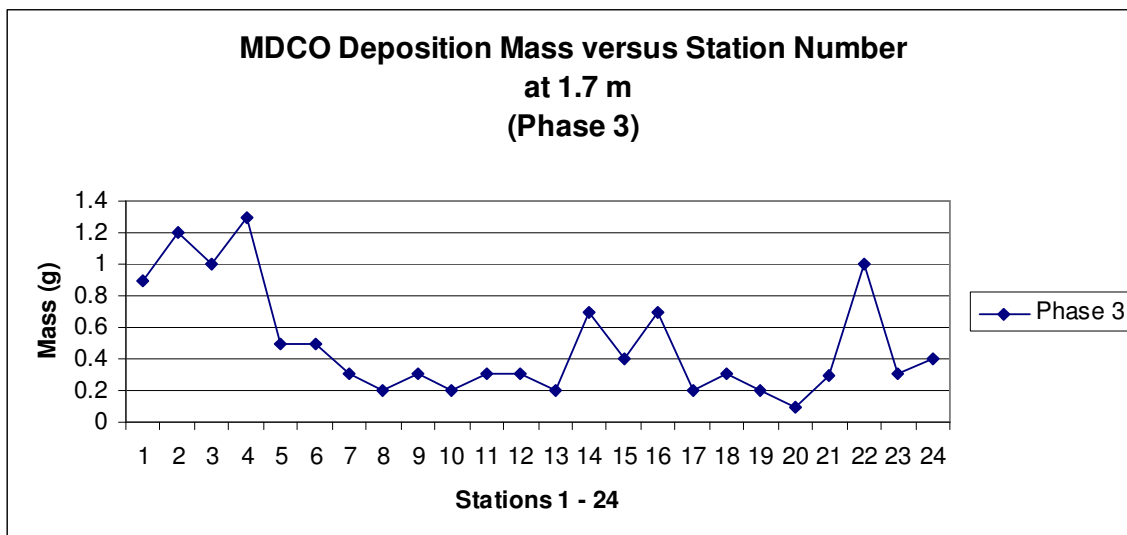


Figure 42: MDCO deposition mass (g) values versus station number for Phase 3.

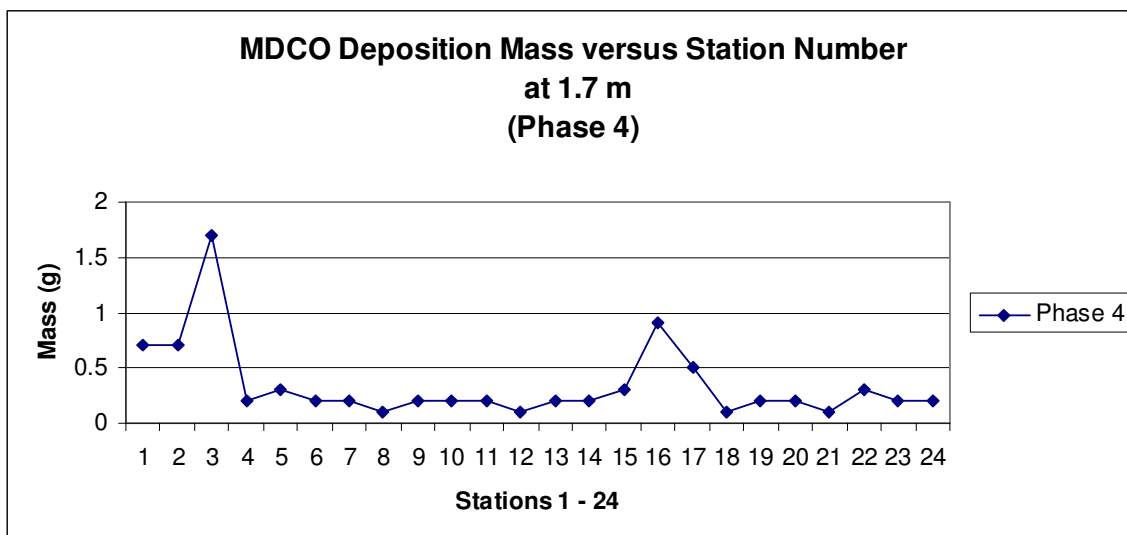


Figure 43: MDCO deposition mass (g) values versus station number for Phase 4.

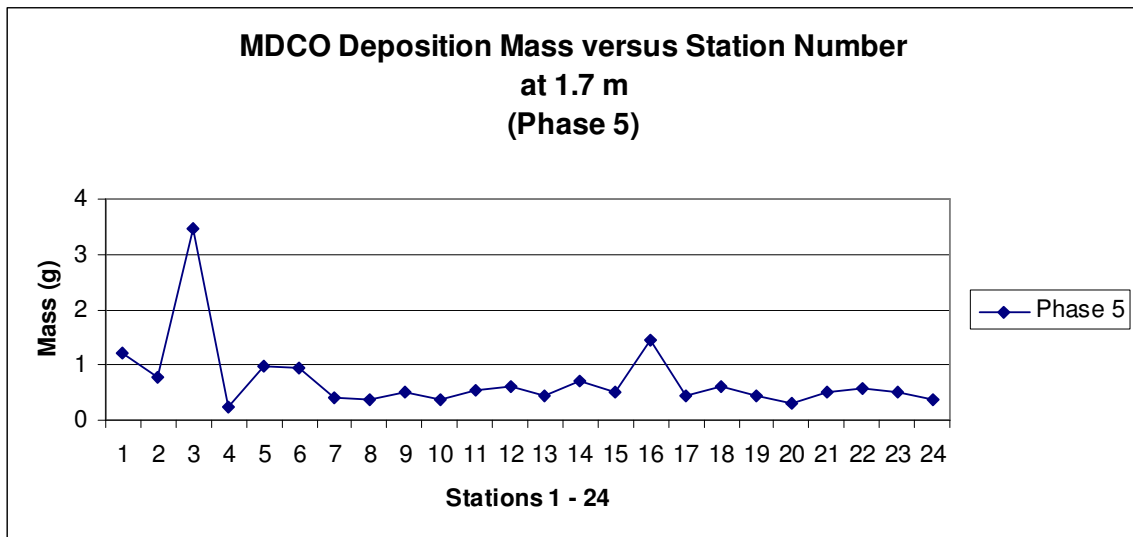


Figure 44: MDCO deposition mass (g) values versus station number for Phase 5.

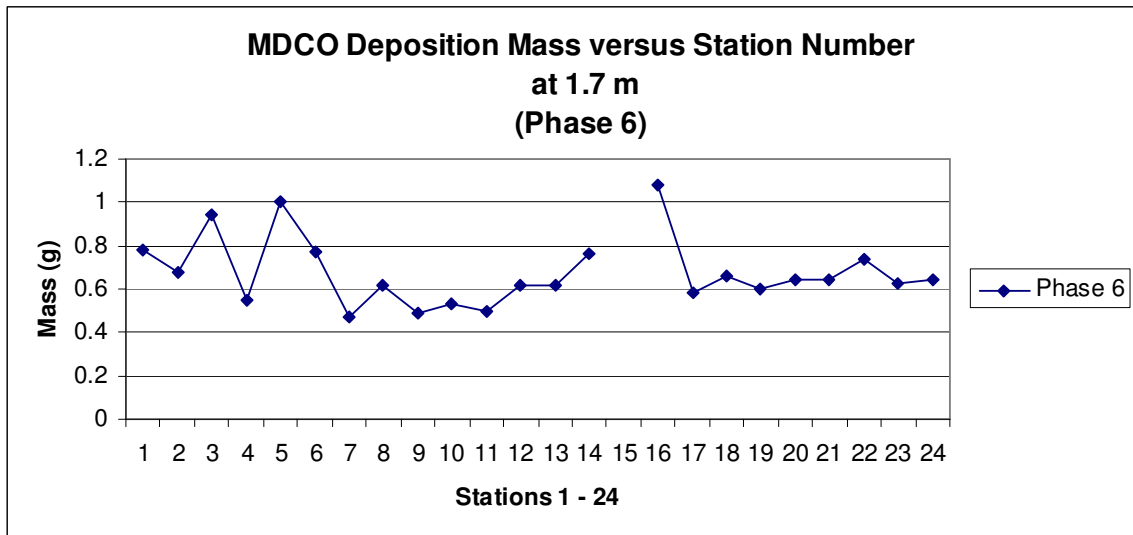


Figure 45: MDCO deposition mass (g) values versus station number for Phase 6.

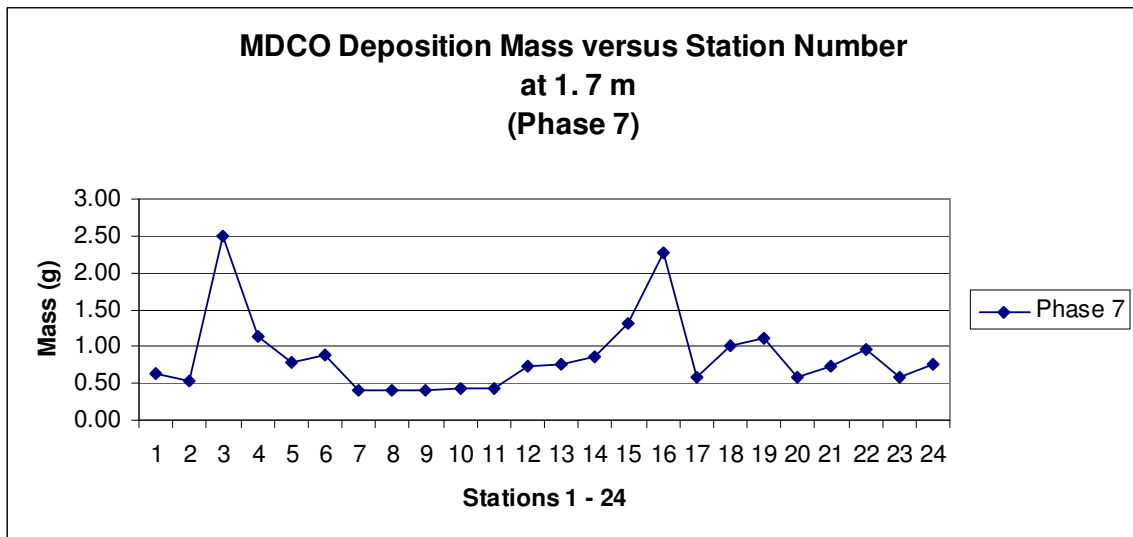


Figure 46: MDCO deposition mass (g) values versus station number for Phase 7.

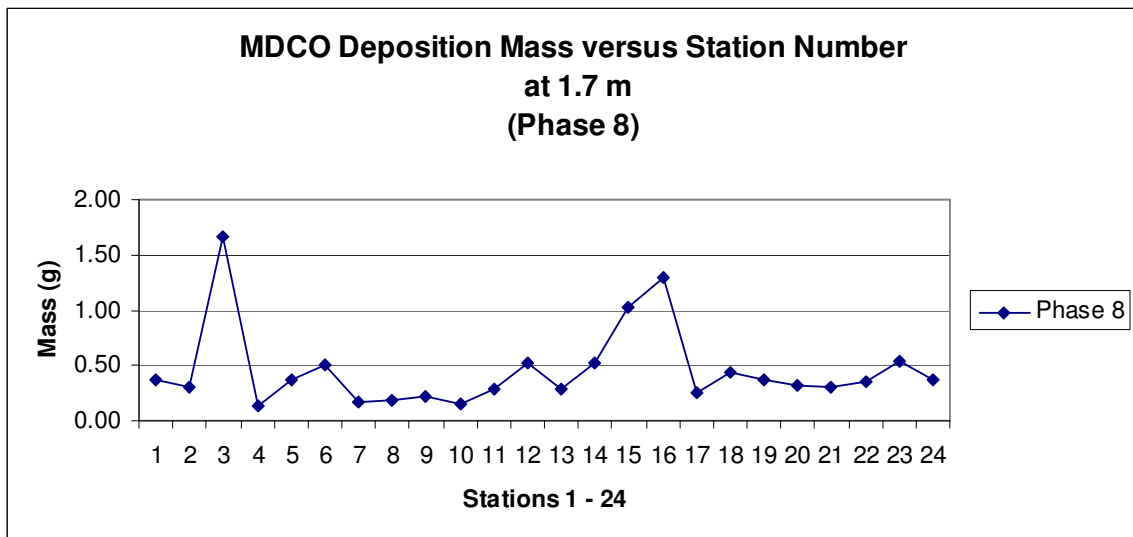


Figure 47: MDCO deposition mass (g) values versus station number for Phase 8.

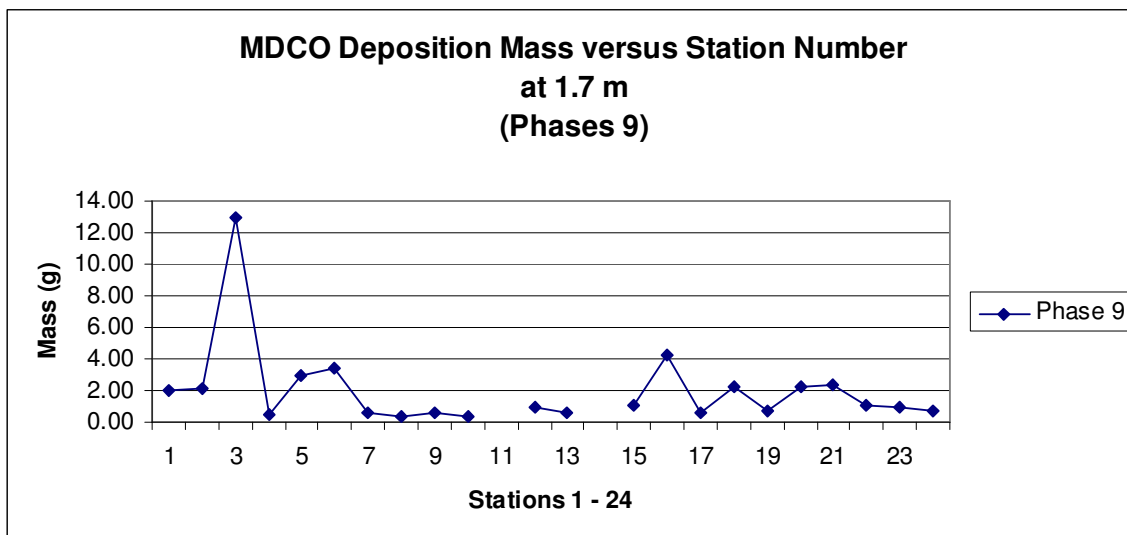


Figure 48: MDCO deposition mass (g) values versus station number for Phase 9.

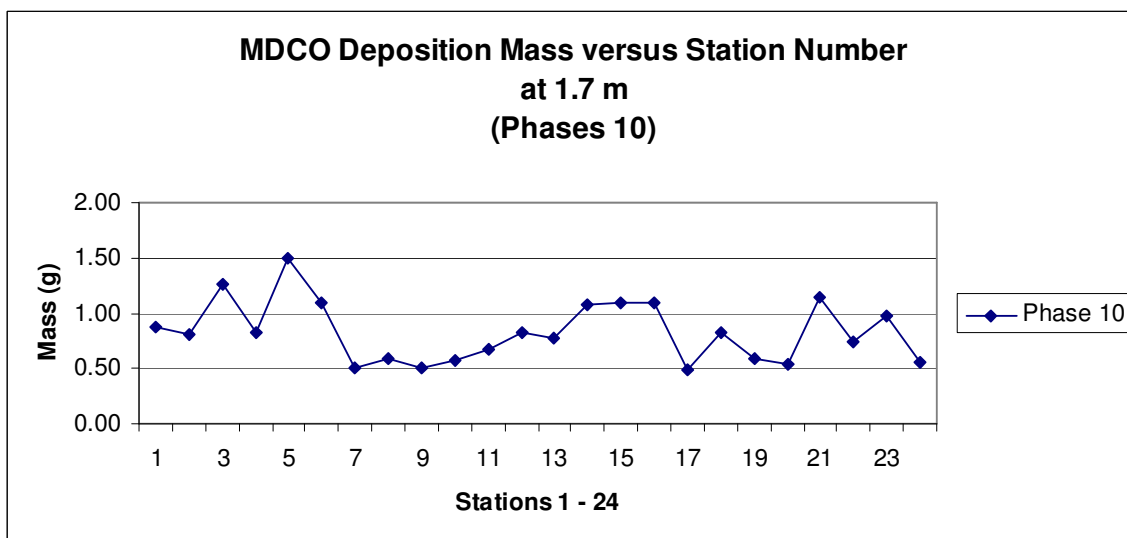


Figure 49: MDCO deposition mass (g) values versus station number for Phase 10.

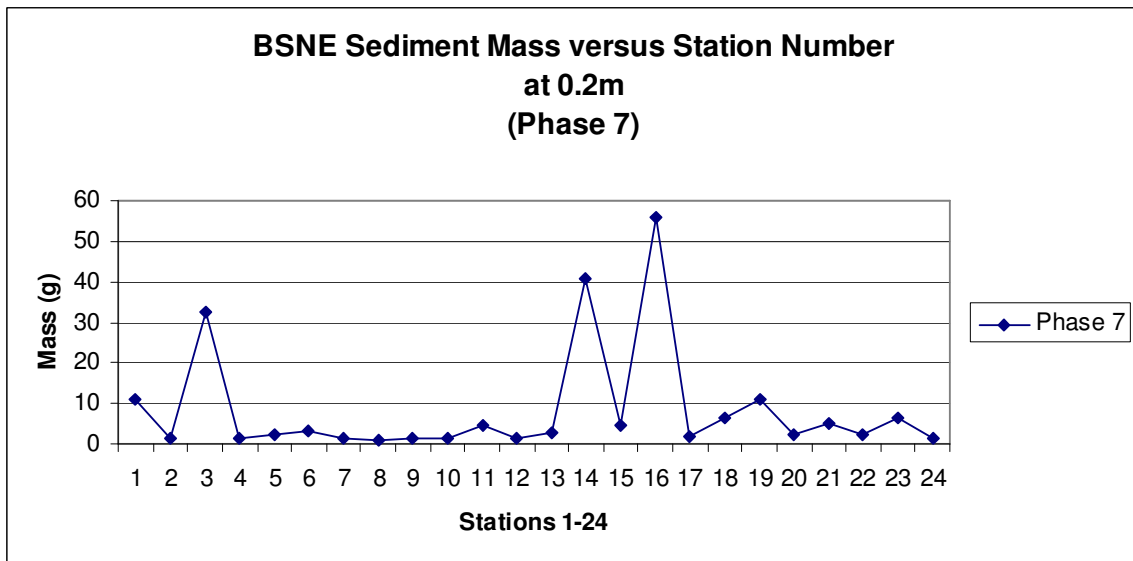


Figure 50: BSNE horizontal sediment mass (g) values versus station number at 0.2 m for Phase 7.

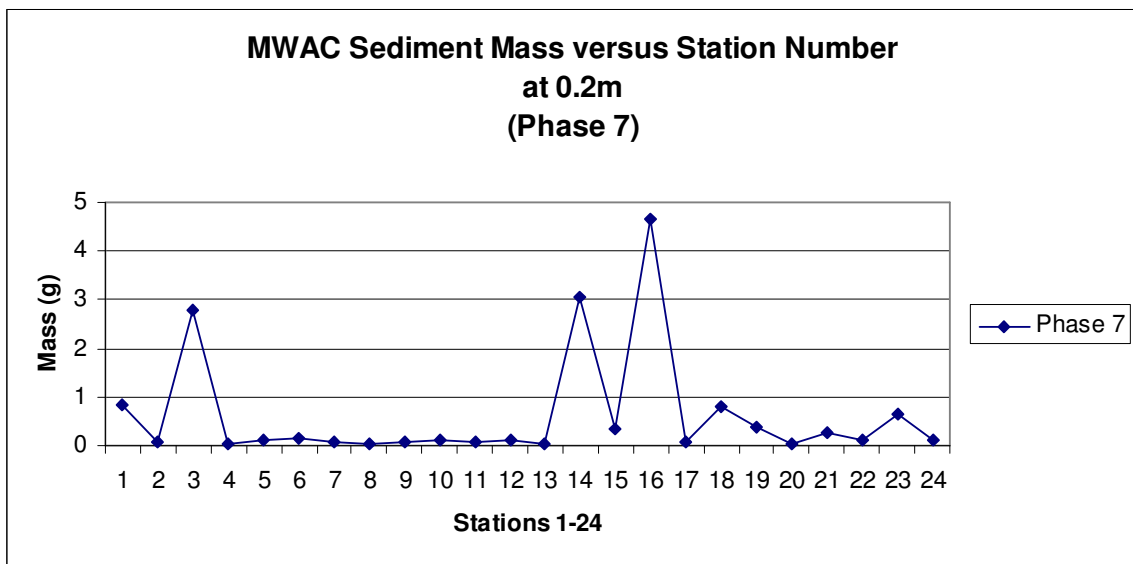


Figure 51: MWAC horizontal sediment mass (g) values versus station number at 0.2 m for Phase 7.

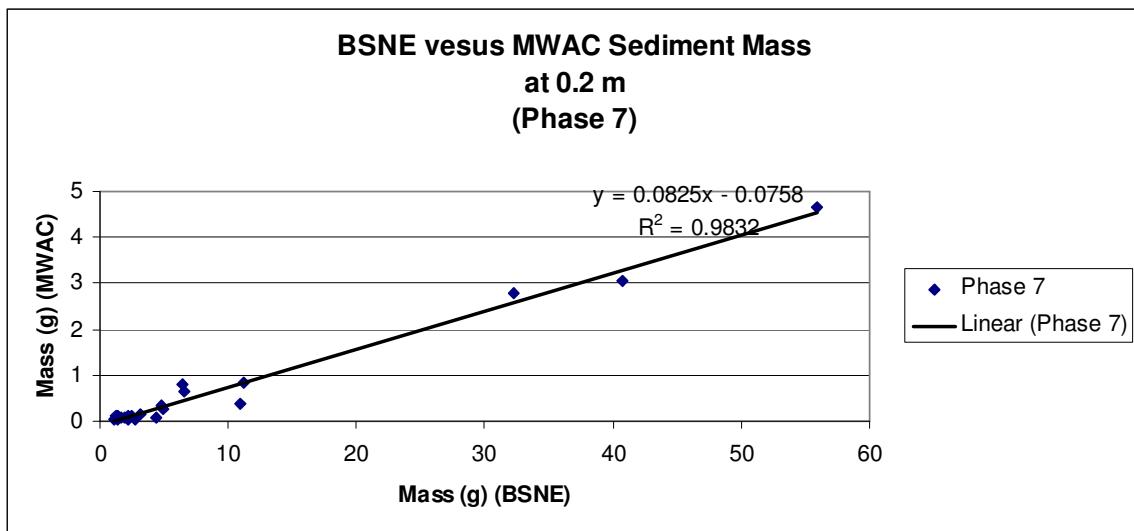


Figure 52: BSNE versus MWAC horizontal sediment mass (g) scattergram at 0.2 m for Phase 7.

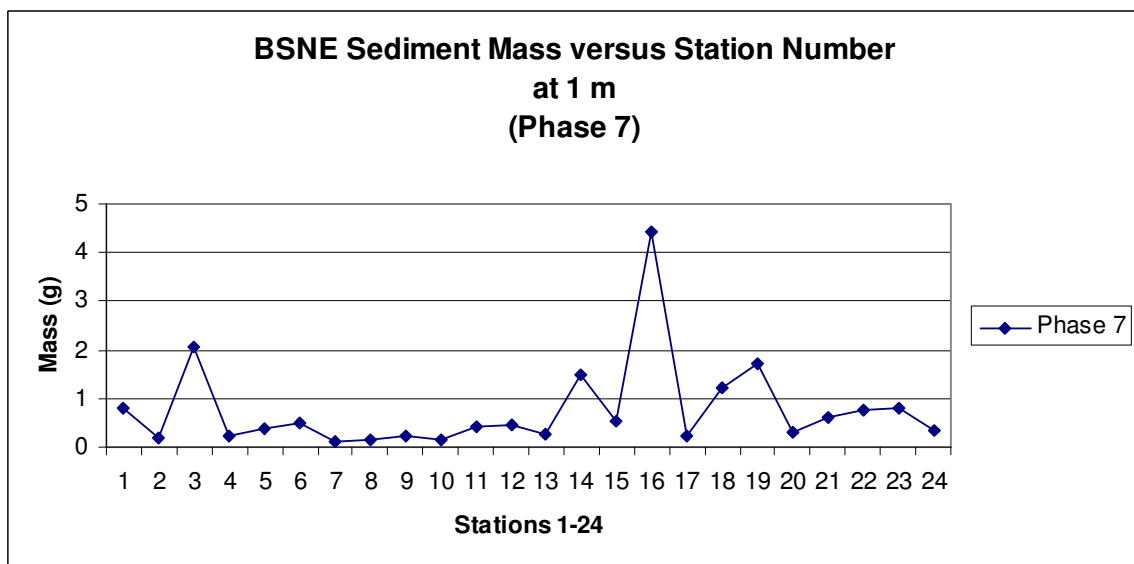


Figure 53: BSNE horizontal sediment mass (g) values versus station number at 1 m for Phase 7.

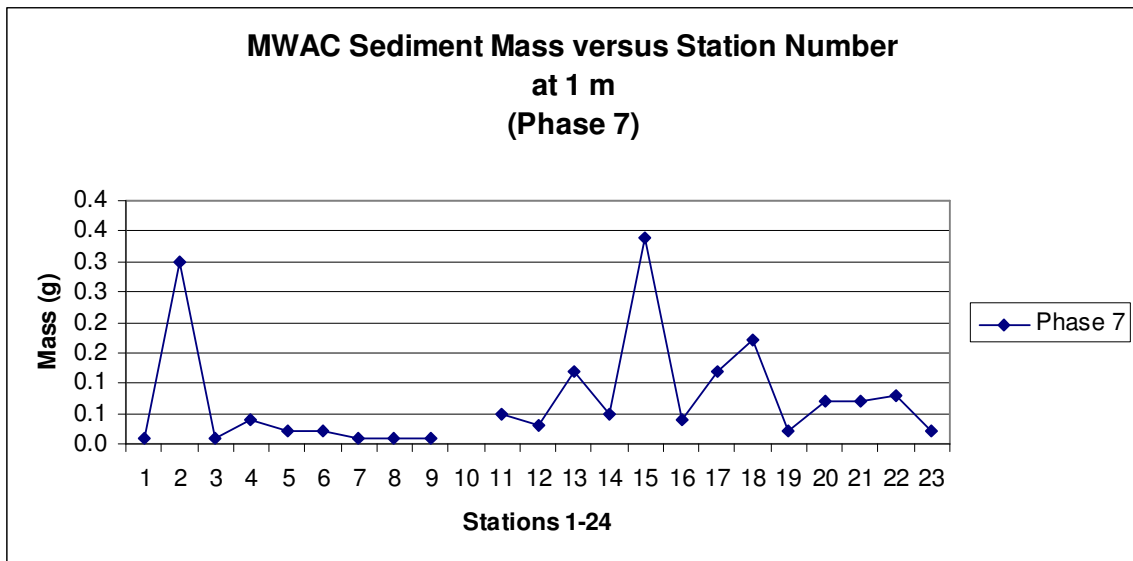


Figure 54: MWAC horizontal sediment mass (g) values versus station number at 1 m for Phase 7.

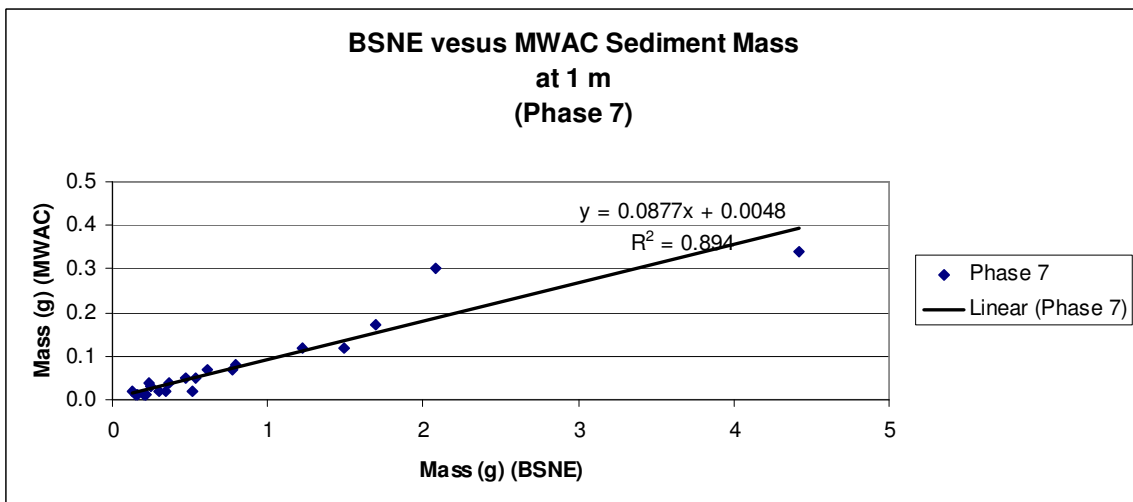


Figure 55: BSNE versus MWAC horizontal sediment mass (g) scattergram at 1 m for Phase 7.

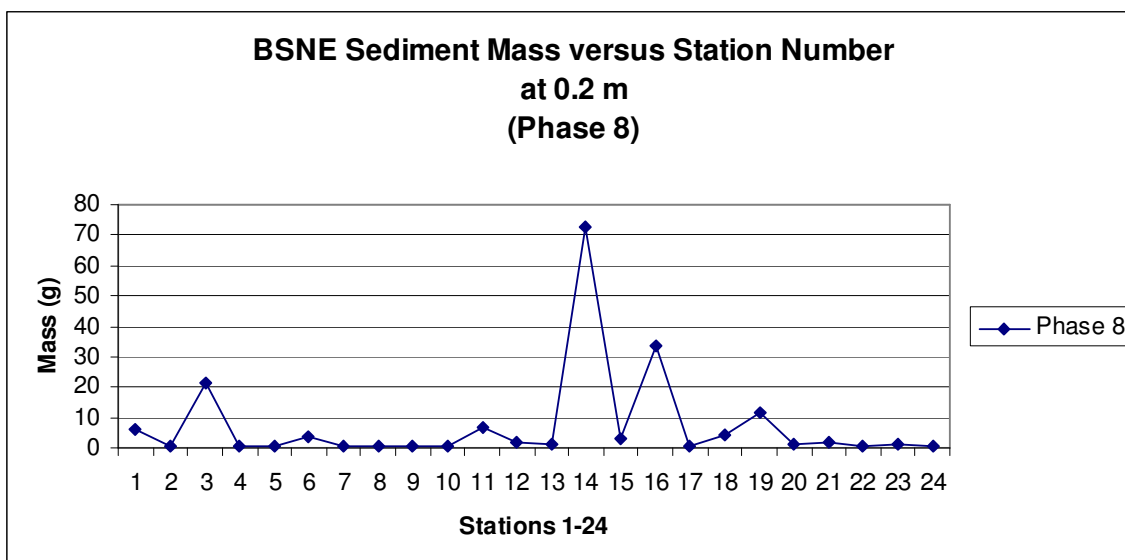


Figure 56: BSNE horizontal sediment mass (g) values versus station number at 0.2 m for Phase 8.

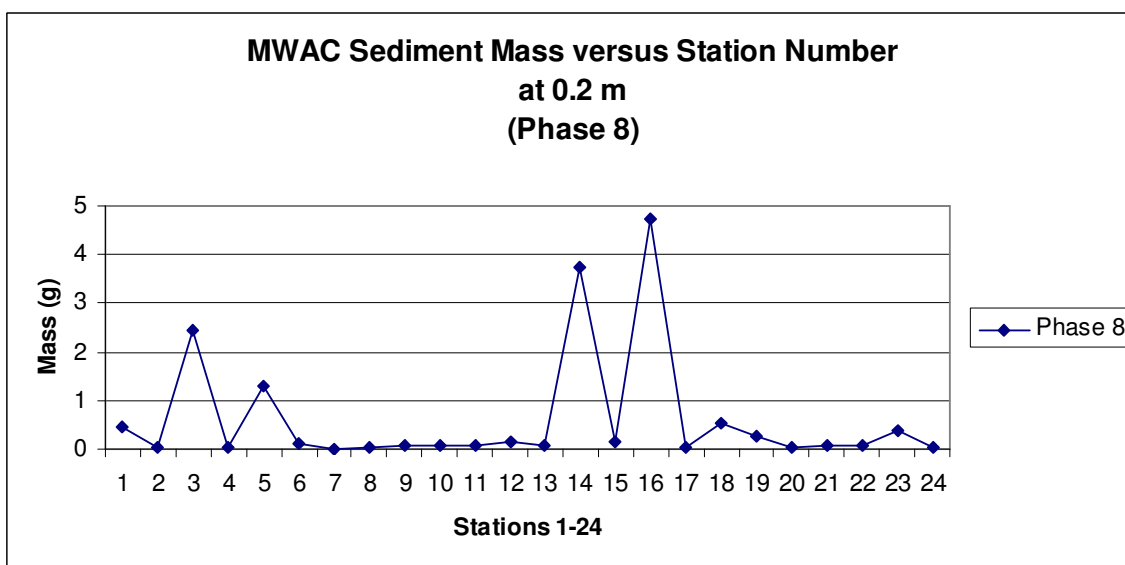


Figure 57: MWAC horizontal sediment mass (g) values versus station number at 0.2 m for Phase 8.

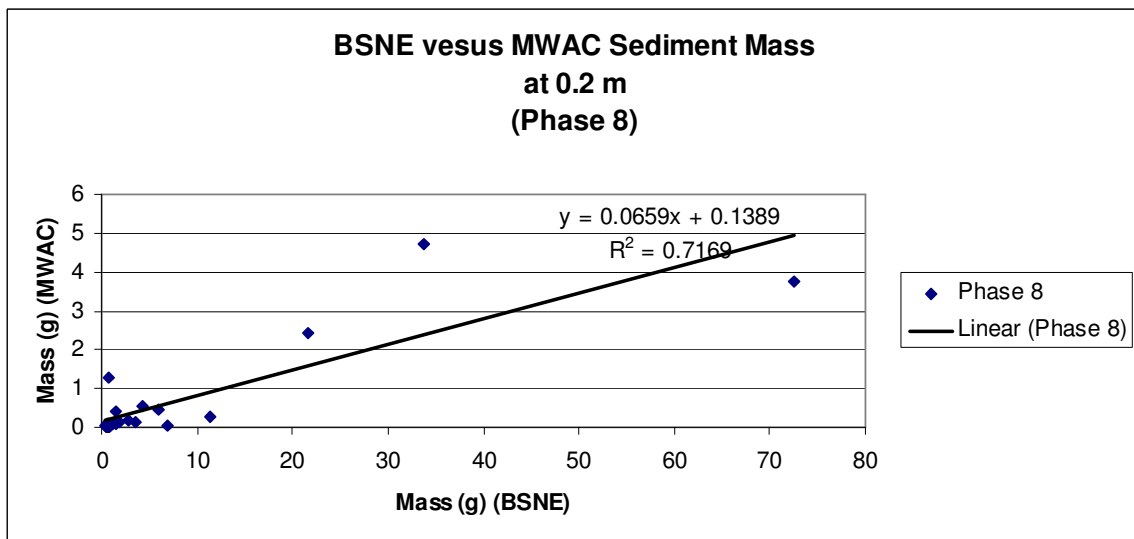


Figure 58: BSNE versus MWAC horizontal sediment mass (g) scattergram at 0.2 m for Phase 8.

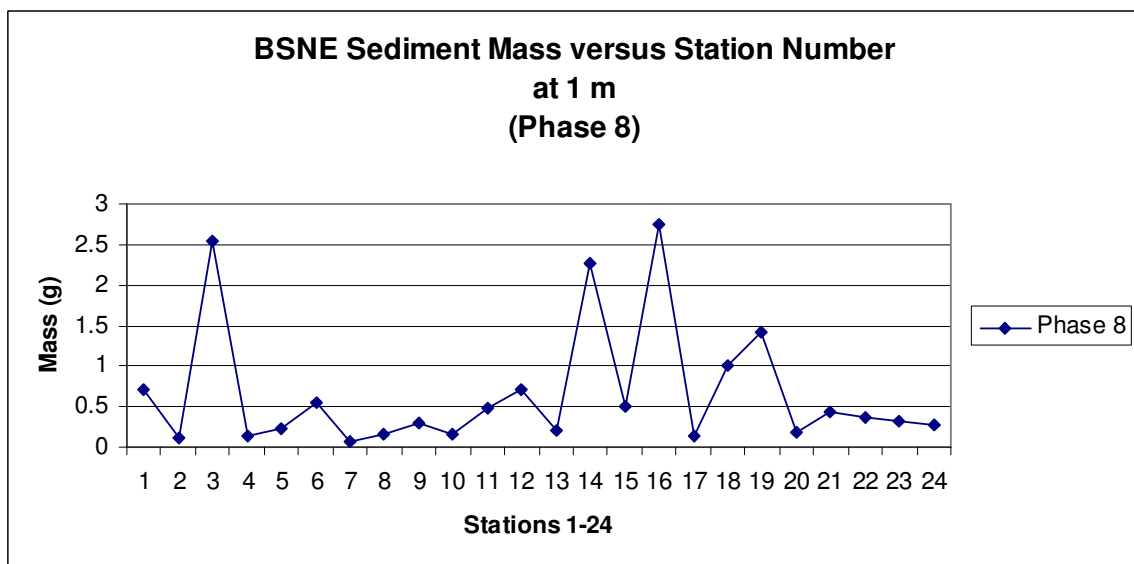


Figure 59: BSNE horizontal sediment mass (g) values versus station number at 1 m for Phase 8.

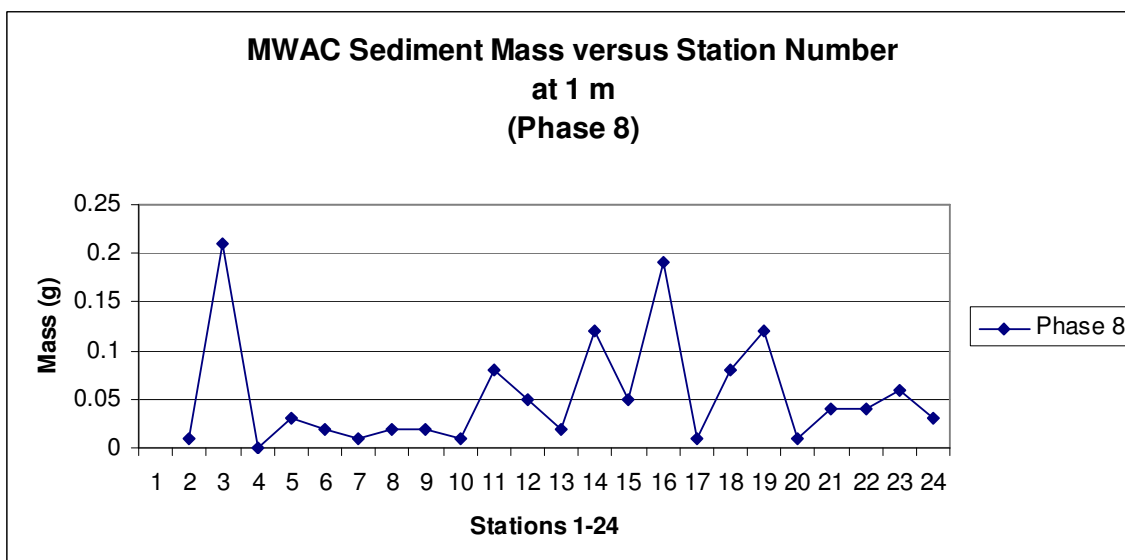


Figure 60: MWAC horizontal sediment mass (g) values versus station number at 1 m for Phase 8.

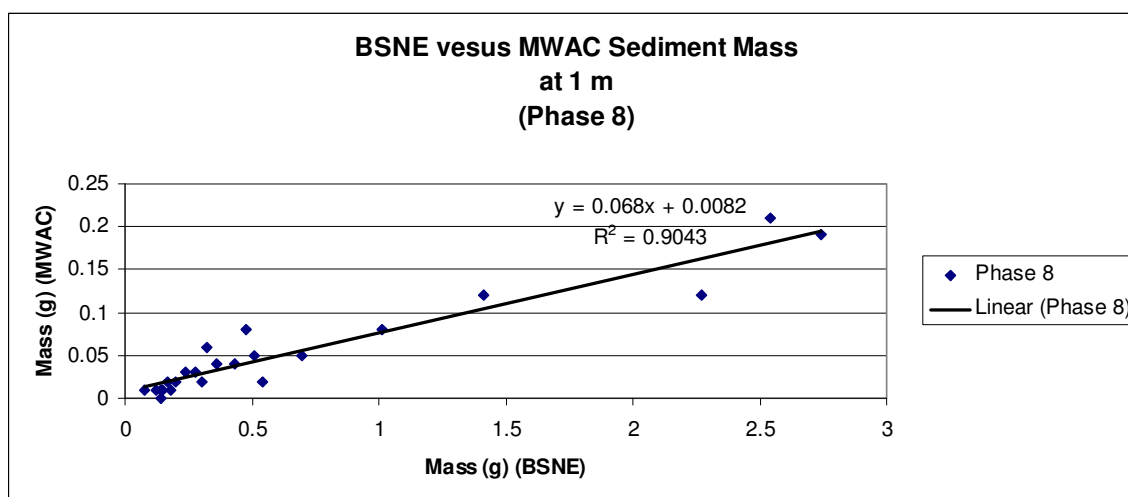


Figure 61: BSNE versus MWAC horizontal sediment mass (g) scattergram at 1 m for Phase 8.

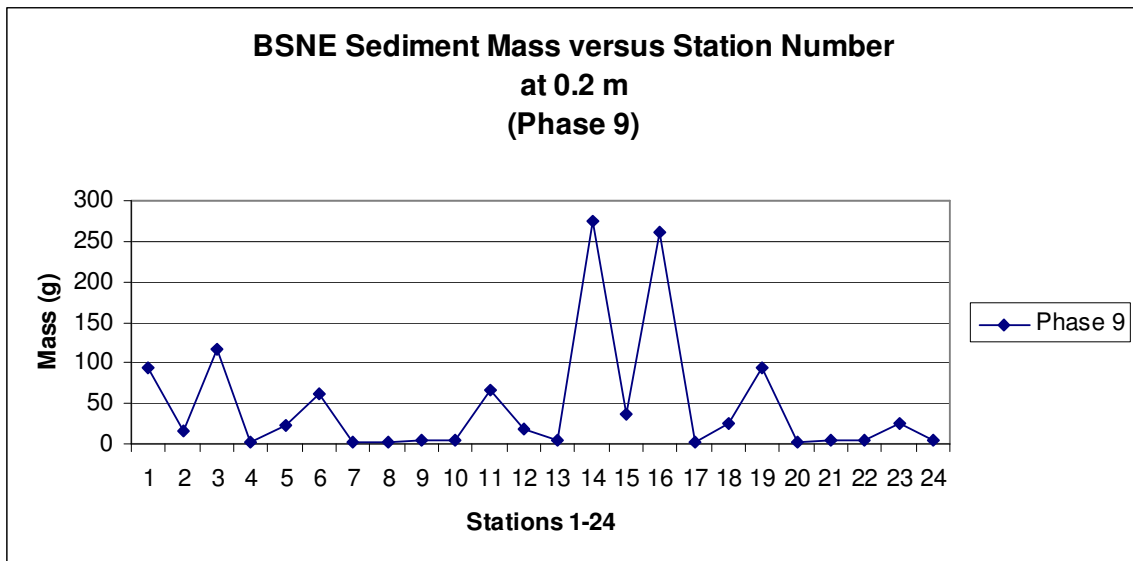


Figure 62: BSNE horizontal sediment mass (g) values versus station number at 0.2 m for Phase 9.

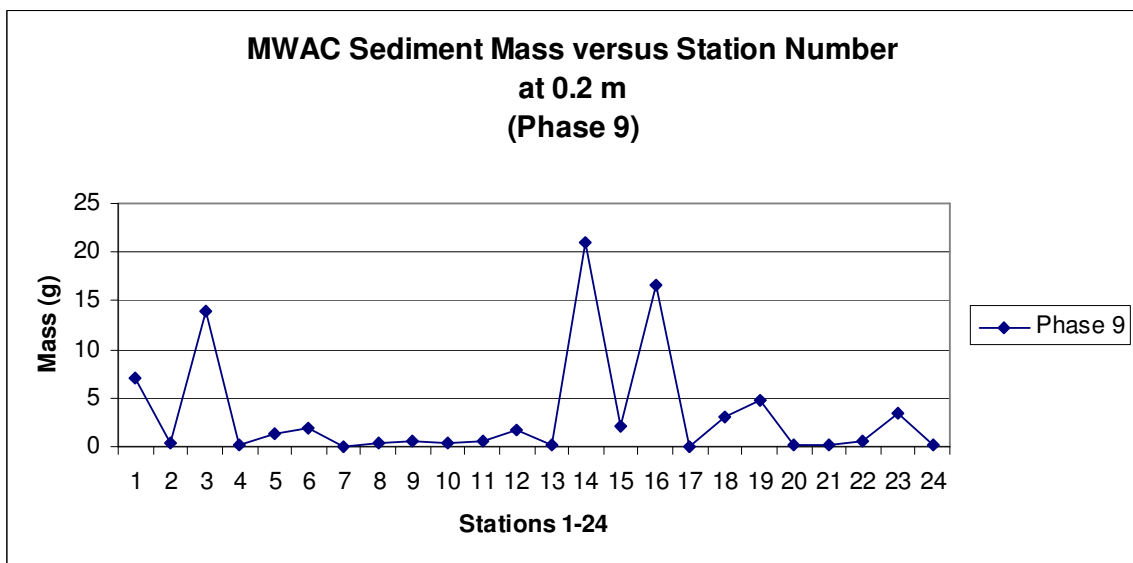


Figure 63: MWAC horizontal sediment mass (g) values versus station number at 0.2 m for Phase 9.

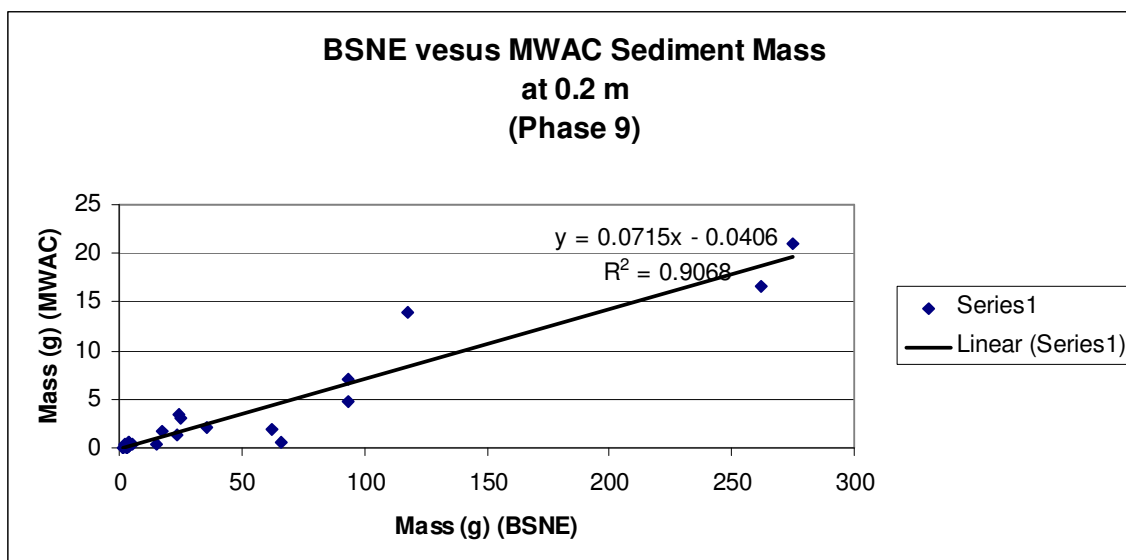


Figure 64: BSNE versus MWAC horizontal sediment mass (g) scattergram at 0.2 m for Phase 9.

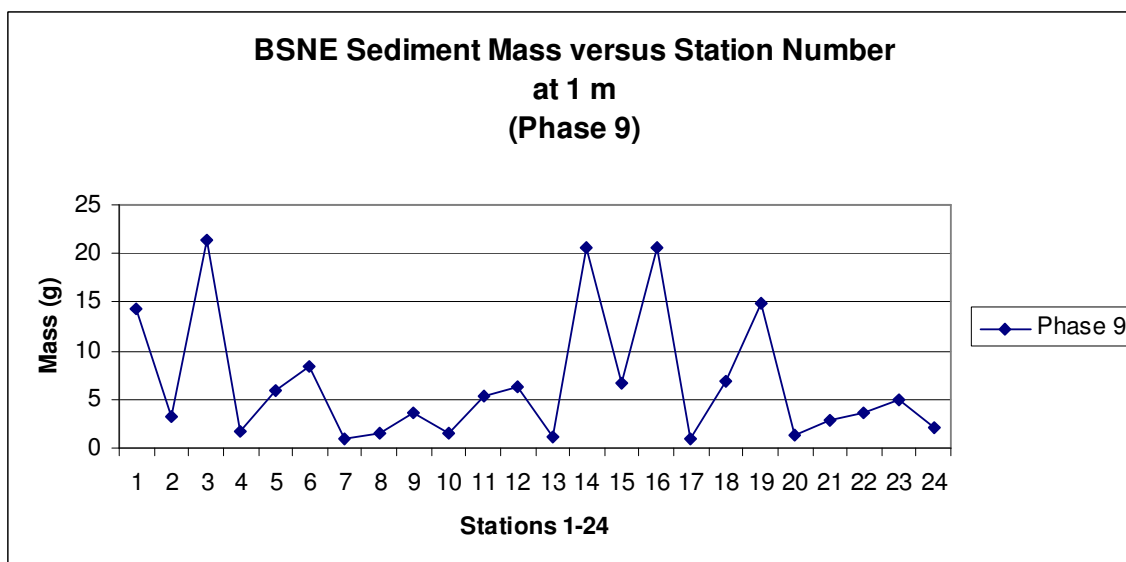


Figure 65: BSNE horizontal sediment mass (g) values versus station number at 1 m for Phase 9.

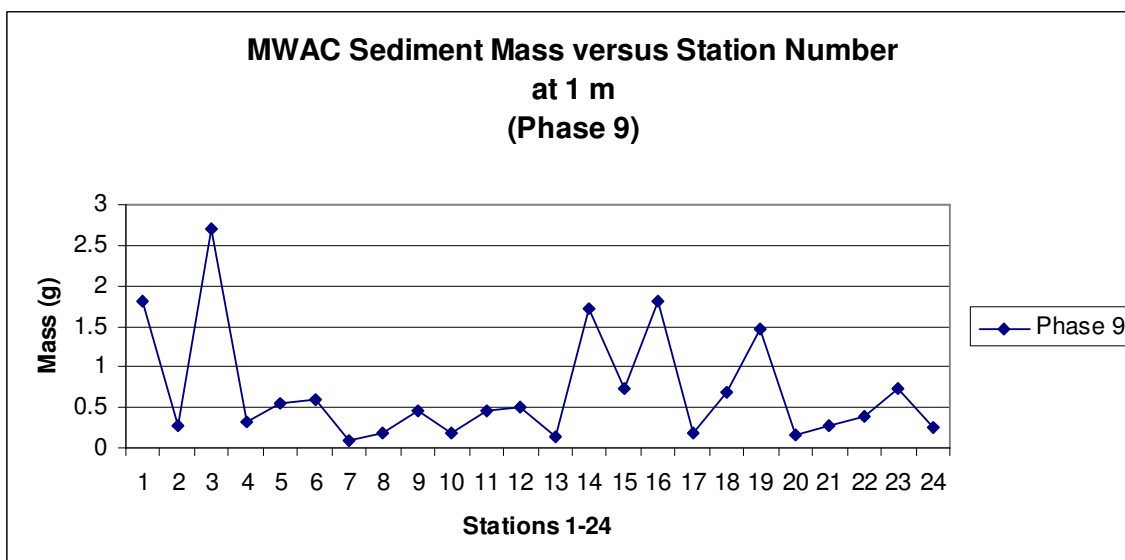


Figure 66: MWAC horizontal sediment mass (g) values versus station number at 1 m for Phase 9.

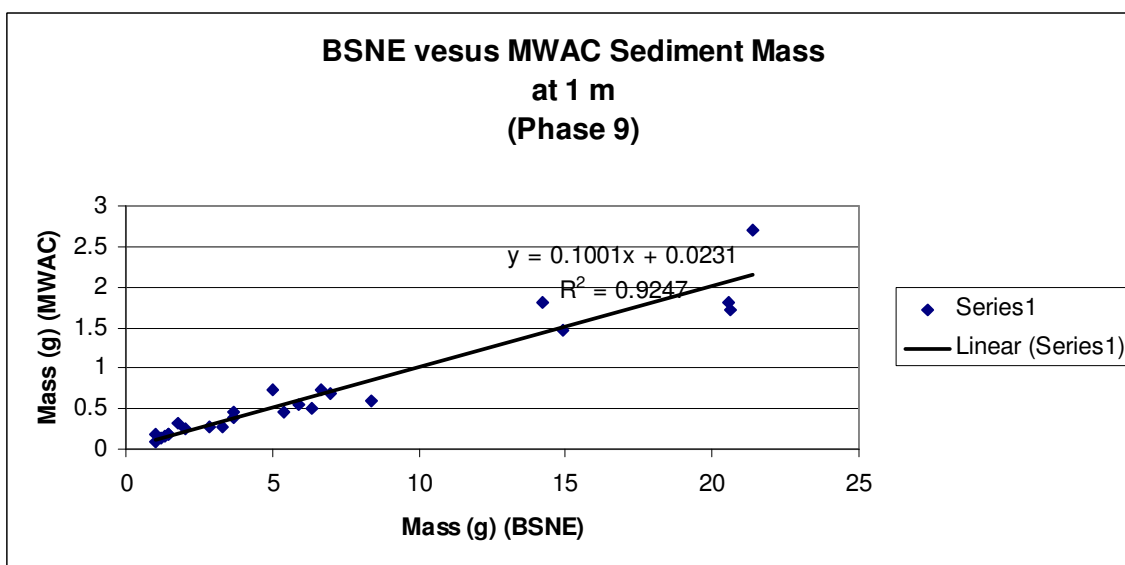


Figure 67: BSNE versus MWAC horizontal sediment mass (g) scattergram at 1 m for Phase 9.

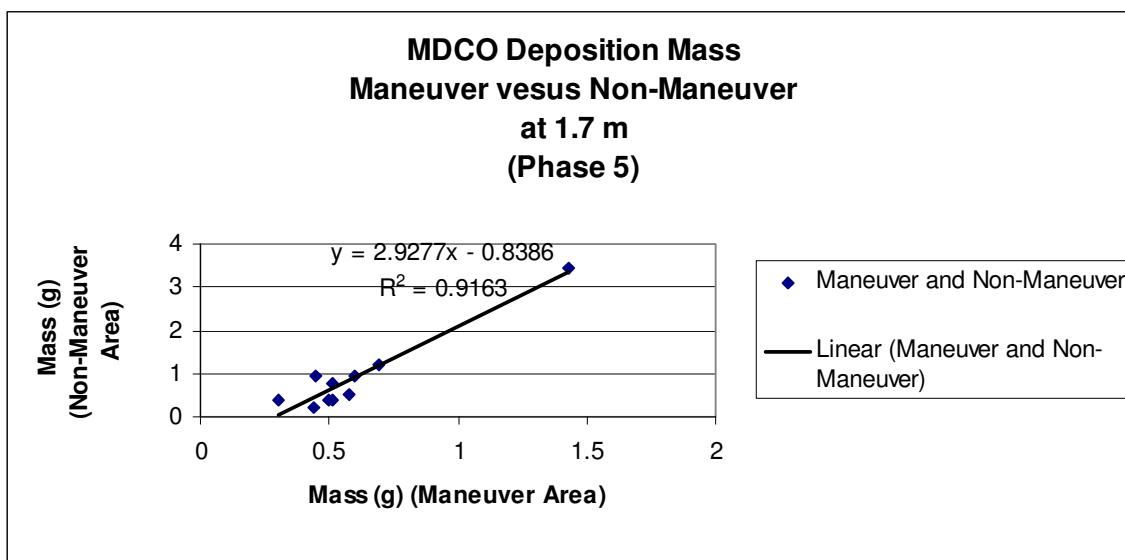


Figure 68: Maneuver versus non-maneuver MDCO deposition mass (g) scattergram at 1.7 m for Phase 5.

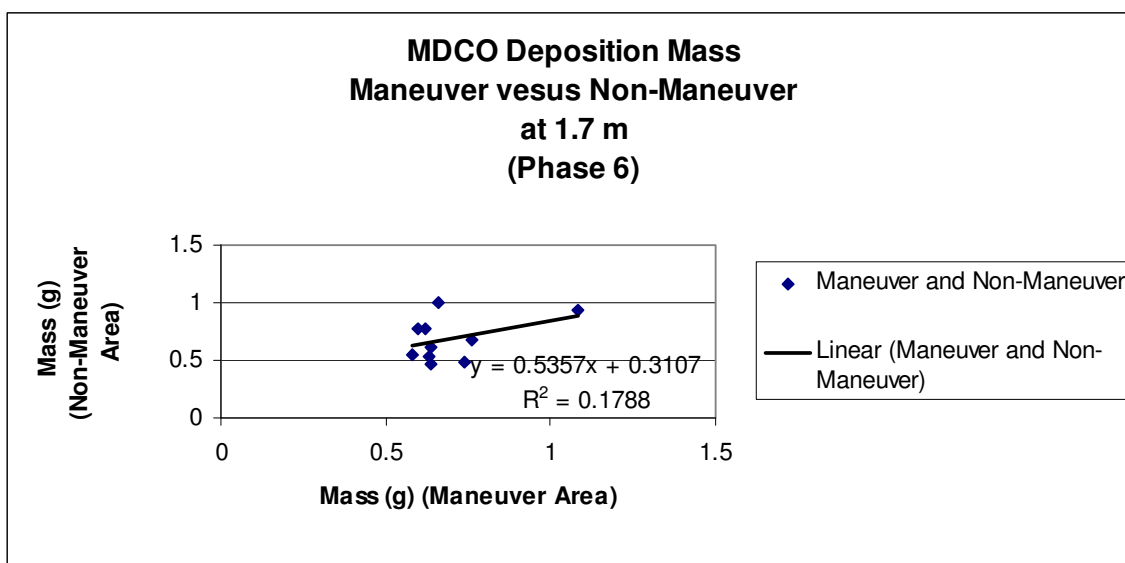


Figure 69: Maneuver versus non-maneuver MDCO deposition mass (g) scattergram at 1.7 m for Phase 6.

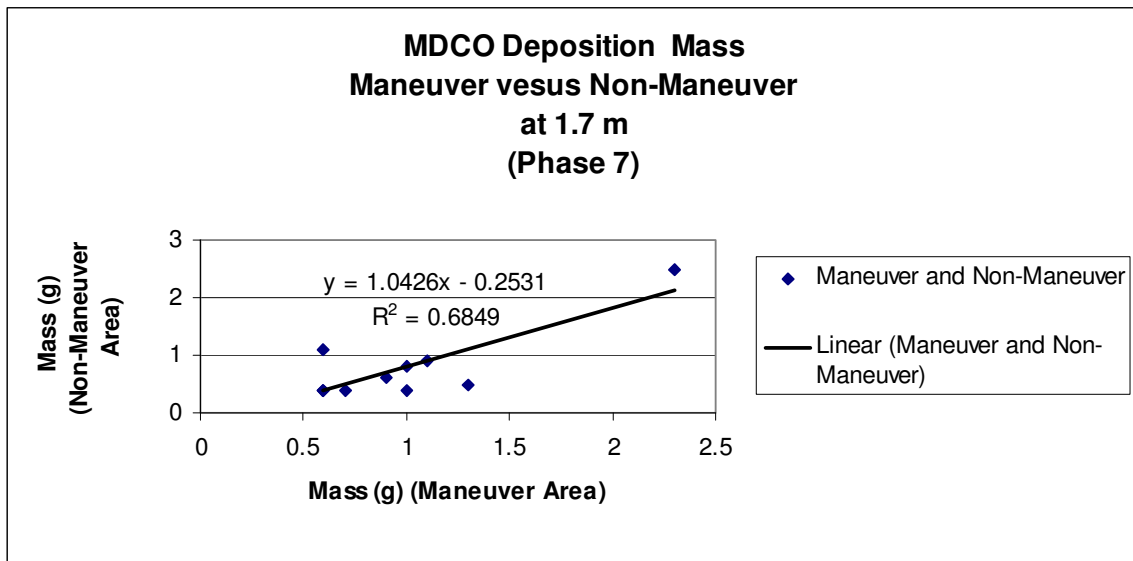


Figure 70: Maneuver versus non-maneuver MDCO deposition mass (g) scattergram at 1.7 m for Phase 7.

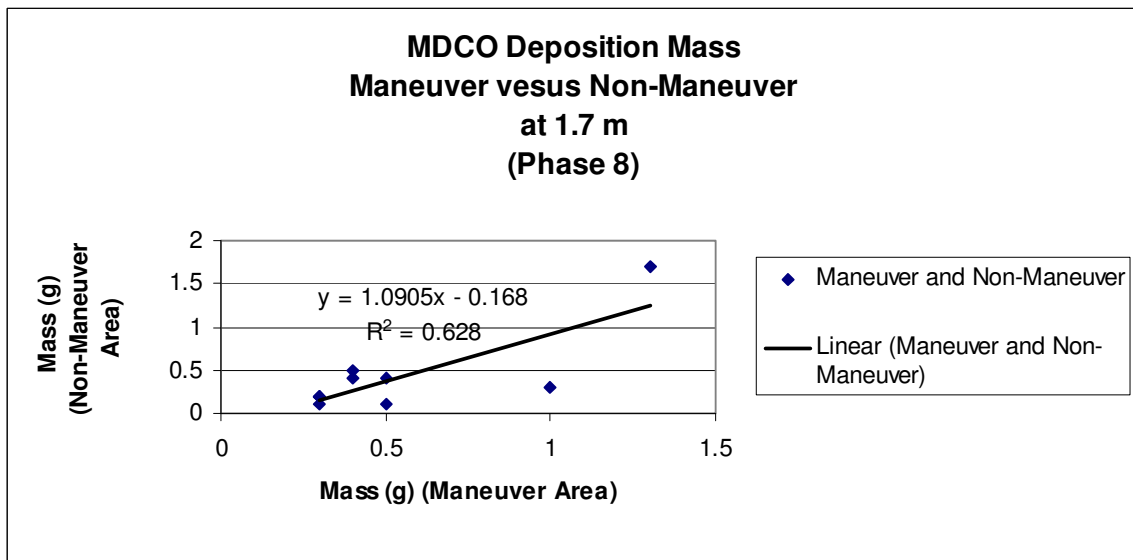


Figure 71: Maneuver versus non-maneuver MDCO deposition mass (g) scattergram at 1.7 m for Phase 8.

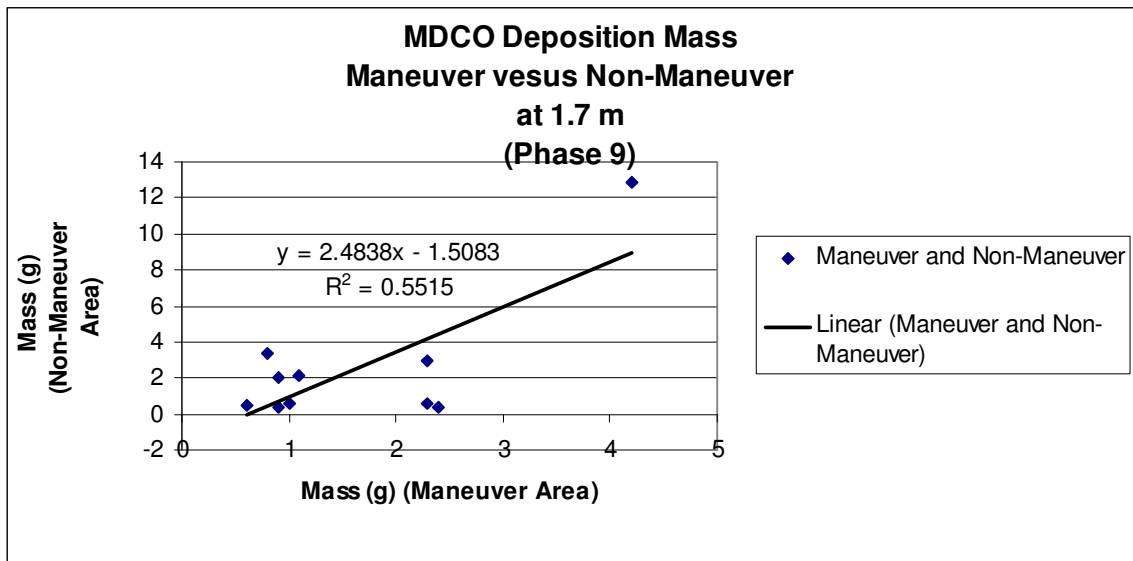


Figure 72: Maneuver versus non-maneuver MDCO deposition mass (g) scattergram at 1.7 m for Phase 9.

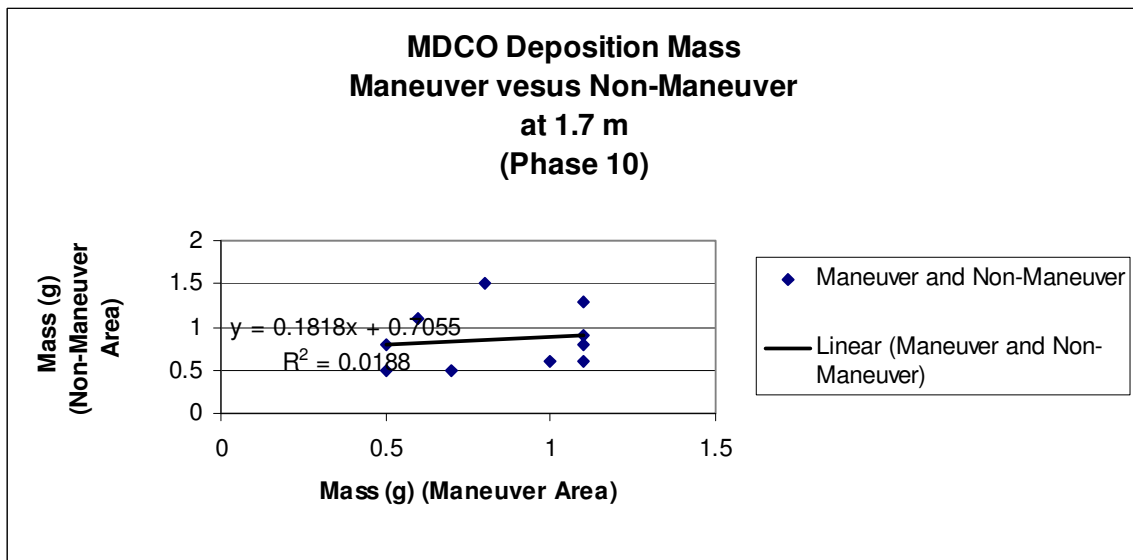


Figure 73: Maneuver versus non-maneuver MDCO deposition mass (g) scattergram at 1.7 m for Phase 10.

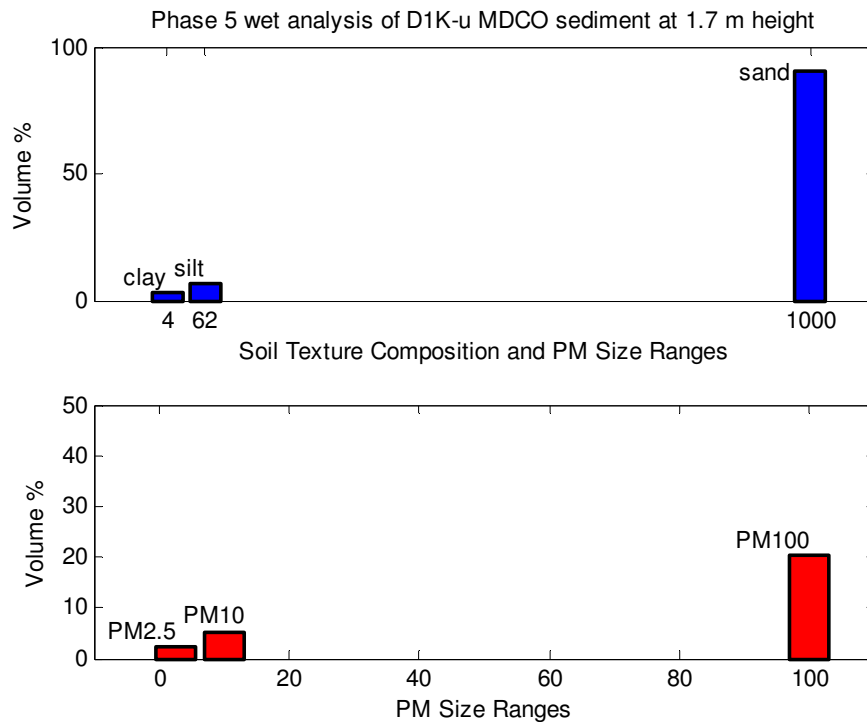


Figure 74: The top (blue) bar graph shows volume percentages versus soil textural composition PM sizes. The bottom (red) bar shows volume percentages versus PM2.5, PM10, and PM100 size ranges. This is at the MDCO Du1K-u station in the non-maneuver area for Phase 5.

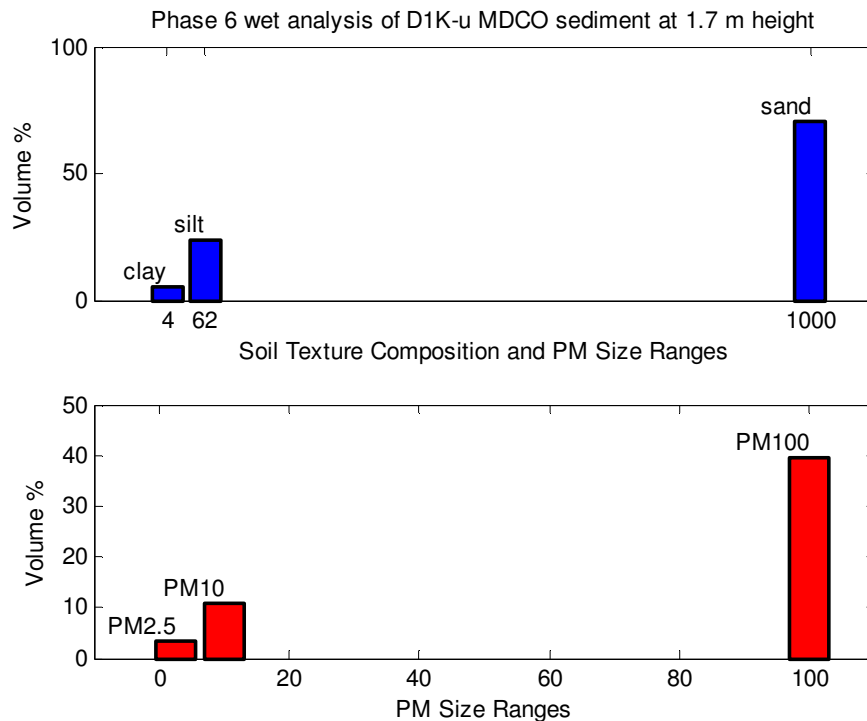


Figure 75: The top (blue) bar graph shows volume percentages versus soil textural composition PM sizes. The bottom (red) bar shows volume percentages versus PM2.5, PM10, and PM100 size ranges. This is at the MDCO Du1K-u station in the non-maneuver area for Phase 6.

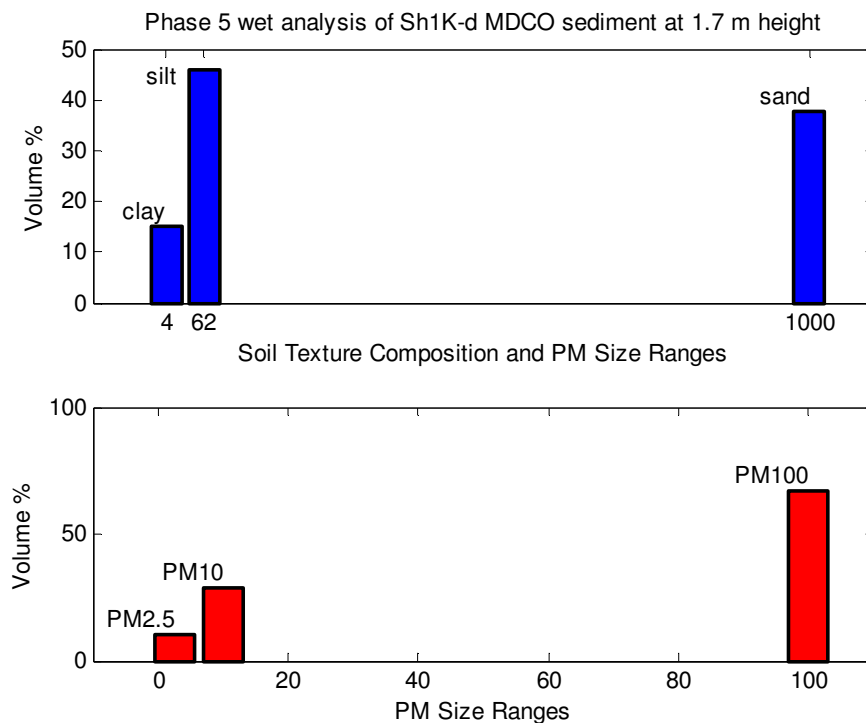


Figure 76: The top (blue) bar graph shows volume percentages versus soil textural composition PM sizes. The bottom (red) bar shows volume percentages versus PM2.5, PM10, and PM100 size ranges. This is at the MDCO Sh1K-d station in the non-maneuver area for Phase 5.

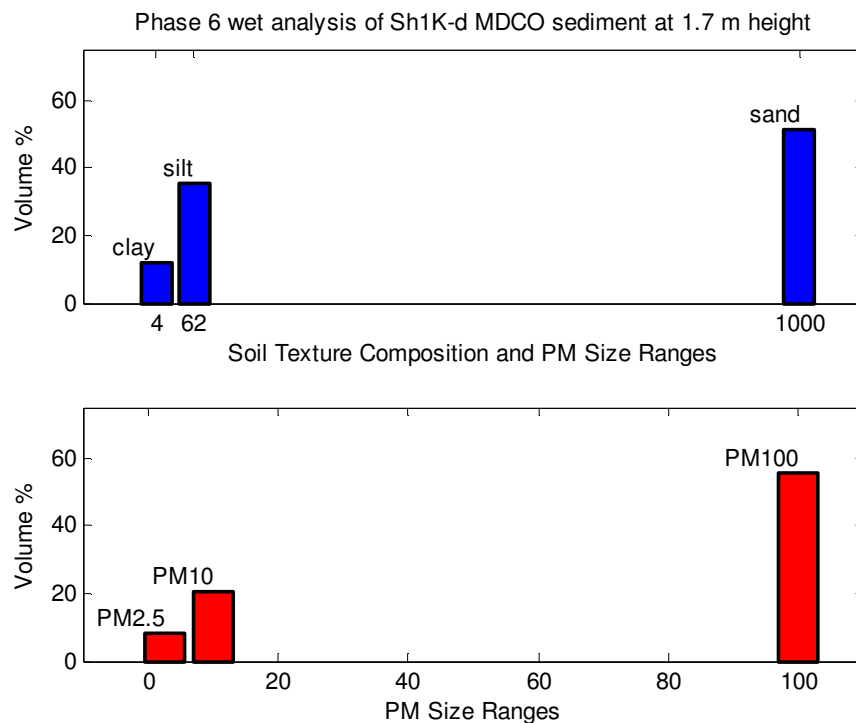


Figure 77: The top (blue) bar graph shows volume percentages versus soil textural composition PM sizes. The bottom (red) bar shows volume percentages versus PM2.5, PM10, and PM100 size ranges. This is at the MDCO Sh1K-d station in the non-maneuver area for Phase 6.

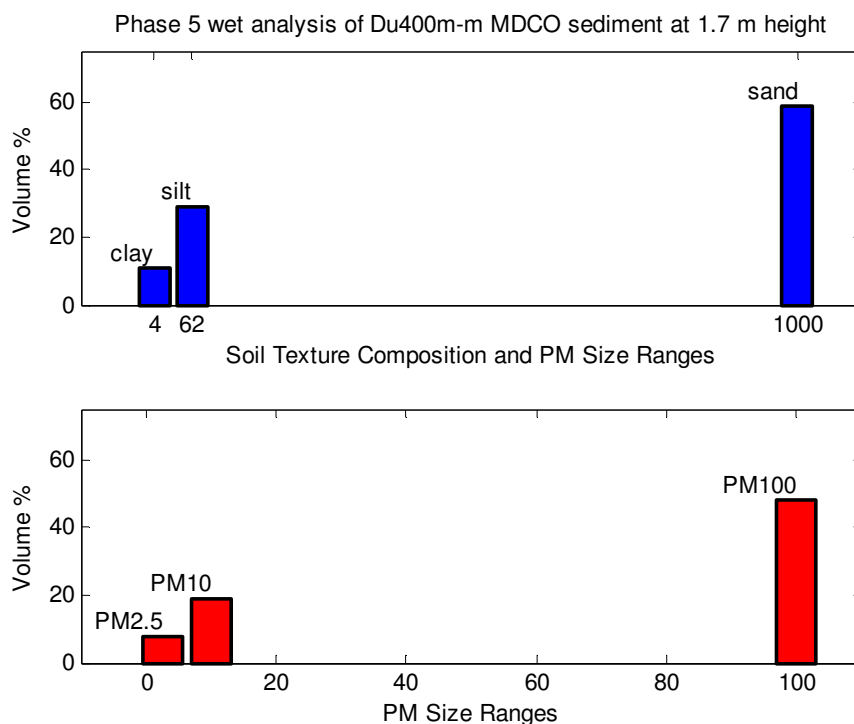


Figure 78: The top (blue) bar graph shows volume percentages versus soil textural composition PM sizes. The bottom (red) bar shows volume percentages versus PM2.5, PM10, and PM100 size ranges. This is at the MDCO Du400m-m station in the maneuver area for Phase 5.

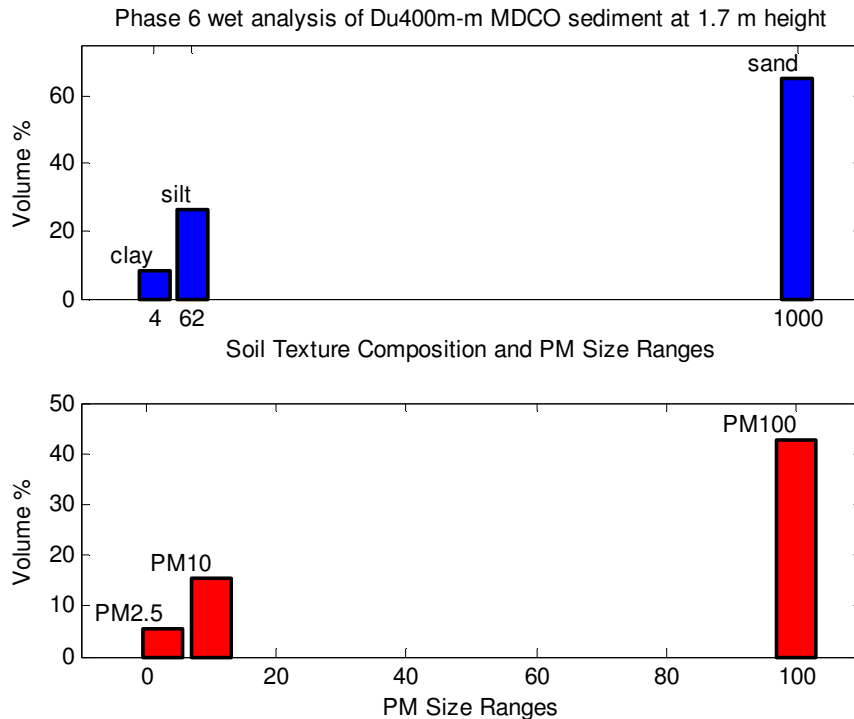


Figure 79: The top (blue) bar graph shows volume percentages versus soil textural composition PM sizes. The bottom (red) bar shows volume percentages versus PM2.5, PM10, and PM100 size ranges. This is at the MDCO Du400m-m station in the maneuver area for Phase 6.

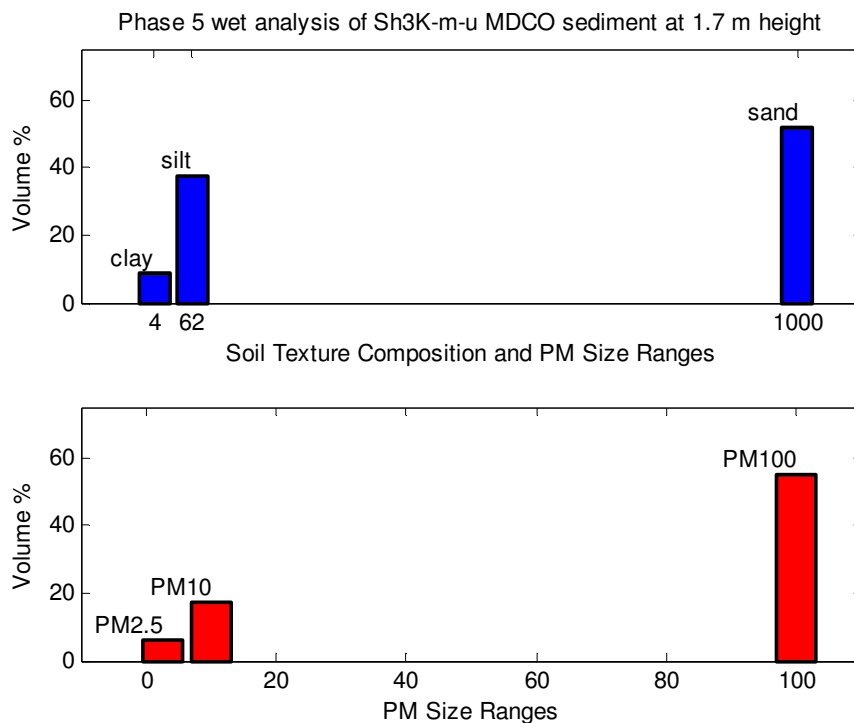


Figure 80: The top (blue) bar graph shows volume percentages versus soil textural composition PM sizes. The bottom (red) bar shows volume percentages versus PM2.5, PM10, and PM100 size ranges. This is at the MDCO Sh3K-m-u station in the maneuver area for Phase 5.

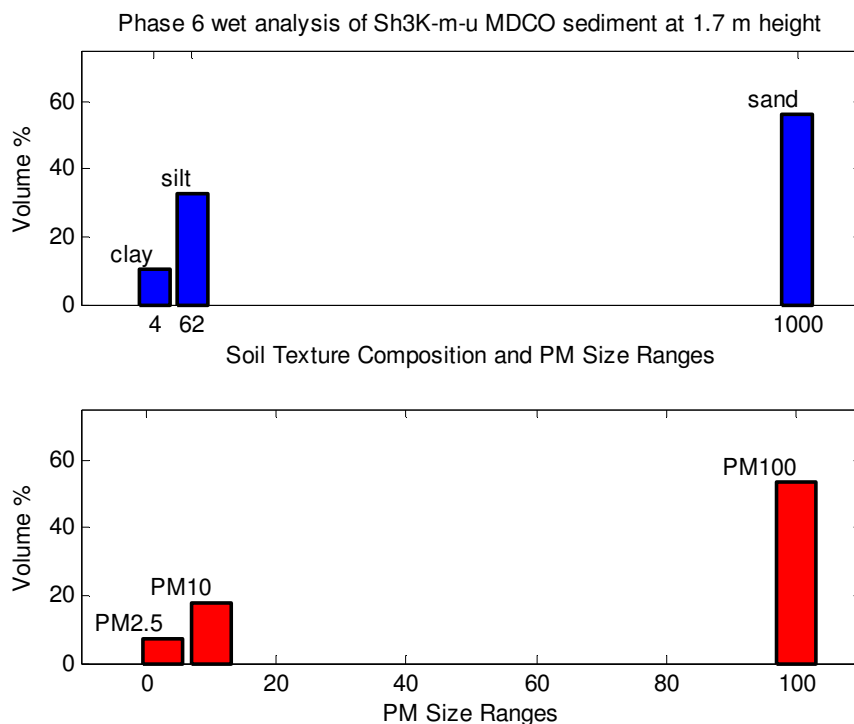


Figure 81: The top (blue) bar graph shows volume percentages versus soil textural composition PM sizes. The bottom (red) bar shows volume percentages versus PM2.5, PM10, and PM100 size ranges. This is at the MDCO Sh3K-m-u station in the maneuver area for Phase 6.

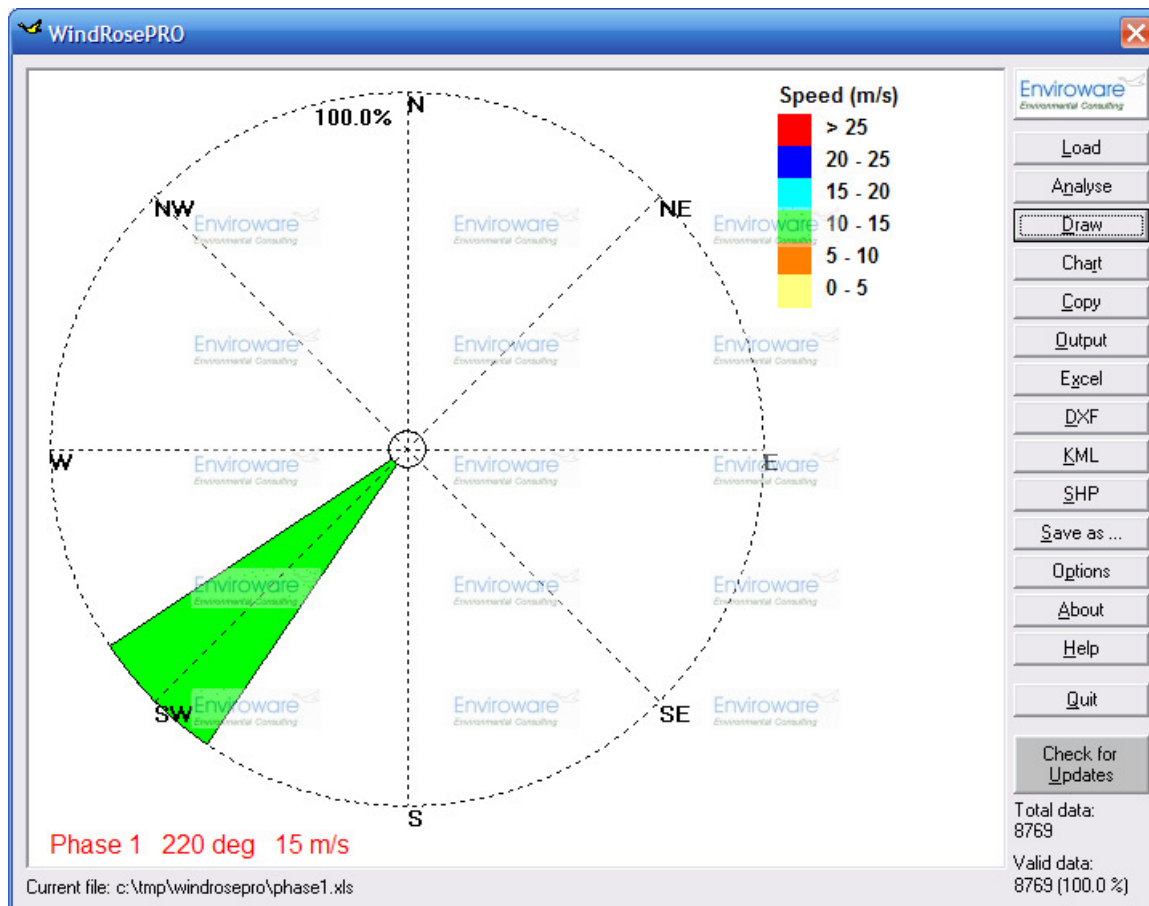


Figure 82: Phase 1 averaged vector wind direction and maximum wind speed.

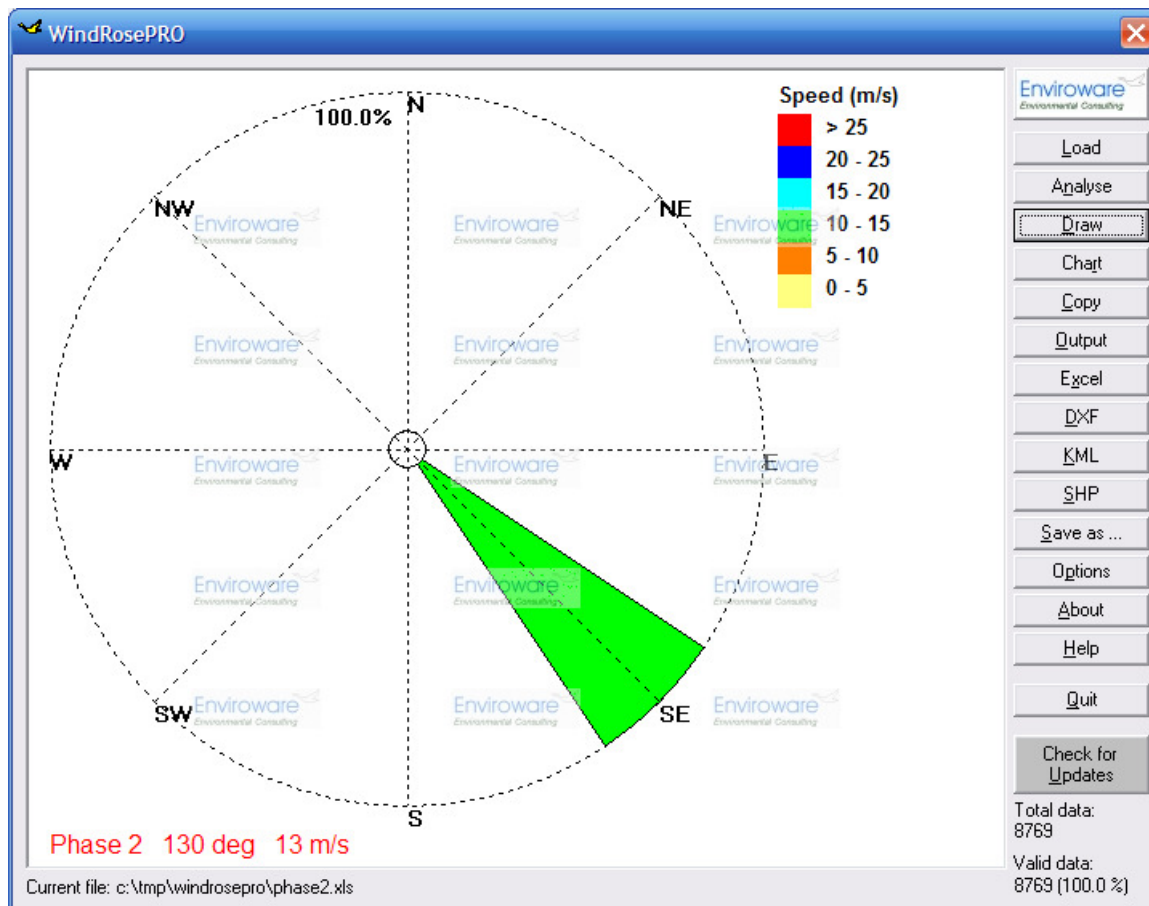


Figure 83: Phase 2 averaged vector wind direction and maximum wind speed.

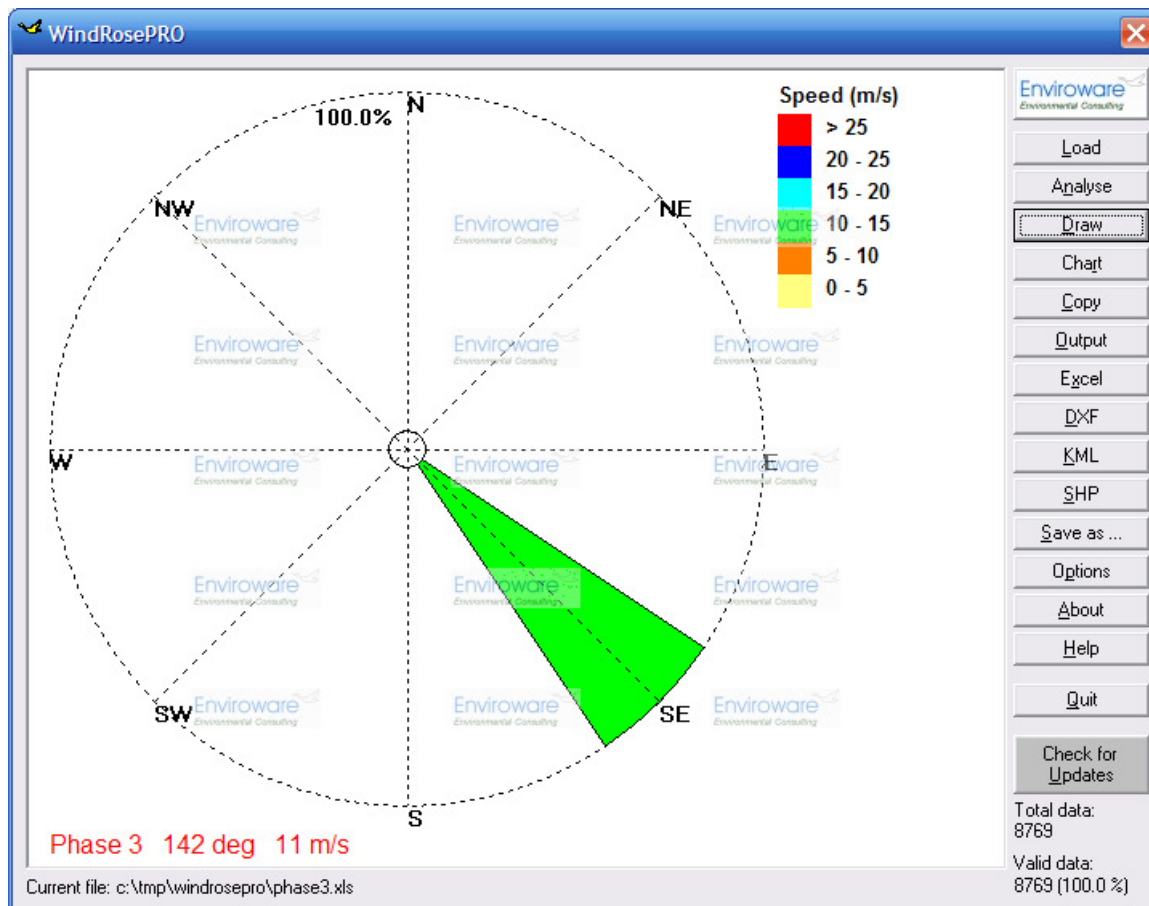


Figure 84: Phase 3 averaged vector wind direction and maximum wind speed.

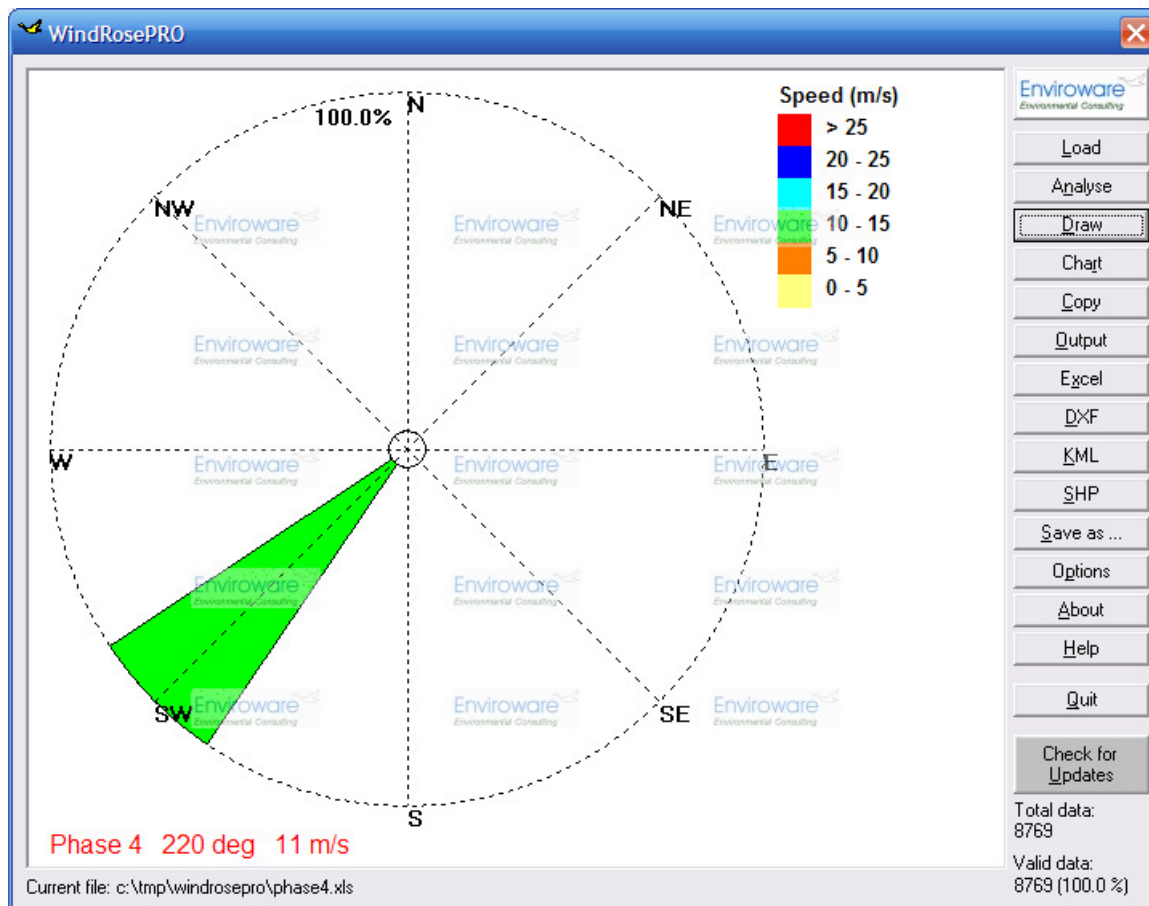


Figure 85: Phase 4 averaged vector wind direction and maximum wind speed.

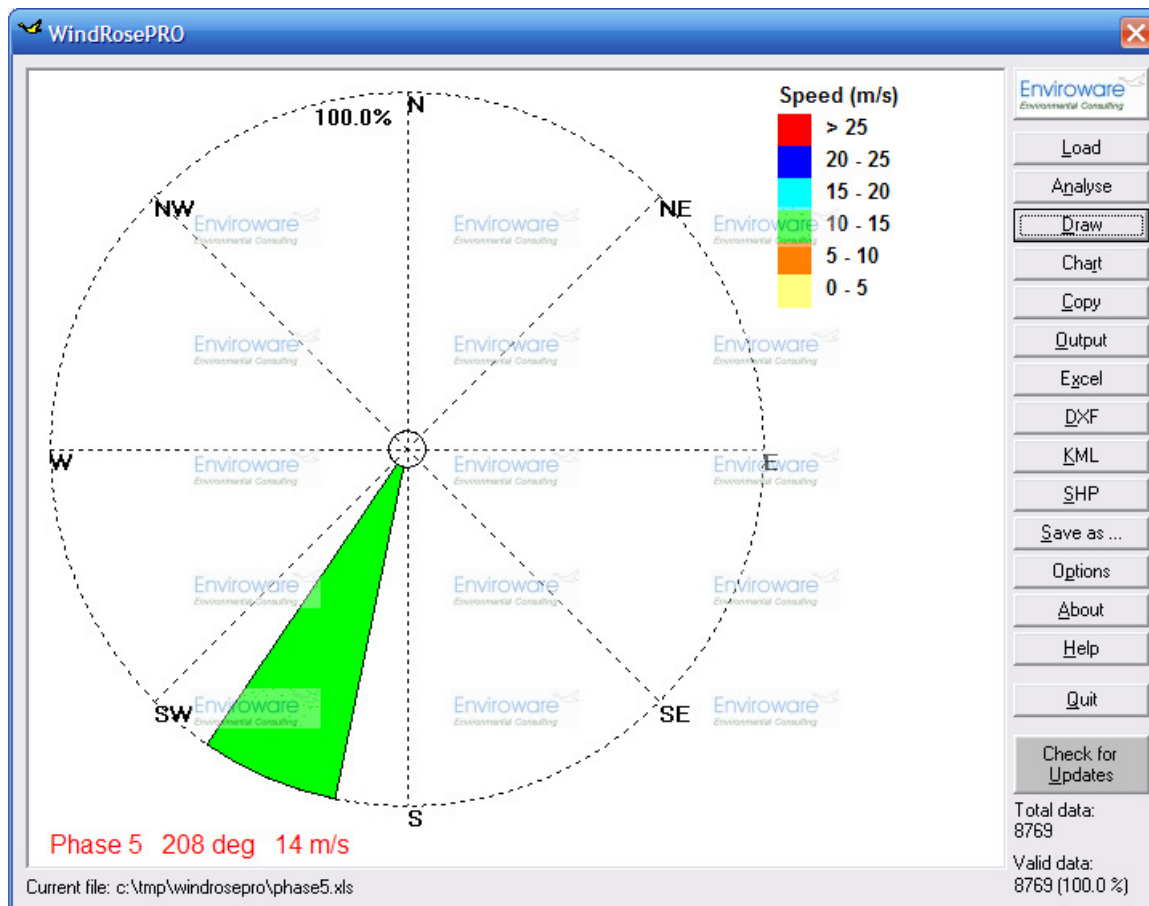


Figure 86: Phase 5 averaged vector wind direction and maximum wind speed.

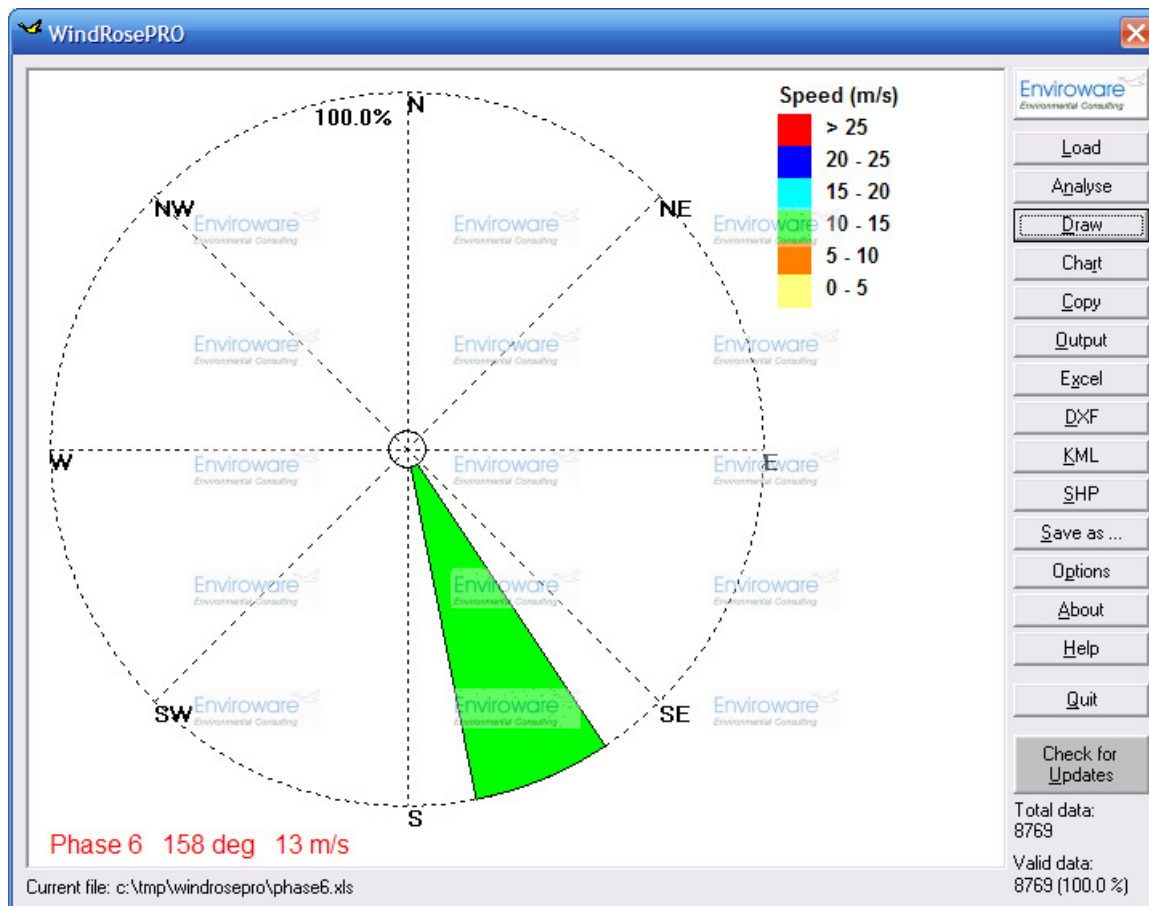


Figure 87: Phase 6 averaged vector wind direction and maximum wind speed.

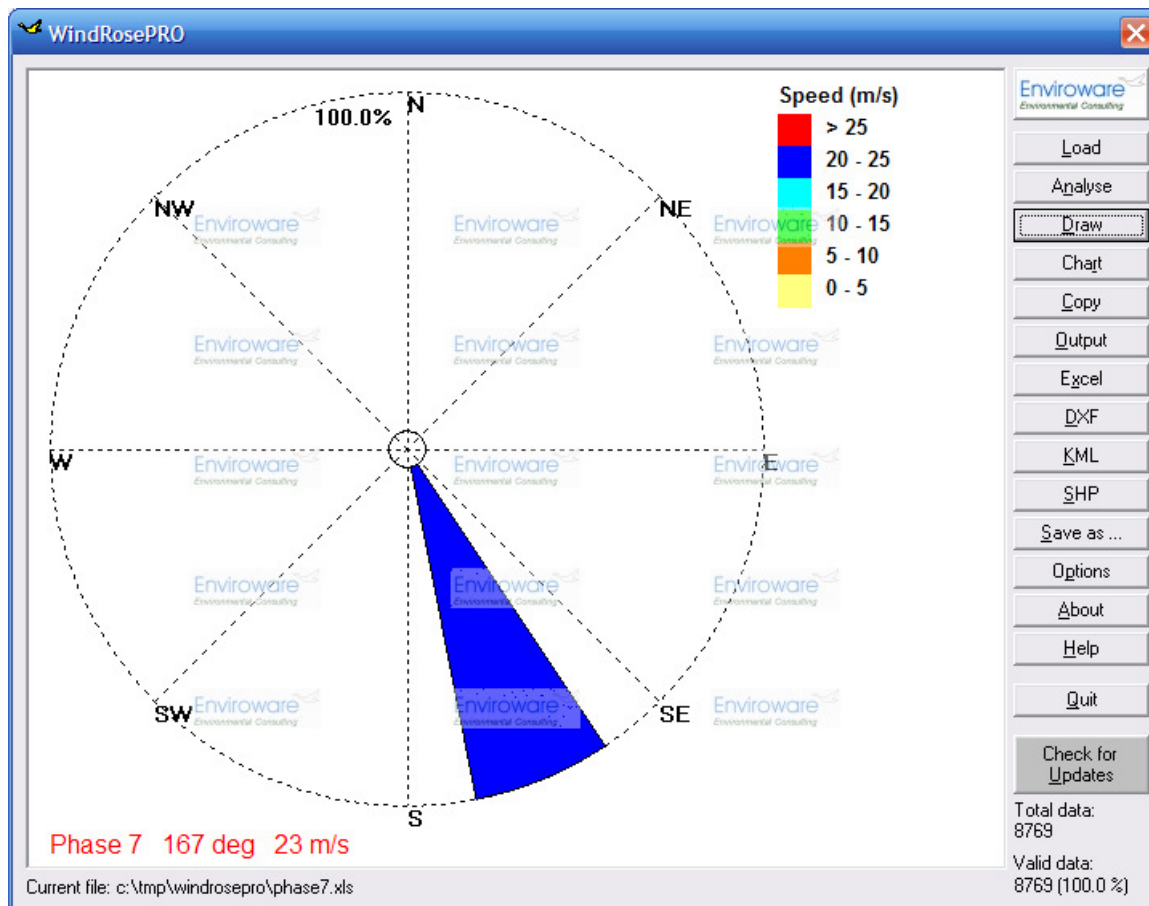


Figure 88: Phase 7 averaged vector wind direction and maximum wind speed.

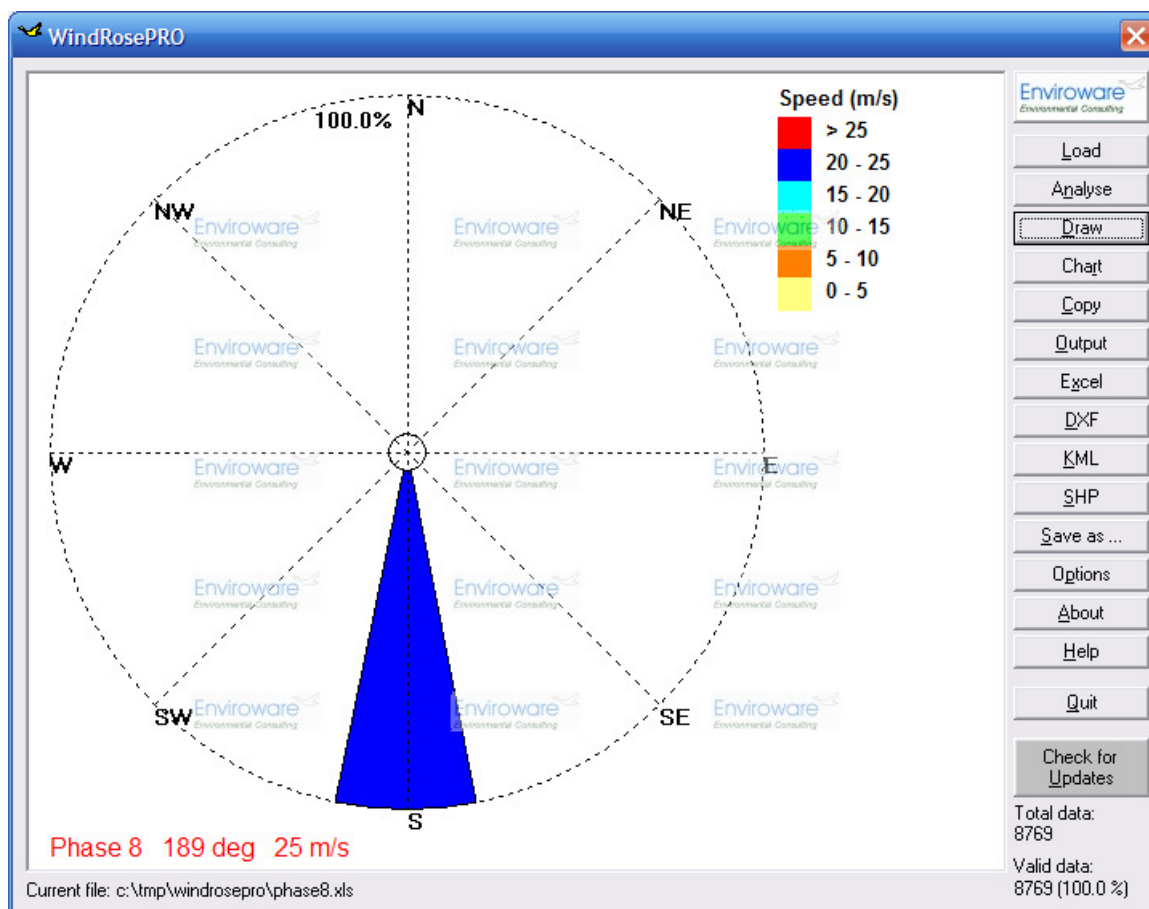


Figure 89: Phase 8 averaged vector wind direction and maximum wind speed.

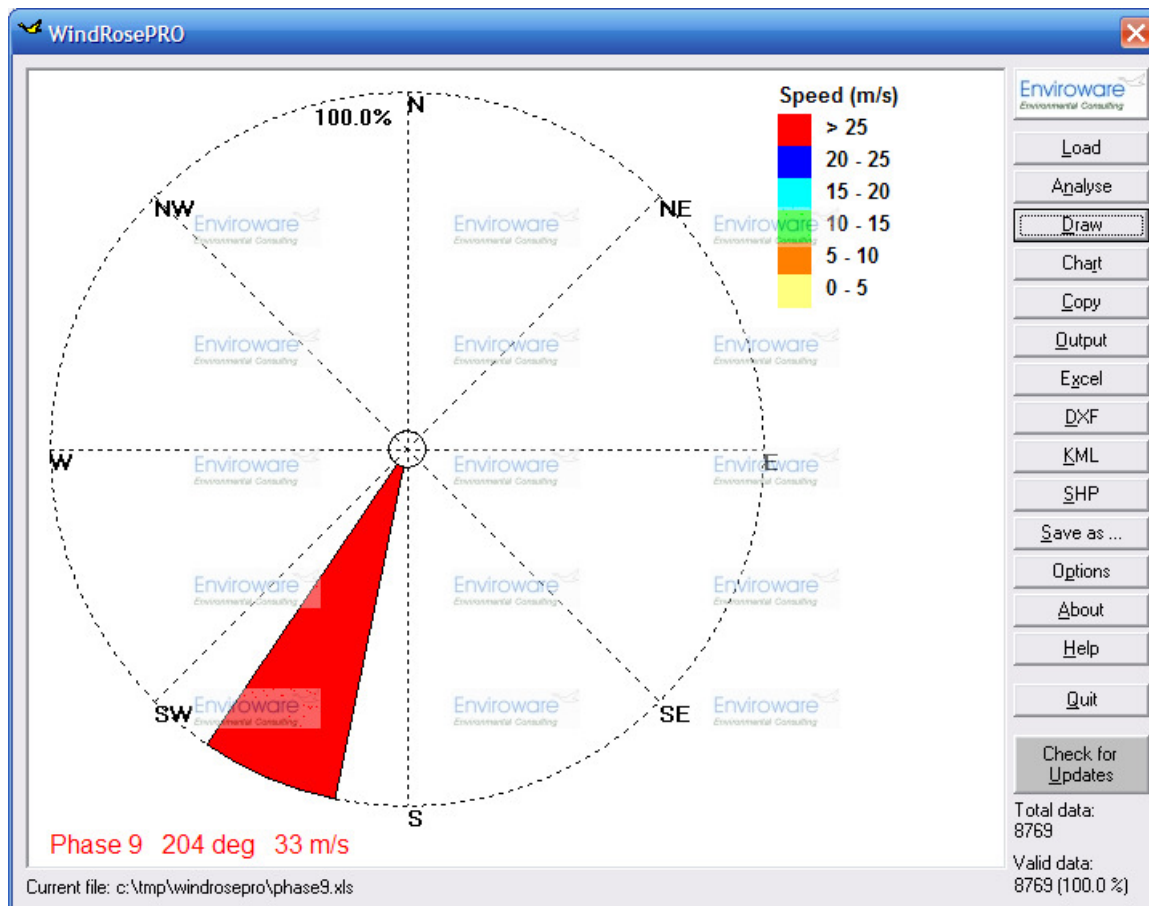


Figure 90: Phase 9 averaged vector wind direction and maximum wind speed.

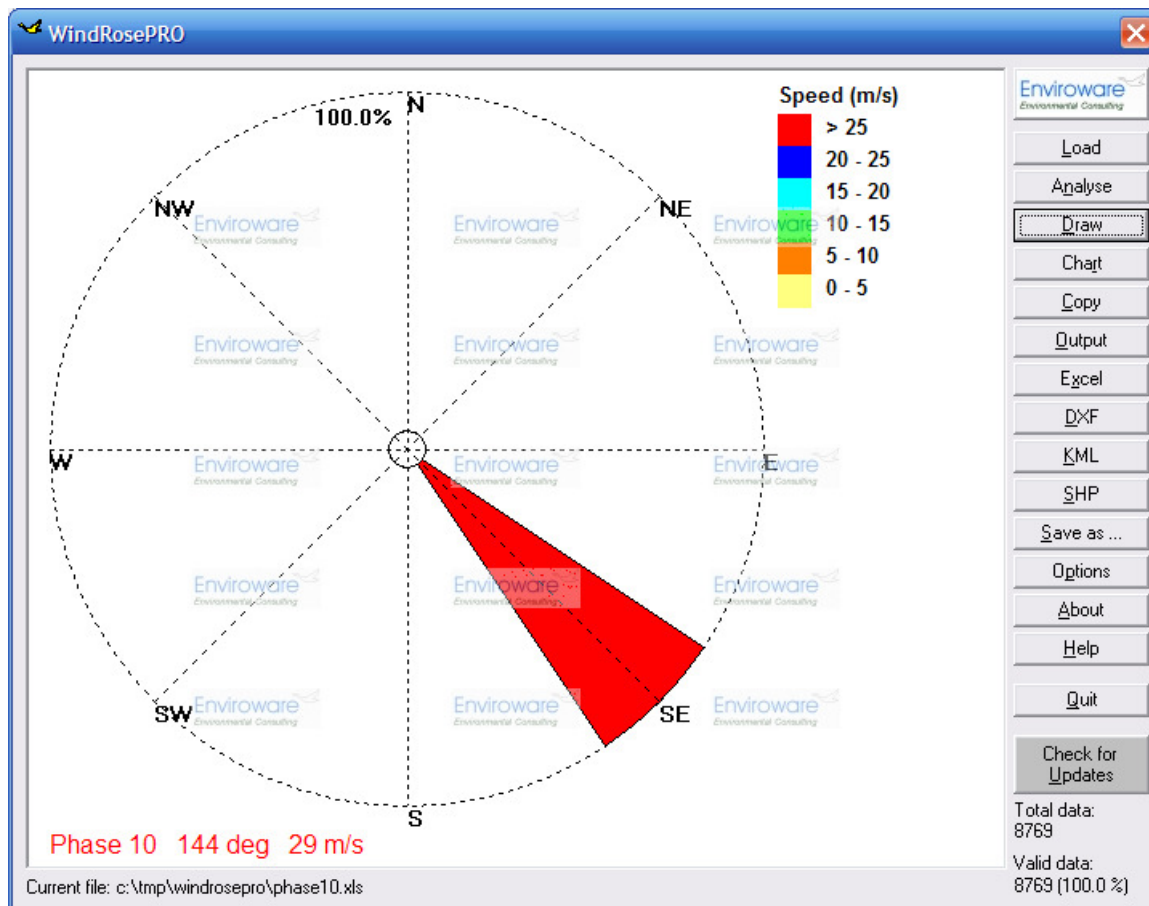


Figure 91: Phase 10 averaged vector wind direction and maximum wind speed.

7. References

- Althoff, P.S., Thien, S.J., 2005. Impact of M1A1 main battle tank disturbance on soil quality, invertebrates, and vegetation characteristics. *Journal of Terramechanics* 42, 159–176.
- American Geological Institute (AGI), 1982, Data Sheet 17.1, Grain-size scale used by American Geologists, 2nd edition, Modified Wentworth Scale, AGI Data Sheets.
- Bagnold, R. A., 1941. *The Physics of Blown Sand and Desert Dunes*, Methuen, London. 241pp.
- Bagnold, R. A., 1954. *The Physics of Blown Sand and Desert Dunes*, Dover, New York, pp. 1-6, 85-95.
- Chappell, A., 1998. Dispersing sandy soil for the measurement of particle size distribution using optical laser diffraction. *Catena* 31, 271-281.
- Choi, Y.-J., Hyde, P., Fernando, H.J.S., 2008. Implementation of a windblown dust parameterization into MODELS-3/CMAQ: Application to episodic PM events in the US/Mexico border. *Atmospheric Environment* 42, 6039–6046.
- Crabtree, G.W., 2005. Dustfall on the southern high plains of Texas. Masters thesis, Texas Tech University, 118 pp.
- Drees, L.R., Manu, A., 1996. Bird urate contamination of atmospheric dust traps. *Catena* 27, 287- 294.
- Eby, G.N., 2004. *Principles of Environmental Geochemistry*. Brooks/Cole - Thomson Learning, Inc., Pacific Grove, California, pp. 289-290.
- Englehardt, R.E., Knebel, G.W., 1968. Characteristics of the Dust Environment in the Vicinity of Military Activities. Final Report No. AR-642. Project No. SWRI No. 11-1689. Southwest Research Institute, San Antonio, Texas.
- Environmental Protection Agency (EPA), 1998. Emission Factor Documentation for AP-42, Section 13.2.2, Unpaved Roads, Final Report, Midwest Research Institute, Kansas City, Missouri.
- Floyd, K.W., Gill, T.E., 2011. The association of land cover with aeolian sediment production at Jornada Basin, New Mexico, USA. *Aeolian Research* 3, 55- 66.
- Fryrear, D.W. 1986. A field dust sampler. *Journal of Soil and Water Conservation* 41, 17-120.
- Fryrear, D.W., Saleh, A., 1993. Field wind erosion: vertical distribution. *Soil Science* 155, 294-300.
- Ganor, E., 1975. Atmospheric dust in Israel. Sedimentological and meteorological analysis of dust deposition. Ph.D. Thesis, Hebrew University of Jerusalem.
- Gile, L. H., Hawley, J. W., Grossman, R. B., 1981. Soils and geomorphology in the Basin and Range area of southern New Mexico—Guidebook to the Desert Project. New Mexico Bureau of Mines and Mineral Resources, Memoir 39, Socorro, New Mexico.

- Gillette, D.A., Fryrear, D.W., Gill, T.E., Ley, T., Cahill, T.A., Gearhart, E.A., 1997a. Relation of vertical flux of particles smaller than 10 μ m to total aeolian Horizontal Flux at Owens Lake. *Journal of Geophysical Research* 102, 26,009-26,015.
- Gillette D.A., Hardebeck, E., Parker, J., 1997b. Large-scale variability of wind erosion mass flux rates at Owens Lake, 2, Role of roughness change, particle limitation, change of threshold friction velocity, and the Owen effect. *J. Geophys. Res.* 102, 25989-25998.
- Gillette, D.A., 1999. A Qualitative Geophysical Explanation for "Hot Spot" Dust Emitting Source Regions. *Contributions to Atmospheric Physics* 72, 67-77.
- Gillette, D. A., Chen, W., 2001. Particle production and aeolian transport from a "supply-limited" source area in the Chihuahuan desert. *Journal of Geophysical Research* 106, 5267-5278.
- Gillette, D. A., Herrick, J.E., Herbert, A., 2006. Wind Characteristics of Mesquite Streets in the Northern Chihuahuan Desert, New Mexico, USA. *Environmental Fluid Mechanics* 6, 241–275.
- Gillette, D.A., Ono, D., 2008. Expressing sand supply limitation using a modified Owen saltation equation. *Earth Surface Processes and Landforms* 33, 1806–1813.
- Goossens D. and Offer, Z.Y. 1988. Loess erosion and loess deposition in the Negev Desert: theoretical modelling and wind tunnel simulations, The Jacob Blaustein Institute for Desert Research, Desert Meteorology Papers, Series A, 13, 65 pp.
- Goossens, D., Offer, Z.Y., 2000. Wind tunnel and field calibration of six aeolian dust samplers. *Atmospheric Environment* 34, 1043-1057.
- Goossens, D., Gross, J., 2002. Similarities and dissimilarities between the dynamics of sand and dust during wind erosion of loamy sandy soil. *Catena*, 47, 269-289.
- Goudie, A.S., 2009. Dust storms: Recent developments. *Journal of Environmental Management* 90, 89-94.
- Grini, A., Zender, C.S., Colarco, P.R., 2002, Saltation Sandblasting behavior during mineral dust aerosol production, *Geophys. Res. Lett.*, 29(18), 1868, doi:10.1029/2002GL015248.
- Hall, D.J., Upton, S.L., Marsland, G.W., 1994. Designs for a deposition gauge and a flux gauge for monitoring ambient dust. *Atmospheric Environment* 28, 2963-2979.
- Hansen, D.J., Ostler, W.K., 2005. Assessment technique for evaluating military vehicular impacts to vegetation in the Mojave desert. *Journal of Terramechanics* 42, 193–205.
- Kuntze, H., Beinhauer, R., Tetzlaff, G., 1990. Quantification of soil erosion by wind, I. Final Report of the BMFT project. Project No. 0339058 A, B, C. Institute of Meteorology and Climatology, University of Hannover, Germany.
- Machenberg, M. D., 1987. Analysis of dust-trap samples collected on the southern High Plains and adjacent areas, in Gustavson, T. C., ed., *Geology and geohydrology of the Palo Duro Basin, Texas Panhandle. Report on the Progress of Nuclear Waste Isolation Feasibility Studies.* Texas Bureau of Economic Geology Publication OF-WTWI-1985-49, pp. 337-343.

- Marston, R.A., 1986. Maneuver-caused wind erosion impacts, south central New Mexico. In: W.G. Nickling, Editor. *Aeolian geomorphology: proceedings of the 17th Annual Binghamton Geomorphology Symposium*. Allen & Unwin, Englewood Cliffs, Boston, Massachusetts, pp. 273-290.
- Miller, I., Freund, J.E., Johnson, R.A., 1990. *Probability and Statistics for Engineers* (4th ed.). Prentice Hall, pp. 210-212, 306-309.
- Monger, H.C., Cole, D.R., Kipp, J., Gish, J.W., Nash, M.H., Khresat, S., Buck, B.J., Giordano, A.J., Cummings, L.S., 1993. *Soil-Geomorphic and Paleoclimatic Characteristics of the Fort Bliss Maneuver Areas, Southern New Mexico and Western Texas*. Historic and Natural Resources Management Program Directorate of Environment, United States Army Air Defense Artillery Center, Ft. Bliss, Texas.
- Novlan, D.J., Hardiman, M., Gill, T.E., 2007. A synoptic climatology of blowing dust events in El Paso, Texas from 1932-2005: 16th Conference on Applied Climatology, American Meteorological Society, paper J3.12.
- Perez, A.E., Gill, T.E., 2009. Salt Flat Basin's Contribution to Regional Dust Production and Potential Influence on Dry Deposition in the Guadalupe Mountains (Texas, USA). *Natural Resources and Environmental Issues* 15, 118- 119.
- Pinnick, R. G., Fernandez, G., Hinds, B. D., Bruce, C. W., Schaefer, R. W., Pendleton, J. D., 1985. Dust Generated by Vehicular Traffic on Unpaved Roadways: Sizes and Infrared Extinction Characteristics. *Aerosol Science and Technology* 4, 99-121.
- Prandtl, L., 1935. The mechanics of viscous fluids. In F. Durand (ed.) *Aerodynamic Theory*, Vol. III. Julius Springer, Berlin, pp. 57-109.
- Prose, D.V., Wilshire, H.G., 2000. *The Lasting Effects of Tank Maneuvers on Desert Soils and Intershrubland Flora*. U.S. Geological Survey Open-File Report OF 00-512.
- Pye, Kenneth, 1987. *Aeolian Dust and Dust Deposits*. Academic Press, Austin, Texas, pp. 29-62.
- Reheis, M.C., 2006. A 16-year record of eolian dust in Southern Nevada and California, USA: Controls on dust generation and accumulation. *Journal of Arid Environments* 67, 487-520.
- Rivera-Rivera, N. I., Bleiweiss, M. P., Fitzgerald, R. M., Gebhart, K. A., Gill, T. E., Hand, J. L., 2009. Wind modeling of Chihuahuan Desert dust outbreaks , *Atmospheric Environment*, 43, 347-354.
- Rose, E.P.F., 2005. Impact of military activities on local and regional geological conditions. *Geological Society of America Reviews in Engineering Geology*, XVI, 51-64.
- Seinfeld, J. H., and S. N. Pandis., 1998, *Atmospheric Chemistry and Physics: From Air Pollution to Climate Change*. Wiley-Interscience, New York, New York, pp. 462-466.
- Shao, Y., McTainsh, G.H., Leys, J.F. and Raupach, M.R. 1993. Efficiencies of sediment samplers for wind erosion measurement, *Australian Journal of Soil Research*, 31 (4), 519-532.
- Shao, Y., 2000. *Physics and Modelling of Wind Erosion*. Kluwer Academic Publishers, pp. 145-158.

Spaan, W.P., van Dijk, P., Hollemans, W. and Eppink, L.A.A.J. 1990. Wind Erosion Measurements on Schiermonnikoog, Report II, Department. of Irrigation and Soil and Water Conservation, Wageningen Agricultural University, 20 pp.

Sperazza, M., Moore, J.N., Hendrix, M.S., 2004. High-Resolution Particle Size Analysis of Naturally Occurring Very Fine-Grained Sediment Through Laser Diffractometry. *Journal of Sedimentary Research* 74, 736-743.

Sterk, G., 1993. Description and calibration of sediment samplers. Sahelian Wind Erosion Research Project, Report III. Department of Irrigation and Soil and Water Conservation, Wageningen Agricultural University, pp. 31.

Stout, J. E., Fryrear, D.W., 1989. Performance of a windblown-particle sampler. *Transactions of the American Society of Agricultural Engineers* 32, 2041-2045.

Strahler, A.N., Strahler, A.H., 1974, *Introduction to Environmental Science*, Hamilton Publishing Company, Santa Barbara, California, pp. 106-108.

U.S. Government, 1986. White Sands Missile Range Technical Capabilities. U.S. Government Printing Office, Denver, Colorado.

U.S. Army Corps of Engineers, 1993. Draft Programmatic Environmental Impact Statement for the Joint Training Exercise Roving Sands at Fort Bliss, Texas and New Mexico and White Sands Missile Range, New Mexico. U.S. Army Corp of Engineers, Fort Worth, Texas.

Van der Hoven, I., 1968. Deposition of particles and gases. In *Meteorology and Atomic Energy*. D. Slade (Ed.), TID-24190, NTIS, Springfield, VA, 445 pp.

van Donk, S.J., Huang, X., Skidmore, E.L., Anderson, A.B., Gebhart, D.L., Prehoda, V.E., Kellogg, E.M., 2003. Wind erosion from military training lands in the Mojave Desert, California, U.S.A. *Journal of Arid Environments* 54, 687-703.

Visher, G.S., 1969. Grain size distributions and depositional processes. *Journal of Sedimentary Petrology* 39: 1074-1106.

von Kármán, T., 1934. Turbulence and skin friction. *Journal of the Aeronautical Sciences* 1, 1-20.

Wiggs, G.F.S., Leys, J., McTainsh, G.H., Heidenrich, S., Strong, C., 2002. A wind tunnel study of the collection efficiency of an aerodynamically improved "Frisbee" dust trap. *Proc. ICAR5/GCTE-SEN Joint Conference*, Int. Center for Arid and Semiarid Land Studies, Texas Tech University, Lubbock, Texas, USA, Publ. 02-2, pp. 133-141.

Williams, D.S., Shukla, M.K., Ross, J., 2008. Particulate matter emission by a vehicle running on unpaved road. *Atmospheric Environment* 42, 3899-3905.

Yaalon, D.H. and Ganor, E. 1979. East Mediterranean trajectories of dust-carrying storms from the Sahara and Sinai, in *Saharan Dust*, Ed. Morales, C., John Wiley and Sons, New York. 187-193.

Zobeck, T.E., 2004. Rapid Soil Particle Size Analyses Using Laser Diffraction. *Applied Engineering in Agriculture* 20, 633-639.

Chapter 5. Conclusions

This dissertation comprised three studies pertinent to wind transported geological particulate matter (PM) in anthropogenically altered lands, namely, the Chihuahuan Desert; and African and Asian deserts. The first study entailed investigating localized wind displacement of uranium and its byproducts by carrier particulates at abandoned high-grade uranium ore storage piles left over from mining operations at Peña Blanca, Chihuahua, Mexico. The second project encompassed intercontinental migration of dust PM bearing plutonium via Saharan and Asian aeolian pathways. The third investigation involved quantifying suspended PM with respect to volume, size, and mass in a military maneuvering area at White Sands Missile Range, New Mexico. Wind-transported particles from these sites can potentially have an environmental impact at regional and global scales.

Chapter 2:

This investigation evaluated potential radionuclide transport during wind erosion of high-grade uranium ore storage piles at Peña Blanca (50 km north of Chihuahua City), Chihuahua, Mexico. Whether or not radionuclides were being transported by aeolian pathways needed to be established. Three aeolian-sediment collecting BSNE (Big Spring Number Eight) stations (S-1, S-2, and S-3) were deployed in December, 2006: S-1 was located 101 meters upwind of the uranium ore stockpiles, S-2 was located on the uranium ore stockpiles, and S-3 was located 89 meters downwind of the uranium ore stockpiles. A leaf blower was utilized to simulate a natural wind gust to collect dust in March, 2007. Sediment accreted naturally for 2.4 years in the BSNE pans which were disassembled in July, 2009.

Grain size, mineralogy, and the potential of radionuclide secular equilibrium were established using various techniques. Element mapping was determined with an electron microprobe; particle size was determined with the Malvern 2000 laser diffraction particle sizer; mineralogy was determined via XRD; elemental concentrations were determined via ICP-MS analysis for two sites (S-1 and S-2); and radioactivity levels were determined by gamma-ray spectrometry (i.e., Canberra HPGe). Results were as follows: S-1: The predominant elements and minerals detected were Si, Al, K, Fe, and Ca; and quartz

and orthoclase, respectively. Approximately 7 ppm (near background for igneous material) of U was detected. No significant amount of radioactivity was detected. Moderate volume percentages of fine particles were found at 0.3 and 1 meter heights, whereas volume percentages of coarse particles were high only at 0.3 meters. S-2: The predominant elements and minerals detected were V, K, U, Si, Al, and Ca; and quartz and kaolinite, respectively. The detected concentrations of U ranged between 1,910 to 4,620 ppm. Radionuclides ^{235}U , ^{234}Pa , ^{226}Ra , ^{214}Pb , ^{214}Bi , ^{211}Bi , and ^{210}Pb were detected in the saltation zone. Significant volume percentages of fine particles were found at 0.3 and 1 meter heights, whereas volume percentages of coarse particles were high only at 0.3 meters. S-3: The predominant elements and minerals detected were Zn, Ca, Si, and Pb; and calcite, quartz, and orthoclase, respectively. Radionuclides ^{226}Ra , ^{214}Pb , ^{214}Bi , and ^{210}Pb were detected in the saltation zone. Significant volume percentages of fine particles were found at 0.3 and 1 meter heights, whereas volume percentages of coarse particles were high only at 0.3 meters. Small concentrations of radionuclides were displaced from S-2 to S-3 (along the path of prevailing winds), but essentially none to S-1. This site can serve as a study site for wind dispersion of radionuclides at similar sites worldwide.

Chapter 3:

Dust resuspended each year from desert soils contains traces of plutonium, derived predominantly from nuclear weapons tests. To evaluate relationships between plutonium activity and mineral dust concentrations (using Al and Ca as dust proxies), high volume aerosol samples were collected from four sites: Izaña, Canary Islands (1989 - 1996) (IZT); Barbados (2005 - 2006) (BAT); Gosan, South Korea (2005 - 2006) (GOS); and Mauna Loa Observatory, Hawaii (2005 - 2006) (MLO). IZT and BAT shared a Saharan aerosol pathway, while GOS and MLO received Asian aerosol. Plutonium activities in the aerosol samples were determined by alpha spectrometry following a series of filter pre-treatments and chemical separations. Concentrations of other elements were determined by a variety of techniques. Plutonium activity levels with respect to dust mass ($\text{Bq}/\mu\text{g}$) for all sites had the following rank order: $\text{GOS} > \text{MLO} > \text{BAT} > \text{IZT}$, respectively. The Pu levels at IZT, BAT,

and MLO were interpreted to be derived from re-entrained global fallout. GOS appears to be a recipient of resuspended plutonium at concentrations above background levels from newly eroding Asian drylands. These results can contribute to the understanding of current global plutonium migration patterns and can be utilized in future environmental change studies employing plutonium as a geochemical tracer.

Chapter 4:

Previous aeolian studies of mesquite coppice dune areas in the Chihuahuan Desert indicate natural processes compositely interacting with anthropogenic disturbances (e.g., military activities) alter vegetation and promote dust suspension. This investigation entailed estimating aeolian sediment transport and deposition in the southern military maneuver area of White Sands Missile Range (WSMR), New Mexico, indentifying spatial and temporal patterns of dust movement, and defining areas potentially more resistant to wind erosion given varied anthropogenic disturbances. Wind transported soil mass and the particle size distribution of airborne sand and dust were measured. Twenty-four passive dust and sand monitoring sites were deployed at WSMR (ten in the non-maneuvering area and fourteen in the maneuvering area) and collected sediment samples over ten seasonal phases from spring 2008 through summer 2010. Consistent with expected seasonal meteorology in the Chihuahuan Desert, more aeolian sediment deposition occurred in late spring than any other period, while summer had the least deposition. Particle size distributions were consistent with saltation-deposition-dust production mechanisms. Concentrations of deposited PM₁₀ (airborne particles smaller than 10 microns diameter) were highest in collectors at 1.7 m height. Results showed that amounts of wind-transported and deposited sediments were generally independent of site location (maneuvering area or non-maneuvering area). The results of this study can provide PM data useful to military officials, atmospheric scientists, land managers, and health officials.

In combination, these three undertakings all entailed investigating dust PM suspension from anthropogenically altered arid lands by aeolian processes. These investigations all evaluated sites where anthropogenic actions (military and mining activities) integrated with their natural desert settings to collectively contribute to suspension and re-suspension of geological particulate matter. Two of the sites entailed radionuclide migration, one driven by localized aeolian processes and the other driven by intercontinental trade wind and jet stream pathways. These studies were investigated with varied and complementary sediment trapping and geochemical and textural analysis methods. Empirical U.S. Environmental Protection Agency (EPA) equations for estimating PM suspension from vehicular activity on unpaved roads were applied to the Chihuahuan study sites where these activities were an additional potential route of dust emission. The results of these studies can potentially aid scientists better understand radionuclide migration behavior on local and global scales, administer land management policies in desert regions, and improve our knowledge of aeolian processes from local to global scales.

Appendices

Appendix A

Electron microprobe results of elements detected at stations S-1, S-2, and S-3.

Crystal names: Lithium fluoride (LIF), Pentaerythritol (PET), and Thallium Acid Phthalate (TAP).

Station	Slide Sample	Microprobe File	Crystal	Shell	Counts per second (cps)	Element
1	S1a and S1b	rb-s1-1	LIF	-	low signal ratio	-
Station	Slide Sample	Microprobe File	Crystal	Shell	Counts per second (cps)	Element
1	S1a and S1b	rb-s1-1	PET	K (beta)	110	K
1	S1a and S1b	rb-s1-1	PET	K (alpha)	600	K
1	S1a and S1b	rb-s1-1	PET	K (alpha)	1,555	Si
Station	Slide Sample	Microprobe File	Crystal	Shell	Counts per second (cps)	Element
1	S1a and S1b	rb-s1-1	TAP	K (alpha)	7,500	Si
1	S1a and S1b	rb-s1-1	TAP	K (alpha)	2,730	Al
1	S1a and S1b	rb-s1-1	TAP	K (alpha2)	565	Si
1	S1a and S1b	rb-s1-1	TAP	K (alpha2)	190	Al

Station	Slide Sample	Microprobe File	Crystal	Shell	Counts per second (cps)	Element
1	S1a and S1b	rb-s1-2	LIF	K (alpha)	125	Fe
Station	Slide Sample	Microprobe File	Crystal	Shell	Counts per second (cps)	Element
1	S1a and S1b	rb-s1-2	PET	K (alpha)	505	K
1	S1a and S1b	rb-s1-2	PET	K (alpha)	1,445	Si
Station	Slide Sample	Microprobe File	Crystal	Shell	Counts per second (cps)	Element
1	S1a and S1b	rb-s1-2	TAP	K (alpha)	5,610	Si
1	S1a and S1b	rb-s1-2	TAP	K (alpha)	2,520	Al
1	S1a and S1b	rb-s1-2	TAP	K (alpha)	185	Mg
1	S1a and S1b	rb-s1-2	TAP	K (alpha2)	400	Si
1	S1a and S1b	rb-s1-2	TAP	K (alpha2)	145	Al

Station	Slide Sample	Microprobe File	Crystal	Shell	Counts per second (cps)	Element
1	S1a and S1b	rb-s1-3	LIF	K (beta)	340	Fe
1	S1a and S1b	rb-s1-3	LIF	K (alpha)	2130	Fe
Station	Slide Sample	Microprobe File	Crystal	Shell	Counts per second (cps)	Element
1	S1a and S1b	rb-s1-3	PET	K (alpha)	105	Ca
1	S1a and S1b	rb-s1-3	PET	K (beta2)	115	Fe
1	S1a and S1b	rb-s1-3	PET	K (alpha2)	155	Fe
1	S1a and S1b	rb-s1-3	PET	K (alpha)	365	Si
Station	Slide Sample	Microprobe File	Crystal	Shell	Counts per second (cps)	Element
1	S1a and S1b	rb-s1-3	TAP	K (alpha)	2,600	Si
1	S1a and S1b	rb-s1-3	TAP	K (alpha)	820	Al
1	S1a and S1b	rb-s1-3	TAP	K (alpha)	120	Mg
1	S1a and S1b	rb-s1-3	TAP	L (alpha)	345	Fe

Station	Slide Sample	Microprobe File	Crystal	Shell	Counts per second (cps)	Element
1	S1a and S1b	rb-s1-4	LIF	K (alpha)	125	Fe
Station	Slide Sample	Microprobe File	Crystal	Shell	Counts per second (cps)	Element
1	S1a and S1b	rb-s1-4	PET	K (alpha)	120	Ca
1	S1a and S1b	rb-s1-4	PET	K (alpha)	245	K
1	S1a and S1b	rb-s1-4	PET	K (alpha)	1,155	Si
Station	Slide Sample	Microprobe File	Crystal	Shell	Counts per second (cps)	Element
1	S1a and S1b	rb-s1-4	TAP	K (alpha)	7,170	Si
1	S1a and S1b	rb-s1-4	TAP	K (alpha)	2,845	Al
1	S1a and S1b	rb-s1-4	TAP	K (alpha) ²	475	Si
1	S1a and S1b	rb-s1-4	TAP	K (alpha) ²	200	Al

Station	Slide Sample	Microprobe File	Crystal	Shell	Counts per second (cps)	Element
1	S1a and S1b	rb-s1-5	LIF	K (alpha)	75	Fe
Station	Slide Sample	Microprobe File	Crystal	Shell	Counts per second (cps)	Element
1	S1a and S1b	rb-s1-5	PET	K (alpha)	180	Ca
1	S1a and S1b	rb-s1-5	PET	K (alpha)	210	K
1	S1a and S1b	rb-s1-5	PET	K (alpha)	740	Si
Station	Slide Sample	Microprobe File	Crystal	Shell	Counts per second (cps)	Element
1	S1a and S1b	rb-s1-5	TAP	K (beta)	160	Si
1	S1a and S1b	rb-s1-5	TAP	K (alpha)	3,295	Si
1	S1a and S1b	rb-s1-5	TAP	K (alpha)	975	Al
1	S1a and S1b	rb-s1-5	TAP	K (alpha)2	300	Si
1	S1a and S1b	rb-s1-5	TAP	K (alpha)2	95	Al

Station	Slide Sample	Microprobe File	Crystal	Shell	Counts per second (cps)	Element
2	S2a and S2b	rb-s2-4	LIF	K (alpha)	50	Fe
2	S2a and S2b	rb-s2-4	LIF	K (beta)	40	V
2	S2a and S2b	rb-s2-4	LIF	K (alpha)	215	V
Station	Slide Sample	Microprobe File	Crystal	Shell	Counts per second (cps)	Element
2	S2a and S2b	rb-s2-4	PET	K (beta)	200	V
2	S2a and S2b	rb-s2-4	PET	K (alpha)	990	V
2	S2a and S2b	rb-s2-4	PET	M (beta)	345	U
2	S2a and S2b	rb-s2-4	PET	K (alpha)	385	K
2	S2a and S2b	rb-s2-4	PET	M (alpha)	345	U
2	S2a and S2b	rb-s2-4	PET	K (alpha)	125	Si
Station	Slide Sample	Microprobe File	Crystal	Shell	Counts per second (cps)	Element
2	S2a and S2b	rb-s2-4	TAP	K (alpha)	1,875	Si
2	S2a and S2b	rb-s2-4	TAP	K (alpha)	1,600	Al
2	S2a and S2b	rb-s2-4	TAP	K (alpha)2	165	Si
2	S2a and S2b	rb-s2-4	TAP	K (alpha)2	125	Al

Station	Slide Sample	Microprobe File	Crystal	Shell		Element
2	S2a and S2b	rb-s2-6a	LIF	-	low signal ratio	-
Station	Slide Sample	Microprobe File	Crystal	Shell	Counts per second (cps)	Element
2	S2a and S2b	rb-s2-6a	PET	K (beta)	125	Ca
2	S2a and S2b	rb-s2-6a	PET	K (alpha)	680	Ca
2	S2a and S2b	rb-s2-6a	PET	M (gamma)	195	U
2	S2a and S2b	rb-s2-6a	PET	M (beta)	1,340	U
2	S2a and S2b	rb-s2-6a	PET	M (alpha)	795	U
2	S2a and S2b	rb-s2-6a	PET	K (alpha)	515	Si
Station	Slide Sample	Microprobe File	Crystal	Shell	Counts per second (cps)	Element
2	S2a and S2b	rb-s2-6a	TAP	K (alpha)	1,220	Si
2	S2a and S2b	rb-s2-6a	TAP	M (beta)2	290	U
2	S2a and S2b	rb-s2-6a	TAP	M (alpha)2	180	U
2	S2a and S2b	rb-s2-6a	TAP	K (alpha)	260	Al

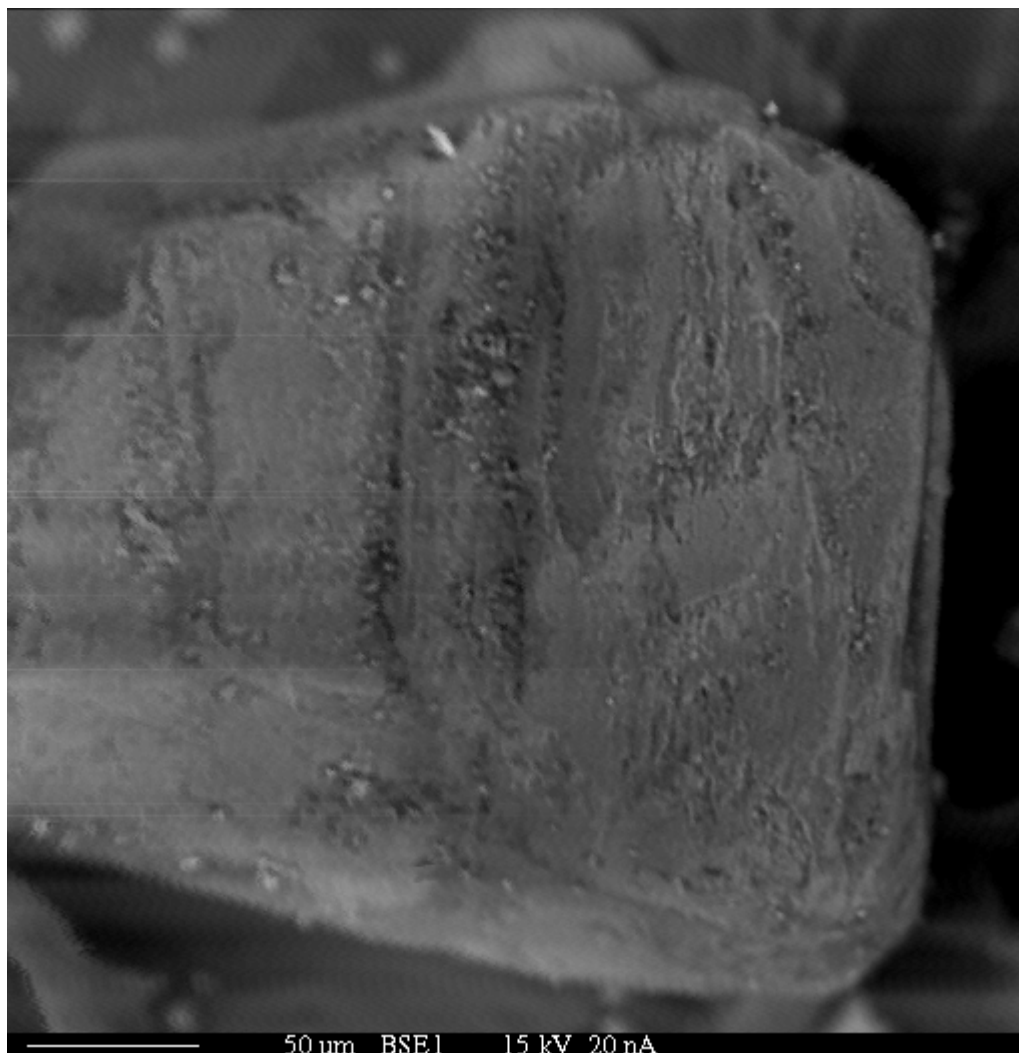
Station	Slide Sample	Microprobe File	Crystal	Shell	Counts per second (cps)	Element
2	S2a and S2b	rb-s2-6b	LIF	-	low signal ratio	-
Station	Slide Sample	Microprobe File	Crystal	Shell	Counts per second (cps)	Element
2	S2a and S2b	rb-s2-6b	PET	K (alpha)	640	Ca
2	S2a and S2b	rb-s2-6b	PET	M (gamma)	180	U
2	S2a and S2b	rb-s2-6b	PET	M (beta)	1,555	U
2	S2a and S2b	rb-s2-6b	PET	M (alpha)	555	U
2	S2a and S2b	rb-s2-6b	PET	K (alpha)	595	Si
Station	Slide Sample	Microprobe File	Crystal	Shell	Counts per second (cps)	Element
2	S2a and S2b	rb-s2-6b	TAP	K (beta)	240	Si
2	S2a and S2b	rb-s2-6b	TAP	K (alpha)	2,280	Si
2	S2a and S2b	rb-s2-6b	TAP	M (beta) ²	250	U
2	S2a and S2b	rb-s2-6b	TAP	M (alpha) ²	250	U
2	S2a and S2b	rb-s2-6b	TAP	K (alpha)	585	Al

Station	Slide Sample	Microprobe File	Crystal	Shell	Counts per second (cps)	Element
3	S3a and S3b	s3-1	LIF	K (beta)	185	Zn
3	S3a and S3b	s3-1	LIF	K (alpha)	1,315	Zn
3	S3a and S3b	s3-1	LIF	K (alpha) ²	70	Zn
Station	Slide Sample	Microprobe File	Crystal	Shell	Counts per second (cps)	Element
3	S3a and S3b	s3-1	PET	K (alpha) ²	35	Zn
3	S3a and S3b	s3-1	PET	K (beta)	40	Ca
3	S3a and S3b	s3-1	PET	K (alpha)	105	Ca
3	S3a and S3b	s3-1	PET	K (alpha)	20	Si
Station	Slide Sample	Microprobe File	Crystal	Shell	Counts per second (cps)	Element
3	S3a and S3b	s3-1	TAP	K (alpha)	205	Si

Station	Slide Sample	Microprobe File	Crystal	Shell	Counts per second (cps)	Element
3	S3a and S3b	s3-8	LIF	L (alpha)	125	Pb
3	S3a and S3b	s3-8	LIF	K (alpha)	90	Zn
Station	Slide Sample	Microprobe File	Crystal	Shell	Counts per second (cps)	Element
3	S3a and S3b	s3-8	PET	K (alpha)	70	Ca
Station	Slide Sample	Microprobe File	Crystal	Shell	Counts per second (cps)	Element
3	S3a and S3b	s3-8	TAP	K (beta)	275	Si
3	S3a and S3b	s3-8	TAP	K (alpha)	325	Si
3	S3a and S3b	s3-8	TAP	K (gamma)2	65	Pb
3	S3a and S3b	s3-8	TAP	M (beta)2	170	Pb
3	S3a and S3b	s3-8	TAP	M (alpha)2	280	Pb

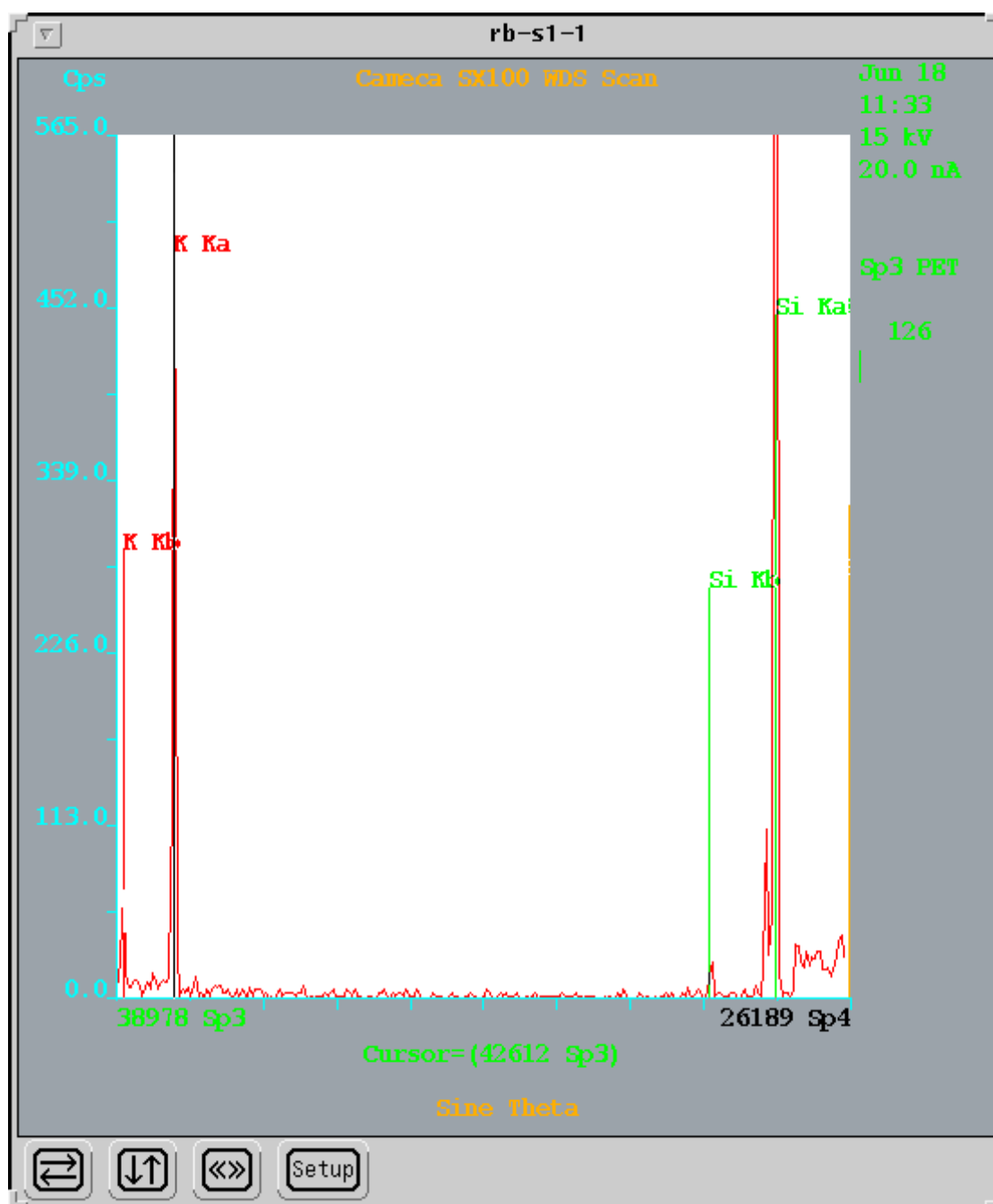
Station	Slide Sample	Microprobe File	Crystal	Shell	Counts per second (cps)	Element
3	S3a and S3b	s3-14s	LIF	L (alpha)	165	Pb
3	S3a and S3b	s3-14s	LIF	K (beta)	115	Zn
3	S3a and S3b	s3-14s	LIF	K (alpha)	120	Zn
Station	Slide Sample	Microprobe File	Crystal	Shell	Counts per second (cps)	Element
3	S3a and S3b	s3-14s	PET	M (beta)	1,005	Pb
3	S3a and S3b	s3-14s	PET	M (alpha)	1,390	Pb
Station	Slide Sample	Microprobe File	Crystal	Shell	Counts per second (cps)	Element
3	S3a and S3b	s3-14s	TAP	K (beta)	250	Si
3	S3a and S3b	s3-14s	TAP	K (alpha)	240	Si
3	S3a and S3b	s3-14s	TAP	M (beta)2	175	Pb
3	S3a and S3b	s3-14s	TAP	M (alpha)2	330	Pb
3	S3a and S3b	s3-14s	TAP	M (alpha)3	95	Pb

Appendix B

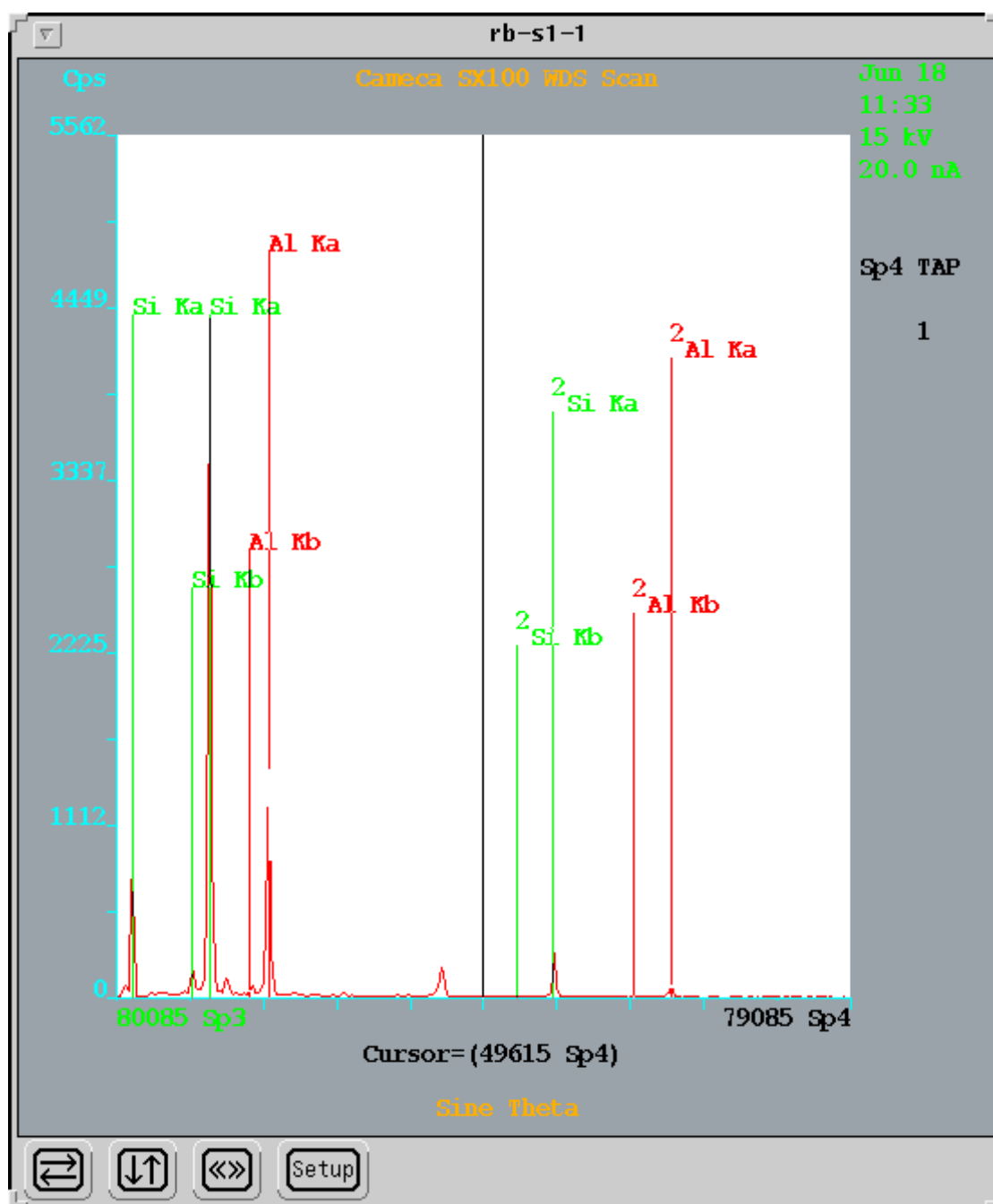


rb-s1-1BSE1

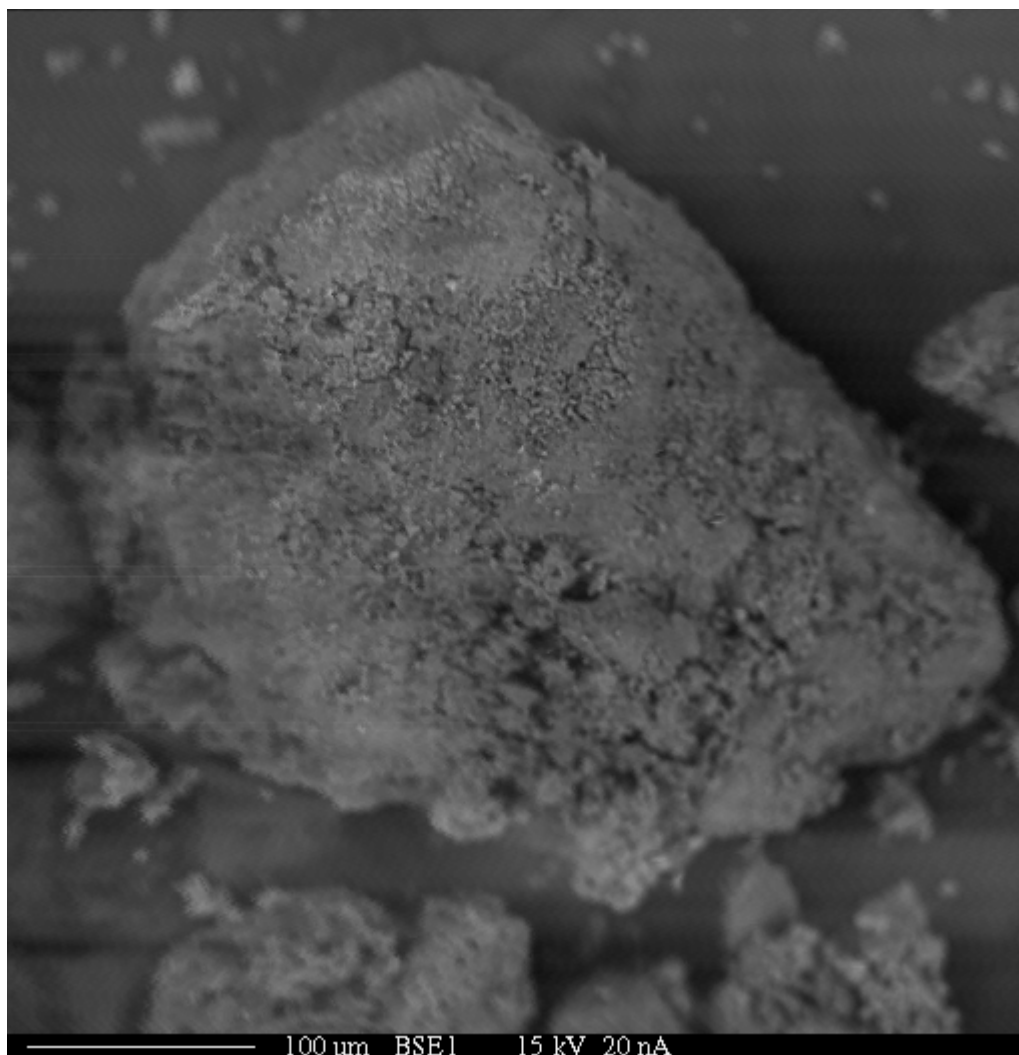
BSE particle grain (simulated wind gust) image from station S-1.
According to the WDS spectra generated, the
inferred mineral is kaolinite and K-feldspar.



Wavelength Dispersive Spectroscopy (WDS)
X-ray scan pentaerythritol (PET) spectrum
for image from station S-1.



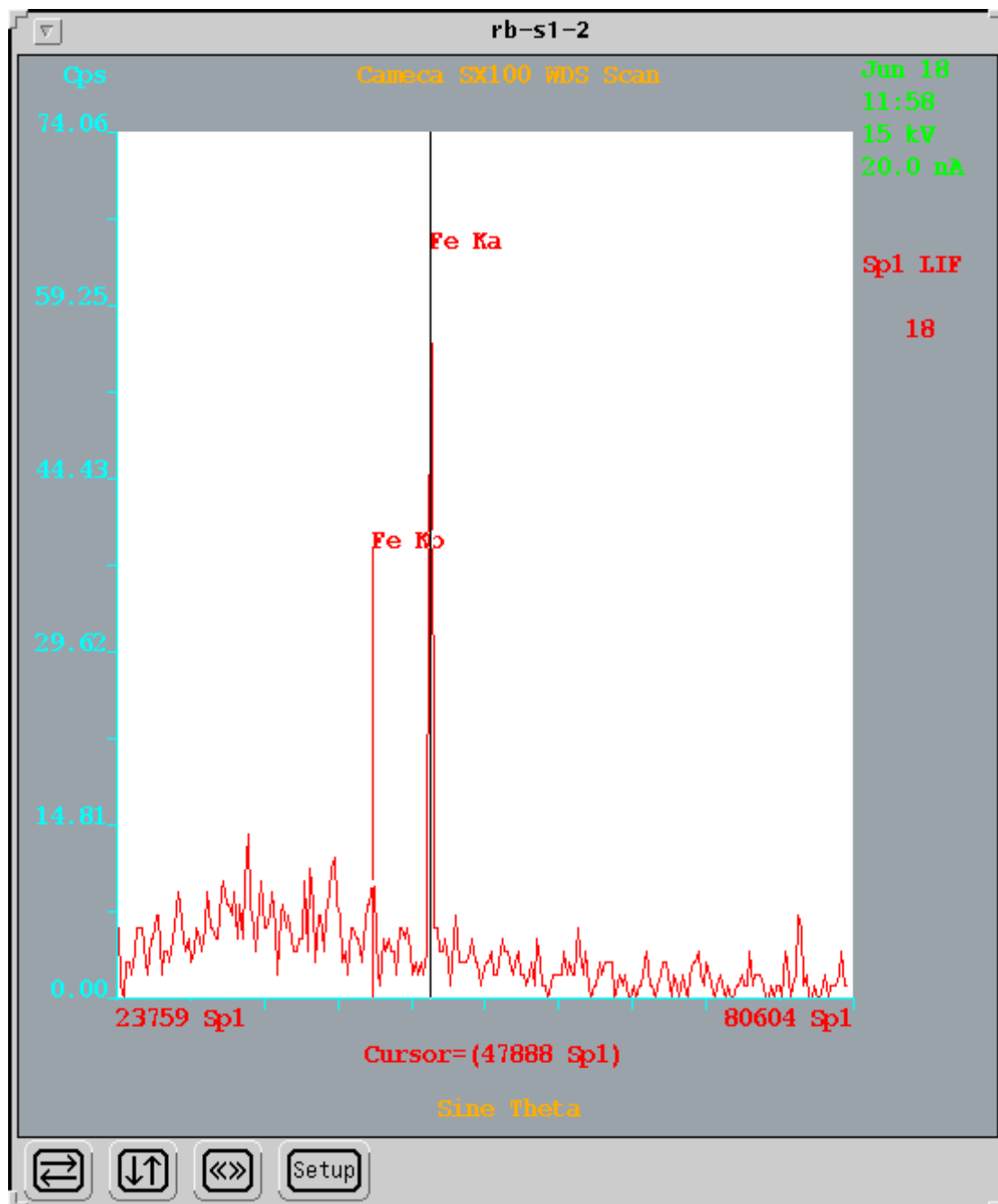
Wavelength Dispersive Spectroscopy (WDS)
X-ray scan thallium acid phthalate (TAP) spectrum
for image from station S-1.



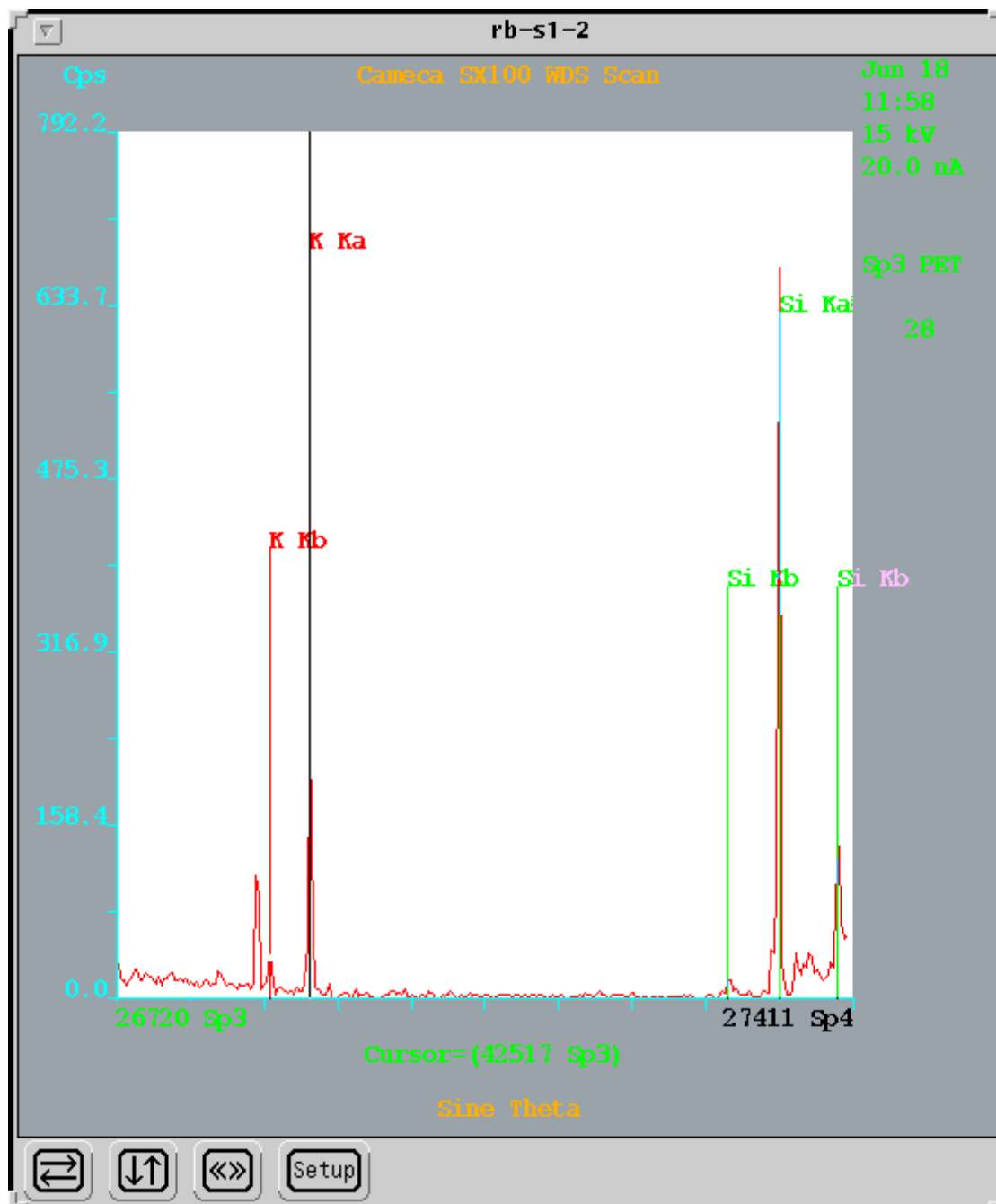
rb-s1-2BSE1

BSE particle grain (simulated wind gust) image from station S-1.

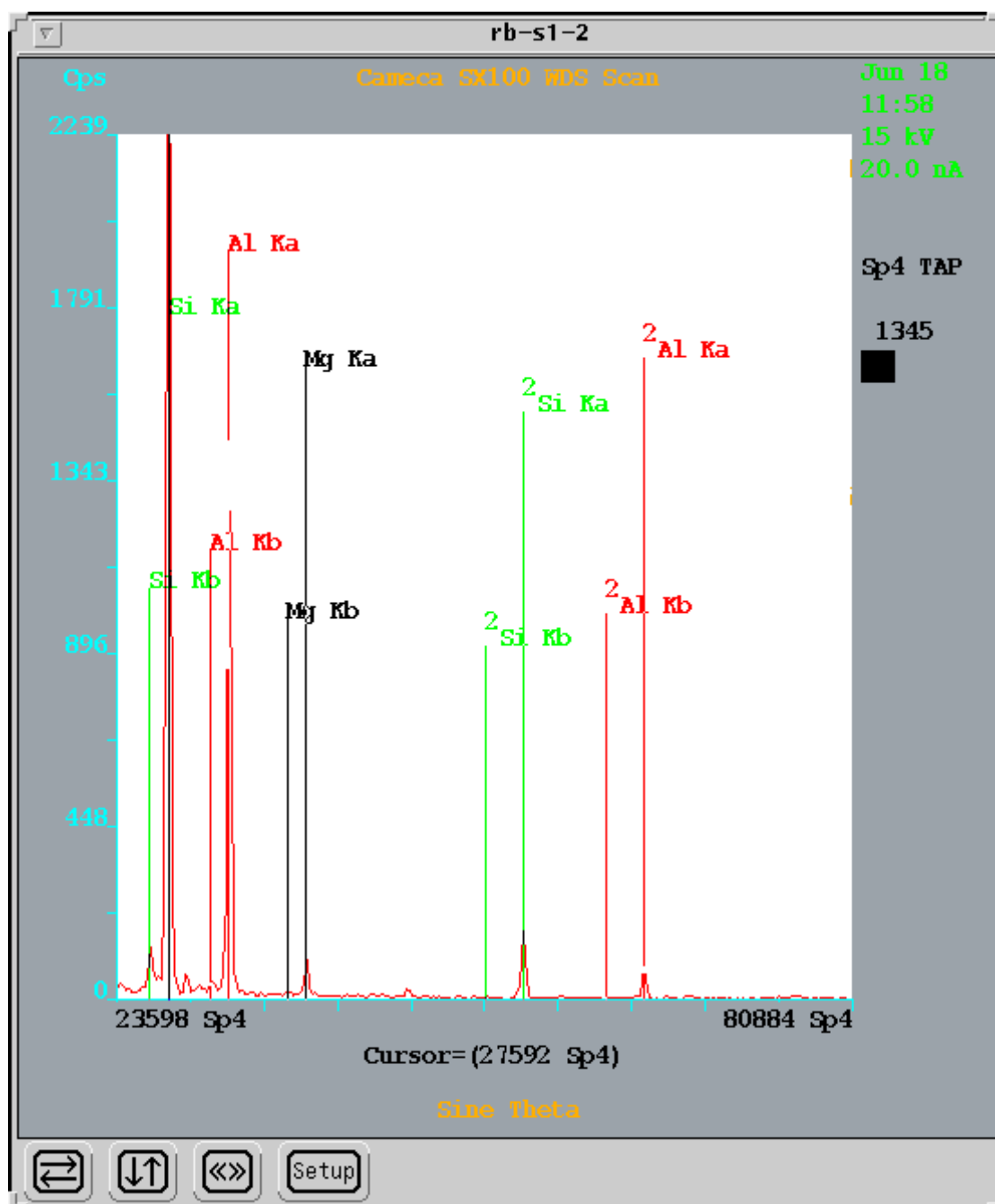
According to the WDS spectra generated, the inferred minerals are kaolinite, K-feldspar and iron oxide.



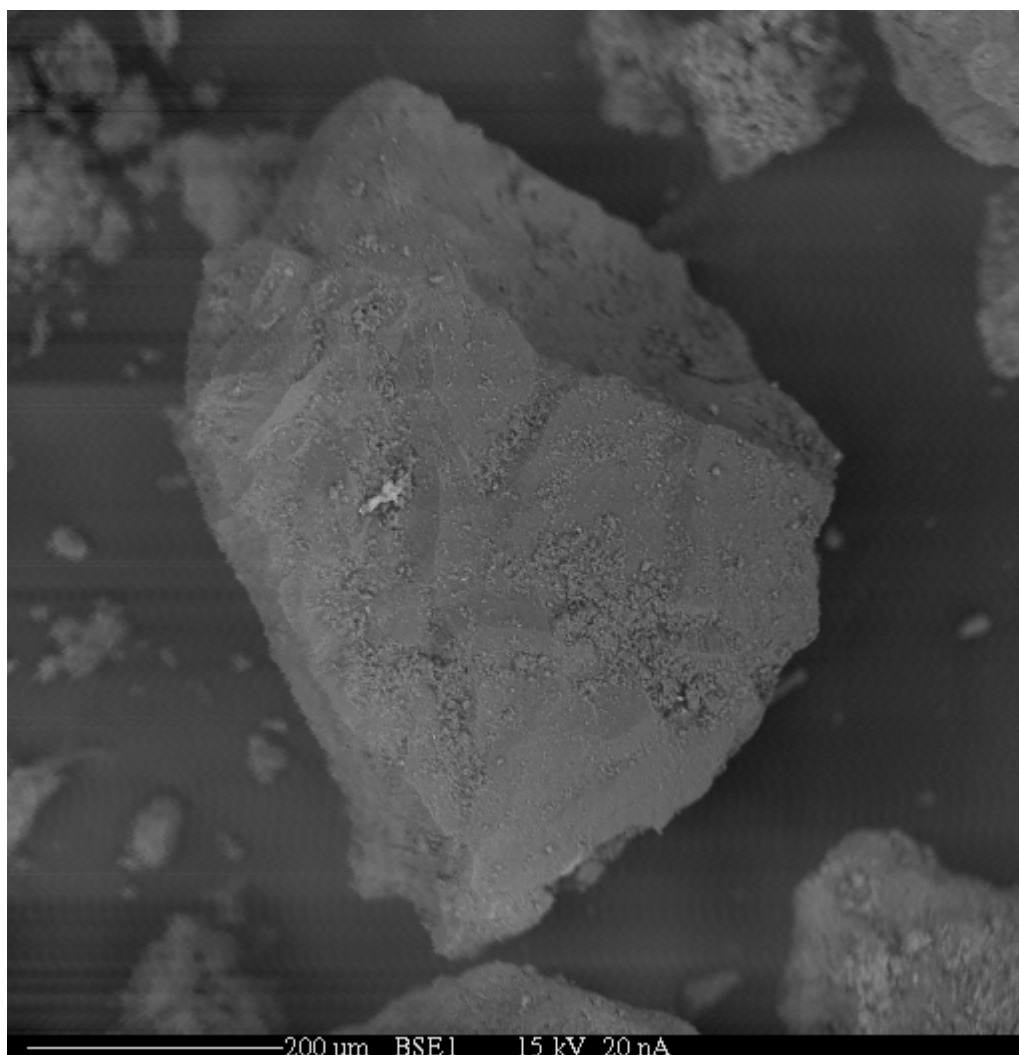
Wavelength Dispersive Spectroscopy (WDS)
X-ray scan lithium fluoride (LIF) spectrum
for image from station S-1.



Wavelength Dispersive Spectroscopy (WDS)
X-ray scan pentaerythritol (PET) spectrum
for image from station S-1.

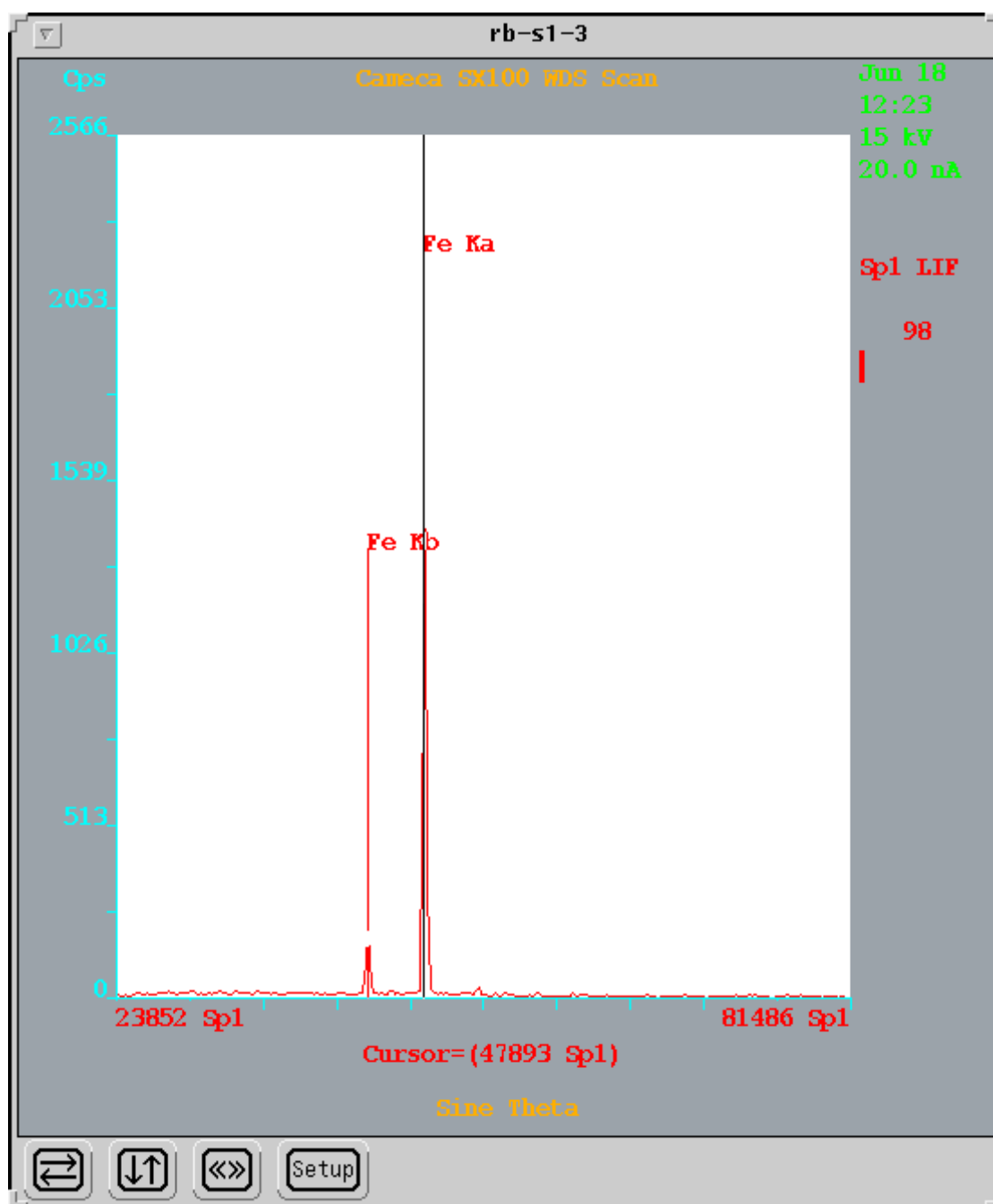


Wavelength Dispersive spectroscopy (WDS)
X-ray scan thallium acid phthalate (TAP) spectrum
for image from station S-1.

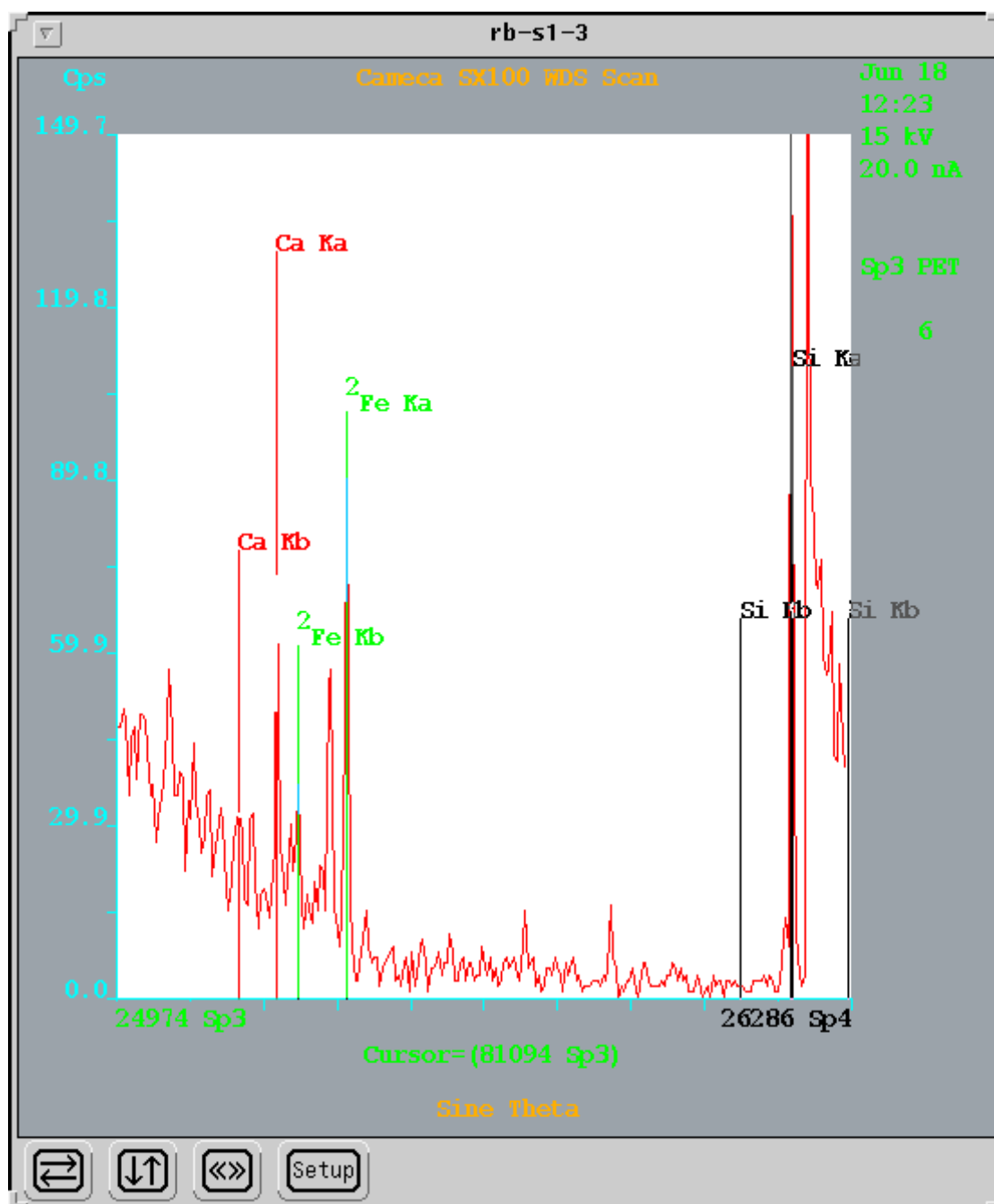


rb-s1-3BSE1

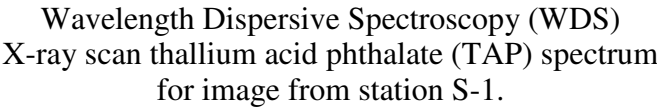
BSE particle grain (simulated wind gust) image from station S-1.
According to the WDS spectra generated, the
inferred minerals are feldspar and iron oxide.

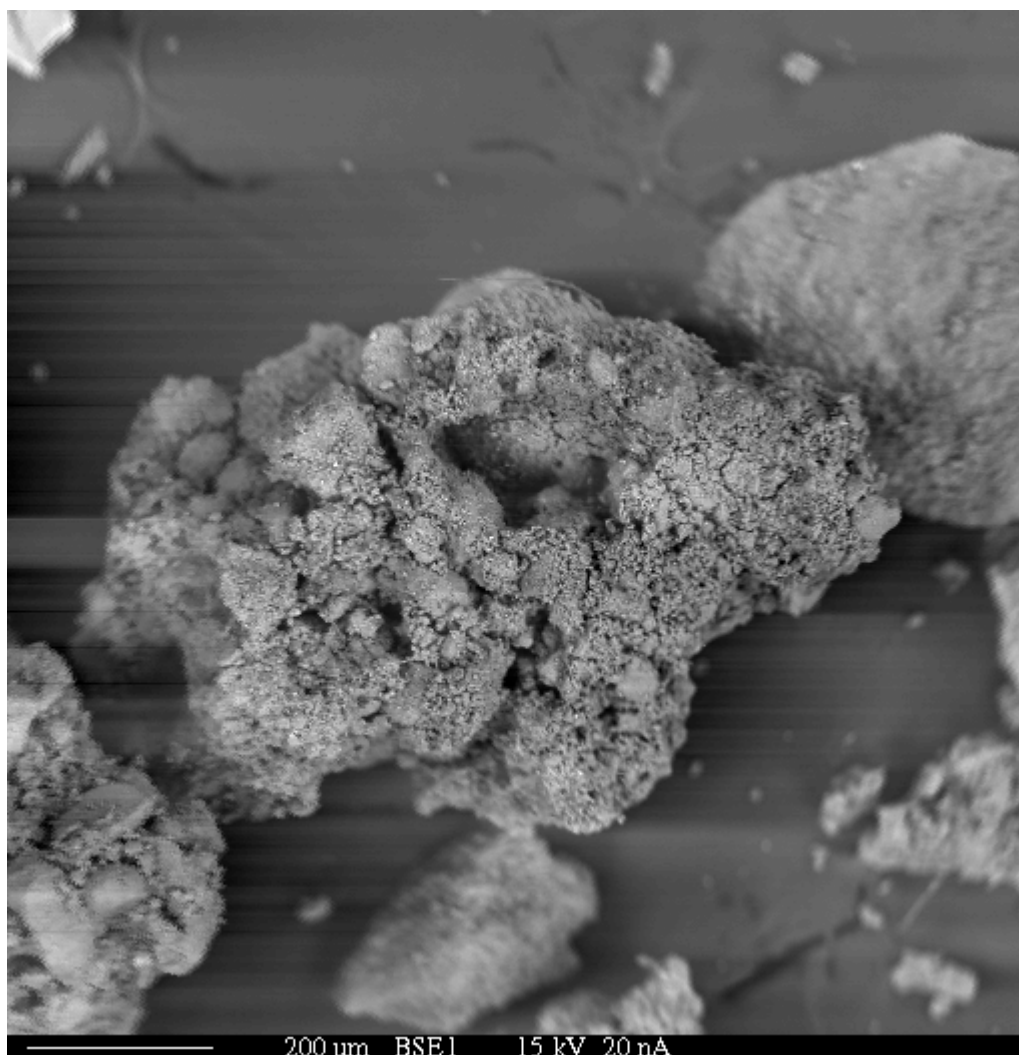


Wavelength Dispersive Spectroscopy (WDS)
X-ray scan lithium fluoride (LIF) spectrum
for image from station S-1.



Wavelength Dispersive Spectroscopy (WDS)
X-ray scan pentaerythritol (PET) spectrum
for image from station S-1.

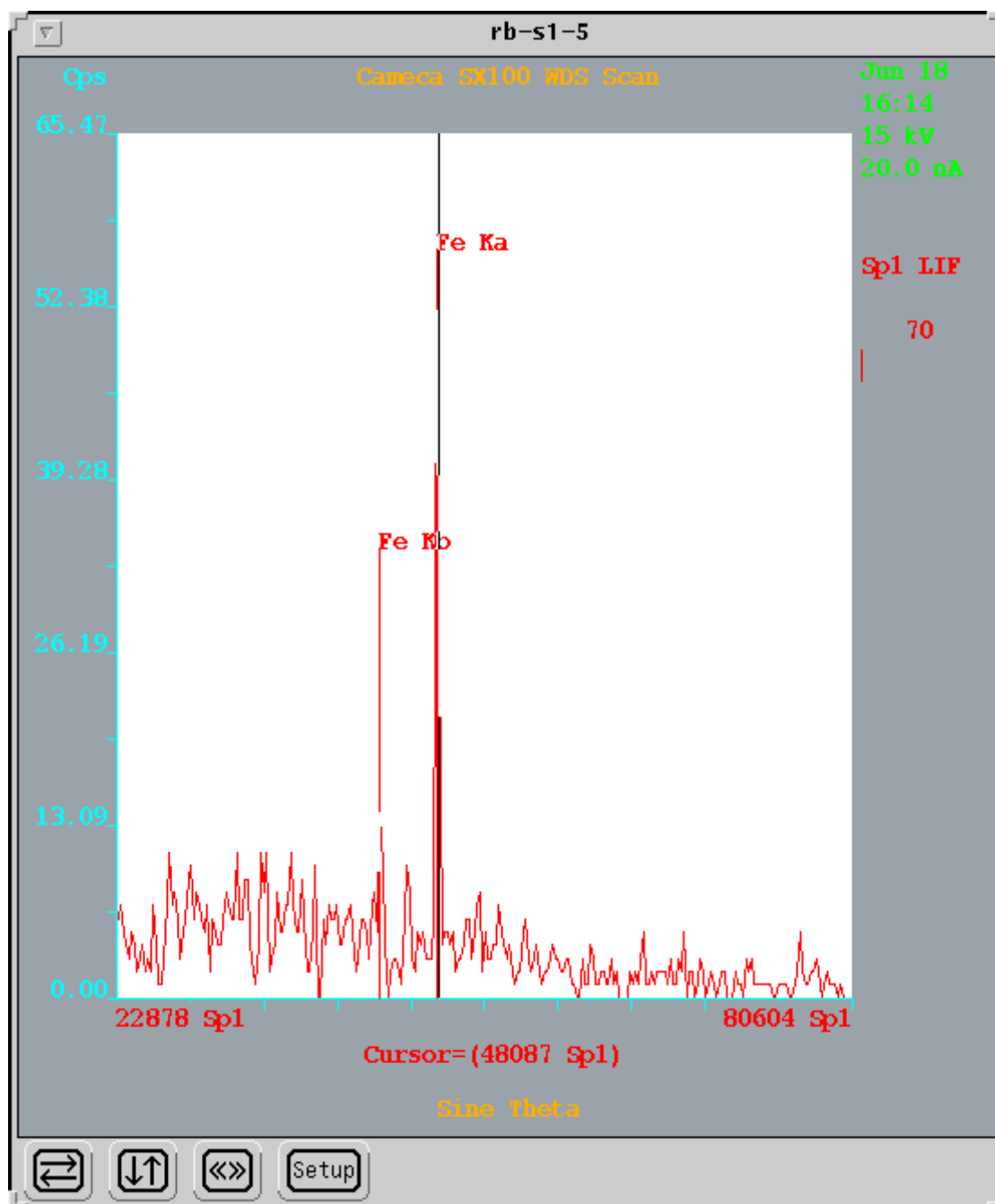




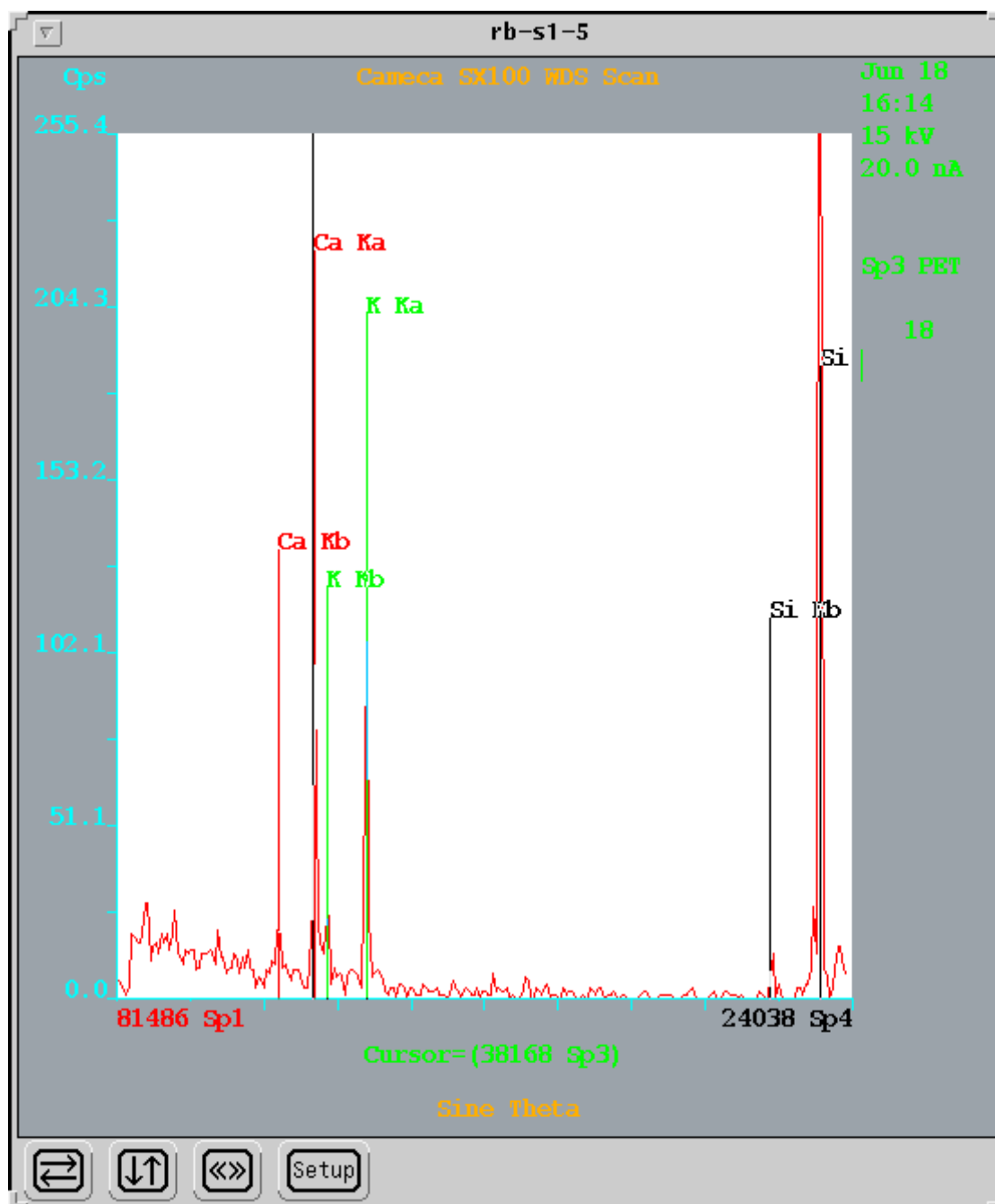
rb-s1-5BSE1

BSE particle grain (simulated wind gust) image from station S-1.

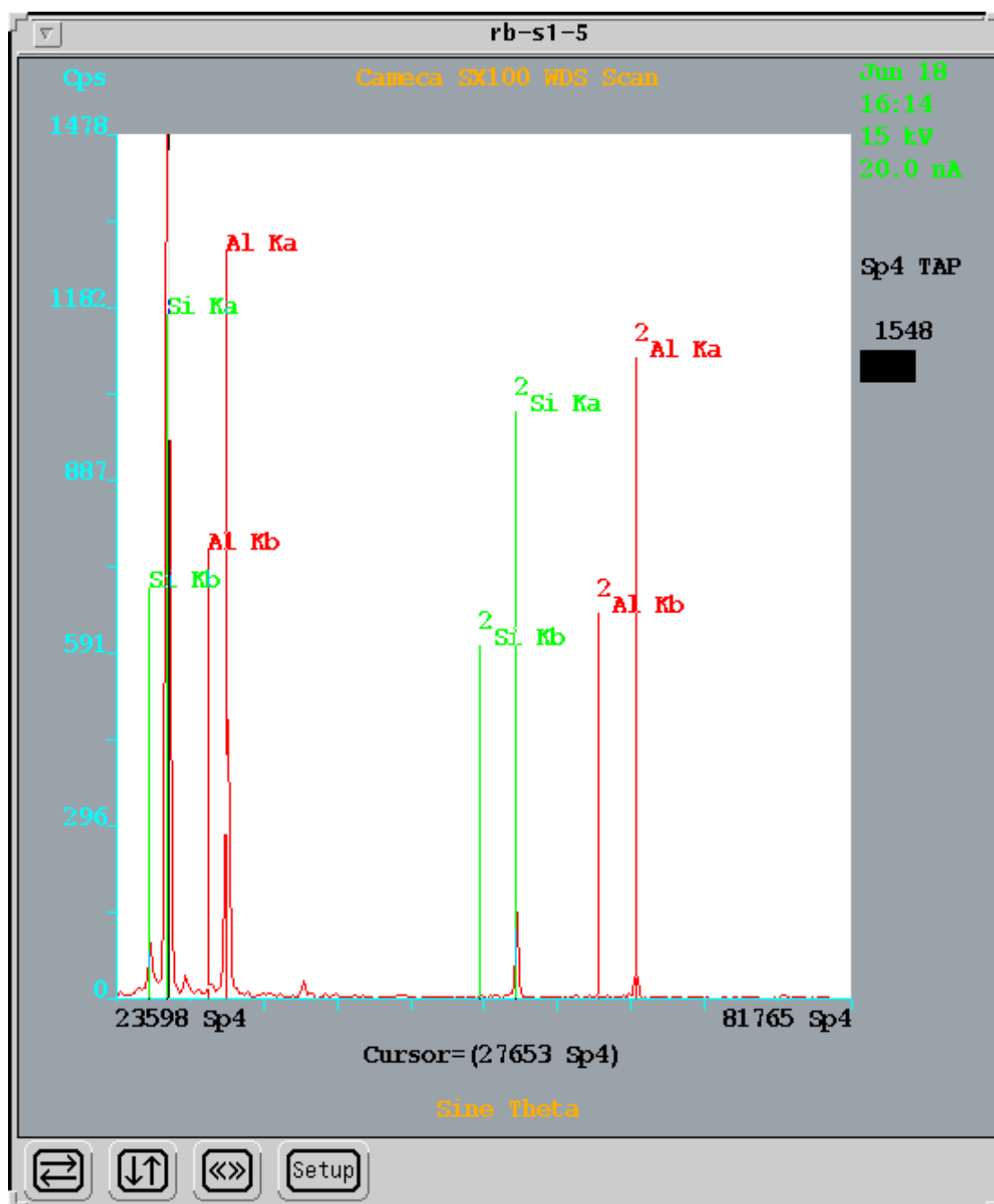
According to the WDS spectra generated, the inferred minerals are kaolinite, feldspar, and iron oxide.



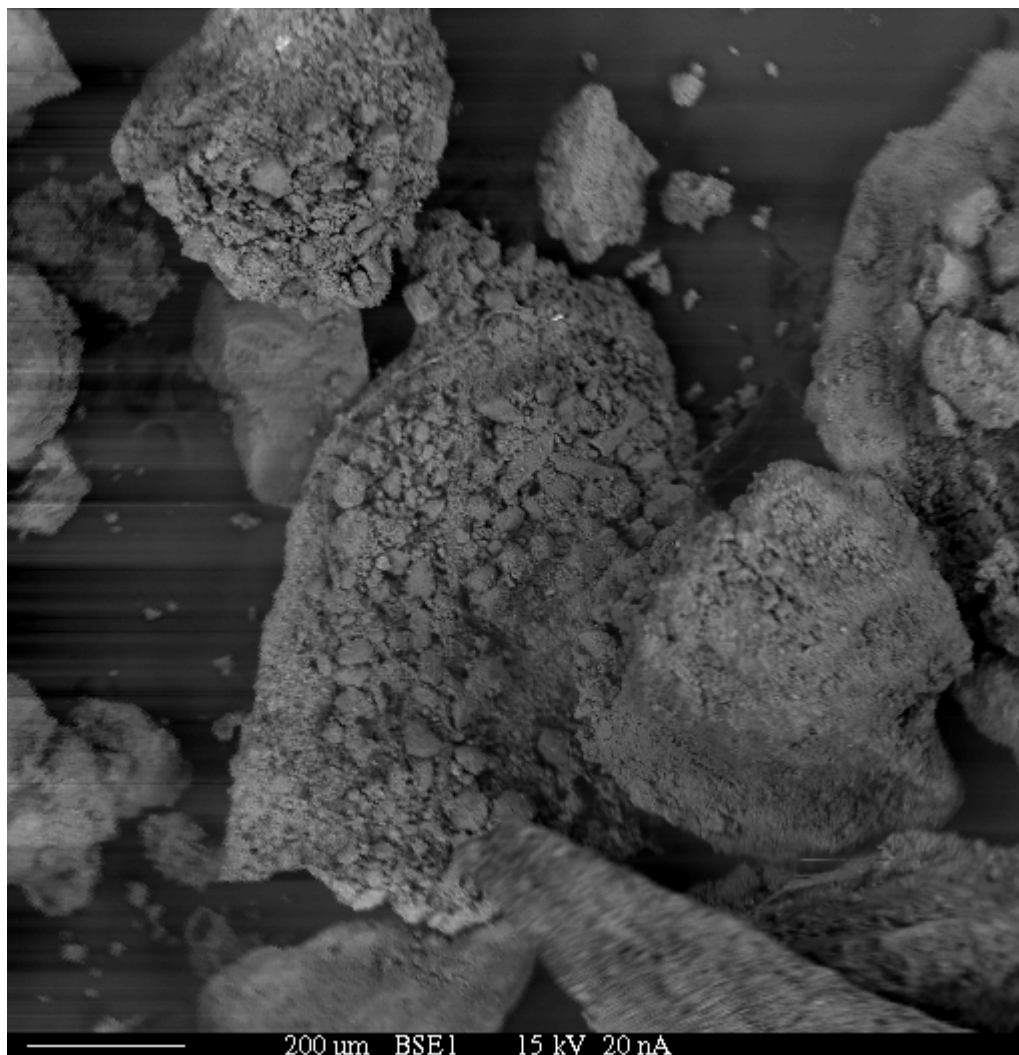
Wavelength Dispersive Spectroscopy (WDS)
X-ray scan lithium fluoride (LIF) spectrum
for image from station S-1.



Wavelength Dispersive Spectroscopy (WDS)
X-ray scan pentaerythritol (PET) spectrum
for image from station S-1.

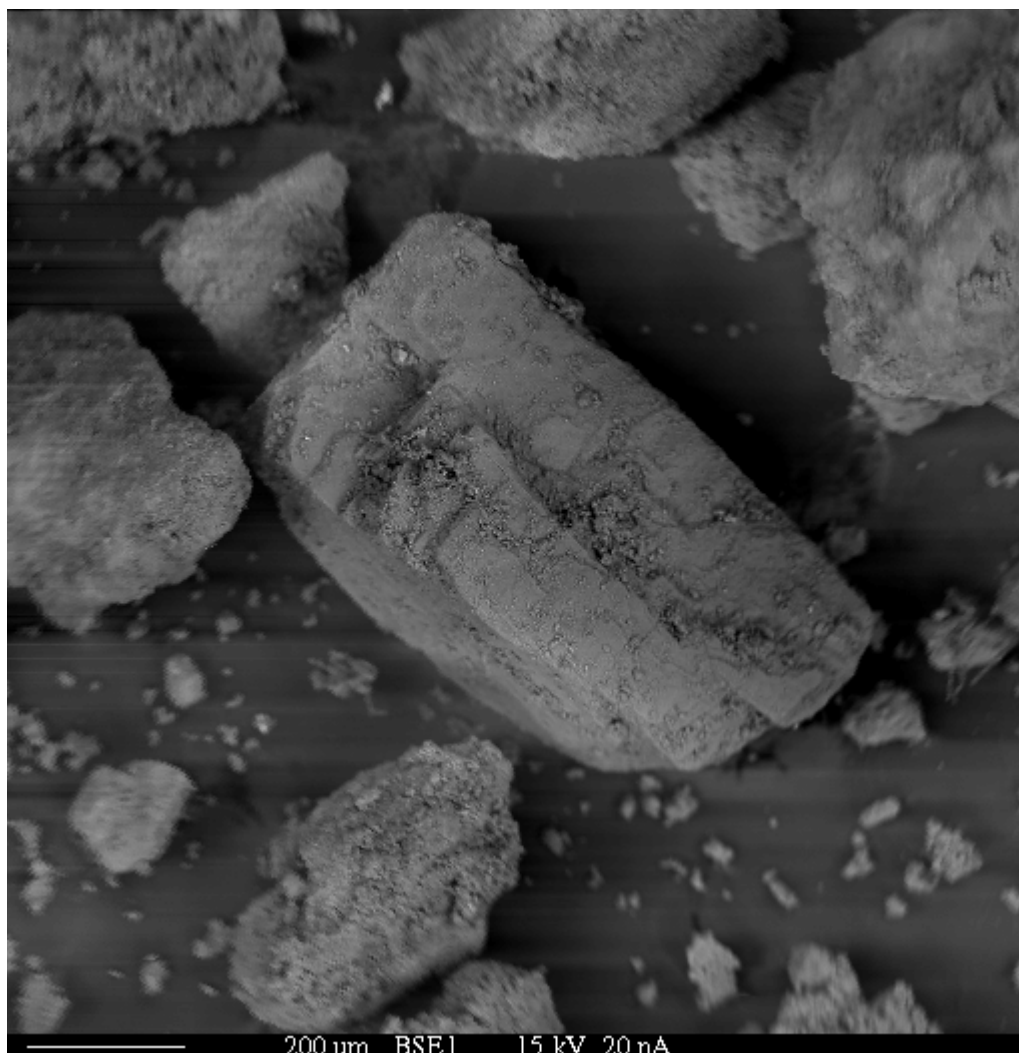


Wavelength Dispersive Spectroscopy (WDS)
X-ray scan thallium acid phthalate (TAP) spectrum
for image from station S-1.



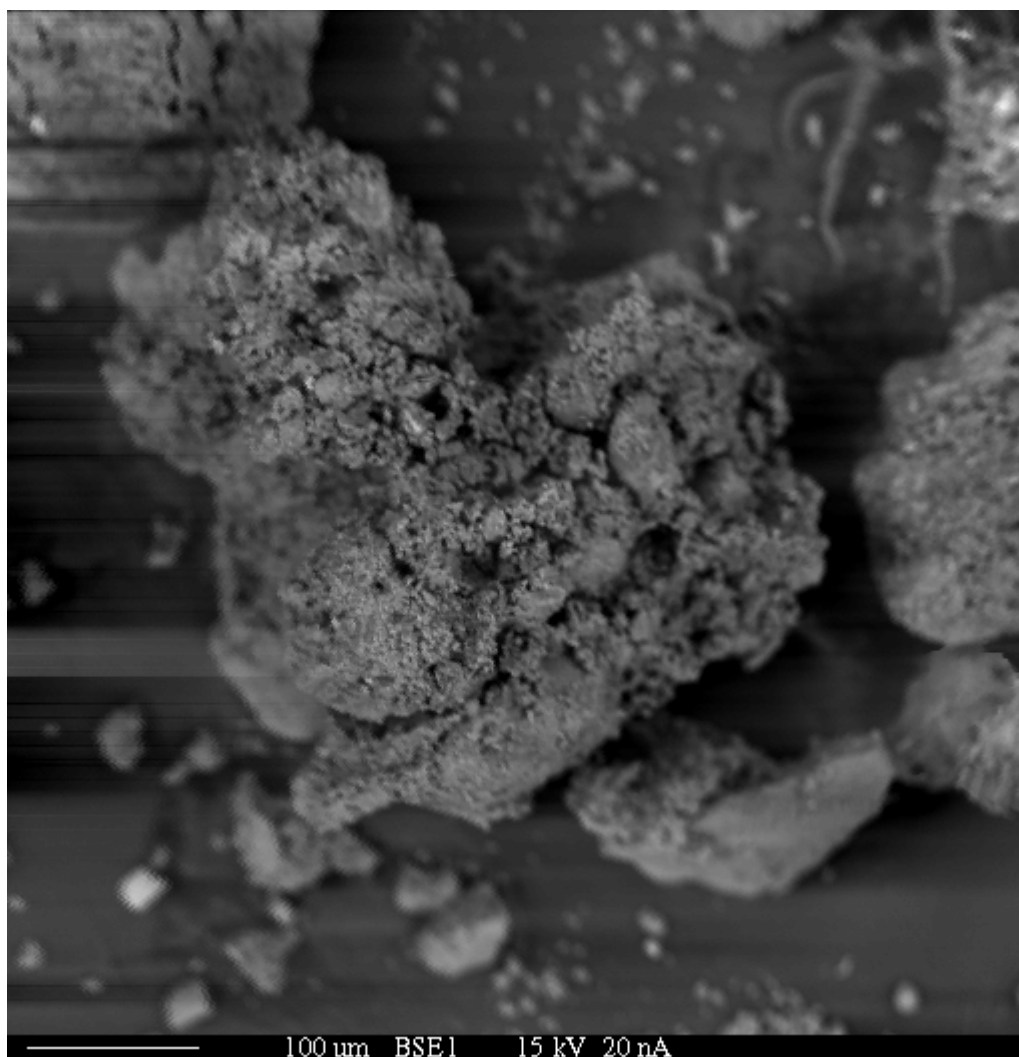
rb-s1-6bBSE1

BSE particle grain (simulated wind gust) image from station S-1.
No WDS was spectra generated.



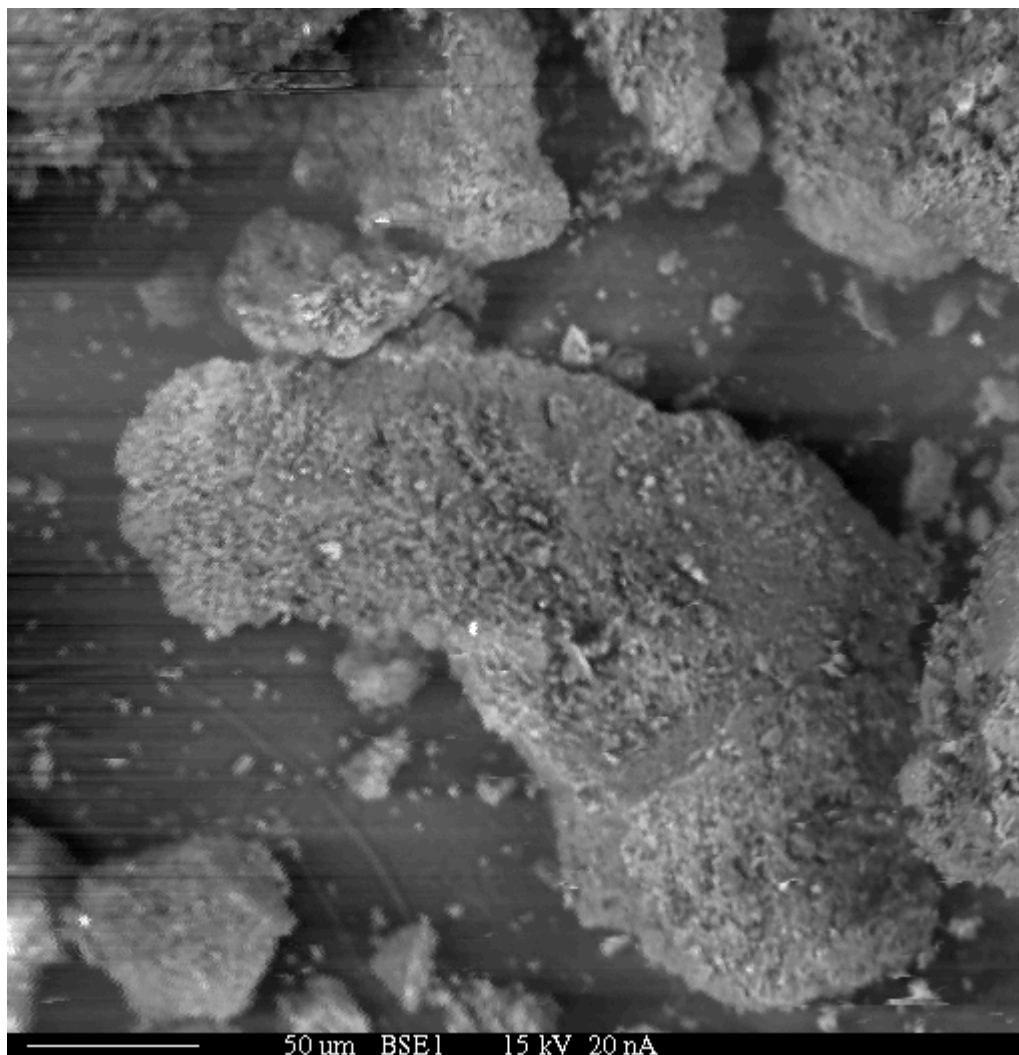
rb-s1-7bBSE1

BSE particle grain (simulated wind gust) image from station S-1.
No WDS was spectra generated.



rb-s1-8bBSE1

BSE particle grain (simulated wind gust) image from station S-1.
No WDS was spectra generated.



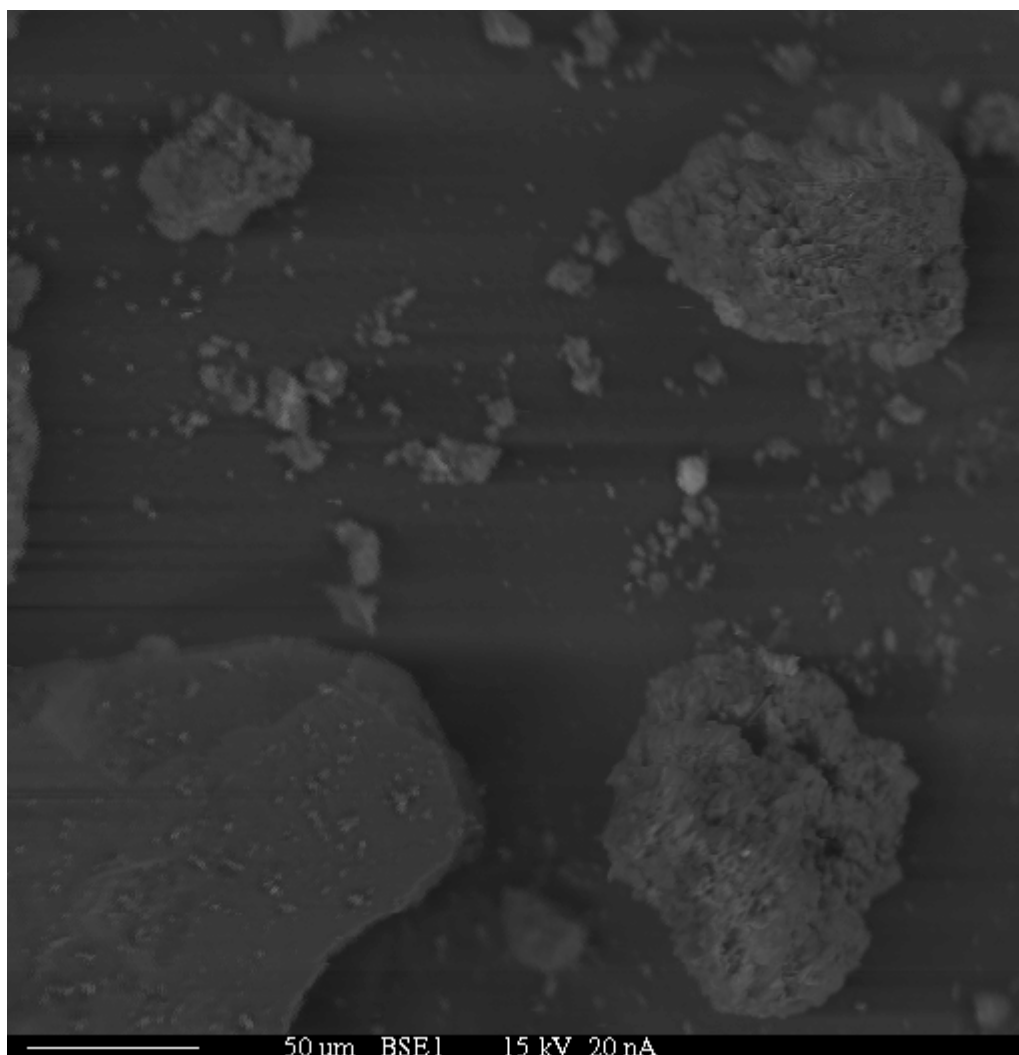
rb-s2-1bse1BSE1

BSE particle grain (simulated wind gust) image from station S-2.
No WDS was spectra generated.



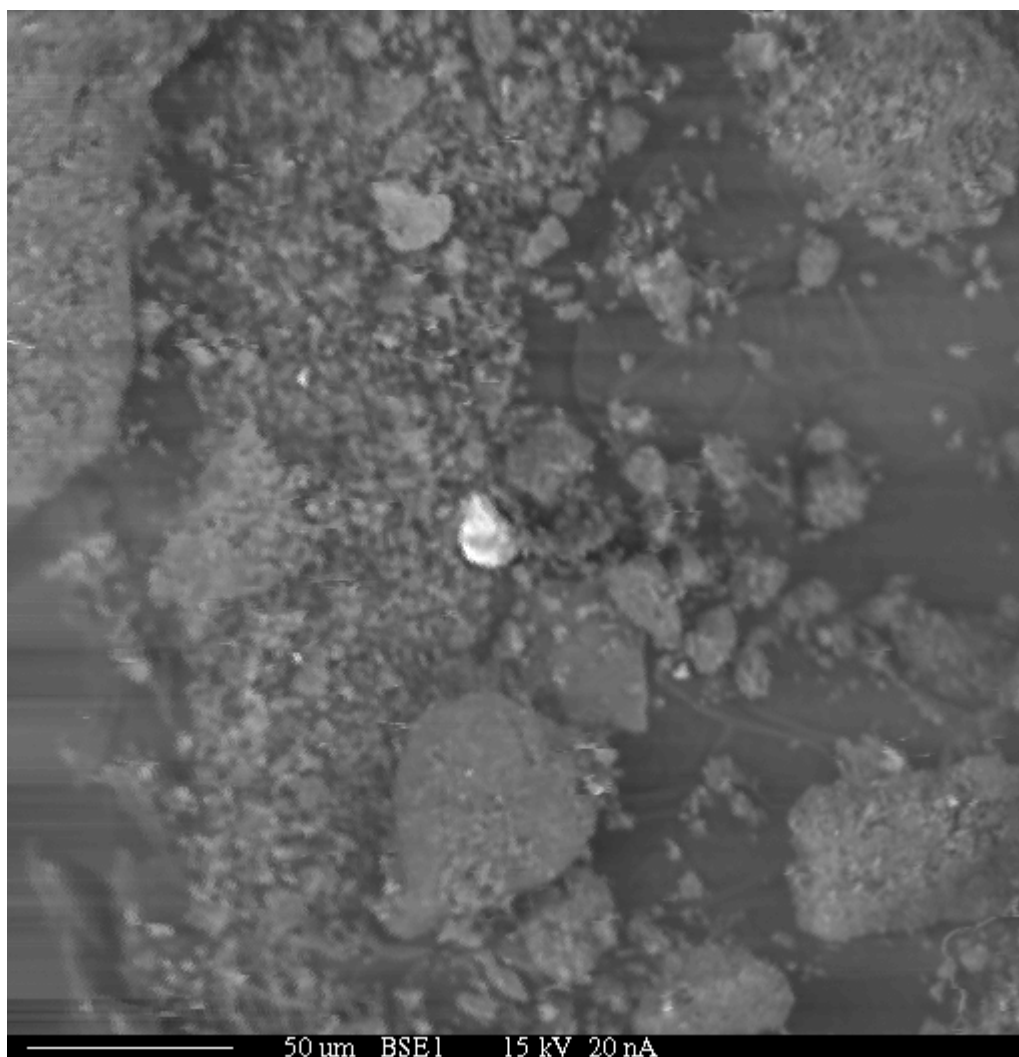
rb-s2-1bse2BSE1

BSE particle grain (simulated wind gust) image from station S-2.
No WDS was spectra generated.



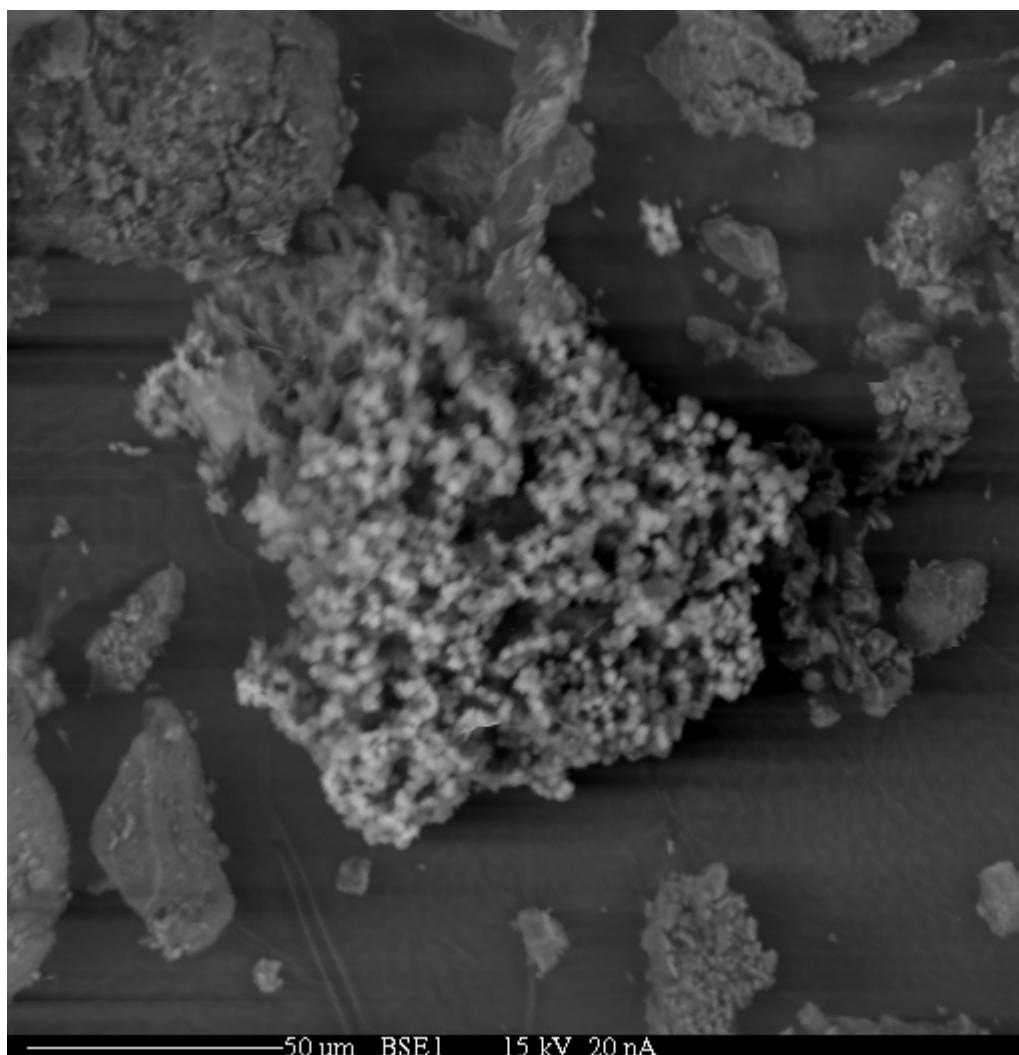
rb-s2-3bse1BSE1

BSE particle grain (simulated wind gust) image from station S-2.
No WDS was spectra generated.



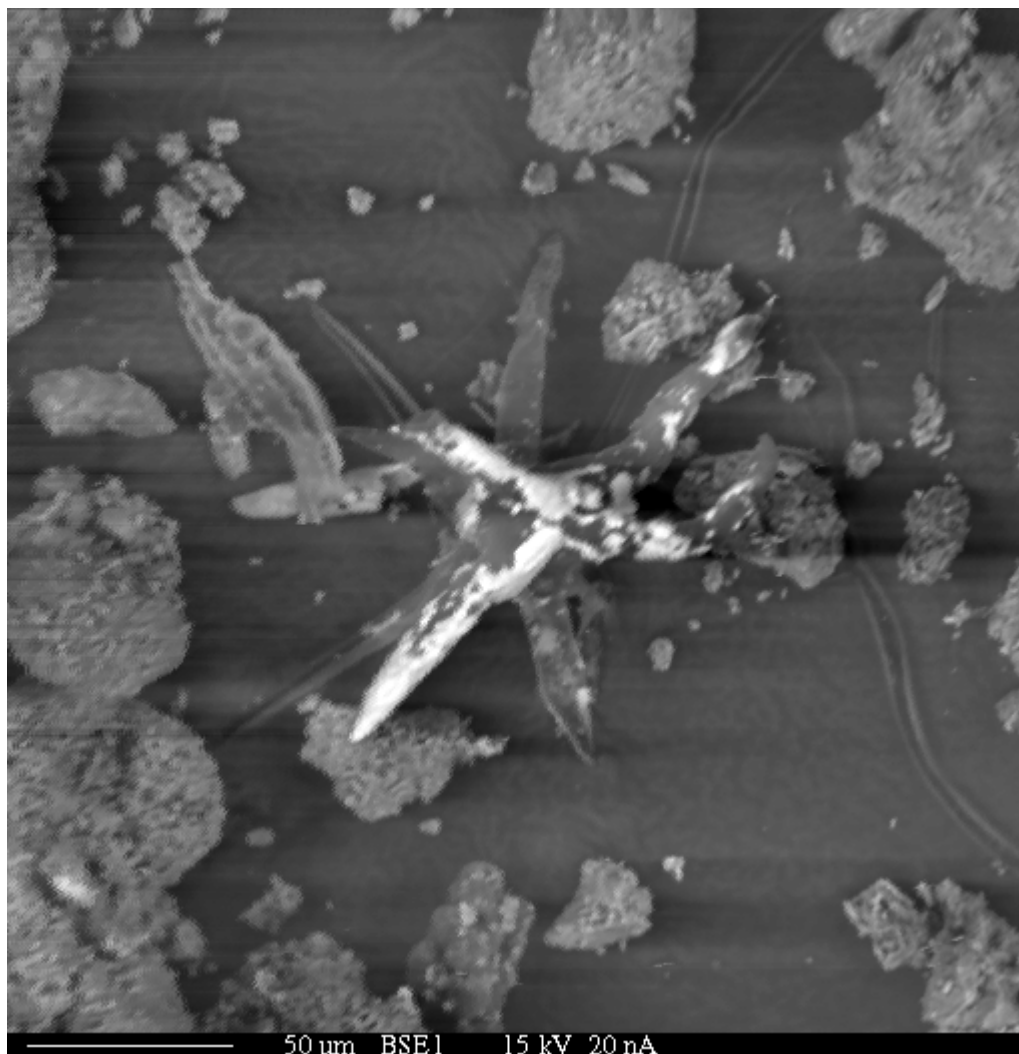
rb-s2-4bse1BSE1

BSE particle grain (simulated wind gust) image from station S-2.
According to the WDS spectra generated, the
inferred minerals are kaolinite, K-feldspar,
uranophane, and carnotite.



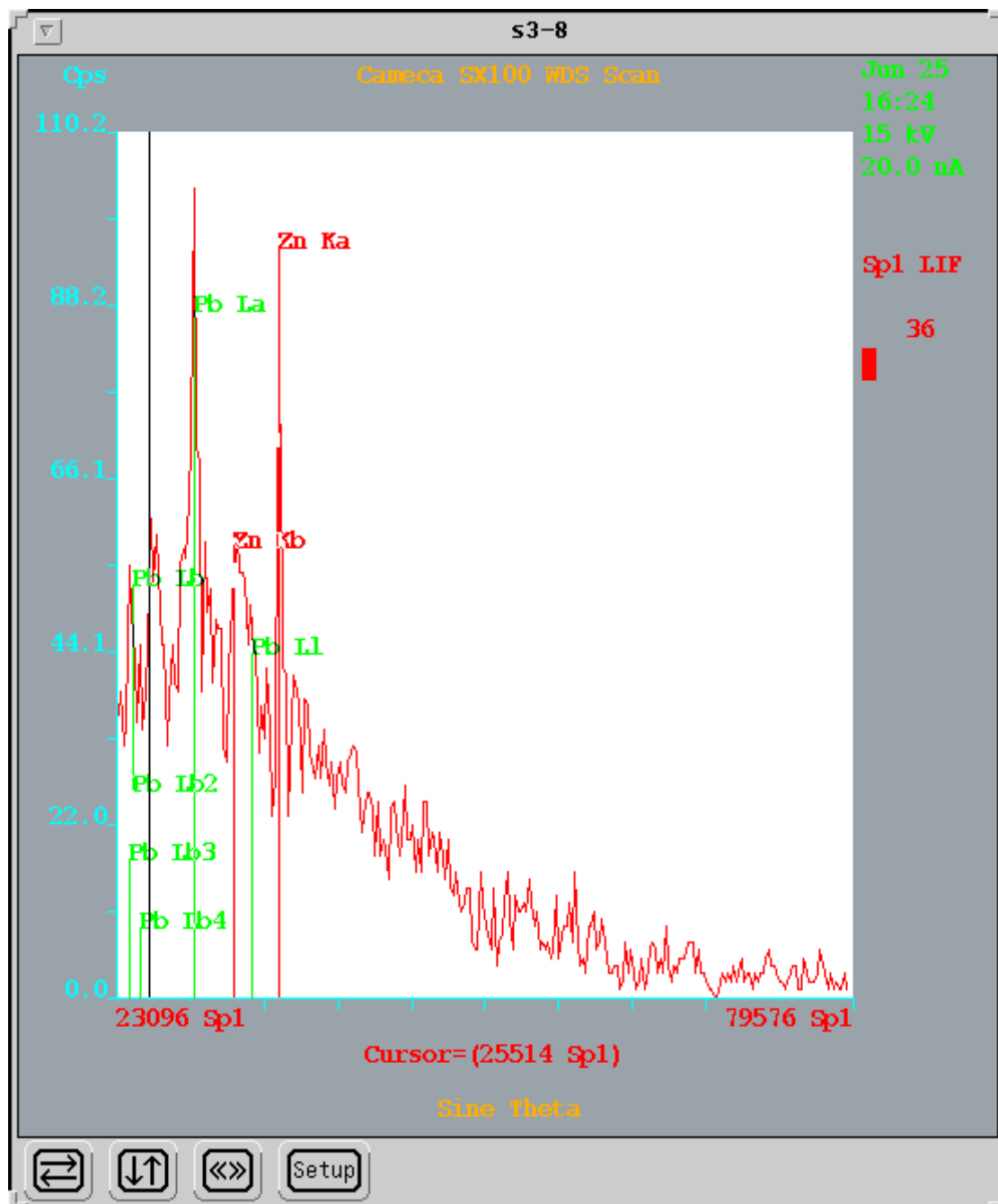
s3-2BSE1

BSE particle grain (simulated wind gust) image from station S-3.
Unintelligible WDS spectra was generated.

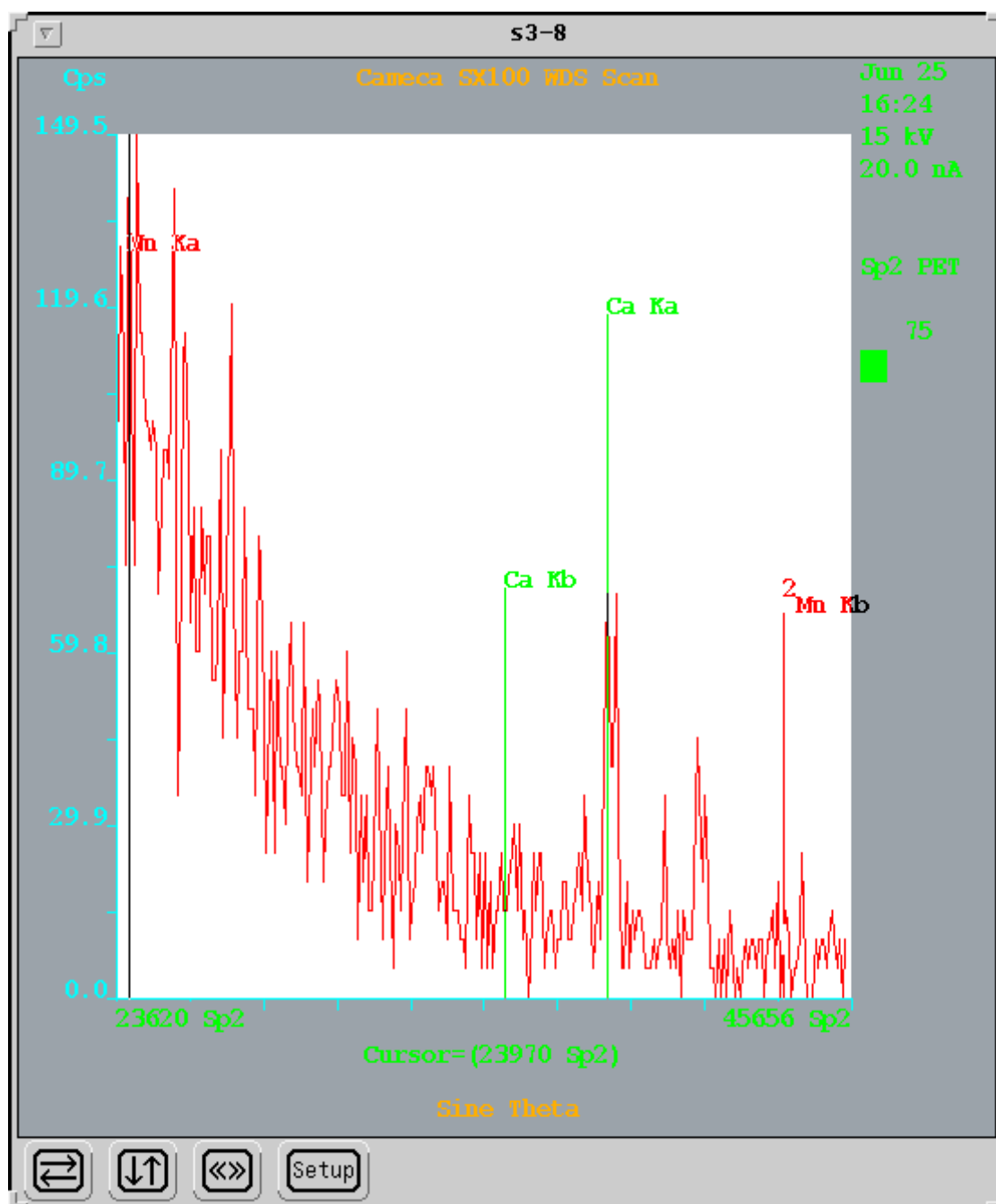


s3-4BSE1

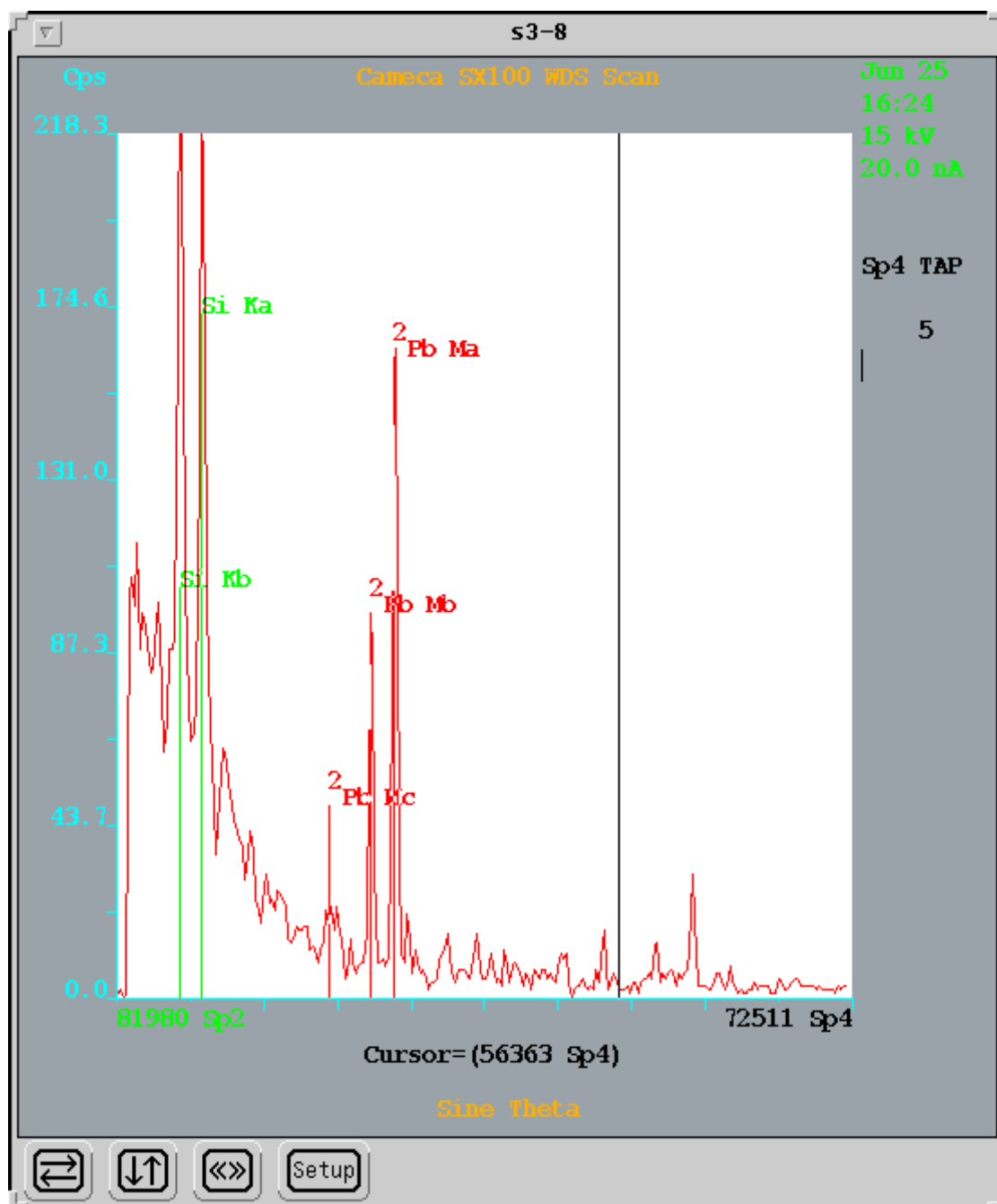
BSE particle grain (simulated wind gust) image from station S-3.
No WDS spectra was generated;
material appears organic.



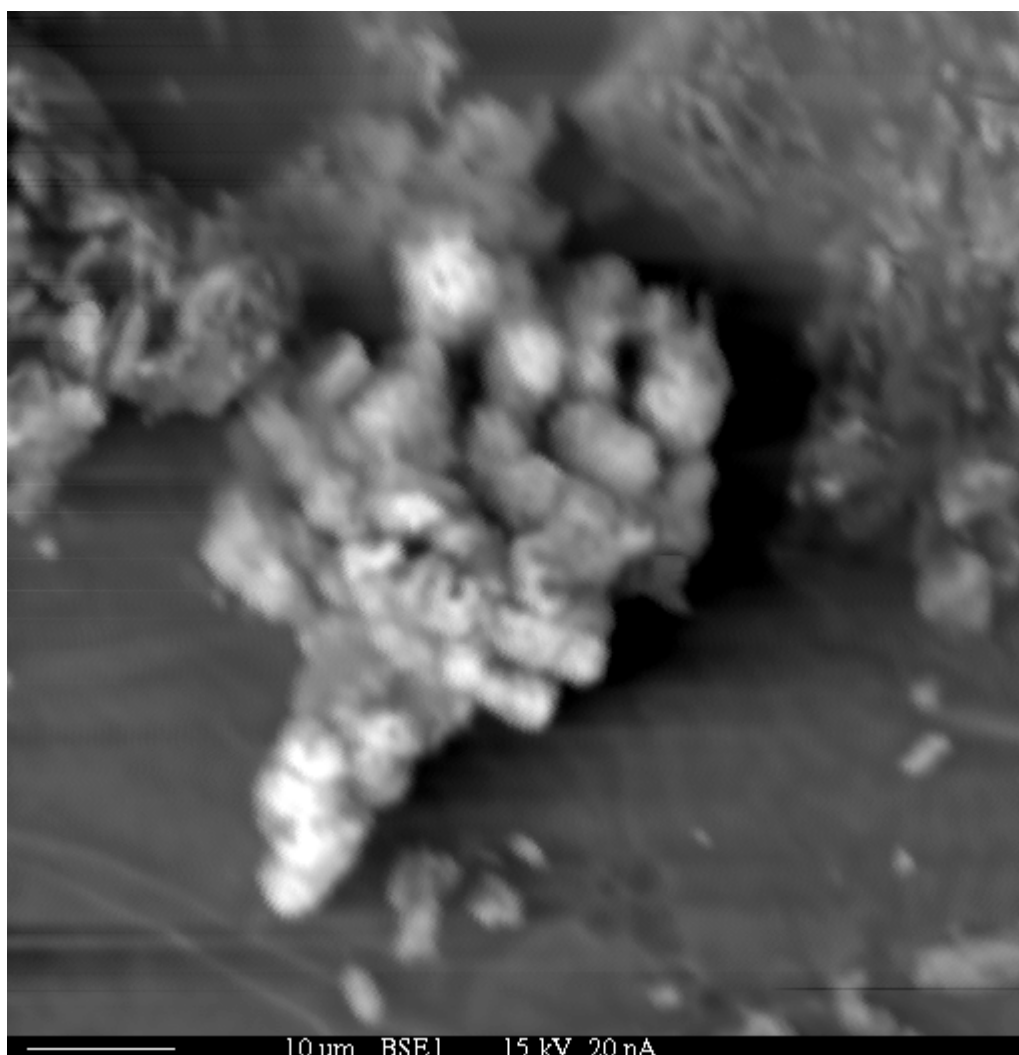
Wavelength Dispersive Spectroscopy (WDS)
X-ray scan lithium fluoride (LIF) spectrum
for sample from station S-3.



Wavelength Dispersive Spectroscopy (WDS)
X-ray scan pentaerythritol (PET) spectrum
for sample from station S-3.

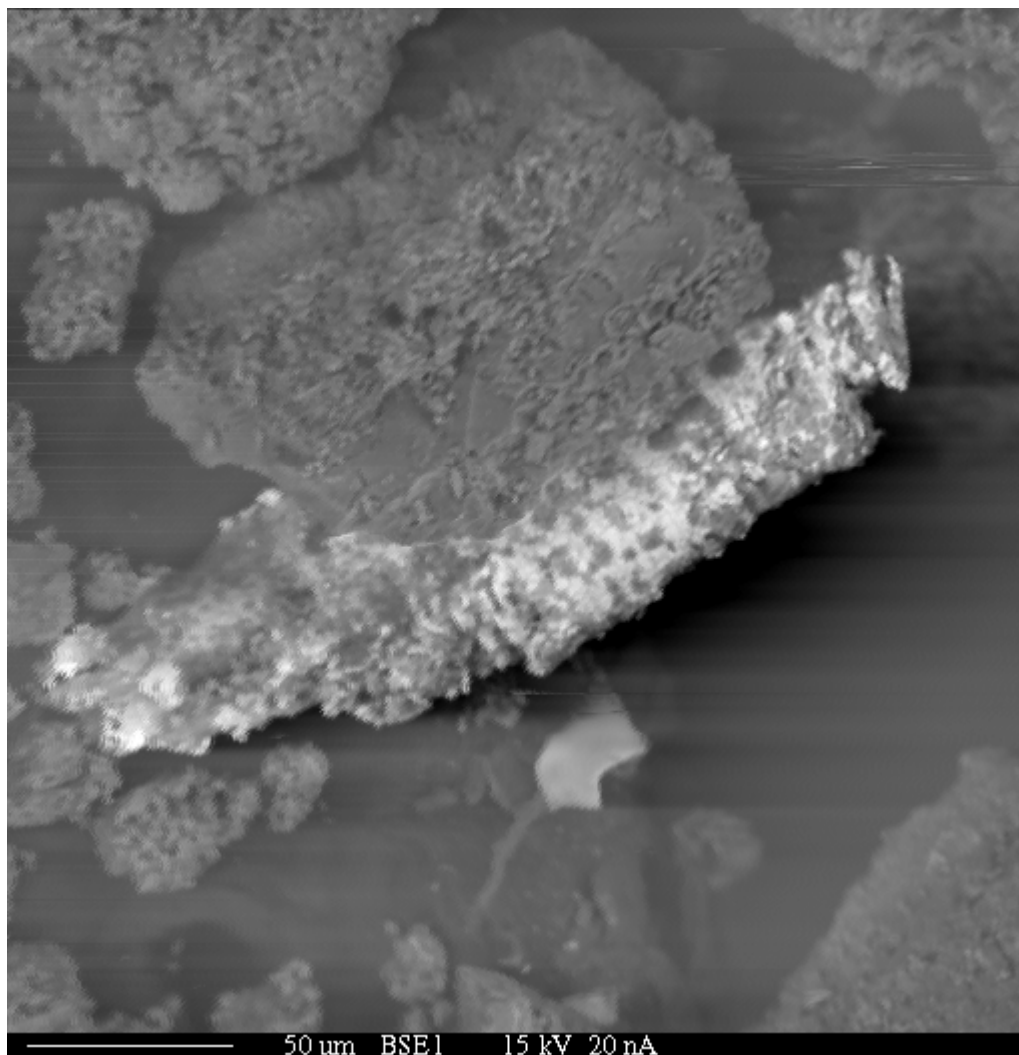


Wavelength Dispersive Spectroscopy (WDS)
X-ray scan thallium acid phthalate (TAP) spectrum
for sample from station S-3.



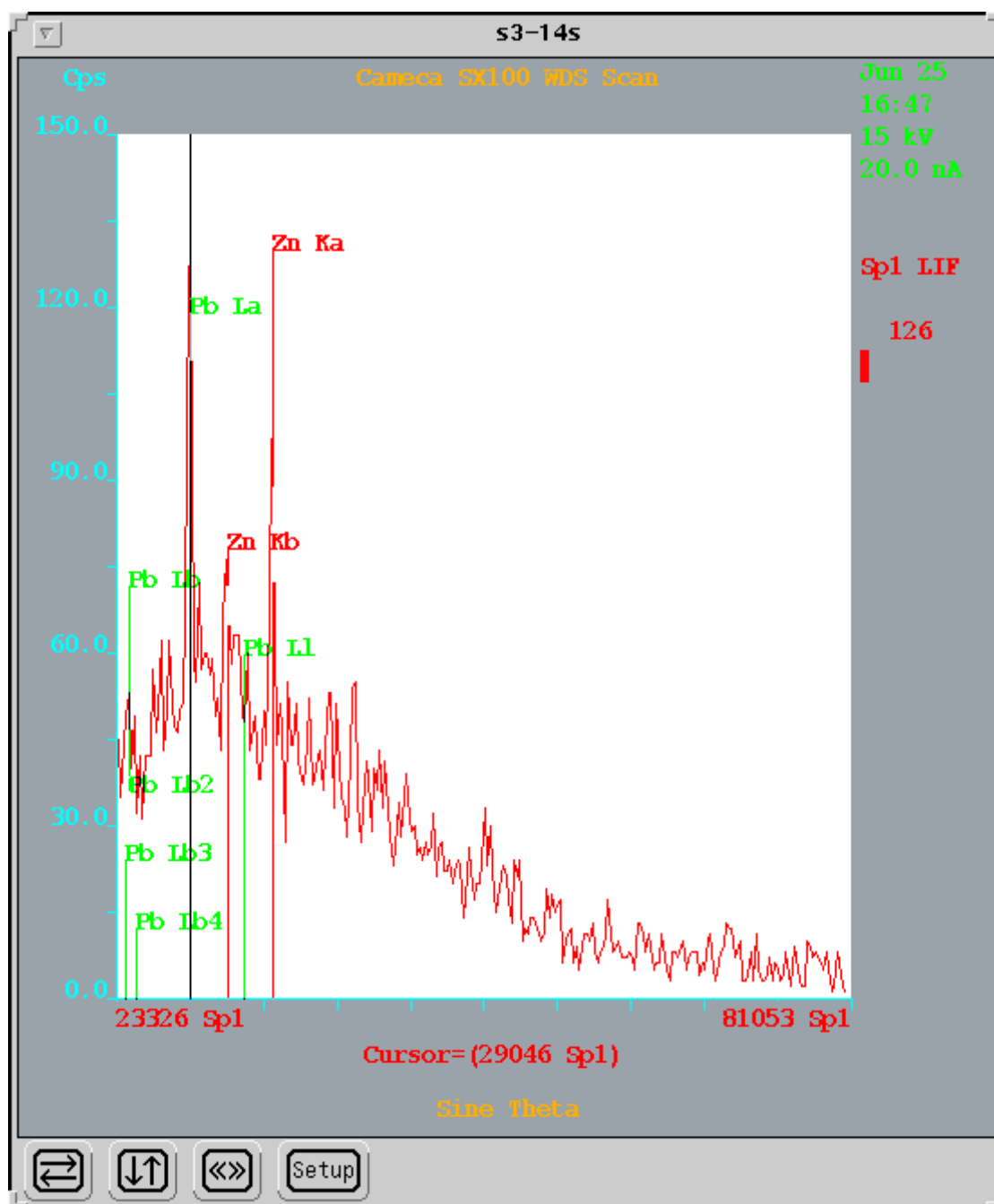
s3-13BSE1

BSE particle grain (simulated wind gust) image from station S-3.
No WDS spectra was generated.

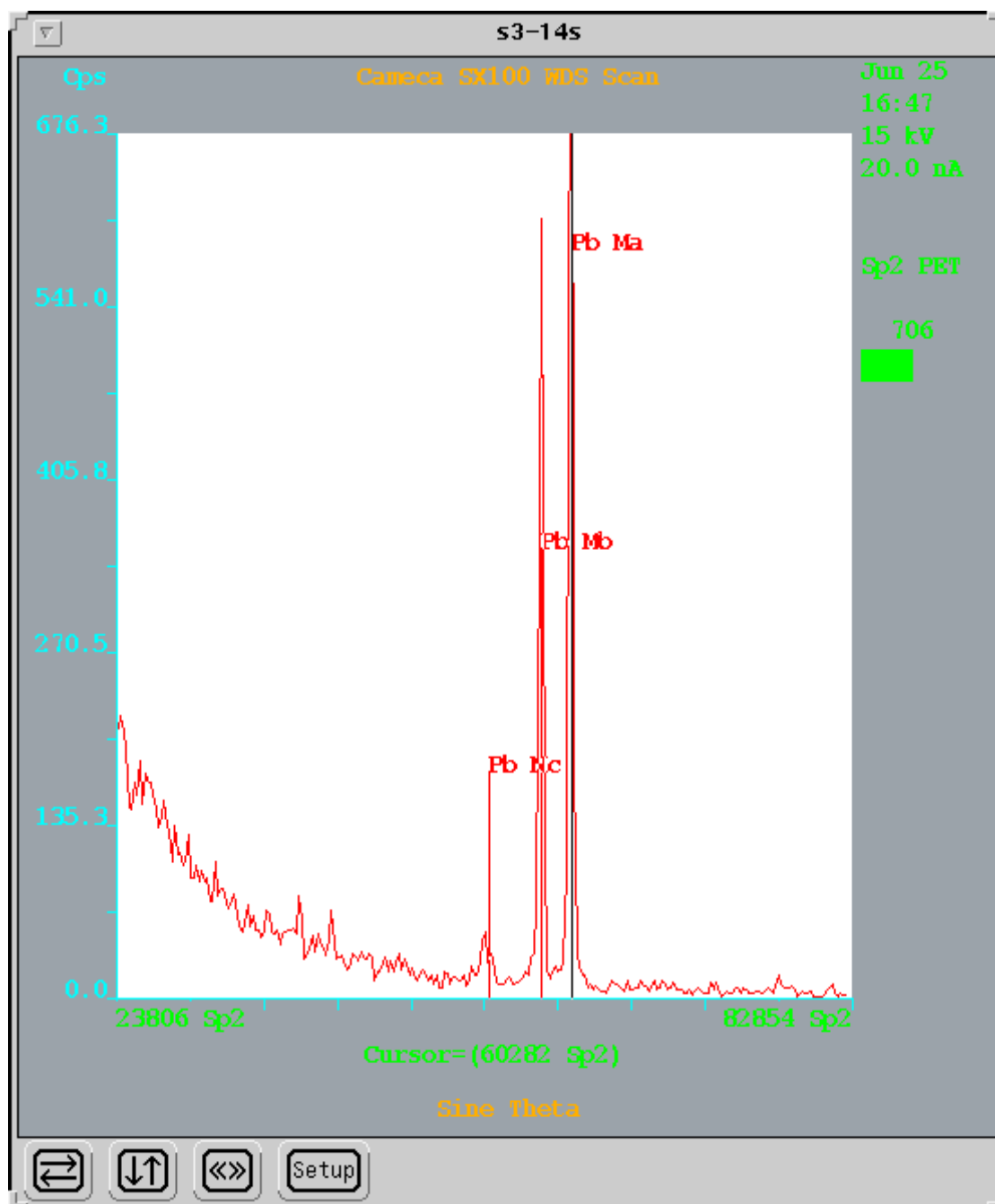


s3-14BSE1

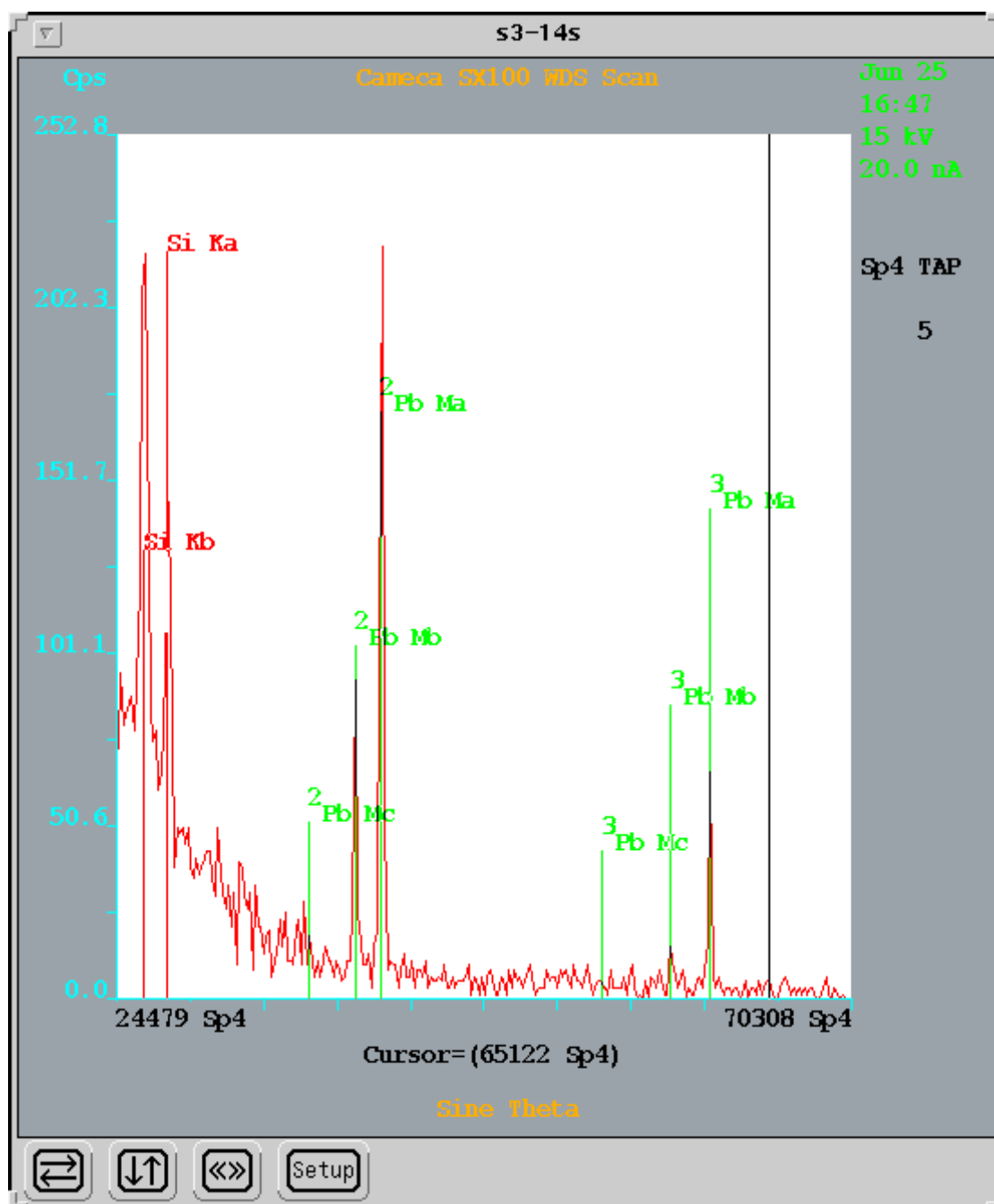
BSE particle grain (simulated wind gust) image from station S-3.
According to the WDS spectra generated.
No mineral was inferred.



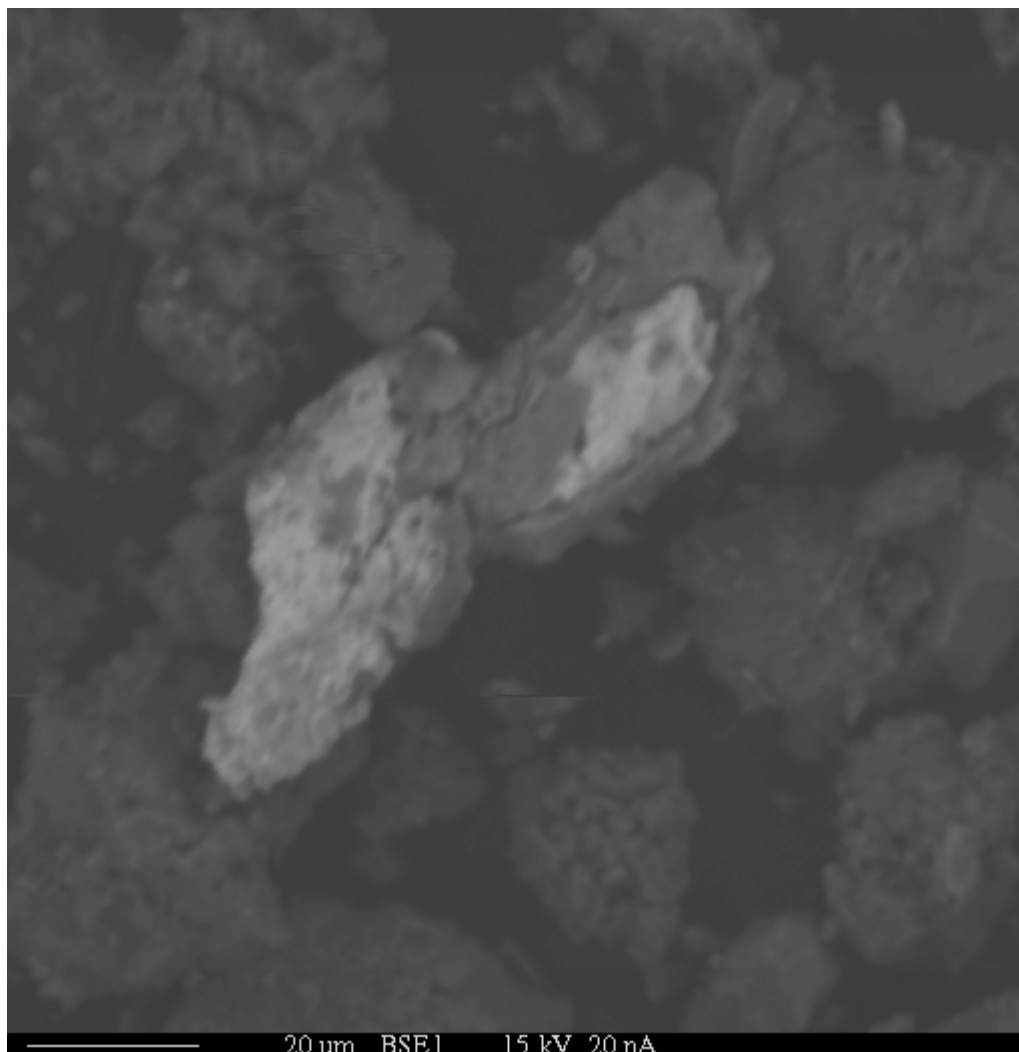
Wavelength Dispersive Spectroscopy (WDS)
X-ray scan lithium fluoride (LIF) spectrum
for image from station S-3.



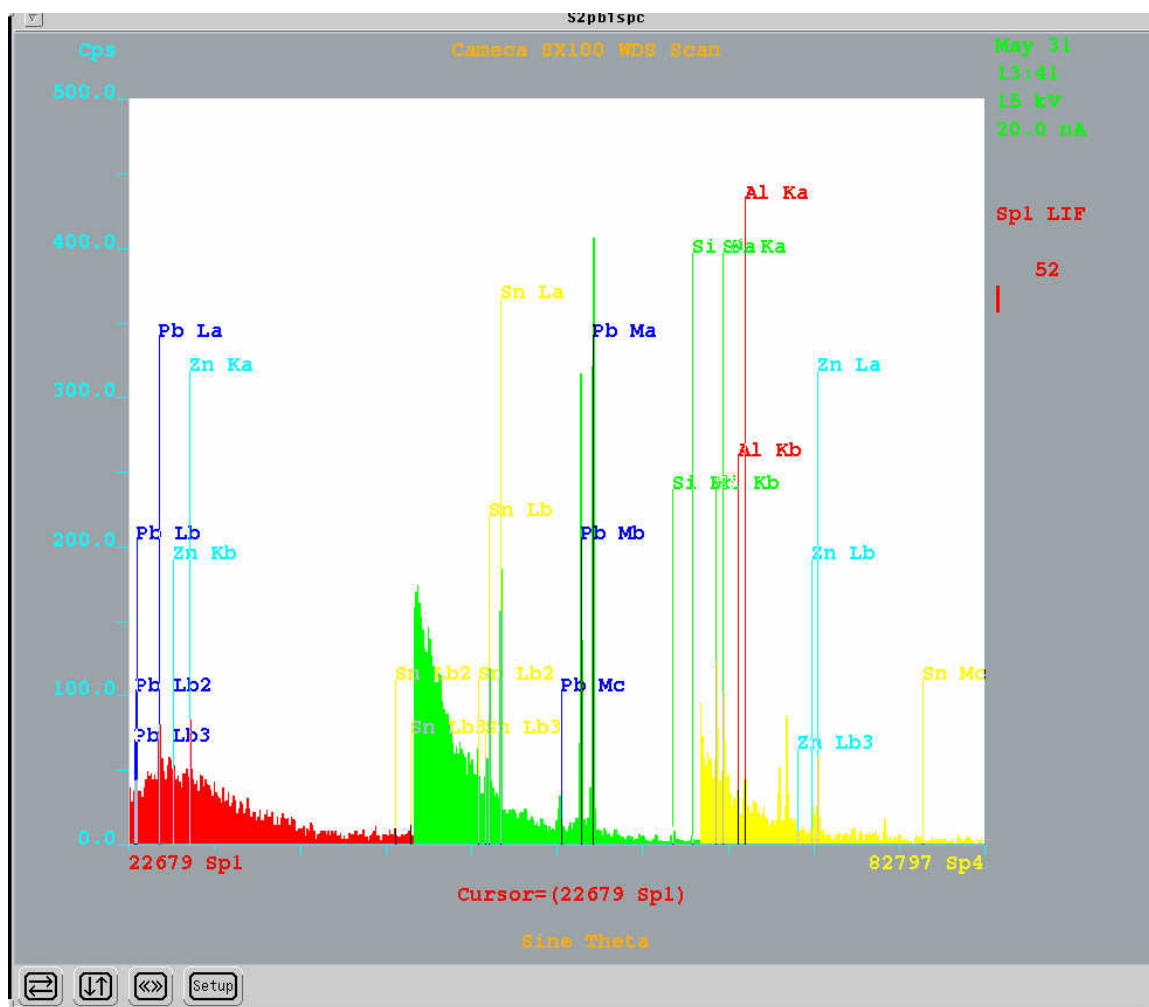
Wavelength Dispersive Spectroscopy (WDS)
X-ray scan pentaerythritol (PET) spectrum
for image from station S-3.



Wavelength Dispersive Spectroscopy (WDS)
X-ray scan thallium acid phthalate (TAP) spectrum
for image from station S-3.



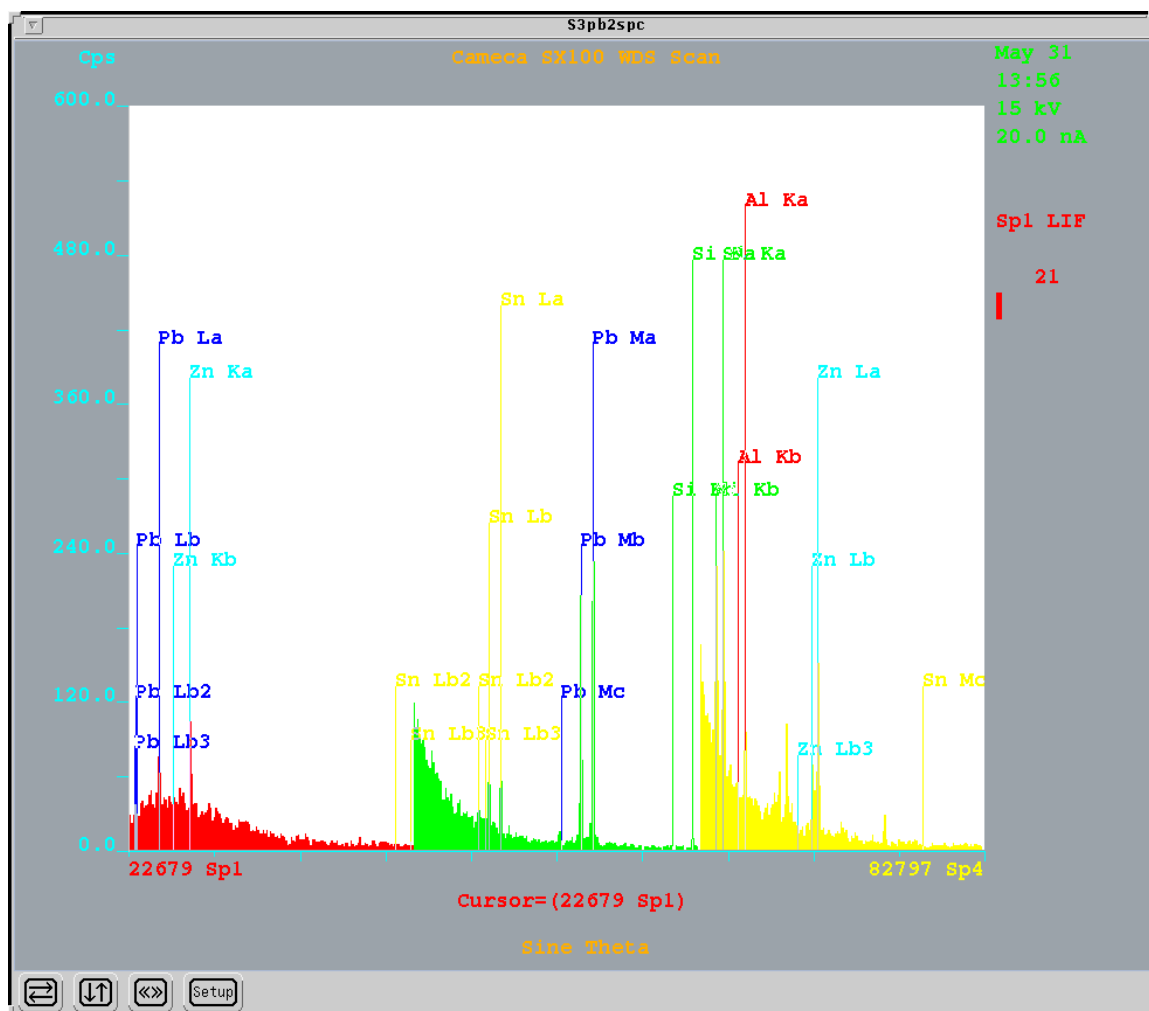
BSE particle grain (naturally accreted) image from station S-2.
According to the WDS spectra generated, the
particle contains lead.



Wavelength Dispersive Spectroscopy (WDS)
X-ray scan lithium fluoride (LIF) spectrum
for image from station S-2.



BSE particle grain (naturally accreted) image from station S-2.
According to the WDS spectra generated, the
particle contains lead.



Curriculum Vita

Roberto Velarde was born on December 24, 1960 in El Paso, Texas and is the oldest son of Irma and Federico Archuleta. He served the United States Air Force with an honorable discharge. He obtained a Bachelor of Science in Civil Engineering and a Bachelor of Architecture from Texas Tech University in 1991. He received a Master's in Environmental Engineering from the University of Texas at El Paso in 2004.

Permanent address: 506 E. University Avenue
El Paso, Texas 79902

This dissertation was typed by Roberto Velarde.